

Feedback Control of Dynamic Bipedal Robot Locomotion

CONTROL AND AUTOMATION

Series Editors

Shuzhi Sam Ge and Frank Lewis

1. Feedback Control of Dynamic Bipedal Robot Locomotion,
*Eric R. Westervelt, Jessy W. Grizzle, Christine Chevallereau,
Jun Ho Choi, and Benjamin Morris*

Feedback Control of Dynamic Bipedal Robot Locomotion

***Eric R. Westervelt
Jessy W. Grizzle
Christine Chevallereau
Jun Ho Choi
Benjamin Morris***



CRC Press
Taylor & Francis Group
Boca Raton London New York

CRC Press is an imprint of the
Taylor & Francis Group, an **informa** business

CRC Press
Taylor & Francis Group
6000 Broken Sound Parkway NW, Suite 300
Boca Raton, FL 33487-2742

© 2007 by Taylor & Francis Group, LLC
CRC Press is an imprint of Taylor & Francis Group, an Informa business

No claim to original U.S. Government works
Printed in the United States of America on acid-free paper
10 9 8 7 6 5 4 3 2 1

International Standard Book Number-10: 1-4200-5372-8 (Hardcover)
International Standard Book Number-13: 978-1-4200-5372-2 (Hardcover)

This book contains information obtained from authentic and highly regarded sources. Reprinted material is quoted with permission, and sources are indicated. A wide variety of references are listed. Reasonable efforts have been made to publish reliable data and information, but the author and the publisher cannot assume responsibility for the validity of all materials or for the consequences of their use.

No part of this book may be reprinted, reproduced, transmitted, or utilized in any form by any electronic, mechanical, or other means, now known or hereafter invented, including photocopying, microfilming, and recording, or in any information storage or retrieval system, without written permission from the publishers.

For permission to photocopy or use material electronically from this work, please access www.copyright.com (<http://www.copyright.com/>) or contact the Copyright Clearance Center, Inc. (CCC) 222 Rosewood Drive, Danvers, MA 01923, 978-750-8400. CCC is a not-for-profit organization that provides licenses and registration for a variety of users. For organizations that have been granted a photocopy license by the CCC, a separate system of payment has been arranged.

Trademark Notice: Product or corporate names may be trademarks or registered trademarks, and are used only for identification and explanation without intent to infringe.

Library of Congress Cataloging-in-Publication Data

Feedback control of dynamic bipedal robot locomotion / Eric R. Westervelt ... [et al.], -- 1st ed.
p. cm. -- (Control and automation ; 1)
Includes bibliographical references and index.
ISBN 978-1-4200-5372-2 (alk. paper)
1. Robotics. 2. Locomotion. I. Westervelt, Eric R. II. Title. III. Series.

TJ211.F43 2007
629.8'932--dc22

2007007727

Visit the Taylor & Francis Web site at
<http://www.taylorandfrancis.com>

and the CRC Press Web site at
<http://www.crcpress.com>

To our loved ones.
A tous ceux que nous aimons.
우리가 사랑하는 이들에게.

Preface

The objective of this book is to present systematic methods for achieving stable, agile and efficient locomotion in bipedal robots. The fundamental principles presented here can be used to improve the control of existing robots and provide guidelines for improving the mechanical design of future robots. The book also contributes to the emerging control theory of hybrid systems. Models of legged machines are fundamentally hybrid in nature, with phases modeled by ordinary differential equations interleaved with discrete transitions and reset maps. Stable walking and running correspond to the design of asymptotically stable periodic orbits in these hybrid systems and not equilibrium points. Past work has emphasized quasi-static stability criteria that are limited to flat-footed walking. This book represents a concerted effort to understand truly dynamic locomotion in planar bipedal robots, from both theoretical and practical points of view.

The emphasis on sound theory becomes evident as early as [Chapter 3](#) on modeling, where the class of robots under consideration is described by lists of hypotheses, and further hypotheses are enumerated to delineate how the robot interacts with the walking surface at impact, and even the characteristics of its gait. This careful style is repeated throughout the remainder of the book, where control algorithm design and analysis are treated. At times, the emphasis on rigor makes the reading challenging for those less mathematically inclined. Do not, however, give up hope! With the exception of [Chapter 4](#) on the method of Poincaré sections for hybrid systems, the book is replete with concrete examples, some very simple, and others quite involved. Moreover, it is possible to cherry-pick one's way through the book in order to "just figure out how to design a controller while avoiding all the proofs." This is mapped out below and in [Appendix A](#).

The practical side of the book stems from the fact that it grew out of a project grounded in hardware. More details on this are given in the acknowledgements, but suffice it to say that every stage of the work presented here has involved the interaction of roboticists and control engineers. This interaction has led to a control theory that is closely tied to the physics of bipedal robot locomotion. The importance and advantage of doing this was first driven home to one of the authors when a multipage computation involving the Frobenius Theorem produced a quantity that one of the other authors identified as angular momentum, and she could reproduce the desired result in two lines! Fortunately, the power of control theory produced its share of eye-opening moments on the robotic side of the house, such as when days and

days of simulations to tune a “physically-based” controller were replaced by a ten minute design of a PI-controller on the basis of a restricted Poincaré map, and the controller worked like a champ. In short, the marriage of mechanics and control is evident throughout the book. The culture of control theory has inspired the hypothesis-definition-theorem-proof-example format of the presentation and many of the mathematical objects used in the analysis, such as zero dynamics and systems with impulse effects, while the culture of mechanics has heavily influenced the vocabulary of the presentation, the understanding of the control problem, the choice of what to control, and ways to render the required computations practical and insightful on complex mechanisms.

Target audience: The book is intended for graduate students, scientists and engineers with a background in either control or robotics—but not necessarily both of these subjects—who seek systematic methods for creating stable walking and running motions in bipedal robots. So that both audiences can be served, an extensive appendix is provided that reviews most of the nonlinear control theory required to read the book, and enough Lagrangian mechanics to be able to derive models of planar bipedal robots comprised of rigid links and joints. Taken together, the control and mechanics overviews provide sufficient tools for representing the robot models in a form that is amenable to analysis. The appendix also contains an intuitive summary of the method of Poincaré sections; this is the primary mathematical tool for studying the existence and stability of periodic solutions of differential equations. The mathematical details of applying the method of Poincaré sections to the hybrid models occurring in bipedal locomotion are sufficiently unfamiliar to both control theorists and roboticists that they are treated in the main part of the book.

Detailed contents: The book is organized into three parts: preliminaries, the modeling and control of robots with point feet, and the control of robots with feet. The preliminaries begin with [Chapter 1](#), which describes particular features of bipedal locomotion that lead to mathematical models possessing both discrete and continuous phenomena, namely, a jump phenomenon that arises when the feet impact the ground, and differential equations (classical Lagrangian mechanics) that describe the evolution of the robot’s motion otherwise. Several challenges that this mix of discrete and continuous phenomena pose for control algorithm design and analysis are highlighted, and how researchers have faced these challenges in the past is reviewed. The chapter concludes with an elementary introduction to a central theme of the book: a method of feedback design that uses virtual constraints to synchronize the movement of the many links comprising a typical bipedal robot. [Chapter 2](#) introduces two bipedal robots that are used as sources of examples of the theory, RABBIT and ERNIE. Both of these machines were specifically designed to study the control of underactuated mechanisms experiencing impacts. A mathematical model of RABBIT is used in many of the simulation examples throughout the book. An extensive set of experiments that have been per-

formed with RABBIT and ERNIE is reported in [Chapter 8](#) and Section 9.9.

Part II begins with [Chapter 3](#) on the modeling of bipedal robots for walking and running motions. For many readers, the differential equation portions of the models, which involve basic Lagrangian mechanics, will be quite familiar, but the presentation of rigid impacts and the interest of angular momentum will be new. The differential equations and impact models are combined to form a special class of hybrid systems called nonlinear systems with impulse effects. The method of Poincaré sections for systems with impulse effects is presented in [Chapter 4](#). Some of the material is standard, but much is new. Of special interest is the treatment of invariant surfaces and the associated restricted Poincaré maps, which are the key to obtaining checkable necessary and sufficient conditions for the existence of exponentially stable walking and running motions. Also of interest is the interpretation of a parameterized family of Poincaré maps as a discrete-time control system upon which event-based or stride-to-stride control decisions can be designed. This leads to an effective means of performing event-based PI control, for example, in order to regulate walking speed in the face of model mismatch and disturbances. [Chapter 5](#) develops the primary design tool of this book, the hybrid zero dynamics of bipedal walking. These dynamics are a low-dimensional controlled-invariant subsystem of the hybrid model that is complex enough to retain the essential features of bipedal walking and simple enough to permit effective analysis and design. Exponentially stable periodic solutions of the hybrid zero dynamics are exponentially stabilizable periodic solutions of the full-dimensional hybrid model of the robot. In other words, they correspond to stable walking motions of the closed-loop system. The hybrid zero dynamics is created by zeroing a set of virtual constraints. How to design the virtual constraints in order to create interesting walking gaits is the subject of [Chapter 6](#). An extensive set of feedback design examples is provided in this chapter. The controllers of Chapter 6 are acting continuously within the stride of a walking motion. [Chapter 7](#) is devoted to control actions that are updated on a stride-to-stride basis. The combined results of Chapters 6 and 7 provide an overall hybrid control strategy that reflects the hybrid nature of a bipedal robot. The practical relevance of the theory is verified in [Chapter 8](#), where RABBIT—a reasonably complex mechanism—is made to walk reliably with just a few days of effort, and not the many months of trial and error that is customary. Part II of the book is concluded with a study of running in [Chapter 9](#). A new element introduced in the chapter is, of course, the flight phase, where the robot has no ground contact; the stance phase of running is similar to the single support phase of walking. Chapter 9 develops natural extensions of the notions of virtual constraints and hybrid zero dynamics to hybrid models with multiple continuous phases. An extensive set of design examples is also provided. An initial experimental study of running is described in Section 9.9; the results are not as resoundingly positive as those of Chapter 8.

The stance foot plays an important role in human walking since it contributes to forward progression, vertical support, and initiation of the lifting

of the swing leg from the ground. Working with a mechanical model, our colleague Art Kuo has shown that plantarflexion of the ankle, which initiates heel rise and toe roll, is the most efficient method to reduce energy loss at the subsequent impact of the swing leg. [Part III](#) of the book is therefore devoted to walking with actuated feet. [Chapter 10](#) addresses a walking motion that allows anthropomorphic foot action. The desired walking motion is assumed to consist of three successive phases: a fully actuated phase where the stance foot is flat on the ground, an underactuated phase where the stance heel lifts from the ground and the stance foot rotates about the toe, and an instantaneous double support phase where leg exchange takes place. It is demonstrated that the feedback design methodology presented for robots with point feet can be extended to obtain a provably asymptotically stabilizing controller that integrates the fully actuated and underactuated phases of walking. By comparison, existing humanoid robots, such as Honda's biped, ASIMO, use only the fully actuated phase (i.e., they only execute flat-footed walking), while RABBIT and ERNIE use only the underactuated phase (i.e., they have no feet, and hence walk as if on stilts). To the best of our knowledge, no other methodology is available for integrating the underactuated and fully actuated phases of walking. Past work that emphasized quasi-static stability criteria and flat-footed walking has primarily been based on the so-called Zero Moment Point (ZMP) or, its extension, the Foot Rotation Indicator (FRI) point. [Chapter 11](#) shows how the methods of the book can be adapted to directly control the FRI point during the flat-footed portion of a walking gait, while maintaining provable stability properties. Importantly, FRI control is done here in such a way that both the fully actuated and underactuated phases of walking are included. For comparison with more standard approaches, a detailed simulation study is performed for flat-footed walking.

Possible paths through the book: This book can be read on many different levels. Most readers will want to peruse [Appendix B](#) in order to fill in gaps on the fundamentals of nonlinear control or Lagrangian mechanics. The serious work can then start with the first three sections of [Chapter 3](#), which develop a hybrid model of bipedal walking. The definition of a periodic solution to the hybrid model of walking, the notion of an exponentially stable periodic orbit and how to test for its existence via a Poincaré map are obtained by reading through Section 4.2.1 of [Chapter 4](#). [Chapters 5](#) and [6](#) then provide a very complete view on designing feedback controllers for walking at a single average speed. If Sections 5.2 and 5.3 seem too technical, then it is advised that the reader skip to Section 6.4, before completing the remainder of Chapter 5. After this, it is really a matter of personal interest whether one continues through the book in a linear fashion or not. A reader whose primary interest is running would complete the above program, read Section 7.3, and finish with [Chapter 9](#), while a reader whose primary interest is walking with feet would proceed to [Chapters 10](#) and [11](#), for example. For a reader whose interests lie primarily in theory, new results for the control of nonlinear

systems with impulse effects are concentrated in [Chapters 4](#) and [5](#), with several interesting twists for systems with multiple phases given in [Chapters 9](#) and [10](#); the other parts of the book could be viewed as a simple confirmation that the theory seems to be worthwhile. The numerous worked-out examples and remarks on interesting special cases make it possible for a practitioner to avoid most of the theoretical considerations when initially working through the book. It is suggested to seek out the two-link walker (a.k.a., the Ac-robot or compass biped) and three-link walker examples in [Chapters 3](#), [5](#), and [6](#), which will provide an introduction to underactuation, hybrid models, the MPFL-normal form, virtual constraints, the swing phase zero dynamics, Bézier polynomials, optimization, and a systematic method to enlarge the basin of attraction of passive gaits. The reader should then be ready to read [Chapter 8](#), with referral to previous chapters as necessary. Further ideas on how to work one's way through the book are given in [Appendix A](#).

Acknowledgements: This book is based on research funded by the National Science Foundation (USA) under grants INT-9980227, ECS-0322395, ECS-0600869, and CMS-0408348 and the CNRS (France). Our work would not have been possible without these foundations' generous support. We are deeply indebted to Gabriel Abba, Yannick Aoustin, Gabriel Buche, Carlos Canudas de Wit, Dalila Djoudi, Alexander Formal'sky, Dan Koditschek, and Franck Plestan with whom we had the great fortune and pleasure of discovering many of the results presented here. Bernard Espiau is offered a special thanks for his active role and constant encouragement in the conception and realization of the bipedal robot RABBIT that inspired our control design and analysis methods. A history of RABBIT's development, along with a listing of the contributors to the project, is given on page 473. Petar Kokotovic and Tamer Basar planted the idea that our research on the control of bipedal robots had matured to the point that organizing it into book form would be a worthwhile endeavor. Dennis Bernstein put RABBIT on the cover of the October 2003 issue of *IEEE Control Systems Magazine*, which was instrumental in bringing our work to the attention of a broader audience in the control field. Laura Bailey believed that control algorithms for bipedal walking and running would appeal to the general public and shared that belief with the *The Economist*, *Wired* magazine, Discovery.com, Reuters and other news outlets, much to our delight and that of our families and friends. As the writing of the book progressed, we benefited from the insightful comments and assistance of Jeff Cook, Kat Farrell, Ioannis Poulakakis, James Schmiedeler, Ching-Long Shih, Aniruddha Sinha, Mark Spong, Theo Van Dam, Giuseppe Viola, Jeff Wensink, and Tao Yang. The team of Frank Lewis, Shuzhi (Sam) Ge, BJ Clark, and Nora Konopka of CRC Press very ably guided us through the publication process.

Book webpage: Supplemental materials are available at the following URL:

www.mecheng.osu.edu/~westerve/biped_book/

The webpage includes links to videos of the experiments reported in the book, MATLAB code for several of the book's robot models, a link to submit errors found in the book, and an erratum.

Eric R. Westervelt, Columbus, Ohio
Jessy W. Grizzle, Ann Arbor, Michigan
Christine Chevallereau, Nantes, France
Jun-Ho Choi, Seoul, Korea
Benjamin Morris, Ann Arbor, Michigan
April 2007

Contents

| | |
|---|-----------|
| I Preliminaries | 1 |
| 1 Introduction | 3 |
| 1.1 Why Study the Control of Bipedal Robots? | 4 |
| 1.2 Biped Basics | 6 |
| 1.2.1 Terminology | 6 |
| 1.2.2 Dynamics | 9 |
| 1.2.3 Challenges Inherent to Controlling Bipedal Locomotion | 11 |
| 1.3 Overview of the Literature | 14 |
| 1.3.1 Polypedal Robot Locomotion | 15 |
| 1.3.2 Bipedal Robot Locomotion | 17 |
| 1.3.3 Control of Bipedal Locomotion | 19 |
| 1.4 Feedback as a Mechanical Design Tool: The Notion of Virtual Constraints | 24 |
| 1.4.1 Time-Invariance, or, Self-Clocking of Periodic Motions | 24 |
| 1.4.2 Virtual Constraints | 25 |
| 2 Two Test Beds for Theory | 29 |
| 2.1 RABBIT | 29 |
| 2.1.1 Objectives of the Mechanism | 29 |
| 2.1.2 Structure of the Mechanism | 30 |
| 2.1.3 Lateral Stabilization | 31 |
| 2.1.4 Choice of Actuation | 33 |
| 2.1.5 Sizing the Mechanism | 33 |
| 2.1.6 Impacts | 35 |
| 2.1.7 Sensors | 35 |
| 2.1.8 Additional Details | 36 |
| 2.2 ERNIE | 37 |
| 2.2.1 Objectives of the Mechanism | 37 |
| 2.2.2 Enabling Continuous Walking with Limited Lab Space | 38 |
| 2.2.3 Sizing the Mechanism | 39 |
| 2.2.4 Impacts | 39 |
| 2.2.5 Sensors | 40 |
| 2.2.6 Additional Details | 40 |

| | |
|---|-----------|
| II Modeling, Analysis, and Control of Robots with Passive Point Feet | 43 |
| 3 Modeling of Planar Bipedal Robots with Point Feet | 45 |
| 3.1 Why Point Feet? | 46 |
| 3.2 Robot, Gait, and Impact Hypotheses | 47 |
| 3.3 Some Remarks on Notation | 52 |
| 3.4 Dynamic Model of Walking | 53 |
| 3.4.1 Swing Phase Model | 53 |
| 3.4.2 Impact Model | 55 |
| 3.4.3 Hybrid Model of Walking | 57 |
| 3.4.4 Some Facts on Angular Momentum | 58 |
| 3.4.5 The MPFL-Normal Form | 60 |
| 3.4.6 Example Walker Models | 63 |
| 3.5 Dynamic Model of Running | 71 |
| 3.5.1 Flight Phase Model | 72 |
| 3.5.2 Stance Phase Model | 73 |
| 3.5.3 Impact Model | 74 |
| 3.5.4 Hybrid Model of Running | 75 |
| 3.5.5 Some Facts on Linear and Angular Momentum | 77 |
| 4 Periodic Orbits and Poincaré Return Maps | 81 |
| 4.1 Autonomous Systems with Impulse Effects | 82 |
| 4.1.1 Hybrid System Hypotheses | 83 |
| 4.1.2 Definition of Solutions | 84 |
| 4.1.3 Periodic Orbits and Stability Notions | 86 |
| 4.2 Poincaré's Method for Systems with Impulse Effects | 87 |
| 4.2.1 Formal Definitions and Basic Theorems | 87 |
| 4.2.2 The Poincaré Return Map as a Partial Function | 90 |
| 4.3 Analyzing More General Hybrid Models | 91 |
| 4.3.1 Hybrid Model with Two Continuous Phases | 92 |
| 4.3.2 Basic Definitions | 92 |
| 4.3.3 Existence and Stability of Periodic Orbits | 94 |
| 4.4 A Low-Dimensional Stability Test Based on Finite-Time Convergence | 96 |
| 4.4.1 Preliminaries | 96 |
| 4.4.2 Invariance Hypotheses | 96 |
| 4.4.3 The Restricted Poincaré Map | 97 |
| 4.4.4 Stability Analysis Based on the Restricted Poincaré Map | 97 |
| 4.5 A Low-Dimensional Stability Test Based on Timescale Separation | 99 |
| 4.5.1 System Hypotheses | 100 |
| 4.5.2 Stability Analysis Based on the Restricted Poincaré Map | 101 |

| | | |
|----------|--|------------|
| 4.6 | Including Event-Based Control | 102 |
| 4.6.1 | Analyzing Event-Based Control with the Full-Order Model | 103 |
| 4.6.2 | Analyzing Event-Based Actions with a Hybrid Restriction Dynamics Based on Finite-Time Attractivity | 107 |
| 5 | Zero Dynamics of Bipedal Locomotion | 111 |
| 5.1 | Introduction to Zero Dynamics and Virtual Constraints | 111 |
| 5.1.1 | A Simple Zero Dynamics Example | 112 |
| 5.1.2 | The Idea of Virtual Constraints | 114 |
| 5.2 | Swing Phase Zero Dynamics | 117 |
| 5.2.1 | Definitions and Preliminary Properties | 117 |
| 5.2.2 | Interpreting the Swing Phase Zero Dynamics | 122 |
| 5.3 | Hybrid Zero Dynamics | 124 |
| 5.4 | Periodic Orbits of the Hybrid Zero Dynamics | 128 |
| 5.4.1 | Poincaré Analysis of the Hybrid Zero Dynamics | 128 |
| 5.4.2 | Relating Modeling Hypotheses to the Properties of the Hybrid Zero Dynamics | 131 |
| 5.5 | Creating Exponentially Stable, Periodic Orbits in the Full Hybrid Model | 132 |
| 5.5.1 | Computed Torque with Finite-Time Feedback Control | 133 |
| 5.5.2 | Computed Torque with Linear Feedback Control | 134 |
| 6 | Systematic Design of Within-Stride Feedback Controllers for Walking | 137 |
| 6.1 | A Special Class of Virtual Constraints | 137 |
| 6.2 | Parameterization of h_d by Bézier Polynomials | 138 |
| 6.3 | Using Optimization of the HZD to Design Exponentially Stable Walking Motions | 144 |
| 6.3.1 | Effects of Output Function Parameters on Gait Properties: An Example | 145 |
| 6.3.2 | The Optimization Problem | 147 |
| 6.3.3 | Cost | 152 |
| 6.3.4 | Constraints | 153 |
| 6.3.5 | The Optimization Problem in Mayer Form | 154 |
| 6.4 | Further Properties of the Decoupling Matrix and the Zero Dynamics | 156 |
| 6.4.1 | Decoupling Matrix Invertibility | 156 |
| 6.4.2 | Computing Terms in the Hybrid Zero Dynamics | 159 |
| 6.4.3 | Interpreting the Hybrid Zero Dynamics | 160 |
| 6.5 | Designing Exponentially Stable Walking Motions on the Basis of a Prespecified Periodic Orbit | 162 |
| 6.5.1 | Virtual Constraint Design | 162 |

| | | |
|----------|--|------------|
| 6.5.2 | Sample-Based Virtual Constraints and Augmentation Functions | 164 |
| 6.6 | Example Controller Designs | 165 |
| 6.6.1 | Designing Exponentially Stable Walking Motions without Invariance of the Impact Map | 165 |
| 6.6.2 | Designs Based on Optimizing the HZD | 173 |
| 6.6.3 | Designs Based on Sampled Virtual Constraints and Augmentation Functions | 178 |
| 7 | Systematic Design of Event-Based Feedback Controllers for Walking | 191 |
| 7.1 | Overview of Key Facts | 192 |
| 7.2 | Transition Control | 195 |
| 7.3 | Event-Based PI-Control of the Average Walking Rate | 199 |
| 7.3.1 | Average Walking Rate | 199 |
| 7.3.2 | Design and Analysis Based on the Hybrid Zero Dynamics | 200 |
| 7.3.3 | Design and Analysis Based on the Full-Dimensional Model | 206 |
| 7.4 | Examples | 208 |
| 7.4.1 | Choice of $\delta\alpha$ | 208 |
| 7.4.2 | Robustness to Disturbances | 210 |
| 7.4.3 | Robustness to Parameter Mismatch | 210 |
| 7.4.4 | Robustness to Structural Mismatch | 210 |
| 8 | Experimental Results for Walking | 213 |
| 8.1 | Implementation Issues | 213 |
| 8.1.1 | RABBIT's Implementation Issues | 213 |
| 8.1.2 | ERNIE's Implementation Issues | 218 |
| 8.2 | Control Algorithm Implementation: Imposing the Virtual Constraints | 220 |
| 8.3 | Experiments | 225 |
| 8.3.1 | Experimental Validation Using RABBIT | 225 |
| 8.3.2 | Experimental Validation Using ERNIE | 241 |
| 9 | Running with Point Feet | 249 |
| 9.1 | Related Work | 250 |
| 9.2 | Qualitative Discussion of the Control Law Design | 251 |
| 9.2.1 | Analytical Tractability through Invariance, Attractivity, and Configuration Determinism at Transitions | 251 |
| 9.2.2 | Desired Geometry of the Closed-Loop System | 252 |
| 9.3 | Control Law Development | 254 |
| 9.3.1 | Stance Phase Control | 255 |
| 9.3.2 | Flight Phase Control | 256 |

| | | |
|------------|---|------------|
| 9.3.3 | Closed-Loop Hybrid Model | 258 |
| 9.4 | Existence and Stability of Periodic Orbits | 258 |
| 9.4.1 | Definition of the Poincaré Return Map | 258 |
| 9.4.2 | Analysis of the Poincaré Return Map | 260 |
| 9.5 | Example: Illustration on RABBIT | 266 |
| 9.5.1 | Stance Phase Controller Design | 267 |
| 9.5.2 | Stability of the Periodic Orbits | 268 |
| 9.5.3 | Flight Phase Controller Design | 268 |
| 9.5.4 | Simulation without Modeling Error | 272 |
| 9.6 | A Partial Robustness Evaluation | 277 |
| 9.6.1 | Compliant Contact Model | 278 |
| 9.6.2 | Simulation with Modeling Error | 279 |
| 9.7 | Additional Event-Based Control for Running | 282 |
| 9.7.1 | Deciding What to Control | 283 |
| 9.7.2 | Implementing Stride-to-Stride Updates of Landing Configuration | 283 |
| 9.7.3 | Simulation Results | 284 |
| 9.8 | Alternative Control Law Design | 287 |
| 9.8.1 | Controller Design | 288 |
| 9.8.2 | Design of Running Motions with Optimization | 292 |
| 9.9 | Experiment | 296 |
| 9.9.1 | Hardware Modifications to RABBIT | 296 |
| 9.9.2 | Result: Six Running Steps | 296 |
| 9.9.3 | Discussion | 298 |
| III | Walking with Feet | 299 |
| 10 | Walking with Feet and Actuated Ankles | 301 |
| 10.1 | Related Work | 302 |
| 10.2 | Robot Model | 302 |
| 10.2.1 | Robot and Gait Hypotheses | 303 |
| 10.2.2 | Coordinates | 305 |
| 10.2.3 | Underactuated Phase | 305 |
| 10.2.4 | Fully Actuated phase | 306 |
| 10.2.5 | Double-Support Phase | 307 |
| 10.2.6 | Foot Rotation, or Transition from Full Actuation to Underactuation | 308 |
| 10.2.7 | Overall Hybrid Model | 309 |
| 10.2.8 | Comments on the FRI Point and Angular Momentum | 309 |
| 10.3 | Creating the Hybrid Zero Dynamics | 315 |
| 10.3.1 | Control Design for the Underactuated Phase | 315 |
| 10.3.2 | Control Design for the Fully Actuated Phase | 317 |
| 10.3.3 | Transition Map from the Fully Actuated Phase to the Underactuated Phase | 318 |

| | | |
|-----------|---|------------|
| 10.3.4 | Transition Map from the Underactuated Phase to the Fully Actuated Phase | 319 |
| 10.3.5 | Hybrid Zero Dynamics | 320 |
| 10.4 | Ankle Control and Stability Analysis | 321 |
| 10.4.1 | Analysis on the Hybrid Zero Dynamics for the Underactuated Phase | 321 |
| 10.4.2 | Analysis on the Hybrid Zero Dynamics for the Fully Actuated Phase with Ankle Torque Used to Change Walking Speed | 322 |
| 10.4.3 | Analysis on the Hybrid Zero Dynamics for the Fully Actuated Phase with Ankle Torque Used to Affect Convergence Rate | 323 |
| 10.4.4 | Stability of the Robot in the Full-Dimensional Model . | 326 |
| 10.5 | Designing the Virtual Constraints | 326 |
| 10.5.1 | Parametrization Using Bézier polynomials | 326 |
| 10.5.2 | Achieving Impact Invariance of the Zero Dynamics Manifolds | 328 |
| 10.5.3 | Specifying the Remaining Free Parameters | 330 |
| 10.6 | Simulation | 331 |
| 10.7 | Special Case of a Gait without Foot Rotation | 332 |
| 10.8 | ZMP and Stability of an Orbit | 334 |
| 11 | Directly Controlling the Foot Rotation Indicator Point | 341 |
| 11.1 | Introduction | 341 |
| 11.2 | Using Ankle Torque to Control FRI Position During the Fully Actuated Phase | 342 |
| 11.2.1 | Ability to Track a Desired Profile of the FRI Point . | 343 |
| 11.2.2 | Analyzing the Zero Dynamics | 344 |
| 11.3 | Special Case of a Gait without Foot Rotation | 347 |
| 11.4 | Simulations | 348 |
| 11.4.1 | Nominal Controller | 348 |
| 11.4.2 | With Modeling Errors | 350 |
| 11.4.3 | Effect of FRI Evolution on the Walking Gait | 351 |
| 11.5 | A Variation on FRI Position Control | 355 |
| 11.6 | Simulations | 357 |
| A | Getting Started | 363 |
| A.1 | Graduate Student | 363 |
| A.2 | Professional Researcher | 368 |
| A.2.1 | Reader Already Has a Stabilizing Controller | 368 |
| A.2.2 | Controller Design Must Start from Scratch | 372 |
| A.2.3 | Walking with Feet | 372 |
| A.2.4 | 3D Robot | 373 |

| | |
|--|------------|
| B Essential Technical Background | 375 |
| B.1 Smooth Surfaces and Associated Notions | 376 |
| B.1.1 Manifolds and Embedded Submanifolds | 376 |
| B.1.2 Local Coordinates and Smooth Functions | 378 |
| B.1.3 Tangent Spaces and Vector Fields | 380 |
| B.1.4 Invariant Submanifolds and Restriction Dynamics . . | 383 |
| B.1.5 Lie Derivatives, Lie Brackets, and Involutive Distributions | 385 |
| B.2 Elementary Notions in Geometric Nonlinear Control | 387 |
| B.2.1 SISO Nonlinear Affine Control System | 388 |
| B.2.2 MIMO Nonlinear Affine Control System | 394 |
| B.3 Poincaré's Method of Determining Limit Cycles | 399 |
| B.3.1 Poincaré Return Map | 400 |
| B.3.2 Fixed Points and Periodic Orbits | 401 |
| B.3.3 Utility of the Poincaré Return Map | 403 |
| B.4 Planar Lagrangian Dynamics | 406 |
| B.4.1 Kinematic Chains | 406 |
| B.4.2 Kinetic and Potential Energy of a Single Link | 408 |
| B.4.3 Free Open Kinematic Chains | 412 |
| B.4.4 Pinned Open Kinematic Chains | 416 |
| B.4.5 The Lagrangian and Lagrange's Equations | 419 |
| B.4.6 Generalized Forces and Torques | 420 |
| B.4.7 Angular Momentum | 420 |
| B.4.8 Further Remarks on Lagrange's Method | 421 |
| B.4.9 Sign Convention on Measuring Angles | 428 |
| B.4.10 Other Useful Facts | 431 |
| B.4.11 Example: The Acrobot | 436 |
| C Proofs and Technical Details | 439 |
| C.1 Proofs Associated with Chapter 4 | 439 |
| C.1.1 Continuity of T_I | 439 |
| C.1.2 Distance of a Trajectory to a Periodic Orbit | 439 |
| C.1.3 Proof of Theorem 4.1 | 440 |
| C.1.4 Proof of Proposition 4.1 | 441 |
| C.1.5 Proofs of Theorem 4.4 and Theorem 4.5 | 442 |
| C.1.6 Proof of Theorem 4.6 | 442 |
| C.1.7 Proof of Theorem 4.8 | 446 |
| C.1.8 Proof of Theorem 4.9 | 448 |
| C.2 Proofs Associated with Chapter 5 | 449 |
| C.2.1 Proof of Theorem 5.4 | 449 |
| C.2.2 Proof of Theorem 5.5 | 450 |
| C.3 Proofs Associated with Chapter 6 | 451 |
| C.3.1 Proof of Proposition 6.1 | 451 |
| C.3.2 Proof of Theorem 6.2 | 451 |
| C.4 Proof Associated with Chapter 7 | 452 |

| | | |
|---------------------|---|------------|
| C.4.1 | Proof of Theorem 7.3 | 452 |
| C.5 | Proofs Associated with Chapter 9 | 454 |
| C.5.1 | Proof of Theorem 9.2 | 454 |
| C.5.2 | Proof of Theorem 9.3 | 455 |
| C.5.3 | Proof of Theorem 9.4 | 455 |
| D | Derivation of the Equations of Motion for Three-Dimensional Mechanisms | 457 |
| D.1 | The Lagrangian | 457 |
| D.2 | The Kinetic Energy | 458 |
| D.3 | The Potential Energy | 462 |
| D.4 | Equations of Motion | 462 |
| D.5 | Invariance Properties of the Kinetic Energy | 464 |
| E | Single Support Equations of Motion of RABBIT | 465 |
| Nomenclature | | 471 |
| End Notes | | 473 |
| References | | 479 |

Part I

Preliminaries

1

Introduction

Locomotion, the ability of a body to move from one place to another, is a defining characteristic of animal life. It is accomplished by manipulating the body with respect to the environment. In the natural setting, locomotion takes on many forms, whether it's the swimming of amoebas, flying of birds, or walking of humans. The diversity of animal locomotion is truly astounding and surprisingly complex. The same is true in objects crafted by man: airplanes have wings that create lift for flight, tanks have tracks for traversing uneven terrain, automobiles have wheels for rolling efficiently—and robots are now walking on their own two legs!

In the case of environments with discontinuous ground support, such as a rocky slope, a flight of stairs, or the rungs of a ladder, it is arguable that the most appropriate and versatile means for locomotion is legs. Legs enable the avoidance of support discontinuities in the environment by stepping over them. Moreover, legs are an obvious choice for locomotion in environments designed for human walking, running, and climbing.

To the extent that a machine equipped with two legs may imitate a human's gait, bipedal robots are biomimetic. In this book, the appeal to biomimetics largely stops here. This is because the material and components available to an engineer for creating a bipedal robot are quite different from those provided by biology. For example, the engineer has at his disposal metal instead of bones, motors instead of muscles, wires instead of nerves, and microprocessors instead of a brain. In addition, there are differences in what quantities can be sensed and the speed and accuracy with which they can be sensed. Just as important, the operational expectations are different. Whereas we are accustomed to many years of training required for a human to acquire a high degree of skill in locomotion related activities (consider a baby learning to walk), and we expect ability to vary greatly from one human to another (consider the sprinter Michael Johnson versus the average runner), we expect that the functioning of machines be exactly reproducible and correct from the moment they are turned on. We would be greatly disappointed in a car, for example, if the automatic transmission's control system took many trials "to learn" how to smoothly shift gears or to maximize the vehicle's intended performance, whether that be speed of acceleration or fuel economy. Similarly, we are disappointed in a legged robot whose control system cannot deliver gaits that utilize the full capabilities of the machine, in terms of elegance, speed, energy economy, and of course, stability.

The theme of this book is the systematic design of feedback control systems for achieving walking and running gaits in bipedal robots. The primary emphasis is on the presentation of a coherent theory for control design, stability analysis, and performance enhancement. The current state of the theory has a number of limitations, the most important being that it applies to planar robots, with rigid links, and at most one degree of underactuation in single support.¹ On the other hand, the principal aspects of the theory have been evaluated on hardware, and they work! Experiments conducted on a bipedal test bed named RABBIT yielded stable walking over a wide range of speeds and with significant robustness to model error and external perturbations; moreover, uncommonly short implementation and debugging times were needed to achieve an elegant stable gait. While this book emphasizes the theoretical aspects of the subject, the reader more concerned with the practice of control system design for bipedal robots will find that the algorithms are presented in a very detailed fashion that aids implementation. In addition, the experimental work provides some guidelines on hardware issues and just how closely an actual bipedal mechanism has to adhere to the theory.

This book is based on theoretical and experimental investigations of the authors and colleagues that have been presented in numerous individual publications, and with varying notation. In addition to gathering all of the peer-reviewed material into one place and applying consistent notation, we have provided considerable additional background material, collected in an appendix, with the objective of making the book largely self-contained.

1.1 Why Study the Control of Bipedal Robots?

Bipedal robots form a subclass of legged robots. On the practical side, the study of mechanical legged locomotion has been motivated by its potential use as a means of locomotion in rough terrain, or environments with discontinuous supports, such as the rungs of a ladder. It must also be acknowledged that much of the current interest in legged robots stems from the appeal of machines that operate in anthropomorphic or animal-like ways (we have in mind several well-known biped and quadruped toys). The motivation for studying bipedal robots in particular arises from diverse sociological and commercial interests, ranging from the desire to replace humans in hazardous occupations (de-mining, nuclear power plant inspection, military interventions, etc.), to the restoration of motion in the disabled (dynamically controlled lower-limb prostheses, rehabilitation robotics, and functional neural stimulation).

¹These limitations are not fundamental to the approach followed in the book and are being actively addressed.

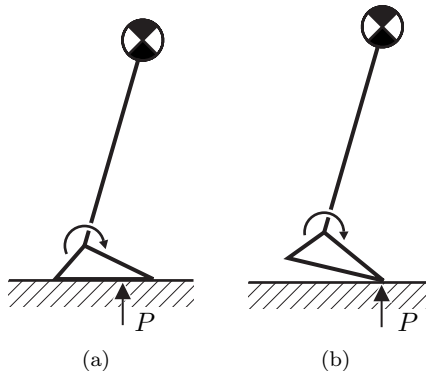


Figure 1.1. The ZMP (Zero Moment Point) criterion in a nutshell. Idealize a robot with one leg in contact with the ground as a planar inverted pendulum that is attached to a base consisting of a foot with torque applied at the ankle, and assume all other joints are independently actuated. In addition, assume adequate friction so that the foot is not sliding. In (a), the robot’s nominal trajectory has been planned so that the center of pressure of the forces on the foot, P , remains strictly within the interior of the footprint. In this case, the foot will not rotate (i.e., the foot is acting as a base, as in a normal robotic manipulator) and the system is therefore fully actuated. It follows that small deviations from the planned trajectory can be attenuated via feedback control, proving stabilizability of the walking motion. In case (b), however, the center of pressure (CoP) has moved to the toe, allowing the foot to rotate. The system is now underactuated (two degrees of freedom and one actuator), and designing a stabilizing controller is nontrivial, especially when impact events are taken into account. The ZMP principle says to design trajectories so that case (a) holds; i.e., walk flat footed. Humans, even with prosthetic legs, use foot rotation to decrease energy loss at impact [72, 144].

An impressive amount of technology has been amassed and specifically developed to build walking robot prototypes. A quick search of the literature, see for example [18], reveals over a hundred walking mechanisms built by public research laboratories, universities, and major companies. Nevertheless, conceptual control breakthroughs have not kept pace with the technological developments. A canonical problem in bipedal robots is how to design a controller that generates closed-loop motions, such as walking or running, that are periodic and stable (i.e., stable limit cycles). There is a huge deficit in fundamental control design concepts in comparison to the number of bipedal prototypes. The state-of-the-art is characterized by a heavy reliance on heuristics or on principles such as the zero moment point (ZMP) criterion [114, 233, 235] that don’t ensure stability; see Fig. 1.1 and [Section 10.8](#). As a result, only slow motions may be achieved. Truly dynamic motions, such as balancing, running or fast walking, are excluded with these approaches [92].

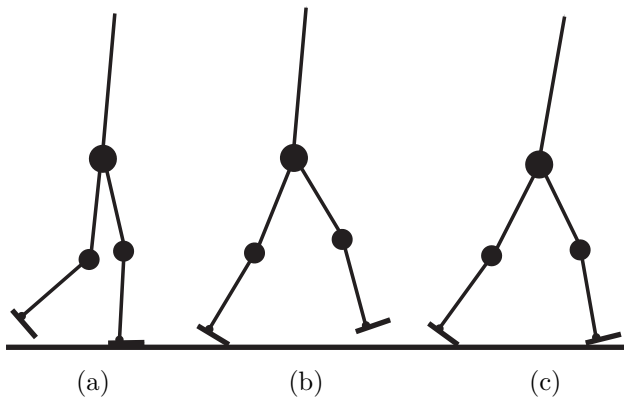


Figure 1.2. Various phases of bipedal walking with nonpoint feet. The single support phase (also called the swing phase) is shown in (a) and (b), while a double support phase is depicted in (c). If all of the joints of the robot are actuated and the feet are not slipping, then comparing the number of degrees of freedom to the number of independent actuators reveals that the robot is fully actuated in (a), underactuated in (b), and overactuated in (c).

1.2 Biped Basics

Before going further, some basic terminology is introduced; more formal definitions of many of these terms will be made later in the text. The terminology will allow an informal description of the essential elements of a dynamic model of a bipedal robot to be given which, in turn, will allow some challenging aspects of the control problem to be raised.

1.2.1 Terminology

A biped is an open kinematic chain consisting of two subchains called *legs* and, often, a subchain called the *torso*, all connected at a common point called the *hip*. One or both of the legs may be in contact with the ground. When only one leg is in contact with the ground, the contacting leg is called the *stance leg* and the other is called the *swing leg*. The end of a leg, whether it has links constituting a foot or not, will sometimes be referred to as a *foot*. The *single support* or *swing phase* is defined to be the phase of locomotion where only one foot is on the ground. Conversely, *double support* is the phase where both feet are on the ground; see Figs. 1.2 and 1.3. *Walking* is then defined as alternating phases of single and double support, with the requirement that the displacement of the horizontal component of the robot's center of mass

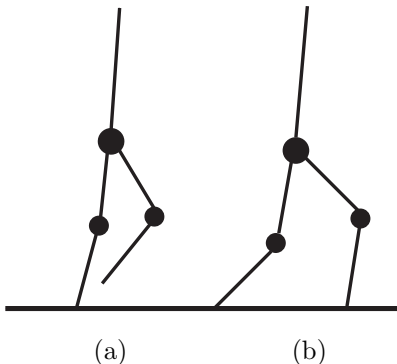


Figure 1.3. Phases of bipedal walking with point feet. In (a), the single support or swing phase, and in (b), the double support phase. If all of the joints of the robot are actuated and the feet are not slipping, then the robot is underactuated in (a) and overactuated in (b).

(COM) is strictly monotonic.² Implicit in this description is the assumption that the feet are not slipping when in contact with the ground. *Running* is defined as sequential phases of single support, flight, and (single-legged) impact, with the additional provision that impacts occur on alternating legs.

The *sagittal plane* is the longitudinal plane that divides the body into right and left sections. The *frontal plane* is the plane parallel to the long axis of the body and perpendicular to the sagittal plane that separates the body into front and back portions. The *transverse plane* is perpendicular to both the sagittal and frontal planes. See Fig. 1.4 for an illustration of these planes of section. A *planar biped* is a biped with motions taking place only in the sagittal plane, whereas a three-dimensional walker has motions taking place in both the sagittal and frontal planes.

A *statically stable gait* is periodic locomotion in which the biped's COM does not leave the *support polygon*, that is, the convex hull formed by all of the contact points with the ground.³ A *quasi-statically stable gait* is one where the center of pressure⁴ (CoP) of the biped's stance foot remains strictly within the interior of the support polygon, and hence does not lie on the boundary. Loosely speaking, a *dynamically stable gait* is then a periodic gait where the biped's CoP is on the boundary of the support polygon for at least part of the cycle and yet the biped does not overturn.

²In dancing, the horizontal component of the COM often rocks forward and backward.

³In particular, for a biped during the swing phase, the support polygon is the convex hull of the set of points where the stance foot is in contact with the ground.

⁴Forces distributed along the base of the stance foot can be equivalently represented by a single force acting at the center of pressure (CoP). To be more precise, the CoP is defined as the point on the ground where the resultant of the ground-reaction force acts [92]. In the legged robotics literature, the CoP is often referred to as the ZMP [235].

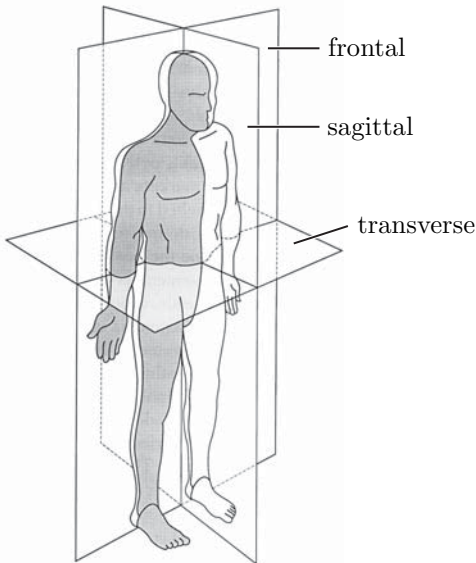


Figure 1.4. The human planes of section. The sagittal plane is the longitudinal plane that divides the body into right and left sections. The frontal plane is the plane parallel to the long axis of the body and perpendicular to the sagittal plane that separates the body into front and back portions. A transverse plane is a plane perpendicular to sagittal and frontal plane. (Image reproduced from [222] with permission.)

1.2.2 Dynamics

The multiple support phases present in a bipedal walking cycle naturally lead to a mathematical model that consists of at least two parts: a set of differential equations describing the dynamics during the single support phase, and a discrete model of the contact event when double support is initiated. For simplicity, during single support, assume either that the biped has point feet as in Fig. 1.3(a) or that the biped has feet and the stance foot remains flat on the ground (i.e., does not rotate), as in Fig. 1.2(a). Assume furthermore that the stance leg end acts as an ideal pivot (the associated *unilateral constraints* required for the validity of this modeling assumption—vertical support force in the positive direction, tangential force no greater than that allowed by the coefficient of friction—will be discussed later). Under these assumptions, the standard robot equations apply, resulting in

$$D(q)\ddot{q} + C(q, \dot{q})\dot{q} + G(q) = Bu, \quad (1.1)$$

where q is a set of generalized coordinates and u denotes the vector of actuator torques [164, 218]. The model is easily converted to state space form by defining $x := (q; \dot{q})$.

A mechanical model is said to be *fully actuated* when the number of independent actuators equals the number of degrees of freedom. If there are fewer actuators than degrees of freedom then it is *underactuated*, and if there are more actuators than degrees of freedom, it is *overactuated*. For a model of a robot in single support to be fully actuated, the robot must have feet, the stance foot must be stationary (i.e., flat on the ground and neither rotating nor slipping), and all of the joints of the robot must be actuated (including the ankles, of course); otherwise, the model is underactuated. In particular, a model of a fully actuated robot (i.e., a robot with feet and all joints actuated) is underactuated when the heel rises and the foot rotates about the toe, as in Fig. 1.2(b). Whenever non-flat-footed walking takes place, underactuation is present.

An impact occurs when the swing leg touches the walking surface. The resulting forces that are generated between the robot and the walking surface depend on whether the surface is springy, like a trampoline, viscous, like a muddy edge of a pond, or essentially rigid, like a solid floor. The first two cases have not been studied in the legged-robot community. In the case of a rigid walking surface, the duration of the impact event is very short [24, 78, 149, 194] and it is common to approximate it as being instantaneous [74, 124, 208]. Under this assumption, the ground reaction forces are replaced with impulses, resulting in a discontinuity in the velocity components of the robot's state. The ultimate result of the impact model is a new initial condition from which the single support model evolves until the next impact, written as

$$x^+ = \Delta(x^-), \quad (1.2)$$

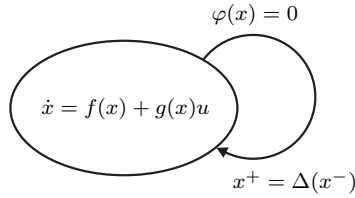


Figure 1.5. Single-mode hybrid model of walking that corresponds either to walking with point feet or to flat-footed walking. Key elements are the continuous dynamics of the single support phase, written in state space form as $\dot{x} = f(x) + g(x)u$, the switching or impact condition, $\varphi = 0$, which detects when the height of the swing leg above the walking surface is zero, and the reinitialization rule coming from the impact map, Δ .

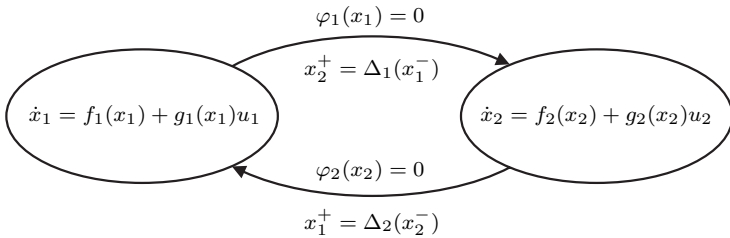


Figure 1.6. Double-mode hybrid model of walking that corresponds to a robot with nontrivial feet that is executing a walking cycle consisting of a flat-footed phase, heel-rise and toe-roll, followed by double support on a flat foot. In this case, there are two dynamic models and two switching conditions. The dynamic model corresponding to toe-roll has one more degree of freedom than the model corresponding to the flat-footed phase and is necessarily underactuated.

where $x^+ := (q^+; \dot{q}^+)$ (resp. $x^- := (q^-; \dot{q}^-)$) is the state value just after (resp. just before) impact. A representation of the resulting model as a simple hybrid system is shown in Fig. 1.5. Models with multiple continuous phases are common; see Fig. 1.6.

A walking motion is then a periodic orbit in a hybrid model, such as Fig. 1.5 or Fig. 1.6. The Poincaré return map⁵ is the appropriate mathematical tool [14, 98, 102, 167, 173] for analyzing the stability of periodic orbits, but its use in the analysis of bipedal robots is more the exception rather than the rule.

⁵See Appendix B.3 for an informal treatment and Chapter 4 for a careful development of this mathematical tool.

1.2.3 Challenges Inherent to Controlling Bipedal Locomotion

Comparing the relatively slow development of algorithms that control bipedal robots with the rapid development of sophisticated prototypes makes one wonder why this discrepancy exists when control is an integral aspect of a functioning biped. We hypothesize that this is due to six reasons that are *inherent* to biped locomotion. The first three difficulties are common to static and dynamic bipedal walking while the final three pertain only to dynamic bipedal locomotion.

1.2.3.1 Common Difficulties

Limb coordination: The first difficulty is *limb coordination*. Bipeds are typically high degree of freedom (DOF) mechanisms but the task of biped walking is inherently a low DOF task—transportation of the robot’s COM from one point to another. Consequently, the task of walking does not uniquely specify how the limbs must be coordinated in order to achieve the desired horizontal displacement of the robot’s center of mass. Typically, when a problem admits many solutions, finding even one can be difficult, and then finding what may be considered a “good” solution may be very difficult.

Hybrid dynamics: The second difficulty is *hybrid dynamics*. The presence of impacts and the varying nature of the contact conditions of the leg ends with the environment throughout a walking cycle—due to foot touchdown, liftoff, and possibly heel strike and heel roll—necessarily lead to models that have multiple phases, and hence are hybrid. A control theory for hybrid systems is just now being developed, and much of the current literature is devoted to equilibrium points instead of limit cycles.

Effective underactuation: The third difficulty is *effective underactuation* during the phase of single support. Unlike traditional robotic manipulators, which are securely fastened to the environment, bipeds are designed to move with respect to the environment. Because of finite foot size, a large torque supplied at the ankle joint may result in foot rollover, in which case the robot is underactuated. Such torque bounds complicate control design, as has been recognized in [83, 92, 119, 133].

Remark 1.1 The latter two complications are both manifestations of the *unilateral constraints* that must be included in order to fully describe the dynamics of a bipedal robot. The ends of the robot’s legs, whether they are terminated with feet or points, are not attached to the walking surface. Consequently, normal forces at the contact points can only act in one direction, and hence are unilateral. Other examples include the following: in order for

the foot not to slip, the ground reaction forces must lie in the *friction cone*,⁶ which can be expressed with multiple unilateral constraints; and if the foot is to remain flat on the ground and not rotate about its extremities, such as the heel or the toe, then there must be a point between the heel and toe where the net moment on the foot is zero (the so-called Zero Moment Point or ZMP), and this condition can be expressed as a pair of unilateral constraints as well. Still other constraints should be specified to guarantee that no other points on the robot—other than its feet—are in contact with the walking surface, though no models known to the authors ever include this. Instead, one typically satisfies the constraints indirectly by specifying that the hips are at least a certain height above the walking surface and the torso is more or less upright.

1.2.3.2 Challenges Associated with Dynamic Locomotion

Several further difficulties arise when one attempts to move beyond the quasi-static locomotion that is obtained with the ZMP criterion.

Static instability: The first difficulty is *static instability* of the biped during portions of the walking cycle. That is, in dynamic walking, the projection of the location of the biped’s COM onto the walking surface is outside the biped’s support polygon—and usually the location of the biped’s CoP is on the boundary of the support polygon—during portions of the walking cycle. This prohibits the use of the popular ZMP criterion to devise walking motions.

Design of limit cycles: The second difficulty is the *design of limit cycles*. Dynamically stable walking corresponds to the existence of limit cycles in the biped’s state space. The design of controllers that induce limit cycles, while a challenge in its own right, is made significantly more difficult by the first four difficulties and by the need for energy efficiency, which will be discussed in the literature review.

Conservation of Angular momentum: The final difficulty is the *conservation of angular momentum* about the robot’s COM during the flight phase of running. One consequence of angular momentum conservation is the impossibility of independently regulating the robot’s shape and absolute orientation during flight phases, which complicates the control of the robot’s configuration at touchdown.

⁶For a given coefficient of static friction, μ_s , the force in the tangent direction, F^T , must satisfy $|F^T| \leq \mu_s |F^N|$, where F^N is the force in the normal direction. This relation specifies a cone in the $(F^T; F^N)$ -plane.

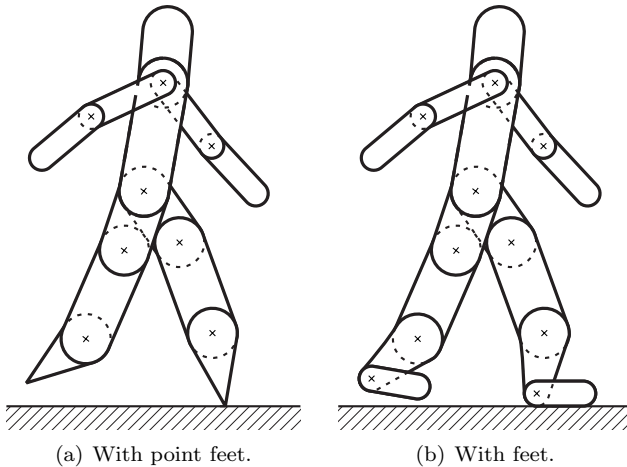


Figure 1.7. Illustrative high DOF planar robot models.

1.2.3.3 Confronting these Challenges

This book studies a class of bipedal robots that are only as complex as required to capture these inherent challenges. Specifically, the book addresses planar bipeds consisting of an N -rigid-link open kinematic chain (see Fig. 1.7); furthermore, the links are connected through ideal revolute joints and are independently actuated. Both the cases of bipeds with point feet (N -DOF during the stance phase and one degree of underactuation) and bipeds with feet and an actuated ankle (fully actuated in single support) are considered.

Restricting attention to the sagittal plane is reasonable since the sagittal plane dynamics are almost decoupled from those in the frontal plane in the sense that stability in the frontal plane can be achieved with only frontal plane control actions, such as step width control [16, 83, 143]. Therefore, it seems reasonable to expect that a control algorithm designed to stabilize walking in the sagittal plane may be coupled with an algorithm designed to stabilize motions in the frontal plane in order to achieve stable three-dimensional walking, as in [143]. Work along this line has been reported in [70, 80] for an underactuated robot and in [6] for a fully actuated robot. Of course, it is not necessary to first address sagittal plane control before attacking the 3D problem; see [212].

Except for [Chapters 10](#) and [11](#), the robots studied in this book are assumed to have point feet with no actuation between the stance leg end and the ground, and actuation at all internal joints. With these assumptions, static, or quasi-static walking is nearly impossible,⁷ thus requiring any walking to

⁷The only class of gaits where static walking would be possible is one where the biped's COM is over the stance leg end for the entire phase of single support and the double support

be dynamic. The model for the swing phase of walking is therefore that of an underactuated mechanical system. Developing controllers to regulate walking in a robot without feet is interesting for at least two reasons. First of all, point feet focus attention on the dynamic aspects of walking, where quasi-static criteria completely breakdown. This has led to the development of new control ideas. Secondly, as shown later in the book, a control theory for point feet serves as a sound foundation for designing controllers for fully actuated robots, that is, robots with feet of nontrivial length and an actuated ankle. With quasi-static criteria, only flat-footed walking has been achieved with such robots, that is, the robot's foot must remain flat on the ground during the entire stance phase, yielding gaits that are visibly awkward or "robotic" looking. Furthermore, based on work in [72, 144], these gaits are likely energetically inefficient. Using the theory developed for walking with point feet, it is possible to design controllers that allow an anthropomorphic walking gait, consisting of a fully actuated phase where the stance foot is flat on the ground, an underactuated phase where the stance heel lifts from the ground and the stance foot rotates about the toe, followed by a double support phase where leg exchange takes place.

1.3 Overview of the Literature

Legged locomotion was investigated by Aristotle as early as 350 B.C. in his work *Progression of Animals* [9] where he asked such questions as, "why are man and bird bipeds, but fish footless?" Actual legged machines can be found as early as the late nineteenth century with Rygg's mechanical horse [197] that used a gear and lever system to generate a fixed gait actuated by a bicycle-like crank system. Since Aristotle and Rygg, research on legged locomotion has grown into a multidisciplinary field spanning physiology, dynamics, computer science, automatic control, and robotics. Despite such great interest, there are almost no legged machines in use today, and those in use are for entertainment purposes only. Some of the industries, other than entertainment, that would benefit from legged machines are prosthetics, orthotics, defense, mining, agriculture, forestry, nuclear facilities inspection, and planetary exploration.

The lack of legged machines being employed to perform real work is certainly not due to a lack of prototype development. In the past 40 years there have been hundreds of prototypes constructed, from lumbering polypeds to hopping monopods, each attempting to improve some aspect of system design, whether that be energy efficiency, autonomy, stability, speed of locomotion, durability, weight reduction, modularity, etc. To give a sense of the

phase is assumed to be of finite duration, i.e., non-instantaneous.

development effort, a few of the pioneering nonbipedal examples will now be highlighted, followed by a discussion of bipedal prototypes.

1.3.1 Polypodal Robot Locomotion

One of the earliest legged machine success stories is the quadrupedal General Electric Walking Truck constructed by Mosher [146] in the late 1960s. Weighing in at 1400 kg, it required an external power source to drive its hydraulic actuation. It carried a single operator who was responsible for controlling each of the twelve servo loops that controlled the legs. It was capable of a top speed of 2.2 m/s and could carry a 220 kg payload. In the early 1980s Odetics, Inc. constructed a series of electro-mechanically powered, autonomous, i.e., untethered, hexapeds serially named the Odex-1, Odex-2, and Odex-3 Functionoids. The Odex-1 weighed 160 kg and had a top speed of about 0.5 m/s [37, 196]. Constructed in the mid 1980s and weighing in at 2700 kg, one of the largest legged machines is Ohio State’s hexapedal, hydraulically actuated Adaptive Suspension Vehicle (ASV) [213]. It operated autonomously with a top speed of 3.6 m/s and could carry a 220 kg payload. In contrast to Mosher’s Walking Truck, the ASV utilized digital feedback control to ease the burden on the operator.

Among the most inspiring of the early efforts is Raibert’s monopod hopper, a one-legged, prismatic-kneed robot that he proposed in the early 1980s as a conceptualization of running [183, 185]. This machine was the first powered legged robot to exhibit dynamic balance. Weighing in at 8.6 kg (neglecting the weight of the boom used to constrain the hopper’s motions to a plane and the weight of the external power source and computation), Raibert’s hopper was capable of a top speed of 1.2 m/s. Even more important than the hopper itself are the control laws which inspired it. Raibert showed that for a class of legged machines, fast, elegant, dynamically stable locomotion could be achieved with simple control actions decomposed into three mutually independent parts—hopping height, foot touchdown angle, and body posture. The remarkable success of Raibert’s control law motivated others to analytically characterize its stability [76, 139], and to further investigate the role of passive elements in achieving efficient running with a hopper [4]. By augmenting his control scheme with leg-switching logic, Raibert successfully demonstrated a three-dimensional version of his monopod hopper, as well as polypodal versions with two and four legs.

In addition to these pioneering machines, there have been a host of other prototypes developed. For more complete treatments of legged machine history see [18, 142, 185, 190, 229, 235].

Despite all of these developments, legged machines have not yet made their way into sectors where their utility exceeds their novelty. One factor contributing to the slow development of usable legged machines is the challenge

of simultaneously achieving energy efficiency and stability,⁸ both important attributes for an autonomous vehicle. Greater energy efficiency translates into the ability to travel farther and longer. Energy efficiency may be achieved in two ways: by machine design and by using (automatic) control to maximize the machine's potential for efficiency. For example, consider the modern automobile. In the years since the Model T, both redesign and control have been used to improve fuel economy. Modern automobiles are lighter, more aerodynamic, and have more efficient engines. To boost fuel economy, modern automobiles also use control to regulate spark timing, meter fuel, etc. The same idea applies to legged machines. Legged machines can be made efficient through the use of light materials, efficient actuators, and improved mechanical design. Through the use of control, a legged machine's gait may be designed and tuned to yield efficient locomotion.

Stability is also of great concern. A vehicle that overturns may damage itself and whatever it falls onto. Of course, any autonomous vehicle will overturn given sufficiently unfavorable circumstances. An objective of vehicle design and control is to maximize stability, that is, to minimize the chance of overturning.

Again, consider the evolution of the modern automobile. Stability is increased by using suspension components that maintain the wheels in contact with the driving surface. Also in use are stability augmentation systems that use the braking system to prevent side-skidding and wheel slippage. In a similar way, legged machines may be designed to have morphologies that enhance stability, for example, feet can be made larger and the number of legs increased. Control may be used to impose gaits that, under some assumptions, have guarantees of stability. Typically, this has been accomplished by controlling the machine's motion to be slow. Slowing the motion minimizes inertial effects so that quasi-static stability measures may be used.

The slow development of legged machines for work arises because machine and control design choices that ensure stability tend to compromise energy efficiency and agility. For example, consider a person walking with snowshoes on fresh, powdery snow. The snowshoes help prevent tipping over by increasing the snowshoer's support polygon. Also to prevent tipping over, the snowshoer uses a slower, more laborious gait than he would if he were walking on a hard surface. By using slower motions and a broader support polygon, he is able to maintain stability by keeping his CoP within his support polygon. The same principles are at work in the General Electric Walking Truck, the Odex Functionoids, the Adaptive Suspension Vehicle, and many of the bipeds to be described shortly. Stability is maintained simply by ensuring that the CoP is within the support polygon. In the case of polypeds with four or more legs, the support polygon is usually large because of sprawled posture and enough

⁸Recall that "stability" is currently being used to mean that the machine does not overturn. By "more stable" it is meant that the machine is further, in some sense, from overturning, and by "less stable" it is meant that the machine is closer, in some sense, to overturning.

legs to maintain a support tripod; however, as speed increases or the support polygon decreases in size, the CoP can more easily reach the boundary of the support polygon making stability difficult to assess. This is the case with bipeds that walk with dynamic gaits and a reason, among others, why almost no bipedal robots currently walk with such gaits.

1.3.2 Bipedal Robot Locomotion

In recent years, there has been a large effort in the development of bipedal robot prototypes and in the control and analysis of bipedal gaits. The literature may be largely divided into two categories: the analysis of *passive walking*—walking where gravity alone powers the walking motion—and the analysis and control of *powered walking*—walking that requires an external power source. The presentation will begin with work on passive, or semi-passive walking, then continue with a presentation on the development of powered walkers, and conclude with a presentation of the various control schemes proposed.

Passive robots: The work on passive walking is primarily motivated by the drive for energy efficiency. A secondary motivation has been the observation that many passive walking gaits have a “natural look” to them. In passive walking, dissipation due to impacts or damping is offset by the use of potential energy supplied by walking down a slope. The recent interest in passive walking can be traced to the seminal research of McGeer in the late 1980s [153, 154]. McGeer built a four-link planar passive walker and performed a detailed parameter variation and stability analysis. McGeer’s mechanism featured locking knees to prevent leg collapse and circular feet to give a rolling ground contact. It weighed 3.5 kg, was 0.5 m tall, and could stably walk down a 1.4 degree slope at about 0.4 m/s. Garcia, Chatterjee, and Ruina [85] duplicated McGeer’s mechanism and performed detailed analysis of its dynamics and the dynamics of several other passive walkers with similar morphologies. In the late 1990s Goswami, Espiau, and Keramane [93] showed that the so-called *compass gait walker*, a two-link planar passive walker with prismatic legs, can also exhibit stable gaits. By adding a torque acting between the legs and adding control to regulate the biped’s total energy, they were able to increase the passive gait’s *basin of attraction*, that is, the set of initial conditions from which solutions converge to the gait in question. Also for the compass gait walker, Thuilot, Goswami, and Espiau [228] showed that this model can exhibit gait bifurcations (in this case, changes in the period of the gait) and apparent chaos under certain conditions. For a model similar to the compass gait walker, but with circular feet, fixed damping and adjustable compliance in series with the stance leg, van der Linde [230] showed that by actively adjusting the leg compliance, the magnitude of the velocity discontinuities that occur upon swing leg touchdown may be reduced. Howell and Baillieul

[118] investigated a planar, semi-passive three-link model with two legs and a torso. With a single actuator to hold the torso parallel to the ground, they found that this model can also exhibit gait bifurcations.

As an approximation to walking in three dimensions, Smith and Berkemeier [210] studied a three-dimensional, spoked, rimless wheel of finite width rolling down a slope. They showed that this tinker toylike model is capable of an asymptotically stable rolling motion. At the end of the 1990s, Collins built a three-dimensional version of McGeer's passive walker. Collin's walker weighed 4.8 kg and measured 0.85 m in height [59]. With carefully designed feet and pendular arms, it was able to walk down a 3.1 degree slope at about 0.5 m/s. Most recent, Adolfsson, Dankowicz, and Nordmark [2] studied a passive, three-dimensional model by beginning with McGeer's planar model and gradually transforming the model into a ten-DOF, three-dimensional model. In this way, stable gaits of the three-dimensional model were found. Gait stability under parameter variations was also investigated.

Powered bipeds: Though it is important and interesting to investigate the properties of passive bipeds and their gaits, any practical biped will require energy input. In recent years, there has also been a large effort in the development of nonpassive bipedal robot prototypes, led primarily by the Japanese. Some of the more noteworthy walkers reported in the literature will now be highlighted in rough chronological order. The first reported biped capable of walking is the WL-5, a three-dimensional, 11-DOF walker constructed by Kato and Tsuiki at Waseda University in Japan in 1972 [136]. By the mid-1980s, the same group developed the WL-10RD, a three-dimensional, 12-DOF walker weighing 80 kg and capable of walking at about 0.1 m/s [225]. In the mid-1980s, Miura and Shimoyama [157] constructed a series of bipeds, named Biper-1 through Biper-5, at least some of which were capable of walking. The bipeds ranged in complexity from planar walkers, Biper-1 and Biper-2, to a three-dimensional walker with all computational facilities on board, Biper-5. Both Biper-3 and Biper-4 weighed about 3 kg and were 0.3 m in height; presumably the rest of the bipeds, which were not documented, were about the same scale. Also in the mid-1980s, Furusho and Masubuchi [82] constructed Kenkyaku, a planar, five-link biped weighing about 23 kg and measuring 0.7 m in height. Kenkyaku had four actuators, at the hip and knees, with no actuation provided between the ground and the biped. It was reported to walk at 0.8 m/s. In the late 1980s, Furusho and Sano constructed BLR-G2, a nine-link, three-dimensional biped [83, 200]. It weighed 25 kg, was 0.97 m tall, and was capable of walking at 0.18 m/s. Early in the 1990s, Kajita and Tani built Meltran II, a planar, six-DOF biped weighing 4.7 kg and standing 0.45 m tall [133, 134]; it was capable of walking successfully over small obstacles at a speed of 0.2 m/s. In the late 1990s, Pratt, at the MIT Leg Lab, built a planar, seven-link walker with feet named Spring Flamingo. It weighed 14 kg and measured 1.2 m in height [180, 181]. Spring Flamingo was capable of walk-

ing at 1.2 m/s, traversing a sloped terrain and featured series elastic elements (i.e., springs) purposefully included between the actuator and load [179]. Also in the late 1990s, the Technical University of Munich began development of Johnnie, a 23-DOF, three-dimensional walker weighing 40 kg and measuring 1.8 m in height [87, 175]. To date, Johnnie has been able to walk at approximately 0.4 m/s. Beginning in the mid-1990s, a group at INRIA in France constructed BIP, a 15-DOF, three-dimensional walker weighing about 100 kg and measuring 1.7 m in height [73]. Currently, BIP is unable to walk.

In the late-1990s, the CNRS and the French National Research Council began the construction of RABBIT, a five-link, planar bipedal walker weighing 32 kg and measuring 1.2 m in height; see [Section 2.1](#) for details on RABBIT's design. RABBIT's stated purpose is to serve as a test bed for the study of control issues related to bipedal walking and running: impacts, limit cycles, and hybrid systems. Following in the series of prototypes that began with the WL-5, the Humanoid Robotics Institute formed at Waseda University in 2000 developed WABIAN [112, 226, 248]. WABIAN is a three-dimensional biped weighing 107 kg and measuring 1.84 m in height. It has 52-DOF and is capable of walking at 0.21 m/s. One of the more famous bipeds to-date is ASIMO (standing for Advanced Step in Innovation MObility) developed by the Honda Corporation [114, 117]. ASIMO is an autonomous three-dimensional walker with 26-DOF weighing 43 kg and measuring 1.2 m in height and is capable of walking at 0.3 m/s on level ground and of climbing and descending stairs. ASIMO's development began in the mid-1980s and continues to the present day. The development has involved ten generations of prototypes, named E0 through E6 and P1 through P3, and has cost hundreds of millions of dollars. Following Honda's success, the Japanese government began the Humanoid Robot Project (HRP) in an attempt to grow Japan's service robot sector. Recently, the HRP project has produced HRP-2, a three-dimensional, 30-DOF biped weighing 58 kg and measuring 1.54 m in height [129, 135].

Hybrids: A type of "hybrid" robot is taking shape in the research literature [58], for which the objective is to use minimal actuation, sensing and control to achieve highly efficient walking on flat ground. The machine designs are based on passive walkers, with the addition of low-power actuators to replace gravity as a source of energy [72, 144]. The interest of these quasi-passive robots lies in the fact that they use less control hardware and less energy than other powered robots, yet walk rather naturally [58]. Current drawbacks include: the range of walking motions is very limited; and the stability of their gaits is not much better than the stability associated with passive walking on slopes, and hence the basins of attraction are very small.

1.3.3 Control of Bipedal Locomotion

An integral but unseen component of each nonpassive biped is its control. From the literature, several categories of control algorithms appear. They

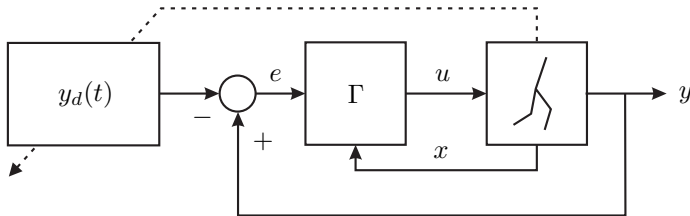


Figure 1.8. Block diagram of a trajectory tracking controller. The controller Γ forces the error $e = y - y_d$ to zero so that output y tracks the desired trajectory $y_d(t)$. The dashed line indicates that the trajectories $y_d(t)$ may be modified on the basis of the robot’s state. A periodic walking motion must be supplied by an external trajectory planner, usually in the form of desired joint trajectories. It is challenging to design the trajectories in such a way that the resulting nonlinear, time-varying, closed-loop system is stable.

fall into two groups: time-dependent and time-invariant algorithms. By far, the most popular algorithms are time-dependent and involve the tracking of precomputed trajectories; see Fig. 1.8.

To control dynamic walking in Biper-3, Miura and Shimoyama [157] approximated the biped as a linearized inverted pendulum and used trajectory tracking. The walking motion produced by this approach might best be described as a shuffle. Katoh and Mori [137] demonstrated in simulation that using PID controllers to track reference trajectories generated by a van der Pol oscillator would induce walking in a model of BIPMAN, a planar, four-DOF biped with prismatic legs. Upon implementation, BIPMAN is reported to have successfully completed only one step. Using PID control, Furusho and Masubuchi [82] were able to control walking in Kenkyaku by tracking piecewise-linear joint reference trajectories. Furusho and Sano [83, 200] were able to control walking in the three-dimensional BLR-G2 by using decoupled control for the frontal and sagittal planes. In the frontal plane, PID control was used to stabilize the upright configuration. In the sagittal plane, joint trajectory tracking was used regulate the robot’s angular momentum to be that of an inverted pendulum. To control walking in Meltran II, Kajita et al. [133, 134] used PID control to track trajectories generated by a length-varying inverted pendulum. The pendulum’s length was varied so as to maintain the biped’s COM at a constant height above the walking surface. To control walking in a three-link, three-DOF planar biped with telescoping legs, Grishin et al. [94] used PID control to track precomputed trajectories that were subsequently modified online to improve stability. To control walking in a planar, five-DOF biped, Mitobe et al. [156] used computed torque to regulate the biped’s COM and swing leg end position. To control walking in a planar, five-DOF biped, Raibert, Tzafestas, and Tzafestas [186] compared in simulation the performance of PID, computed torque, and sliding mode control in the tracking of

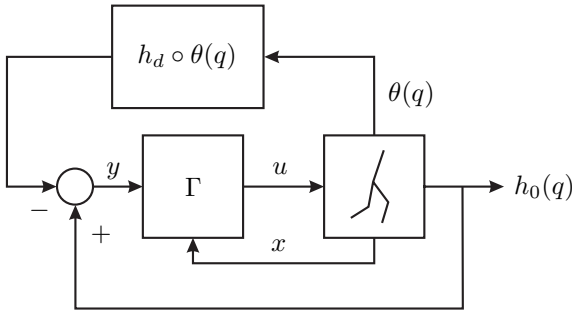


Figure 1.9. Block diagram of a time-invariant controller. The controller Γ forces the signal $y = h_0(q) - h_d \circ \theta(q)$ to zero so that the signal $h_0(q)$ tracks the function $h_d \circ \theta(q)$. In this way, the control action is “clocked” to events on the robot’s path and not to an externally supplied time-based trajectory. With proper design of $h_0(q)$ and $h_d \circ \theta(q)$, a self-generated limit cycle exists through the combined actions of the controller and the environment on the robot.

piecewise linear joint trajectories. In simulation, Fujimoto [78, 79] applied trajectory tracking, augmented with foot force control, to a three-dimensional, 20-axis biped. In simulation, to control walking in a three-dimensional biped, Park and Kim [172] used computed torque with gravity compensation to track reference trajectories generated by a length-varying inverted pendulum. In a similar scheme, Kajita et al. [129, 130] tracked trajectories generated by an inverted pendulum to control walking in HRP-2. To simplify the analysis, the pendulum height was constrained to be constant.

The most pervasive scheme used to augment trajectory tracking controllers is the ZMP criterion; its use is commonly taken as a proof of stability.⁹ The ZMP is defined to be the point on the ground where the resultant of the ground-reaction force acts and is, consequently, always contained in the robot’s support polygon [92]; recall Fig. 1.1. The ZMP criterion states that when the ZMP is contained within the interior of the support polygon, the robot is stable, i.e., will not topple. The ZMP criterion has been used to augment trajectory tracking in WABIAN [145, 248] and ASIMO [114]. The ZMP criterion has also been used to analyze the stability of the control algorithms of [129, 130, 148, 172].

In contrast to the heavy use of ZMP-based, time-dependent (trajectory tracking) control algorithms, there have been only a few time-invariant control schemes proposed; see Fig. 1.9 for an example. In a simulation study, Hürmüzlü [120, 121] controlled the motion of a fully actuated, planar, five-link biped by using feedback to impose a mix of holonomic and non-holonomic con-

⁹For clarification on stability and the ZMP, see Section 10.8.

straints on the robot's state. This permitted a closed-form computation of the robot's trajectory as a function of time. The important role of impacts was underlined in [125]. To control dynamic walking in Spring Flamingo, Pratt et al. [181] used what they termed "virtual model control." Virtual model control consists of a collection of intuitive constraints¹⁰ and a set of *ad hoc* rules for switching among them as a function of the robot's state. For the planar Spring Flamingo it works well, but for the more complicated M2, a 3D biped, it has not worked. For a fully actuated version of the compass gait walker, Spong [216] used potential energy shaping and passivity-based feedback to render passive gaits slope invariant. In particular, the robot in closed loop then admitted provably asymptotically stable periodic walking motions on flat surfaces, upwardly sloped surfaces, and down larger slopes than was possible without feedback control, all with a larger basin of attraction than was possible when walking passively down a shallow slope. Spong and Bullo [216, 217] have since extended the result to a class of three-dimensional walkers of arbitrary DOF; the stability of the associated periodic walking motions is carefully proved and the role of symmetry has been clarified.

The studies just cited are important because they represent pioneering attempts to move away from trajectory tracking and the ZMP. Instead of the periodicity of the robot's motion coming from an external clock-driven source, a controller has been designed so that the interaction of the robot with the walking surface intrinsically produces a stable limit cycle, analogous to the stable periodic motion exhibited by a van der Pol oscillator, and much more in line with the pioneering work of Raibert on the hopper. An additional important point represented by the work of Spong is the emphasis on establishing analytically—and not through simulations—the existence and asymptotic stability of a periodic motion.

These studies also have a significant shortcoming, namely the assumption of full actuation in single support, which limits the motion to flat-footed walking. Moreover, the required ground reaction forces to maintain the foot flat on the ground have not been analyzed. In order to move beyond flat-footed walking, underactuation must be addressed, which makes the control law design and analysis considerably more difficult.

Chevallereau, Aouustin, and Formal'sky developed a systematic method for computing periodic solutions for a biped model with one degree of underactuation in single support [45]. Later work addressed optimal reference trajectories for both walking and running [44].

¹⁰For example, to achieve an upright posture, one may imagine a *virtual sky hook* attached to the head of the robot, holding the body upright. One must then compute feasible actuator torques at the joints to achieve the effect of the virtual force supplied by the sky hook. Clearly, such intuitive notions may work well for quasi-static tasks, but for more dynamic tasks where one must simultaneously deal with the unilateral forces at the leg ends and stability, more systematic methods are required.

The first control law design that analytically established the stability of the walking motion of an underactuated, powered biped as an asymptotically stable periodic orbit was provided by Grizzle, Plestan, and Abba [97–99] in the context of a three-link planar biped. The robot consisted of two legs without knees and a torso, with actuation between each leg and the torso, and no actuation between the leg ends and ground. The robot thus had one degree of underactuation in single support. The key innovation was the use of feedback control to impose holonomic constraints on the robot’s motion during the single support phase. When combined with a continuous finite-time converging controller, the existence and stability of an orbit could be established with a one-dimensional Poincaré map, though this map had to be computed numerically. Plestan et al. extended the control method and illustrated it on a simulation model of RABBIT. In [8], Aoustin and Formal’sky also used holonomic constraints to control a simulation model of RABBIT. In closely related work, Ono, Takahashi, and Shimada [169] successfully controlled dynamic walking in a four-link, planar biped prototype with locking knees by using the single actuator at the hip to impose a holonomic constraint between the crotch angle (the angle between the legs) and the swing leg tibia angle (see also [170] where this idea is applied to the Acrobot). Using this method, their 0.8 m biped successfully walked at 0.29 m/s.

In the above work, the holonomic constraints were imposed during the single support phase without regard to the impacts that occur at double support. A key contribution was made by Westervelt, Grizzle, and Koditschek [244, 245] where they placed the single support phase and the impact phase on more equal footing. This work recognized that the holonomic constraints were creating an invariant surface in the continuous phase of the model, and it showed how to design the constraints so that the surface became invariant under the impact model as well. The resulting notion of *hybrid invariance*—being invariant under the continuous part of the model as well as the discrete part—yielded the concept of the *hybrid zero dynamics* (HZD), a low-dimensional submodel of the closed-loop hybrid robot model. The HZD led to fast algorithms for designing the holonomic constraints in order to minimize torque requirements, for example, and subject to meeting the natural unilateral constraints associated with bipedal locomotion. Very successful implementations of the method on RABBIT were reported by Chevallereau et al. [43] and by Westervelt, Buche, and Grizzle [241, 242]. This body of work has been followed by extensions to running in an underactuated biped by Chevallereau, Westervelt, and Grizzle [50, 51]; related experiments by Morris et al. are reported in [163]. Work by Choi and Grizzle on robots with feet allows both fully actuated and underactuated phases in the walking gait [54]. The work of Morris and Grizzle removed the need to use a finite-time converging controller [161].

Song and Zefran [211, 212] have developed a general computational framework for the stabilization of periodic orbits in nonlinear systems with impulse effects. The results have been illustrated through simulations on planar and 3D robot models.

1.4 Feedback as a Mechanical Design Tool: The Notion of Virtual Constraints

Successful control design must address the challenges in legged robots that arise from the many degrees of freedom in the mechanisms, the intermittent nature of the contact conditions with the environment, multiple phases or hybrid nature of the models, and underactuation. Since walking (and running) can be viewed as a periodic solution of the robot model, the method of Poincaré sections is the natural means to study asymptotic stability of a walking cycle. Due to the complexity of the associated dynamic models, however, this approach has had limited success. One of the contributions of this book is to show that a control strategy can be designed in a way that greatly simplifies the application of the method of Poincaré to a class of biped models, and in many cases, to reduce the stability assessment problem to the calculation of a scalar map. Our philosophy is that if stability analysis can be rendered sufficiently simple, then it becomes possible to efficiently explore a large set of asymptotically stable gaits in order to find one that meets additional performance objectives, such as minimum energy consumption per distance traveled for a given average speed, or minimum peak-actuator power demand.

Consummate with the hybrid nature of biped models, the controllers we develop will be hybrid, with continuous-time feedback signals applied in stance and/or flight phases, and discrete (or event-based) updates of controller parameters performed at transitions between phases. The controller designs will use two principles that are ubiquitous in nonhybrid systems, namely invariance and attractivity, with the notion of invariance being extended to hybrid systems so as to address the discrete transitions as well as the continuous phases. Hybrid invariance will lead to the creation of a low-dimensional hybrid subsystem of the full-dimensional closed-loop system. The low-dimensional hybrid subsystem is called the hybrid zero dynamics (HZD). Attractivity will mean that trajectories of the full-dimensional closed-loop system converge locally and sufficiently rapidly to those of the hybrid zero dynamics so that existence and stability of periodic walking and running motions can be restricted to the study of the hybrid zero dynamics. The Poincaré return map for the hybrid zero dynamics will turn out to be one-dimensional.

1.4.1 Time-Invariance, or, Self-Clocking of Periodic Motions

The controller designs that we propose for walking will not involve trajectory tracking. Why? One reason is that time-varying, nonlinear, hybrid systems are extremely hard to analyze. Here is another reason: In a controller based upon tracking, if a disturbance affects the robot and causes its motion to be retarded with respect to the planned motion, for example, the feedback system

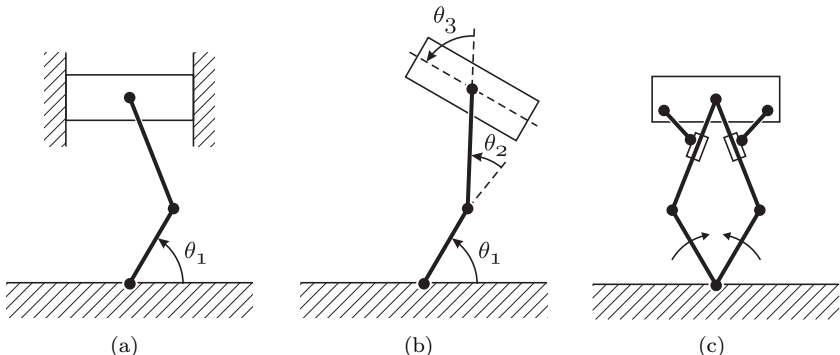


Figure 1.10. Virtual Constraints in a simpler context. (a) Piston constrained to move in a cylinder; this is a one degree of freedom mechanical system. (b) Piston without the constraints; this is a three degree of freedom mechanical system. (c) Hypothetical, Rube Goldberg realization of a piston constrained via additional links to have the kinematics of a piston in a cylinder; the arrows represent the two cranks rotating synchronously in opposite directions. By using virtual constraints to achieve link coordination on a bipedal robot, different gaits can be more easily programmed than if the links were coordinated by hardware constraints.

is obliged to play catch up in order to regain synchrony with the reference trajectory. Presumably, what is more important is the orbit of the robot’s motion, that is, the path in state space traced out by the robot, and not the slavish notion of time imposed by a reference trajectory (think about how you respond to a heavy gust of wind when walking). A preferable situation, therefore, would be for the robot in response to a disturbance to converge back to the periodic orbit, but not to attempt otherwise re-synchronizing itself with time. One way to achieve this is by parameterizing the orbit (i.e., the walking motion) with respect to (a scalar-valued function of) the state of the robot, instead of time [14, 98, 244]. In this way, when a disturbance perturbs the motion of the robot, the feedback controller can focus solely on maintaining limb positions and velocities that are appropriate for that point of the orbit, without the additional burden of re-synchronizing with an external clock. As a bonus, the controller is time invariant, which helps analytical tractability.

1.4.2 Virtual Constraints

A concept we will use over and over again in our feedback designs is to asymptotically impose holonomic constraints on a dynamic system through feedback control. This idea has a long history, but its development in nonlinear control theory, which is what we will use, is primarily due to Byrnes and Isidori [31, 32, 128]. We introduce the idea by considering something less com-

plicated than a biped. [Figure 1.10\(a\)](#) depicts a planar piston in an open cylinder. The system has one DOF, which means that a model can be given in terms of the angle of the “crank,” θ_1 , and its derivatives. [Figure 1.10\(b\)](#) represents the planar piston without the constraints imposed by the walls of the cylinder. The system now has three degrees of freedom involving three coupled equations in the angles $\theta_1, \theta_2, \theta_3$, and their derivatives. Only one degree of motion freedom remains when two constraints are imposed: (a) the center of the piston lies always on a vertical line passing through the rotation point of the crank and (b), the angle of the piston head is horizontal throughout the stroke. Mathematically, this is “equivalent” to imposing

$$0 = L_1 \cos(\theta_1) + L_2 \cos(\theta_1 + \theta_2), \quad (1.3a)$$

$$\pi = \theta_1 + \theta_2 + \theta_3, \quad (1.3b)$$

where L_1 is the length of the crank, and L_2 is the length of the second link (due to the existence of multiple solutions, one must choose the solution corresponding to the piston being above the crank). These two constraints can be imposed through the physical means of the cylinder walls shown in [Fig. 1.10\(a\)](#), or, through the use of additional links as shown in [Fig. 1.10\(c\)](#).

If the system is appropriately actuated, the constraints can also be *asymptotically* imposed through feedback control. To see this, assume that the joints θ_2 and θ_3 are actuated. Define two outputs in such a way that zeroing the outputs is equivalent to satisfying the constraints; for example

$$y_1 = L_1 \cos(\theta_1) + L_2 \cos(\theta_1 + \theta_2), \quad (1.4a)$$

$$y_2 = \theta_1 + \theta_2 + \theta_3 - \pi. \quad (1.4b)$$

The constraints will then be asymptotically imposed by any feedback controller that asymptotically drives y_1 and y_2 to zero; for the design of the feedback controller, one could use computed torque, PD control, etc.

When the outputs (1.4) are zeroed, the actuated joint angles become implicit functions of the unactuated joint angle. Sometimes it is more convenient to relate the actuated joint angles to the unactuated angle in an explicit form. As long as $L_1 < L_2$, the constraints (1.3) can also be rewritten as explicit functions of the crank angle, θ_1 , per

$$\theta_2 = \pi - \theta_1 - \arccos\left(\frac{L_1}{L_2} \cos(\theta_1)\right), \quad (1.5a)$$

$$\theta_3 = \arccos\left(\frac{L_1}{L_2} \cos(\theta_1)\right), \quad (1.5b)$$

leading to the alternative output functions

$$y_1 = \theta_2 - \left(\pi - \theta_1 - \arccos\left(\frac{L_1}{L_2} \cos(\theta_1)\right)\right), \quad (1.6a)$$

$$y_2 = \theta_3 - \arccos\left(\frac{L_1}{L_2} \cos(\theta_1)\right). \quad (1.6b)$$

We have used both explicit and implicit forms of the constraints when controlling a biped.

When constraints are imposed on a system via feedback control, we call them *virtual constraints*¹¹ [35,43]. The planar three DOF piston of Fig. 1.10(b) can be virtually constrained to achieve asymptotically the same *kinematic behavior* as the one DOF piston in Fig. 1.10(a); the resulting dynamic models are different because the constraint forces are applied at different points of the 3 DOF piston.¹² The virtual constraints can be imposed through the implicit constraints given in (1.3) or the explicit constraints in (1.5). In the case of a bipedal robot, the advantage of imposing the constraints on the mechanism virtually (i.e., via feedback control) rather than physically (i.e., through complicated couplings between the links or the environment), is evident: the robot can then be “electronically reconfigured” to achieve different tasks, such as walking at different speeds, going up stairs, and running.

The above discussion has focused on the aspects of a model that can be described by differential equations. As such, a very important feature of bipedal locomotion has been ignored, namely, impacts [125]. Suppose that during the swing phase of a given step, the time evolution of a robot under feedback control is respecting a set of virtual constraints. At the end of the step, the impact map comes into play when the swing leg contacts the ground, providing a new initial condition for the ensuing step. In general, there is no reason for the new initial condition to satisfy the virtual constraints! In this case, the feedback controller will have to expend effort to rezero the outputs encoding the virtual constraint during the swing phase, only to have the next impact once again push the robot’s state off the constraint surface. Hence, when designing virtual constraints, some care should be taken to account for the impacts. This aspect of the theory requires an important extension of the classical notion of the zero dynamics of a nonlinear control system [31,32,128]. Bipedal robots are fundamentally hybrid systems and a theory of their control must be hybrid as well.

¹¹The term “virtual constraints” was coined by Carlos Canudas de Wit.

¹²This important point will be illustrated fully on the Acrobot in Chapter 5.

Two Test Beds for Theory

2.1 RABBIT

2.1.1 Objectives of the Mechanism

The RABBIT test bed shown in Fig. 2.1 is the result of a joint effort by several French research laboratories, encompassing mechanical engineering, automatic control, and robotics [26]; the University of Michigan joined in the control effort in late 1998, as the result of a sabbatical in Strasbourg, France. The effort was funded by the CNRS and the National Research Council, with the following primary objectives:

- Study powered (i.e., actuated) bipedal robot locomotion, as opposed to passive (i.e., unactuated) locomotion, so that the robot would be able to perform a wide range of gaits on a flat surface, with various step lengths and average speeds, and study whether feedback control would lead to stable locomotion with a large basin of attraction.
- Study quasi-statically unstable phases of motion that have been ignored in most powered walking robots.
- Understand the influence of the mechanical and control design choices on the robot's locomotion.
- To be able to walk and to run. Walking robots typically use rigid links and joints, while hoppers (which have a flight phase) usually employ springs to store and release energy. The decision was made to design a robot with rigid links and joints and to make it walk and run.

The [End Notes](#) provide a detailed history of the RABBIT project.

RABBIT's lateral stabilization is ensured by a rotating bar, and thus only 2D motion in the sagittal plane is considered. Except for this limitation, the prototype captures the main difficulties inherent in this type of nonlinear system: underactuation (no feet), variable structure (the state dimension varies as a function of the motion phase), and state jumps (sudden state variations resulting from impacts with the ground). Asymptotically stable locomotion is thus only achievable through a detailed study of the robot's full dynamics, including impact phases.

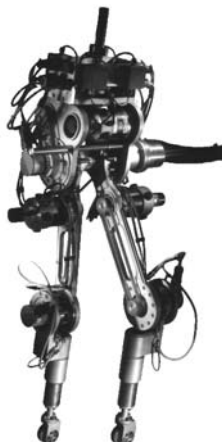


Figure 2.1. Photo of RABBIT. The robot was designed to facilitate the development of theoretically sound control algorithms for walking and running. RABBIT is located at the Automatic Control Laboratory of Grenoble (LAG), France. See the [End Notes](#) for a detailed history of the RABBIT project.

2.1.2 Structure of the Mechanism

RABBIT was conceived to have the simplest mechanical structure that is still representative of human walking. The requirement of mechanical simplicity naturally led to restricting its motion to the sagittal plane, with lateral stabilization being achieved by external means. However, many of the other design decisions that went into the prototype are less obvious, involving numerous tradeoffs to achieve dynamic performance, scientific objectives, simplicity, and robustness at a cost compatible with a university budget. This section gives an overview of the key design decisions that went into the conception and construction of RABBIT. Additional photographs of the mechanism are available at [26, 43]. Some of the components are specified in [Table 2.1](#).

Work conducted in recent years on passive bipedal walking has shown that it is possible to design three-dimensional, anthropomorphic robots that can walk stably down a sloped surface without any actuation whatsoever [59, 153]! One must therefore reflect on the essential role of each link in the design of a walking mechanism, and, in particular, one must question whether a given joint needs to be actuated or not.

Numerous studies on controlled bipedal robots have shown that actuation of the hips and knees is essential for providing locomotive power to the robot for walking on a flat or upwardly sloped surface, and for ensuring clearance of the swing leg during a step. However, the case for including actuation at the ankles is less clear. From the start of the RABBIT project, one of the goals was to demonstrate that actuated ankles are *not* absolutely necessary for the existence of asymptotically stable locomotion, and thus RABBIT has

no feet. Without actuated ankles, lighter feet can be designed, which is more efficient for walking and running. If the robot can still be shown to achieve stable walking or running over a wide range of speeds on flat ground, then actuation of the ankles must be justified on the basis of improved traction with the walking surface, better adaptability over nonsmooth surfaces, or for ameliorating the shocks associated with the feet impacting the ground. Finally, without feet, the ZMP principle is not applicable, and thus underactuation must be explicitly addressed in the feedback control design, leading to the development of new feedback stabilization methods.

For the RABBIT project, a mechanism design was sought that would enable running as well as walking. Because it was also desired that the robot could perform anthropomorphic gaits, RABBIT had to have at least a hip and two knees, giving a minimum of four links. For the robot to be able to carry a load, a torso was necessary, making a total of five links. RABBIT is thus a seven-degree-of-freedom mechanism (when there is no contact with the ground), with four degrees of actuation. In the upright position, with both legs together and straight, the hip is 80 cm above the ground and the tip of the torso is at 1.43 m. RABBIT's total mass is 32 kg. See [Table 6.3](#) on page 177 for the lengths, masses, and inertias of each link of the robot.

2.1.3 Lateral Stabilization

Without active lateral stabilization [143], a biped *walker* can still be designed to maintain its lateral stability by means of “laterally pointing feet,” that is, bars or plates attached at the leg ends that extend laterally and prevent the robot from tipping over sideways [59, 152, 153]. But in the case of a *runner*, where a flight phase exists (i.e., ballistic motion—no contact with the walking surface), some means is required to maintain lateral stability. In order for this external stabilization device not to limit the displacement of the robot, the choice of a circular path was made. Hence, the robot is guided around a central column by means of a boom; see [Fig. 2.2](#). The same solution for lateral stabilization had been implemented in the design of Kenkyaku [82], Meltran II [133], and robots in the MIT Leg Lab [178, 182]. The robot is attached to the radial bar via a revolute joint that is aligned with the axes of the hips, and it is attached to the central column with a universal joint.

With this lateral support device, the robot's sagittal plane is tangent to a sphere centered on the universal joint. As explained in [Fig. 2.3](#), it follows that the distance between the stance leg end and the central column must be allowed to vary with the position of the hip. To permit frictionless radial displacement of the supporting leg end, wheels directed in the frontal plane (i.e., normal to the sagittal plane) are used. In this way, no mobility of the leg end exists in the sagittal plane of the robot, and therefore, with a sufficiently long boom (the nominal boom length is two meters), the robot's motion is tangential to the sphere can be accurately modeled as that of a perfectly planar robot.



Figure 2.2. RABBIT's setup, which includes a boom to constrain the robot's path to a circle. The boom is attached at the robot's hip, via a revolute joint. The boom only provides lateral stabilization; it does not prevent the robot from falling forward, backward, or down. The counter balance can be used to offset the weight of the lateral stabilization bar or to modify the effective gravitational field. Not shown are the dSPACE module and power electronics that are mounted on top of the central tower.

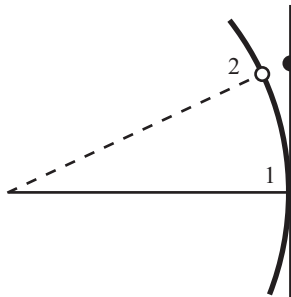


Figure 2.3. Top view of RABBIT's circular walking path. To see why wheels in the frontal plane are necessary on the leg ends, consider the robot when the hip is in position 1, and the stance leg is in front of the robot, as marked by the solid dot. The leg end must lie on the robot's sagittal plane, which is tangent to the circle, and thus the leg end is not on the circle. However, as the robot advances to point 2 where the hips are now over the stance leg end, the leg end now must touch the circle as shown by the unfilled dot. This mobility is supplied by a wheel that is directed normal to the sagittal plane of the robot. A related but less significant effect is associated with changes in the height of the hip; this bit of geometry is left to the reader.

2.1.4 Choice of Actuation

Specifying the actuation is a key step in the design process of a robot. This includes the choice and sizing of actuation technology. The use of electric motors allows for simpler low-level joint control, higher bandwidth, and easier construction than hydraulic or pneumatic drives. The choice of the type of electric motor usually comes down to quality measures, such as power-to-weight ratio. The project designers chose DC motors with Samarium Cobalt magnets, though nearly identical performance in terms of torque density and peak torque could have been had with brushless motors. A gear reducer and belt were used to connect the motors to each of the four actuated joints. The motors for the knees were mounted as close as possible to the hips in order to minimize the inertia of the legs about the hip axes; this decreases the coupling in the dynamic model as well as the required motor torques.

2.1.5 Sizing the Mechanism

Once the motor technology was selected, sizing was determined on the basis of dynamic simulations and offline trajectory optimization [1, 38]. Indeed, in order to check if the proposed structure would be able to walk and run, a simulation study was conducted. Feasible trajectories were computed, along with the torque needed to achieve them in open loop. One difficulty is that in both flight and single support, RABBIT is underactuated. During the single support phase, the degree of underactuation is one (five degrees of motion freedom due to the constraint that the stance leg end does not slip, and four actuators), while during the flight phase, the degree of underactuation is three (seven degrees of motion freedom and four actuators). Hence, even though a given motion of the robot may be kinematically realizable, it may not be dynamically feasible [29], so a kinematic analysis combined with an inverse torque model is definitely not sufficient for determining possible walking and running motions.

Generally speaking, it is desirable that the robot be able to walk and run efficiently, in the sense that the energy cost per distance traveled for a given motion will be as small as possible. Thus, dynamic optimization [49] was used to compute optimal walking and running trajectories, assuming nominal values for the mechanical parameters as well as for the motor characteristics, specifically their torque and speed limits. Reaction forces at the leg ends were calculated to check that all contact conditions were met (the stance leg remains in contact with the walking surface and does not slip). These calculations provided for each joint the torque-speed curve as a function of walking and running speed, as illustrated in Figs. 2.4 and 2.5. By carrying out this analysis for a wide range of walking and running speeds, it was possible to determine the total operating range required of each motor, and thereby arrive at its required size. These specifications were then matched to off-the-shelf components, both for the motors and the gear reducers. In the end,

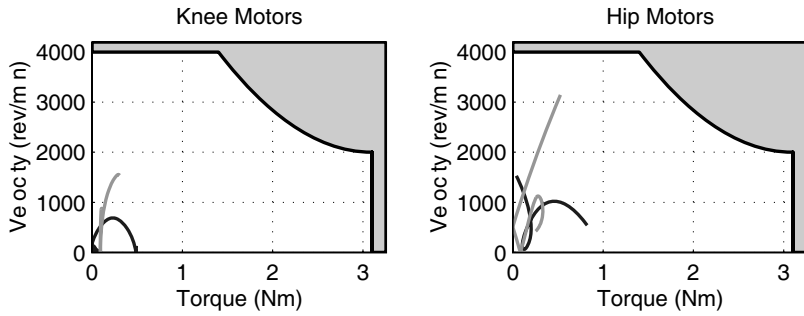


Figure 2.4. Plot of motor speed versus torque for an optimal walking motion of RABBIT at 0.75 m/s; the gear ratio is 50:1.

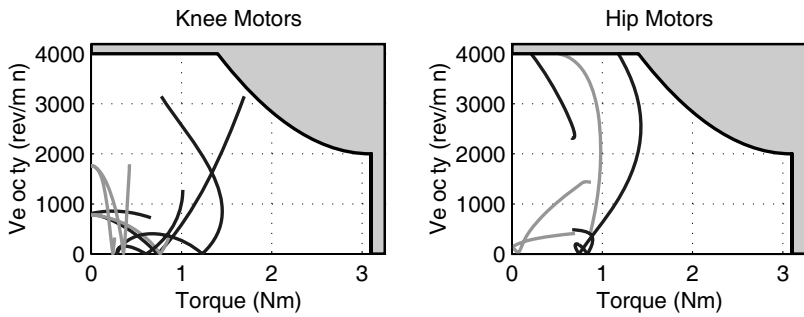


Figure 2.5. Plot of motor speed versus torque for an optimal running motion of RABBIT at 1.2 m/s; the gear ratio is 50:1.

RABBIT was designed to be able to walk with an average forward speed of at least 5 km/h and to run at more than 12 km/h.

2.1.6 Impacts

An impact or shock occurs in the majority of cases when the swing leg contacts the ground. The only way to avoid a shock is for the velocity of the leg end to be zero at the contact moment, which is not feasible in practice. Shocks have obvious deleterious effects on the durability and life of a mechanical system. The most affected components are the bearings, gear-reducers, and sensors. It is therefore indispensable from the beginning to plan for a source of compliance in the system in order to prevent the transmission of large shocks to the most sensitive parts. The magnitude of the shock is determined by the nature of the walking surface (hard, soft, absorbing) and the material used at the end of the leg. The frontal wheels on the leg ends were therefore constructed of a stiff, shock absorbing, polymer. The belts between the motors and the gear boxes were designed to provide additional protection.

2.1.7 Sensors

The speed of response or bandwidth of each axis of the robot is determined by the transfer function of the mechanical powertrain (motors, gears, and belts) and the power amplifiers that drive each motor. In the case of RABBIT, the approximate bandwidth of the mechanical portion of each actuated joint is 12 Hz, and approximately 250 Hz for the amplifiers.

Because RABBIT is an experimental apparatus, a maximal sensor set was installed. The four actuated joints of the robot are each equipped with two encoders to measure angular position; velocity must be calculated from position. One encoder is attached directly to the motor shaft, while the second is attached to the output shaft of the gear-reducer; this configuration allows any compliance between the motor and the joint angle to be detected, though subsequent experimentation has shown that the connection is adequately rigid for control purposes. Identical encoders are used at each joint. The mechanism has three additional encoders. One measures the angle of the torso with respect to a vertical axis established by the central column around which RABBIT walks. The second measures the horizontal (surge) angle of the stabilizing bar with respect to the central column; this allows the distance traveled by the robot to be computed. The final encoder measures the pitch angle of the stabilizing bar, which allows the height of the hips to be measured; in single or double support this information is redundant, but when both feet are off the ground, as in running, it is not.

The robot was initially equipped with two force sensors, one at the end of each leg, to measure the tangential and normal components of the forces exerted at the contact of the robot and the ground. These turned out to be insufficiently robust, and were replaced with contact switches. The support

Table 2.1. Components used in RABBIT.

| Component | Model (Specification) | Manufacturer |
|------------------------------------|--|---|
| DC motors | RS420J | Parvex SA, Dijon, France |
| Motor current drives | RS420 RTS10/20-60 | |
| Motor incremental encoders | C4 (250 counts/rev) | |
| Joint absolute encoders | CHM 506 P426R/8192/16 (8192 counts/rev) | Ideacod, Strasbourg, France |
| Central tower incremental encoders | GHM5 | |
| Gear Reducers | HFUS-2UH, size: 25 (ratio: 1/50) | Harmonic Drive Technologies, Peabody, MA, US |
| Real-time Controller | DS1103 (400 MHz PowerPC 604e DSP) | dSpace, Paderborn, Germany |

leg and double support phases are easily distinguished through the positions of the contact switches. Estimating contact moment through swing leg height as determined by the position measurements is not sufficiently accurate.

2.1.8 Additional Details

After the robot was built, its link-parameter values were identified by a group associated with the project and are given in [Table 6.3](#), with the measurement conventions given in [Fig. 6.14](#).

For a real-time control platform, RABBIT uses a dSPACE DS1103 system. With the DS1103 system, run-time software is created by automatic translation and cross-compiling of Simulink diagrams for the system's 400 MHz PowerPC 604e DSP, allowing the real-time controller software to be developed in a high-level language. This obviates the need for low-level I/O programming and facilitates debugging. In addition, the system provides low-level computation, digital-to-analog and analog-to-digital conversion, as well as a user interface, all in a single package.

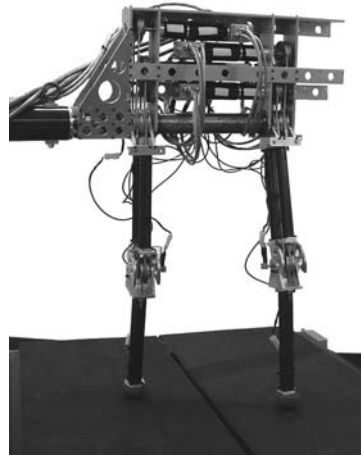


Figure 2.6. Photo of ERNIE walking on a treadmill. ERNIE was designed to have morphology that is similar to RABBIT's, to allow the addition of parallel joint compliance at the knees, and to walk on a treadmill. ERNIE is located at the Locomotion and Biomechanics Laboratory at the Department of Mechanical Engineering, The Ohio State University, Columbus, OH, USA.

2.2 ERNIE

2.2.1 Objectives of the Mechanism

The ERNIE test bed, shown in Fig. 2.6, was designed at The Ohio State University by Ryan Bockbrader, Adam Dunki-Jacobs, Jim Schmiedeler, and Eric Westervelt during the period of September 2005 to January 2006. The primary motivation for the design and construction of ERNIE was to provide a scientific and educational platform at OSU for the development of novel control strategies for bipedal walking and running. The general morphology of ERNIE was inspired by that of RABBIT: two legs with knees, no feet, and a torso. Nevertheless, there are a number of unique features in the mechanical design of ERNIE, and these impact the range of experiments that can be carried out as well as controller design and implementation.

ERNIE's legs are modular: By making ERNIE's legs modular, the leg lengths, the leg ends, and the joint offsets may be changed with minimal redesign. In this way, modularity facilitates the study of robot asymmetry, walking with feet, etc.

ERNIE’s design uses carbon fiber: ERNIE’s boom and legs are made primarily of carbon fiber, whereas RABBIT’s boom is made of tubular steel and its legs are made of aluminium. Connections between ERNIE’s carbon fiber tubes are made with aluminum plugs epoxied into the tubing’s ends. Using carbon fiber in place of aluminium and steel reduces mass and increases rigidity. Decreasing the mass of the legs is important because it lowers the torque required to accelerate the legs, thus enabling the use of smaller motors.

All of ERNIE’s actuators are located in the torso: Locating all of the actuators in the torso reduces the mass that is distal to the robot’s center of mass. The result is lighter legs, thus enabling smaller motors to be used. The downside of locating the actuators in the body is that the needed transmissions are more complicated than locating the knee actuators on the femurs, as is the case with RABBIT. ERNIE’s transmissions consist of drive pulley’s at the motors and joints connected by polymer-coated steel cabling. Idler pulleys are used at the hip for the knee joints.

Parallel compliance may be easily added at ERNIE’s knees: The addition of compliance at the knees in parallel with the actuators has the potential to reduce the peak power requirements of walking and running, thus enabling more aggressive motions to be achieved with a given set of actuators.

ERNIE’s joints have relatively low friction: Compared with the joints of RABBIT, ERNIE’s joints have low friction. The friction of RABBIT’s joint’s drivetrains is due to the use of harmonic drives. ERNIE’s drivetrains use gear reducers with staged planetary gear sets, which have considerably less friction.

2.2.2 Enabling Continuous Walking with Limited Lab Space

Due to limited lab space, ERNIE was designed to walk on a treadmill. ERNIE’s treadmill is a split-track treadmill with force plates under each belt. The treadmill was manufactured by the Bertec Corporation, Columbus, Ohio, USA. Among the treadmill’s many features, the positions of the individual tracks may be directly measured, and the speeds of the tracks may be set independently. Since the tracks’ belts have significant lateral flexibility, ERNIE does not require wheels at its leg ends as does RABBIT; see Fig. 2.3.

So that ERNIE may walk either on the ground or on a treadmill, the mechanism that affixes ERNIE’s boom to the wall allows the height of the attachment point (sphere center) to be adjusted. Affixing the boom to the wall, however, prevents the use of a counterbalance.

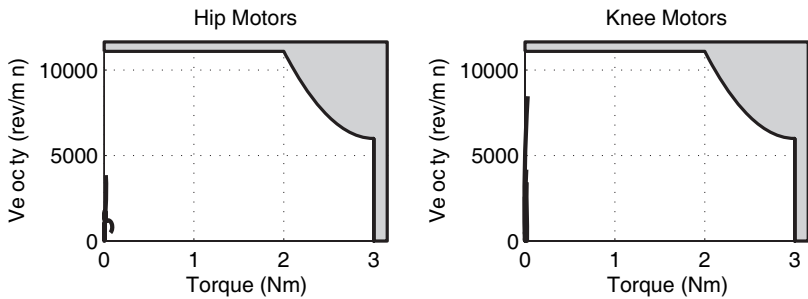


Figure 2.7. Plot of motor speed versus torque for an optimal walking motion of ERNIE at 0.6 m/s; the gear ratio is 91:1.

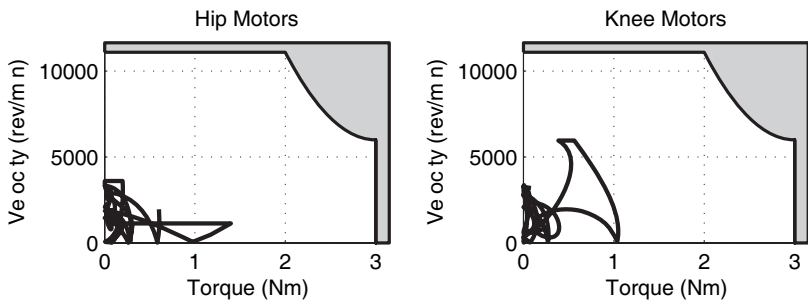


Figure 2.8. Plot of motor speed versus torque for an optimal running motion of ERNIE at 0.8 m/s; the gear ratio is 91:1.

2.2.3 Sizing the Mechanism

ERNIE's actuation was chosen based upon simulations of a detailed model of the robot in closed-loop with a feedback controller.¹ With this technique, the effects of disturbances and perturbations on power consumption could be studied. Using these simulations, the design of ERNIE was iterated until the needed components' specifications matched those that were available off the shelf. Typical torque-speed curves for walking and running corresponding to ERNIE's final design are given in Figs. 2.7 and 2.8.

2.2.4 Impacts

To ameliorate the effects of shocks, ERNIE's aluminum hemispherical leg ends are covered with half of a racquetball. In addition to being shock-absorbing,

¹Recall that RABBIT was sized on the basis of open-loop trajectory optimization. When RABBIT was designed, a method for controlling it had not yet been invented!

the racquetball has a high coefficient of friction, which helps prevent foot slippage. Compliance in the transmissions protect the gear reducer's teeth.

2.2.5 Sensors

As in the case of RABBIT, ERNIE has a maximal sensor set with sensors located at the same locations as RABBIT. Unlike RABBIT, however, the sensors at ERNIE's joints and the sensor that measures ERNIE's absolute orientation are rotary potentiometers. In addition to being lighter, potentiometers are less expensive, have greater shock tolerance, and require less cabling than encoders.

Force sensitive resistors are used at the leg ends to detect ground contact. Since force sensitive resistors suffer from significant drift, their signals are numerically differentiated to make easier the detection of impact events. Force sensitive resistors were also used in RABBIT's running experiments; see [Section 9.9](#).

2.2.6 Additional Details

Some of ERNIE's components are specified in [Table 2.2](#). Note that published peak torque capability of the selected motor and gearhead pairs is 28 Nm; however, experience with these motors and gearhead pairs suggests that the published component specifications are extremely conservative and that producing peak torques of more than three times the rated value is not a problem.

ERNIE's total mass is 18.6 kg. In the upright position, with both legs together and straight, its hip is 72 cm above the ground and the tip of the torso is at 1.0 m. See [Table 8.2](#) for a complete list of ERNIE's parameters, which were determined from the 3D solid modeling software used in its design.

ERNIE's real-time control platform is a newer version of the dSPACE DS1103 system used for RABBIT. ERNIE's system has increased processor speed and greater data transfer rate between the host and target computers.

Table 2.2. Components used in ERNIE.

| Component | Model (Specification) | Manufacturer |
|----------------------------|--------------------------------------|---|
| Brushless DC motors | EC 45-136212 | Maxon Precision Motors, Inc. Fall River, MA, USA |
| Motor incremental encoders | HEDL 9140 (500 PPR) | |
| Motor gearheads | GP 42C-203125 | |
| Brushless servo amplifiers | B60A40AC | Advanced Motion Controls Camarillo, CA, USA |
| Boom encoders | NSO-S10000-2MD-10-050 (10000 PPR) | CUI Inc. Tualatin, OR, USA |
| Joint potentiometers | 308 NPC (5 kΩ) | Clarostat Sensors and Controls, USA |
| Real-time controller | DS1103 (1 GHz PPC 750GX DSP) | dSpace, Paderborn, Germany |

Part II

Modeling, Analysis, and Control of Robots with Passive Point Feet

3

Modeling of Planar Bipedal Robots with Point Feet

This chapter introduces dynamic models for walking and running motions of planar bipedal robots with point feet. The robots are assumed to consist of rigid links with mass, connected via rigid, frictionless, revolute joints to form a single open kinematic chain lying in a plane. It is further assumed that there are two identical subchains called the legs, connected at a common point called the hip, and, optionally, additional subchains that may be identified as a torso, arms, tail, etc. Each leg end is terminated in a point so that, in particular, either the robot does not have feet, or it is walking tiptoe. A typical allowed robot is depicted in Fig. 3.1, which is intentionally suggestive of a human form. All motions will be assumed to take place in the sagittal plane and consist of successive phases of single support and double support in the case of walking, or single support and flight in the case of running. Conditions that guarantee the leg ends alternate in ground contact—while other links such as the torso or arms remain free in the air—will be imposed during control design in later chapters. Motions such as crawling, tumbling, skipping, hopping, dancing, and brachiation will not be studied.

The distinct phases of walking and running motions naturally lead to mathematical models that are comprised of distinct parts: the differential equations describing the dynamics during a single support phase, the differential equations describing the dynamics during a flight phase, and a model that describes the dynamics when a leg end impacts the ground. For the models developed here, the ground—also called a walking or running surface—is assumed to be smooth and perpendicular to the gravitational field, that is, the ground is assumed to be flat as opposed to sloped or terraced.¹

Impacts with the ground can be compliant or inelastic.² In a compliant model, the reaction forces between the ground and the leg ends are often modeled with nonlinear spring-dampers [24, 149, 194]. For common walking surfaces—such as a tile floor, as opposed to a trampoline, the impact duration

¹A walking surface that is spatially periodic, such as a uniform flight of stairs or a constant slope, and compatible with the robot's workspace, for example, the step height is not too large, can be addressed with the methods of this book. In particular, a surface of constant slope is easily addressed; see Section 6.6.3.

²An inelastic model can be rigid (as used in this book) or plastic (beyond the elastic limit, a material undergoes a permanent shape change called plastic deformation).

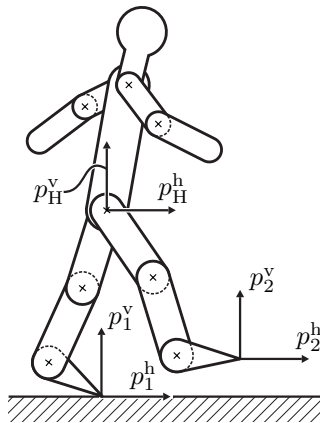


Figure 3.1. A typical planar robot model meeting the hypotheses of this book. For later use, Cartesian coordinates are indicated at the hip and the leg ends.

or transient phase of the impact model is very short. The corresponding differential equations are numerically very stiff and including them can greatly complicate the simulation and analysis of a walking or running gait; moreover, determining physically reasonable parameters for a compliant impact model is itself a very challenging problem. To avoid these difficulties, throughout the book, a rigid (i.e., perfectly inelastic) contact model will be assumed for the purposes of control design and analysis.³ The rigid contact model of [74, 208] effectively collapses the impact phase to an instant in time. The impact forces are consequently modeled by impulses, and a discontinuity or jump is allowed in the velocity component of the robot's state, with the configuration variables remaining continuous or constant during the impact. The dynamic models of walking and running are thus *hybrid* in nature, consisting of continuous dynamics and a reinitialization rule at the impact event.

3.1 Why Point Feet?

An important source of complexity in a biped system is the degree of actuation of the system, or more precisely, the degree of *underactuation* of the system. It will be assumed in this part of the book that the legs are terminated in

³The compliant impact model of [176] will be introduced in Chapter 9 for the purpose of investigating the robustness of a proposed feedback control law.

points, and consequently, no actuation is possible at the end of the stance leg. It follows that the system is underactuated during single support, as opposed to fully actuated (a control at each joint and at the contact point with the ground). During the flight phase of a running gait, the system is underactuated in any case.

One could be concerned that “real robots have feet,” and thus, while the analysis of point-feet models may be of interest mathematically, it is “misguided for practical robotics.” Hopefully, Part III of the book, which addresses walking with feet and an actuated ankle, will allay any such misgivings. If one takes human walking as the defacto standard against which mechanical bipedal walking is to be compared, then the flat-footed walking achieved by current robots needs to be improved. In particular, toe roll toward the end of the single support phase needs to be allowed as part of the gait design. Currently, this is not allowed specifically because it leads to underactuation,⁴ which cannot be treated with the control design philosophy based on trajectory tracking and a quasi-static stability criterion, such as the ZMP; see Figs. 1.1 and 1.8.

A model of an anthropomorphic walking gait should at least consider a fully actuated phase where the stance foot is flat on the ground, followed by an underactuated phase where the stance heel lifts from the ground and the stance foot rotates about the toe, and a double support phase where leg exchange takes place; optionally, heel strike and heel roll could also be included, which would yield a second underactuated phase in the gait. In either case, a model of walking with a point contact is an integral part of an overall model of walking that is more anthropomorphic in nature than the current flat-footed walking paradigm. Because the model with point feet is simpler than a more complete anthropomorphic gait model, it facilitates the development of new feedback designs and dynamic stability analysis methods that are appropriate for moving beyond quasi-static walking.

3.2 Robot, Gait, and Impact Hypotheses

The following comments on terminology are expanded from Chapter 1. The *single support* or *swing phase* is defined to be the phase of locomotion where only one leg is in contact with the ground. Conversely, *double support* is the phase where both feet are on the ground; see Figs. 1.2 and 1.3. When only one leg is in contact with the ground, the contacting leg is called the *stance leg* and the other is called the *swing leg*. *Walking* is then defined as

⁴When the foot is rotating about the toe, one effectively has a point contact with no actuation. To see this, take another look at Fig. 3.1.

alternating phases of single and double support, with the requirement that the displacement of the horizontal component of the robot's center of mass (COM) is strictly monotonic and the swing leg is placed strictly in front of the stance leg at impact. Implicit in this description is the assumption that the feet are not slipping when in contact with the ground. The end of a leg, even when it does not have links constituting a foot, will sometimes be referred to as a *foot*.

The robot is said to be in *flight phase* when there is no contact with the ground and the displacement of the horizontal component of the robot's center of mass is strictly monotonic; sometimes this is referred to as *ballistic motion*.⁵ In the flight phase, the robot has two more degrees of freedom than when it is in the stance phase. In the stance phase, each of the robot's degrees of freedom can be identified with the orientation of a link, while in flight phase, the robot has an additional two degrees of freedom associated with the horizontal and vertical displacements of the center of mass within the sagittal plane. *Running* is defined as alternating phases of single support, flight, and (single-legged) impact, with the additional provision that impact does not occur on the former stance leg, but rather on the former swing leg. Note that during the flight phase, the notion of swing leg is ambiguous and hence one refers to the roles the legs held in the previous single support phase.

With this terminology in mind, complete lists of hypotheses are now enumerated for the robot model, the desired walking and running gaits, and the impact model.

Robot with Point Feet Hypotheses

The robot is assumed to be:

- HR1) comprised of N rigid links connected by $(N - 1)$ ideal revolute joints (i.e., rigid and frictionless) to form a single open kinematic chain; furthermore, each link has nonzero mass and its mass is distributed (i.e., each link is not modeled as a point mass);
- HR2) planar, with motion constrained to the sagittal plane;
- HR3) bipedal, with two symmetric legs connected at a common point called the hip, and both leg ends are terminated in points;
- HR4) independently actuated at each of the $(N - 1)$ ideal revolute joints; and
- HR5) unactuated at the point of contact between the stance leg and ground.

⁵There are no external forces, other than gravity, acting on the robot.

Remark 3.1 The properties of the robot are independent of coordinate choice, but at times it will be convenient to choose the coordinates such that

- HR6) the model is expressed in $N - 1$ *body* coordinates $q_b = (q_1; \dots; q_{N-1})$ plus one *absolute* angular coordinate q_N .

Gait Hypotheses for Walking

Conditions on the controller will be imposed and shown to ensure that the robot's consequent motion satisfies the following properties consistent with the notion of a simple walking gait:

- HGW1) there are alternating phases of single support and double support;
- HGW2) during the single support phase, the stance leg end acts as an ideal pivot, that is, throughout the contact, it can be guaranteed that the vertical component of the ground reaction force is positive and that the ratio of the horizontal component to the vertical component does not exceed the coefficient of static friction;
- HGW3) the double support phase is instantaneous and the associated impact can be modeled as a rigid contact [124];
- HGW4) at impact, the swing leg neither slips nor rebounds, while the former stance leg releases without interaction with the ground;
- HGW5) in steady state, the motion is symmetric with respect to the two legs;
- HGW6) in each step, the swing leg starts from strictly behind the stance leg and is placed strictly in front of the stance leg at impact; and
- HGW7) walking is from left to right and takes place on a level surface.

In particular, Hypotheses HGW5 and HGW6 impose the swapping of the roles of the two legs at impact so that walking does not consist of rocking back and forth on the same support leg. The symmetric nature of the gait is a natural requirement for a simple walking motion, but is not a necessary condition for applying the methods of this book. For example, it is possible to analyze a model of a pathological gait arising from injury or asymmetry. With small extensions to the methodology of this book, it is possible to analyze a model with one passive (prosthetic) knee and one actuated knee.

Remark 3.2 Hypotheses HR1 and HR2 imply the robot has $(N+2)$ -degrees of freedom (DOF) (N joint angles plus the Cartesian coordinates of the hip, for example). Hypothesis HGW2 implies that in single support, the robot has N -DOF (the N joint angles, for example). Hypotheses HR4, HR5 and HGW2 imply that in single support, the robot has one degree of underactuation, i.e., one less actuator than DOF.

Gait Hypotheses for Running

Conditions on the controller will be imposed and shown to ensure that the robot's consequent motion satisfies the following properties consistent with the notion of a simple running gait:

- HGR1) there are alternating phases of single support, flight, and impact;
- HGR2) during the single support phase, the stance leg end acts as an ideal pivot joint, in particular, throughout the contact, it can be guaranteed that the vertical component of the ground reaction force is non-negative and that the ratio of the horizontal component to the vertical component does not exceed the coefficient of static friction;
- HGR3) the center of mass of the robot travels a nonzero horizontal distance during the flight phase;
- HGR4) the flight phase terminates with the former swing leg end impacting the ground;
- HGR5) at impact, the leg end neither slips nor rebounds;
- HGR6) in steady state, the motion over successive single support and flight phases is symmetric with respect to the two legs;
- HGR7) running is from left to right and takes place on a level surface.

Rigid Impact Model Hypotheses

An impact occurs when the swing leg contacts the ground.⁶ The impact is modeled as a contact between two rigid bodies. There are many rigid impact models in the literature [12, 23, 24, 124, 174], and all of them can be used to obtain an expression for the generalized velocity just after the impact of the swing leg with the walking surface in terms of the generalized velocity and position just before the impact. The model from [124] is used here for both walking and running. The model is essentially identical in the two cases. The one difference is noted in the list of hypotheses:

- HI1) an impact results from the contact of the swing leg end with the ground;
- HI2) the impact is instantaneous;
- HI3) the impact results in no rebound and no slipping of the swing leg;

⁶Recall that in running, this means when the former swing leg (i.e., future stance leg) impacts the ground.

- HI4) in the case of walking, at the moment of impact, the stance leg lifts from the ground without interaction,⁷ while in the case of running, at the moment of impact, the former stance leg is not in contact with the ground;
- HI5) the externally applied forces during the impact can be represented by impulses;
- HI6) the actuators cannot generate impulses and hence can be ignored during impact; and
- HI7) the impulsive forces may result in an instantaneous change in the robot's velocities, but there is no instantaneous change in the configuration.

Remark 3.3 To aid in understanding this last assumption, consider the following scalar, second-order linear time-invariant system with an impulsive input at $t = t_0 > 0$,

$$\ddot{x}(t) + a\dot{x}(t) + bx(t) = c\delta(t - t_0), \quad (3.1)$$

where δ is the unit impulse and $a, b, c \in \mathbb{R}$. Integrating (3.1) once yields

$$\dot{x}(t) = \dot{x}(0) + \int_0^t (-a\dot{x}(\tau) - bx(\tau) + c\delta(\tau - t_0)) d\tau \quad (3.2)$$

$$= \dot{x}(0) - ax(t) + ax(0) - \int_0^t bx(\tau) d\tau + c\mathbb{1}(t - t_0) \quad (3.3)$$

where $\mathbb{1}(t)$ is the unit step function and hence $\dot{x}(t)$ is discontinuous at $t = t_0$. Integrating (3.3) yields

$$\begin{aligned} x(t) &= x(0) + \int_0^t (\dot{x}(0) - ax(\sigma) + ax(0)) d\sigma \\ &\quad - \int_0^t \left(\int_0^\sigma bx(\tau) d\tau + c\mathbb{1}(\sigma - t_0) \right) d\sigma \end{aligned} \quad (3.4)$$

$$\begin{aligned} &= x(0) + (\dot{x}(0) + ax(0)) t - \int_0^t ax(\sigma) d\sigma \\ &\quad - \int_0^t \int_0^\sigma bx(\tau) d\tau d\sigma + c(t - t_0)\mathbb{1}(t - t_0). \end{aligned} \quad (3.5)$$

Let x and \dot{x} evaluated at t_0^+ (resp., t_0^-) denote the limits from the right (resp., limits from the left) at time t_0 , and interpret $x(t_0^-)$ and $\dot{x}(t_0^-)$ as the position

⁷The vertical component of the velocity of the swing leg end must be positive after impact.

and velocity just before the impulsive input occurs and $x(t_0^+)$ and $\dot{x}(t_0^+)$ as the position and velocity just after the impulsive input occurs. Equation (3.5) shows that $x(t_0^+) - x(t_0^-) = 0$, implying continuity in position across the impulse (read impact), whereas from (3.3), $\dot{x}(t_0^+) - \dot{x}(t_0^-) = c$, the magnitude of the impulsive input, implying a jump in the velocity across the impulse (read impact).

3.3 Some Remarks on Notation

Throughout this chapter, while developing the dynamic models of walking and running, the generalized coordinates for the stance (or single-support) phase will be denoted by $(q_s; \dot{q}_s)$ and the generalized coordinates for the flight phase of running will be denoted by $(q_f; \dot{q}_f)$. The importance of distinguishing between these two phases is evident when walking and running are being treated in the same chapter. Elsewhere in the book, however, if only walking is being treated, then there is no longer a compelling need to distinguish between stance and flight phases, and the generalized coordinates will be denoted simply by $(q; \dot{q})$; the subscript “*s*” will be dropped in order to simplify the notation.

In general, a point on the robot (or its center of mass) will be denoted by its Cartesian coordinates $p = (p^h; p^v)$ with respect to the inertial frame. Some points and forces of particular interest are identified in Fig. 3.2, namely, the ends of the stance and swing legs, denoted respectively by p_1 and p_2 , the position of the hips, p_H , and the position of the center of mass, p_{cm} . In the stance phase, each of these points can be expressed as smooth functions of the generalized configuration variables, q_s .

For the flight phase of running, it is natural and always possible—though not required—to construct generalized coordinates by starting with a set of generalized coordinates for the stance phase and then appending the Cartesian position and velocity of a single point on the robot (or its center of mass). In this case, in order to emphasize its potential role as an independent variable, we have chosen to denote the point by its “**x-y**” coordinates, as shown in Fig. 3.2(c). In particular, the generalized configuration variables for the flight phase of running will be selected as $q_f = (q_s; \mathbf{x}_{cm}; \mathbf{y}_{cm})$.

Finally, semicolons will be used to form column vectors in-line, for example, $(q_s; \mathbf{x}_{cm}; \mathbf{y}_{cm})$ to denote

$$\begin{bmatrix} q_s \\ \mathbf{x}_{cm} \\ \mathbf{y}_{cm} \end{bmatrix} \quad (3.6)$$

instead of $(q'_s, \mathbf{x}_{cm}, \mathbf{y}_{cm})'$. The utility of avoiding additional superscripts for

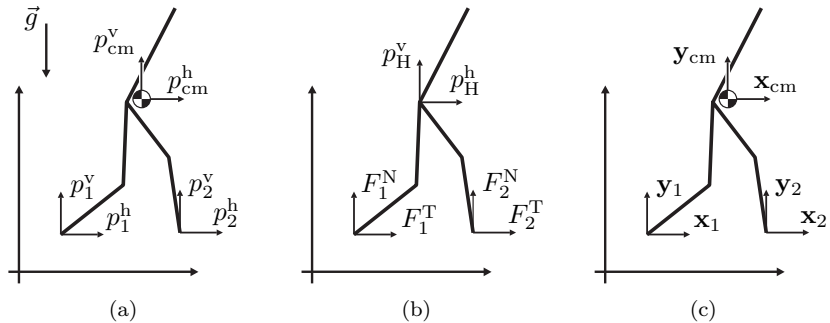


Figure 3.2. Key position and force nomenclature. For any robot satisfying HR1–HR5, the Cartesian positions of the leg ends, hip, and center of mass are identified, as well as possible forces acting on the leg ends. The position nomenclature used in (a) and (b) applies to walking whereas the alternative position nomenclature used in (c) applies to running.

transposes will become clear when the model of the impact phase is treated in Section 3.4.2. The arguments of a multivariable function will continue to be separated by a comma.

3.4 Dynamic Model of Walking

This section develops a mathematical model for the study of a walking gait of a biped satisfying Robot Hypotheses HR1–HR5, Gait Hypotheses HGW1– HGW7, and Impact Hypotheses HI1–HI7. An inertial reference frame is assumed to be given and oriented in the standard manner with respect to gravity. From Hypothesis HGW7, the walking surface is flat, and thus it can be assumed without loss of generality that the ground height is zero with respect to the inertial frame. As in Fig. 3.2(a), let $p_1 = (p_1^h; p_1^v)$ denote the position of the end of leg-1 with respect to the inertial frame and, similarly, let $p_2 = (p_2^h; p_2^v)$ denote the position of the end of leg-2.

3.4.1 Swing Phase Model

The swing phase model corresponds to a pinned open kinematic chain. Since by Hypothesis HGW5, the gait is assumed to be symmetric, it does not matter which leg end is pinned, so assume it is leg-1. The swapping of the roles of leg-1 and leg-2 will be accounted for in the impact model of the next section.

Let \mathcal{Q}_s be the N -dimensional configuration space of the robot when the stance leg end is acting as a pivot and let $q_s := (q_1; \dots; q_N) \in \mathcal{Q}_s$ be a

set of generalized coordinates. The dynamic model is easily obtained with the method of Lagrange, which consists of first computing the kinetic energy and potential energy of each link, and then summing terms to compute the total kinetic energy, K_s , and the total potential energy, V_s ; see [Appendix B.4](#). Denote the Lagrangian by

$$\mathcal{L}_s(q_s, \dot{q}_s) := K_s(q_s, \dot{q}_s) - V_s(q_s). \quad (3.7)$$

Applying the method of Lagrange (see [Appendix B.4.4](#)), the model is written in the form

$$D_s(q_s)\ddot{q}_s + C_s(q_s, \dot{q}_s)\dot{q}_s + G_s(q_s) = B_s(q_s)u. \quad (3.8)$$

The matrix D_s is the inertia matrix; C_s is the Coriolis matrix; G_s is the gravity vector; and B_s maps the joint torques to generalized forces. In accordance with HR4 and HR5, $u := (u_1; \dots; u_{N-1}) \in \mathbb{R}^{(N-1)}$, where u_i is the torque applied between the two links connected by joint- i , *and there is no torque applied between the stance leg and ground*. Letting $\theta_i^{\text{rel}}(q_s)$ denote the relative angle of the i -th actuated joint, the matrix B_s is computed as

$$B_s(q_s) := \left(\frac{\partial}{\partial q_s} \begin{bmatrix} \theta_1^{\text{rel}} \\ \vdots \\ \theta_{N-1}^{\text{rel}} \end{bmatrix} \right)'; \quad (3.9)$$

see (B.147). Under HR6, B_s is

$$B_s = \begin{bmatrix} I_{N-1 \times N-1} \\ 0_{1 \times N-1} \end{bmatrix}, \quad (3.10)$$

and, hence, for every $q_s \in \mathcal{Q}_s$,

$$\text{rank } B_s(q_s) = N - 1. \quad (3.11)$$

The model is written in state space form by defining

$$\dot{x} = \begin{bmatrix} \dot{q}_s \\ D_s^{-1}(q_s) [-C_s(q_s, \dot{q}_s)\dot{q}_s - G_s(q_s) + B_s(q_s)u] \end{bmatrix} \quad (3.12)$$

$$=: f_s(x) + g_s(x)u \quad (3.13)$$

where $x := (q_s; \dot{q}_s)$. The state space of the model is $\mathcal{X}_s = T\mathcal{Q}_s$. Note that for each $x \in T\mathcal{Q}_s$, $g_s(x)$ is a $2N \times (N - 1)$ matrix; its i -th column is denoted by g_{si} . Note also that in natural coordinates $(q_s; \dot{q}_s)$ for $T\mathcal{Q}_s$, g_s is independent of \dot{q}_s , and thus sometimes we abuse notation and write this as $g_s(q_s)$.

It is clear that not all configurations of the model are physically compatible with our notion of the single support phase of walking. For example, with the exception of the end of the stance leg, all points of the robot should be

above the walking surface, and for human-like walking, the knees should not hyperextend. In addition, there are kinetic constraints, such as, for the leg end to act like a pivot, the forces on the leg end must lie in the static friction cone, and the normal component of the reaction force must be positive. These issues will be addressed in the motion design phase of the controller design.

Remark 3.4 A more formal approach to dealing with the issue of “physically admissible” states of the robot’s model is to define them through *viability* or *unilateral constraints* [12,24]: these are scalar valued functions of the states, $\lambda_i : \mathcal{X}_s \rightarrow \mathbb{R}$, chosen in such a way that $x \in \mathcal{X}_s$ is admissible if, and only if, $\lambda_i(x) \geq 0$.

3.4.2 Impact Model

The development of the impact model involves the reaction forces at the leg ends, and thus requires the unpinned or $(N + 2)$ -DOF model of the robot. Let q_s be the generalized coordinates used in the single support model and complete these to a set of generalized coordinates for the unpinned model by letting $p_e = (p_e^h; p_e^v)$ be the Cartesian coordinates of some fixed point on the robot or its center of mass. Using the generalized coordinates $q_e = (q_s; p_e)$, the method of Lagrange results in

$$D_e(q_e)\ddot{q}_e + C_e(q_e, \dot{q}_e)\dot{q}_e + G_e(q_e) = B_e(q_e)u + \delta F_{\text{ext}}, \quad (3.14)$$

where δF_{ext} represents the vector of external forces acting on the robot due to the contact between the swing leg end and the ground. From Hypothesis HI5, these forces are impulsive, hence the notation δF_{ext} . Under Hypotheses HI1–HI7, (3.14) is “integrated” over the “duration” of the impact to obtain [124]

$$D_e(q_e^+)\dot{q}_e^+ - D_e(q_e^-)\dot{q}_e^- = F_{\text{ext}}, \quad (3.15)$$

where $F_{\text{ext}} := \int_{t_-}^{t_+} \delta F_{\text{ext}}(\tau) d\tau$ is the result of integrating the impulsive contact force over the impact duration, \dot{q}_e^- is the velocity just before the impact and \dot{q}_e^+ is the velocity just after the impact; see Remark 3.3. By Hypothesis HI7, the positions do not change during the impact, and thus $q_e^+ = q_e^-$. Equation (3.15) expresses conservation of momentum [124], a point to which we will return during the control analysis.

By definition, the velocity just before impact is determined from the single support model. During the single support phase, p_e , the Cartesian coordinate added to the robot’s body, can be determined from q_s ; denote this by $p_e = \Upsilon_e(q_s)$. Thus

$$q_e^- = \begin{bmatrix} q_s^- \\ \Upsilon_e(q_s^-) \end{bmatrix} \quad (3.16)$$

and

$$\dot{q}_e^- = \begin{bmatrix} I_{N \times N} \\ \frac{\partial}{\partial q_s} \Upsilon_e(q_s^-) \end{bmatrix} \dot{q}_s^- . \quad (3.17)$$

From Hypothesis HI4, F_{ext} is the reaction force at the end of the swing leg, that is, leg-2. Letting $p_2(q_e)$ denote the position of the end of the swing leg with respect to the inertial frame, it follows from the principle of virtual work that

$$F_{\text{ext}} = E_2(q_e^-)' F_2, \quad (3.18)$$

where, $E_2(q_e) = \frac{\partial}{\partial q_e} p_2(q_e)$ and $F_2 = (F_2^T; F_2^N)$ is the vector of forces acting at the end of the swing leg. Note that $E_2(q_e)$ has full rank because p_2 can be written in the form $p_2(q_e) = p_e + \Upsilon_2(q_s)$, and thus, $E_2 = [\partial \Upsilon_2(q_s)/\partial q_s, I_{2 \times 2}]$.

Equation (3.15) represents $(N + 2)$ equations and $(N + 4)$ unknowns; the unknowns are \dot{q}_e^+ , F_2^T , and F_2^N . The two additional required equations come from the no slip and rebound condition of Hypothesis HI3, which may be written as

$$E_2(q_e^-) \dot{q}_e^+ = 0. \quad (3.19)$$

The combined set of equations (3.15) and (3.19) yields

$$\begin{bmatrix} D_e(q_e^-) & -E_2(q_e^-)' \\ E_2(q_e^-) & 0_{2 \times 2} \end{bmatrix} \begin{bmatrix} \dot{q}_e^+ \\ F_2 \end{bmatrix} = \begin{bmatrix} D_e(q_e^-) \dot{q}_e^- \\ 0_{2 \times 1} \end{bmatrix}, \quad (3.20)$$

or,

$$\begin{bmatrix} D_e(q_e^-) & -E_2(q_e^-)' \\ E_2(q_e^-) & 0_{2 \times 2} \end{bmatrix} \begin{bmatrix} \dot{q}_e^+ \\ F_2 \end{bmatrix} = \begin{bmatrix} D_e(q_e^-) \begin{bmatrix} I_{N \times N} \\ \frac{\partial}{\partial q_s} \Upsilon_e(q_s^-) \end{bmatrix} \\ 0_{2 \times N} \end{bmatrix} \dot{q}_s^-, \quad (3.21)$$

where q_e^- is evaluated with (3.16).

Because D_e is positive definite and E_2 is full rank, the matrix on the left-hand side of (3.21) is easily proved to be invertible.⁸ Solving (3.21) yields

$$\begin{bmatrix} \dot{q}_e^+ \\ F_2 \end{bmatrix} = \begin{bmatrix} \bar{\Delta}_{\dot{q}_e}(q_s^-) \\ \Delta_{F_2}(q_s^-) \end{bmatrix} \dot{q}_s^-, \quad (3.22)$$

where,

$$\Delta_{F_2} = - (E_2 D_e^{-1} E_2')^{-1} E_2 \begin{bmatrix} I_{N \times N} \\ \frac{\partial}{\partial q_s} \Upsilon_e(q_s^-) \end{bmatrix} \quad (3.23)$$

⁸Denote the matrix on the left-hand side of (3.21) by Π . Suppose that $(\dot{q}_e; F_2)$ is in the (right) nullspace of Π . Then $\dot{q}_e = D_e^{-1} E_2' F_2$ and $E_2 \dot{q}_e = 0$, which in turn implies that $F_2' E_2 D_e^{-1} E_2' F_2 = 0$. But, D_e positive definite and E_2 full rank imply that $E_2 D_e^{-1} E_2'$ is positive definite. Hence $F_2 = 0$ and $\dot{q}_e = 0$. Therefore, Π is invertible.

and

$$\bar{\Delta}_{\dot{q}_e} = D_e^{-1} E'_2 \Delta_{F_2} + \begin{bmatrix} I_{N \times N} \\ \frac{\partial}{\partial q_s} \Upsilon_e \end{bmatrix}. \quad (3.24)$$

The first N rows of (3.22) should then be used to reinitialize (3.13), the state space model of the single support phase, so that the next step may be undertaken. Since we are assuming a symmetric walking gait, we can avoid having to use two single support models, one for each leg playing the role of the stance leg, by relabeling the coordinates at impact. The coordinates must be relabeled because the roles of the legs must be swapped: the former swing leg is now in contact with the ground and is poised to take on the role of the stance leg. Express the *relabeling* of the generalized coordinates as a matrix, R , acting on q_s with the property that $RR = I$, i.e., R is a circular matrix. The result of the impact and the relabeling of the states is then an expression

$$x^+ = \Delta(x^-) \quad (3.25)$$

where $x^+ := (q_s^+; \dot{q}_s^+)$ (resp. $x^- := (q_s^-; \dot{q}_s^-)$) is the state value just after (resp. just before) impact and

$$\Delta(x^-) := \begin{bmatrix} \Delta_{q_s} q_s^- \\ \Delta_{\dot{q}_s}(q_s^-) \dot{q}_s^- \end{bmatrix}, \quad (3.26)$$

where

$$\Delta_{q_s} := R \quad (3.27)$$

and

$$\Delta_{\dot{q}_s}(q_s^-) := [R \ 0_{N \times 2}] \bar{\Delta}_{\dot{q}_e}(q_s^-). \quad (3.28)$$

Remark 3.5 The validity of the impact model must be checked at each impact. Upon evaluating (3.23) at an impact, it must be verified that $F_2^N > 0$ and $|F_2^T| \leq \mu_s F_2^N$, where μ_s is the assumed coefficient of static friction. In addition, it must be verified that the stance leg “lifts from the ground without interaction,” that is, letting $(p_1^h(q_e); p_1^v(q_e))$ denote the position of the end of the stance leg with respect to the inertial frame, it must be the case that

$$\dot{p}_1^v = \frac{\partial}{\partial q_e} p_1^v(q_e^-) \dot{q}_e^+ \geq 0, \quad (3.29)$$

where \dot{q}_e^+ is determined from (3.22). If any of these three conditions is violated, then the computed post-impact velocity is meaningless and appropriate action must be taken, such as stopping a simulation or redesigning a walking gait.

3.4.3 Hybrid Model of Walking

An overall model of walking is obtained by combining the swing phase model and the impact model to form a system with impulse effects. Assume that the

trajectories of the swing phase model possess finite left and right limits, and denote them by $x^-(t) := \lim_{\tau \nearrow t} x(\tau)$ and $x^+(t) := \lim_{\tau \searrow t} x(\tau)$, respectively. The model is then

$$\Sigma : \begin{cases} \dot{x} = f_s(x) + g_s(x)u & x^- \notin \mathcal{S} \\ x^+ = \Delta(x^-) & x^- \in \mathcal{S}, \end{cases} \quad (3.30)$$

where the switching set is chosen⁹ to be

$$\mathcal{S} := \{(q_s, \dot{q}_s) \in T\mathcal{Q}_s \mid p_2^v(q) = 0, p_2^h(q) > 0\}. \quad (3.31)$$

The mathematical meaning of a solution of the model will be made precise in Section 4.1. In simple words, a trajectory of the hybrid model is specified by the swing phase model until an impact occurs. An impact occurs when the state “attains” the set \mathcal{S} , which represents the walking surface. At this point, the impact of the swing leg with the walking surface results in a very rapid change in the velocity components of the state vector. The impulse model of the impact compresses the impact event into an instantaneous moment in time, resulting in a discontinuity in the velocities.¹⁰ The ultimate result of the impact model is a new initial condition from which the swing phase model evolves until the next impact. In order for the state not to be obliged to take on two values at the “impact time,” the impact event is, roughly speaking, described in terms of the values of the state “just prior to impact” at time “ t^- ,” and “just after impact” at time “ t^+ .¹⁰ These values are represented by the left and right limits, x^- and x^+ , respectively. Solutions are taken to be right continuous and must have finite left and right limits at each impact event. [Figure 3.3](#) gives a graphical representation of this discrete event system.

A *step* of the robot is a solution of (3.30) that starts with the robot in double support, ends in double support with the configurations of the legs swapped, and contains only one impact event. *Walking* is a sequence of steps.

3.4.4 Some Facts on Angular Momentum

At this point, the sign convention for measuring angles with respect to the inertial frame must be discussed. If angles are *positive* when measured in the *clockwise direction*, that is, they increase when rotated clockwise, then the angular momentum of a link rotating clockwise has positive angular momentum. With this convention, when a robot walks left to right, it will have positive angular momentum about its stance leg end. The opposite holds with a *councclockwise* convention. See [Appendix B.4.9](#) for more details on the consequences of making one choice versus another.

⁹Recall that Hypothesis HGW6 specifies the swing leg is placed strictly ahead of the stance leg.

¹⁰The relabeling results in a discontinuity in position, and, after impact, $p_2^h(q) < 0$.

$$p_2^v(x) = 0 \text{ and } p_2^h(x) > 0$$

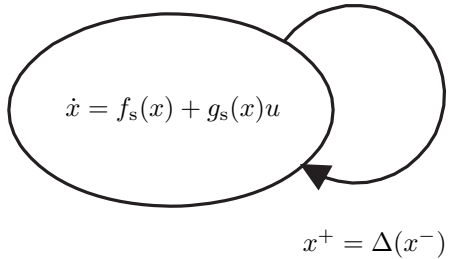


Figure 3.3. Hybrid model of walking with point feet. Key elements are the continuous dynamics of the single support phase, written in state space form as $\dot{x} = f_s(x) + g_s(x)u$, the switching or impact condition, $p_2^v(q) = 0, p_2^h(q) > 0$, which detects when the height of the swing leg above the walking surface is zero and the swing leg is in front of the stance leg, and the reinitialization rule coming from the impact map, Δ .

3.4.4.1 The Role of Gravity in Walking

The modeled robot has no actuation at the leg ends. So, what causes the robot to rotate about the support leg end and thus advance forward in a step? The answer is gravity. Let σ_1 be the angular momentum of the robot about the stance leg end, which is assumed to act as an ideal pivot (i.e., it does not slip and remains in contact with the walking surface). The angular momentum balance theorem says that the time derivative of the angular momentum about a fixed point equals the sum of the moments of the external forces about that point. Since the motor torques act internally to the robot, their contribution to the moment balance is zero, leaving only gravity

$$\dot{\sigma}_1 = \begin{cases} g_0 m_{\text{tot}} (p_{\text{cm}}^h - p_1^h), & \text{clockwise convention} \\ -g_0 m_{\text{tot}} (p_{\text{cm}}^h - p_1^h), & \text{counterclockwise convention,} \end{cases} \quad (3.32)$$

where m_{tot} is the total mass of the robot, g_0 is the gravitational constant, p_{cm}^h is the horizontal component of the position of the center mass, and p_1^h is the horizontal component of the position of the stance foot. In this regard, a robot with point feet functions like a passive bipedal walker [58, 59, 153].

So what is the role of the actuators at the hips, knees, and other joints? The actuators directly act on the shape or posture of the robot, thereby changing the position of the center of mass, and, thus, the moment arm through which gravity acts on the robot. The posture of the robot also has a large effect on the energy lost at impact [125] and whether or not the required contact conditions at the leg ends are respected. The challenge for control design is to bring all of this together in a manner that ensures the creation of a desired asymptotically stable, periodic motion.

3.4.4.2 Momentum Transfer at Impact

The evolution of the angular momentum about the stance foot is explained by (3.32). The effect of an impact on the angular momentum of the robot is investigated next.

As before, let σ_1^- denote the angular momentum about the stance foot just before impact. Let σ_2^- represent the angular momentum about the swing foot just before impact. Then, according to the principle of angular momentum transfer, see (B.153),

$$\sigma_2^- = \sigma_1^- + (p_1^- - p_2^-) \wedge m_{\text{tot}} \dot{p}_{\text{cm}}^-, \quad (3.33)$$

where \wedge is the planar “equivalent” of the vector cross product (see (B.198) when using the clockwise convention and (B.148) when using the counter-clockwise convention for measuring angles), \dot{p}_{cm} is the velocity of the center of mass, and as before, m_{tot} is the total mass of the robot and p_1 and p_2 are the positions of the stance foot and the swing foot, respectively.

At impact, the impulsive reaction force from the ground is applied at the end of the swing leg. Since the force acts at p_2 , σ_2 is not affected by the reaction force, and therefore,

$$\sigma_2^+ = \sigma_2^-, \quad (3.34)$$

before relabeling of the coordinates is taken into account. After relabeling of the coordinates, the roles of the legs are swapped, so σ_2^+ becomes σ_1^+ . This observation combined with (3.34) and (3.33) gives

$$\sigma_1^+ = \sigma_1^- + (p_1^- - p_2^-) \wedge m_{\text{tot}} \dot{p}_{\text{cm}}^-. \quad (3.35)$$

Note that if the robot walks on a level surface (3.35) becomes

$$\sigma_1^+ = \begin{cases} \sigma_1^- + L_s m_{\text{tot}} \dot{p}_{\text{cm}}^{v-}, & \text{clockwise convention} \\ \sigma_1^- - L_s m_{\text{tot}} \dot{p}_{\text{cm}}^{v-}, & \text{counterclockwise convention,} \end{cases} \quad (3.36)$$

where $L_s = p_2^{h-} - p_1^{h-}$ is the step length of the robot and \dot{p}_{cm}^{v-} is the vertical component of the velocity of the center of mass just before impact.

3.4.5 The MPFL-Normal Form

The objective of this subsection is to indicate a set of generalized coordinates and a preliminary state variable feedback that places the swing phase model (3.8) or (3.13) in a particularly convenient form for subsequent analysis. The main idea for the normal form, which is based on partial feedback linearization, is taken from [187, 220].

Choose generalized coordinates $q_s = (q_b; q_N)$, where $q_b = (q_1; \dots; q_{N-1})$ is a set of body coordinates and q_N provides the orientation of the robot with respect to the inertial frame. For example, q_b could be selected as a set of

relative angles, $(\theta_1^{\text{rel}}; \dots; \theta_{N-1}^{\text{rel}})$, and q_N could be the absolute orientation of any link of the robot or the angle of the center of mass with respect to the end of the stance leg. By Proposition B.8 on p. 424, q_N is a cyclic coordinate, meaning that the inertia matrix in (3.8) is independent of q_N , that is, $D_s(q_s) = D_s(q_b)$. Because $\frac{\partial \theta_i^{\text{rel}}}{\partial q_N} \equiv 0$, $1 \leq i \leq N-1$, (3.9) and (3.11) together imply that the input matrix has the form

$$B_s(q_s) = \begin{bmatrix} B_1(q_b) \\ 0 \end{bmatrix}, \quad (3.37)$$

where $B_1(q_b)$ is a square and invertible matrix for all $(q_b; q_N) \in \mathcal{Q}_s$.

Let $\Omega(q_s, \dot{q}_s) := C_s(q_s, \dot{q}_s)\dot{q}_s + G_s(q_s)$ and partition the model (3.8) as

$$\begin{aligned} D_{11}(q_b)\ddot{q}_b + D_{12}(q_b)\ddot{q}_N + \Omega_1(q_s, \dot{q}_s) &= B_1(q_b)u \\ D_{21}(q_b)\ddot{q}_b + D_{22}(q_b)\ddot{q}_N + \Omega_2(q_s, \dot{q}_s) &= 0. \end{aligned} \quad (3.38)$$

For later use, we note that

$$\begin{aligned} D_{21}(q_b) &= [d_{N1}(q_b), \dots, d_{NN-1}(q_b)] \\ D_{22}(q_b) &= d_{NN}(q_b), \end{aligned} \quad (3.39)$$

where d_{ij} is the ij -element of D_s . Because D_s is positive definite, D_{11} and D_{22} are both positive definite and hence invertible. Define

$$\bar{D} := D_{11} - D_{12}D_{22}^{-1}D_{21} \quad J^{\text{norm}} := D_{22}^{-1}D_{21} \quad (3.40)$$

$$\bar{\Omega}_1 := \Omega_1 - D_{12}D_{22}^{-1}\Omega_2 \quad \bar{\Omega}_2 := -D_{22}^{-1}\Omega_2. \quad (3.41)$$

Then the regular¹¹ static state feedback

$$u = B_1^{-1}(q_b) (\bar{D}(q_b)v + \bar{\Omega}_1(q_s, \dot{q}_s)), \quad (3.42)$$

results in

$$\begin{aligned} \ddot{q}_b &= v \\ \ddot{q}_N &= \bar{\Omega}_2(q_s, \dot{q}_s) - J^{\text{norm}}(q_b)v, \end{aligned} \quad (3.43)$$

which is called the *Partial-Feedback-Linearized (PFL)* normal form. Because $D_{22} = d_{NN}$ is scalar, recall Hypothesis HR4, computing the various terms defined in (3.40) is straightforward.

Expressing (3.43) in state variable form using $x := (q_s; \dot{q}_s)$, results in

$$\dot{x} = \begin{bmatrix} \dot{q}_s \\ v \\ \bar{\Omega}_2(q_s, \dot{q}_s) - J^{\text{norm}}(q_b)v \end{bmatrix} \quad (3.44)$$

$$=: \tilde{f}_s(x) + \tilde{g}_s(x)v. \quad (3.45)$$

¹¹In general, a static state variable feedback $u = \alpha(x) + \beta(x)v$ is said to be *regular* if $\beta(x)$ is square and invertible. The feedback defined in (3.42) is regular because the matrix multiplying the new input, v , is the product of two invertible matrices; indeed, $(\det \bar{D}) d_{NN} = \det D_s$ and D_s is positive definite.

The above state variable model is precisely the result of applying the state variable feedback (3.42) to the state variable model (3.13). An advantage of this form of the model over (3.13) is that (3.45) can be computed without inverting the inertia matrix. Secondly, it can be advantageous to design a state variable feedback controller in a two stage process: first, determine $v = \gamma(x)$ on the basis of (3.45), because this form of the model typically has many fewer terms than (3.13), and then determine the equivalent feedback controller for (3.13) as

$$u = B_1^{-1}(q_b) (\bar{D}(q_b)\gamma(x) + \bar{\Omega}_1(q_s, \dot{q}_s)). \quad (3.46)$$

An even more convenient normal form for the state variable model (3.8) is obtained from (3.43) by a simple coordinate change. Denote the generalized momentum conjugate to q_N by $\bar{\sigma}_N = \frac{\partial \mathcal{L}_s}{\partial \dot{q}_N}$; see (B.181). From (B.182),

$$\bar{\sigma}_N = \sum_{k=1}^N d_{N,k}(q_1, \dots, q_{N-1}) \dot{q}_k. \quad (3.47)$$

Because there is no actuation at the stance leg end and q_N is cyclic,

$$\dot{\bar{\sigma}}_N = -\frac{\partial V_s}{\partial q_N}(q). \quad (3.48)$$

Using (3.47) and (3.48), the normal form (3.43) can be expressed as

$$\begin{aligned} \ddot{q}_b &= v \\ \dot{q}_N &= \frac{\bar{\sigma}_N}{d_{N,N}(q_b)} - J^{\text{norm}}(q_b) \dot{q}_b \\ \dot{\bar{\sigma}}_N &= -\frac{\partial V_s}{\partial q_N}(q_b, q_N), \end{aligned} \quad (3.49)$$

which will be called the *Mixed-Partial-Feedback-Linearized (MPFL)*¹² normal form. Define

$$\varpi_s := \begin{bmatrix} \dot{q}_b \\ \bar{\sigma}_N \end{bmatrix} = \underbrace{\begin{bmatrix} I_{N-1 \times N-1} & 0_{N-1 \times 1} \\ d_{N,N}(q_b) J^{\text{norm}}(q_b) & d_{N,N}(q_b) \end{bmatrix}}_{M(q_b)} \begin{bmatrix} \dot{q}_b \\ \dot{q}_N \end{bmatrix} \quad (3.50)$$

and note that

$$\underbrace{\begin{bmatrix} \dot{q}_b \\ \dot{q}_N \end{bmatrix}}_{\dot{q}_s} = \underbrace{\begin{bmatrix} I_{N-1 \times N-1} & 0_{N-1 \times 1} \\ -J^{\text{norm}}(q_b) & \frac{1}{d_{N,N}(q_b)} \end{bmatrix}}_{M^{-1}(q_b)} \underbrace{\begin{bmatrix} \dot{q}_b \\ \bar{\sigma}_N \end{bmatrix}}_{\varpi_s}. \quad (3.51)$$

¹²The normal form (3.49) *mixes* the Lagrangian and Hamiltonian formalisms because it uses angular velocity and momentum.

Writing the model (3.49) in state variable form, with $\tilde{x} := (q_s; \varpi_s)$, results in

$$\begin{aligned}\dot{\tilde{x}} &= \begin{bmatrix} \dot{q}_b \\ \frac{\bar{\sigma}_N}{d_{N,N}(q_b)} - J^{\text{norm}}(q_b)\dot{q}_b \\ v \\ -\frac{\partial V_s}{\partial q_N}(q_b, q_N) \end{bmatrix} \\ &=: \tilde{f}_s(\tilde{x}) + \tilde{g}_s(\tilde{x})v.\end{aligned}\quad (3.52)$$

Because a change of state variables has been made, the feedback required to go from (3.8) to (3.53) is given by (3.42) with \dot{q}_s given in terms of ϖ_s , per (3.51). The impact map must be modified as well to take into account the change of coordinates, so that (3.26) becomes

$$\tilde{\Delta}(\tilde{x}^-) := \begin{bmatrix} \tilde{\Delta}_{q_s} q_s^- \\ \tilde{\Delta}_{\varpi_s}(q_s^-) \varpi_s^- \end{bmatrix} \quad (3.54)$$

where

$$\tilde{\Delta}_{q_s} := R \quad (3.55)$$

is unchanged from (3.27), while (3.28) becomes

$$\tilde{\Delta}_{\varpi_s}(q_s^-) := [RM(q_b) \ 0_{N \times 2}] \tilde{\Delta}_{\dot{q}_e}(q_s^-) M^{-1}(q_b). \quad (3.56)$$

The overall model with impulse effects is

$$\tilde{\Sigma} : \begin{cases} \dot{\tilde{x}} = \tilde{f}_s(\tilde{x}) + \tilde{g}_s(\tilde{x})u & \tilde{x}^- \notin \mathcal{S} \\ \tilde{x}^+ = \tilde{\Delta}(\tilde{x}^-) & \tilde{x}^- \in \mathcal{S}, \end{cases} \quad (3.57)$$

where the switching set is unchanged from (3.31).

3.4.6 Example Walker Models

This section presents three bipedal robot models of increasing complexity. The first and third models will be used repeatedly.

3.4.6.1 The Acrobot as a Walker: A Two-link Example Model

The *Acrobot* is a simple biped model that will be used to illustrate key points developed in later chapters. In the passive bipedal robot literature, it is usually known as a *compass model* or a compass-gait biped. The model consists of two symmetric links with a single actuator at the link connection point, the hip; see Fig. 3.4. In the swing phase, the model corresponds to that of the Acrobot [17, 93, 215] with symmetric links. It is very similar to the simplest walking model of Garcia et al. [84], except that the mass is distributed along the leg as opposed to being concentrated at the hip.

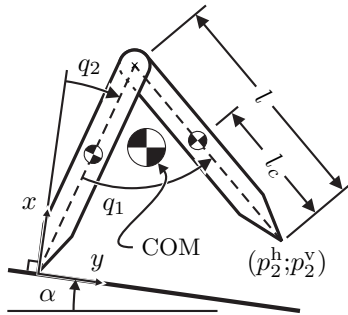


Figure 3.4. Schematic indicating the definition of the generalized coordinates and the mechanical data of a two-link bipedal robot. The legs are symmetric, with length l , and with center of mass location l_c . The ground slope is α . The dynamics during the single support phase is that of the Acrobot [215].

Because of its extremely simple morphology, this is not a physically realizable model of bipedal walking: with equal leg lengths, the swing foot will scuff, i.e., prematurely contact the walking surface. Common arguments for overcoming this deficiency involve assumptions of small, retractable leg ends which allow the swing leg to be shortened enough to achieve ground clearance [98], or, the observation that in three-dimensions, frontal plane hip sway would allow foot clearance [143]. The interest here is not the physical realizability of this model, but its illustrative utility since it is the simplest model for walking which satisfies HR1–HR5.

A detailed derivation of the Acrobot using the method of Lagrange can be found in [Appendix B.4.11](#). Specializing the model to the case of symmetric legs¹³ and using the coordinates of Fig. 3.4 yields the equations of motion during the swing phase; they are given by (3.8) with

$$(D_s(q_1))_{1,1} = (l - l_c)^2 m + I \quad (3.58a)$$

$$(D_s(q_1))_{1,2} = m l(l - l_c) \cos(q_1) - (l - l_c)^2 m - I \quad (3.58b)$$

$$(D_s(q_1))_{2,2} = -2 m l(l - l_c) \cos(q_1) + (2(l_c^2 + l^2) - 2 l_c l) m + 2 I, \quad (3.58c)$$

with the remaining entries of D_s completed by symmetry. The nonzero entries of C_s are

$$(C_s(q_1, \dot{q}_1))_{1,2} = -m l \sin(q_1)(l - l_c) \dot{q}_2 \quad (3.59a)$$

$$(C_s(q_1, \dot{q}_2))_{2,1} = -m l \sin(q_1)(l - l_c)(\dot{q}_1 - \dot{q}_2) \quad (3.59b)$$

$$(C_s(q_1, \dot{q}_2))_{2,2} = m l \sin(q_1)(l - l_c) \dot{q}_1. \quad (3.59c)$$

¹³More precisely, the following substitutions should be made: $m_1 = m_2 = m$, $J_{cm,1} = J_{cm,2} = I$, $L_1 = L_2 = l$, $\ell_{cm,1}^h = l_c$, $\ell_{cm,2}^h = l - l_c$, q_1 becomes $\pi - q_1$, and q_2 becomes $3\pi/2 - q_2$.

Table 3.1. Parameters of the two-link model.

| Parameter | Units | Value |
|------------------------------------|-------------------|-------|
| Leg length, l | m | 1.0 |
| Leg COM location, l_c | m | 0.8 |
| Leg mass, m | kg | 0.3 |
| Leg inertia about leg COM, I | kg·m ² | 0.03 |
| Acceleration due to gravity, g_0 | m/s ² | 9.81 |

The vector G_s and the input matrix B_s are given by

$$(G_s(q_1, q_2))_1 = m g_0 \sin(q_1 - q_2 - \alpha)(l - l_c) \quad (3.60a)$$

$$(G_s(q_1, q_2))_2 = m g_0 ((l_c - l) \sin(q_1 - q_2 - \alpha) - \sin(q_2 + \alpha)(l_c + l)) \quad (3.60b)$$

and

$$B_s = \begin{bmatrix} 1 \\ 0 \end{bmatrix}. \quad (3.61)$$

The state space is taken as

$$T\mathcal{Q}_s := \{x := (q_1; q_2; \dot{q}_1; \dot{q}_2) \mid (q_1; q_2) \in \mathcal{Q}_s, (\dot{q}_1; \dot{q}_2) \in \mathbb{R}^2\} \quad (3.62)$$

where \mathcal{Q}_s is an open subset of $(-\pi/2, \pi/2) \times (0, 2\pi)$. The model parameters are given in Table 3.1. The parameters were taken from [84, Tab. 4.1]. Note that D_s is independent of q_2 , which is the case for any N -link robot satisfying HR1–HR5 when the coordinates are chosen as $(N - 1)$ shape (relative) coordinates plus one absolute coordinate, i.e., a coordinate referencing the angle of a point on the robot to a world coordinate frame. This will be important for the zero dynamics development in [Chapter 5](#).

Following the procedure of Section 3.4.2, the impact model is computed to be

$$\Delta_q = R = \begin{bmatrix} -1 & 0 \\ -1 & 1 \end{bmatrix} \quad (3.63)$$

and

$$\begin{aligned} (\Delta_{\dot{q}})_{1,1} &= \frac{1}{\text{den}} (l_c l m - I - m l_c^2) [m l l_c \cos(q_1) - m l^2 \cos(q_1) \\ &\quad + I + m l^2 + m l_c^2 - 2 l_c l m] \end{aligned} \quad (3.64a)$$

$$\begin{aligned} (\Delta_{\dot{q}})_{1,2} &= \frac{-l_c l m}{\text{den}} [m l^2 + 2 I + m l^2 \cos(2q_1) - 3 l_c l m \\ &\quad - 2 m l^2 \cos(q_1) - m l_c l \cos(2q_1) - 2 m \cos(q_1) l_c^2 \\ &\quad + 4 m l l_c \cos(q_1) + 2 m l_c^2 - 2 I \cos(q_1)] \end{aligned} \quad (3.64b)$$

Table 3.2. Parameters of the three-link model.

| Parameter | Units | Value |
|------------------------------------|------------------|-------|
| Torso length, l | m | 0.5 |
| Leg length, r | m | 1.0 |
| Torso mass, M_T | kg | 10 |
| Hip mass, M_H | kg | 15 |
| Leg mass, m | kg | 5 |
| Acceleration due to gravity, g_0 | m/s ² | 9.81 |

$$(\Delta_{\dot{q}})_{2,1} = \frac{1}{\text{den}}(-I + l_c l m - m l_c^2)(m l^2 + m l_c^2 + I - 2 l_c l m) \quad (3.64c)$$

$$\begin{aligned} (\Delta_{\dot{q}})_{2,2} = & \frac{1}{\text{den}} [m^2 l^3 l_c \cos(q_1) - 3 I l_c l m + I l_c l m \cos(q_1) \\ & + m l^2 I + m l^2 I \cos(q_1) + m^2 l_c^3 l \cos(q_1) \\ & - 2 m^2 l^2 \cos(q_1) l_c^2 - m^2 l^3 l_c + 3 m^2 l^2 l_c^2 \\ & - 3 m^2 l_c^3 l + 2 m l_c^2 I + m^2 l_c^4 + I^2] \end{aligned} \quad (3.64d)$$

$$\begin{aligned} \text{den} = & -m^2 l^4 \cos(q_1)^2 - 2 I l_c l m + 2 m^2 l^3 l_c \cos(q_1)^2 \\ & - m^2 l^2 l_c^2 \cos(q_1)^2 + m^2 l^4 + 2 m l^2 I - 2 m^2 l^3 l_c \\ & + 2 m^2 l^2 l_c^2 - 2 m^2 l_c^3 l + 2 m l_c^2 I + m^2 l_c^4 + I^2. \end{aligned} \quad (3.64e)$$

Using (3.49), the MPFL-normal form is

$$\begin{aligned} \ddot{q}_1 &= v_1 \\ \dot{q}_2 &= \frac{\bar{\sigma}_2}{(D_s(q_1))_{2,2}} - \frac{(D_s(q_1))_{2,1}}{(D_s(q_1))_{2,2}} \dot{q}_1 \\ \dot{\bar{\sigma}}_2 &= -(G_s(q))_2, \end{aligned} \quad (3.65)$$

where the required elements of the dynamic model are obtained from (3.58) and (3.60b). Clearly, (3.65) is much simpler than (3.8) with (3.58)–(3.60).

3.4.6.2 Three-Link Walker

A *three-link walker* is depicted in Fig. 3.5. Like the Acrobot, the robot has no knees and hence suffers from scuffing. Whereas the uncontrolled Acrobot is known to possess stable walking motions (i.e., asymptotically stable periodic orbits) when walking down a sufficiently gentle constant slope, this robot model does not possess any stable walking motions without feedback control. The three-link walker provides the simplest example where torso stabilization is important. The model is given in two sets of coordinates. The model parameters are given in Table 3.2.

Consider first the coordinates shown in Fig. 3.5(a), where $q = (\theta_1; \theta_2; \theta_3)$ and the θ_i are absolute orientations of the various links. The stance leg is

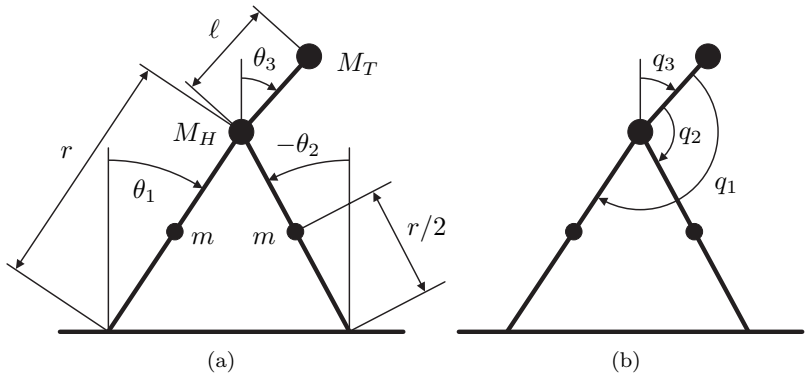


Figure 3.5. Schematic indicating the definition of the generalized coordinates and the mechanical data of a three-link bipedal robot. All masses are lumped. The legs are symmetric, with length r , and the mass of each leg is lumped at $r/2$. The distance from the hips to the center of mass of the torso is denoted by ℓ . In (a), the model is indicated in a set of absolute coordinates, that is θ_1 , θ_2 , and θ_3 are each referenced with respect to the inertial frame. The label $-\theta_2$ indicates that the angle is negative as labeled. In (b), the model is indicated in body (also called shape) coordinates, where q_1 and q_2 are measured relative to the body and only q_3 is referenced to the inertial frame.

the leg parameterized with θ_1 . Applying the method of Lagrange yields the following data for the model (3.8):

$$(D_s(q))_{1,1} = \left(\frac{5}{4}m + M_H + M_T \right) r^2 \quad (3.66a)$$

$$(D_s(q))_{1,2} = -\frac{1}{2}mr^2 \cos(\theta_1 - \theta_2) \quad (3.66b)$$

$$(D_s(q))_{1,3} = M_T r \ell \cos(\theta_1 - \theta_3) \quad (3.66c)$$

$$(D_s(q))_{2,2} = \frac{1}{4}mr^2 \quad (3.66d)$$

$$(D_s(q))_{2,3} = 0 \quad (3.66e)$$

$$(D_s(q))_{3,3} = M_T \ell^2, \quad (3.66f)$$

with the remaining entries completed by symmetry. The inertia matrix depends on all three of the generalized coordinates, θ_1 , θ_2 , and θ_3 . The nonzero entries of C_s are

$$(C_s(q, \dot{q}))_{1,2} = -\frac{1}{2}mr^2 \sin(\theta_1 - \theta_2) \dot{\theta}_2 \quad (3.67a)$$

$$(C_s(q, \dot{q}))_{1,3} = M_T r \ell \sin(\theta_1 - \theta_3) \dot{\theta}_3 \quad (3.67b)$$

$$(C_s(q, \dot{q}))_{2,1} = \frac{1}{2}mr^2 \sin(\theta_1 - \theta_2) \dot{\theta}_1 \quad (3.67c)$$

$$(C_s(q, \dot{q}))_{3,1} = -M_T r \ell \sin(\theta_1 - \theta_3) \dot{\theta}_1. \quad (3.67d)$$

The vector G_s and the input matrix B_s are given by

$$G_s = \begin{bmatrix} -\frac{1}{2}g_0(2M_H + 3m + 2M_T)r \sin(\theta_1) \\ \frac{1}{2}g_0mr \sin(\theta_2) \\ -g_0M_Tl \sin(\theta_3) \end{bmatrix} \quad (3.68)$$

and

$$B_s = \begin{bmatrix} -1 & 0 \\ 0 & -1 \\ 1 & 1 \end{bmatrix}. \quad (3.69)$$

Following the procedure of Section 3.4.2, the impact model is computed to be

$$\Delta_q = R = \begin{bmatrix} 0 & 1 & 0 \\ 1 & 0 & 0 \\ 0 & 0 & 1 \end{bmatrix} \quad (3.70)$$

and

$$(\Delta_{\dot{q}})_{1,1} = \frac{1}{\text{den}} [2M_T \cos(-\theta_1 + 2\theta_3 - \theta_2) - (2m + 4M_H + 2M_T) \cos(\theta_1 - \theta_2)] \quad (3.71a)$$

$$(\Delta_{\dot{q}})_{1,2} = \frac{m}{\text{den}} \quad (3.71b)$$

$$(\Delta_{\dot{q}})_{1,3} = 0 \quad (3.71c)$$

$$(\Delta_{\dot{q}})_{2,1} = \frac{1}{\text{den}} [m - (4m + 4M_H + 2M_T) \cos(2\theta_1 - 2\theta_2) + 2M_T \cos(2\theta_1 - 2\theta_3)] \quad (3.71d)$$

$$(\Delta_{\dot{q}})_{2,2} = \frac{1}{\text{den}} 2m \cos(\theta_1 - \theta_2) \quad (3.71e)$$

$$(\Delta_{\dot{q}})_{2,3} = 0 \quad (3.71f)$$

$$(\Delta_{\dot{q}})_{3,1} = \frac{r}{\ell \text{den}} [(2m + 2M_H + 2M_T) \cos(\theta_3 + \theta_1 - 2\theta_2) - (2m + 2M_H + 2M_T) \cos(-\theta_1 + \theta_3) + m \cos(-3\theta_1 + 2\theta_2 + \theta_3)] \quad (3.71g)$$

$$(\Delta_{\dot{q}})_{3,2} = -\frac{r}{\ell \text{den}} m \cos(-\theta_2 + \theta_3) \quad (3.71h)$$

$$(\Delta_{\dot{q}})_{3,3} = 1 \quad (3.71i)$$

$$\text{den} = -3m - 4M_H - 2M_T + 2m \cos(2\theta_1 - 2\theta_2) + 2M_T \cos(-2\theta_2 + 2\theta_3). \quad (3.71j)$$

Consider next the coordinates shown in Fig. 3.5(b), where $q = (q_1; q_2; q_3)$, with q_1 and q_2 relative angles and q_3 the absolute orientation of the torso. From the diagram, it follows that

$$\begin{bmatrix} \theta_1 \\ \theta_2 \\ \theta_3 \end{bmatrix} = \begin{bmatrix} 1 & 0 & 1 \\ 0 & 1 & 1 \\ 0 & 0 & 1 \end{bmatrix} \begin{bmatrix} q_1 \\ q_2 \\ q_3 \end{bmatrix} - \begin{bmatrix} \pi \\ \pi \\ 0 \end{bmatrix} \quad (3.72)$$

and

$$\begin{bmatrix} q_1 \\ q_2 \\ q_3 \end{bmatrix} = \begin{bmatrix} 1 & 0 & -1 \\ 0 & 1 & -1 \\ 0 & 0 & 1 \end{bmatrix} \begin{bmatrix} \theta_1 \\ \theta_2 \\ \theta_3 \end{bmatrix} + \begin{bmatrix} \pi \\ \pi \\ 0 \end{bmatrix}. \quad (3.73)$$

The model in the new coordinates can be obtained either by re-deriving the Lagrangian in the new coordinates, or by applying relations (B.203)–(B.205) for canonical changes of coordinates. The resulting model is

$$(D_s(q))_{1,1} = \left(\frac{5m}{4} + M_H + M_T \right) r^2 \quad (3.74a)$$

$$(D_s(q))_{1,2} = -\frac{1}{2}mr^2 \cos(q_1 - q_2) \quad (3.74b)$$

$$(D_s(q))_{1,3} = \left(\frac{5}{4}m + M_H + M_T - \frac{m}{2} \cos(q_1 - q_2) \right) r^2 - M_T r \ell \cos(q_1) \quad (3.74c)$$

$$(D_s(q))_{2,2} = \frac{1}{4}mr^2 \quad (3.74d)$$

$$(D_s(q))_{2,3} = \left(\frac{m}{4} - \frac{m}{2} \cos(q_1 - q_2) \right) r^2 \quad (3.74e)$$

$$(D_s(q))_{3,3} = \left(M_H + \frac{3m}{2} + M_T - m \cos(q_1 - q_2) \right) r^2 - 2M_T r \ell \cos(q_1) + M_T \ell^2, \quad (3.74f)$$

with the remaining entries completed by symmetry. Note that in these coordinates, D_s is independent of q_3 . The nonzero entries of C_s are

$$(C_s(q, \dot{q}))_{1,2} = -\frac{1}{2}mr^2 \sin(q_1 - q_2)(\dot{q}_2 + \dot{q}_3) \quad (3.75a)$$

$$(C_s(q, \dot{q}))_{1,3} = -\frac{r}{2} (mr \sin(q_1 - q_2)\dot{q}_2 + mr \sin(q_1 - q_2)\dot{q}_3) \quad (3.75b)$$

$$+ 2M_T r \ell \sin(q_1) \dot{q}_3 \quad (3.75c)$$

$$(C_s(q, \dot{q}))_{2,1} = \frac{1}{2}mr^2 \sin(q_1 - q_2)(\dot{q}_1 + \dot{q}_3) \quad (3.75d)$$

$$(C_s(q, \dot{q}))_{2,3} = \frac{1}{2}mr^2 \sin(q_1 - q_2)(\dot{q}_1 + \dot{q}_3) \quad (3.75e)$$

$$(C_s(q, \dot{q}))_{3,1} = \frac{1}{2} (mr^2 \sin(q_1 - q_2) + 2M_T r \ell \sin(q_1)) (\dot{q}_1 + \dot{q}_3) \quad (3.75f)$$

$$(C_s(q, \dot{q}))_{3,2} = -\frac{1}{2}mr^2 \sin(q_1 - q_2)(\dot{q}_2 + \dot{q}_3) \quad (3.75g)$$

$$\begin{aligned} (C_s(q, \dot{q}))_{3,3} = & \frac{1}{2} (mr^2 \sin(q_1 - q_2)\dot{q}_1 + 2M_T r \ell \sin(q_1)\dot{q}_1 \\ & - mr^2 \sin(q_1 - q_2)\dot{q}_2). \end{aligned} \quad (3.75h)$$

The vector G_s and the input matrix B_s are given by

$$(G_s(q))_1 = \frac{1}{2}g_0(3m + 2M_H + 2M_T)r \sin(q_1 + q_3) \quad (3.76a)$$

$$(G_s(q))_2 = -\frac{1}{2}g_0mr \sin(q_2 + q_3) \quad (3.76b)$$

$$\begin{aligned} (G_s(q))_3 = & \frac{1}{2}g_0 ((2M_H + 2M_T + 3m)r \sin(q_1 + q_3) - mr \sin(q_2 + q_3)) \\ & - g_0 M_T \ell \sin(q_3) \end{aligned} \quad (3.76c)$$

and

$$B_s = \begin{bmatrix} -1 & 0 \\ 0 & -1 \\ 0 & 0 \end{bmatrix}. \quad (3.77)$$

Similarly, the impact map can be re-derived in the new coordinates. It is most easily obtained by applying the change of coordinates (3.72) and (3.73) to (3.70) and (3.71).

The MPFL-normal form is easily determined in the coordinates of Fig. 3.5(b). From (3.49), the normal form is

$$\begin{aligned} \ddot{q}_1 &= v_1 \\ \ddot{q}_2 &= v_2 \\ \ddot{q}_3 &= \frac{\bar{\sigma}_3}{(D_s(q_1, q_2))_{3,3}} - \frac{(D_s(q_1, q_2))_{3,1}}{(D_s(q_1, q_2))_{3,3}}\dot{q}_1 - \frac{(D_s(q_1, q_2))_{3,2}}{(D_s(q_1, q_2))_{3,3}}\dot{q}_2 \\ \dot{\bar{\sigma}}_3 &= -(G_s(q))_3, \end{aligned} \quad (3.78)$$

where the four required elements of the dynamic model are read from (3.74a) through (3.76c). Clearly, (3.78) is much simpler than (3.8).

3.4.6.3 Five-Link Model: RABBIT

A model of the five-link walker RABBIT is developed in Section 6.6.2.1. The detailed equations of motion are given in Appendix E. While the equations of motion for the two-link and three-link walker models can be derived by hand, symbolic tools are necessary for RABBIT. Having the equations of motion available in symbolic form is useful when performing the calculations required for the control laws developed in later chapters. Computing the impact model in closed form (symbolically or otherwise) is not necessary and has not been done for RABBIT; instead, (3.26) is evaluated numerically.

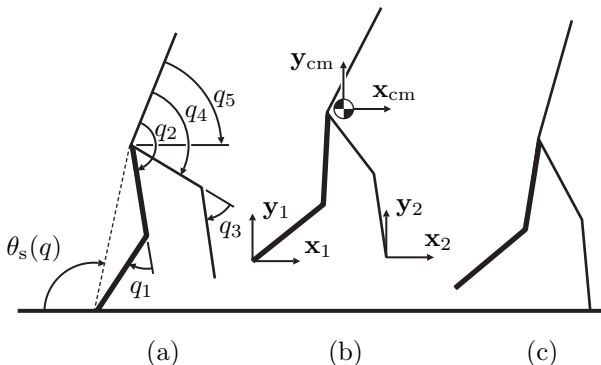


Figure 3.6. Different phases of running with coordinate conventions labeled on an example five-link model. The robot is shown (a) at the end of the stance phase; (b) during flight; and (c) at the beginning of the stance phase just after impact. To avoid clutter, the coordinate conventions have been spread out over the single support and flight phases even though they apply to all three phases. leg-1 is presented in bold. Angles are positive in the clockwise direction.

3.5 Dynamic Model of Running

This section develops a mathematical model for the study of a running gait of a biped satisfying Robot Hypotheses HR1–HR5, Gait Hypotheses HGR1–HGR7, and Impact Hypotheses HI1–HI7. The development parallels the corresponding section on walking models. As in Section 3.4, an inertial reference frame is assumed to be given and oriented in the standard manner with respect to gravity. From Hypothesis HGR7, the running surface is flat, and thus it can be assumed without loss of generality that ground height is zero with respect to the inertial frame. Furthermore, it will be assumed that all angles are positive in the clockwise direction.

As in Fig. 3.2, let $(\mathbf{x}_1; \mathbf{y}_1)$ denote the position of the end of leg-1 with respect to the inertial frame, let $(\mathbf{x}_2; \mathbf{y}_2)$ denote the position of the end of leg-2, and let $(\mathbf{x}_{cm}; \mathbf{y}_{cm})$ denote the position of the center of mass.

Recall that the robot is said to be in *flight phase* when there is no contact with the ground, and in *stance phase* when one leg end is in stationary contact with the ground (that is, the leg end is acting as an ideal pivot) and the other leg is free. For the stance phase, the leg in contact with the ground is called the *stance leg* and the other leg is the *swing leg*.

In the flight phase, the robot has $N + 2$ degrees of freedom (DOF): a degree of freedom associated with the orientation of each link, plus two DOF associated with the horizontal and vertical displacement of the center of mass

within the sagittal plane. The state vector of the dynamical model is thus $2(N + 2)$ -dimensional: there are $N + 2$ configuration variables required to describe the position of the robot, plus the associated velocities. In the stance phase, the robot has only N DOF because the position of the center of mass is determined by the orientation of the N links (plus a horizontal, constant offset of the stance leg end with respect to the origin of the inertial frame). The state vector of the dynamical model is thus $2N$ -dimensional.

3.5.1 Flight Phase Model

The flight phase model corresponds to a free open kinematic chain. The model will be presented in a particular set of body coordinates. Let $q_b = (q_1; \dots; q_{N-1})$ be $N - 1$ relative angles of the actuated joints, as shown in Fig. 3.6. The coordinates q_b describe the shape of the biped and are referenced to the body of the biped and not the inertial frame. Let the biped's absolute orientation with respect to the inertial frame be given by q_N , with a clockwise convention adopted for angle measurement.¹⁴ The biped's absolute position is specified by the Cartesian coordinates of the center of mass, $(\mathbf{x}_{cm}; \mathbf{y}_{cm})$. The vector of generalized coordinates is denoted as $q_f := (q_b; q_N; \mathbf{x}_{cm}; \mathbf{y}_{cm})$.

The dynamic model is easily obtained with the method of Lagrange, which consists of first computing the kinetic energy and potential energy of each link, and then summing terms to compute the total kinetic energy, K_f , and the total potential energy, V_f ; see Appendix B.4. The Lagrangian is defined as $\mathcal{L}_f = K_f - V_f$, and the dynamical model is determined from Lagrange's equation

$$\frac{d}{dt} \frac{\partial \mathcal{L}_f}{\partial \dot{q}_f} - \frac{\partial \mathcal{L}_f}{\partial q_f} = \Gamma_f, \quad (3.79)$$

where Γ_f is the vector of generalized forces and torques applied to the robot.

In terms of the generalized coordinates of the robot, q_f , the total kinetic energy becomes

$$K_f = \frac{1}{2} \dot{q}_f^T D_f(q_b) \dot{q}_f, \quad (3.80)$$

where

$$D_f = \begin{bmatrix} A(q_b) & 0_{N \times 2} \\ 0_{2 \times N} & m_{tot} I_{2 \times 2} \end{bmatrix}, \quad (3.81)$$

m_{tot} is the total mass of the robot, and A depends only on q_b because the total kinetic energy is invariant under rotations and translations of the body; see Proposition B.10. The potential energy is

$$V_f = m_{tot} g_0 \mathbf{y}_{cm}. \quad (3.82)$$

¹⁴This convention only applies to q_N . Because the angles in q_b are not referenced to the inertial frame, any convention can be used.

The principle of virtual work yields that the external torques are

$$\Gamma_f = B_f u = \begin{bmatrix} I_{N-1 \times N-1} \\ 0_{3 \times N-1} \end{bmatrix} u, \quad (3.83)$$

where u is the vector of actuator torques applied at the $N - 1$ actuated joints of the robot. Applying Lagrange's equation leads to a model of the form

$$D_f(q_b)\ddot{q}_f + C_f(q_b, \dot{q}_f)\dot{q}_f + G_f(q_f) = B_f u, \quad (3.84)$$

where D_f is the inertia matrix, the matrix C_f contains Coriolis and centrifugal terms, and G_f is the gravity vector. Introducing the state vector $x_f := (q_f; \dot{q}_f)$, the mechanical model (3.84) is easily expressed as

$$\dot{x}_f = f_f(x_f) + g_f(x_f)u. \quad (3.85)$$

The configuration space \mathcal{Q}_f is taken as a simply connected, open subset of ${}^{15}\mathbb{T}^N \times \mathbb{R}^2$ corresponding to physically reasonable configurations of the robot, and the state space is taken as $T\mathcal{Q}_f := \{x_f := (q_f; \dot{q}_f) \mid q_f \in \mathcal{Q}_f, \dot{q}_f \in \mathbb{R}^{N+2}\}$.

3.5.2 Stance Phase Model

The stance phase model of running is identical to the stance phase model of walking. Here, it is developed in the generalized coordinates $q_s := (q_b; q_N) = (q_1; \dots; q_N)$, and the relation with the flight phase model is brought out. Since the robot's legs are identical, in the stance phase, it will be assumed without loss of generality that leg-1 is in contact with the ground. Moreover, the Cartesian position of the stance leg end will be identified with the origin of the $(x - y)$ -axes of the inertial frame.

The position of the center of mass can be expressed in terms of q_s per

$$\begin{bmatrix} \mathbf{x}_{cm}(q_s) \\ \mathbf{y}_{cm}(q_s) \end{bmatrix} = \mathbf{f}_{cm}(q_s), \quad (3.86)$$

where \mathbf{f}_{cm} is determined from the robot's geometric parameters (link lengths, masses, positions of the centers of mass). Hence

$$\dot{q}_f = \begin{bmatrix} I_{N \times N} \\ \frac{\partial \mathbf{f}_{cm}}{\partial q_s} \end{bmatrix} \dot{q}_s. \quad (3.87)$$

Substituting (3.87) into (3.80) yields the kinetic energy of the stance phase,

$$K_s = \frac{1}{2} \dot{q}'_s D_s(q_b) \dot{q}_s, \quad (3.88)$$

¹⁵ \mathbb{T}^n denotes the n -Torus, which is equal to $\underbrace{\mathbb{S}^1 \times \mathbb{S}^1 \times \dots \times \mathbb{S}^1}_{n-\text{times}}$.

with

$$D_s(q_b) = A(q_b) + m_{\text{tot}} \frac{\partial \mathbf{f}_{\text{cm}}(q_s)}{\partial q_s} \frac{\partial \mathbf{f}_{\text{cm}}(q_s)}{\partial q_s}; \quad (3.89)$$

because the kinetic energy is invariant under rotations of the body, D_s depends only on q_b . The potential energy remains $V_s(q_s) = m_{\text{tot}} g_0 \mathbf{y}_{\text{cm}}(q_s)$. Lagrange's equation becomes

$$\frac{d}{dt} \frac{\partial \mathcal{L}_s}{\partial \dot{q}_s} - \frac{\partial \mathcal{L}_s}{\partial q_s} = \Gamma_s, \quad (3.90)$$

and the external torques are

$$\Gamma_s = B_s u = \begin{bmatrix} I_{N-1 \times N-1} \\ 0_{1 \times N-1} \end{bmatrix} u. \quad (3.91)$$

The dynamic model can therefore be written as

$$D_s(q_b)\ddot{q}_s + C_s(q_b, \dot{q}_s)\dot{q}_s + G_s(q_s) = B_s u. \quad (3.92)$$

Introducing the state vector $x_s := (q_s; \dot{q}_s)$, the mechanical model (3.92) is easily expressed as

$$\dot{x}_s = f_s(x_s) + g_s(x_s)u. \quad (3.93)$$

The state space is taken as $T\mathcal{Q}_s := \{(q_s; \dot{q}_s) \mid q_s \in \mathcal{Q}_s, \dot{q}_s \in \mathbb{R}^N\}$, where the configuration space \mathcal{Q}_s is a simply connected, open subset of \mathbb{T}^N corresponding to physically reasonable configurations.

3.5.3 Impact Model

The Cartesian position of the end of leg-2 can be expressed in terms of the Cartesian position of the center of mass and the robot's angular coordinates as

$$\begin{bmatrix} \mathbf{x}_2 \\ \mathbf{y}_2 \end{bmatrix} = \begin{bmatrix} \mathbf{x}_{\text{cm}} \\ \mathbf{y}_{\text{cm}} \end{bmatrix} - \mathbf{f}_2(q_s), \quad (3.94)$$

where \mathbf{f}_2 is determined from the robot's parameters (links lengths, masses, positions of the centers of mass); see (3.86). When leg-2 touches the ground at the end of a flight phase, an impact takes place. The impact model of [75, 124] is used, which represents the ground reaction forces at impact as impulses with intensity I_R . The impact is assumed inelastic, with the velocity of the contact leg end becoming zero instantaneously; furthermore, after impact, the contact leg end is assumed to act as an ideal pivot. This model yields that the robot's configuration q_f is unchanged during impact and there are instantaneous changes in the velocities.

The velocity vector *just before* impact is denoted by \dot{q}_f^- . After impact, with the assumption that the leg neither rebounds nor slides after impact, the robot is in stance phase. During the stance phase leg-2 acts as an ideal pivot and

thus the linear velocity of the center of mass center can be expressed in terms of the angular velocities *just after impact*, \dot{q}_s^+ , yielding

$$\begin{bmatrix} 0 \\ 0 \end{bmatrix} = \begin{bmatrix} \dot{\mathbf{x}}_{\text{cm}}^+ \\ \dot{\mathbf{y}}_{\text{cm}}^+ \end{bmatrix} - \frac{\partial \mathbf{f}_2(q_s)}{\partial q_s} \dot{q}_s^+. \quad (3.95)$$

The impact model of [75, 124] is expressed as

$$\begin{bmatrix} A(q_b) & 0_{N \times 2} \\ 0_{2 \times N} & m_{\text{tot}} I_{2 \times 2} \end{bmatrix} \left(\begin{bmatrix} \dot{q}_s^+ \\ \dot{\mathbf{x}}_{\text{cm}}^+ \\ \dot{\mathbf{y}}_{\text{cm}}^+ \end{bmatrix} - \dot{q}_f^- \right) = \begin{bmatrix} -\frac{\partial \mathbf{f}_2'(q_s)}{\partial q_s} \\ I_{2 \times 2} \end{bmatrix} I_R. \quad (3.96)$$

The vector I_R of the ground reaction impulses can be expressed using the last two lines of the matrix equation (3.96) in combination with (3.95):

$$I_R = m_{\text{tot}} \left(\frac{\partial \mathbf{f}_2(q_s)}{\partial q_s} \dot{q}_s^+ - \begin{bmatrix} \dot{\mathbf{x}}_{\text{cm}}^- \\ \dot{\mathbf{y}}_{\text{cm}}^- \end{bmatrix} \right). \quad (3.97)$$

Substituting this into the first N lines of (3.96) and rearranging yields that the robot's angular velocity vector after impact is given by a linear expression with respect to the velocity before impact:

$$\dot{q}_s^+ = \left[A + m_{\text{tot}} \frac{\partial \mathbf{f}_2}{\partial q_s} \frac{\partial \mathbf{f}_2'}{\partial q_s} \right]^{-1} \left[A \mid m_{\text{tot}} \frac{\partial \mathbf{f}_2'}{\partial q_s} \right] \dot{q}_f^-, \quad (3.98)$$

which, for later use, is written as

$$\dot{q}_s^+ = \tilde{\Delta}(q_f^-) \dot{q}_f^-. \quad (3.99)$$

Remark 3.6 In the case of running, since the robot has $N + 2$ DOF before impact and only N DOF after impact, for any post-impact velocity, there is a two-dimensional set of velocities in the flight phase that gets mapped onto that same vector. This is different from walking where, generically, the double support impact results in a one-to-one mapping between pre-impact and post-impact velocity vectors.

3.5.4 Hybrid Model of Running

The overall bipedal robot model can be expressed as a *nonlinear hybrid system* containing two state manifolds (called “charts” in [103]):

$$\Sigma_f : \begin{cases} \mathcal{X}_f = T\mathcal{Q}_f \\ \mathcal{F}_f : (\dot{x}_f) = f_f(x_f) + g_f(x_f)u \\ \mathcal{S}_f^s = \{x_f \in \mathcal{X}_f \mid H_f^s(x_f) = 0\} \\ T_f^s : x_s^+ = \Delta_f^s(x_f^-) \end{cases}$$

(3.100)

$$\Sigma_s : \begin{cases} \mathcal{X}_s = T\mathcal{Q}_s \\ \mathcal{F}_s : (\dot{x}_s) = f_s(x_s) + g_s(x_s)u \\ \mathcal{S}_s^f = \{x_s \in \mathcal{X}_s \mid H_s^f(x_s) = 0\} \\ \mathcal{T}_s^f : x_f^+ = \Delta_s^f(x_s^-) \end{cases}$$

where, for example, \mathcal{F}_f is the flow on state manifold \mathcal{X}_f , \mathcal{S}_f^s is the switching hyper-surface for transitions between \mathcal{X}_f and \mathcal{X}_s , and $\mathcal{T}_f^s : \mathcal{S}_f^s \rightarrow \mathcal{X}_s$ is the transition function applied when $x_f \in \mathcal{S}_f^s$.

The transition from flight phase to stance phase occurs when leg-2 impacts the ground. Hence, $H_f^s(x_f) = y_2$; see Fig. 3.6. The ensuing initial value of the stance phase, x_s^+ , is determined from the impact model of Section 3.5.3. As in walking, a relabeling matrix R is applied to the angular coordinates to account for the impact occurring on leg-2 while the stance model assumes leg-1 is in contact with the ground:

$$\Delta_f^s(x_f^-) = \begin{bmatrix} [R \ 0_{N \times 2}] q_f^- \\ R \tilde{\Delta}(q_f^-) \dot{q}_f^- \end{bmatrix}, \quad (3.101)$$

where (3.99) has been used. The relabeling matrix must satisfy $RR = I$, i.e., R is a circular matrix.

The transition from stance phase to flight phase can be initiated by causing the acceleration of the stance leg end to become positive. If torque discontinuities¹⁶ are allowed—as they are assumed to be in this treatment of running—when to transition into the flight phase becomes a control decision. Here, in view of simplifying the analysis of periodic orbits as part of the control design, the transition is assumed to occur at a predetermined point in the stance phase. In particular, the transition will be determined by a function of the form $H_s^f = \theta_s(q_s) - \theta_{s,0}$, where $\theta_s(q_s)$ is the angle of the hips with respect to end of the stance leg (see Fig. 3.6) and $\theta_{s,0}$ is a constant to be determined as part of the control design.

The ensuing initial value of the flight phase, x_f^+ , is defined so as to achieve continuity in the position and velocity variables, using (3.86) and (3.87):

$$\Delta_s^f(x_s^-) = \begin{bmatrix} \left[\begin{array}{c} q_s^- \\ \mathbf{f}_{cm}(q_s^-) \end{array} \right] \\ \left[\begin{array}{c} \dot{q}_s^- \\ \frac{\partial \mathbf{f}_{cm}}{\partial q_s} \Big|_{q_s^-} \dot{q}_s^- \end{array} \right] \end{bmatrix}. \quad (3.102)$$

¹⁶This is a modeling decision. In practice, the torque is continuous due to actuator dynamics. It is assumed here that the actuator time constant is small enough that it need not be modeled.

Continuity of the torques is not imposed, and hence neither is continuity of the accelerations. It is assumed that the control law in the flight phase will be designed to result in $\ddot{\mathbf{y}}_1$ at the beginning of the flight phase being greater than zero; see [44].

The definition of a solution of the hybrid model is adopted from [103], and amounts to piecing together solutions in an appropriate manner, just as in the hybrid model of walking. Appropriate definitions of orbital stability in the sense of Lyapunov, attractivity, and orbital asymptotic stability in the sense of Lyapunov can be taken from [98, 167, 193].

Remark 3.7 Note that for a solution of the model to correspond to running, HGR3 requires that $\dot{\mathbf{x}}_{\text{cm}} > 0$ during the flight phase; otherwise, the robot is jogging in place. Though not done here, this requirement could be built into the model by redefining the state manifold of the flight phase as

$$\mathcal{X}_f := \{x_f := (q_f; \dot{q}_f) \mid q_f \in \mathcal{Q}_f, \dot{q}_f \in \mathbb{R}^{N+2}, \dot{\mathbf{x}}_{\text{cm}} > 0\}. \quad (3.103)$$

Instead, we will simply seek solutions of (3.100) respecting $\dot{\mathbf{x}}_{\text{cm}} > 0$.

3.5.5 Some Facts on Linear and Angular Momentum

A few linear and angular momentum properties of the mechanical models for stance and flight are noted. Let σ_{cm} denote the angular momentum of the biped about its center of mass. In the flight phase, σ_{cm} can be computed by $\sigma_{\text{cm}} = \frac{\partial K_f}{\partial \dot{q}_N} = A_N \dot{q}_s$, where A_N is the N -th row of A . The N -th row of (3.79) yields conservation of σ_{cm} ,

$$\dot{\sigma}_{\text{cm}} = 0. \quad (3.104)$$

In addition, the last two rows of (3.79) correspond to Newton's second law in a central gravity field:

$$m_{\text{tot}} \ddot{\mathbf{x}}_{\text{cm}} = 0 \quad \text{and} \quad m_{\text{tot}} \ddot{\mathbf{y}}_{\text{cm}} = -m_{\text{tot}} g_0. \quad (3.105)$$

As before, let σ_i denote the angular momentum of the biped about the end of leg- i , for $i = 1, 2$. The three angular momenta are related by

$$\sigma_i = \sigma_{\text{cm}} + m_{\text{tot}} \begin{bmatrix} \mathbf{x}_{\text{cm}} - \mathbf{x}_i \\ \mathbf{y}_{\text{cm}} - \mathbf{y}_i \end{bmatrix} \wedge \begin{bmatrix} \dot{\mathbf{x}}_{\text{cm}} \\ \dot{\mathbf{y}}_{\text{cm}} \end{bmatrix} \quad (3.106)$$

$$= \sigma_{\text{cm}} + m_{\text{tot}} ((\mathbf{y}_{\text{cm}} - \mathbf{y}_i) \dot{\mathbf{x}}_{\text{cm}} - (\mathbf{x}_{\text{cm}} - \mathbf{x}_i) \dot{\mathbf{y}}_{\text{cm}}), \quad (3.107)$$

where the last line assumes a clockwise convention on angle measurement. This expression is valid in both the stance and flight phases. In the stance phase, σ_1 is determined by $\sigma_1 = \frac{\partial K_s}{\partial \dot{q}_N} = D_{s,N} \dot{q}_s$, where $D_{s,N}$ is the N -th row of D_s . The N -th row of (3.90) yields the angular momentum balance theorem:

$$\dot{\sigma}_1 = -\frac{\partial V_s}{\partial q_N} = m_{\text{tot}} g_0 \mathbf{x}_{\text{cm}}. \quad (3.108)$$

The impact model of [75, 124] yields conservation of angular momentum about the impact point. Indeed, because the only external impulsive force is applied at the impact point, the N -th row of (3.96) can be written as

$$\sigma_{\text{cm}}^+ - \sigma_{\text{cm}}^- = -m_{\text{tot}} \begin{bmatrix} \mathbf{x}_{\text{cm}} - \mathbf{x}_2 \\ \mathbf{y}_{\text{cm}} - \mathbf{y}_2 \end{bmatrix} \wedge \begin{bmatrix} \dot{\mathbf{x}}_{\text{cm}}^+ - \dot{\mathbf{x}}_{\text{cm}}^- \\ \dot{\mathbf{y}}_{\text{cm}}^+ - \dot{\mathbf{y}}_{\text{cm}}^- \end{bmatrix} \quad (3.109)$$

$$= -m_{\text{tot}} [\mathbf{y}_{\text{cm}} - \mathbf{y}_2 | - \mathbf{x}_{\text{cm}} + \mathbf{x}_2] \begin{bmatrix} \dot{\mathbf{x}}_{\text{cm}}^+ - \dot{\mathbf{x}}_{\text{cm}}^- \\ \dot{\mathbf{y}}_{\text{cm}}^+ - \dot{\mathbf{y}}_{\text{cm}}^- \end{bmatrix} \quad (3.110)$$

because

$$\frac{\partial f_2}{\partial q_N} = \begin{bmatrix} \mathbf{y}_{\text{cm}} - \mathbf{y}_2 \\ -\mathbf{x}_{\text{cm}} + \mathbf{x}_2 \end{bmatrix} \quad (3.111)$$

and

$$I_R = m_{\text{tot}} \begin{bmatrix} \dot{\mathbf{x}}_{\text{cm}}^+ - \dot{\mathbf{x}}_{\text{cm}}^- \\ \dot{\mathbf{y}}_{\text{cm}}^+ - \dot{\mathbf{y}}_{\text{cm}}^- \end{bmatrix}. \quad (3.112)$$

Using (3.107) results in

$$\sigma_2^+ - \sigma_2^- = \sigma_{\text{cm}}^+ - \sigma_{\text{cm}}^- + m_{\text{tot}} \begin{bmatrix} \mathbf{x}_{\text{cm}} - \mathbf{x}_2 \\ \mathbf{y}_{\text{cm}} - \mathbf{y}_2 \end{bmatrix} \wedge \begin{bmatrix} \dot{\mathbf{x}}_{\text{cm}}^+ - \dot{\mathbf{x}}_{\text{cm}}^- \\ \dot{\mathbf{y}}_{\text{cm}}^+ - \dot{\mathbf{y}}_{\text{cm}}^- \end{bmatrix} \quad (3.113)$$

and thus

$$\sigma_2^+ = \sigma_2^-, \quad (3.114)$$

meaning the value of σ_2 is unchanged during the impact. Since the stance phase model assumes that the stance leg is leg-1, for later use, (3.114) is rewritten as

$$\sigma_1^{s+} = \sigma_2^{f-} \quad (3.115)$$

to reflect the swapping of the roles of the legs; see (3.101).

Remark 3.8 The notation $s+$ emphasizes that σ_1 is being evaluated at the *beginning of the stance phase* and the notation $f-$ emphasizes that σ_2 is being evaluated at the *end of the flight phase*. If no confusion is possible, the notation $+$ and $-$ will be used. For example, the variable θ_s only makes sense in the stance phase, and hence θ_s^{s-} would be redundant. On the other hand, for a variable such as \mathbf{x}_{cm} , it is important to distinguish among $\mathbf{x}_{\text{cm}}^{s+}$, $\mathbf{x}_{\text{cm}}^{s-}$, $\mathbf{x}_{\text{cm}}^{f+}$, and $\mathbf{x}_{\text{cm}}^{f-}$.

Remark 3.9 The robot is assumed to advance from left to right that is, in the positive direction of the horizontal component of the inertial frame. In this section, angles were assumed to be positive when measured in the clockwise direction so that the angular momenta about the stance leg end and the center

of mass will be positive. A more classical choice of measuring the angles in the trigonometric sense, that is, positive is counterclockwise, would lead to negative angular momenta for left-to-right movement of the robot. In this case, (3.107) would become

$$\sigma_i = \sigma_{\text{cm}} + m_{\text{tot}} ((\mathbf{x}_{\text{cm}} - \mathbf{x}_i)\dot{\mathbf{y}}_{\text{cm}} - (\mathbf{y}_{\text{cm}} - \mathbf{y}_i)\dot{\mathbf{x}}_{\text{cm}}), \quad (3.116)$$

(3.108) would become

$$\dot{\sigma}_1 = -\frac{\partial V_s}{\partial q_N} = -m_{\text{tot}} g_0 \mathbf{x}_{\text{cm}}, \quad (3.117)$$

(3.110) would become

$$\sigma_{\text{cm}}^+ - \sigma_{\text{cm}}^- = -m_{\text{tot}} [-\mathbf{y}_{\text{cm}} + \mathbf{y}_2 | \mathbf{x}_{\text{cm}} - \mathbf{x}_2] \begin{bmatrix} \dot{\mathbf{x}}_{\text{cm}}^+ - \dot{\mathbf{x}}_{\text{cm}}^- \\ \dot{\mathbf{y}}_{\text{cm}}^+ - \dot{\mathbf{y}}_{\text{cm}}^- \end{bmatrix}, \quad (3.118)$$

and (3.111) would become

$$\frac{\partial f_2}{\partial q_N} = \begin{bmatrix} -\mathbf{y}_{\text{cm}} - \mathbf{y}_2 \\ \mathbf{x}_{\text{cm}} - \mathbf{x}_2 \end{bmatrix}. \quad (3.119)$$

In turn, certain equations derived from these would have to be modified in [Chapter 9](#).

4

Periodic Orbits and Poincaré Return Maps

This chapter develops effective methods for determining the existence and stability properties of periodic orbits in nonlinear systems with impulse effects. By effective methods, we first of all mean methods that lead to rigorous conclusions. We also mean that the methods are systematic, broadly applicable, and practical in terms of computations. Ultimately, our aim is to design feedback loops that create provably asymptotically (or exponentially) stable walking and running motions in bipedal robots, and we want analysis techniques that can assist us in this endeavor.

In this book, periodic locomotion patterns such as walking and running are interpreted as periodic orbits traced out in the state space of a robot's model. The classical technique for determining the existence and stability properties of periodic orbits in nonlinear systems involves Poincaré sections and Poincaré return maps. The Poincaré return map transforms the problem of finding periodic orbits into one of finding fixed points of a map, which in turn can also be viewed as the problem of finding equilibrium points of a particular discrete-time nonlinear system. The method of Poincaré sections is certainly rigorous: it provides necessary and sufficient conditions for the existence of (stable, asymptotically stable, or exponentially stable) periodic orbits. The difficulty is that determining the return map for a typical system is impossible to do analytically because it requires the closed-form solution of a nonlinear ordinary differential equation. Certainly, numerical schemes can be used to find fixed points of the return map and to estimate eigenvalues for determining exponential stability. Often, this numerical process is computationally intensive. The more important drawback is that the numerical computations are not insightful, by which we mean that it is very difficult to establish a cause-and-effect relationship between the existence or stability properties of a periodic orbit and properties of the system (robot) that may be altered by a designer.¹

In this chapter, the method of Poincaré sections will be augmented with notions of timescale decomposition, invariance, and attractivity in order to simplify its application to complex systems, while maintaining analytical rigor.

¹Of course, difficult does not mean impossible. There has been success with numerical implementations of Poincaré methods in the passive robot community in terms of finding parameter values—masses, inertias, link lengths—for a given robot that yield asymptotically stable periodic orbits.

The underlying idea is the following: The robot models addressed in this book are underactuated in one or more phases. The unactuated degrees of freedom in these models must be controlled indirectly through the actuated degrees of freedom. A good feedback design typically results in relatively higher bandwidth—that is, faster rates of convergence—for variables that are closer² to the actuators. Also, with feedback, it is often possible to create invariant manifolds—that is, lower-dimensional surfaces with the property that if the system is initialized on the surface, its evolution remains on the surface. It is often quite advantageous to exploit timescale and invariance properties in stability analysis.

Finally, it is very natural to organize the feedback control of a hybrid system, such as a bipedal robot, around the various modes or phases of the system's dynamics. Control actions can be updated continuously within each phase and discretely at transitions between phases. This chapter will also address how to formally include discrete control actions in the stability analysis.

4.1 Autonomous Systems with Impulse Effects

An *autonomous system with impulse effects* consists of three things: an autonomous ordinary differential equation, $\dot{x}(t) = f(x(t))$, defined on some state space \mathcal{X} ; a hyper surface \mathcal{S} at which solutions of the differential equation undergo a discrete transition that is modeled as an instantaneous reinitialization of the differential equation; and a rule $\Delta : \mathcal{S} \rightarrow \mathcal{X}$ that specifies the new initial condition as a function of the point at which the solution impacts \mathcal{S} . Such a system will be denoted by

$$\Sigma : \begin{cases} \dot{x}(t) = f(x(t)) & x^-(t) \notin \mathcal{S} \\ x^+(t) = \Delta(x^-(t)) & x^-(t) \in \mathcal{S}. \end{cases} \quad (4.1)$$

\mathcal{S} will be called the *impact surface* and Δ the *impact map*. The terminology *switching surface* and *reset map*, respectively, is also common and will be used occasionally.

A formal definition of a solution $\varphi(t)$ of (4.1) is developed on the basis of solutions to the associated ordinary differential equation

$$\dot{x} = f(x). \quad (4.2)$$

As a point of notation, φ^f will denote a solution of the ordinary differential equation (4.2) while φ will denote a solution of the system with impulse effects

²As measured by the number of integrations separating a variable from the inputs. This is called the relative degree in control parlance.

(4.1). The point of introducing φ^f is that, firstly, a lot is known about solutions of ordinary differential equations with continuous right-hand sides [110]; for example, if f is continuous, then solutions always exist over sufficiently small intervals of time. Secondly, in the proofs of various results, it is sometimes necessary to extend a solution of (4.2) “through” \mathcal{S} , while this does not make sense for (4.1).

4.1.1 Hybrid System Hypotheses

The following hypotheses concern the elements of (4.1).

A minimal set of hypotheses:

HSH1) \mathcal{X} is a smooth embedded submanifold of \mathbb{R}^n .

HSH2) $f : \mathcal{X} \rightarrow T\mathcal{X}$ is continuous and a solution of $\dot{x} = f(x)$ from a given initial condition is unique and depends continuously on the initial condition.

HSH3) \mathcal{S} is nonempty and there exist an open set $\check{\mathcal{X}} \subset \mathcal{X}$ and a differentiable function $H : \check{\mathcal{X}} \rightarrow \mathbb{R}$ such that

$$\mathcal{S} := \{x \in \check{\mathcal{X}} \mid H(x) = 0\}; \quad (4.3)$$

moreover, for every $s \in \mathcal{S}$, $\frac{\partial H}{\partial x}(s) \neq 0$.

HSH4) $\Delta : \mathcal{S} \rightarrow \mathcal{X}$ is continuous, where \mathcal{S} is given the subset topology from \mathcal{X} .

HSH5) $\overline{\Delta(\mathcal{S})} \cap \mathcal{S} = \emptyset$, where $\overline{\Delta(\mathcal{S})}$ is the set closure of $\Delta(\mathcal{S})$.

Since we will only be doing local analysis, without any essential loss of generality, we can in fact assume that \mathcal{X} is a simply connected open subset of \mathbb{R}^n . The more general setting of “smooth surfaces” in \mathbb{R}^n is useful when we look at subsystems in Section 4.4. The first part of Hypothesis HSH2, namely the continuity of f , implies that at any point $x_0 \in \mathcal{X}$, a solution to (4.2) will exist over a sufficiently small interval of time [110]. This solution may not be unique, and may not depend continuously on the initial condition; whence the second part of Hypothesis HSH2. Under HSH2, there always exist solutions of (4.2) with a maximal interval of existence. Hypothesis HSH3 implies that \mathcal{S} is a smooth hypersurface in \mathcal{X} , that is, an embedded submanifold [127] with dimension one less than the dimension of \mathcal{X} . Hypothesis HSH4 ensures that the result of an impact varies continuously with respect to where it occurs on \mathcal{S} . Hypothesis HSH5 ensures that the result of an impact does not lead immediately to another impact event because every point in $\Delta(\mathcal{S})$ is a positive distance away from \mathcal{S} .

Remark 4.1 When defining the impact (or switching) surface \mathcal{S} for use in bipedal robot models, H is typically the height of the swing leg end above the walking surface, p_2^y ; see Fig. 3.1. It is often desirable to add further restrictions on the nature of the impact, such as, an impact can only occur when the swing leg is strictly in front of the stance leg, that is, $p_2^h > p_1^h$, as in Fig. 3.3 and (3.31). In this case, $\tilde{\mathcal{X}} := \{x \in \mathcal{X} \mid p_2^h - p_1^h > 0\}$. However, from a practical perspective, the same ends can be met by simply modifying the state space \mathcal{X} to exclude points where the swing leg end has non-positive velocity whenever it is not strictly in front of the stance leg and its vertical height does not exceed a given threshold. Hence, there is no essential loss of generality in assuming $\tilde{\mathcal{X}} = \mathcal{X}$ and using Hypothesis HSH3 in the simpler form

HSH3) \mathcal{S} is nonempty and there exists a differentiable function $H : \mathcal{X} \rightarrow \mathbb{R}$ such that

$$\mathcal{S} := \{x \in \mathcal{X} \mid H(x) = 0\}; \quad (4.4)$$

moreover, for every $s \in \mathcal{S}$, $\frac{\partial H}{\partial x}(s) \neq 0$.

A stronger set of hypotheses: An autonomous system with impact effects (4.1) is said to be continuously differentiable or C^1 if it satisfies HSH1–HSH5 with HSH2 and HSH4 strengthened to:

HSH2') $f : \mathcal{X} \rightarrow T\mathcal{X}$ is continuously differentiable

HSH4') $\Delta : \mathcal{S} \rightarrow \mathcal{X}$ is continuously differentiable.

4.1.2 Definition of Solutions

A function $\varphi : [t_0, t_f] \rightarrow \mathcal{X}$, $t_f \in \mathbb{R} \cup \{\infty\}$, $t_f > t_0$, is a *solution*³ of (4.1) if (i) $\varphi(t)$ is right continuous on $[t_0, t_f]$, (ii) left and right limits exist at each point $t \in (t_0, t_f)$, denoted by $\varphi^-(t) := \lim_{\tau \nearrow t} \varphi(\tau)$ and $\varphi^+(t) := \lim_{\tau \searrow t} \varphi(\tau)$; and (iii) there exists a closed discrete subset $\mathcal{T} \subset [t_0, t_f]$ called impact times such that, (a) for every $t \notin \mathcal{T}$, $\varphi(t)$ is differentiable, $\frac{d\varphi(t)}{dt} = f(\varphi(t))$, and $\varphi(t) \notin \mathcal{S}$, and (b) for $t \in \mathcal{T}$, $\varphi^-(t) \in \mathcal{S}$ and $\varphi^+(t) = \Delta(\varphi^-(t))$. The difference between left and right continuity is illustrated in Fig. 4.1.

The condition that the set of impact times \mathcal{T} is closed and discrete means that there is no “chattering” about an impact point,⁴ which simplifies the construction of solutions; on the other hand, this condition also means that a maximal interval of existence⁵ of a solution may not exist because it may

³The definition is based on [250]. For a careful study of the existence of solutions of mechanical systems with shocks, see [24, 221].

⁴See the notion of a Zeno solution in the hybrid systems literature.

⁵Suppose that $t_f < \infty$. Then $\varphi : [t_0, t_f] \rightarrow \mathcal{X}$ is a *maximal solution* of (4.1) if whenever $\mathcal{T} \neq \emptyset$, $\varphi : [\max(\mathcal{T}), t_f] \rightarrow \mathcal{X}$ is a maximal solution of (4.2), and whenever $\mathcal{T} = \emptyset$,

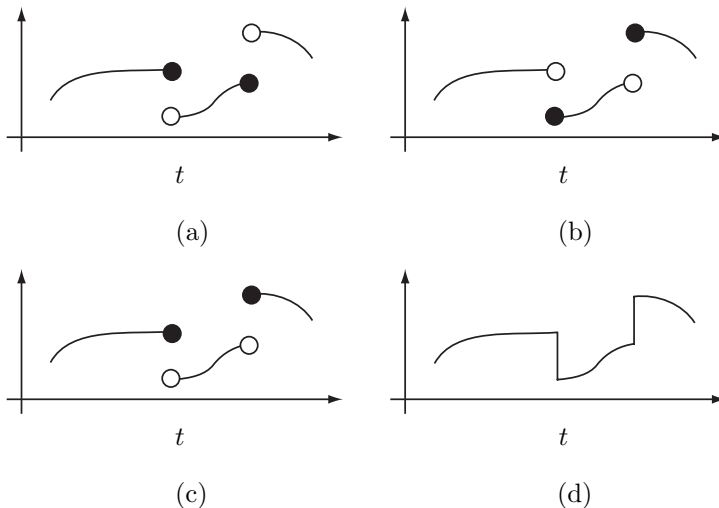


Figure 4.1. Left and right continuity. In (a), the function is left continuous, in (b), the function is right continuous, and in (c), the function is neither right nor left continuous. The plot in (d) is not the graph of a function because it takes on multiple values at the jumps. Despite this, common practice will be followed and in most simulation plots found in future chapters, the jumps will be shown as in (d) and the reader must understand that the solution is being taken as in (b).

involve a sequence of impact times with an accumulation point. Because a solution φ is assumed to be right continuous, $\varphi(t) = \varphi^+(t) := \lim_{\tau \searrow t} \varphi(\tau)$ at all points in its domain of definition. Under HSH2, solutions to (4.1) are unique. For $x_0 \in \mathcal{X}$, the solution of (4.1) corresponding to the initial condition x_0 at time t_0 is denoted $\varphi(t, x_0)$. When $x_0 \notin \mathcal{S}$, $\varphi(t_0, x_0) = x_0$ because this property holds for φ^f . When $x_0 \in \mathcal{S}$, then $\varphi(t_0, x_0) = \Delta(x_0) = \varphi(t_0, \Delta(x_0))$ because of right continuity and HSH5. Generally, there is never a value of t where $\varphi(t) \in \mathcal{S}$, for any solution of (4.1). Hence, for initial conditions in \mathcal{S} , we will systematically write the corresponding solution as $\varphi(t_0, \Delta(x_0))$ to emphasize that the impact map must be applied first.

4.1.3 Periodic Orbits and Stability Notions

A solution $\varphi : [t_0, \infty) \rightarrow \mathcal{X}$ of the autonomous system with impact effects (4.1) is *periodic* if there exists a finite $T > 0$ such that $\varphi(t + T) = \varphi(t)$ for all $t \in [t_0, \infty)$. A set $\mathcal{O} \subset \mathcal{X}$ is a *periodic orbit* of (4.1) if $\mathcal{O} = \{\varphi(t) \mid t \geq t_0\}$ for some periodic solution $\varphi(t)$. An orbit is *nontrivial* if it contains more than one point.

Remark 4.2 Note that a periodic orbit of a system with impulse effects may not be a closed set, since, for $\bar{t} \in \mathcal{T}$, the set of impact times, $\varphi^-(\bar{t}) \notin \mathcal{O}$ (if solutions were assumed to be left continuous, instead of right continuous, then $\varphi^+(\bar{t}) \notin \mathcal{O}$). Indeed, a periodic orbit is closed if, and only if, $\mathcal{T} = \emptyset$. For a bipedal robot, a closed periodic orbit would not correspond to walking or running because there would be no impact with the ground.

A periodic orbit \mathcal{O} is *stable in the sense of Lyapunov* if for every $\epsilon > 0$, there exists an open neighborhood \mathcal{V} of \mathcal{O} such that for every $p \in \mathcal{V}$, there exists a solution $\varphi : [0, \infty) \rightarrow \mathcal{X}$ of (4.1) satisfying $\varphi(0) = p$, $\text{dist}(\varphi(t), \mathcal{O}) < \epsilon$ for all $t \geq 0$, where $\text{dist}(p_1, p_2)$ is the usual Euclidean distance between points $p_1, p_2 \in \mathbb{R}^n$ and $\text{dist}(p_1, \mathcal{O}) := \inf_{p_2 \in \mathcal{O}} \text{dist}(p_1, p_2)$. \mathcal{O} is *attractive* if there exists an open neighborhood \mathcal{V} of \mathcal{O} such that for every $p \in \mathcal{V}$, there exists a solution $\varphi : [0, \infty) \rightarrow \mathcal{X}$ of (4.1) satisfying $\varphi(0) = p$ and $\lim_{t \rightarrow \infty} \text{dist}(\varphi(t), \mathcal{O}) = 0$. \mathcal{O} is *asymptotically stable in the sense of Lyapunov* if it is both stable and attractive. From here on, the qualifier, “in the sense of Lyapunov,” will be systematically assumed if it is not made explicit when speaking of stability or asymptotic stability. \mathcal{O} is *exponentially stable* if there exists an open neighborhood \mathcal{V} of \mathcal{O} and positive constants N and γ such that for every $p \in \mathcal{V}$, there exists a solution $\varphi : [0, \infty) \rightarrow \mathcal{X}$ of (4.1) satisfying $\varphi(0) = p$ and $\text{dist}(\varphi(t), \mathcal{O}) \leq N \exp(-\gamma t) \text{dist}(p, \mathcal{O})$.

$\varphi : [t_0, t_f] \rightarrow \mathcal{X}$ is a maximal solution of (4.2). When $t_f = \infty$, the solution is obviously maximal.

A periodic orbit \mathcal{O} is *transversal* to \mathcal{S} if its closure intersects \mathcal{S} in exactly one point, and for $\bar{x} := \bar{\mathcal{O}} \cap \mathcal{S}$, $L_f H(\bar{x}) := \frac{\partial H}{\partial x}(\bar{x})f(\bar{x}) \neq 0$ (in words, at the intersection, $\bar{\mathcal{O}}$ is not tangent to \mathcal{S} , where $\bar{\mathcal{O}}$ is the set closure of \mathcal{O}). In the case of a bipedal robot, a nontrivial periodic orbit transversal to \mathcal{S} will also be referred to as *periodic locomotion*.

Remark 4.3 The above definition has explicitly ruled out multiple (distinct) intersections with \mathcal{S} , that is, orbits corresponding to *m-periodic solutions*, where $m \geq 2$ is the number of distinct intersections with \mathcal{S} . These more general periodic orbits are important when studying asymmetric gaits or the period-doubling path to chaos [64, 84, 122, 228]. An *m*-periodic orbit is transversal to \mathcal{S} if each of its intersections with \mathcal{S} is transversal.

4.2 Poincaré’s Method for Systems with Impulse Effects

The method of Poincaré sections is developed for systems with impulse effects (4.1) for the study of nontrivial periodic orbits that are transversal to the impact surface. This will be done in a certain amount of generality so that a wide class of bipedal robot models and controllers can be treated. In particular, some of the stabilizing controllers of Chapters 6 and 7 will make use of feedbacks that are continuous, but not Lipschitz continuous. While Poincaré’s method carries over nicely to the hybrid setting with non-Lipschitz continuous differential equations, the proof differs considerably from the standard one in [138, 173], for example.⁶ All proofs and several lemmas are available in Appendix C.1. Sources for results and pertinent references are provided in the End Notes.

4.2.1 Formal Definitions and Basic Theorems

The first aim is to define the Poincaré return map. There is a natural choice for the Poincaré section, namely \mathcal{S} . Define the *time-to-impact function*, $T_I : \mathcal{X} \rightarrow \mathbb{R} \cup \{\infty\}$, by

$$T_I(x_0) := \begin{cases} \inf\{t \geq 0 \mid \varphi^f(t, x_0) \in \mathcal{S}\} & \text{if } \exists t \text{ such that } \varphi^f(t, x_0) \in \mathcal{S} \\ \infty & \text{otherwise,} \end{cases} \quad (4.5)$$

From Lemma C.1 in Appendix C.1, Hypotheses HSH1–HSH3 imply that T_I is continuous at points x_0 where $0 < T_I(x_0) < \infty$ and $L_f H(\varphi^f(T_I(x_0), x_0))$

⁶The standard development assumes that the flow is a local diffeomorphism, while, here, it may be not even a homeomorphism.

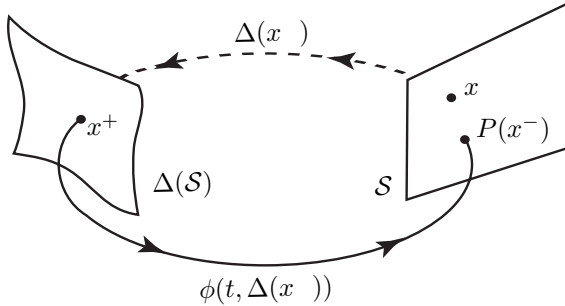


Figure 4.2. Geometric interpretation of a Poincaré return map $P : \mathcal{S} \rightarrow \mathcal{S}$ for a system with impulse effects. The Poincaré section is selected as the switching surface, \mathcal{S} . A periodic orbit exists when $P(x^-) = x^-$. Due to right-continuity of the solutions, x^- is not an element of the orbit. With left-continuous solutions, $\Delta(x^-)$ would not be an element of the orbit.

$\neq 0$. Hence, under HSH1–HSH3,

$$\tilde{\mathcal{X}} := \{x \in \mathcal{X} \mid 0 < T_I(x) < \infty \text{ and } L_f H(\varphi^f(T_I(x), x)) \neq 0\} \quad (4.6)$$

is open. If HSH4 also holds, then

$$\tilde{\mathcal{S}} := \Delta^{-1}(\tilde{\mathcal{X}}) \quad (4.7)$$

is an open subset of \mathcal{S} . It immediately follows that under HSH1–HSH5, the *Poincaré return map*, $P : \tilde{\mathcal{S}} \rightarrow \mathcal{S}$ by

$$P(x) := \varphi^f(T_I(\Delta(x)), \Delta(x)), \quad (4.8)$$

is well defined and continuous. In the case of a robot, the return map represents the evolution of the robot from just before an impact with the walking surface to just before the next impact, assuming that a next impact does occur. If it does not, that is, the robot falls due to the preceding impact or fails in some other manner to complete a forward step, the point being analyzed is not in the domain of definition of the return map. The notion of a Poincaré map and a periodic orbit in a system with impact effects is depicted in Fig. 4.2.

Next, note that under HSH1–HSH5, if \mathcal{O} is any periodic orbit of (4.1) that is transversal to \mathcal{S} , then $\mathcal{O} \subset \tilde{\mathcal{X}}$ (this is essentially by the definitions of $\tilde{\mathcal{X}}$ and transversal). Thus, there exists $x_0 \in \tilde{\mathcal{S}}$ that generates \mathcal{O} in the sense that $\Delta(x_0) \in \mathcal{O}$; indeed, $x_0 = \bar{\mathcal{O}} \cap \tilde{\mathcal{S}}$. It makes sense therefore to denote the orbit by $\mathcal{O}(\Delta(x_0))$. The Poincaré return map gives rise to a discrete-time system on the Poincaré section, \mathcal{S} , by defining

$$x[k + 1] = P(x[k]). \quad (4.9)$$

This system corresponds to sampling φ^- at each impact with \mathcal{S} ; in other words, the sampling process is event based. A point $x^* \in \tilde{\mathcal{S}}$ is said to be a *fixed point* of P if $P(x^*) = x^*$. Thus a fixed point is an equilibrium point of (4.9), and vice-versa. A fixed point generates a periodic orbit of the hybrid model (4.1) per $\mathcal{O} = \mathcal{O}(\Delta(x^*)) := \{\varphi(t, \Delta(x^*)) \mid 0 \leq t < T_I(\Delta(x^*))\}$. The method of Poincaré sections is based on the equivalence between periodic orbits of the system with impulse effects (4.1) and equilibrium points of the sampled system (4.9). Furthermore, it establishes the equivalence between the stability properties of periodic orbits of (4.1) and equilibrium points of (4.9).

Theorem 4.1 (Method of Poincaré Sections for Systems with Impulse Effects)

Under HSH1–HSH5, the following statements hold:

- a) If \mathcal{O} is a periodic orbit of (4.1) that is transversal to \mathcal{S} , then there exists a point $x^* \in \tilde{\mathcal{S}}$ that generates \mathcal{O} .
- b) $x^* \in \tilde{\mathcal{S}}$ is a fixed point of P if, and only if, $\Delta(x^*)$ generates a periodic orbit that is transversal to \mathcal{S} .
- c) $x^* \in \tilde{\mathcal{S}}$ is a stable equilibrium point of $x[k+1] = P(x[k])$ if, and only if, the orbit $\mathcal{O}(\Delta(x^*))$ is stable.
- d) $x^* \in \tilde{\mathcal{S}}$ is an asymptotically stable equilibrium point of $x[k+1] = P(x[k])$ if, and only if, the orbit $\mathcal{O}(\Delta(x^*))$ is asymptotically stable.

Moreover, if the system with impulse effects is continuously differentiable, that is, Hypotheses HSH2 and HSH4 are strengthened to HSH2' and HSH4', then

- e) $x^* \in \tilde{\mathcal{S}}$ is an exponentially stable equilibrium point of $x[k+1] = P(x[k])$ if, and only if, the orbit $\mathcal{O}(\Delta(x^*))$ is exponentially stable.

The proof of the theorem is given in [Appendix C.1.3](#). It is often convenient to check exponential stability in terms of eigenvalues. When f is continuously differentiable, the time-to-impact function T_I is a continuously-differentiable function on $\tilde{\mathcal{X}}$ [173] and, for each t in its domain of definition, $\varphi^f(t, x_0)$ is a continuously-differentiable function of x_0 [138]. When combined with the continuous differentiability of Δ and Hypothesis HSH3 (\mathcal{S} is an embedded submanifold of \mathcal{X}), the Poincaré map (4.8) is a continuously-differentiable function on $\tilde{\mathcal{S}}$. Thus, the corresponding sampled-data system (4.9) is continuously differentiable, which means that exponential stability of its equilibrium points can be completely characterized through eigenvalues of its linearization [138].

Corollary 4.1 (Method of Poincaré Sections for Differentiable Systems with Impulse Effects)

Consider Hypotheses HSH1–HSH5 and assume that HSH2 and HSH4 are strengthened to HSH2' and HSH4'. Then $T_I : \tilde{\mathcal{X}} \rightarrow \mathbb{R}$ and $P : \tilde{\mathcal{S}} \rightarrow \mathcal{S}$ are continuously differentiable, and, consequently,

- f) $x^* \in \tilde{\mathcal{S}}$ is an exponentially stable equilibrium point of $x[k+1] = P(x[k])$ if, and only if, the eigenvalues⁷ of $D_x P(x^*)$, the Jacobian linearization of P at x^* , have magnitude strictly less than one.

4.2.2 The Poincaré Return Map as a Partial Function

So far, when using the Poincaré return map $P : \tilde{\mathcal{S}} \rightarrow \mathcal{S}$, we have been very careful to first define the set of points $x_0 \in \mathcal{S}$ at which P is well defined and has nice properties, such as continuity and $P(x_0)$ results in a transversal intersection with \mathcal{S} (i.e., $L_f H(P(x_0)) \neq 0$). It is common practice—and much more convenient—to simply write $P : \mathcal{S} \rightarrow \mathcal{S}$ for the Poincaré return map and to understand that by this collection of symbols we mean the following rule: take a point $x_0 \in \mathcal{S}$ and apply the impact map to obtain $\Delta(x_0)$; initialize the differential equation (4.2) at $\Delta(x_0)$ and compute its maximal solution, $x : [0, t_f) \rightarrow \mathcal{X}$; if there does not exist any finite t such that $x(t) \in \mathcal{S}$, then P is not defined at x_0 ; otherwise, $P(x_0) = x(t_1)$, where t_1 is the smallest t such that $x(t) \in \mathcal{S}$. In particular, we allow that P does not assign a value to all points in \mathcal{S} . This is formalized in mathematics with the notion of a *partial map* or a *partial function*.

A partial function $f : A \rightarrow B$ is a rule that associates to every element of A *at most one* element in B . A is called the domain and B is called the codomain. If a partial function associates *precisely one element* in B to every element in A , then it is a function. One says that a partial function $f : A \rightarrow B$ is *well defined* at a point $a \in A$ if there exists a point $b \in B$ such that $b = f(a)$, and f is well defined when it is well defined at every point in its domain. In this sense, a function is a well-defined partial function, and every partial function is well defined on $f^{-1}(B) := \{a \in A \mid \exists b \in B, f(a) = b\}$, the inverse image of B under f .

It is important to note that by writing the Poincaré return map as a partial map, $P : \mathcal{S} \rightarrow \mathcal{S}$, the notion of a fixed point of P does not change, because if $x^* = P(x^*)$ for some $x^* \in \mathcal{S}$, then P is necessarily well defined at x^* . The same goes for continuity at a point, differentiability, and so forth: *to possess a certain property at a given point, the partial map must first be well defined at that point*.

⁷It is important to note that $D_x P(x^*)$ is the Jacobian of the Poincaré map viewed as a mapping from $\tilde{\mathcal{S}} \rightarrow \mathcal{S}$ and not as a mapping from $\mathbb{R}^n \rightarrow \mathbb{R}^n$; consequently, there is not a supplemental eigenvalue with value 1 as in [173], for example.

Proposition 4.1

Consider the system with impulse effects (4.1) and assume Hypotheses HSH1–HSH5 hold. Let $P : \mathcal{S} \rightarrow \mathcal{S}$ be the partial Poincaré map.

- a) Let the set $\tilde{\mathcal{S}}$ be defined as in (4.7). Then,

$$\tilde{\mathcal{S}} = \{x \in \mathcal{S} \mid P \text{ is continuous at } x \text{ and } L_f H(P(x)) \neq 0\}. \quad (4.10)$$

- b) If $x^* \in \mathcal{S}$ is a stable equilibrium point of $x[k+1] = P(x[k])$, then P is continuous at x^* . Consequently, if $x^* \in \mathcal{S}$ is a stable equilibrium point of $x[k+1] = P(x[k])$ and $L_f H(x^*) \neq 0$, then $x^* \in \tilde{\mathcal{S}}$.

The proof of the proposition is given in [Appendix C.1.4](#). In terms of the partial Poincaré map, Theorem 4.1 on the stability of periodic orbits can be restated as follows.

Theorem 4.2 (Method of Poincaré Sections with a Partial Map)

Assume HSH1–HSH5 and let $P : \mathcal{S} \rightarrow \mathcal{S}$ be the partial Poincaré map. Suppose that $x^* \in \mathcal{S}$ satisfies $P(x^*) = x^*$ and $L_f H(x^*) \neq 0$. Then,

- a) x^* is a stable equilibrium point of $x[k+1] = P(x[k])$ if, and only if, the orbit $\mathcal{O}(\Delta(x^*))$ is stable and its closure $\bar{\mathcal{O}}(\Delta(x^*))$ intersects \mathcal{S} only once.
- b) x^* is an asymptotically stable equilibrium point of $x[k+1] = P(x[k])$ if, and only if, the orbit $\mathcal{O}(\Delta(x^*))$ is asymptotically stable and its closure $\bar{\mathcal{O}}(\Delta(x^*))$ intersects \mathcal{S} only once.

Moreover, if the Hypotheses HSH2 and HSH4 are strengthened to HSH2' and HSH4', then

- c) x^* is an exponentially stable equilibrium point of $x[k+1] = P(x[k])$ if, and only if, the orbit $\mathcal{O}(\Delta(x^*))$ is exponentially stable and its closure $\bar{\mathcal{O}}(\Delta(x^*))$ intersects \mathcal{S} only once.

In summary, the Poincaré return map can be viewed as a partial map on all of \mathcal{S} or as a (well-defined) map on a subset of \mathcal{S} . At times, it is quite convenient to discuss P without first specifying $\tilde{\mathcal{S}}$, and we often will do that. The same stability results can be proven in either case, and $\tilde{\mathcal{S}}$ can be determined from the partial map, if it is needed.

4.3 Analyzing More General Hybrid Models

This section will address systems with two continuous phases and discrete transitions between the phases. Such models occur in running with point feet

and in walking with nontrivial feet. Models with three or more continuous phases will not be addressed, but the reader will easily see how their analysis would proceed. Such models would occur, for example, in running with nontrivial feet and in walking with nontrivial feet where the gait consists of successive phases of heel strike and roll, the foot flat on the ground, toe roll, followed by an instantaneous double support phase.

4.3.1 Hybrid Model with Two Continuous Phases

Let \mathcal{X}_1 and \mathcal{X}_2 be embedded submanifolds of \mathbb{R}^{n_1} and \mathbb{R}^{n_2} , respectively, upon which are defined the differential equations \mathcal{F}_1 and \mathcal{F}_2 . Let \mathcal{S}_1^2 be a hyper surface in the state space \mathcal{X}_1 that determines when a transition from \mathcal{X}_1 to \mathcal{X}_2 takes place, according to the transition function \mathcal{T}_1^2 , and similarly for \mathcal{S}_2^1 and \mathcal{T}_2^1 . The corresponding *hybrid model* is written as follows.

$$\Sigma_1 : \begin{cases} \mathcal{X}_1 \subset \mathbb{R}^{n_1} \\ \mathcal{F}_1 : (\dot{x}_1) = f_1(x_1) \\ \mathcal{S}_1^2 = \{x_1 \in \mathcal{X}_1 \mid H_1^2(x_1) = 0\} \\ \mathcal{T}_1^2 : x_2^+ = \Delta_1^2(x_1^-) \end{cases} \quad (4.11)$$

$$\Sigma_2 : \begin{cases} \mathcal{X}_2 \subset \mathbb{R}^{n_2} \\ \mathcal{F}_2 : (\dot{x}_2) = f_2(x_2) \\ \mathcal{S}_2^1 = \{x_2 \in \mathcal{X}_2 \mid H_2^1(x_2) = 0\} \\ \mathcal{T}_2^1 : x_1^+ = \Delta_2^1(x_2^-). \end{cases}$$

It is assumed that Hypotheses HSH1–HSH5 hold for (4.11) when applied to Σ_1 and Σ_2 in the obvious manner.

4.3.2 Basic Definitions

The mathematical meaning of a solution of the multiphase model (4.11) is quite similar to the one given for (4.1) and will be expressed using a formalism adopted from [103]. As in Section 4.1.2 and [167], the idea is to piece together trajectories of the flows \mathcal{F}_1 and \mathcal{F}_2 in such a way that a transition occurs when a flow intersects a switching hyper-surface, and at each transition the new initial condition is determined by the transition functions. This is formalized as follows. Denote $\mathcal{X} = \mathcal{X}_1 \cup \mathcal{X}_2$ as the union of the two state manifolds. A function $\varphi : [t_0, t_f] \rightarrow \mathcal{X}$, $t_f \in \mathbb{R} \cup \{\infty\}$, $t_f > t_0$, is a *solution* of (4.11) if there exists a closed discrete subset $\mathcal{T} \subset [t_0, t_f]$, $\mathcal{T} = \{t_0 < t_1 < \dots < t_j < \dots\}$,

called the set of switching times, and a function $i : \mathcal{T} \rightarrow \{1, 2\}$, which specifies the model's phase or mode, such that

- (a) for all⁸ $j \geq 0$, $i(j) \neq i(j+1)$;
- (b) for all $j \geq 0$, φ restricted to $[t_j, t_{j+1})$ takes values in $\mathcal{X}_{i(j)}$;
- (c) for all $j \geq 0$, φ restricted to $[t_j, t_{j+1})$ is right continuous, and hence, in particular, for every point $t \in [t_j, t_{j+1})$, the limit from the right, $\varphi^+(t) := \lim_{\tau \searrow t} \varphi(\tau)$, exists and is finite;
- (d) for all $j \geq 0$, φ restricted to (t_j, t_{j+1}) satisfies the differential equation $\dot{\varphi} = f_{i(j)}(\varphi)$;
- (e) for all $j \geq 0$ and for every point $t \in (t_j, t_{j+1})$, the limit from the left, $\varphi^-(t) := \lim_{\tau \nearrow t} \varphi(\tau)$, exists and is finite;
- (f) for all $j \geq 0$, and $t \in (t_j, t_{j+1})$, $\varphi(t) \notin \mathcal{S}_{i(j)}^{i(j+1)}$;
- (g) for all $j \geq 1$, and $t_j < \infty$, $\varphi^+(t_j) = \Delta_{i(j)}^{i(j+1)}(\varphi^-(t_j))$.

The condition that the set of switching times is closed and discrete implies that there is no “chattering.”

A solution $\varphi(t)$ of (4.11) is *periodic* if there exists a finite $T > 0$ such that $\varphi(t+T) = \varphi(t)$ for all $t \in [t_0, \infty)$. A set $\mathcal{O} \subset \mathcal{X}$ is a *periodic orbit* of (4.11) if $\mathcal{O} = \{\varphi(t) \mid t \geq t_0\}$ for some periodic solution $\varphi(t)$. The definitions of *orbital stability in the sense of Lyapunov*, *orbital asymptotic stability* and *orbital exponential stability* are identical to those given in Section 4.1.3 once an appropriate notion of distance is defined on $\mathcal{X} = \mathcal{X}_1 \cup \mathcal{X}_2$. Define $\text{dist} : \mathcal{X} \times \mathcal{X} \rightarrow \mathbb{R} \cup \{\infty\}$ to be

$$\text{dist}(p_1, p_2) := \begin{cases} \|p_1 - p_2\| & p_1, p_2 \in \mathcal{X}_1 \text{ or } p_1, p_2 \in \mathcal{X}_2 \\ \infty & \text{otherwise,} \end{cases} \quad (4.12)$$

and

$$\text{dist}(p_1, \mathcal{O}) := \inf_{p_2 \in \mathcal{O}} \text{dist}(p_1, p_2). \quad (4.13)$$

As an example, a periodic orbit \mathcal{O} of (4.11) is *stable in the sense of Lyapunov* if for every $\epsilon > 0$, there exists an open neighborhood⁹ \mathcal{V} of \mathcal{O} such that for every $p \in \mathcal{V}$, there exists a solution $\varphi : [0, \infty) \rightarrow \mathcal{X}$ of (4.11) satisfying $\varphi(0) = p$, $\text{dist}(\varphi(t), \mathcal{O}) < \epsilon$ for all $t \geq 0$.

A periodic orbit \mathcal{O} is *transversal* to \mathcal{S}_1 and \mathcal{S}_2 if its closure intersects \mathcal{S}_1 and \mathcal{S}_2 in exactly one point each, and for $\bar{x}_1 := \bar{\mathcal{O}} \cap \mathcal{S}_1$, $L_{f_1} H_1^2(\bar{x}_1) :=$

⁸In an abuse of notation, $i(j)$ is written for $i(t_j)$.

⁹That is, both $\mathcal{V} \cap \mathcal{X}_1$ and $\mathcal{V} \cap \mathcal{X}_2$ are open.

$\frac{\partial H_1^2}{\partial x_1}(\bar{x}_1)f_1(\bar{x}_1) \neq 0$ and similarly for \bar{x}_2 . In the case of a bipedal robot, a nontrivial periodic orbit transversal to \mathcal{S}_1 and \mathcal{S}_2 will also be referred to as *periodic locomotion*.

4.3.3 Existence and Stability of Periodic Orbits

The Poincaré return map remains the mathematical tool of choice for determining the existence and stability properties of periodic orbits. This section first defines the Poincaré section and the Poincaré return map that will be used for analyzing periodic orbits of (4.11). It is then shown how its use can be reduced to applying the corresponding results for systems with impulse effects, that is, the stability theorems presented in Section 4.2 through Section 4.6.

4.3.3.1 Definition of the Poincaré Return Map

Following Section 4.2, define the phase two *time-to-impact function*,¹⁰ $T_{I,2} : \mathcal{X}_2 \rightarrow \mathbb{R} \cup \{\infty\}$, by

$$T_{I,2}(x_0) := \begin{cases} \inf\{t \geq 0 \mid \varphi_2(t, x_0) \in \mathcal{S}_2^1\} & \text{if } \exists t \text{ such that } \varphi_2(t, x_0) \in \mathcal{S}_2^1 \\ \infty & \text{otherwise,} \end{cases} \quad (4.14)$$

where $\varphi_2(t, x_0)$ is an integral curve of (4.11) corresponding to $\varphi_2(0, x_0) = x_0$. From Lemma C.1, $T_{I,2}$ is continuous at points x_0 where $0 < T_{I,2}(x_0) < \infty$ and the intersection with \mathcal{S}_2^1 is transversal. Hence, $\tilde{\mathcal{X}}_2 := \{x_2 \in \mathcal{X}_2 \mid 0 < T_{I,2}(x_2) < \infty \text{ and } L_{f_2}H_2^1(\varphi_2(T_{I,2}(x_2), x_2)) \neq 0\}$ is open, and consequently, $\tilde{\mathcal{S}}_1^2 := \Delta_1^{2-1}(\tilde{\mathcal{X}}_2)$ is an open subset of \mathcal{S}_1^2 . It follows that under Hypotheses HSH1–HSH5 the *generalized Poincaré phase two map* $P_2 : \tilde{\mathcal{S}}_1^2 \rightarrow \mathcal{S}_2^1$ defined by

$$P_2(x_1) := \varphi_2(T_{I,2}(\Delta_1^2(x_1)), \Delta_1^2(x_1)), \quad (4.15)$$

is well defined and continuous (the terminology of a *generalized-Poincaré map* follows Appendix D of [173]). Moreover, when Hypotheses HSH2 and HSH4 are strengthened to HSH2' and HSH4', [173, Appendix D] proves that it is continuously differentiable.

Similarly, the *generalized Poincaré phase one map* $P_1 : \tilde{\mathcal{S}}_2^1 \rightarrow \tilde{\mathcal{S}}_1^2$, is defined by

$$P_1(x_2) := \varphi_1(T_{I,1}(\Delta_2^1(x_2)), \Delta_2^1(x_2)), \quad (4.16)$$

¹⁰Flows from one surface to another are sometimes called impact maps or functions, as they are here.

where, $T_{I,1} : x_0 \in \mathcal{X}_2 \rightarrow \mathbb{R} \cup \{\infty\}$ by

$$T_{I,1}(x_0) := \begin{cases} \inf\{t \geq 0 \mid \varphi_1(t, x_0) \in \tilde{\mathcal{S}}_1^2\} & \text{if } \exists t \text{ such that } \varphi_1(t, x_0) \in \tilde{\mathcal{S}}_1^2 \\ \infty & \text{otherwise,} \end{cases} \quad (4.17)$$

and

$$\tilde{\mathcal{S}}_2^1 = \{x_2 \in \mathcal{S}_2^1 \mid 0 < T_{I,1}(\Delta_2^1(x_2)) < \infty, \\ L_{f_1} H_1^2(\varphi_1(T_{I,1}(\Delta_2^1(x_2)), \Delta_2^1(x_2))) \neq 0\}. \quad (4.18)$$

When Hypotheses HSH2 and HSH4 are strengthened to HSH2' and HSH4', P_1 is continuously differentiable.

The *Poincaré return map* $P : \tilde{\mathcal{S}}_2^1 \rightarrow \mathcal{S}_2^1$ for (4.11) is defined by¹¹

$$P := P_2 \circ P_1. \quad (4.19)$$

4.3.3.2 Analysis of the Poincaré Return Map

Theorem 4.3 (Connecting Two-Phase Models to Single-Phase Models)

Let P be the Poincaré return map defined in (4.19) for the two-phase model in (4.11). P is also the Poincaré return map for the system with impulse effects

$$\Sigma : \begin{cases} \dot{x}(t) = f_2(x(t)) & x^-(t) \notin \mathcal{S} \\ x^+(t) = \Delta(x^-(t)) & x^-(t) \in \mathcal{S}, \end{cases} \quad (4.20)$$

where $\mathcal{S} := \tilde{\mathcal{S}}_2^1$ and $\Delta := \Delta_1^2 \circ P_1$.

Proof This follows immediately from the construction of the Poincaré return map in (4.8).

It is emphasized that this observation is important because it allows results developed for models of the form (4.20) to be applied to models with multiple phases. In particular, the material developed in Section 4.2 and Sections 4.4–4.6 is available when analyzing the Poincaré map of (4.11).

¹¹Clearly, the relative roles of phases one and two can be reversed, in which case $P := P_1 \circ P_2 : \tilde{\mathcal{S}}_1^2 \rightarrow \mathcal{S}_1^2$.

4.4 A Low-Dimensional Stability Test Based on Finite-Time Convergence

The Poincaré methods developed in the previous sections are fundamental for characterizing stable periodic locomotion in bipedal robots. However, the computations required to apply them in their current form can be prohibitive. The aim of this section is to present special circumstances where the application of Poincaré methods can be carried out in a straightforward and insightful manner. The additional hypotheses used here are motivated in part by the hybrid zero dynamics developed in Chapter 5 and in part by the desire to achieve analytical simplicity. These additional hypotheses will be achieved with specific feedback designs in Chapter 6 and Chapters 8–11.

4.4.1 Preliminaries

Consider the system with impulse effects (4.1) with the differential equation $\dot{x} = f(x)$ and impact map $\Delta : \mathcal{S} \rightarrow \mathcal{X}$. A set $\mathcal{Z} \subset \mathcal{X}$ is *forward invariant* if for each $x_0 \in \mathcal{Z}$, there exists $t_1 > 0$ such that $\varphi^f(t, x_0) \in \mathcal{Z}$ for $t \in [0, t_1]$. \mathcal{Z} is *impact invariant* if $\mathcal{S} \cap \mathcal{Z} \neq \emptyset$ and $\Delta(\mathcal{S} \cap \mathcal{Z}) \subset \mathcal{Z}$. \mathcal{Z} is *hybrid invariant* if it is both forward invariant and impact invariant.

Define the *settling time to \mathcal{Z}* , $T_{\mathcal{Z}}^{\text{set}} : \mathcal{X} \rightarrow \mathbb{R} \cup \{\infty\}$, by

$$T_{\mathcal{Z}}^{\text{set}}(x_0) := \begin{cases} \inf\{\tau \geq 0 \mid \exists \tau_1 > \tau, \text{ s.t.} & \text{if } \exists t \text{ such that} \\ & \varphi^f(t, x_0) \in \mathcal{Z}, t \in [\tau, \tau_1)\} & \varphi^f(t, x_0) \in \mathcal{Z} \\ \infty & \text{otherwise.} \end{cases} \quad (4.21)$$

\mathcal{Z} is *locally continuously finite-time attractive* if \mathcal{Z} is forward invariant and there exists an open set \mathcal{V} containing \mathcal{Z} such that $T_{\mathcal{Z}}^{\text{set}}$ is finite and continuous at each point of \mathcal{V} .

Remark 4.4 From [138], if f is locally Lipschitz continuous on an open neighborhood of $\mathcal{Z} \subset \mathcal{X}$ and \mathcal{Z} is locally continuously finite-time attractive, then \mathcal{Z} has nonempty interior (in particular, it cannot have dimension lower than that of \mathcal{X}). Hence, interesting examples of sets that are locally continuously finite-time attractive necessarily involve differential equations that are not locally Lipschitz continuous. As an example, the origin is continuously finite-time attractive for the differential equation $\dot{x} = -\text{sgn}(x)\sqrt{|x|}$.

4.4.2 Invariance Hypotheses

The autonomous system with impulse effects (4.1) will be analyzed when it possesses a subset $\mathcal{Z} \subset \mathcal{X}$ satisfying some or all of the hypotheses below.

- HInv1) \mathcal{Z} is an embedded submanifold of \mathcal{X} .
- HInv2) $\mathcal{S} \cap \mathcal{Z}$ is an embedded submanifold with dimension one less than the dimension of \mathcal{Z} .
- HInv3) \mathcal{Z} is locally continuously finite-time attractive.
- HInv4) \mathcal{Z} is hybrid invariant (forward invariant and impact invariant).

Lemma 4.1

Assume Hypotheses HInv1–HInv3.

1. The set

$$\hat{\mathcal{S}} := \{x_0 \in \mathcal{S} \mid T_{\mathcal{Z}}^{\text{set}}(\Delta(x_0)) < T_I(\Delta(x_0)) < \infty, \\ L_f H(\phi^f(T_I(\Delta(x_0)), \Delta(x_0))) \neq 0\} \quad (4.22)$$

is an open subset of $\tilde{\mathcal{S}}$, as defined in (4.7).

2. Let $P : \mathcal{S} \rightarrow \mathcal{S}$ be the Poincaré return map. Then $P : \hat{\mathcal{S}} \rightarrow \mathcal{S} \cap \mathcal{Z}$.

The straightforward proof is skipped.

4.4.3 The Restricted Poincaré Map

Define the *restricted Poincaré map*

$$\rho : \hat{\mathcal{S}} \cap \mathcal{Z} \rightarrow \mathcal{S} \cap \mathcal{Z} \text{ by } \rho(x) := P(x). \quad (4.23)$$

For $x^* \in \hat{\mathcal{S}}$, $P(x^*) \in \mathcal{S} \cap \mathcal{Z}$. Thus, by the definition of ρ , $P(x^*) = x^*$ if, and only if, $x^* \in \hat{\mathcal{S}} \cap \mathcal{Z}$ and $\rho(x^*) = x^*$. Suppose that for some $x_0 \in \hat{\mathcal{S}}$, the sequence $x[k+1] := P(x[k])$ is well defined for $k \geq 0$, and remains in some open neighborhood of x_0 . Then for all $k \geq 1$, $x[k+1] = \rho(x[k])$. It follows that $x^* \in \hat{\mathcal{S}}$ is a stable (resp., asymptotically stable, exponentially stable) equilibrium point of P if, and only if, it is a stable (resp., asymptotically stable, exponentially stable) equilibrium point of ρ . Thus, the determination of the existence and stability properties of periodic orbits that are transversal to $\hat{\mathcal{S}}$ can be reduced to the analysis of a low-dimensional map.

4.4.4 Stability Analysis Based on the Restricted Poincaré Map

The above remarks are summarized in the following theorem.

Theorem 4.4 (Low-Dimensional Stability Test-I)

Assume that the autonomous system with impulse effects (4.1) satisfies Hypotheses HSH1–HSH5. Suppose furthermore that $\mathcal{Z} \subset \mathcal{X}$ satisfies HInv1–HInv3. Then,

1. A periodic orbit is transversal to $\hat{\mathcal{S}}$ if, and only if, it is transversal to $\hat{\mathcal{S}} \cap \mathcal{Z}$.
2. $x^* \in \hat{\mathcal{S}} \cap \mathcal{Z}$ gives rise to a periodic orbit of (4.1) if, and only if, $\rho(x^*) = x^*$.
3. $x^* \in \hat{\mathcal{S}} \cap \mathcal{Z}$ gives rise to a stable (resp., asymptotically stable) periodic orbit of (4.1) if, and only if, x^* is a stable (resp., asymptotically stable) equilibrium point of ρ .

Theorem 4.4 identifies conditions under which periodic orbits of (4.1) may be rigorously characterized without computing the full Poincaré map: it is only necessary to evaluate a restriction of the Poincaré map to the set $\hat{\mathcal{S}} \cap \mathcal{Z}$. The computational savings can be substantial when \mathcal{Z} has relatively low dimension. It must be emphasized however that the determination of $\rho := P|_{\mathcal{Z}}$ still requires the solution of the differential equation (4.1) on \mathcal{X} , even though its initial conditions are being taken from $\hat{\mathcal{S}} \cap \mathcal{Z}$. It would be computationally advantageous if the restricted Poincaré map could be computed on the basis of a lower-order differential equation. The additional assumption required to achieve this is impact invariance. Note that \mathcal{Z} is impact invariant and locally continuously finite-time attractive if, and only if, \mathcal{Z} is hybrid invariant and locally continuously finite-time attractive; this is because local continuous finite-time attractivity includes, as part of its definition, forward invariance.

By forward invariance, solutions of $\dot{x} = f(x)$ initialized in \mathcal{Z} remain in \mathcal{Z} . Denote the restriction of f to \mathcal{Z} by $f|_{\mathcal{Z}}$ and the associated differential equation by $\dot{z} = f|_{\mathcal{Z}}(z)$. Similarly, let $H|_{\mathcal{Z}}$ and $\Delta|_{\mathcal{S} \cap \mathcal{Z}}$ denote the restriction of H and Δ to \mathcal{Z} . We note that Hypotheses HSH1–HSH5 on (4.1) imply the corresponding properties on the restriction dynamics. Indeed, $H|_{\mathcal{Z}}$ clearly satisfies HSH3, and by impact invariance, $\Delta|_{\mathcal{S} \cap \mathcal{Z}} : \mathcal{S} \cap \mathcal{Z} \rightarrow \mathcal{Z}$ by $\Delta|_{\mathcal{S} \cap \mathcal{Z}}(z) := \Delta(z)$, $z \in \mathcal{Z}$, satisfies HSH4 and HSH5. Hence, the *hybrid restriction dynamics*

$$\Sigma|_{\mathcal{Z}} : \begin{cases} \dot{z}(t) = f|_{\mathcal{Z}}(z(t)) & z^-(t) \notin \mathcal{S} \cap \mathcal{Z} \\ z^+(t) = \Delta|_{\mathcal{S} \cap \mathcal{Z}}(z^-(t)) & z^-(t) \in \mathcal{S} \cap \mathcal{Z} \end{cases} \quad (4.24)$$

is a system with impulse effects in its own right, verifying Hypotheses HSH1–HSH5 with respect to its state space, \mathcal{Z} . Therefore, Theorem 4.1 and Corollary 4.1 on the method of Poincaré sections can be applied to characterize periodic orbits in (4.24). In order to profitably use this observation, two further observations need to be made: (1) By construction, periodic orbits of the hybrid restriction dynamics are also periodic orbits of the full-dimensional model (4.1); (2) The Poincaré map of the hybrid restriction dynamics is the

restriction of the Poincaré map of the full-dimensional dynamics to \mathcal{Z} , that is, $P|_{\mathcal{Z}}$ is the Poincaré map of the hybrid restriction dynamics. Hence, by Theorem 4.4, the stability properties of orbits of the hybrid restriction dynamics carry over to the full-dimensional dynamics. In other words, the properties of certain periodic orbits of the full-dimensional dynamic can be completely determined on the basis of a lower-dimensional model. This is formalized in the next theorem.

Theorem 4.5 (Low-Dimensional Stability Test-II)

Assume that the autonomous system with impulse effects, (4.1), satisfies Hypotheses HSH1–HSH5. Suppose furthermore that $\mathcal{Z} \subset \mathcal{X}$ satisfies HInv1–HInv4. Then, all of the conclusions of Theorem 4.4 hold. Moreover, the restricted Poincaré map $\rho := P|_{\mathcal{Z}}$ is precisely the Poincaré map of the hybrid restriction dynamics (4.24). Consequently, stable (resp., asymptotically stable) orbits of the reduced-dimensional system with impulse effects, (4.24), are also stable (resp., asymptotically stable) orbits of the full-dimensional system with impulse effects, (4.1), and if both $f|_{\mathcal{Z}}$ and $\Delta|_{\mathcal{Z}}$ in (4.24) are continuously differentiable, then the correspondence extends to exponentially stable orbits.

The straightforward proof of Theorem 4.4 is not given; only the proof of the last part of Theorem 4.5 is sketched in [Appendix C.1.5](#). Using Proposition 4.1 and the partial Poincaré map yields a convenient restatement of Theorem 4.5:

Corollary 4.2

Assume that the autonomous system with impulse effects, (4.1), satisfies Hypotheses HSH1–HSH5. Suppose furthermore that $\mathcal{Z} \subset \mathcal{X}$ satisfies HInv1–HInv4. Then (4.1) has a stable (resp., asymptotically stable) orbit transversal to \mathcal{S} if, and only if, the discrete-time system

$$x[k+1] = \rho(x[k]) \quad (4.25)$$

with state space $\mathcal{S} \cap \mathcal{Z}$ has a stable (resp., asymptotically stable) equilibrium point x^* such that $L_f H(x^*) \neq 0$. Moreover, if $f|_{\mathcal{Z}}$ and $\Delta|_{\mathcal{S} \cap \mathcal{Z}}$ are continuously differentiable, then the equivalence also holds for exponential stability.

4.5 A Low-Dimensional Stability Test Based on Timescale Separation

Using the notion of finite-time convergence, the previous section established conditions under which a periodic orbit in a system with impulse effects is

stable or asymptotically stable, if, and only if, the orbit is stable or asymptotically stable in a hybrid restriction dynamics. It will be seen later that this provides an interesting “recipe” for designing feedback laws, namely, the feedback law should ensure three things: the creation of a hybrid invariant surface, the finite-time attractivity of the surface, and the creation of an asymptotically stable orbit in the restriction dynamics.

This section establishes a similar low-dimensional stability result when the invariant surface is “sufficiently rapidly exponentially attractive” instead of being finite-time attractive. The result is reminiscent of classical singular perturbation or timescale separation arguments [140]. Roughly speaking, the previous section on finite-time convergence can be viewed as the *ultimate* in timescale separation, since the dynamics transversal to the invariant surface were *infinitely fast* when compared to the dynamics on the surface. The result here replaces “infinitely fast” with “sufficiently fast.”

4.5.1 System Hypotheses

Consider a system with impulse effects that depends on a real parameter $\epsilon > 0$,

$$\Sigma^\epsilon : \begin{cases} \dot{x} = f^\epsilon(x), & x^- \notin \mathcal{S} \\ x^+ = \Delta(x^-), & x^- \in \mathcal{S}, \end{cases} \quad (4.26)$$

and suppose that for each value of $\epsilon > 0$, Hypotheses HSH1, HSH2', HSH3, HSH4', and HSH5 hold. For later use, a solution of $\dot{x} = f^\epsilon(x)$ is written as $\phi^\epsilon(t, x_0)$. The time-to-impact function is T_I^ϵ , and the Poincaré map is $P^\epsilon : \mathcal{S} \rightarrow \mathcal{S}$. In addition, suppose that the following structural hypotheses are met:

- HS1) there exist global coordinates $x = (z; \eta)$ for $\mathcal{X} \subset \mathbb{R}^n$, such that $z \in \mathbb{R}^k$, and $\eta \in \mathbb{R}^{n-k}$, $1 < k < n$, in which f^ϵ has the form

$$f^\epsilon(x) := f^\epsilon(z, \eta) := \begin{bmatrix} f_{1:k}(z, \eta) \\ f_{k+1:n}^\epsilon(\eta) \end{bmatrix}; \quad (4.27)$$

- HS2) for $\mathcal{Z} := \{(z; \eta) \in \mathcal{X} \mid \eta = 0\}$, $\mathcal{S} \cap \mathcal{Z}$ is a $(k - 1)$ -dimensional, C^1 -embedded submanifold of \mathcal{Z} , and

$$\Delta(\mathcal{S} \cap \mathcal{Z}) \subset \mathcal{Z}; \quad (4.28)$$

- HS3) (4.26) has a periodic orbit \mathcal{O} that is contained in \mathcal{Z} , and hence the orbit is independent of ϵ ;

- HS4) $x^* := \bar{\mathcal{O}} \cap \mathcal{S} \cap \mathcal{Z}$ is a singleton;

- HS5) $L_{f^\epsilon} H(x^*) \neq 0$; and

HS6) $f_{k+1:n}^\epsilon(\eta) = A(\epsilon)\eta$, and $\lim_{\epsilon \searrow 0} e^{A(\epsilon)} = 0$.

Hypotheses HS1 and HS6 imply that the set \mathcal{Z} is invariant under the continuous part of the model, $\dot{x} = f^\epsilon(x)$, so that if $x_0 \in \mathcal{Z}$ then for all t in its maximal domain of existence, $\phi^\epsilon(t, x_0) \in \mathcal{Z}$. Hypothesis HS2 implies that \mathcal{Z} remains invariant across the impact event, and hence the solution of (4.1) satisfies $x_0 \in \mathcal{Z}$ implies $\varphi(t, x_0) \in \mathcal{Z}$ on its domain of existence. Together, Hypotheses HS1 and HS2 imply that the restriction of Σ^ϵ to the manifold \mathcal{Z} is a well-defined system with impulse effects, which will be called the *restriction dynamics*, $\Sigma_{\mathcal{Z}}$,

$$\Sigma_{\mathcal{Z}} : \begin{cases} \dot{z} = f_{\mathcal{Z}}(z) & z^- \notin \mathcal{S} \cap \mathcal{Z} \\ z^+ = \Delta_{\mathcal{Z}}(z^-) & z^- \in \mathcal{S} \cap \mathcal{Z}, \end{cases} \quad (4.29)$$

where $f_{\mathcal{Z}}(z) := f^\epsilon(z, 0)$, and $\Delta_{\mathcal{Z}} = \Delta(z, 0)$. Whenever convenient, z will also be viewed as an element of \mathcal{X} by the identification $z = (z; 0)$. The invariance of \mathcal{Z} also yields

$$P^\epsilon(\mathcal{S} \cap \mathcal{Z}) \subset \mathcal{S} \cap \mathcal{Z}. \quad (4.30)$$

From Hypothesis HS3, \mathcal{O} is a periodic orbit of the restriction dynamics. The restriction of f^ϵ to \mathcal{Z} removes any dependence on ϵ . This fact may be used to show that $\phi_{\mathcal{Z}} := \phi^\epsilon|_{\mathcal{Z}}$, $T_{I,\mathcal{Z}} := T_I^\epsilon|_{\mathcal{Z}}$, and $P^\epsilon|_{\mathcal{Z}}$ are also independent of ϵ , and hence,

$$t^* := T_I^\epsilon(\Delta(x^*)) = T_{I,\mathcal{Z}}(\Delta_{\mathcal{Z}}(x^*)), \quad (4.31)$$

is independent of ϵ .

On the basis of (4.30), the *restricted Poincaré map*, $\rho : \mathcal{S} \cap \mathcal{Z} \rightarrow \mathcal{S} \cap \mathcal{Z}$, may be defined as $\rho := P^\epsilon|_{\mathcal{Z}}$, or equivalently,

$$\rho(z) := \phi_{\mathcal{Z}}(T_{I,\mathcal{Z}}(\Delta_{\mathcal{Z}}(z)), \Delta_{\mathcal{Z}}(z)), \quad (4.32)$$

and is independent of ϵ . From HS4, it follows that x^* is a fixed point of P^ϵ and ρ , and from HS5, the orbit is transversal to \mathcal{S} , and hence also to $\mathcal{S} \cap \mathcal{Z}$.

Hypothesis HS6 says that the dynamics transversal to \mathcal{Z} is “sufficiently rapidly” exponentially contracting. When the solution of (4.1) is not on the periodic orbit, $\eta(t) \neq 0$. In many situations, such as bipedal walking, the impact map increases the norm of η at each impact. Hypothesis HS6 provides control over the speed with which $\eta(t)$ converges to zero during the continuous phase, so that, over a cycle consisting of an impact event followed by continuous flow, the solution may converge to the orbit.

4.5.2 Stability Analysis Based on the Restricted Poincaré Map

Theorem 4.6 (Low-Dimensional Stability Test-III)

Under Hypotheses HSH1, HSH2', HSH3, HSH4', HSH5, and HS1–HS6, there exists $\bar{\epsilon} > 0$ such that for $0 < \epsilon < \bar{\epsilon}$, the following are equivalent:

- a) x^* is an exponentially stable fixed point of ρ ;
- b) x^* is an exponentially stable fixed point of P^ϵ .

In other words, for $\epsilon > 0$ sufficiently small, an exponentially stable periodic orbit of the restriction dynamics is also an exponentially stable periodic orbit of the full-dimensional model. The proof is given in [Appendix C.1.6](#). An interesting structural property of the Jacobian of the Poincaré map evaluated at the fixed point is brought out in Lemma C.5.

4.6 Including Event-Based Control

In this section, we assume that various elements of the system with impulse effects (4.1) depend on one or more parameters that are to be held constant between impact events, but at each impact, the parameters may be updated. The utility of this feature becomes apparent, for example, when a within-stride controller has been designed to depend on a parameter in such a way that by changing the parameter's value, different locomotion characteristics may be achieved, such as walking at a different speed, or with a different step length. We will analyze two situations.

In the first situation, the parameter takes on discrete values and is updated infrequently at impact events. Our objective is to transfer the system from a neighborhood of one asymptotically stable periodic orbit to another, while "guaranteeing stability." The method we follow is motivated by a switching idea presented in [30]. In this reference, controllers were designed to accomplish the individual tasks of juggling, catching, and palming a ping-pong ball by a robot arm. The domains of attraction of each controller were empirically estimated within the full state space of the robot. The controllers were then sequentially composed via switching to accomplish the complex task of maneuvering the ping-pong ball in a three-dimensional workspace with an obstacle. Switching from one controller to another without loss of stability was accomplished by allowing a switch to occur only if the current state of the robot was in the domain of attraction of the next desired task. The problem we analyze here is more challenging than the situation faced in [30] in the sense that we allow that the domains of attraction of any two of the individual periodic orbits may have empty intersection, and hence a transition phase will be required to steer the system from the domain of attraction of one periodic orbit into the domain of attraction of another periodic orbit.

In the second situation, the parameter will take on a continuum of values and may be updated at each impact event. Our objective is to analyze when a given event-based update rule for the parameter will result in a stable, periodic

orbit. The parameter update rule will be thought of as an event-driven, static or dynamic, feedback law.

4.6.1 Analyzing Event-Based Control with the Full-Order Model

Infrequent switching or transition control: Consider a collection of systems with impulse effects, indexed by a parameter a ,

$$\Sigma_a : \begin{cases} \dot{x}(t) = f(x(t), a) & x^-(t) \notin \mathcal{S} \\ x^+(t) = \Delta(x^-(t), a) & x^-(t) \in \mathcal{S}, \end{cases} \quad (4.33)$$

with common state space $x \in \mathcal{X}$ and impact set \mathcal{S} . Assume that a takes values in a set \mathcal{A} , and that for each value of a , Hypotheses HSH1–HSH5 are satisfied. For $a \in \mathcal{A}$, let $P_a : \mathcal{S} \rightarrow \mathcal{S}$ be the Poincaré return map and denote the corresponding difference equation on \mathcal{S} by $x[k+1] = P_a(x[k])$. Suppose that two elements α and β belonging to \mathcal{A} give rise to asymptotically stable periodic orbits \mathcal{O}_α and \mathcal{O}_β of (4.33) that are transversal to \mathcal{S} . The goal is to understand when (or how) it is possible to synthesize a solution of (4.33) that starts near \mathcal{O}_α and converges to \mathcal{O}_β , where a solution consists of piecing together trajectories in which the parameter is held constant between impacts. In other words, a solution corresponds to a switching policy, where switches are only allowed to occur at impacts.

Denote the fixed points of the Poincaré return maps P_α and P_β by x_α^* and x_β^* . It is supposed the Poincaré maps are continuous at their fixed points and that the fixed points are transversal to \mathcal{S} . Finally, let $\mathcal{D}_\alpha \subset \mathcal{S}$ and $\mathcal{D}_\beta \subset \mathcal{S}$ be the corresponding domains of attraction.

In terms of synthesizing a control law to transfer from a neighborhood of \mathcal{O}_α to a neighborhood of \mathcal{O}_β , the simplest situation occurs when $x_\alpha^* \in \mathcal{D}_\beta$. Indeed, in this case, any solution of (4.33) that enters \mathcal{D}_α will eventually enter \mathcal{D}_β , at which time, switching the parameter value from α to β and keeping it constant thereafter will result in convergence to x_β^* , and consequently, to \mathcal{O}_β . Conversely, if $x_\alpha^* \notin \mathcal{D}_\beta$, there is no guarantee that a simple switch in parameter value from α to β will result in a solution that converges to \mathcal{O}_β . Indeed, such a simple switching policy would be guaranteed to fail when (4.33) with $a = \alpha$ is initialized sufficiently closely to \mathcal{O}_α . A richer family of trajectories is thus required for synthesizing a switching policy.

Proposition 4.2 (Transition Control-I)

Consider the parameterized system with impulse effects (4.33), which is assumed to satisfy Hypotheses HSH1–HSH5 for parameters taking values in \mathcal{A} . Let $\alpha, \beta, \mathcal{O}_\alpha, \mathcal{O}_\beta, \mathcal{D}_\alpha \subset \mathcal{S}$, and $\mathcal{D}_\beta \subset \mathcal{S}$ be as above. Suppose that \mathcal{A} contains

a third element denoted $(\alpha \rightarrow \beta)$ such that¹² $x_\alpha^* \in \mathcal{D}_{(\alpha \rightarrow \beta)} := P_{(\alpha \rightarrow \beta)}^{-1}(\mathcal{D}_\beta)$. Then, any solution of (4.33) that is initialized in the domain of attraction of \mathcal{O}_α will asymptotically converge to \mathcal{O}_β under the following switching policy: hold the parameter constant and equal to α until the trajectory impacts $\mathcal{D}_{(\alpha \rightarrow \beta)}$; immediately switch the parameter value to $(\alpha \rightarrow \beta)$; at the very next impact, switch the parameter value to β and hold it constant thereafter.

Proof Any solution of $x[k+1] = P_\alpha(x[k])$ that is initialized in \mathcal{D}_α will converge to x_α^* , and thus eventually enter $\mathcal{D}_{(\alpha \rightarrow \beta)}$. The set of points in \mathcal{D}_α that can be steered in one step to \mathcal{D}_β under $a = (\alpha \rightarrow \beta)$ is $\mathcal{D}_\alpha \cap P_{(\alpha \rightarrow \beta)}^{-1}(\mathcal{D}_\beta)$. Any solution of $x[k+1] = P_\beta(x[k])$ that is initialized in \mathcal{D}_β will converge to x_β^* . By Theorem 4.1, the corresponding solution of (4.33) converges to \mathcal{O}_β .

The parameter value $(\alpha \rightarrow \beta)$ has served to steer—or transition—solutions from a neighborhood of x_α^* to a neighborhood of x_β^* in one step. $(\alpha \rightarrow \beta)$ is called a *transition parameter*. The extension of the analysis to encompass a finite set of two or more transition parameters to effect a multistep transition between two periodic orbits is obvious. Note that a transition parameter need not give rise to a periodic orbit itself, that is, $P_{(\alpha \rightarrow \beta)}$ need not have a fixed point.

Continual switching: Consider again the collection of systems with impulse effects, (4.33), with common state space $x \in \mathcal{X}$ and impact set \mathcal{S} , and suppose that Hypotheses HSH1 and HSH3–HSH5 hold. Assume this time that a takes values in \mathcal{A} , an open subset of \mathbb{R}^p , and that Hypothesis HSH2 is strengthened to hold for the associated differential equation

$$\begin{aligned}\dot{x} &= f(x, a) \\ \dot{a} &= 0,\end{aligned}\tag{4.34}$$

that is, f is continuous on $\mathcal{X} \times \mathcal{A}$ and solutions exist, are unique, and depend continuously on initial conditions.

As before, for $a \in \mathcal{A}$, let $P_a : \mathcal{S} \rightarrow \mathcal{S}$ be the Poincaré return map. However, instead of considering the difference equation $x[k+1] = P_a(x[k])$ on \mathcal{S} , we now invoke the fact that a can be changed at each impact and we view the difference equation as a discrete-time control system on \mathcal{S} with the parameter vector $a \in \mathcal{A}$ as the control:

$$x[k+1] = P(x[k], a[k]),\tag{4.35}$$

¹²This is the inverse image of the set \mathcal{D}_β under the map $P_{(\alpha \rightarrow \beta)}$. Thus,

$$\mathcal{D}_{(\alpha \rightarrow \beta)} := \{x \in \mathcal{S} \mid P_{(\alpha \rightarrow \beta)}(x) \in \mathcal{D}_\beta\}.$$

where $P(x, a) := P_a(x)$. It will now be established that there is a one-to-one correspondence between static (resp., dynamic) state-variable feedback control laws for (4.35) and static (resp., dynamic) parameter update laws for (4.33). Moreover, thanks to Poincaré analysis, this correspondence extends to periodic orbits and their stability properties. In other words, the design of a parameter update law for (4.33) that creates an asymptotically stable periodic orbit can be performed by designing a feedback controller for (4.35) that creates an asymptotically stable equilibrium point. Even more specifically, suppose there exists a parameter value a^* for which (4.33) possesses a desired periodic orbit, but the orbit is either not stable, or it is asymptotically stable, but the rate of convergence is too slow. Let x^* be the corresponding fixed point of P_{a^*} . Then designing a parameter update law for (4.33) that preserves the orbit and stabilizes it (or increases the rate of convergence) is equivalent to designing a feedback controller for (4.35) that preserves the equilibrium point and stabilizes it (or increases the rate of convergence).

Suppose that $a = v(x)$ is a static state-variable feedback control law for (4.35) and consider the discrete-time closed-loop system

$$x[k+1] = P(x[k], v(x[k])), \quad (4.36)$$

and a deadbeat dynamic extension

$$\begin{aligned} x[k+1] &= P(x[k], v(x[k])) \\ a[k+1] &= v(x[k]). \end{aligned} \quad (4.37)$$

Note that (4.36) has an equilibrium point if, and only if, (4.37) has an equilibrium point, and moreover, x^* is a stable (resp., asymptotically stable, or exponentially stable) equilibrium point for (4.36) if, and only if, $(x^*; a^* = v(x^*))$ is a stable (resp., asymptotically stable, or exponentially stable) equilibrium point for (4.37). The importance of this formal looking observation is that

$$P_{aux}(x, a) := \begin{bmatrix} P(x, v(x)) \\ v(x) \end{bmatrix} \quad (4.38)$$

is the Poincaré return map of the following system with impulse effects:

$$\Sigma_{aux} : \begin{cases} \begin{bmatrix} \dot{x}(t) \\ \dot{a}(t) \end{bmatrix} = \begin{bmatrix} f(x(t), a(t)) \\ 0 \end{bmatrix} & \begin{bmatrix} x^-(t) \\ a^-(t) \end{bmatrix} \notin \mathcal{S}_{aux} \\ \begin{bmatrix} x^+(t) \\ a^+(t) \end{bmatrix} = \begin{bmatrix} \Delta(x^-(t), v(x^-(t))) \\ v(x^-(t)) \end{bmatrix} & \begin{bmatrix} x^-(t) \\ a^-(t) \end{bmatrix} \in \mathcal{S}_{aux}, \end{cases} \quad (4.39)$$

where the state space is $\mathcal{X}_{aux} := \mathcal{X} \times \mathcal{A}$ and the impact surface is $\mathcal{S}_{aux} := \mathcal{S} \times \mathcal{A}$. Hence, by Theorem 4.1 and Corollary 4.1, designing a memoryless parameter-update law for (4.33) that results in (4.39) possessing a stable (resp., asymptotically stable, or exponentially stable) periodic orbit is precisely equivalent

to designing a static state-feedback control law for (4.35) that results in (4.36) possessing a stable (resp., asymptotically stable, or exponentially stable) equilibrium point. Since the same reasoning applies *mutatis mutandis* for the more general case of a parameter update law with memory (i.e., a dynamic event-based feedback controller), we have the following result.

Theorem 4.7 (Stability under Event-Based Parameter Updates-I)

Consider the collection of systems with impulse effects, (4.33), with $a \in \mathcal{A}$, an open subset of \mathbb{R}^p . Suppose that \mathcal{X} and \mathcal{S} satisfy Hypotheses HSH1, HSH3–HSH5. Suppose furthermore that Hypothesis HSH2 holds for the differential equation (4.34). Let \mathcal{W} be an open subset of \mathbb{R}^ℓ for some integer ℓ , and define $\mathcal{X}_{aux} := \mathcal{X} \times \mathcal{A} \times \mathcal{W}$ and $\mathcal{S}_{aux} := \mathcal{S} \times \mathcal{A} \times \mathcal{W}$. Suppose that $v_1 : \mathcal{S} \times \mathcal{W} \rightarrow \mathcal{A}$ and $v_2 : \mathcal{S} \times \mathcal{W} \rightarrow \mathcal{W}$ are continuous. Then,

$$\Sigma_{aux} : \begin{cases} \begin{bmatrix} \dot{x}(t) \\ \dot{a}(t) \\ \dot{w}(t) \end{bmatrix} = \begin{bmatrix} f(x(t), a(t)) \\ 0 \\ 0 \end{bmatrix}, & \begin{bmatrix} x^-(t) \\ a^-(t) \\ w^-(t) \end{bmatrix} \notin \mathcal{S}_{aux} \\ \begin{bmatrix} x^+(t) \\ a^+(t) \\ w^+(t) \end{bmatrix} = \begin{bmatrix} \Delta(x^-(t), v_1(x^-(t), w^-(t))) \\ v_1(x^-(t), w^-(t)) \\ v_2(x^-(t), w^-(t)) \end{bmatrix}, & \begin{bmatrix} x^-(t) \\ a^-(t) \\ w^-(t) \end{bmatrix} \in \mathcal{S}_{aux}, \end{cases} \quad (4.40)$$

has a stable (resp., asymptotically stable) orbit transversal to \mathcal{S}_{aux} if, and only if, the discrete-time system

$$\begin{aligned} x[k+1] &= P(x[k], v_1(x[k], w[k])) \\ w[k+1] &= v_2(x[k], w[k]) \end{aligned} \quad (4.41)$$

on $\mathcal{S} \times \mathcal{W}$ has a stable (resp., asymptotically stable) equilibrium point $(x^*; w^*)$ such that $L_f H(x^*, a^*) \neq 0$, where $a^* = v_1(x^*, w^*)$. Moreover, if HSH2' and HSH4' hold and v_1 and v_2 are continuously differentiable, then the equivalence also holds for exponential stability.

The special case of a memoryless parameter update for (4.33), and hence, static state-feedback control of (4.35), is obtained by letting \mathcal{W} be empty. Integral feedback control action, either to reject a constant disturbance or to track a constant reference, is also a special case: If d and r are constants (possibly, vector valued) representing disturbances and references, respectively, then formally define $f(x, a) = \tilde{f}(x, a, d)$, $v_1(x, w) = \tilde{v}_1(x, w, r)$ and $v_2(x, w) = \tilde{v}_2(x, w, r)$ in the above analysis.

4.6.2 Analyzing Event-Based Actions with a Hybrid Restriction Dynamics Based on Finite-Time Attractivity

The previous subsection reduced the study of orbits in a collection of systems with impulse effects, having a common state space and a common impact surface, to the study of equilibrium points of a discrete-time control system evolving on the impact surface. This subsection will identify circumstances in which analysis and feedback controller design for the discrete-time control system can be performed on the restriction dynamics, thereby reducing the dimension of the problem. The significant payoff in terms of computational tractability will become evident in [Chapters 7 and 8](#).

Infrequent switching or transition control: Under the hypothesis of finite-time attractivity, the problem of transitioning between two orbits follows very closely the corresponding development in the previous subsection. For this reason, we pass straight to the main result.

Proposition 4.3 (Transition Control-II)

Consider the parameterized system with impulse effects (4.33), where \mathcal{X} and \mathcal{S} satisfy Hypotheses HSH1 and HSH3–HSH5, and where \mathcal{A} is an open subset of \mathbb{R}^p such that Hypothesis HSH2 holds for the differential equation (4.34). Suppose that there exist embedded submanifolds $\mathcal{Z}_a \subset \mathcal{X}$ such that

1. for $a \in \{\alpha, \beta\} \subset \mathcal{A}$, \mathcal{Z}_a is forward invariant under f_a ;
2. for $a \in \{\alpha, \beta\}$, \mathcal{Z}_a is continuously finite-time attractive under f_a , $\mathcal{S} \cap \mathcal{Z}_a$ is a nonempty embedded submanifold of \mathcal{X} , and $\Delta(\mathcal{Z}_a, a) \subset \mathcal{Z}_a$;
3. for $a \in \{\alpha, \beta\}$, there exists an asymptotically (exponentially) stable, periodic orbit \mathcal{O}_a transversal to $\mathcal{S} \cap \mathcal{Z}_a$ so that the domain of attraction $\mathcal{D}_a \subset \mathcal{S} \cap \mathcal{Z}_a$ of the restricted Poincaré map ρ_a is nonempty and open; denote the associated fixed point by x_a^* ; and
4. $\Delta(\mathcal{Z}_\alpha, (\alpha \rightarrow \beta)) \subset \mathcal{Z}_{(\alpha \rightarrow \beta)}$ and $\Delta(\mathcal{Z}_{(\alpha \rightarrow \beta)}, \beta) \subset \mathcal{Z}_\beta$.

If $x_\alpha^* \in \mathcal{D}_{(\alpha \rightarrow \beta)} := \rho_{(\alpha \rightarrow \beta)}^{-1}(\mathcal{D}_\beta)$, then any solution of (4.33) with $a = \alpha$ that is initialized in the domain of attraction of \mathcal{O}_α will asymptotically (exponentially) converge to \mathcal{O}_β under the following switching policy: hold the parameter constant and equal to α until the trajectory impacts $\mathcal{D}_{(\alpha \rightarrow \beta)}$; immediately switch the parameter value to $(\alpha \rightarrow \beta)$; at the very next impact, switch the parameter to β and hold it constant thereafter.

The proof is quite trivial once it is noted that the hypotheses imply that $P_{(\alpha \rightarrow \beta)}(\mathcal{S} \cap \mathcal{Z}_\alpha) \subset \mathcal{Z}_\beta$. Hence, $\rho_{(\alpha \rightarrow \beta)} : \mathcal{S} \cap \mathcal{Z}_\alpha \rightarrow \mathcal{Z}_\beta$ is a restriction of $P_{(\alpha \rightarrow \beta)}$ to \mathcal{Z}_α and \mathcal{Z}_β .

Continual switching: We present two refinements of Theorem 4.7 to allow the event-based feedback design to be performed on the basis of the restriction dynamics. Consider a collection of subsets $\{\mathcal{Z}_a \mid a \in \mathcal{A}\} \subset \mathcal{X}$. In the first case, we suppose that $\mathcal{S} \cap \mathcal{Z}_a$ is independent of $a \in \mathcal{A}$. We denote the common intersection by $\mathcal{S} \cap \mathcal{Z}_\diamond$. Under this assumption, hybrid invariance leads to a restricted Poincaré map, $\rho_a : \mathcal{S} \cap \mathcal{Z}_\diamond \rightarrow \mathcal{S} \cap \mathcal{Z}_\diamond$. Under appropriate hypotheses, the reduction method of Theorem 4.5 can be combined with Theorem 4.7 so that event-based feedback design can be carried out on the control system $x[k+1] = \rho(x[k], a[k])$ evolving on the state space $\mathcal{S} \cap \mathcal{Z}_\diamond$ with controls taking values in \mathcal{A} .

Theorem 4.8 (Stability under Event-Based Parameter Updates-II)
Consider the collection of systems with impulse effects, (4.33), with the parameter a taking values in \mathcal{A} . Suppose that \mathcal{X} and \mathcal{S} satisfy Hypotheses HSH1 and HSH3–HSH5. Suppose furthermore that \mathcal{A} is an open subset of \mathbb{R}^p such that Hypothesis HSH2 holds for the differential equation (4.34) and there exists a collection of subsets $\{\mathcal{Z}_a \mid a \in \mathcal{A}\} \subset \mathcal{X}$ such that:

1. $\forall a \in \mathcal{A}$, $\mathcal{Z}_a \subset \mathcal{X}$ satisfies Hypotheses HInv1 and HInv2;
2. $\forall a \in \mathcal{A}$, $\mathcal{S} \cap \mathcal{Z}_a$ is independent of a ; denote the common intersection with \mathcal{S} by $\mathcal{S} \cap \mathcal{Z}_\diamond$;
3. $\forall a \in \mathcal{A}$, $\Delta(\mathcal{S} \cap \mathcal{Z}_\diamond, a) \subset \mathcal{Z}_a$; and
4. $\mathbf{Z} := \{(x, a) \mid x \in \mathcal{Z}_a, a \in \mathcal{A}\}$ is an embedded submanifold of $\mathcal{X} \times \mathcal{A}$ and is locally continuously finite-time attractive for (4.34).

Let \mathcal{W} be an open subset of \mathbb{R}^ℓ and suppose that $v_1 : \mathcal{S} \times \mathcal{W} \rightarrow \mathcal{A}$ and $v_2 : \mathcal{S} \times \mathcal{W} \rightarrow \mathcal{W}$ are given continuous maps. Define $\mathcal{X}_{aux} := \mathcal{X} \times \mathcal{A} \times \mathcal{W}$, $\mathcal{S}_{aux} := \mathcal{S} \times \mathcal{A} \times \mathcal{W}$, and $\mathcal{Z}_{aux} := \mathbf{Z} \times \mathcal{W}$. Then (4.40) has a stable (resp., asymptotically stable) orbit transversal to $\mathcal{S}_{aux} \cap \mathcal{Z}_{aux}$ if, and only if, the discrete-time system

$$\begin{aligned} x[k+1] &= \rho(x[k], v_1(x[k], w[k])) \\ w[k+1] &= v_2(x[k], w[k]) \end{aligned} \tag{4.42}$$

on $\mathcal{S} \cap \mathcal{Z}_\diamond \times \mathcal{W}$ has a stable (resp., asymptotically stable) equilibrium point (x^*, w^*) such that $L_f H(x^*, a^*) \neq 0$, where $a^* = v_1(x^*, w^*)$. Moreover, if $f|_{\mathbf{Z}}$, $\Delta|_{(\mathcal{S} \times \mathcal{A}) \cap \mathbf{Z}}$, v_1 , and v_2 are continuously differentiable, then the equivalence also holds for exponential stability.

In the second case, we allow $\mathcal{S} \cap \mathcal{Z}_a$ to depend on $a \in \mathcal{A}$ and hence impact invariance must be replaced by a more general notion that is closer to what was used in transition control.

Theorem 4.9 (Stability under Event-Based Parameter Updates-III)

Consider the collection of systems with impulse effects, (4.33), with the parameter taking values in $\mathcal{A} := \mathcal{A}_1 \times \mathcal{A}_2$, where \mathcal{A}_1 is an open subset of \mathbb{R}^{p_1} and \mathcal{A}_2 is an open subset of \mathbb{R}^{p_2} . Suppose that \mathcal{X} and \mathcal{S} satisfy Hypotheses HSH1 and HSH3–HSH5. Suppose furthermore that Hypothesis HSH2 holds for the differential equation (4.34) and there exists a collection of subsets of \mathcal{X} such that:

1. $\forall (a_1, a_2) \in \mathcal{A}_1 \times \mathcal{A}_2$, $\mathcal{Z}_{a_1, a_2} \subset \mathcal{X}$ satisfies Hypotheses HInv1 and HInv2;
2. $\forall (a_1, a_2) \in \mathcal{A}_1 \times \mathcal{A}_2$, $\mathcal{S} \cap \mathcal{Z}_{a_1, a_2}$ is independent of a_1 ; denote the intersection with \mathcal{S} by $\mathcal{S} \cap \mathcal{Z}_{\diamond, a_2}$;
3. there exists a continuous function $\psi : \mathcal{A}_2 \rightarrow \mathcal{A}_1$ such that, $\forall a_2^-, a_2^+ \in \mathcal{A}_2$, $\Delta(\mathcal{S} \cap \mathcal{Z}_{\diamond, a_2^-}, \psi(a_2^-), a_2^+) \subset \mathcal{Z}_{\psi(a_2^-), a_2^+}$; and
4. $\mathbf{Z} := \{(x, a_1, a_2) \mid x \in \mathcal{Z}_{a_1, a_2}, a_1 \in \mathcal{A}_1, a_2 \in \mathcal{A}_2\}$ is an embedded submanifold of $\mathcal{X} \times \mathcal{A}_1 \times \mathcal{A}_2$ and is locally continuously finite-time attractive for (4.34).

Let \mathcal{W} be an open subset of \mathbb{R}^ℓ . Suppose that $v_1 : \mathcal{S} \times \mathcal{W} \rightarrow \mathcal{A}_2$ and $v_2 : \mathcal{S} \times \mathcal{W} \rightarrow \mathcal{W}$ are continuous. Define $\mathcal{X}_{aux} := \mathcal{X} \times \mathcal{A} \times \mathcal{W}$, $\mathcal{S}_{aux} := \mathcal{S} \times \mathcal{A} \times \mathcal{W}$, and $\mathcal{Z}_{aux} := \mathbf{Z} \times \mathcal{W}$. Then,

$$\Sigma_{aux} : \begin{cases} \begin{bmatrix} \dot{x}(t) \\ \dot{a}_1(t) \\ \dot{a}_2(t) \\ \dot{w}(t) \end{bmatrix} = \begin{bmatrix} f(x(t), a_1(t), a_2(t)) \\ 0 \\ 0 \\ 0 \end{bmatrix}, & \begin{bmatrix} x^-(t) \\ a_1^-(t) \\ a_2^-(t) \\ w^-(t) \end{bmatrix} \notin \mathcal{S}_{aux} \\ \begin{bmatrix} x^+(t) \\ a_1^+(t) \\ a_2^+(t) \\ w^+(t) \end{bmatrix} = \begin{bmatrix} \Delta(x^-(t), \psi(a_2^-(t)), \\ v_1(x^-(t), w^-(t))) \\ \psi(a_2^-(t)) \\ v_1(x^-(t), w^-(t)) \\ v_2(x^-(t), w^-(t)) \end{bmatrix}, & \begin{bmatrix} x^-(t) \\ a_1^-(t) \\ a_2^-(t) \\ w^-(t) \end{bmatrix} \in \mathcal{S}_{aux}, \end{cases} \quad (4.43)$$

has a stable (resp., asymptotically stable) orbit transversal to $\mathcal{S}_{aux} \cap \mathcal{Z}_{aux}$ if, and only if, the discrete-time system

$$\begin{aligned} x[k+1] &= \rho(x[k], \psi(a_2[k]), v_1(x[k], w[k])) \\ a_2[k+1] &= v_1(x[k], w[k]) \\ w[k+1] &= v_2(x[k], w[k]) \end{aligned} \quad (4.44)$$

on $\{(\mathcal{S} \cap \mathcal{Z}_{\diamond, a_2}, a_2) \mid a_2 \in \mathcal{A}_2\} \times \mathcal{W}$ has a stable (resp., asymptotically stable) equilibrium point $(x^*; a_2^*; w^*)$ such that $L_f H(x^*, a_1^*, a_2^*) \neq 0$, where $a_1^* =$

$\psi(a_2^*)$. Moreover, if $f|_{\mathbf{Z}}$, $\Delta|_{(\mathcal{S} \times \mathcal{A}) \cap \mathbf{Z}}$, ψ , v_1 , and v_2 are continuously differentiable, then the equivalence also holds for exponential stability.

The proofs of these two theorems are given in Appendices C.1.7 and C.1.8. The theorems can be modified to replace finite-time attractivity with sufficiently fast exponential convergence, as in Theorem 4.6.

5

Zero Dynamics of Bipedal Locomotion

The method of computed torque, also known as inverse dynamics, is ubiquitous in the field of robotics [60, 164, 218]. It consists of defining a set of outputs, equal in number to the inputs, and then designing a feedback controller that asymptotically drives the outputs to zero. In this manner, a geometric task for the robot may be encoded into a set of outputs in such a way that the zeroing of the outputs is asymptotically equivalent to achieving the task, whether the task be asymptotic convergence to an equilibrium point, a surface, or a time trajectory. For a system modeled by ordinary differential equations (in particular, without impact dynamics), the maximal internal dynamics of the system that is compatible with the output being identically zero is called the *zero dynamics* [127, 128, 168]. Hence, the method of computed torque can be seen as an indirect means of designing a set of zero dynamics for the robot. Since, in general, the dimension of the zero dynamics is considerably less than the dimension of the model itself, the task to be achieved by the robot is *implicitly* encoded into a lower-dimensional system.

One of the main points of this chapter is that this process can be *explicitly* exploited in the design of feedback controllers for walking mechanisms *even in the presence of impacts*. Here, the outputs will be thought of as defining virtual constraints, that is, holonomic relationships among the system's states that are imposed asymptotically via a state-variable feedback controller. As opposed to physical constraints, that is, constraints that are imposed mechanically, for example, with cams and links, and hence for obvious reasons are not easily reconfigured, virtual constraints may be easily redefined (reconfigured).

5.1 Introduction to Zero Dynamics and Virtual Constraints

This section introduces zero dynamics and virtual constraints via two examples. The first example uses a SISO linear system with a single zero and two poles to develop the notion of zero dynamics. The second example uses a pendulum evolving in a horizontal plane (i.e., normal to the gravitational field) to develop the notion of virtual constraints. A more general overview of the

notion of zero dynamics for a system modeled by a set of nonlinear ordinary differential equations is provided in [Appendix B.2](#).

5.1.1 A Simple Zero Dynamics Example

Consider the single-input, single-output linear system described by the transfer function

$$H(s) = \frac{s + \alpha}{s^2 - s - 6} \quad (5.1)$$

where $\alpha \in \mathbb{R}$. $H(s)$ has a zero at $-\alpha$ and two poles, at 3 and -2 . A state space realization of $H(s)$ is

$$\begin{bmatrix} \dot{x}_1 \\ \dot{x}_2 \end{bmatrix} = \begin{bmatrix} 0 & 1 \\ 6 & 1 \end{bmatrix} \begin{bmatrix} x_1 \\ x_2 \end{bmatrix} + \begin{bmatrix} 0 \\ 1 \end{bmatrix} u \quad (5.2a)$$

$$y = [\alpha \ 1] \begin{bmatrix} x_1 \\ x_2 \end{bmatrix}. \quad (5.2b)$$

The origin is not stable in the sense of Lyapunov due to the eigenvalue at 3. Differentiating the output once gives

$$\dot{y} = \alpha \dot{x}_1 + \dot{x}_2 \quad (5.3a)$$

$$= 6x_1 + (1 + \alpha)x_2 + u, \quad (5.3b)$$

and hence the system has relative degree one. Applying the preliminary feedback

$$u = -6x_1 - (1 + \alpha)x_2 + v, \quad (5.4)$$

where $v \in \mathbb{R}$, yields the output dynamics $\dot{y} = v$. The choice of $v = -y$ results in the output converging exponentially to zero according to $\dot{y} = -y$. In order to understand what this implies about the full state of (5.2a), suppose that $y \equiv 0$, that is, $x_2 \equiv -\alpha x_1$. Under this constraint, the system's state must evolve on the set

$$\mathcal{Z} := \{x \in \mathbb{R}^2 \mid \alpha x_1 + x_2 = 0\}, \quad (5.5)$$

which is called the *zero dynamics manifold*.¹ The dynamics of the system restricted to this set is known as the *zero dynamics*—the maximal internal dynamics compatible with the output being identically zero. For this example, the zero dynamics is

$$\dot{x}_2 = -\alpha \dot{x}_1 \quad (5.6a)$$

$$= -\alpha x_2. \quad (5.6b)$$

¹In the case of a linear system, \mathcal{Z} is a subspace. The terminology of a manifold is used for consistency with the case of a nonlinear system.

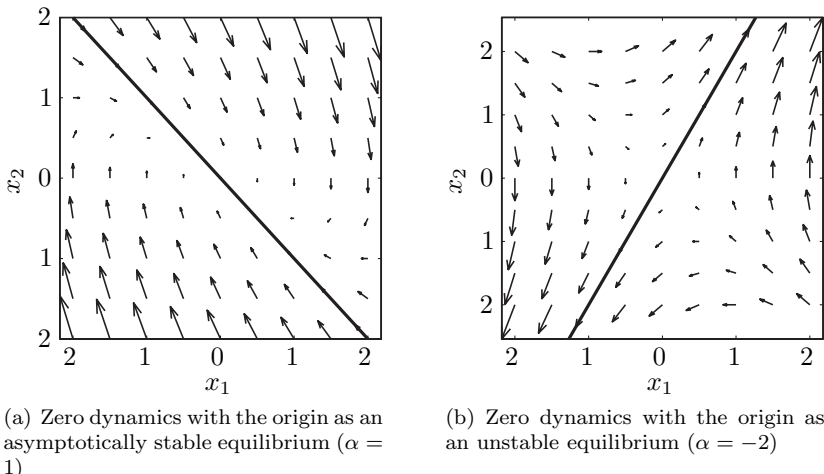


Figure 5.1. Vector fields for a zero dynamics example using a second order linear system. The bold line corresponds to the zero dynamics manifold, $\mathcal{Z} := \{x \in \mathbb{R}^2 \mid \alpha x_1 + x_2 = 0\}$.

It is no accident that the eigenvalue of (5.6b) corresponds to the zero of $H(s)$. For a minimal linear system, it is always the case that the eigenvalues of the zero dynamics correspond to the zeros of the corresponding transfer function; see [127, Sec. 4.3].

The input compatible with $x \in \mathcal{Z}$ is obtained from (5.4) by setting $v = 0$, yielding

$$u^* = -6x_1 - (1 + \alpha)x_2 \quad (5.7a)$$

$$= (\alpha^2 + \alpha - 6)x_1. \quad (5.7b)$$

Notice that the feedback u^* is *independent* of the feedback chosen to stabilize the output dynamics (5.3b) and that $y \equiv 0$ implies $u \equiv u^*$. More generally, any state variable feedback applied to (5.2a) that results in \mathcal{Z} being an invariant manifold (i.e., invariant subspace) of the closed-loop system can always be decomposed as $u = u^* + v$, where v vanishes on \mathcal{Z} .

In this example, the parameter α can be thought of as a design parameter that selects the zero dynamics manifold along with the corresponding zero dynamics. Figure 5.1 gives the vector fields (i.e., phase plane plot) for (5.2a) in closed loop with (5.4) and $v = -y$ for two values of α . For both values of α , the output dynamics (5.3b) with (5.4) and $v = -y$ are identical and stable; indeed, the outputs satisfy $\dot{y} = -y$, which causes the solutions of the closed-loop systems to converge exponentially to \mathcal{Z} . However, the zero dynamics manifold itself and the dynamics of the closed-loop system restricted to this manifold vary with α : for $\alpha = 1$, the zero dynamics is stable whereas with $\alpha = -2$, the zero dynamics is unstable.

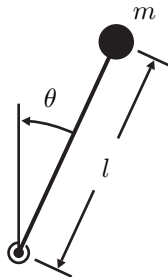


Figure 5.2. A horizontal, variable-length pendulum used to explain virtual constraints.

For a thorough discussion of zero dynamics, see [127,138]. The basic notions are summarized in [Appendix B.2](#).

5.1.2 The Idea of Virtual Constraints

For a mechanical system with generalized coordinates partitioned as $q = (q_1; q_2)$, a relation of the form

$$q_2 = h_d(q_1) \quad (5.8)$$

that is achieved by generalized forces or torques that do no work on the system is called a (workless) *holonomic constraint*; see [Appendix B.4.10](#). A typical example of this was illustrated in [Fig. 1.10](#). On the other hand, a relation achieved by a feedback controller that asymptotically zeros an output of the form

$$y = q_2 - h_d(q_1) \quad (5.9)$$

is termed a *virtual constraint*. The constraint is *virtual* because it does not arise from a *physical connection* between the two variables but rather from the actions of a *feedback controller*. Virtual constraints will be used in the next section to synchronize the evolution of the joints of a robot in order to design walking motions. An obvious advantage of a virtual constraint over a physical constraint is that it can be reprogrammed on the fly.

It is important to understand that while virtual constraints and physical constraints impose the same kinematic behavior on a system, the resulting dynamic behaviors are different. To see this distinction between virtual and physical constraints, consider a planar variable-length pendulum evolving in the absence of gravity, as depicted in Fig. 5.2. In the absence of gravity, the pendulum's Lagrangian is equal to its kinetic energy,

$$\mathcal{L} = K = \frac{1}{2}m \left(\dot{l}^2 + l^2\dot{\theta}^2 \right). \quad (5.10)$$

Two scenarios will be considered. First, the pendulum's length, l , will be constrained to evolve as a function of θ via a physical constraint. Second, l will be constrained via a virtual constraint.

In the first case, suppose that the end of the pendulum is constrained to evolve in a smooth frictionless slot about the pivot point in such a manner that

$$l = l_d(\theta). \quad (5.11)$$

In this case, the principle of virtual work gives that the external force acting on the pendulum due to the slot can be written as

$$\Gamma = \begin{bmatrix} -\frac{\partial l_d(\theta)}{\partial \theta} \\ 1 \end{bmatrix} \lambda^*, \quad (5.12)$$

where λ^* is a scalar. From (5.11), the generalized velocity of the system is

$$\dot{q} = \begin{bmatrix} \dot{\theta} \\ \dot{l} \end{bmatrix} = \begin{bmatrix} 1 \\ \frac{\partial l_d(\theta)}{\partial \theta} \end{bmatrix} \dot{\theta}. \quad (5.13)$$

The instantaneous power given by the inner product of Γ and \dot{q} is zero, showing that the physical constraint (5.11) does no work on the system. Moreover, the Lagrangian of the constrained system is

$$\mathcal{L} = \frac{1}{2}m \left(\left(\frac{\partial l_d(\theta)}{\partial \theta} \right)^2 + l_d(\theta)^2 \right) \dot{\theta}^2, \quad (5.14)$$

which is easily recognized as (5.10) with l given by (5.11) and \dot{l} given by (5.13). The equation of motion is therefore

$$m \left(\left(\frac{\partial l_d(\theta)}{\partial \theta} \right)^2 + (l_d(\theta))^2 \right) \ddot{\theta} + m \frac{\partial l_d(\theta)}{\partial \theta} \left(\frac{\partial^2 l_d(\theta)}{\partial \theta^2} + l_d(\theta) \right) \dot{\theta}^2 = 0. \quad (5.15)$$

It is supposed next that the pendulum's length varies according to a virtual constraint, in which case the length l is treated as a controlled quantity. The equations of motion may be calculated from the Lagrangian (5.10) to be

$$\underbrace{\begin{bmatrix} ml^2 & 0 \\ 0 & m \end{bmatrix}}_{D(q)} \underbrace{\begin{bmatrix} \ddot{\theta} \\ \ddot{l} \end{bmatrix}}_{\ddot{q}} + \underbrace{\begin{bmatrix} ml\dot{l} & ml\dot{\theta} \\ -ml\dot{\theta} & 0 \end{bmatrix}}_{C(q, \dot{q})} \underbrace{\begin{bmatrix} \dot{\theta} \\ \dot{l} \end{bmatrix}}_{\dot{q}} = \underbrace{\begin{bmatrix} 0 \\ 1 \end{bmatrix}}_B u, \quad (5.16)$$

where u corresponds to an actuator used to regulate the pendulum's length. Define an output

$$y = l - l_d(\theta) \quad (5.17)$$

and note that $y = 0$ means $l = l_d(\theta)$. Differentiating y once gives

$$\dot{y} = \dot{l} - \frac{\partial l_d(\theta)}{\partial \theta} \dot{\theta}, \quad (5.18)$$

and differentiating one more time gives

$$\ddot{y} = \ddot{l} - \frac{\partial^2 l_d(\theta)}{\partial \theta^2} \dot{\theta}^2 - \frac{\partial l_d(\theta)}{\partial \theta} \ddot{\theta} \quad (5.19a)$$

$$= l \dot{\theta}^2 - \frac{\partial^2 l_d(\theta)}{\partial \theta^2} \dot{\theta}^2 + \frac{2}{l} \frac{\partial l_d(\theta)}{\partial \theta} \dot{l} \dot{\theta} + \frac{1}{m} u. \quad (5.19b)$$

The state variable feedback

$$u = u^* + v \quad (5.20a)$$

$$u^* = m \left(-l \dot{\theta}^2 + \frac{\partial^2 l_d(\theta)}{\partial \theta^2} \dot{\theta}^2 - \frac{2}{l} \frac{\partial l_d(\theta)}{\partial \theta} \dot{l} \dot{\theta} \right) \quad (5.20b)$$

$$v = -m (K_D \dot{y} + K_P y), \quad (5.20c)$$

results in

$$\ddot{y} + K_D \dot{y} + K_P y = 0. \quad (5.21)$$

For $K_D, K_P > 0$, the solutions of (5.21) converge exponentially quickly to zero. For $y \equiv 0$, that is, $l \equiv l_d(\theta)$, the system's state evolves on the set

$$\mathcal{Z} := \left\{ (\theta, \dot{\theta}, l, \dot{l}) \in \mathbb{S} \times \mathbb{R}^3 \mid l - l_d(\theta) = 0, \dot{l} - \frac{\partial l_d(\theta)}{\partial \theta} \dot{\theta} = 0 \right\}. \quad (5.22)$$

Evaluating the model (5.16) on the zero dynamics manifold (5.22), with u equal to u^* in (5.20b), yields the zero dynamics

$$m (l_d(\theta))^2 \ddot{\theta} + 2m \frac{\partial l_d(\theta)}{\partial \theta} l_d(\theta) \dot{\theta}^2 = 0, \quad (5.23)$$

which, except for the special case of $l_d(\theta)$ being constant, is not equal to (5.15). Therefore, while the system (5.16) under the feedback law (5.20), that is, under the virtual constraint $y = l - l_d(\theta)$, asymptotically has the same kinematic behavior as the system (5.15) resulting from the physical constraint $l = l_d(\theta)$, the two constraints yield different dynamic behaviors. [Figure 5.3](#) illustrates this point for the constraint $l_d = 1.5 + \sin(\theta)$. For this example, $m = 1$ and the system (5.15) was initialized with $(\theta; \dot{\theta}) = (0; 1)$ and the system (5.16) was initialized with $(\theta; \dot{\theta}; l; \dot{l}) = (0; 1; 1.5; 1) \in \mathcal{Z}$. The source of the different dynamic behavior is the power injected into the closed-loop system via the virtual constraint. Indeed, the injected power is

$$\dot{q}' B u^* = m \dot{l} \left(-l \dot{\theta}^2 + \frac{\partial^2 l_d(\theta)}{\partial \theta^2} \dot{\theta}^2 - \frac{2}{l} \frac{\partial l_d(\theta)}{\partial \theta} \dot{l} \dot{\theta} \right), \quad (5.24)$$

which, when evaluated along the constraint surface \mathcal{Z} , yields

$$\dot{q}' B u^*|_{\mathcal{Z}} = m \frac{\partial l_d(\theta)}{\partial \theta} \left(\frac{\partial^2 l_d(\theta)}{\partial \theta^2} - \frac{2}{l_d(\theta)} \left(\frac{\partial l_d(\theta)}{\partial \theta} \right)^2 - l_d(\theta) \right) \dot{\theta}^3. \quad (5.25)$$

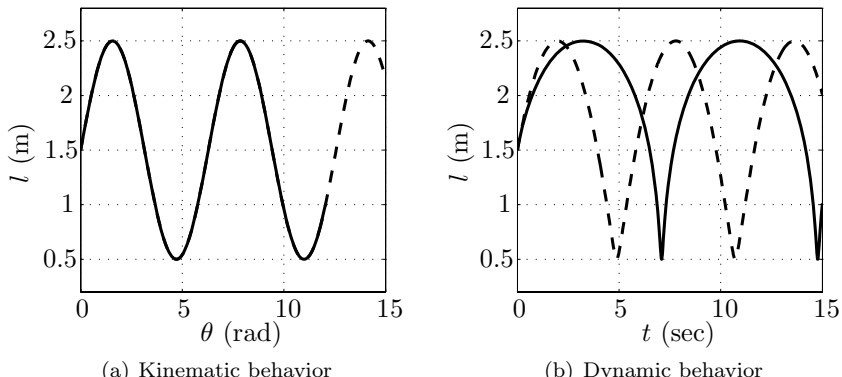


Figure 5.3. Kinematic and dynamic behaviors of the horizontal pendulum. The dashed lines correspond to the constraint $l = \sin(\theta) + 1.5$ imposed via a physical constraint, whereas the solid corresponds to the same constraint imposed via a virtual constraint.

Remark 5.1 The instantaneous power injected by the virtual constraint vanishes along \mathcal{Z} if, and only if, either l_d is constant or l_d satisfies the differential equation

$$\frac{\partial^2 l_d(\theta)}{\partial \theta^2} - \frac{2}{l_d(\theta)} \left(\frac{\partial l_d(\theta)}{\partial \theta} \right)^2 - l_d(\theta) = 0. \quad (5.26)$$

This equation has the general solution

$$l_d(\theta) = \frac{c_0}{\cos(\theta - \theta_0)}, \quad (5.27)$$

where c_0 and θ_0 are arbitrary constants. A virtual constraint for which the instantaneous injected power is zero along the constraint surface is said to be *passive*. For this example, physically meaningful solutions (i.e., $l_d > 0$) can only be found for θ restricted to a subset of the circle.

5.2 Swing Phase Zero Dynamics

5.2.1 Definitions and Preliminary Properties

This section identifies the swing phase zero dynamics for a particular class of outputs that has proven useful in constructing feedback controllers for bipedal walkers. Since no impact dynamics are involved, the work here is simply a

specialization of the general results in [127] to a model of the form

$$\dot{x} = \begin{bmatrix} \dot{q} \\ D^{-1}(q) [-C(q, \dot{q})\dot{q} - G(q) + B(q)u] \end{bmatrix} \quad (5.28)$$

$$=: f(x) + g(x)u \quad (5.29)$$

and an output that is independent of velocity. The results summarized here will form the basis for defining a zero dynamics of the complete hybrid model of a planar bipedal walker, which is the desired object for study.

Note that if an output

$$y = h(q) \quad (5.30)$$

depends only on the configuration variables, then, due to the second order nature of the robot model, the derivative of the output along solutions of (5.29) does not depend directly on the inputs,

$$\frac{dy}{dt} = \frac{\partial h}{\partial x} \dot{x} \quad (5.31a)$$

$$= \left[\frac{\partial h}{\partial q} \quad \frac{\partial h}{\partial \dot{q}} \right] \left[\underbrace{\begin{bmatrix} \dot{q} \\ D^{-1} [-C\dot{q} - G] \end{bmatrix}}_f + \underbrace{\begin{bmatrix} 0 \\ D^{-1}B \end{bmatrix}}_g u \right] \quad (5.31b)$$

$$= \underbrace{\left[\frac{\partial h}{\partial q} \quad 0 \right]}_{L_f h} \underbrace{\begin{bmatrix} \dot{q} \\ D^{-1} [-C\dot{q} - G] \end{bmatrix}}_f + \underbrace{\left[\frac{\partial h}{\partial q} \quad 0 \right]}_{L_g h} \underbrace{\begin{bmatrix} 0 \\ D^{-1}B \end{bmatrix}}_u u \quad (5.31c)$$

$$= L_f h(q, \dot{q}), \quad (5.31d)$$

because $L_g h$ is zero. Hence, the relative degree of the output is at least two. Differentiating the output once again computes the accelerations, resulting in

$$\frac{d^2 y}{dt^2} = \left[\frac{\partial}{\partial q} \left(\frac{\partial h}{\partial q} \dot{q} \right) \quad \frac{\partial h}{\partial q} \right] \left[\begin{bmatrix} \dot{q} \\ D^{-1} [-C\dot{q} - G] \end{bmatrix} + \begin{bmatrix} 0 \\ D^{-1}B \end{bmatrix} u \right] \quad (5.32a)$$

$$= \underbrace{\left[\frac{\partial}{\partial q} \left(\frac{\partial h}{\partial q} \dot{q} \right) \quad \frac{\partial h}{\partial q} \right]}_{L_f^2 h} \underbrace{\begin{bmatrix} \dot{q} \\ D^{-1} [-C\dot{q} - G] \end{bmatrix}}_f + \underbrace{\frac{\partial h}{\partial q} D^{-1} B u}_{L_g L_f h} \quad (5.32b)$$

$$= L_f^2 h(q, \dot{q}) + L_g L_f h(q)u. \quad (5.32c)$$

The matrix $L_g L_f h(q)$ is called the *decoupling matrix* and depends only on the configuration variables. A consequence of the general results in [127] is that the invertibility of this matrix at a given point ensures the existence and uniqueness of the zero dynamics in a neighborhood of that point. With a few extra hypotheses, these properties can be ensured on a given open set.

Lemma 5.1 (Swing Phase Zero Dynamics)

Suppose that a smooth function h is selected so that

HH1) h is a function of only the configuration coordinates;

HH2) there exists an open set $\tilde{\mathcal{Q}} \subset \mathcal{Q}$ such that for each point $q \in \tilde{\mathcal{Q}}$, the decoupling matrix $L_g L_f h(q)$ is square and invertible (i.e., the dimension of u equals the dimension of y , and h has vector relative degree $(2, \dots, 2)$);

HH3) there exists a smooth real-valued function $\theta(q)$ such that

$$[h(q); \theta(q)] : \tilde{\mathcal{Q}} \rightarrow \mathbb{R}^N \quad (5.33)$$

is a diffeomorphism onto its image; and

HH4) there exists at least one point in $\tilde{\mathcal{Q}}$ where h vanishes.

Then,

1. the set

$$\mathcal{Z} := \{x \in T\tilde{\mathcal{Q}} \mid h(x) = 0, L_f h(x) = 0\} \quad (5.34)$$

is a smooth two-dimensional embedded submanifold of $T\mathcal{Q}$; and

2. the feedback control

$$u^*(x) = -(L_g L_f h(x))^{-1} L_f^2 h(x) \quad (5.35)$$

renders \mathcal{Z} invariant under the swing phase dynamics; that is, for every $z \in \mathcal{Z}$,

$$f_{\text{zero}}(z) := f(z) + g(z)u^*(z) \in T_z \mathcal{Z}. \quad (5.36)$$

\mathcal{Z} is called the zero dynamics manifold and $\dot{z} = f_{\text{zero}}(z)$ is called the zero dynamics.

Lemma 5.1 follows immediately from general results in [127]; a few of the details are outlined here for later use. From Hypotheses HH1 and HH3, $\Phi(q) := [h; \theta(q)]$ is a valid coordinate transformation on $\tilde{\mathcal{Q}}$, and thus

$$\begin{aligned} \eta_1 &= h(q), & \eta_2 &= L_f h(q, \dot{q}), \\ \xi_1 &= \theta(q), & \xi_2 &= L_f \theta(q, \dot{q}), \end{aligned} \quad (5.37)$$

is a coordinate transformation on $T\tilde{\mathcal{Q}}$. In these coordinates, the system consisting of (5.29) and (5.30) takes the form

$$\begin{aligned} \dot{\eta}_1 &= \eta_2, & \dot{\eta}_2 &= L_f^2 h + L_g L_f h u, \\ \dot{\xi}_1 &= \xi_2, & \dot{\xi}_2 &= L_f^2 \theta + L_g L_f \theta u, \end{aligned} \quad (5.38)$$

$$y = \eta_1$$

where $(q; \dot{q})$ is evaluated at

$$q = \Phi^{-1}(\eta_1, \xi_1) \quad (5.39a)$$

$$\dot{q} = \left(\frac{\partial \Phi}{\partial q} \right)^{-1} \begin{bmatrix} \eta_2 \\ \xi_2 \end{bmatrix}. \quad (5.39b)$$

Enforcing $y \equiv 0$ results in $(\eta_1 = h = 0; \eta_2 = L_f h = 0)$, the input being equal to u^* in (5.35), and the zero dynamics becoming

$$\dot{\xi}_1 = \xi_2 \quad (5.40a)$$

$$\dot{\xi}_2 = L_f^2 \theta + L_g L_f \theta u^*. \quad (5.40b)$$

While it is useful to know that the zero dynamics can be expressed as a second-order system, this form of the equations is very difficult to compute directly due to the need to invert the decoupling matrix. However, this can be avoided. Indeed, since the columns of g in (5.29) are involutive, by [127, p. 222], in a neighborhood of any point where the decoupling matrix is invertible, there exists a smooth scalar function γ such that

$$\begin{aligned} \eta_1 &= h(q), \quad \eta_2 = L_f h(q, \dot{q}), \\ \xi_1 &= \theta(q), \quad \xi_2 = \gamma(q, \dot{q}), \end{aligned} \quad (5.41)$$

is a valid coordinate transformation and

$$L_g \gamma = 0. \quad (5.42)$$

Moreover, by applying the constructive proof of the Frobenius theorem of [127, p. 23] in a set of coordinates for the robot such that HR6 holds, one obtains that γ can be explicitly computed to be the last entry of $D(q)\dot{q}$, and hence it can be assumed that $\gamma(q, \dot{q})$ has the form $\gamma_0(q)\dot{q}$. It follows that (5.41) is a valid coordinate change on all of $T\bar{Q}$ and in these coordinates the system has the form

$$\begin{aligned} \dot{\eta}_1 &= \eta_2 \\ \dot{\eta}_2 &= L_f^2 h(q, \dot{q}) + L_g L_f h(q) u \\ \dot{\xi}_1 &= L_f \theta(q, \dot{q}) \\ \dot{\xi}_2 &= L_f \gamma(q, \dot{q}), \end{aligned} \quad (5.43)$$

where the right-hand side is evaluated at

$$q = \Phi^{-1}(\eta_1, \xi_1) \quad (5.44a)$$

$$\dot{q} = \left[\begin{array}{c} \frac{\partial h}{\partial q} \\ \gamma_0 \end{array} \right]^{-1} \begin{bmatrix} \eta_2 \\ \xi_2 \end{bmatrix}. \quad (5.44b)$$

The swing phase zero dynamics is then

$$\begin{aligned}\dot{\xi}_1 &= L_f \theta \\ \dot{\xi}_2 &= L_f \gamma,\end{aligned}\tag{5.45}$$

where the right-hand side is evaluated at

$$q = \Phi^{-1}(0, \xi_1) \tag{5.46a}$$

$$\dot{q} = \left[\begin{array}{c} \frac{\partial h}{\partial q} \\ \gamma_0 \end{array} \right]^{-1} \left[\begin{array}{c} 0 \\ \xi_2 \end{array} \right]. \tag{5.46b}$$

Theorem 5.1 (Swing Phase Zero Dynamics Form)

Under the hypotheses of Lemma 5.1, $(\xi_1; \xi_2) = (\theta(q); \gamma_0(q) \dot{q})$ is a valid set of coordinates on \mathcal{Z} , and in these coordinates the zero dynamics takes the form

$$\dot{\xi}_1 = \kappa_1(\xi_1)\xi_2 \tag{5.47a}$$

$$\dot{\xi}_2 = \kappa_2(\xi_1). \tag{5.47b}$$

Moreover, if the model (5.29) is expressed in coordinates satisfying HR6, the following interpretations can be given for the various functions appearing in the zero dynamics:

$$\xi_1 = \theta|_{\mathcal{Z}} \tag{5.48a}$$

$$\xi_2 = \left. \frac{\partial K}{\partial \dot{q}_N} \right|_{\mathcal{Z}} \tag{5.48b}$$

$$\kappa_1(\xi_1) = \left. \frac{\partial \theta}{\partial q} \left[\begin{array}{c} \frac{\partial h}{\partial q} \\ \gamma_0 \end{array} \right]^{-1} \left[\begin{array}{c} 0 \\ 1 \end{array} \right] \right|_{\mathcal{Z}} \tag{5.48c}$$

$$\kappa_2(\xi_1) = -\left. \frac{\partial V}{\partial q_N} \right|_{\mathcal{Z}}, \tag{5.48d}$$

where $K(q, \dot{q}) = \frac{1}{2} \dot{q}' D(q) \dot{q}$ is the kinetic energy of the robot, $V(q)$ is its potential energy, and γ_0 is the last row of D , the inertia matrix.

Proof The form of (5.47a) is immediate by the form of (5.45) and (5.46b) since both h and γ_0 are functions of q , and hence when restricted to \mathcal{Z} , are functions of ξ_1 only.

Suppose now that the model (5.29) is expressed in coordinates satisfying HR6. Since the kinetic energy of the robot, $K(q, \dot{q})$, is independent of the choice of world coordinate frame [219, p. 140], and since q_N fixes this choice, $K(q, \dot{q})$ is independent of q_N (i.e., q_N is a cyclic coordinate). Since $D = \partial[(\partial K / \partial \dot{q})'] / \partial \dot{q}$ [219, p. 141], it follows that $\partial D / \partial q_N = 0$. Let D_N , C_N , and

G_N be the last rows of D , C , and G , respectively. Then $\dot{\xi}_2 = \gamma_0(q) \dot{q}$ is equal to $D_N(q) \dot{q}$, and thus is equal to $\partial K / \partial \dot{q}_N$ since $K = \frac{1}{2} \dot{q}' D \dot{q}$. Continuing, $\dot{\xi}_2 := L_f \gamma$ becomes

$$L_f \gamma = \begin{bmatrix} \dot{q}' \frac{\partial D'_N}{\partial q} & D_N \end{bmatrix} \begin{bmatrix} \dot{q} \\ -D^{-1}[C \dot{q} + G] \end{bmatrix} \quad (5.49a)$$

$$= \dot{q}' \frac{\partial D'_N}{\partial q} \dot{q} - C_N \dot{q} - G_N. \quad (5.49b)$$

Noting that since (see [219, p. 142])

$$C_N = \dot{q}' \frac{\partial D'_N}{\partial q} - \frac{1}{2} \dot{q}' \frac{\partial D}{\partial q_N}, \quad (5.50)$$

(5.49b) becomes $L_f \gamma = -G_N = -\partial V / \partial q_N$, which, when evaluated on \mathcal{Z} , is a function of ξ_1 only.

Remark 5.2 The second state of the zero dynamics, (5.47b), can also be derived directly from the Lagrangian [43]. If the robot's Lagrangian, L , is expressed in coordinates satisfying HR6, then since q_N is unactuated

$$\frac{d}{dt} \frac{\partial L}{\partial \dot{q}_N} - \frac{\partial L}{\partial q_N} = 0. \quad (5.51)$$

Since q_N is a cyclic coordinate (i.e., $\partial K / \partial q_N = 0$), (5.51) reduces to

$$\frac{d}{dt} \frac{\partial K}{\partial \dot{q}_N} = -\frac{\partial V}{\partial q_N}. \quad (5.52)$$

5.2.2 Interpreting the Swing Phase Zero Dynamics

Much in the way that it has been proposed that a spring-loaded inverted pendulum is a template for running [185, 205], it has been proposed, though less formally, that an inverted pendulum is an appropriate template for walking [83, 129, 133, 134, 172]. From Fig. 5.4 it might seem that the dynamics that result from imposing virtual constraints—the swing phase zero dynamics, (5.47)—should be the dynamics of a *length- and inertia-varying inverted pendulum*, that is, a pendulum where the length, l , and the inertia about the center of mass, J , vary as functions of ξ_1 . If this were true, it would suggest this physical pendulum model as a new control template (or target) in the design of controllers for walking robots. It will be shown that such an interpretation of the swing phase zero dynamics is not valid. The reason for this will be traced back to the fact that while virtual constraints may induce the same kinematic behavior as a physical constraint, the induced dynamic behavior is in general different from that imposed by a physical constraint, as was discussed in Section 5.1.2.

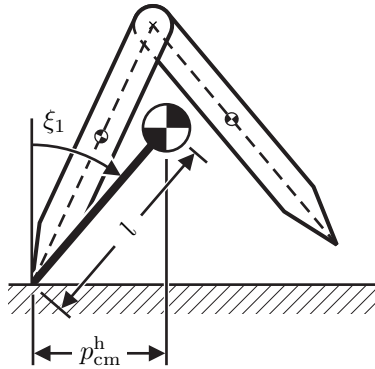


Figure 5.4. A robot with its center of mass labeled. The robot has mass m_{tot} and the inertia about the COM is J . Angles are measured here with a clockwise convention, that is, they increase in the clockwise direction.

Consider Fig. 5.4. Using the angular momentum balance theorem, the rate of change of the angular momentum of the robot about the stance leg end during the swing phase, $\dot{\xi}_2$, is equal to the external applied torque,

$$\dot{\xi}_2 = g_0 m_{\text{tot}} p_{\text{cm}}^h, \quad (5.53)$$

where g_0 is the acceleration due to gravity, m_{tot} is the robot's mass and p_{cm}^h is the horizontal position of the robot's center of mass, measured relative to the end of the stance leg. Suppose ξ_1 is defined as in Fig. 5.4. Then, for an output (5.30) satisfying Lemma 5.1, on the set \mathcal{Z} in (5.34), it follows that $p_{\text{cm}}^h = p_{\text{cm}}^h(\xi_1)$ and $l = l(\xi_1)$ so that

$$\kappa_2(\xi_1) = g_0 m_{\text{tot}} l(\xi_1) \sin(\xi_1). \quad (5.54)$$

Expressing (5.47a) as $\dot{\xi}_2 = I_{\text{zero}}(\xi_1)\dot{\xi}_1$, where² $I_{\text{zero}}(\xi_1) = 1/\kappa_1(\xi_1)$ is an inertial term, allows the zero dynamics (5.47a) and (5.47b) to be written as a second-order system,

$$I_{\text{zero}}(\xi_1)\ddot{\xi}_1 + \frac{\partial I_{\text{zero}}(\xi_1)}{\partial \xi_1}(\dot{\xi}_1)^2 - g_0 m_{\text{tot}} l(\xi_1) \sin(\xi_1) = 0. \quad (5.55)$$

The equation of motion for a length- and inertia-varying pendulum can be easily derived using the method of Lagrange. The kinetic energy is $K(\xi_1) = \frac{1}{2}I(\xi_1)\dot{\xi}_1^2$ where

$$I(\xi_1) = m_{\text{tot}} \left(\frac{\partial l(\xi_1)}{\partial \xi_1} \right)^2 + m_{\text{tot}}(l(\xi_1))^2 + J(\xi_1). \quad (5.56)$$

²A later result will ensure that $\kappa_1(\xi_1)$ is never zero whenever the robot successfully completes a step.

The potential energy is $V(\xi_1) = m_{\text{tot}}g_0 l(\xi_1) \cos(\xi_1)$, and, hence, the equation of motion³ is,

$$I(\xi_1) \ddot{\xi}_1 + \frac{1}{2} \frac{\partial I(\xi_1)}{\partial \xi_1} \dot{\xi}_1^2 + m_{\text{tot}}g_0 \left(\frac{\partial l(\xi_1)}{\partial \xi_1} \cos(\xi_1) - l(\xi_1) \sin(\xi_1) \right) = 0. \quad (5.57)$$

Comparing the swing phase zero dynamics (5.55) and the dynamics for the length- and inertia-varying pendulum (5.57), it is evident that the swing phase zero dynamics does not correspond to an inverted pendulum, despite what may be suggested by Fig. 5.4. It is interesting to note, however, that if the length- and inertia-varying inverted pendulum had a torque, u , acting between the pendulum and ground, i.e.,

$$I(\xi_1) \ddot{\xi}_1 + \frac{1}{2} \frac{\partial I(\xi_1)}{\partial \xi_1} \dot{\xi}_1^2 + m_{\text{tot}}g_0 \left(\frac{\partial l(\xi_1)}{\partial \xi_1} \cos(\xi_1) - l(\xi_1) \sin(\xi_1) \right) = u, \quad (5.58)$$

where

$$u = -\frac{1}{2} \frac{\partial I(\xi_1)}{\partial \xi_1} \dot{\xi}_1^2 + m_{\text{tot}}g_0 \frac{\partial l(\xi_1)}{\partial \xi_1} \cos(\xi_1), \quad (5.59)$$

then, the forms of (5.55) and (5.58) with u as in (5.59) would be identical.⁴ Matching the inertial terms, I and I_{zero} , however, does not yield a positive definite J . That is, supposing I_{zero} has the form of I given in (5.56) implies $J(\xi_1) = I_{\text{zero}} - m_{\text{tot}} (\partial l(\xi_1)/\partial \xi_1) - m_{\text{tot}} (l(\xi_1))^2$ where l is the distance from the stance leg end to the COM. For every example worked by the authors, J is sign indefinite, indicating that even with the addition of u as in (5.59), the interpretation of the swing phase zero dynamics as a length- and inertia-varying inverted pendulum does not hold.

5.3 Hybrid Zero Dynamics

The goal of this section is to incorporate the impact model into the notion of the maximal internal dynamics compatible with the output being identically zero, to obtain a zero dynamics of the complete model of the bipedal walker, (3.30). Toward this goal, let $y = h(q)$ be an output satisfying the hypotheses of Lemma 5.1 and suppose there exists a trajectory, $x(t)$, of the hybrid model (3.30) along which the output is identically zero. If the trajectory contains no impacts with \mathcal{S} , then $x(t)$ is a solution of the swing phase dynamics and

³If l and J do not vary as a function of ξ_1 , then $I(\xi_1) = I$, $l(\xi_1) = l$ and (5.57) reduces to the equation of motion for an inverted pendulum, $I \ddot{\xi}_1 - m_{\text{tot}}g_0 l \sin(\xi_1) = 0$.

⁴The justification for this input is to account for the energy entering the robot's dynamics via the control u^* given in (5.35).

also of its zero dynamics. If the trajectory does contain impact events, then let (t_0, t_f) be an open interval of time containing exactly one impact at t_e . By definition, on the intervals (t_0, t_e) and (t_e, t_f) , $x(t)$ is a solution of the swing phase dynamics and hence also of its zero dynamics, so $x(t) \in \mathcal{Z}$; since also by definition of a solution, $x^- := \lim_{t \nearrow t_e} x(t)$ exists, is finite, and lies in \mathcal{S} , it follows that $x^- \in \mathcal{S} \cap \mathcal{Z}$. Moreover, by definition of a solution of (3.30), $x(t_e) := x^+ := \Delta(x^-)$, from which it follows that $\Delta(x^-) \in \mathcal{Z}$. On the other hand, if $\Delta(\mathcal{S} \cap \mathcal{Z}) \subset \mathcal{Z}$, then from solutions of the swing phase zero dynamics it is clearly possible to construct solutions to the complete model of the bipedal walker along which the output $y = h(q)$ is identically zero. This leads to the following definition.

Definition 5.1 Let $y = h(q)$ be an output satisfying the hypotheses of Lemma 5.1, and let \mathcal{Z} and $\dot{z} = f_{\text{zero}}(z)$ be the associated zero dynamics manifold and zero dynamics of the swing phase model. Suppose that $\mathcal{S} \cap \mathcal{Z}$ is a smooth, one-dimensional, embedded submanifold of $T\mathcal{Q}$. If $\Delta(\mathcal{S} \cap \mathcal{Z}) \subset \mathcal{Z}$, then the nonlinear system with impulse effects,

$$\Sigma_{\text{zero}} : \begin{cases} \dot{z} = f_{\text{zero}}(z), & z^- \notin \mathcal{S} \cap \mathcal{Z} \\ z^+ = \Delta(z^-), & z^- \in \mathcal{S} \cap \mathcal{Z}, \end{cases} \quad (5.60)$$

with $z \in \mathcal{Z}$, is the hybrid zero dynamics of the model (3.30).

Remark 5.3 From standard results in [22], $\mathcal{S} \cap \mathcal{Z}$ will be a smooth one-dimensional embedded submanifold if $\mathcal{S} \cap \mathcal{Z} \neq \emptyset$ and the map $[h; (L_f h); p_2^y]$ has constant rank equal to $2N - 1$ on $\mathcal{S} \cap \mathcal{Z}$. Since

$$\frac{\partial}{\partial x} \begin{bmatrix} h \\ L_f h \\ p_2^y \end{bmatrix} = \begin{bmatrix} \frac{\partial h}{\partial q} & 0 \\ \frac{\partial}{\partial q} \left(\frac{\partial h}{\partial q} \dot{q} \right) & \frac{\partial h}{\partial q} \\ \frac{\partial p_2^y}{\partial q} & 0 \end{bmatrix}, \quad (5.61)$$

it is clear that this rank condition will be met if

$$\text{rank } [h; p_2^y] = N, \quad (5.62)$$

and under this rank condition, $\mathcal{S} \cap \mathcal{Z} \cap \tilde{\mathcal{Q}}$ consists of the isolated zeros of $[h; p_2^y]$. Let q_0^- be a solution of $[h(q); p_2^y(q)] = [0; 0]$, $p_2^h(q) > 0$. Then the connected component of $\mathcal{S} \cap \mathcal{Z}$ containing q_0^- is diffeomorphic to \mathbb{R} per $\bar{\lambda} : \mathbb{R} \rightarrow \mathcal{S} \cap \mathcal{Z}$, where

$$\bar{\lambda}(\omega) := \begin{bmatrix} \bar{\lambda}_q \\ \bar{\lambda}_{\dot{q}} \omega \end{bmatrix} \quad (5.63)$$

$\bar{\lambda}_q := q_0^-$, and

$$\bar{\lambda}_{\dot{q}} := \begin{bmatrix} \frac{\partial h}{\partial q}(q_0^-) \\ \gamma_0(q_0^-) \end{bmatrix}^{-1} \begin{bmatrix} 0 \\ 1 \end{bmatrix}. \quad (5.64)$$

In view of this, the following additional assumption is made about the output h and the open set $\tilde{\mathcal{Q}}$

- HH5) there exists a unique point $q_0^- \in \tilde{\mathcal{Q}}$ such that $[h(q_0^-); p_2^y(q_0^-)] = [0; 0]$, $p_2^h(q_0^-) > 0$, and the rank of $[h; p_2^y]$ at q_0^- equals N .

The next result characterizes when the swing phase zero dynamics is compatible with the impact model, leading to a nontrivial hybrid zero dynamics.

Theorem 5.2 (Hybrid Zero Dynamics Existence)

Consider the model (3.30), satisfying Hypotheses HR1–HR5 on the robot, HGW1–HGW7 on the robot's gait, and HI1–HI7 on the impact model, with a smooth function h satisfying Hypotheses HH1–HH5. Then, the following statements are equivalent:

- (a) $\Delta(\mathcal{S} \cap \mathcal{Z}) \subset \mathcal{Z}$;
- (b) $h \circ \Delta|_{(\mathcal{S} \cap \mathcal{Z})} = 0$ and $L_f h \circ \Delta|_{(\mathcal{S} \cap \mathcal{Z})} = 0$; and
- (c) there exists at least one point $(q_0^-; \dot{q}_0^-) \in \mathcal{S} \cap \mathcal{Z}$ such that $\gamma_0(q_0^-) \dot{q}_0^- \neq 0$, $h \circ \Delta_q(q_0^-) = 0$, and $L_f h \circ \Delta(q_0^-, \dot{q}_0^-) = 0$.

Proof The equivalence of (a) and (b) is immediate from the definition of \mathcal{Z} as the zero set of h and $L_f h$. The equivalence of (b) and (c) follows from Remark 5.3 once it is noted from (3.26) that $L_f h \circ \Delta$ is linear in \dot{q} .

Under the hypotheses of Theorem 5.2, the hybrid zero dynamics is well-defined. Let $z^- \in \mathcal{S} \cap \mathcal{Z}$, and suppose that $T_I \circ \Delta(z^-) < \infty$. Set $z^+ = \Delta(z^-)$ and let $\varphi : [0, t_f] \rightarrow \mathcal{Z}$, $t_f = T_I(z^+)$, be a solution of the zero dynamics, (5.47), such that $\varphi(0) = z^+$. Define $\hat{\theta}(t) := \theta \circ \varphi(t)$ and $\dot{\hat{\theta}} := d\hat{\theta}(t)/dt$.

Proposition 5.1

Assume the hypotheses of Theorem 5.2. Then over any step of the robot resulting in a transversal impact, $\dot{\hat{\theta}} : [0, t_f] \rightarrow \mathbb{R}$ is never zero. In particular, $\hat{\theta} : [0, t_f] \rightarrow \mathbb{R}$ is strictly monotonic and thus achieves its maximum and minimum values at the end points.

Proof Without loss of generality, assume $\hat{\theta}(0) < \hat{\theta}(t_f)$. By HH3, the configuration of the robot at time t is determined by $\hat{\theta}(t)$. By HGW1 and HI7,

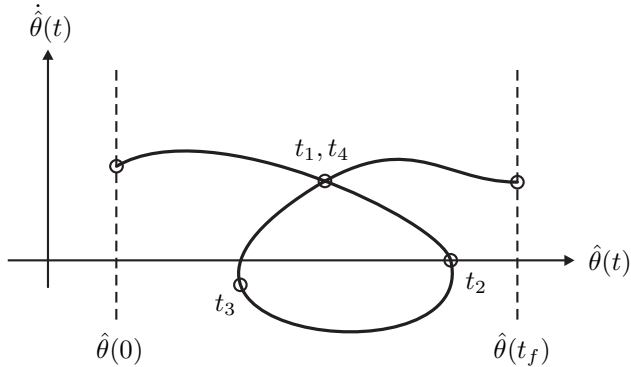


Figure 5.5. Impossible integral curve of the zero dynamics.

the height of the swing leg above the ground is zero at 0 and t_f , and hence, for all $0 < t < t_f$, $\hat{\theta}(0) < \hat{\theta}(t) < \hat{\theta}(t_f)$, for otherwise there is an intermediate impact with the ground. To show that $\dot{\hat{\theta}}(t)$ is monotonic it suffices to show that $\dot{\hat{\theta}}(t) > 0$ for all $0 < t < t_f$. Suppose there exists some t_2 (see Fig. 5.5) such that $0 < t_2 < t_f$ and $\dot{\hat{\theta}}(t_2) = 0$. Let t_2 be the smallest such t . The point $(\hat{\theta}(t_2); 0)$ cannot be an equilibrium point of (5.40) because $\dot{\hat{\theta}}(t_2) < \dot{\hat{\theta}}(t_f)$. Hence, there exists some $t_3 > t_2$ such that for all $t_2 < t < t_3$, $\dot{\hat{\theta}}(t) < 0$ and $\hat{\theta}(t) < \hat{\theta}(t_2)$. By the assumption that $\dot{\hat{\theta}}(t) > \dot{\hat{\theta}}(0)$ for all $t > 0$ and because $\dot{\hat{\theta}}(t_f) > \dot{\hat{\theta}}(t_2)$, there must exist a $t_4 > t_3$ such that $\dot{\hat{\theta}}(t_4) = \dot{\hat{\theta}}(t_1)$ for some $0 < t_1 < t_2$. This contradicts the uniqueness of solutions of (5.40). Hence, there can be no t_2 such that $\dot{\hat{\theta}}(t_2) = 0$ and thus $\dot{\hat{\theta}}(t) > 0$ for all $0 < t < t_f$. By HI4, $\dot{\hat{\theta}}(0) \neq 0$, because $\dot{\hat{\theta}}(0) = 0$ implies $\dot{q}(0) = 0$, which in turn implies that the velocity of the end of the swing leg is zero, which contradicts the hypothesis that the swing leg lifts from the ground without interaction at the beginning of the step. Because the impact at the end of the step is transversal, $\dot{\hat{\theta}}(t_f) \neq 0$. Therefore, by continuity, $\dot{\hat{\theta}}(t) > 0$ for all $t \in [0, t_f]$, establishing that $\hat{\theta} : [0, t_f] \rightarrow \mathbb{R}$ is strictly monotonic.

By Remark 5.3, it follows that $\hat{\theta}(0) = \theta \circ \Delta_q(q_0^-)$ and $\hat{\theta}(t_f) = \theta(q_0^-)$, that is, the extrema can be computed *a priori*. Denote these by

$$\theta^- := \theta(q_0^-) \tag{5.65a}$$

$$\theta^+ := \theta \circ \Delta_q(q_0^-). \tag{5.65b}$$

Without loss of generality, it is assumed that $\theta^+ < \theta^-$; that is, along any step of the hybrid zero dynamics, θ is *monotonically increasing*.

Remark 5.4 The fact that θ evaluated along a step of the zero dynamics

must be monotonic implies that there are restrictions on the walking gaits that can be achieved by zeroing an output that depends only on the configuration variables.

5.4 Periodic Orbits of the Hybrid Zero Dynamics

The hybrid zero dynamics (5.60) is a particular case of the hybrid restriction dynamics defined in (4.24), corresponding to the case that the invariant manifold arises from a set of virtual constraints. It is shown here that the Poincaré return map associated with (5.60) is diffeomorphic to a scalar LTI system, thereby reducing determination of the existence of a fixed point and its local stability properties to a simple explicit computation. Fixed points of the Poincaré return map of the hybrid zero dynamics correspond to periodic orbits of the hybrid zero dynamics. The analysis of periodic orbits of the hybrid zero dynamics will form the basis for proposing feedback laws that induce exponentially stable walking motions in the full-dimensional hybrid model.

5.4.1 Poincaré Analysis of the Hybrid Zero Dynamics

Assume the hypotheses of Theorem 5.2 and consider the hybrid zero dynamics expressed in the form of a system with impulse effects, as in (5.60). Take the Poincaré section to be $\mathcal{S} \cap \mathcal{Z}$ and let the Poincaré map $\rho : \mathcal{S} \cap \mathcal{Z} \rightarrow \mathcal{S} \cap \mathcal{Z}$ be defined on its domain of definition⁵ as in (4.23). In a special set of local coordinates, the return map can be explicitly computed. Indeed, express the hybrid zero dynamics in the coordinates of Theorem 5.1, namely, $(\xi_1; \xi_2) = (\theta; \gamma)$. In these coordinates, $\mathcal{S} \cap \mathcal{Z}$ and $\Delta : (\xi_1^-; \xi_2^-) \rightarrow (\xi_1^+; \xi_2^+)$ simplify to

$$\mathcal{S} \cap \mathcal{Z} = \{(\xi_1^-; \xi_2^-) \mid \xi_1^- = \theta^-, \xi_2^- \in \mathbb{R}\} \quad (5.66a)$$

$$\xi_1^+ = \theta^+ \quad (5.66b)$$

$$\xi_2^+ = \delta_{\text{zero}} \xi_2^-, \quad (5.66c)$$

where

$$\delta_{\text{zero}} := \gamma_0(q_0^+) \Delta_{\dot{q}}(q_0^-) \bar{\lambda}_{\dot{q}}, \quad (5.67)$$

a constant that may be computed *a priori*. The hybrid zero dynamics is thus given by (5.47) during the swing phase, and at impact with $\mathcal{S} \cap \mathcal{Z}$, the reinitialization rules (5.66b) and (5.66c) are applied. By Proposition 5.1, over any step resulting in a transversal impact, ξ_1 is nonzero, and thus (5.47) is

⁵Here, the interpretation as a partial map is being used; see Section 4.2.2.

equivalent to

$$\frac{d\xi_2}{d\xi_1} = \frac{\kappa_2(\xi_1)}{\kappa_1(\xi_1)\xi_2}. \quad (5.68)$$

From (5.47), $\dot{\xi}_1 \neq 0$ implies $\xi_2 \neq 0$, and thus $\zeta_2 := \frac{1}{2}(\xi_2)^2$ is a valid change of coordinates on (5.68). In these coordinates, (5.68) becomes

$$\frac{d\zeta_2}{d\xi_1} = \frac{\kappa_2(\xi_1)}{\kappa_1(\xi_1)}. \quad (5.69)$$

For $\theta^+ \leq \xi_1 \leq \theta^-$, define⁶

$$V_{\text{zero}}(\xi_1) := - \int_{\theta^+}^{\xi_1} \frac{\kappa_2(\xi)}{\kappa_1(\xi)} d\xi \quad (5.70)$$

and

$$\zeta_2^- := \frac{1}{2}(\xi_2^-)^2 \quad (5.71a)$$

$$\zeta_2^+ := \delta_{\text{zero}}^2 \zeta_2^-. \quad (5.71b)$$

Then (5.69) may be integrated over a step to obtain

$$\zeta_2^- = \zeta_2^+ - V_{\text{zero}}(\theta^-), \quad (5.72)$$

as long as⁷

$$\zeta_2^+ - V_{\text{zero}}^{\text{MAX}} > 0, \quad (5.73)$$

where,

$$V_{\text{zero}}^{\text{MAX}} := \max_{\theta^+ \leq \xi_1 \leq \theta^-} V_{\text{zero}}(\xi_1). \quad (5.74)$$

Theorem 5.3 (Poincaré Map for Hybrid Zero Dynamics)

Consider the robot model (3.30) satisfying Hypotheses HR1–HR6 and HI1–HI7 with a smooth function h satisfying Hypotheses HH1–HH5, and let $(\theta; \gamma)$ be as in Theorem 5.1. Then in the coordinates $(\zeta_1; \zeta_2) = (\theta; \frac{1}{2}\gamma^2)$, the Poincaré return map of the hybrid zero dynamics, $\rho : \mathcal{S} \cap \mathcal{Z} \rightarrow \mathcal{S} \cap \mathcal{Z}$, is given by

$$\rho(\zeta_2^-) = \delta_{\text{zero}}^2 \zeta_2^- - V_{\text{zero}}(\theta^-), \quad (5.75)$$

with domain of definition

$$\mathcal{D}_{\text{zero}} := \left\{ \zeta_2^- > 0 \mid \delta_{\text{zero}}^2 \zeta_2^- - V_{\text{zero}}^{\text{MAX}} > 0 \right\}. \quad (5.76)$$

If $\delta_{\text{zero}}^2 \neq 1$ and

$$\zeta_2^* := -\frac{V_{\text{zero}}(\theta^-)}{1 - \delta_{\text{zero}}^2} \quad (5.77)$$

⁶In general, V_{zero} must be computed numerically.

⁷By definition, $\zeta_2 := \frac{1}{2}(\xi_2)^2$ must be positive along any solution.

is in the domain of definition of ρ , then it is the fixed point of ρ . Moreover, if $\zeta_2^* \in \mathcal{D}_{\text{zero}}$ is a fixed point, then ζ_2^* is an exponentially stable equilibrium point of

$$\zeta_2(k+1) = \rho(\zeta_2(k)) \quad (5.78)$$

if, and only if, $0 < \delta_{\text{zero}}^2 < 1$, and in this case, its domain of attraction is (5.76), the entire domain of definition of ρ .

Proof Equation (5.75) follows from substituting (5.66c) into (5.72), and (5.76) follows from (5.73). Note that because $V_{\text{zero}}(\theta^+) = 0$, $V_{\text{zero}}^{\text{MAX}} \geq 0$, and thus $\mathcal{D}_{\text{zero}}$ is nonempty if, and only if, $\delta_{\text{zero}}^2 > 0$. On the other hand, from the affine form of ρ , a fixed point will be exponentially stable, if, and only if, $\delta_{\text{zero}}^2 < 1$, and in this case, solutions of (5.78) are monotonic, which implies that the domain of attraction is all of $\mathcal{D}_{\text{zero}}$.

Remark 5.5 The domain of definition (5.76) specifies a lower bound on the Poincaré map ρ . That is, if $\zeta_2^- < V_{\text{zero}}^{\text{MAX}}/\delta_{\text{zero}}^2$, then the robot will not successfully complete a step. Viewed another way, $\delta_{\text{zero}}^2 \zeta_2^- - V_{\text{zero}}^{\text{MAX}}$ is the amount of energy that may be removed from the system during a step—through perturbations, for example—before the robot will not be able to successfully complete the step.

Using Corollary 4.2, these results on the hybrid zero dynamics can be reformulated in the following way:

Corollary 5.1

Consider the robot model (3.30) satisfying Hypotheses HR1–HR6 and HI1–HI7 with a smooth function h satisfying Hypotheses HH1–HH5, and let $(\theta; \gamma)$ be as in Theorem 5.1.

- (a) The hybrid zero dynamics has a nontrivial periodic orbit transversal to $\mathcal{S} \cap \mathcal{Z}$ if, and only if, $\delta_{\text{zero}}^2 \neq 1$ and

$$\frac{\delta_{\text{zero}}^2}{1 - \delta_{\text{zero}}^2} V_{\text{zero}}(\theta^-) + V_{\text{zero}}^{\text{MAX}} < 0. \quad (5.79)$$

- (b) The hybrid zero dynamics has an exponentially stable periodic orbit transversal to $\mathcal{S} \cap \mathcal{Z}$ if, and only if, (5.79) holds and

$$0 < \delta_{\text{zero}}^2 < 1. \quad (5.80)$$

Proof Since (3.30) is smooth, Hypotheses HSH1–HSH5 are met and $f|_{\mathcal{Z}} = f_{\text{zero}}$ and $\Delta|_{\mathcal{S} \cap \mathcal{Z}}$ are smooth. In addition, Hypotheses HH1–HH5 imply Hypotheses HIInv1–HIInv4. Hence, all of the conditions of Corollary 4.2 are met.

It remains to show that a fixed point of ρ is transversal to $\mathcal{S} \cap \mathcal{Z}$. But from (5.76), a fixed point must have $\zeta_2^* \neq 0$, which in combination with (5.62) proves that $L_{f_{\text{zero}}} p_2^y(z^*) \neq 0$, where $z^* \in \mathcal{S} \cap \mathcal{Z}$ is the fixed point of ρ .

The computation of the closed-form representation of the Poincaré map has shown the following result.

Corollary 5.2

A Lagrangian of the swing phase zero dynamics (5.47) is $\mathcal{L}_{\text{zero}} := K_{\text{zero}} - V_{\text{zero}}$, where V_{zero} is given by (5.70) and

$$K_{\text{zero}} = \frac{1}{2} \left(\frac{\dot{\xi}_1}{\kappa_1(\xi_1)} \right)^2. \quad (5.81)$$

Remark 5.6 The time-to-impact function, $T_I(\xi_2^-)$, may be calculated from (5.47a) as

$$T_I(\xi_2^-) = \int_{\theta^+}^{\theta^-} \frac{1}{\kappa_1(\xi_1) \xi_2(\xi_1, \xi_2^-)} d\xi_1, \quad (5.82)$$

where $\xi_2(\xi_1, \xi_2^-)$ is a solution of (5.68). Because $\xi_2(\xi_1, \xi_2^-)$ is strictly increasing in ξ_2^- , it follows that $T_I(\xi_2^-)$ is strictly decreasing in ξ_2^- .

5.4.2 Relating Modeling Hypotheses to the Properties of the Hybrid Zero Dynamics

Although the domain of definition of the Poincaré map is as given in (5.76), not all solutions of the zero dynamics satisfy the modeling hypotheses; in particular, walking Hypothesis HGW2 limits the ratio and sign of the ground reaction forces of the stance leg end during phases of single support. These limits are reflected as an upper bound on the domain of definition of ρ . To see this, let F_1^T and F_1^N be the tangential and normal forces experienced at the end of the stance leg. The upper bound on ζ_2^- will be the largest ζ_2^- such that during the associated phase of single support, F_1^N is non-negative and $|F_1^T/F_1^N|$ is less than or equal to the maximum allowed static Coulomb friction coefficient.

The calculation of F_1^T and F_1^N requires the full $(N + 2)$ -DOF model. Consider the model (3.14) and apply the feedback u^* from (5.35). Let $\dot{x}_e = f_e(x_e) + g_e(x_e)[F_1^T; F_1^N]$ be the resulting closed-loop system written in state space form, where, $x_e := (q_e; \dot{q}_e)$ and $y_e = h_e(q_e) := (p_1^h(q_e); p_1^v(q_e))$ is the 2-vector of outputs corresponding to the position of the end of the stance leg. It is easily checked that the decoupling matrix $L_{g_e} L_{f_e} h_e$ is always invertible,

thus the forces F_1^T and F_1^N may be calculated as

$$\begin{bmatrix} F_1^T \\ F_1^N \end{bmatrix} = -(L_{g_e} L_{f_e} h_e)^{-1} L_{f_e}^2 h_e. \quad (5.83)$$

The above expression is quadratic in \dot{q}_e , and, when restricted to \mathcal{Z} , is affine in ζ_2 . Combining this with the solution of (5.69) results in an expression for the forces over a step of the robot that depends only on ξ_1 and ζ_2^- , viz

$$\begin{bmatrix} F_1^N(\xi_1, \zeta_2^-) \\ F_1^T(\xi_1, \zeta_2^-) \end{bmatrix} = \Lambda_1(\xi_1) \zeta_2^- + \Lambda_0(\xi_1), \quad (5.84)$$

where Λ_0 and Λ_1 are smooth functions of ξ_1 . Thus, an upper bound on ζ_2^- so that the pivot assumption holds is given by

$$\zeta_{2,F_1^N}^{\max} := \sup \left\{ \zeta_2^- > 0 \mid \min_{\theta^+ \leq \xi_1 \leq \theta^-} F_1^N(\xi_1, \zeta_2^-) \geq 0 \right\} \quad (5.85a)$$

$$\zeta_{2,|F_1^T/F_1^N|}^{\max} := \sup \left\{ 0 < \zeta_2^- < \zeta_{2,F_1^N}^{\max} \mid \max_{\theta^+ \leq \xi_1 \leq \theta^-} \left| \frac{F_1^T(\xi_1, \zeta_2^-)}{F_1^N(\xi_1, \zeta_2^-)} \right| \leq \mu_s \right\}, \quad (5.85b)$$

where μ_s is the static Coulomb friction coefficient of the walking surface [124], and the domain of definition of the Poincaré return map should thus be restricted to

$$\left\{ \zeta_2^- > 0 \mid \delta_{\text{zero}}^2 \zeta_2^- - V_{\text{zero}}^{\text{MAX}} > 0, \ zeta_2^- < \zeta_{2,|F_1^T/F_1^N|}^{\max} \right\}. \quad (5.86)$$

On a practical note, if the modeling hypotheses included bounds on the maximum actuator torque, then, in the same manner, these bounds could also be explicitly included in the domain of definition of the Poincaré map.

5.5 Creating Exponentially Stable, Periodic Orbits in the Full Hybrid Model

Fixed points of the Poincaré return map of the hybrid zero dynamics correspond to periodic orbits of the hybrid zero dynamics. By construction of the hybrid zero dynamics, these are also periodic orbits of the full model, (3.30). Indeed, suppose that Hypotheses HH1–HH5 hold and that, in addition, there exists a fixed point, $z^* \in \mathcal{S} \cap \mathcal{Z}$, of the Poincaré return map for the hybrid zero dynamics. Let \mathcal{O} be the periodic orbit in \mathcal{Z} corresponding to z^* ; that is,

$$\mathcal{O} := \{z \in \mathcal{Z} \mid z = \varphi(t, \Delta(z^*)), \ 0 \leq t < T_I \circ \Delta(z^*)\}, \quad (5.87)$$

where φ is a solution of the hybrid zero dynamics, (5.60). \mathcal{O} is then a periodic orbit of the full model corresponding to initial condition z^* and control input $u(t) = u^* \circ \varphi(t, \Delta(z^*))$, for $0 \leq t < T_I \circ \Delta(z^*)$, where u^* is given by (5.35).

The objective is to now show that *exponentially stable orbits* of the hybrid zero dynamics correspond to *exponentially stabilizable orbits* of the full model. This is developed using two approaches to the design of a feedback control that imposes the virtual constraints, (5.30). Application of the prefeedback

$$u(x) = (L_g L_f h(x))^{-1}(v - L_f^2 h(x)) \quad (5.88)$$

to (5.29) with an output satisfying HH1–HH4 results in the chain of $N - 1$ double integrators,

$$\frac{d^2y}{dt^2} = v; \quad (5.89)$$

see (5.32). Two choices of a feedback v are now made for which the periodic orbit \mathcal{O} can be shown to be exponentially attractive.

5.5.1 Computed Torque with Finite-Time Feedback Control

Let

$$v(y, \dot{y}) \quad (5.90)$$

be any feedback controller on (5.89) satisfying conditions HC1–HC4 below.

Controller Hypotheses: for the closed-loop chain of double integrators, $\ddot{y} = v(y, \dot{y})$,

HC1) solutions globally exist on \mathbb{R}^{2N-2} , and are unique;

HC2) solutions depend continuously on the initial conditions;

HC3) the origin is globally asymptotically stable, and convergence is achieved in finite time; and

HC4) the *settling time function*,⁸ $T_{\text{set}} : \mathbb{R}^{2N-2} \rightarrow \mathbb{R}$ by

$$\begin{aligned} T_{\text{set}}(y_0, \dot{y}_0) := \inf\{t > 0 \mid (y(t); \dot{y}(t)) = (0; 0), \\ (y(0); \dot{y}(0)) = (y_0; \dot{y}_0)\} \end{aligned} \quad (5.91)$$

depends continuously on the initial condition, $(y_0; \dot{y}_0)$.

Hypotheses HC1–HC3 correspond to the definition of *finite-time stability* [20, 21, 108]; Hypothesis HC4 is also needed, and it is not implied by HC1–HC3 [20]. These requirements rule out traditional sliding mode control, with its

⁸That is, the time it takes for a solution initialized at $(y_0; \dot{y}_0)$ to converge to the origin. The terminology is taken from [20].

well-known discontinuous action. One possibility is the *continuous* feedback law presented in [20],

$$v = \Psi(y, \dot{y}) := \frac{1}{\epsilon^2} \cdot \begin{bmatrix} \psi_1(y_1, \epsilon \dot{y}_1) \\ \vdots \\ \psi_{N-1}(y_{N-1}, \epsilon \dot{y}_{N-1}) \end{bmatrix}, \quad (5.92)$$

where

$$\psi_i(y_i, \epsilon \dot{y}_i) := -\text{sign}(\epsilon \dot{y}_i) |\epsilon \dot{y}_i|^\alpha - \text{sign}(\phi_i(y_i, \epsilon \dot{y}_i)) |\phi_i(y_i, \epsilon \dot{y}_i)|^{\frac{\alpha}{2-\alpha}}, \quad (5.93)$$

$0 < \alpha < 1$, and

$$\phi_i(y_i, \epsilon \dot{y}_i) := y_i + \frac{1}{2-\alpha} \cdot \text{sign}(\epsilon \dot{y}_i) |\epsilon \dot{y}_i|^{2-\alpha}. \quad (5.94)$$

The settling time of the controller is adjusted by the parameter $\epsilon > 0$.

The state feedback controller is

$$u_{FT}(x) = (L_g L_f h(x))^{-1} (v(h(x), L_f h(x)) - L_f^2 h(x)), \quad (5.95)$$

for any choice of v in (5.90) satisfying HC1–HC4.

Theorem 5.4 (Exponentially Stable Walking Motions-I)

Consider the hybrid model of walking (3.30) for a robot satisfying Hypotheses HR1–HR5 and HI1–HI7, and a set of virtual constraints (5.30) satisfying Hypotheses HH1–HH5. Suppose that the hybrid zero dynamics has an exponentially stable periodic orbit \mathcal{O} transversal to $\mathcal{S} \cap \mathcal{Z}$. Then for any function v satisfying Hypotheses HC1–HC4, \mathcal{O} is also an exponentially stable periodic orbit transversal to \mathcal{S} of the closed-loop system consisting of (3.30) and the state variable feedback (5.95).

The proof is given in [Appendix C.2](#). By this result, it follows that if an output can be selected so that the resulting 1-DOF hybrid zero dynamics admits an exponentially stable orbit, then an exponentially stable walking motion can be achieved for the full-dimensional model of the robot. Moreover, by the results of Section 5.4.2, it can be ensured that key modeling assumptions are met for the steady state walking motion. [Chapter 6](#) will give a means of systematically selecting the output function.

5.5.2 Computed Torque with Linear Feedback Control

Suppose that the decoupling matrix $L_g L_f h$ is invertible. Let $K_D > 0$ and $K_P > 0$ be $N-1 \times N-1$ positive definite matrices and let $\epsilon > 0$ be a positive scalar “tuning parameter.” Then the feedback

$$u_{LIN}(x) = -(L_g L_f h(x))^{-1} \left(L_f^2 h(x) + \frac{1}{\epsilon} K_D L_f h(x) + \frac{1}{\epsilon^2} K_P h(x) \right) \quad (5.96)$$

applied to the swing phase portion of (3.30) results in

$$\ddot{y} = -\frac{1}{\epsilon} K_D \dot{y} - \frac{1}{\epsilon^2} K_P y. \quad (5.97)$$

The solutions of (5.97) converge exponentially to zero. In bipedal walking, the impact map tends to increase the norm of \dot{y} at each impact. The parameter $\epsilon > 0$ provides control over the speed with which $y(t)$ and $\dot{y}(t)$ converge to zero during the continuous phase, so that, over a cycle consisting of an impact event followed by a swing phase, the contraction taking place in the swing phase dominates the expansion coming from the impact. In this way, the solution of the closed-loop system may converge to the hybrid zero dynamics, and hence to an exponentially stable periodic orbit of the hybrid zero dynamics. The theorem below makes this intuitive idea rigorous.

Theorem 5.5 (Exponentially Stable Walking Motions-II)

Consider the hybrid model of walking (3.30) for a robot satisfying Hypotheses HR1–HR5 and HI1–HI7, and a set of virtual constraints (5.30) satisfying Hypotheses HH1–HH5. Suppose that the hybrid zero dynamics has an exponentially stable periodic orbit \mathcal{O} transversal to $\mathcal{S} \cap \mathcal{Z}$. Then for any choice of positive definite matrices $K_D > 0$ and $K_P > 0$, there exists $\bar{\epsilon} > 0$ such that for $0 < \epsilon < \bar{\epsilon}$, \mathcal{O} is also an exponentially stable periodic orbit transversal to \mathcal{S} of the closed-loop system consisting of (3.30) and the state variable feedback (5.96).

In short, for $\epsilon > 0$ sufficiently small, an exponentially stable periodic orbit of the hybrid zero dynamics is also an exponentially stable periodic orbit of the full-dimensional closed-loop system. The proof is given in [Appendix C.2](#).

6

Systematic Design of Within-Stride Feedback Controllers for Walking

Chapter 5 provided the conditions for the existence of a zero dynamics for the complete robot model with impacts and established a number of its properties. However, in a concrete manner, the results are not yet practicable for feedback design for at least two reasons. First, the issue of how to choose the virtual constraints has not been addressed, and second, in general, the coordinate transformation used in the explicit computation of the hybrid zero dynamics can be very difficult to perform. This chapter has two principal objectives: to present a class of output functions that leads to computable, closed-form representations of the zero dynamics and to introduce a finite parameterization of the outputs in a convenient form that will permit the shaping of the zero dynamics by parameter optimization.

Throughout the chapter, the robot is assumed to satisfy Hypotheses HR1–HR6 and HI1–HI7. Its model in the form of a system with impulse effects is expressed as

$$\Sigma : \begin{cases} \dot{x} = f(x) + g(x)u & x^- \notin \mathcal{S} \\ x^+ = \Delta(x^-) & x^- \in \mathcal{S}, \end{cases} \quad (6.1)$$

where $x = (q; \dot{q})$, and

$$f(x) = \begin{bmatrix} \dot{q} \\ D^{-1}(q) [-C(q, \dot{q})\dot{q} - G(q)] \end{bmatrix} \quad \text{and} \quad g(x) = \begin{bmatrix} 0 \\ D^{-1}(q)B(q) \end{bmatrix}. \quad (6.2)$$

In addition, a gait is sought that satisfies Hypotheses HGW1–HGW7.

6.1 A Special Class of Virtual Constraints

Associate to (6.1) and (6.2) the following output function

$$y = h(q) := h_0(q) - h_d \circ \theta(q), \quad (6.3)$$

where $h_0(q)$ specifies $(N - 1)$ independent quantities that are to be controlled and $h_d \circ \theta(q)$ specifies the desired evolution of these quantities as a function of

the scalar quantity $\theta(q)$. Driving y to zero will force $h_0(q)$ to track $h_d \circ \theta(q)$, see Fig. 1.9. The posture of the robot is then being controlled to evolve according to the virtual constraints $h_0(q) - h_d \circ \theta(q) = 0$ —that is, a set of holonomic constraints parameterized by $\theta(q)$. It is important to note that this is not a classical trajectory tracking scheme because the desired evolution of $h_0(q)$ is slaved to $\theta(q)$, a function of the robot’s state, and not time. Slaving $h_0(q)$ to $\theta(q)$ results in a closed-loop system which is autonomous.

Choosing

$$h_0(q) := H_0 q \quad (6.4a)$$

$$\theta(q) := c q \quad (6.4b)$$

where H_0 is an $(N - 1) \times N$ real matrix and c is a $1 \times N$ real row vector, allows the hypotheses of Lemma 5.1 to be easily satisfied. Specifically, the output function structure of (6.3) with $h_0(q)$ and $\theta(q)$ as in (6.4), satisfies Hypothesis HH1 (the output only depends on the configuration variables) and will satisfy Hypothesis HH3 (invertibility of the coordinate transformation on the configuration variables) if, and only if,

$$H := \begin{bmatrix} H_0 \\ c \end{bmatrix} \quad (6.5)$$

is full rank. Hence, if Hypotheses HH2 and HH4 hold (invertibility of the decoupling matrix and \mathcal{Z} is nonempty), the swing phase zero dynamics can be computed in closed form. Indeed, the coordinate inverse required in (5.46a) is given by

$$q = H^{-1} \begin{bmatrix} h_d(\xi_1) \\ \xi_1 \end{bmatrix}. \quad (6.6)$$

In Section 6.2, h_d will be specialized to a vector of Bézier polynomials, which will make it straightforward to achieve the invariance condition, $\Delta(\mathcal{S} \cap \mathcal{Z}) \subset \mathcal{Z}$. Finally, note that due to the structure of the output (6.3) with h_0 and θ as in (6.4), Hypotheses HH2 and HH3 imply Hypothesis HH4.

6.2 Parameterization of h_d by Bézier Polynomials

Let $1 \leq i \leq (N - 1)$. A one-dimensional Bézier polynomial [19] of degree M is a polynomial, $b_i : [0, 1] \rightarrow \mathbb{R}$, defined by $M + 1$ coefficients, α_k^i , per

$$b_i(s) := \sum_{k=0}^M \alpha_k^i \frac{M!}{k!(M-k)!} s^k (1-s)^{M-k}. \quad (6.7)$$

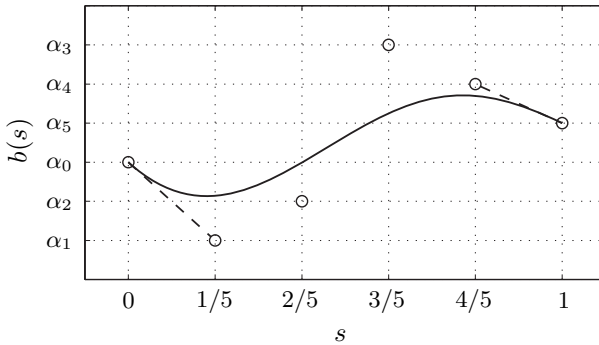


Figure 6.1. An example Bézier degree five ($M = 5$) polynomial curve. Note that (i) the curve is contained within the convex hull of the 6 coefficients (as viewed as points in \mathbb{R}^2 , $\{(0; \alpha_0), (1/5; \alpha_1), \dots, (1; \alpha_5)\}$), (ii) the curve begins at $(0; \alpha_0)$ and ends at $(1; \alpha_5)$, and (iii) the curve is tangent to the line segments connecting $(0; \alpha_0)$ and $(1/5; \alpha_1)$, and $(4/5; \alpha_4)$ and $(1; \alpha_5)$ at the start and end points, respectively.

For later use, note that

$$\frac{\partial b_i(s)}{\partial s} = \sum_{k=0}^{M-1} (\alpha_{k+1}^i - \alpha_k^i) \frac{M!}{k!(M-k-1)!} s^k (1-s)^{M-k-1}. \quad (6.8)$$

Some particularly useful features of Bézier polynomials are (see [189, p. 291])

1. the image of the Bézier polynomial is contained in the convex hull of the $M + 1$ coefficients (as viewed as points in \mathbb{R}^2 , $\{(0; \alpha_0^i), (1/M; \alpha_1^i), (2/M; \alpha_2^i), \dots, (1; \alpha_M^i)\}$);
2. $b_i(0) = \alpha_0^i$ and $b_i(1) = \alpha_M^i$; and
3. $(\partial b_i(s)/\partial s)|_{s=0} = M(\alpha_1^i - \alpha_0^i)$ and $(\partial b_i(s)/\partial s)|_{s=1} = M(\alpha_M^i - \alpha_{M-1}^i)$.

The first feature implies that the polynomial does not exhibit large oscillations with small parameter variations, which is useful for numerical calculations. The second two features are exactly those used to achieve $\Delta(\mathcal{S} \cap \mathcal{Z}) \subset \mathcal{Z}$. See Fig. 6.1 for an example Bézier polynomial curve.

A given function $\theta(q)$ of the generalized coordinates will not, in general, take values in the unit interval over a phase of single support. Therefore, to appropriately compose a Bézier polynomial with $\theta(q)$, it is necessary to normalize θ by

$$s(q) := \frac{\theta(q) - \theta^-}{\theta^+ - \theta^-}, \quad (6.9)$$

which takes values in $[0, 1]$; recall that θ^- is the value of θ at the end of the step and θ^+ is the value at the beginning of the step. Define $h_d \circ \theta(q)$ by

$$h_d \circ \theta(q) := \begin{bmatrix} b_1 \circ s(q) \\ b_2 \circ s(q) \\ \vdots \\ b_{N-1} \circ s(q) \end{bmatrix}. \quad (6.10)$$

Group the parameters α_k^i into an $(N - 1) \times (M + 1)$ matrix, α , and denote the columns of α by $\alpha_k := (\alpha_k^1; \dots; \alpha_k^{N-1})$. For most of this book, the output will be chosen to be of the form (6.3) to (6.4b) with h_d chosen as in (6.10). An important class of parameters, α , is now defined.

Definition 6.1 *The matrix of parameters α is said to be a regular parameter of an output of the form (6.3) to (6.4b) with h_d chosen as in (6.10) if the resulting output satisfies Hypotheses HH1–HH5, that is, the conditions for the invertibility of the decoupling matrix and the existence of a two-dimensional, smooth, zero dynamics associated with the single support phase of the robot.*

In later chapters it will be important to distinguish between different output functions—and hence walking motions—which differ only in the choice of the Bézier parameters. For this reason, from this point forward, quantities related to an output will be labeled with its grouped Bézier coefficients; for example, the beginning and ending values of θ associated with α will be written as θ_α^+ and θ_α^- , and the Bézier polynomial degree will be written M_α .

Evaluating (6.10) and its derivative with respect to θ_α at the beginning (respectively end) of a phase of single support, that is, where $\theta(q) = \theta_\alpha^+$ (respectively $\theta(q) = \theta_\alpha^-$) will lead to a convenient means of ensuring $\Delta(\mathcal{S} \cap \mathcal{Z}_\alpha) \subset \mathcal{Z}_\alpha$. Evaluation of $h_{d,\alpha}$ is particularly trivial,

$$h_{d,\alpha}(\theta_\alpha^+) = \alpha_0 \quad (6.11a)$$

$$h_{d,\alpha}(\theta_\alpha^-) = \alpha_M, \quad (6.11b)$$

and therefore (6.6) evaluated at θ_α^+ and θ_α^- becomes

$$q_\alpha^+ = H^{-1} \begin{bmatrix} \alpha_0 \\ \theta_\alpha^+ \end{bmatrix} \quad (6.12a)$$

$$q_\alpha^- = H^{-1} \begin{bmatrix} \alpha_M \\ \theta_\alpha^- \end{bmatrix}. \quad (6.12b)$$

Differentiation of (6.6) with respect to time yields

$$\dot{q}_\alpha = H^{-1} \begin{bmatrix} \frac{\partial h_{d,\alpha}}{\partial \theta} \\ 1 \end{bmatrix} \dot{\theta}_\alpha. \quad (6.13)$$

Taking the partial derivative of (6.10) required by (6.13) yields

$$\frac{\partial h_{d,\alpha}}{\partial \theta} = \frac{\partial b_\alpha}{\partial s_\alpha} \frac{\partial s_\alpha}{\partial \theta} \quad (6.14a)$$

$$= \left(\sum_{k=0}^{M_\alpha} \alpha_k \frac{M_\alpha!}{k!(M_\alpha-k)!} \left(ks_\alpha^{k-1} (1-s_\alpha)^{M_\alpha-k} - (M_\alpha-k)s_\alpha^k (1-s_\alpha)^{M_\alpha-k-1} \right) \right) \frac{1}{\theta_\alpha^- - \theta_\alpha^+} \quad (6.14b)$$

which when evaluated at θ_α^+ and θ_α^- gives

$$\frac{\partial h_{d,\alpha}}{\partial \theta} \Big|_{\theta=\theta_\alpha^+} = \frac{M_\alpha}{\theta_\alpha^- - \theta_\alpha^+} (\alpha_1 - \alpha_0) \quad (6.15a)$$

$$\frac{\partial h_{d,\alpha}}{\partial \theta} \Big|_{\theta=\theta_\alpha^-} = \frac{M_\alpha}{\theta_\alpha^- - \theta_\alpha^+} (\alpha_{M_\alpha} - \alpha_{M_\alpha-1}) \quad (6.15b)$$

and therefore (6.13) evaluated at θ_α^+ and θ_α^- becomes

$$\dot{q}_\alpha^+ = H^{-1} \begin{bmatrix} \frac{M_\alpha}{\theta_\alpha^- - \theta_\alpha^+} (\alpha_1 - \alpha_0) \\ 1 \end{bmatrix} \dot{\theta}_\alpha^+ \quad (6.16a)$$

$$\dot{q}_\alpha^- = H^{-1} \begin{bmatrix} \frac{M_\alpha}{\theta_\alpha^- - \theta_\alpha^+} (\alpha_{M_\alpha} - \alpha_{M_\alpha-1}) \\ 1 \end{bmatrix} \dot{\theta}_\alpha^- \quad (6.16b)$$

For notational convenience, define

$$\omega_\alpha^- := H^{-1} \begin{bmatrix} \frac{M_\alpha}{\theta_\alpha^- - \theta_\alpha^+} (\alpha_M - \alpha_{M-1}) \\ 1 \end{bmatrix}. \quad (6.17)$$

For two regular parameter sets, α and β , the following theorem gives the conditions under which $\Delta(\mathcal{S} \cap \mathcal{Z}_\alpha) \subset \mathcal{Z}_\beta$. This theorem will be key in the construction of controllers with invariant zero dynamics manifolds and when performing event-based PI control in the next chapter.

Theorem 6.1 (Achieving $\Delta(\mathcal{S} \cap \mathcal{Z}_\alpha) \subset \mathcal{Z}_\beta$)

Assume the hypotheses of Theorem 5.2 and two outputs h_α and h_β of the form (6.3) with h_0 , h_d , and θ as in (6.4) and (6.10). Then, $h_\beta \circ \Delta(\mathcal{S} \cap \mathcal{Z}_\alpha) = 0$ if, and only if,

$$\begin{bmatrix} \beta_0 \\ \theta_\beta^+ \end{bmatrix} = H \Delta_q H^{-1} \begin{bmatrix} \alpha_{M_\alpha} \\ \theta_\alpha^- \end{bmatrix}. \quad (6.18)$$

Moreover, if $c\Delta_{\dot{q}}\omega_{\alpha}^{-} \neq 0$, then $L_f h_{\beta} \circ \Delta(\mathcal{S} \cap \mathcal{Z}_{\alpha}) = 0$ if, and only if,

$$\beta_1 = H_0 \Delta_{\dot{q}}\omega_{\alpha}^{-} \frac{\theta_{\beta}^{-} - \theta_{\beta}^{+}}{M_{\beta}} (c\Delta_{\dot{q}}\omega_{\alpha}^{-})^{-1} + \beta_0. \quad (6.19)$$

That is, (6.18) and (6.19) are equivalent to $\Delta(\mathcal{S} \cap \mathcal{Z}_{\alpha}) \subset \mathcal{Z}_{\beta}$ as long as $c\Delta_{\dot{q}}\omega_{\alpha}^{-} \neq 0$.

Proof Using Theorem 5.2, it suffices to show that there exists at least one point $x_{\alpha}^{-} = (q_{0,\alpha}^{-}; \dot{q}_{0,\alpha}^{-}) \in \mathcal{S} \cap \mathcal{Z}_{\alpha}$ such that $\gamma_0(q_{0,\alpha}^{-}) \dot{q}_{0,\alpha}^{-} \neq 0$, $h_{\beta} \circ \Delta_q q_{0,\alpha}^{-} = 0$, and $L_f h_{\beta} \circ \Delta(q_{0,\alpha}^{-}, \dot{q}_{0,\alpha}^{-}) = 0$. Evaluating (6.6) on $\mathcal{S} \cap \mathcal{Z}_{\alpha}$, $h_{\beta} \circ \Delta(x_{\alpha}^{-}) = 0$ means that $q_{\beta}^{+} = \Delta_q q_{\alpha}^{-}$. Equating (6.12) with Δ_q yields

$$H^{-1} \begin{bmatrix} \beta_0 \\ \theta_{\beta}^{+} \end{bmatrix} = \Delta_q H^{-1} \begin{bmatrix} \alpha_{M_{\alpha}} \\ \theta_{\alpha}^{-} \end{bmatrix}, \quad (6.20)$$

which may be solved for $(\beta_0; \theta_{\beta}^{+})$. Achieving $L_f h_{\beta} \circ \Delta(x_{\alpha}^{-}) = 0$ means that $\dot{q}_{\beta}^{+} = \Delta_{\dot{q}}(q_{\alpha}^{-}) \dot{q}_{\alpha}^{-}$. Equating (6.16) with $\Delta_{\dot{q}}$ yields

$$H^{-1} \begin{bmatrix} \frac{M_{\beta}}{\theta_{\beta}^{-} - \theta_{\beta}^{+}} (\beta_1 - \beta_0) \\ 1 \end{bmatrix} \dot{q}_{\beta}^{+} = \Delta_{\dot{q}} H^{-1} \begin{bmatrix} \frac{M_{\alpha}}{\theta_{\alpha}^{-} - \theta_{\alpha}^{+}} (\alpha_{M_{\alpha}} - \alpha_{M_{\alpha}-1}) \\ 1 \end{bmatrix} \dot{q}_{\alpha}^{-} \quad (6.21)$$

and consequently

$$\frac{M_{\beta}}{\theta_{\beta}^{-} - \theta_{\beta}^{+}} (\beta_1 - \beta_0) \dot{q}_{\beta}^{+} = H_0 \Delta_{\dot{q}}\omega_{\alpha}^{-} \dot{q}_{\alpha}^{-} \quad (6.22)$$

and

$$\dot{q}_{\beta}^{+} = c\Delta_{\dot{q}}\omega_{\alpha}^{-} \dot{q}_{\alpha}^{-}, \quad (6.23)$$

which implies

$$\beta_1 = H_0 \Delta_{\dot{q}}\omega_{\alpha}^{-} \frac{\theta_{\beta}^{-} - \theta_{\beta}^{+}}{M_{\beta}} \frac{\dot{q}_{\alpha}^{-}}{\dot{q}_{\beta}^{+}} + \beta_0 \quad (6.24)$$

and

$$\frac{\dot{q}_{\beta}^{+}}{\dot{q}_{\alpha}^{-}} = c\Delta_{\dot{q}}\omega_{\alpha}^{-}. \quad (6.25)$$

Hence,

$$\beta_1 = H_0 \Delta_{\dot{q}}\omega_{\alpha}^{-} \frac{\theta_{\beta}^{-} - \theta_{\beta}^{+}}{M_{\beta}} (c\Delta_{\dot{q}}\omega_{\alpha}^{-})^{-1} + \beta_0 \quad (6.26)$$

as long as $c\Delta_{\dot{q}}\omega_{\alpha}^{-} \neq 0$.

Corollary 6.1 (Achieving $\Delta(\mathcal{S} \cap \mathcal{Z}_\alpha) \subset \mathcal{Z}_\alpha$)

Assume the hypotheses of Theorem 5.2 and an output h_α of the form (6.3) with h_0 , $h_{d,\alpha}$, and θ_α as in (6.4) and (6.10). Then, $h_\alpha \circ \Delta(\mathcal{S} \cap \mathcal{Z}_\alpha) = 0$ if, and only if,

$$\begin{bmatrix} \alpha_0 \\ \theta_\alpha^+ \end{bmatrix} = H \Delta_q H^{-1} \begin{bmatrix} \alpha_{M_\alpha} \\ \theta_\alpha^- \end{bmatrix}. \quad (6.27)$$

Moreover, if $c\Delta_{\dot{q}}\omega_\alpha^- \neq 0$, then $L_f h_\alpha \circ \Delta(\mathcal{S} \cap \mathcal{Z}_\alpha) = 0$ if, and only if,

$$\alpha_1 = H_0 \Delta_{\dot{q}} \omega_\alpha^- \frac{\theta_\alpha^- - \theta_\alpha^+}{M_\alpha} (c\Delta_{\dot{q}}\omega_\alpha^-)^{-1} + \alpha_0. \quad (6.28)$$

That is, (6.27) and (6.28) are equivalent to $\Delta(\mathcal{S} \cap \mathcal{Z}_\alpha) \subset \mathcal{Z}_\alpha$ as long as $c\Delta_{\dot{q}}\omega_\alpha^- \neq 0$.

Remark 6.1 Corollary 6.1 constrains the coefficients α_0 and α_1 to be functions of α_{M_α} and $\alpha_{M_\alpha-1}$. Hence, M_α must be chosen to be three or greater to impose the invariance condition.

The following two lemmas give the conditions under which two regular parameter sets, α and β , satisfy $\mathcal{S} \cap \mathcal{Z}_\beta = \mathcal{S} \cap \mathcal{Z}_\alpha$ and $\Delta(\mathcal{S} \cap \mathcal{Z}_\beta) = \Delta(\mathcal{S} \cap \mathcal{Z}_\alpha)$. These lemmas will be the key to achieving transitions between two walking gaits in the next chapter.

Lemma 6.1 (Achieving $\mathcal{S} \cap \mathcal{Z}_\alpha = \mathcal{S} \cap \mathcal{Z}_\beta$)

Assume the hypotheses of Theorem 5.2 and two outputs h_α and h_β of the form (6.3) with h_0 , h_d , and θ as in (6.4) and (6.10). Then, $\mathcal{S} \cap \mathcal{Z}_\alpha = \mathcal{S} \cap \mathcal{Z}_\beta$ if, and only if,

$$\alpha_{M_\alpha} = \beta_{M_\beta}, \quad \theta_\alpha^- = \theta_\beta^- \quad (6.29)$$

and

$$\alpha_{M_\alpha-1} = \frac{M_\beta}{M_\alpha} \frac{\theta_\alpha^- - \theta_\alpha^+}{\theta_\beta^- - \theta_\beta^+} (\beta_{M_\beta-1} - \beta_{M_\beta}) + \beta_{M_\beta}. \quad (6.30)$$

Proof The result follows directly from equating (6.12b) for β and α and equating (6.16b) for β and α .

Lemma 6.2 (Achieving $\Delta(\mathcal{S} \cap \mathcal{Z}_\beta) = \Delta(\mathcal{S} \cap \mathcal{Z}_\alpha)$)

Assume the hypotheses of Theorem 5.2 and two outputs h_α and h_β of the form (6.3) with h_0 , h_d , and θ as in (6.4) and (6.10). Then, $\Delta(\mathcal{S} \cap \mathcal{Z}_\beta) = \Delta(\mathcal{S} \cap \mathcal{Z}_\alpha)$ if, and only if,

$$\beta_0 = \alpha_0, \quad \theta_\beta^+ = \theta_\alpha^+ \quad (6.31)$$

and

$$\beta_1 = \frac{M_\alpha}{M_\beta} \frac{\theta_\beta^- - \theta_\beta^+}{\theta_\alpha^- - \theta_\alpha^+} (\alpha_1 - \alpha_0) + \alpha_0. \quad (6.32)$$

Proof The result follows directly from equating (6.12a) for β and α and equating (6.16a) for β and α .

6.3 Using Optimization of the HZD to Design Exponentially Stable Walking Motions

The previous two Sections have specified a set of outputs (or virtual constraints) for which the existence of the hybrid zero dynamics can be ensured in a straightforward manner. In particular, the invariance of the zero dynamics manifold under the impact map can be worked out in closed form when Bézier polynomials are used. This section presents a method for choosing the remaining free parameters in the Bézier polynomials to design a walking gait. The main idea is to pose the gait design problem as a parameter optimization problem.

The use of optimization in the analysis and design of bipedal walking motions has a relatively long history. Work as early as the 1970s can be found in the biomechanics literature (see [55, 113], for example). In more recent years, the design of optimal or approximately optimal trajectories for bipedal robots has become a popular topic [33, 44, 49, 109, 111, 191, 192, 195]. In each case the approach has been to design time trajectories such that a defined cost is minimized, or approximately minimized, subject to a set of constraints. The particular optimization technique employed varies considerably. CaboDevila and Abba [33] parameterized the robot state as a finite Fourier series and compared the performance of three algorithms: Nelder and Mead, Genetic, and Simulated Annealing. Chevallereau and Aoustin [44], and Chevallereau and Sardain [49] rewrote the actuated dynamics of the robot as a polynomial function of the unactuated dynamics and used Sequential Quadratic Programming (SQP). Hasegawa, Arakawa, and Fukuda [111] used a modified genetic algorithm to generate reference trajectories parameterized as cubic splines. Hardt [109] used an optimization package, DIRCOL [232], which implements a sparse SQP algorithm and uses a variable number of cubic splines to approximate the state and piecewise linear functions to approximate the control signals. Rostami and Bessonnet [192] applied Pontryagin's Maximum Principle. Roussel, Canudas de Wit, and Goswami [195] approximated the dynamics and used a direct shooting optimization algorithm.

Optimization will be used here to design walking motions via the selection of the parameters in the output functions, specifically, the Bézier polynomial

coefficients of h_d . The optimization process will not result in an optimal or approximately optimal open-loop trajectory, but rather a *closed-loop system* which possesses an exponentially stable orbit, and along this orbit a cost function will have been approximately minimized while satisfying other natural kinematic and dynamic constraints.

It is emphasized that the choice of the output function structure, H_0 , c , and the use of Bézier polynomials for h_d is based on analytical and computational tractability. Other output function structures have been explored. For example, in [176], which addresses the control of the five-link model presented in Section 3.4.6, a Cartesian approach is taken to the design of output functions. In that work, virtual constraints are posed on absolute torso angle, hip height, horizontal hip position, and swing leg end height. These virtual constraints, however, were not chosen so that the corresponding swing phase zero dynamics would be invariant under the impact map, and thus the stability results of Chapter 5 could not be applied.¹ Another choice of output function was explored in [120]. In that work, a fully actuated model is assumed and the output is designed to depend upon the horizontal component of the velocity of the robot's center of mass. In particular, the horizontal velocity of the center of mass is controlled to be a constant. Although the class of output functions chosen in this chapter does not allow explicit dependence upon velocity, the effect of velocity dependence used in [120] may be achieved via the event-based PI control scheme given in the next chapter.

Before the optimization problem is posed, it is worth illustrating how the parameters in an output function can affect gait properties, such as stability and energy expenditure.

6.3.1 Effects of Output Function Parameters on Gait Properties: An Example

The purpose of this example is to illustrate how the coefficients in the Bézier polynomial h_d can affect gait properties. Consider the two-link walker presented in Section 3.4.6.1 with a scalar output² of the form (6.3) to (6.4b) with h_d chosen³ as in (6.10). In the process of analyzing the example, the details of hypothesis verification will be illustrated and the need for a systematic approach to parameter selection—namely, optimization—will be motivated.

The first step in the design of the output function is to select the quantity to be controlled. The controlled quantity is selected here to be the hip angle, q_1 , because it is the directly actuated coordinate. Hence, $H_0 = [1 \ 0]$. The function $\theta(q)$ is selected to be $\theta(q) = q_2$ because, as the robot pivots from

¹Stability was analyzed using a version of Theorem 4.4.

²Because the two-link model has only one actuated joint, the output is scalar.

³In this section, α refers to the output function parameters and not the ground slope, which is assumed to be zero.

left to right about the stance foot, $\theta(q)$ is monotonically increasing; moreover, $H_0 q$ and $\theta(q) = c q = [0 \ 1] q$ are independent. Indeed

$$H = \begin{bmatrix} 1 & 0 \\ 0 & 1 \end{bmatrix} \quad (6.33)$$

is full rank. As a result, HH3 is clearly satisfied. Computing the decoupling matrix yields

$$\begin{aligned} L_g L_f h(q_1, q_2) = \\ \frac{\left(I - m l (l - l_c) \cos(q_1) + m(l - l_c)^2 \right) \left(\frac{\partial h_d}{\partial q_2} - 2 \right) - 2m l_c l}{\left(m l (l - l_c) \cos(q_1) \right)^2 - ((l^2 + l_c^2)m + I) \left((l - l_c)^2 m + I \right)}. \end{aligned} \quad (6.34)$$

The decoupling matrix will be invertible, c.f. Hypothesis HH2, whenever the numerator of (6.34) is different from zero, which can be ensured by appropriately choosing h_d and $\tilde{\mathcal{Q}} \subset \mathcal{Q}$ for given l and l_c . The Bézier polynomial degree, M_α , is selected to be four. The first two parameters, α_0 and α_1 , are constrained to impose invariance per Corollary 6.1, leaving three free parameters α_2 , α_3 , and α_4 . For simplicity, fix $\alpha_4 = \pi/7$, which leaves α_2 and α_3 as the only free parameters to be selected.

Because HH5 only depends upon q_α^- , given by (6.12b), which depends only upon α_3 and α_4 , HH5 is verified because

$$\frac{\partial}{\partial q} \begin{bmatrix} h_\alpha \\ p_2^v \end{bmatrix} \Big|_{q_\alpha^-} \approx \begin{bmatrix} 1 & \frac{28}{\pi} \alpha_3 - 4 \\ 0.223 & -0.445 \end{bmatrix} \quad (6.35)$$

is full rank for $\alpha_3 \not\approx 0.225$.

For a scalar output and two free parameters, it is feasible to numerically explore which parameter values give rise to motions that satisfy stability conditions (5.79) and (5.80) of Corollary 5.1 and also satisfy the remaining unverified hypotheses: HGW2, HI3, HH2, and HH4.⁴ These conditions and hypotheses were checked on a 500 by 500 grid for $0.5 \leq \alpha_2 \leq 7$ and $-0.85 \leq \alpha_3 \leq 2.2$. Figure 6.2(a) gives the region in which the two stability conditions (5.79) and (5.80) are satisfied. The linear shape of the left side of the shaded region is a consequence of δ_{zero} being greater than one and δ_{zero} only depending upon α_3 and α_4 (see Fig. 6.2(b)). Output Hypotheses HH2 and HH4 are satisfied for the entire walking motion inside the darkly shaded region of Fig. 6.2(a). Inside the lightly shaded region the decoupling matrix is singular for at least one point along the walking motion. Inside the darkly shaded region of Fig. 6.2(c), the two ground contact assumptions given in Hypotheses HGW2 and HI3 are

⁴For this two-link model, HGW6 will never be satisfied due to the simplicity of the model. See Section 3.4.6.1 for a discussion of this issue.

Table 6.1. Example gait statistics for the two-link walker with $\alpha_2 = 1.4$ and $\alpha_3 = 0.8$.

| $J(\alpha)$ ($N^2 m$) | ζ_2^* (kgm^2/s^2) | δ_{zero}^2 | $V_{zero}(\theta^-)$ (kgm^2/s^2) | V_{zero}^{MAX} (kgm^2/s^2) | $\bar{\nu}$ (m/s) |
|----------------------------|--------------------------------|-------------------|---|-------------------------------------|----------------------|
| 0.211 | 0.101 | 0.813 | -0.0340 | 0.0631 | 0.363 |

met; namely, the vertical component of the ground reaction force is positive, the ratio of the horizontal component to the vertical component does not exceed the coefficient of static friction (assumed here to be 0.6), and at impact, the swing leg neither slips nor rebounds. Points inside this region satisfy gait Hypotheses HGW1–HGW5 and output Hypotheses HH1–HH6. The grid was refined about this region and the average walking rate, $\bar{\nu}$, and cost given by the integral over the step of squared torque divided by distance traveled,⁵

$$J(\alpha) = \frac{1}{p_2^h(q_0^-)} \int_0^{T_I(\xi_2^-)} \|u_\alpha^*(t)\|_2^2 dt, \quad (6.36)$$

were calculated for points inside the region; Fig. 6.3 and Fig. 6.4 present the contour plots.

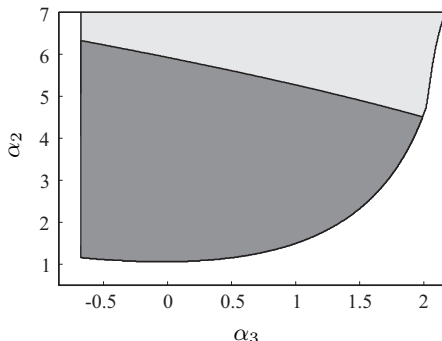
For $\alpha_2 = 1.4$ and $\alpha_3 = 0.8$, the system was simulated for three steps. Table 6.1 and Fig. 6.5 give various statistics and plots of interest. Note that the discontinuities in the plots of Fig. 6.5 are due to impacts and coordinate relabeling. The swing foot height, see Fig. 6.5(f), becomes negative due to the foot scuffing that is unavoidable with this simple model (see Section 3.4.6.1). A stick-figure animation of the simulation is provided in Fig. 6.6.

In this simple example, a few simulations were sufficient to determine how to choose α_2 and α_3 in order to achieve stable walking with desirable characteristics. As the Bézier polynomial degree, M_α , and the number of links, N , increase, determining desirable parameter values becomes significantly more difficult. This motivates the use of optimization as an automated means of parameter selection.

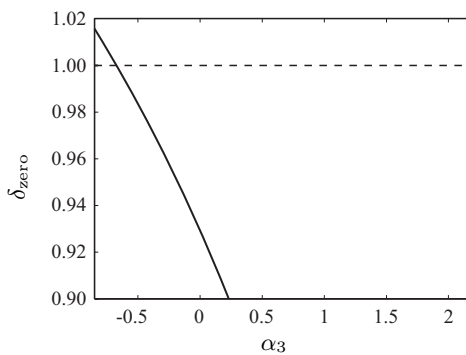
6.3.2 The Optimization Problem

The parameter selection problem will now be cast as a constrained nonlinear optimization problem that may be solved with many of the numerical optimization tools currently available. The objective will be to choose the matrix of output function parameters, α , such that hybrid model (6.1), the virtual constraint specified by (6.3) with h_0 , h_d , and θ as in (6.4) and (6.10), and either of the state variable feedbacks given in (5.95) and (5.96), will possess

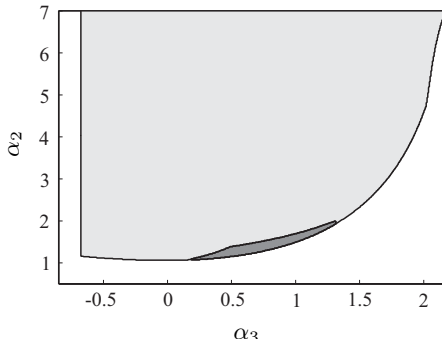
⁵See the next subsection for a discussion of this cost function.



(a) Inside the lightly shaded region, requirements (5.79) and (5.80) are met. Inside the darkly shaded region, Hypotheses HH2 and HH4 are met.



(b) Stability requirement (5.80) is met below the dashed line. Note δ_{zero} depends only on α_3 and α_4 , and for the example, α_4 is fixed at $\pi/7$.



(c) Inside the darkly shaded region, the ground contact assumptions given in Hypotheses HGW2 and HI3 are met. Outside this region, one or the other is not met. The coefficient of friction is assumed to be 0.6.

Figure 6.2. Determining which parameters give rise to a valid walking gait for the two-link walker. Note that $\alpha_4 = \pi/7$.

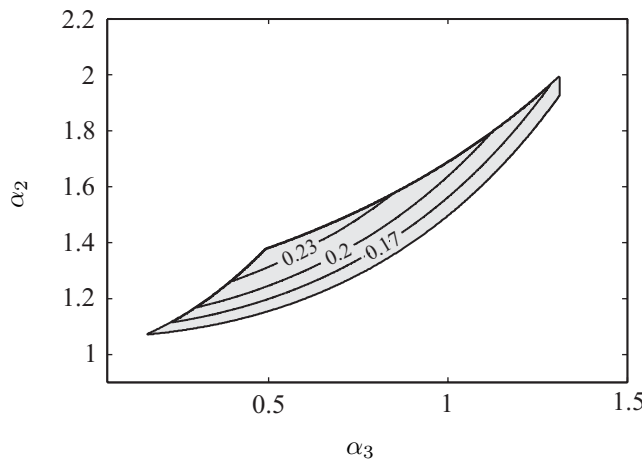


Figure 6.3. Contour plot of average walking rate for parameters which give rise to stable walking. The contour units are meters per second.

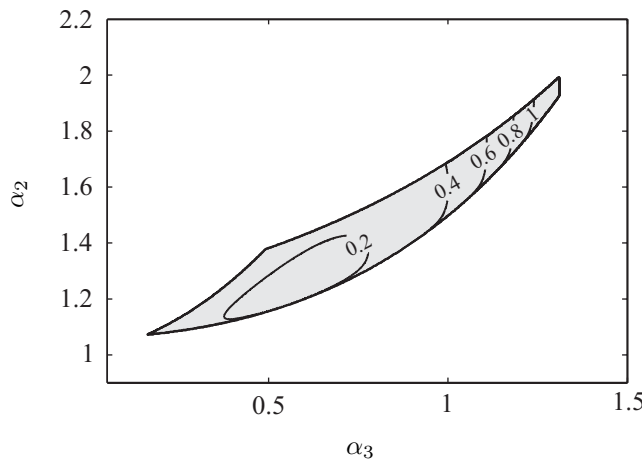


Figure 6.4. Contour plot of the cost for parameters which give rise to stable walking. The cost is $J(\alpha) = \frac{1}{p_2^h(q_0^-)} \int_0^{T_f(\xi_2^-)} (u^*(t))^2 dt$, with units of Joules squared per meter.

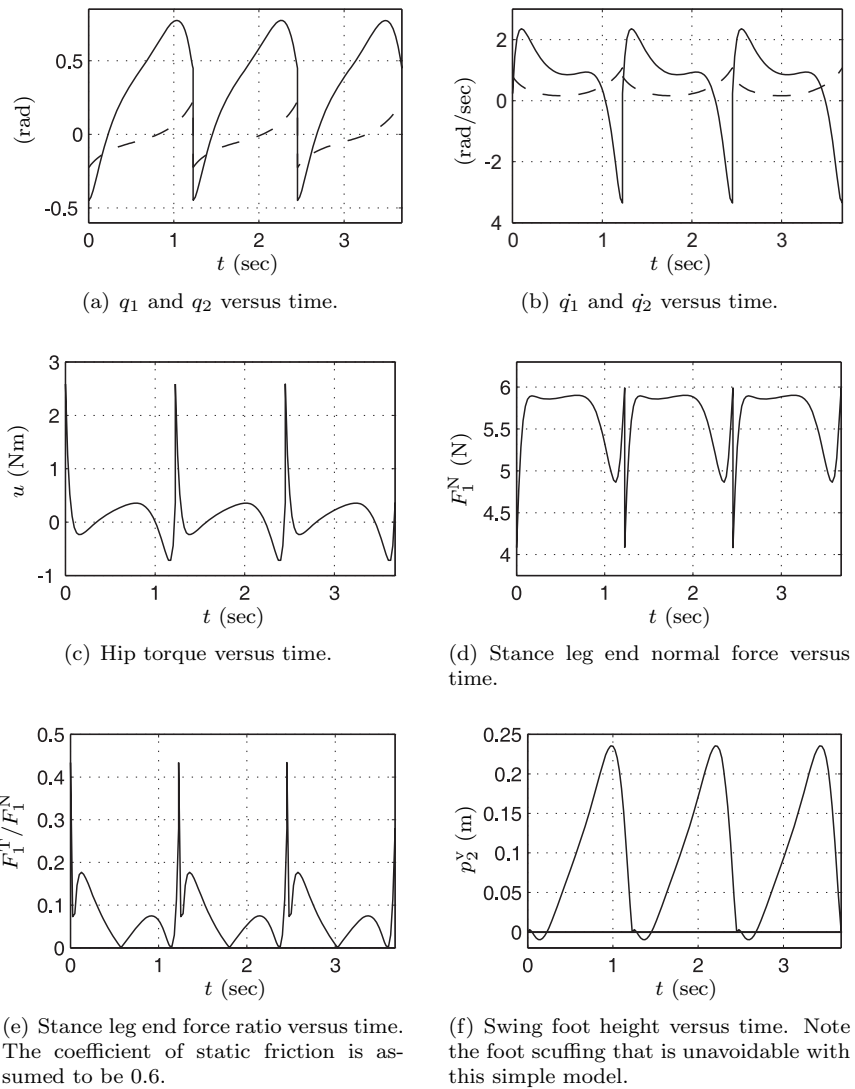


Figure 6.5. Plots corresponding to an example two-link walker gait at 0.363 m/s for three steps along a periodic orbit. The discontinuities are due to impacts and coordinate relabeling. Plots corresponding to q_2 are dashed.

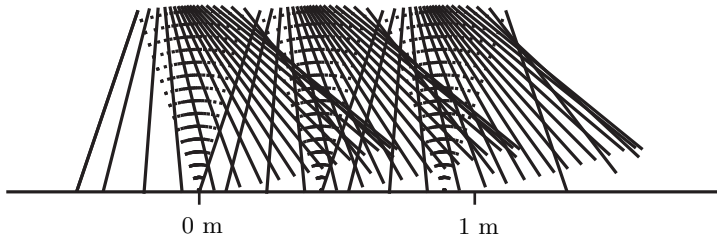


Figure 6.6. Stick animation of two-link walker taking three steps from left to right. The stance leg is dotted.

an exponentially stable periodic orbit while approximately minimizing a given cost function and satisfying a set of physically and mathematically motivated constraints along the periodic orbit.

A solution to the optimization problem may be sought on the full hybrid model (6.1), but it is computationally expensive, and increasingly so as the degree of the Bézier polynomials in the virtual constraints or the number of links in the model becomes large. However, if the parameters of (6.4) and (6.10) are chosen to meet the conclusions of Corollary 6.1, then the hybrid zero dynamics given in (5.60) exists; moreover, the control u^* associated with motion within the zero dynamics manifold is unique and is given by (5.35). This allows control effort within the hybrid zero dynamics to be computed independently of how the outputs corresponding to the virtual constraints are zeroed. Since periodic orbits of the hybrid zero dynamics are also orbits of the full-dimensional model, the optimization problem may be posed on the (two-dimensional) hybrid zero dynamics (5.60) instead of on the full ($2N$ -dimensional) hybrid model (6.1).

6.3.2.1 Parameter-Dependent Dynamic Model for Optimization

For the convenience of the reader, the key equations used in setting up the optimization problem are collected in one place. An output of the form

$$y = h_\alpha(q) = H_0 q - h_{d,\alpha} \circ \theta(q) \quad (6.37a)$$

$$\theta(q) = cq \quad (6.37b)$$

is assumed, with the parameter dependence arising from the Bézier polynomials used in Section 6.2. The zero dynamics manifold depends on α :

$$\mathcal{Z}_\alpha = \{x \in T\tilde{\mathcal{Q}} \mid h_\alpha(x) = 0, L_f h_\alpha(x) = 0\}. \quad (6.38)$$

The control enforcing the virtual constraints, which is unique on \mathcal{Z}_α , is

$$u_\alpha^*(x) = -(L_g L_f h_\alpha(x))^{-1} L_f^2 h_\alpha(x). \quad (6.39)$$

The hybrid zero dynamics is

$$\Sigma_{\text{zero},\alpha} : \begin{cases} \dot{z} = f_{\text{zero},\alpha}(z), & z^- \notin \mathcal{S} \cap \mathcal{Z}_\alpha \\ z^+ = \Delta(z^-), & z^- \in \mathcal{S} \cap \mathcal{Z}_\alpha, \end{cases} \quad (6.40)$$

where,

$$f_{\text{zero},\alpha}(z) = f(z) + g(z)u_\alpha^*(z) \in T_z \mathcal{Z}. \quad (6.41)$$

In coordinates $z = (\xi_1; \xi_2)$ for \mathcal{Z}_α chosen as in Theorem 5.1, the zero dynamics have the simple form

$$\dot{\xi}_1 = \kappa_{1,\alpha}(\xi_1)\xi_2 \quad (6.42a)$$

$$\dot{\xi}_2 = \kappa_{2,\alpha}(\xi_1). \quad (6.42b)$$

The state $x(t) = (q(t); \dot{q}(t))$ of the full-dimensional system (6.1) is easily reconstructed from $(\xi_1(t); \xi_2(t))$ using (5.46a). Substituting $x(t)$ into (6.39) yields the associated control signal, $u_\alpha^*(t) := u_\alpha^*(x(t))$.

6.3.3 Cost

In the optimization literature on bipedal gait design, the two most popular cost functions over a single step are

$$J_1(\alpha) := \frac{1}{p_2^h(q_0^-)} \int_0^{T_I(\xi_2^-)} \|u_\alpha^*(t)\|_2^2 dt \quad (6.43)$$

and

$$J_2(\alpha) := \frac{1}{p_2^h(q_0^-)} \int_0^{T_I(\xi_2^-)} \langle \dot{q}(t), Bu_\alpha^*(t) \rangle dt, \quad (6.44)$$

where $T_I(\xi_2^-)$ is the step duration, $p_2^h(q_0^-)$ corresponds to step length, $u_\alpha^*(t)$ is the result of evaluating (6.39) along a solution of the hybrid zero dynamics, and $\langle a, b \rangle := a'b$. The cost (6.43) roughly represents electric motor energy⁶ per distance traveled, and minimizing this cost function tends to reduce peak torque demands over a step. The cost (6.44) is the integral of the instantaneous mechanical power delivered by the actuators, per distance traveled. In both cases, the total number of parameters for optimization is $(N-1)(M_\alpha-1)$: there are $M_\alpha - 1$ free parameters for each output component; see Remark 6.1.

Remark 6.2 A diagonal weighting matrix

$$W := \text{diag}(w_1, \dots, w_N), \quad (6.45)$$

⁶Torque is roughly proportional to current in a DC motor, and the square of the current is proportional to electrical power.

with

$$w_i := \begin{cases} w_{i,0}, & \dot{q}_i(Bu_\alpha^*)_i \leq 0 \\ w_{i,1}, & \dot{q}_i(Bu_\alpha^*)_i > 0, \end{cases} \quad (6.46)$$

$w_{i,0}, w_{i,1} \neq 0$ for $i = 1, \dots, N$, is often included in the inner product of (6.44) so that $\langle \cdot, \cdot \rangle$ is replaced with

$$\langle a, b \rangle_W := a' W b. \quad (6.47)$$

This permits, for example, positive and negative work to be penalized differently.

6.3.4 Constraints

The constraints will be chosen to ensure, if a solution exists, that the following are met:

1. the stability conditions (5.79) and (5.80);
2. the gait Hypotheses HGW2, HI3 and HGW6;
3. the output function Hypotheses HH2, HH4, HH5 and HH6; and
4. a desired average walking speed is achieved.

In the examples, how to achieve other desirable gait properties will be illustrated. The constraints may be divided into two classes: nonlinear inequality constraints (NICs) and nonlinear equality constraints (NECs).

Nonlinear inequality constraints: The following constraints are typically required: The following three NICs enforce modeling assumptions per constraints on

NIC1) minimum normal ground reaction force experienced by the stance leg end,

$$F_1^N > 0; \quad (6.48)$$

NIC2) maximum ratio of tangential to normal ground reaction forces experienced by the stance leg end,

$$\left| \frac{F_1^T}{F_1^N} \right| < \mu_s; \quad (6.49)$$

NIC3) swing leg end height to ensure \mathcal{S} intersects \mathcal{Z} (only) at the end of the step.

Note that other NICs, such as a constraint on minimum hip height, maximum swing leg deflections, etc., are in general required to achieve a desired walking “style.”

Nonlinear equality constraints: There are five natural NECs that enforce:

NEC1) the average walking rate, $\bar{\nu}$, defined as step length divided by step duration

$$\bar{\nu} := \frac{p_2^h(q_0^-)}{T_I(\xi_2^-)}, \quad (6.50)$$

NEC2) the vertical component of the post-impact swing-leg velocity is positive;

NEC3) the validity of the impact of the swing leg end with the walking surface;

NEC4) the existence of a fixed point, $\zeta_2^* > V_{\text{zero}}^{\text{MAX}}/\delta_{\text{zero}}^2$; and

NEC5) the stability of the fixed point, $0 < \delta_{\text{zero}}^2 < 1$.

In this generic form, the parameter optimization problem may be solved with any number of the numerical optimization tools available. For the work reported in this book, the optimization problem was solved with MATLAB's constrained nonlinear optimization tool `fmincon` with the hybrid zero dynamics implemented in C as a MATLAB mex function.

It is important to emphasize that the use of the hybrid zero dynamics greatly reduces the computational cost of evaluating the cost function (6.43) or (6.44). Moreover, stability of the closed-loop system may be included as a simple optimization constraint. After optimization, Hypothesis HH2, the invertibility of the decoupling matrix, must be checked. This condition is essentially guaranteed whenever $J(\alpha)$ is finite, since singularities in $L_g L_f h$ will normally result in u^* taking on unbounded values. A method for *explicitly* computing, if it exists, a simply connected, open set about the periodic orbit where the decoupling matrix is invertible, is given in [176]. An analytical investigation of this question is given in Section 6.4.

6.3.5 The Optimization Problem in Mayer Form

The optimization problem may also be expressed in Mayer form [15, p. 332] as

$$\dot{\xi}_1 = \kappa_{1,\alpha}(\xi_1)\xi_2 \quad (6.51a)$$

$$\dot{\xi}_2 = \kappa_{2,\alpha}(\xi_1) \quad (6.51b)$$

$$\dot{\xi}_3 = J(\xi_1, \xi_2, \alpha) \quad (6.51c)$$

where J is the time derivative of the cost. The Mayer form is useful in parameter optimization algorithms that construct an approximate solution to a parameterized set of first order differential equations such that a static function of the state is minimized. Appending the cost as a state enables the

cost calculation and solution approximation to be performed with the same algorithm. The cost function (6.43), for example, may be appended as

$$\dot{J}_1(\xi_1, \xi_2, \alpha) := \frac{1}{p_2^h(q_0^-)} \|u_\alpha^*(\xi_1, \xi_2)\|_2^2 \quad (6.52)$$

so that

$$\xi_3(t) = \frac{1}{p_2^h(q_0^-)} \int_0^t \|u_\alpha^*(t)\|_2^2 dt. \quad (6.53)$$

Posing the problem in Mayer form requires another class of constraints, explicit boundary constraints (EBCs), that fix the initial or final state. The following EBCs are required.

Explicit boundary constraints: Let ζ_2^* be the fixed point of Poincaré return map of the hybrid zero dynamics, as defined in (5.77). Let $\gamma^* := \pm\sqrt{2\zeta_2^*}$, where the sign is chosen depending on the assumed angle convention,⁷ and, based on (5.63), compute

$$\dot{q}^* := \bar{\lambda}_{\dot{q}} \gamma^* = \begin{bmatrix} \frac{\partial h}{\partial q}(q_0^-) \\ \gamma_0(q_0^-) \end{bmatrix}^{-1} \begin{bmatrix} 0 \\ 1 \end{bmatrix} \gamma^*, \quad (6.54)$$

where q_0^- is the solution of $[h(q); p_2^v(q)] = [0; 0]$, $p_2^h(q) > 0$. There are five EBCs that relate the state of the hybrid zero dynamics at $t = 0$ and $t = T_I(\xi_2^-)$ to the fixed point

$$\text{EBC1}) \quad \xi_1(0) = c \Delta_q q_0^-;$$

$$\text{EBC2}) \quad \xi_2(0) = \gamma \circ \Delta(q_0^-, \dot{q}^*);$$

$$\text{EBC3}) \quad \xi_3(0) = 0;$$

$$\text{EBC4}) \quad \xi_1(T_I(\xi_2^-)) = c q_0^-; \text{ and}$$

$$\text{EBC5}) \quad \xi_2(T_I(\xi_2^-)) = \gamma(q_0^-, \dot{q}^*).$$

Note that $\xi_3(T_I(\xi_2^-))$ cannot be explicitly given as its calculation requires knowledge of ξ_1 and ξ_2 over the entire time interval of optimization. Also note that without use of the hybrid zero dynamics, the optimization in Mayer form would have $2N$ states, the derivative of the cost, and $N - 1$ control signals to be included in the problem formulation.

Remark 6.3 When the EBC1 and EBC2 hold, EBC4 and EBC5 are equivalent to ζ_2^* belonging to the domain of definition of the Poincaré map; see (5.76). Hence, an equivalent formulation is to keep EBC1–EBC3 and add one further inequality condition, namely, $\delta_{\text{zero}}^2 \zeta_2^* - V_{\text{zero}}^{\text{MAX}} > 0$.

⁷For example, with a counterclockwise sign convention on angles, the robot has negative angular momentum when walking from left to right.

6.4 Further Properties of the Decoupling Matrix and the Zero Dynamics

6.4.1 Decoupling Matrix Invertibility

A key hypothesis in the development of the control laws given in Theorems 5.4 and 5.5, as well as in the development of the swing phase zero dynamics, is the invertibility of the decoupling matrix. Since the decoupling matrix can of course have singularities even at points where the Jacobian of the output, $\partial h/\partial q$, has full row rank,⁸ an analysis of its invertibility is required. This turns out to be especially insightful if one further assumption is made on how the output (6.3) is chosen, namely,

- HH6) In (6.4), $q_b := H_0 q$ is a set of body coordinates for the robot and $\theta = cq$ is an absolute angle, that is, it represents the angle of some point of the body or its center of mass with respect to the inertial frame. It is further assumed that θ is measured in the clockwise⁹ direction.

On the basis of HH6, define a change of coordinates on the configuration variables by

$$\tilde{q} := Hq = \begin{bmatrix} H_0 \\ c \end{bmatrix} q =: \begin{bmatrix} q_b \\ \theta \end{bmatrix}, \quad (6.55)$$

which induces a canonical change of coordinates¹⁰ on the velocity variables per

$$\dot{\tilde{q}} := H\dot{q} = \begin{bmatrix} H_0 \\ c \end{bmatrix} \dot{q} =: \begin{bmatrix} \dot{q}_b \\ \dot{\theta} \end{bmatrix}. \quad (6.56)$$

In these coordinates, the potential energy is

$$\tilde{V}(\tilde{q}) = V(q) |_{q=H^{-1}\tilde{q}}. \quad (6.57)$$

The inertia matrix becomes

$$\tilde{D}(\tilde{q}) = (H^{-1})' D(q) H^{-1} \Big|_{q=H^{-1}\tilde{q}}; \quad (6.58)$$

⁸First note that $L_g L_f h = \partial h / \partial q D^{-1} B$. Although $D^{-1} B$ has full column rank (since $D(q)$ is positive definite and B is a constant, full column rank matrix), application of Sylvester's inequality [40, p. 31] shows that the rank of $L_g L_f h$ is strictly greater than $N - 2$, not $N - 1$.

⁹The consequences of clockwise versus counterclockwise are summarized in Proposition B.8 and Proposition B.10.

¹⁰See Appendix B.4.10 for the definition of a canonical change of coordinates.

moreover, θ is cyclic¹¹ and hence

$$\tilde{D}(\tilde{q}) = \tilde{D}(q_b). \quad (6.59)$$

Finally, the output (6.3) becomes

$$y = h(\tilde{q}) := q_b - h_d(\theta). \quad (6.60)$$

Expressing the swing phase model in the MPFL-normal form on the basis of the coordinates $\tilde{q} = (q_b; \theta)$ then gives

$$\begin{aligned} \ddot{q}_b &= v \\ \dot{\theta} &= \frac{\bar{\sigma}_N}{\tilde{d}_{N,N}(q_b)} - \tilde{J}^{\text{norm}}(q_b)\dot{q}_b \\ \dot{\bar{\sigma}}_N &= -\frac{\partial \tilde{V}}{\partial \theta}(q_b, \theta), \end{aligned} \quad (6.61)$$

where

$$\tilde{J}^{\text{norm}}(q_b) = \frac{1}{\tilde{d}_{N,N}(q_b)} \left[\tilde{d}_{N,1}(q_b), \dots, \tilde{d}_{N,N-1}(q_b) \right], \quad (6.62)$$

$\tilde{d}_{j,k}$ is the $j-k$ -element of \tilde{D} , and $\bar{\sigma}_N$ is the generalized momentum conjugate to $\tilde{q}_N = \theta$. Taking $\tilde{x} := (q_b; \theta; \dot{q}_b; \bar{\sigma}_N)$, the swing phase model is expressed in state variable form as

$$\begin{aligned} \dot{\tilde{x}} &= \begin{bmatrix} \dot{q}_b \\ \frac{\bar{\sigma}_N}{\tilde{d}_{N,N}(q_b)} - \tilde{J}^{\text{norm}}(q_b)\dot{q}_b \\ v \\ -\frac{\partial \tilde{V}}{\partial \theta}(q_b, \theta) \end{bmatrix} \\ &=: \tilde{f}(\tilde{x}) + \tilde{g}(\tilde{x})v. \end{aligned} \quad (6.63)$$

A simple calculation¹² then gives that the decoupling matrix for the output (6.60) is

$$L_{\tilde{g}} L_{\tilde{f}} h(\tilde{q}) = I_{(N-1) \times (N-1)} + \underbrace{\frac{\partial h_d(\theta)}{\partial \theta}}_{(N-1) \times 1} \underbrace{\tilde{J}^{\text{norm}}(q_b)}_{1 \times (N-1)}. \quad (6.65)$$

¹¹See Proposition B.9, part (d).

¹²The easiest way to obtain this is to compute the second derivative of the output, using (6.61), and then to recognize that the matrix multiplying v is the decoupling matrix.

Proposition 6.1 (Decoupling Matrix Properties)

(a) $\det(L_{\tilde{g}}L_{\tilde{f}}h)(\tilde{q}) = 1 + \tilde{J}^{\text{norm}}(q_b)\frac{\partial h_d(\theta)}{\partial \theta}$ and is nonzero if, and only if

$$\tilde{d}_{N,N}(q_b) + [\tilde{d}_{N,1}(q_b), \dots, \tilde{d}_{N,(N-1)}(q_b)] \frac{\partial h_d(\theta)}{\partial \theta} \neq 0. \quad (6.66)$$

(b) At all points where the determinant of the decoupling matrix is nonzero, the inverse of the decoupling matrix is

$$\left[L_{\tilde{g}}L_{\tilde{f}}h(\tilde{q}) \right]^{-1} = I_{(N-1) \times (N-1)} + \frac{1}{\det(L_{\tilde{g}}L_{\tilde{f}}h)(\tilde{q})} \frac{\partial h_d(\theta)}{\partial \theta} \tilde{J}^{\text{norm}}(q_b). \quad (6.67)$$

(c) The inverse of the decoupling matrix can be equivalently written as

$$\begin{aligned} \left[L_{\tilde{g}}L_{\tilde{f}}h(\tilde{q}) \right]^{-1} &= I_{(N-1) \times (N-1)} \\ &+ \left(\frac{1}{\tilde{d}_{N,N}(q_b) + [\tilde{d}_{N,1}(q_b), \dots, \tilde{d}_{N,(N-1)}(q_b)] \frac{\partial h_d(\theta)}{\partial \theta}} \right. \\ &\quad \left. \left(\frac{\partial h_d(\theta)}{\partial \theta} [\tilde{d}_{N,1}(q_b), \dots, \tilde{d}_{N,(N-1)}(q_b)] \right) \right). \end{aligned} \quad (6.68)$$

(d) Let L_gL_fh be the decoupling matrix of (6.2) and (6.3). Then L_gL_fh is invertible at q if, and only if, $L_{\tilde{g}}L_{\tilde{f}}h$ is invertible at $\tilde{q} = Hq$.

The proof is given in [Appendix C.3.1](#).

Remark 6.4 Note that from (6.61) and (6.60), it follows that

$$L_{\tilde{f}}^2h(\tilde{q}, \dot{\tilde{q}}) = -\frac{\partial h_d(\theta)}{\partial \theta} \ddot{\theta} \Big|_{v=0} - \frac{\partial^2 h_d(\theta)}{\partial \theta^2} \dot{\theta}^2, \quad (6.69)$$

where

$$\dot{\theta} = \frac{\bar{\sigma}_N}{\tilde{d}_{N,N}(q_b)} - \tilde{J}^{\text{norm}}(q_b)\dot{q}_b \quad (6.70a)$$

$$\begin{aligned} \ddot{\theta} \Big|_{v=0} &= -\frac{1}{\tilde{d}_{N,N}(q_b)} \frac{\partial \tilde{V}}{\partial \theta}(q_b, \theta) \\ &- \frac{\bar{\sigma}_N}{\tilde{d}_{N,N}^2(q_b)} \frac{\partial \tilde{d}_{N,N}(q_b)}{\partial q_b} \dot{q}_b - \frac{\partial \tilde{J}^{\text{norm}}(q_b)}{\partial q_b} \dot{q}_b. \end{aligned} \quad (6.70b)$$

6.4.2 Computing Terms in the Hybrid Zero Dynamics

Attention is now turned to the zero dynamics. In the coordinates $(q_b; \theta; \dot{q}_b; \dot{\theta})$, the zero dynamics manifold can be written as

$$\mathcal{Z} := \left\{ (q_b; \theta; \dot{q}_b; \dot{\theta}) \mid q_b = h_d(\theta), \dot{q}_b = \frac{\partial h_d(\theta)}{\partial \theta} \dot{\theta} \right\}. \quad (6.71)$$

On \mathcal{Z} , the generalized momentum conjugate to θ becomes

$$\bar{\sigma}_N = I(\theta) \dot{\theta}, \quad (6.72)$$

where the *virtual inertia* $I(\theta)$ is given by

$$I(\theta) := \left[\tilde{d}_{N,N}(q_b) + \left[\tilde{d}_{N,1}(q_b), \dots, \tilde{d}_{N,(N-1)}(q_b) \right] \frac{\partial h_d(\theta)}{\partial \theta} \right] \Big|_{q_b=h_d(\theta)}. \quad (6.73)$$

From (a) of Proposition 6.1, on \mathcal{Z} , there is a bijective relationship¹³ between $\bar{\sigma}_N$ and $\dot{\theta}$ if, and only if, the decoupling matrix is invertible on \mathcal{Z} , in which case one has

$$\dot{\theta} = \frac{\bar{\sigma}_N}{I(\theta)}. \quad (6.74)$$

The same conclusion can be reached by starting with the second line of (6.61) and seeking to solve for $\dot{\theta}$ in terms of $\bar{\sigma}_N$ after substituting in $\dot{q}_b = \frac{\partial h_d(\theta)}{\partial \theta} \dot{\theta}$.

Restricting the last line of (6.61) to \mathcal{Z} ,

$$\dot{\bar{\sigma}}_N = -\frac{\partial \tilde{V}}{\partial \theta}(q_b, \theta) \Big|_{q_b=h_d(\theta)}. \quad (6.75)$$

The potential energy is given by $\tilde{V}(q_b, \theta) = m_{\text{tot}} g_0 p_{\text{cm}}^{\text{v}}(q_b, \theta)$. From Proposition B.10, $\frac{\partial p_{\text{cm}}^{\text{v}}}{\partial \theta} = -p_{\text{cm}}^{\text{h}}$, and thus

$$\dot{\bar{\sigma}}_N = m_{\text{tot}} g_0 p_{\text{cm}}^{\text{h}}(q_b, \theta) \Big|_{q_b=h_d(\theta)}. \quad (6.76)$$

Identifying ξ_1 with θ and ξ_2 with $\bar{\sigma}_N$, it follows that

$$\kappa_1(\xi_1) = \frac{1}{I(\xi_1)} \quad (6.77a)$$

$$\kappa_2(\xi_1) = m_{\text{tot}} g_0 p_{\text{cm}}^{\text{h}}(h_d(\xi_1), \xi_1). \quad (6.77b)$$

It is emphasized that these terms can be determined directly from the Lagrangian of the swing phase model and the term h_d of the virtual constraints.

¹³Comparing (6.73) to (6.66), it follows that on \mathcal{Z} , the decoupling matrix is invertible if, and only if, $I(\theta) \neq 0$.

In particular, there is no need to invert the inertia matrix, as would be required if the zero dynamics were computed as the restriction of $f + gu^*$ to \mathcal{Z} , with f and g as in (6.2).

Turning to the impact map on the zero dynamics manifold, δ_{zero} , Hypothesis HH6 gives that $\bar{\sigma}_N = \sigma_1$, the angular momentum of the robot about the stance leg end. Recalling (3.36), it follows that

$$\xi_2^+ = \xi_2^- + L_s m_{\text{tot}} \dot{p}_{\text{cm}}^{\text{v}-}. \quad (6.78)$$

On \mathcal{Z} , $\dot{p}_{\text{cm}}^{\text{v}}$ can be expressed in the form

$$\ddot{p}_{\text{cm}}^{\text{v}} = \lambda^{\text{v}}(\xi_1) \xi_2, \quad (6.79)$$

which then yields

$$\begin{aligned} \xi_2^+ &= \xi_2^- + L_s m_{\text{tot}} \lambda^{\text{v}}(\xi_1^-) \xi_2^- \\ &= (1 + L_s m_{\text{tot}} \lambda^{\text{v}}(\xi_1^-)) \xi_2^-, \end{aligned} \quad (6.80)$$

and therefore,

$$\delta_{\text{zero}} = 1 + L_s m_{\text{tot}} \lambda^{\text{v}}(\xi_1^-). \quad (6.81)$$

Hence, an analytical expression for the impact map Δ of the full-dimensional model is not needed to compute the impact map on the zero dynamics.

Finally, the control u^* that zeros the virtual constraints can be computed as well without inverting the inertia matrix. Let v^* denote the equivalent of u^* for the system written in MPFL-normal form, as in (6.61). Then part (d) of Proposition 6.1 and Remark 6.4 establishes that v^* is easy to compute. Recalling (3.42), it follows that

$$u^* = B_1^{-1}(q_b) (\bar{D}(q_b)v^* + \bar{\Omega}_1(q, \dot{q})), \quad (6.82)$$

where the various terms are given in (3.40).

6.4.3 Interpreting the Hybrid Zero Dynamics

A physical interpretation of the necessary and sufficient conditions provided in Corollary 5.1 for the existence of an exponentially stable orbit of the hybrid zero dynamics involves the essential interplay of kinetic and potential energy that is taking place throughout a step. Analyzing this helps to understand the inherent robustness of solutions of the hybrid zero dynamics. Because the swing phase zero dynamics is Lagrangian, the total energy $K_{\text{zero}} + V_{\text{zero}}$ is conserved along solutions of the zero dynamics [90]; it follows that energy may be gained or lost only at impacts. This property is similar to the energy conservation in the case of an inverted pendulum subject only to gravity. Assuming that angles are measured positive in the clockwise direction and the robot is walking left to right, the angular momentum $\bar{\sigma}_N$ is always positive. In the beginning of the swing phase, the center of mass of the robot is behind

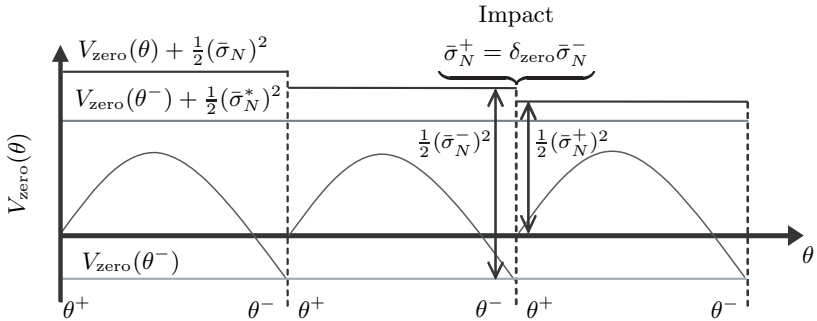


Figure 6.7. A qualitative look at stability through energy. The zero dynamics is Lagrangian, and thus throughout the single support phase, the corresponding total energy $V_{\text{zero}}(\theta) + \frac{1}{2}\bar{\sigma}_N^2$ is constant. At impact, the change in total energy depends on the angular momentum through $\delta_{\text{zero}}\bar{\sigma}_N^-$ and the potential energy through $V_{\text{zero}}(\theta^-)$. The total energy corresponding to the periodic orbit is $V_{\text{zero}}(\theta^-) + \frac{1}{2}(\bar{\sigma}_N^*)^2$. Convergence to this total energy level occurs if the angular momentum decreases during impact, namely, $\delta_{\text{zero}} < 1$. From the expression for the existence of a periodic orbit, $\delta_{\text{zero}} < 1$ is equivalent to $V_{\text{zero}}(\theta^-) < 0$.

the support leg end. Thus, by (6.76), gravity initially decreases the angular momentum of the robot, and $V_{\text{zero}}(\theta)$ increases. If the angular momentum is not large enough, then the angular momentum goes to zero while the center of mass is still behind the support leg end, and, due to gravity, the robot falls backward. If the initial angular momentum is sufficiently large to overcome the potential energy barrier corresponding to $V_{\text{zero}}^{\text{MAX}}$, the center of mass will move past the support leg end, inducing the reverse exchange of energy, until the swing leg impacts the ground, see Fig. 6.7. An impact induces a change in the total energy in two ways. A constant change of V_{zero} occurs at impact, from $V_{\text{zero}}(\theta^-)$ at the end of the step to $V_{\text{zero}}(\theta^+)$ at the beginning of the step; see Fig. 6.7. The angular momentum changes also, through multiplication by δ_{zero} . From this, one can compute an angular momentum just before impact, $\bar{\sigma}_N^-$, that results in the conservation of the total energy *during the impact*, so that periodicity is enforced. Condition (5.79) stipulates that $\delta_{\text{zero}}\bar{\sigma}_N^-$ must be large enough to overcome the barrier posed by gravity, $V_{\text{zero}}^{\text{MAX}}$. For the periodic orbit, the total energy has a constant value $V_{\text{zero}}(\theta^-) + \frac{1}{2}(\bar{\sigma}_N^*)^2$. Since the angular momentum is scaled by δ_{zero} at impact, the same is true of the difference between the angular momentum and its value on the periodic orbit, given by $\bar{\sigma}_N - \bar{\sigma}_N^*$. Thus, if angular momentum decreases at impacts, then it converges to $\bar{\sigma}_N^*$. Exponential stability is thus ensured by condition (5.80).

From the above analysis, it follows that once an exponentially stable orbit

exists for the model of the robot, modeling errors will tend to destroy it only if they are sufficiently large to drive the angular momentum of the robot to zero before its center of mass is above the support leg end. Interpreted loosely, deliberate forward gaits, that is, gaits with a periodic motion that has significant angular momentum reserve at the point of maximum potential energy, will be quite robust; modeling error will significantly alter the average walking speed before it destabilizes the robot.

6.5 Designing Exponentially Stable Walking Motions on the Basis of a Prespecified Periodic Orbit

This section explains how to design virtual constraints that will realize a prespecified, period-one walking gait as a periodic orbit of a hybrid zero dynamics. Moreover, it will be shown how to determine *a priori* if the resulting HZD controller will exponentially stabilize the orbit or not. It will also be shown how to systematically modify a given period-one walking gait through HZD control so as to obtain additional functionality. Illustrations of these ideas will be given in Section 6.6.3.

6.5.1 Virtual Constraint Design

Let $q = (q_b; \theta)$ be a set of generalized coordinates for the swing phase model, where q_b are body coordinates and θ is an absolute angle (i.e., it is measured with respect to the inertial frame). Let $\mathbf{q}(t)$, $0 \leq t < T$ be the time evolution of the configuration variables q for a periodic solution of (6.1), with period T . Similarly, let $\dot{\mathbf{q}}(t)$, $\ddot{\mathbf{q}}(t)$, $\Theta(t)$, $\dot{\Theta}(t)$, $\ddot{\Theta}(t)$, and $\sigma_1(t)$ denote the corresponding time evolutions of \dot{q} , \ddot{q} , θ , $\dot{\theta}$, $\ddot{\theta}$, σ_1 along the periodic orbit.¹⁴ The following are the key hypotheses:

- HO1) $\mathbf{q}(t)$ is three-times continuously differentiable on $[0, T]$.
- HO2) $(\mathbf{q}(t); \dot{\mathbf{q}}(t))$ is a T -periodic solution of (6.1) and is transversal to \mathcal{S} .
- HO3) $\Theta(t)$ is strictly increasing on $[0, T]$; that is, $\inf_{t \in [0, T]} \dot{\Theta}(t) > 0$.
- HO4) $\sigma_1(t)$, the angular momentum about the stance leg end, is nonzero on $[0, T]$.

Note that by Hypothesis HO3, $\theta = \Theta(t)$ has a well-defined inverse, $t = \Theta^{-1}(\theta)$, and it is three-times continuously differentiable.

¹⁴Because the model is given, knowing $\mathbf{q}(t)$, $\dot{\mathbf{q}}(t)$, and $\ddot{\mathbf{q}}(t)$ is equivalent to knowing $\mathbf{q}(t)$, $\dot{\mathbf{q}}(t)$ and the input.

Theorem 6.2 (The HZD of a Prespecified Periodic Orbit)

Consider the model (3.30), satisfying Hypotheses HR1–HR6 on the robot, HGW1–HGW7 on the robot's gait, and HI1–HI6 on the impact model. Let $\mathcal{O} = \{(\mathbf{q}(t); \dot{\mathbf{q}}(t)) \mid 0 \leq t < T\}$ be a periodic orbit satisfying Hypotheses HO1–HO4, where the configuration variables $q = (q_b; \theta)$ are expressed as a set of body coordinates and an absolute angle. Consider an output of the form (6.60) and define

$$h_d(\theta) := \mathbf{q}_b(t)|_{t=\Theta^{-1}(\theta)}. \quad (6.83)$$

Then,

1. the hybrid zero dynamics exist for $h(q) = q_b - h_d(\theta)$, and
2. \mathcal{O} is a periodic orbit of the hybrid zero dynamics.
3. Moreover, the periodic orbit \mathcal{O} is exponentially stable within the hybrid zero dynamics if, and only if,

$$\lim_{t \nearrow T} \frac{\sigma_1(0)}{\sigma_1(t)} < 1. \quad (6.84)$$

The proof is provided in [Appendix C.3.2](#).

Given a periodic solution of the model, it is possible to compute directly the various derivatives of h_d that are required for implementing a controller based on the hybrid zero dynamics, that is, either the feedback given in Theorem 5.4 or Theorem 5.5. See [part \(d\)](#) of Proposition 6.1 and [Remark 6.4](#).

Proposition 6.2 (Constructing Output Function Derivatives from a Prespecified Periodic Orbit)

Under the hypotheses of Theorem 6.2,

$$\frac{\partial h_d}{\partial \theta}(\theta) = \left. \frac{\dot{\mathbf{q}}_b(t)}{\dot{\Theta}(t)} \right|_{t=\Theta^{-1}(\theta)} \quad (6.85a)$$

$$\frac{\partial^2 h_d}{\partial \theta^2}(\theta) = \left. \left(\frac{\ddot{\mathbf{q}}_b(t)}{\dot{\Theta}^2(t)} - \frac{\dot{\mathbf{q}}_b(t)\ddot{\Theta}(t)}{\dot{\Theta}^3(t)} \right) \right|_{t=\Theta^{-1}(\theta)}. \quad (6.85b)$$

Proof On the periodic orbit $y(t) \equiv 0$ by construction of h_d . Hence,

$$0 = q_b(t) - h_d(\theta(t)) \quad (6.86a)$$

$$0 = \dot{q}_b(t) - \frac{\partial h_d(\theta(t))}{\partial \theta} \dot{\theta}(t) \quad (6.86b)$$

$$0 = \ddot{q}_b(t) - \frac{\partial^2 h_d(\theta(t))}{\partial \theta^2} \dot{\theta}(t)^2 - \frac{\partial h_d(\theta(t))}{\partial \theta} \ddot{\theta}(t). \quad (6.86c)$$

Evaluating (6.86) at $t = \Theta^{-1}(\theta)$ and solving for the required terms completes the proof.

6.5.2 Sample-Based Virtual Constraints and Augmentation Functions

As a practical matter, it may be impossible to solve for $t = \Theta^{-1}(\theta)$ in closed form. Cubic spline interpolation can be used to circumvent this problem, as well as to improve the efficiency of computing the control law $u(x)$.

Proposition 6.3 (Construction of Virtual Constraints from a Sampled Periodic Orbit)

The term $h_d(\theta)$ and its derivatives can be reproduced with arbitrary accuracy by sampling the periodic orbit and applying cubic spline interpolation between sample points.

Proof First, sample the full-state information associated with the periodic orbit: $\mathbf{q}(t)$, $\dot{\mathbf{q}}(t)$, $\ddot{\mathbf{q}}(t)$, $\Theta(t)$, $\dot{\Theta}(t)$, $\ddot{\Theta}(t)$. Calculate the quantities of Proposition 6.2 for each unique value of θ . Cubic spline interpolation between sample points will result in estimates of $h_d(\theta)$, $\partial h_d(\theta)/\partial\theta$, and $\partial^2 h_d(\theta)/\partial\theta^2$ each having an accuracy of $\mathcal{O}(|\tau^4|)$, where τ is the distance to the nearest sample point [63, Ch. 5].

Thus, for a given periodic orbit, the terms in a HZD controller, $h_d(\theta)$, $\partial h_d(\theta)/\partial\theta$, and $\partial^2 h_d(\theta)/\partial\theta^2$ can be approximated arbitrarily accurately using *sample-based virtual constraints*, without a closed-form representation of $h_d(\theta)$. For computational efficiency, the sampled functions may be precomputed and stored in a lookup table. Note that the method of Proposition 6.3 is *not* equivalent to fitting $h_d(\theta)$ to a set of splines and then differentiating the splines to obtain $\partial h_d(\theta)/\partial\theta$ and $\partial^2 h_d(\theta)/\partial\theta^2$. If $h_d(\theta)$ were interpolated with an accuracy of $\mathcal{O}(|\tau^4|)$, differentiation would give an accuracy of $\mathcal{O}(|\tau^3|)$ for $\partial h_d(\theta)/\partial\theta$ and an accuracy of $\mathcal{O}(|\tau^2|)$ for $\partial^2 h_d(\theta)/\partial\theta^2$ [63, Ch. 5]. An alternative method of approximating $h_d(\theta)$ would be to regress joint trajectories against a single polynomial of θ . In practice, the authors have observed that the use of polynomials of sufficiently high degree to obtain accurate fits to joint trajectories often results in poor fits to the derivatives of the trajectories.

On another practical note, it can be interesting to construct a new walking gait on the basis of a previously computed gait. A *constraint augmentation function* is a finitely parameterized function, such as a Bézier polynomial, that provides a means to systematically modify a set of previously computed virtual constraints, such as the sample-based virtual constraints just described. The parameters of the augmentation function may be chosen via optimization, as in Section 6.3. It will be shown in Section 6.6.3.2 how augmentation functions may be used to transform a passive compass gait into a gait that can be executed on flat ground, while retaining, as much as possible, the robot's

original passive (i.e., unactuated) dynamic behavior.¹⁵

Consider once again an output of the form $y = q_b - h_d(\theta)$, and decompose h_d , into

$$h_d(\theta) = h_{d,0}(\theta) + h_{d,\text{aug}}(\theta), \quad (6.87)$$

where $h_{d,0}$ is the nominal virtual constraint and $h_{d,\text{aug}}$ is an augmentation function. The function $h_{d,\text{aug}}$ will be finitely parameterized and used to modify the properties of the nominal motion associated with $h_{d,0}$.

6.6 Example Controller Designs

Three different methods of controller design are illustrated. The first method takes a step back and looks at feedback design without using the hybrid zero dynamics. A three-link walker is used to show that a more “intuitive” approach to feedback design may have practical, computational, and analytical drawbacks. The second example uses optimization of the hybrid zero dynamics to design a controller for a five-link walker. The last set of examples illustrates just how easy it is to perform feedback design on the basis of a given periodic orbit.

6.6.1 Designing Exponentially Stable Walking Motions without Invariance of the Impact Map

The objective of this section is to present a feedback design that uses many of the ideas presented in this book, namely, virtual constraints, swing phase zero dynamics, and restricted Poincaré maps, but which does not insist upon invariance of the swing phase zero dynamics manifold under the impact map. Because a hybrid zero dynamics will not be created, the analysis will have to be performed on the full-dimensional hybrid model, (6.1). The feedback design will be explained and illustrated on the three-link walker presented in Section 3.4.6. The coordinates of Fig. 3.5(a) are assumed, as are the model parameters given in Table 3.2.

As discussed in Section 3.4.6, in the case of a stiff-legged robot on a flat surface, the notion of the contact point of the swing leg with the walking surface is physically ambiguous, because, without a knee, and with equal length legs, the swing leg must scuff along the ground if it remains in the sagittal plane. McGeer [153, 154] has shown with his ballistic walkers, both theoretically and experimentally, that one can basically ignore the leg clearance issue for stiff-legged models. He has done this in two ways: in one realization, he

¹⁵This result is similar to work in [217], except here the biped will be underactuated as opposed to fully actuated.

puts additional small motors on the legs that allow him to push the swing leg just slightly out of the sagittal plane during the swing phase and to pull the leg back into the sagittal plane whenever he wishes to initiate contact. The second way he has done this is to put small (essentially massless) flaps on the ends of the legs, and to fold up the flap of the swing leg during the swing phase, and to unfold it whenever he wants to initiate contact. With McGeer's first method in mind, it is hereafter assumed that contact is initiated when the angle of the stance leg attains a desired value, θ_1^d . Hence, the impact surface is taken as

$$\mathcal{S} := \{(\theta; \dot{\theta}) \in T\mathcal{Q} \mid \theta_1 - \theta_1^d = 0\}. \quad (6.88)$$

In order for the swing leg end to be at ground level at the end of the step, it must be the case that

$$\theta_2 = -\theta_1 \quad (6.89)$$

at contact. This will be taken care of in the control law design. Finally, in the impact model, (3.70) and (3.71), it is supposed that the friction coefficient satisfies $\mu_s = 2/3$. For each of the simulations presented below, it has been verified that the impact model is valid, so this point will not be discussed further.

6.6.1.1 Encoding a Walking Pattern or Choosing What to Control

At its most basic level, walking consists of two things: posture control, that is, maintaining the torso in a semierect position, and swing leg advancement, that is, causing the swing leg to come from behind the stance leg, pass it by a certain amount, and prepare for contact with the ground. This motivates the direct control of the angles θ_3 (describing the torso) and θ_2 (describing the swing leg). On a periodic orbit corresponding to a normal walking motion, it is clear that the horizontal motion of the hips is monotonically strictly increasing. For the three-link walker, this is equivalent to $\theta_1(t)$ strictly increasing over each step of the walking cycle. Thus, for any desired trajectories $\theta_2(t)$ and $\theta_3(t)$ that express (encode) a desired walking pattern for the biped, it is therefore reasonable to assume that the corresponding trajectory for θ_1 has the property that $\theta_1(t)$ is strictly monotonic. It follows that $\theta_2(t)$ and $\theta_3(t)$ can each be re-parameterized in terms of θ_1 . That is, without loss of generality, it can be supposed that $\theta_3(t) = h_{d,1}(\theta_1(t))$ and $\theta_2(t) = h_{d,2}(\theta_1(t))$, for some functions $h_{d,1}$ and $h_{d,2}$.

The simplest version of posture control is to maintain the angle of the torso at some constant value, say θ_3^d , while the simplest version of swing leg advancement is to command the swing leg to behave as the mirror image of the stance leg, that is, $\theta_2 = -\theta_1$. Thus the "behavior" of walking can be "encoded" into the dynamics of the robot by defining outputs

$$y := \begin{bmatrix} y_1 \\ y_2 \end{bmatrix} := \begin{bmatrix} h_1(\theta) \\ h_2(\theta) \end{bmatrix} := \begin{bmatrix} \theta_3 - h_{d,1}(\theta_1) \\ \theta_2 - h_{d,2}(\theta_1) \end{bmatrix} := \begin{bmatrix} \theta_3 - \theta_3^d \\ \theta_2 + \theta_1 \end{bmatrix}, \quad (6.90)$$

with the control objective being to drive the outputs to zero. Driving y to zero will force θ_2 and θ_3 to converge to known functions of θ_1 (here, θ_3^d , being a constant, should be viewed as a trivial function of θ_1).

6.6.1.2 Controller Design

It is proposed to use a feedback controller of the form specified in (5.88), (5.92) and (5.93). The details associated with such a controller are now developed.

As a first step, a tedious but otherwise straightforward computation gives that the decoupling matrix is

$$L_g L_f h = \frac{1}{\det(D_s)} \begin{bmatrix} R_{11} & R_{12} \\ R_{21} & R_{22} \end{bmatrix} \quad (6.91)$$

where,

$$R_{11} = \frac{mr^3}{4} \left(\frac{5}{4}mr + M_H r + M_T r - mr(c_{12})^2 + M_T l c_{13} \right) \quad (6.92a)$$

$$R_{12} = \frac{mr^3}{4} \left(\frac{5}{4}mr + M_H r + M_T r - mr(c_{12})^2 + 2M_T l c_{12} c_{13} \right) \quad (6.92b)$$

$$R_{21} = \frac{-mM_T lr^2}{4} (1 + 2c_{12})(rc_{13} + l) \quad (6.92c)$$

$$R_{22} = \frac{-M_T lr^2}{4} \left(5ml + 4M_H l + 4M_T l + mrc_{13} + 2mrc_{12}c_{13} - 4M_T l(c_{13})^2 + 2mlc_{12} \right) \quad (6.92d)$$

$$\det(D_s) = \frac{mM_T r^4 l^2}{4} \left(\frac{5}{4}m + M_H + M_T - m(c_{12})^2 - M_T(c_{13})^2 \right), \quad (6.92e)$$

and

$$c_{ij} := \cos(\theta_i - \theta_j). \quad (6.93)$$

A further tedious computation reveals that the determinant of the decoupling matrix is zero if, and only if,

$$-r(rM_H + rm + rM_T + lM_T \cos(\theta_1 - \theta_3)) = 0. \quad (6.94)$$

Thus, the decoupling matrix is invertible for all $x \in T\mathcal{Q}$ as long as

$$0 < lM_T < r(m + M_T + M_H), \quad (6.95)$$

which imposes a very mild constraint on the position of the center of gravity of the torso of the robot in relation to the length of its legs. The parameter values in [Table 3.2](#) satisfy this condition.

Next, a controller is designed that drives the output (6.90) to zero in finite time. The easiest way to do this is to input-output linearize the swing phase

dynamics and then impose a desired dynamic response on the outputs. In preparation for doing this, note that

$$\begin{bmatrix} y_1 \\ y_2 \\ \theta_1 \end{bmatrix} = \Phi(\theta) := \begin{bmatrix} \theta_3 - \theta_3^d \\ \theta_1 + \theta_2 \\ \theta_1 \end{bmatrix} \quad (6.96)$$

is a diffeomorphism onto its range. With this coordinate transformation, and upon defining

$$v := L_f^2 h + L_g L_f h u, \quad (6.97)$$

the swing phase dynamics can be written in the form

$$\begin{bmatrix} \ddot{y} \\ \ddot{\theta}_1 \end{bmatrix} = \begin{bmatrix} v \\ \zeta_0(y, \dot{y}, \theta_1, \dot{\theta}_1) + \zeta_1(y, \dot{y}, \theta_1, \dot{\theta}_1)v \end{bmatrix}. \quad (6.98)$$

The next step is to impose a continuous feedback $v = v(y, \dot{y})$ on (6.98) so that the pair of double integrators $\ddot{y} = v$ is globally finite-time stabilized. If this is done in such a way that Hypotheses HC1–HC4 are met, then it follows that all of the hypotheses of Theorem 4.4 are met [98], leading to a simplified stability test.

Let

$$v := \Psi(y, \dot{y}) := \begin{bmatrix} \frac{1}{\epsilon^2} \psi_\alpha(y_1, \epsilon \dot{y}_1) \\ \frac{1}{\epsilon^2} \psi_\alpha(y_2, \epsilon \dot{y}_2) \end{bmatrix}, \quad (6.99)$$

where

$$\psi_\alpha(x_1, x_2) = -\text{sign}(x_2)|x_2|^\alpha - \text{sign}(\phi_\alpha(x_1, x_2))|\phi_\alpha(x_1, x_2)|^{\frac{\alpha}{2-\alpha}} \quad (6.100a)$$

$$\phi_\alpha(x_1, x_2) := x_1 + \frac{1}{2-\alpha} \text{sign}(x_2)|x_2|^{2-\alpha}, \quad (6.100b)$$

and set $\epsilon = 0.1$ and $\alpha = 0.9$. The parameter $\epsilon > 0$ allows the settling time of the controller to be adjusted. The controller is then

$$u(x) := (L_g L_f h(x))^{-1} (\Psi(h(x), L_f h(x)) - L_f^2 h(x)). \quad (6.101)$$

Denote the right-hand side of the swing phase closed-loop system by

$$f_{cl}(x) := f(x) + g(x)u(x). \quad (6.102)$$

The hybrid model of the bipedal robot in closed loop with the controller is thus:

$$\Sigma_{cl} : \begin{cases} \dot{x} = f_{cl}(x) & x^- \notin \mathcal{S} \\ x^+ = \Delta(x^-) & x^- \in \mathcal{S}. \end{cases} \quad (6.103)$$

Theorem 4.4 allows the existence and stability of periodic orbits of (6.103) to be deduced from the solutions of

$$\dot{x} = f_{cl}(x) \quad (6.104)$$

corresponding to a one-dimensional subset of initial conditions.

6.6.1.3 Checking Existence and Stability of an Orbit

The swing phase zero dynamics manifold (5.5) is computed from (6.98) to be

$$\begin{aligned} \mathcal{Z} = \{(\theta; \dot{\theta}) \in T\mathcal{Q} \mid \theta_3 - \theta_3^d = 0, \theta_1 + \theta_2 = 0, \dot{\theta}_3 = 0, \\ \dot{\theta}_1 + \dot{\theta}_2 = 0, -\pi < \theta_1 < \pi, \dot{\theta}_1 \in \mathbb{R}\}. \end{aligned} \quad (6.105)$$

The feedback (6.101) renders \mathcal{Z} invariant under the closed-loop swing phase dynamics. \mathcal{Z} is not invariant, however, under the impact map, that is, $\Delta(\mathcal{Z} \cap \mathcal{S}) \not\subset \mathcal{S}$. Hence, the hybrid zero dynamics does not exist. The swing phase zero dynamics (5.36) will not be computed here because it is not needed directly in the stability analysis.¹⁶

In terms of the original coordinates $(\theta; \dot{\theta})$ of the robot,

$$\mathcal{S} \cap \mathcal{Z} = \{(\theta; \dot{\theta}) \in T\mathcal{Q} \mid \theta_3 = \theta_3^d, \theta_1 + \theta_2 = 0, \dot{\theta}_3 = 0, \quad (6.106)$$

$$\dot{\theta}_1 + \dot{\theta}_2 = 0, \theta_1 = \theta_1^d, \dot{\theta}_1 \in \mathbb{R}\}, \quad (6.107)$$

a one-dimensional (embedded) submanifold of $T\mathcal{Q}$. To determine if a particular choice of parameters in the feedback law results in an exponentially stable walking cycle that is transversal to \mathcal{S} , the restricted Poincaré map,¹⁷ $\rho : \mathcal{S} \cap \mathcal{Z} \rightarrow \mathcal{S} \cap \mathcal{Z}$ of Theorem 4.4 is evaluated. This is conveniently done as follows. Define the insertion map $\iota : \mathbb{R} \rightarrow \mathcal{S} \cap \mathcal{Z}$ by $\iota(\dot{\theta}_1^-) := (\theta_1^d; -\theta_1^d, \theta_3^d; \dot{\theta}_1^-; -\dot{\theta}_1^-; 0)$, where $\dot{\theta}_1^-$ denotes the angular velocity of the stance leg just before impact. Define $\hat{\rho} := \iota^{-1} \circ \rho \circ \iota$, which is just a local coordinate representation of ρ . A straightforward procedure for evaluating $\hat{\rho}$ on the basis of a simulation model¹⁸ of the closed-loop system is now given.

Numerical Procedure to Test for Walking Cycles:

1. For a point $\dot{\theta}_1^- > 0$, compute $x^- := \iota(\dot{\theta}_1^-)$, the position of the robot just before impact (the restriction to positive velocities corresponds to the robot walking from left to right).
2. Apply the impact model to x^- , that is, compute $x^+ := \Delta(x^-)$.
3. Use x^+ as the initial condition in (6.104), the robot in closed loop with the controller, and simulate until one of the following happens:

¹⁶The swing phase zero dynamics of the three-link walker is computed in [98, Sec. V]. In addition, the relation of the swing phase zero dynamics and the high-gain limit of the closed-loop hybrid system is analyzed for the controller of (6.97) and (6.99).

¹⁷This is really a partial map, with domain spelled out in Section 4.4.3.

¹⁸A numerical simulator is used to compute an approximation of $\hat{\rho}$. Since the feedback in (6.99) can be uniformly approximated by a Lipschitz continuous function, a standard numerical integrator can be used to approximately compute $\hat{\rho}$ to any desired degree of accuracy.

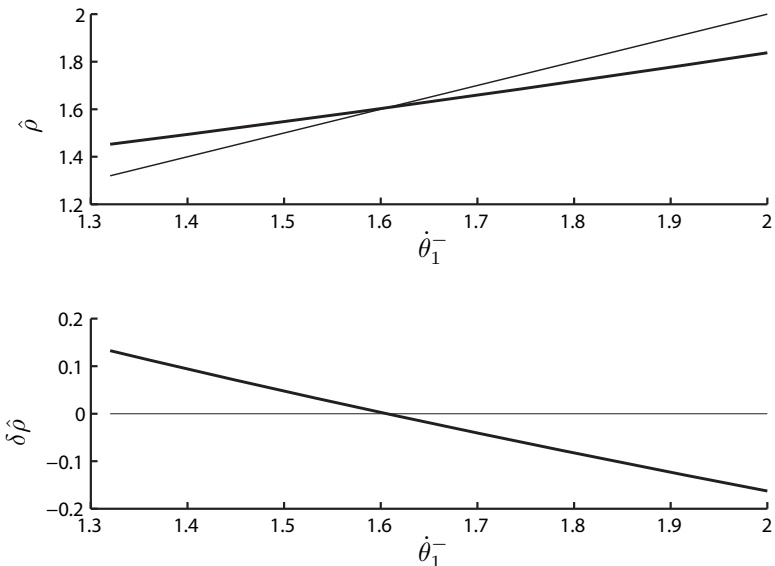


Figure 6.8. The top graph presents the function $\hat{\rho}$ (bold line) and, for visualization purposes, the identity function (thin line); the bottom graph presents the function $\delta\hat{\rho}$ (bold line) and the zero line (thin line). From either graph, it is seen that there exists a periodic orbit and that it is asymptotically stable.

- (a) there exists a time $T > 0$ where $\theta_1(T) = \theta_1^d$; if T is greater than the settling time of the controller (in other words, the output y is identically zero), then $x^+ \in \hat{S} \cap \mathcal{Z}$, and $\dot{\rho}(\theta_1^-) = \dot{\theta}_1(T)$; else, $x^+ \notin \hat{S} \cap \mathcal{Z}$, and $\dot{\rho}(\dot{\theta}_1^-)$ is undefined at this point.
 - (b) there does not exist a $T > 0$ such that $\theta_1(T) = \theta_1^d$ (which is normally detected by one of the angles exceeding $\pm\pi/2$ during the simulation); in this case, it is also true that $x^+ \notin \hat{S} \cap \mathcal{Z}$, and $\dot{\rho}(\dot{\theta}_1^-)$ is undefined at this point.

Figure 6.8 depicts the function $\hat{\rho}$ for $\theta_3^d = \pi/6$; it also displays the related function $\delta\hat{\rho}(\dot{\theta}_1^-) := \hat{\rho}(\dot{\theta}_1^-) - \dot{\theta}_1^-$, which represents the change in velocity over successive cycles, from just before an impact to just before the next one. It is seen that $\hat{\rho}$ is undefined for $\dot{\theta}_1^-$ less than approximately 1.32 rad/sec (for initial $\dot{\theta}_1^-$ less than this value, the robot falls backward). The plot was truncated at 2 rad/sec because nothing interesting occurs beyond this point (except an upper bound on its domain of existence will eventually occur due to the impact model becoming invalid or the controller not having enough time to settle over one walking cycle). A fixed point occurs at approximately 1.6 rad/sec, and, from the graph of $\hat{\rho}$, it clearly corresponds to an asymptotically stable walking

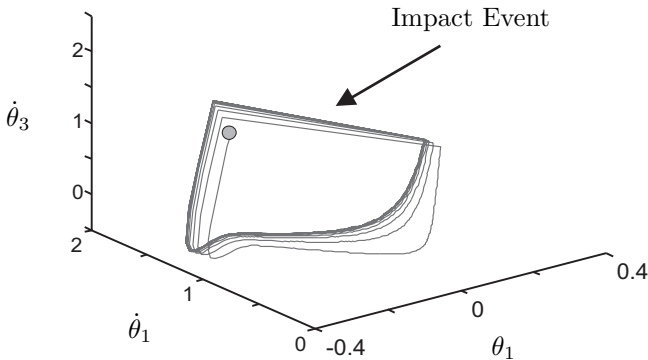


Figure 6.9. Projection onto $(\theta_1; \dot{\theta}_1; \dot{\theta}_3)$ of a trajectory asymptotically converging to an orbit. Note that the straight portion of the curve is really an instantaneous transition due to the impact of the swing leg with the ground. The dot is the initial point.

cycle, whose projection is shown in Fig. 6.9. The corresponding control signals are given in Fig. 6.10.

To illustrate the role played by the inclination of the torso, suppose that θ_3^d is reduced by half to $\pi/12$. Figure 6.11 displays $\hat{\rho}$ and $\delta\hat{\rho}$ for this case. It is seen that there is no fixed point, and hence no periodic orbit that is transversal to \mathcal{S} .

6.6.1.4 Discussion

The virtual constraints selected in (6.90) have the advantage of being simple and intuitive. They do not, however, provide very much design freedom. The only parameter that may be varied is the torso lean angle, which can be used to vary walking speed to a certain extent, but there is no possibility of minimizing torque requirements for a given walking speed, for example. For this reason, [97] considers a set of outputs of the form

$$y := \begin{bmatrix} y_1 \\ y_2 \end{bmatrix} := \begin{bmatrix} h_1(\theta, a) \\ h_2(\theta, a) \end{bmatrix} := \begin{bmatrix} \theta_3 - h_{d,1}(\theta_1, a) \\ \theta_2 - h_{d,2}(\theta_1, a) \end{bmatrix}, \quad (6.108)$$

where

$$h_{d,1}(\theta_1, a) := a_1^0 + \cdots + a_1^3(\theta_1)^3 \quad (6.109a)$$

$$h_{d,2}(\theta_1, a) := -\theta_1 + (a_2^0 + \cdots + a_2^3(\theta_1)^3)(\theta_1 + \theta_1^d)(\theta_1 - \theta_1^d). \quad (6.109b)$$

The rather particular form of $h_{d,2}$ was arrived at by imposing that $h_{d,2}(\theta_1^d, a) = h_{d,2}(-\theta_1^d, a) = 0$, which is the condition needed for the swing leg end to have

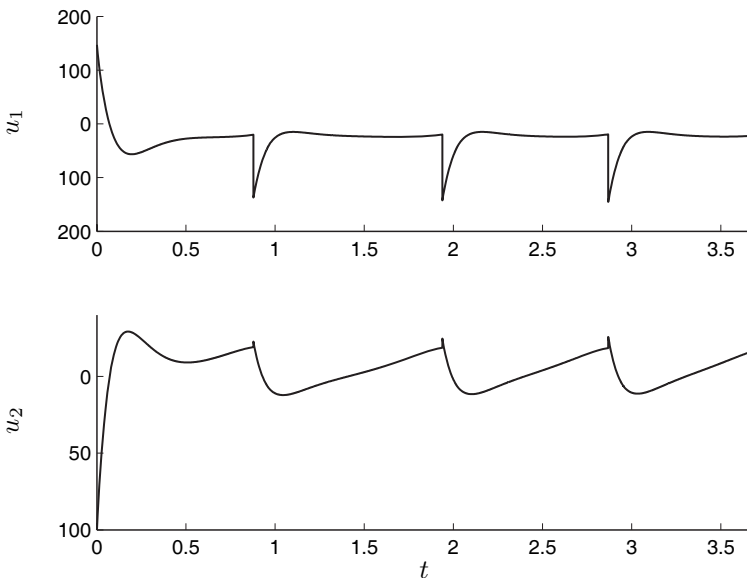


Figure 6.10. Plot of applied torques versus time for a finite-time feedback computed on the basis of (6.90); units of Newton-meters.

height zero at impact. The “intuitive” justification for this more complicated output is that (i) keeping the torso at a constant angle does not allow it to respond “naturally” to the shocks that occur at impact, and (ii) advancing the swing leg more or less quickly during the stance may improve energy efficiency or reduce peak torque requirements. A cost function of the form

$$J(a) := \int_0^T (u_1^2(t) + u_2^2(t)) dt \quad (6.110)$$

was defined, where \$T\$ is such that \$\theta_1(T) - \theta_1^d = 0\$ and \$u(t)\$ is the result of applying (6.101) to (6.102), with \$h_d\$ as in (6.109), and for an initial condition \$x_0 \in \Delta(\mathcal{S} \cap \mathcal{Z})\$ that gives rise to a periodic orbit. A gradient descent algorithm was used to minimize (6.110), initialized at values of the parameters \$a\$ for which the new outputs were equivalent to the original outputs with \$\theta_3^d = \pi/6\$; see Table 6.2. As seen from Fig. 6.12, the process of minimizing the integral of squared torque also fortuitously reduced the peak torque magnitude from approximately 145 Nm to 85 Nm.

These results indicate that the use of a more complicated, less “intuitive” set of virtual constraints should be considered. Once the decision is made to go from (6.90) to (6.109), then it is just a small step further to use \$y = h_0(q) - h_d \circ \theta(q)\$ with \$h_d\$ parameterized via Bézier polynomials, as in (6.3) and (6.10). There are advantages to taking this last step because it is then straightforward to choose the coefficients in the virtual constraints in such

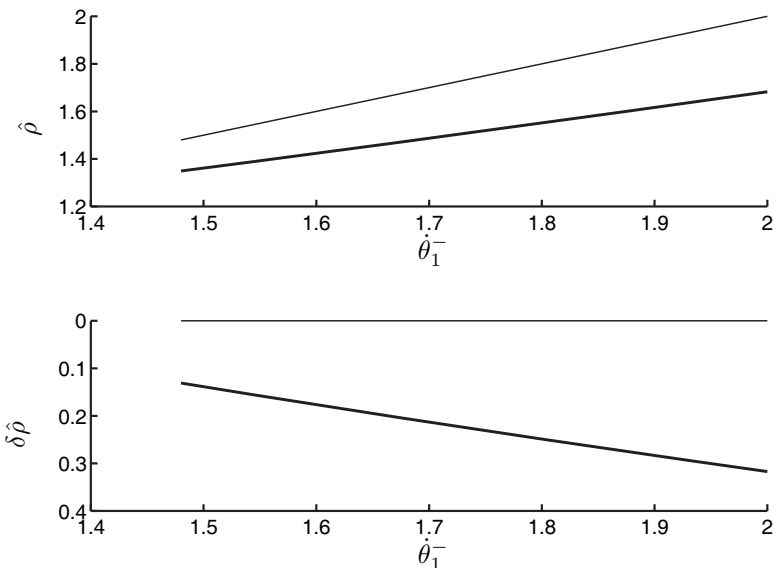


Figure 6.11. The top graph presents the function $\hat{\rho}$ (bold line) and, for visualization purposes, the identity function (thin line); the bottom graph presents the function $\delta\hat{\rho}$ (bold line) and the zero line (thin line). From either graph, it is seen that there does not exist a periodic orbit.

a way that the machinery of the hybrid zero dynamics may be employed, which then provides very significant computational advantages when trying to minimize a cost function over a periodic orbit and very significant analytical advantages as well.

6.6.2 Designs Based on Optimizing the HZD

6.6.2.1 Application: Design of a Gait for RABBIT

This section illustrates how the techniques developed in Section 6.3 may be applied to the design of controllers that induce stable gaits in a five-link robot, RABBIT.

A controller that induces walking at 0.8 m/s is designed and simulated for the five-link walker model of Section 3.4.6; see Fig. 6.13. The control design method of Section 6.3 begins by specifying an output of the form given in (6.3), namely, $y = h_0(q) - h_d \circ \theta(q)$, with $h_0(q)$ and $\theta(q)$ as in (6.4). Hence, the controller design process begins with the choice of (i) the quantities to be controlled, H_0 , (ii) the function $\theta(q) = cq$ used to parameterize a periodic orbit (i.e., a walking gait), and (iii) the degree of the Bézier polynomials, M . The specific choice of (iv) the Bézier polynomial coefficients, α , is accom-

Table 6.2. Result of optimizing the virtual constraints for minimal energy consumption.

| | i | a_0^i | a_1^i | a_2^i | a_3^i | J |
|-------------------------|-----|---------|---------|---------|---------|-------|
| Original Values | 1 | 0.523 | 0 | 0 | 0 | 1,360 |
| | 2 | 0 | 0 | 0 | 0 | |
| Optimized Values | 1 | 0.512 | 0.073 | 0.035 | -0.819 | 761 |
| | 2 | -2.27 | 3.26 | 3.11 | 1.89 | |

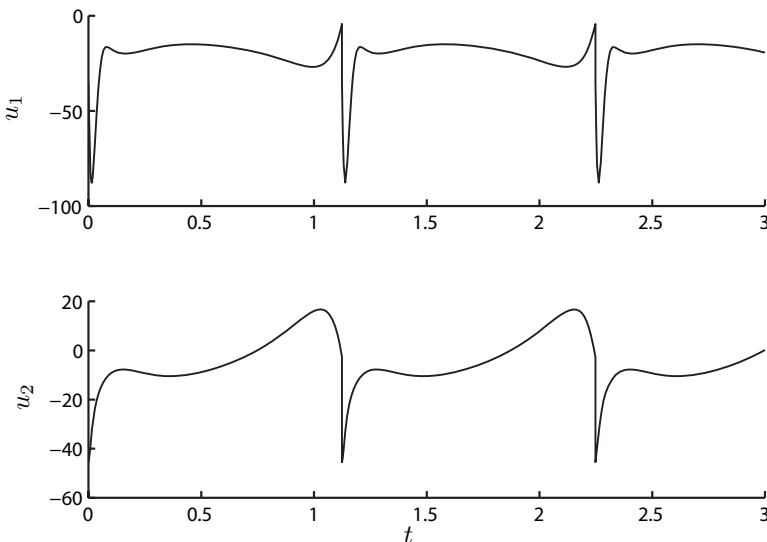


Figure 6.12. Plot of applied torques versus time for a finite-time feedback computed on the basis of (6.109); units of Newton-meters.

plished on the basis of achieving invariance of the induced swing phase zero dynamics under the impact map per Corollary 6.1 and the minimization of a cost function along the periodic orbit per Section 6.3.2.

Following Section 6.4, the relative angles of the actuated joints are selected as the controlled quantities. In a normal gait, absolute angle of the line connecting the stance leg end to the hip is strictly monotonic, and this is taken as $\theta(q)$; see Fig. 6.13(b). Hence,

$$H_0 = [I_{4 \times 4} \ 0_{4 \times 1}] \quad (6.111a)$$

$$c = [-1 \ 0 \ -1/2 \ 0 \ -1], \quad (6.111b)$$

which clearly guarantees that $H = [H_0; c]$ is invertible, satisfying HH3. The

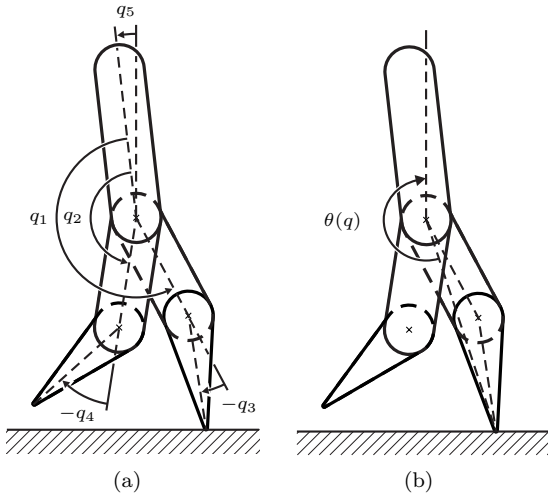


Figure 6.13. Schematic of the prototype RABBIT with measurement conventions.

output is then

$$y = h_0(q) - h_d \circ \theta(q) \quad (6.112a)$$

$$= \begin{bmatrix} q_1 \\ q_2 \\ q_3 \\ q_4 \end{bmatrix} - h_d \circ \theta(q). \quad (6.112b)$$

In light of Remark 6.1, M is chosen to be 6, which leaves five free parameters to be chosen for each output. This implies a total of 20 output function parameters to be chosen via optimization. For a particular choice of α , HH5 must be checked to ensure smoothness of $\mathcal{S} \cap \mathcal{Z}$. This entails evaluating the rank¹⁹ of

$$\frac{\partial}{\partial q} \begin{bmatrix} h(q) \\ p_2^v(q) \end{bmatrix} \Big|_{x \in \mathcal{S} \cap \mathcal{Z}} = \begin{bmatrix} H_0 - \frac{M}{\theta^- - \theta^+} (\alpha_M - \alpha_{M-1}) c \\ \frac{\partial p_2^v(q)}{\partial q} \Big|_{q=q_0^-} \end{bmatrix}, \quad (6.113)$$

where $p_2^v(q)$ is the height of the swing end. Hypothesis HH2, the invertibility of the decoupling matrix, is checked for a choice of α through the results of Section 6.4. If the optimization constraints are satisfied, as detailed in

¹⁹See Remark 5.3 on page 125.

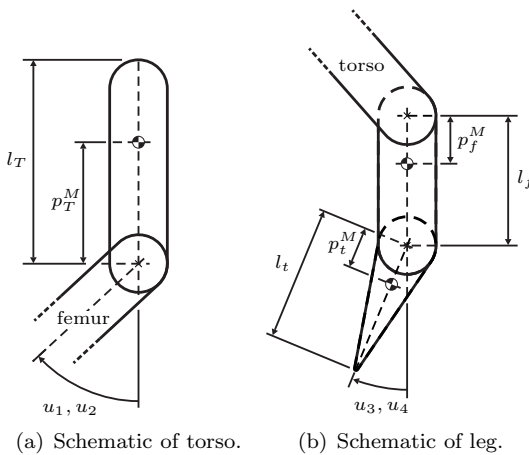


Figure 6.14. Schematic of RABBIT’s link parameter measurement conventions.

Section 6.3, the remaining gait, impact model, and output function hypotheses will also be satisfied.

The optimization problem is posed as described in Section 6.3.2 to choose the 20 free parameters of α . Three additional nonlinear inequality constraints are imposed to obtain a human-like gait. The first two, when satisfied, prevent the stance and swing leg knees from hyperextending,

NIC4)

$$q_3 < 0, \quad (6.114)$$

NIC5)

$$q_4 < 0, \quad (6.115)$$

and the third is used to prevent the hip from dropping too low,

NIC6)

$$p_H^V - p_{H,\min}^V > 0, \quad (6.116)$$

where $p_{H,\min}^V$ is the minimum hip height. MATLAB’s constrained nonlinear optimization tool `fmincon` was used to approximately minimize the cost $J_1(\alpha)$, (6.43), subject to NIC1–NIC6 and NEC1–NEC5.

Table 6.3 gives RABBIT’s link parameter values as identified by a group associated with the project. For the measurement conventions of the parameters see Fig. 6.14. A discussion of the prototype’s design is given in Section 2.1. **Table 6.4** summarizes the result of optimizing for a desired average walking rate of 0.8 m/s. From a reasonable initial condition, the optimization took

Table 6.3. Identified link parameters for RABBIT.

| Model Parameter | Units | Label | Value |
|---------------------|----------------------------|-----------|-------|
| Mass | kg | M_T | 12 |
| | | M_f | 6.8 |
| | | M_t | 3.2 |
| Length | m | l_T | 0.63 |
| | | l_f | 0.4 |
| | | l_t | 0.4 |
| Inertia | $\text{kg}\cdot\text{m}^2$ | I_T | 1.33 |
| | | I_f | 0.47 |
| | | I_t | 0.20 |
| Mass center | m | p_T^M | 0.24 |
| | | p_f^M | 0.11 |
| | | p_t^M | 0.24 |
| Viscous friction | Ns | $F_{v,H}$ | 16.5 |
| | | $F_{v,K}$ | 5.48 |
| Static friction | Nm | $F_{s,H}$ | 15.0 |
| | | $F_{s,K}$ | 8.84 |
| Gear ratio | - | n_g | 50 |
| Motor rotor inertia | $\text{kg}\cdot\text{m}^2$ | I_a | 0.83 |

approximately 1 min on a PC based computer with a 2 GHz Pentium IV processor. The walking motion is exponentially stable since

$$\frac{\delta_{\text{zero}}^2}{1 - \delta_{\text{zero}}^2} V_{\text{zero}}(\theta^-) + V_{\text{zero}}^{\text{MAX}} = -224 < 0 \quad (6.117)$$

and $0 < \delta_{\text{zero}}^2 < 1$ per Corollary 5.1. This controller was initialized on $\mathcal{S} \cap \mathcal{Z}$ at the fixed point and simulated for three steps.

Figure 6.15 is a stick figure animation of the result. The walking motion appears quite natural. Figure 6.16 gives the joint trajectories. Figures 6.17(a) and 6.17(b) are the motor torques for the hip and knees. Of the four associated torques, the peak torque occurs at the stance leg hip and is approximately

Table 6.4. Example gait statistics for RABBIT.

| $J(\alpha)$ (N^2m) | ζ_2^* (kgm^2/s) ² | δ_{zero}^2 | $V_{\text{zero}}(\theta^-)$ (kgm^2/s) ² | $V_{\text{zero}}^{\text{MAX}}$ (kgm^2/s) ² | $\bar{\nu}$ (m/s) |
|---|---|--------------------------|---|--|----------------------|
| 91.0 | 549 | 0.741 | -142 | 182 | 0.800 |

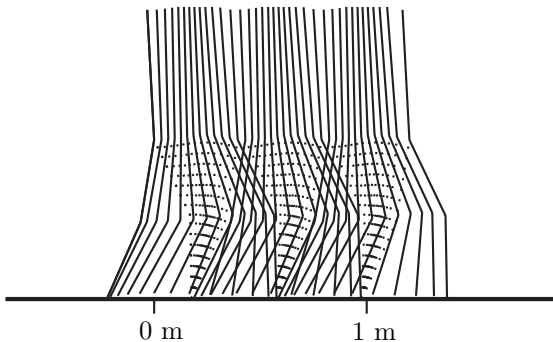


Figure 6.15. Stick animation of a simulation of RABBIT taking three steps. Note that walking is from left to right and that the stance leg is dotted.

64 Nm. [Figures 6.17\(c\)](#) and 6.17(d) are plots of the motor speed versus torque requirements for one step of the walking motion. Note that the requirements for this motion are well below the manufacturer's limits indicated by the shaded region. [Figures 6.18\(a\)](#) and 6.18(b) are normal and tangential ground reaction forces. Figure 6.18(c) is a plot of their ratio. Note that the ratio F_1^T/F_1^N is substantially below the assumed static friction limit, $\mu_s = 0.6$. The trajectory of the swing leg end height is given in Fig. 6.18(d).

6.6.3 Designs Based on Sampled Virtual Constraints and Augmentation Functions

This section uses the two-link walker to illustrate some of the flexibility available when designing controllers on the basis of virtual constraints and the hybrid zero dynamics. In the first example, a periodic torque is found that creates a periodic walking motion. On the basis of this motion, the corresponding virtual constraints and feedback controller are found that realize this gait on the biped, illustrating the considerable range of motions that can be achieved using these methods. In the second example, a passive walking motion on a slope is first found and then a feedback controller is designed that significantly increases the basin of attraction of the passive motion. Continuing with the example, starting from the same passive motion, a feedback controller is found that allows the robot to walk on flat ground, and even up a slight incline, further illustrating the range of motions that can be achieved using virtual constraints and hybrid zero dynamics.

6.6.3.1 Application: The design of a Gait via Torque Specification

This example applies the method of Section 6.5 to design a virtual constraint that can achieve, with arbitrary accuracy, a periodic walking motion found by direct optimization of the steady-state torque profile. In the first part of the

example, a periodic walking motion is computed. A set of virtual constraints that implement this walking motion are calculated in the second part of the example. With this approach, the joint motions of the robot are not limited to those achievable through a set of finitely-parameterized functions. Instead, they asymptotically converge to their values on the limit cycle specified by a torque profile.

Consider again the two-link walking model of Section 3.4.6.1 with parameters given in [Table 3.1](#) and assume that the robot is walking on level ground, so that $\alpha = 0$. A family of steady-state torque profiles is selected to have the form

$$u(t) = A \cos \left(\left(\frac{2\pi}{T} \right) (t - t^+) + \phi \right), \quad (6.118)$$

where A , T , and ϕ are to be chosen and t^+ is the time of the most recent initialization of the stance phase. To specify a walking motion, the model's initial condition x_0 and values for the parameters A , T , and ϕ must be found such that the corresponding trajectory is a periodic solution of the hybrid model, (6.1). Using numerical optimization, valid parameters for the torque profile were found to be $A = 0.445$, $T = 0.728$, $\phi = -1.22$, and the initial condition of the model was $x_0 = (-0.356; -0.178; 0.135; 0.756)$.

To determine virtual constraints for implementing this torque-specified walking gait, the periodic orbit is densely sampled to obtain the output function and its derivatives per Proposition 6.3; the results are depicted in [Fig. 6.19](#). A plot of the virtual inertia, $I(\theta)$, is also given in Fig. 6.19; because the virtual inertia does not vanish, the decoupling matrix is nonsingular on the periodic orbit. [Figure 6.20](#) illustrates the response of the closed-loop system to a perturbation in the initial condition off the periodic orbit. As the robot approaches steady state, the controller's torque converges to the sinusoidal torque profile, (6.118), of the periodic walking motion used to design the virtual constraints.

6.6.3.2 Application: Making Passive Bipedal Gaits More Robust

Next, two examples are used to illustrate how the feedback control designs of Section 6.5 can be used to achieve a stable periodic walking motion that is based on a passive gait. Before presenting the examples, a few remarks on passive bipedal walking are given.

Passive walking: A passive bipedal walker is mechanism that is capable of walking (stably) down a slope without active feedback control and with gravity as the sole energy source.²⁰ Since McGeer first simulated and built such a mechanism in the 1980s [153], passive bipedal walkers have been objects of

²⁰The energetic cost of passive dynamic walking is, in fact, nonzero—because work must be done to lift the mechanism to the top of the slope!

substantial interest, primarily as a point of departure for building energetically efficient, powered bipedal robots [58]. Passive walkers, however, have two fundamentally limiting features. The first limitation is that the basins of attraction associated with their orbits are small—meaning the robots are easily toppled. The second limitation is their very limited repertoire of walking motions: the features of their gaits can only be modified by redesigning the robot or by changing the ground slope.

Actuation, sensing and feedback can remedy both of these shortcomings [217]. Ideal actuation²¹ and feedback control can be used to increase the basin of attraction of a walking gait and to change other characteristics, such as the minimum or maximum slope on which the biped is able to walk.²² Assuming *full* actuation, the work of [217] shows how to design a controller that allows a robot to execute on flat ground any of its stable and passive walking motions arising from walking on a sloped surface. A result is given here that is similar—but conceptually stronger—because the use of the hybrid zero dynamics removes the need for full actuation.

The remainder of the section is organized into two examples. In the first example, a sample-based HZD controller is designed that increases the robustness of a passive gait and is such that control effort is used only to increase the region of attraction of the nominal motion—*no control effort is required in steady state*.²³ The example is concluded with an illustration of the robustness of the controller to external force perturbations and parameter variations. The second example illustrates how various features of an existing gait can be modified through sample-based HZD control and an augmentation function.

Enlarging the Basin of Attraction of a Stable, Passive Gait of a Two-Link Biped: Consider the two-link biped of Fig. 3.4, with mechanical parameters given in Table 3.1. A passive periodic walking motion was found for a ground slope of 0.02 rad (1.15 deg) and a maximum coefficient of static friction at the stance leg end of 0.6. The basin of attraction of the walking motion is depicted in Fig. 6.21.

²¹Here, the term “ideal actuator” is used to indicate a torque source with no power losses, zero mass, and zero inertia. The addition of nonideal actuation typically results in the loss of all stable, passive gaits. This is because the usual means of powering a biped is with actuators that are collocated with the biped’s joints, connected through a lossy drive train (typically, gears). An example where passive gaits are not lost is Collins’s quasi-passive 3D biped [58], which is powered through impulsive foot action. The loss of stable passive gaits does not preclude the use of energy efficiency as a performance metric when evaluating walking at a given rate, walking on flat ground, or walking with increased robustness.

²²Although stable gaits exist for arbitrarily small downward slopes, the basins of attractions of such gaits become impractically small [85].

²³When using nonideal actuators, zero control effort is achieved only in the sense that the actuator performs no *mechanical work* on the system. With electric motors, for example, electrical energy will be consumed to compensate for friction and rotor inertia.

Following the method suggested in Section 6.5, a sample-based virtual constraint of the form

$$y = q_1 - h_d(\theta), \quad (6.119a)$$

$$\theta = q_2, \quad (6.119b)$$

was designed on the basis of the passive orbit for a slope of 0.02 rad. The corresponding controller was realized with input-output linearization, as in (5.96), with $K_P = 200$ and $K_D = 25$. The basin of attraction of the biped in closed loop with this controller is given in Fig. 6.21. It is observed that the basin of attraction of the controlled walker is significantly larger than that of the passive walker, but it does not fully contain it: the basin of attraction of the controlled walker does not include a small region in the upper left of the graph, corresponding to extreme combinations of velocity and position.

The closed-loop system was simulated for thirty steps with an initial condition $x_0 = x_{0,\text{nom}} + \delta x_0$, where $x_{0,\text{nom}}$ is the state of the biped at the beginning of the step on the periodic orbit of the passive gait and $\delta x_0 = (0.2; 0.1; -1; 0)$. Figure 6.22 gives the evolution of the applied control torque u . Note that the peak control effort is relatively small and that the control effort goes to zero as the state approaches the passive orbit.

An interesting observation for this example is that increasing the controller gains K_P and K_D may result in a smaller basin of attraction. This effect is more pronounced when increasing K_D , as illustrated in Fig. 6.23. Larger controller gains result in larger transient control signals, and, potentially, larger ground reaction force magnitudes. The former may result in actuator saturation, and the latter may result in the coefficient of static friction being exceeded.

As a test of robustness, the closed-loop system with feedback gains $K_P = 200$ and $K_D = 25$ was simulated for horizontal, aperiodic forces acting on the robot's hip and swing leg end and mismatch between the model and controller in leg mass, m , and leg inertia, I . Between 4.6 and 4.75 seconds, a horizontal force of 15 Nm acted at the hips opposite to the direction of forward progression, and between 6.1 and 6.3 seconds, a horizontal force of 9.25 Nm acted at the swing leg end, also opposing the direction of motion. The design model for the controller used values for the leg mass and leg inertia set to 80% and 120% of nominal, respectively, of the parameters given in Table 3.1.

The resulting joint angles, joint velocities, and joint torque are depicted in Fig. 6.24. Because of the parameter mismatch, the steady-state control effort is no longer zero. It is seen that rather modest control effort is required to reject the force perturbations.

Changing the minimum slope capability of a motion: For the closed-loop robot of the previous example, a numerical search was performed to find the minimum ground slope on which the robot was able to walk stably. The minimum slope was found to be 0.0171 rad (0.980 deg). A new output of the

form $y = q_1 - h_d(\theta)$, $\theta = q_2$, is proposed where h_d is decomposed into

$$h_d(\theta) = h_{d,0}(\theta) + h_{d,\text{aug}}(\theta), \quad (6.120)$$

with $h_{d,0}$ the nominal virtual constraint of Fig. 6.19 and $h_{d,\text{aug}}$, the augmentation function, parameterized with a degree-seven Bézier polynomial. The function $h_{d,\text{aug}}$ is used to modify the properties of the nominal motion associated with $h_{d,0}$.

The numerical optimization approach of Section 6.3 was applied to determine the augmentation function, with the ground slope in the model set to zero so that the closed-loop system would be capable of walking on flat ground. This yielded the new $h_d(\theta)$ depicted in Fig. 6.25. The new closed-loop system was simulated on zero slope, for an initial condition $x_0 = x_{0,\text{nom}} + \delta x_0$, where $x_{0,\text{nom}}$ is the state of the biped at the beginning of a step on the (passive) periodic orbit for the nominal slope ($\alpha = 0.02$ rad) and $\delta x_0 = (0.025; 0.0125; 3; 0)$. Figure 6.26 gives the evolution of the applied torque, u . Note that peak control effort is relatively small. Through numerical simulation, it was found that the robot under this feedback controller was in fact capable of walking on a slope of -0.01 rad (-0.523 deg), that is, uphill.

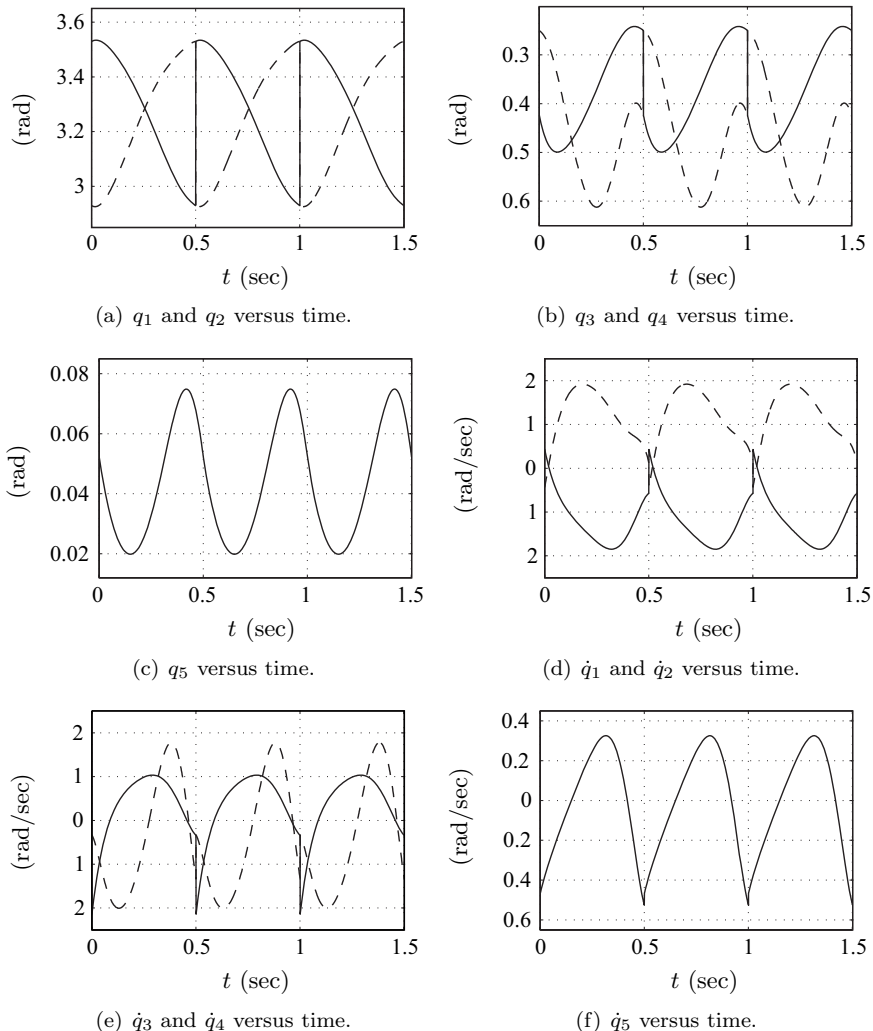


Figure 6.16. State trajectory plots corresponding to a simulated gait of RABBIT. Three steps are taken at an average walking rate of 0.8 m/s each step. The discontinuities are due to impacts and coordinate relabeling. Plots associated with q_2 and q_4 are dashed.

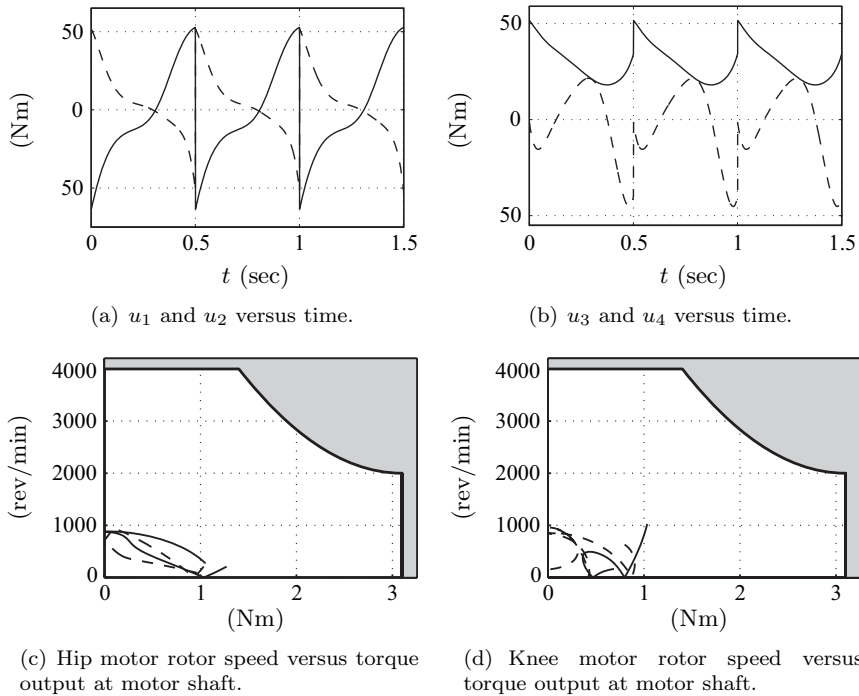


Figure 6.17. Commanded control signals corresponding to a simulated gait of RABBIT. Three steps are taken at an average walking rate of 0.8 m/s each step. The discontinuities are due to impacts and coordinate relabeling. Plots associated with u_2 and u_4 , the joint torques of the swing leg, are dashed.

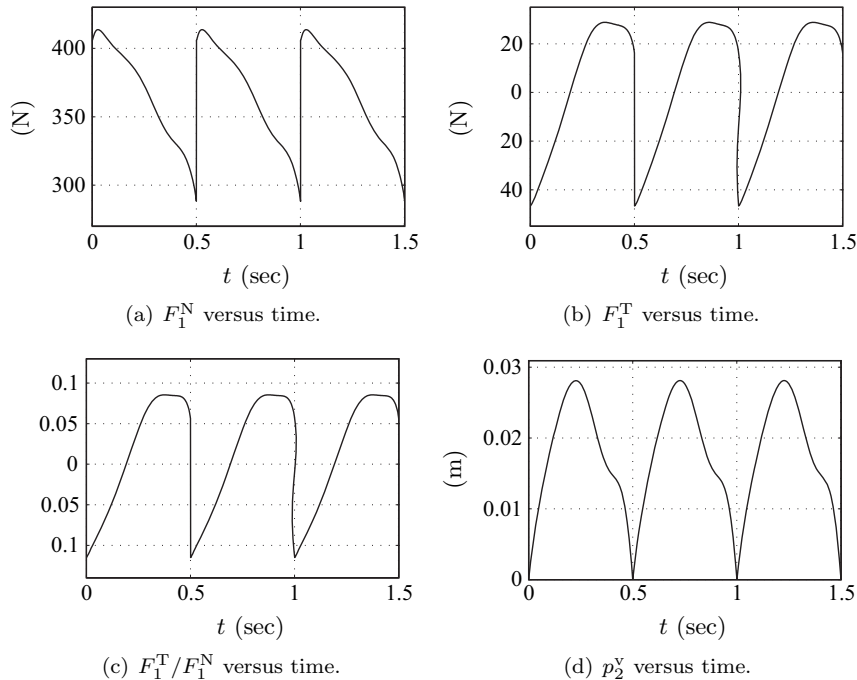


Figure 6.18. Additional plots corresponding to a simulated gait of RABBIT. Three steps are taken at an average walking rate of 0.8 m/s each step. The discontinuities are due to impacts and coordinate relabeling.

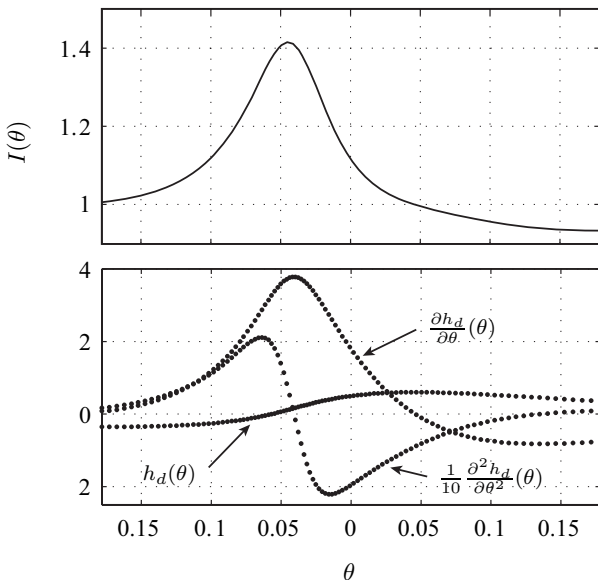


Figure 6.19. The top graph verifies that the decoupling matrix is nonsingular along the periodic orbit, as indicated by the virtual inertia $I(\theta)$ being bounded away from zero. The bottom graph displays the sample-based virtual constraint given in Theorem 6.2 and its derivatives given in Proposition 6.2.

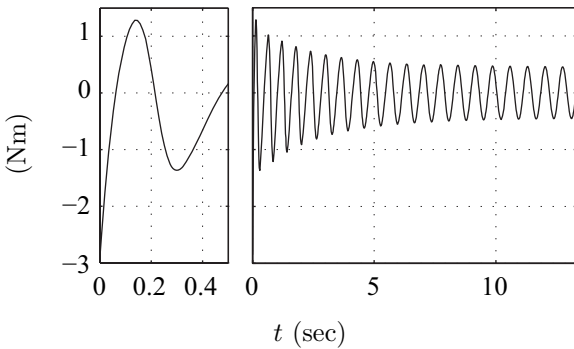


Figure 6.20. Torque evolution for a simulation of twenty (20) steps on level ground for the torque specified gait designed in Section 6.6.3.1. Torque evolution over first step is left and the torque evolution over all steps is right. The initial error is $\delta x_0 = (0.025; 0.0125; 3; 0)$. Note that the torque requirements converge rapidly to the steady-state sinusoidal profile.

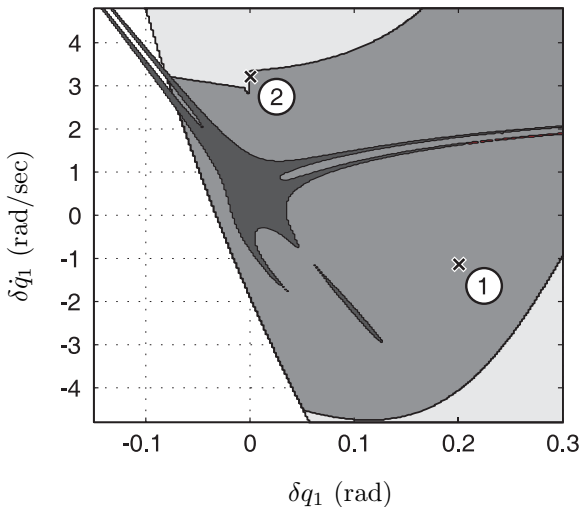


Figure 6.21. Two-dimensional slices of the basin of attraction when walking on a 0.02 rad slope. The basin for the passive walker is dark gray and the basin for the controlled walker is light gray. Shown in medium gray is the basin of attraction for the controlled walker when a peak torque magnitude of 3 Nm is imposed by saturating the output of the control law. In all cases, the coefficient of static friction at the stance leg end is assumed to be 0.6 and $\delta\dot{q}_2 = 0$. Other slices of the basins of attraction for $\delta\dot{q}_2 \neq 0$ are similarly proportioned. The initial conditions used to generate Fig. 6.22 are indicated with a 1 and those used to generate Fig. 6.24 are indicated with a 2.

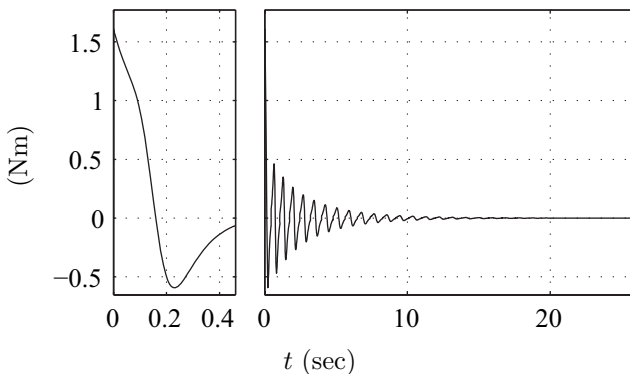


Figure 6.22. Torque evolution for a simulation of thirty (30) steps on a ground slope of $\alpha = 0.02$ rad using a sample-based HZD controller. Torque evolution over first step is left and the torque evolution over all steps is right. Note that the applied torque approaches zero as the state converges to the limit cycle. The peak torque is 1.6 Nm.

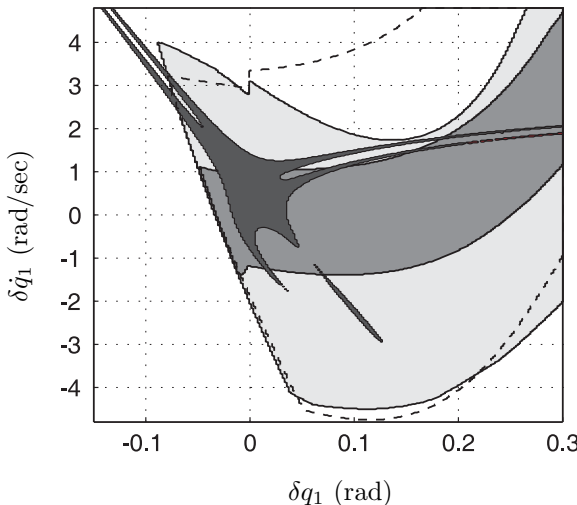


Figure 6.23. Two-dimensional slices of the basin of attraction for three different sets of controller gains, when walking on a 0.02 rad slope. The basin for the passive walker is dark gray. The basin with $K_P = 200$ and $K_D = 25$ is outlined with a dashed line, the basin with $K_P = 700$ and $K_D = 25$ is light gray, and the basin with $K_P = 500$ and $K_D = 75$ is medium gray. In all cases, a torque limit of 3 Nm is assumed, the coefficient of static friction at the stance leg end of is 0.6, and $\delta \dot{q}_2 = 0$.

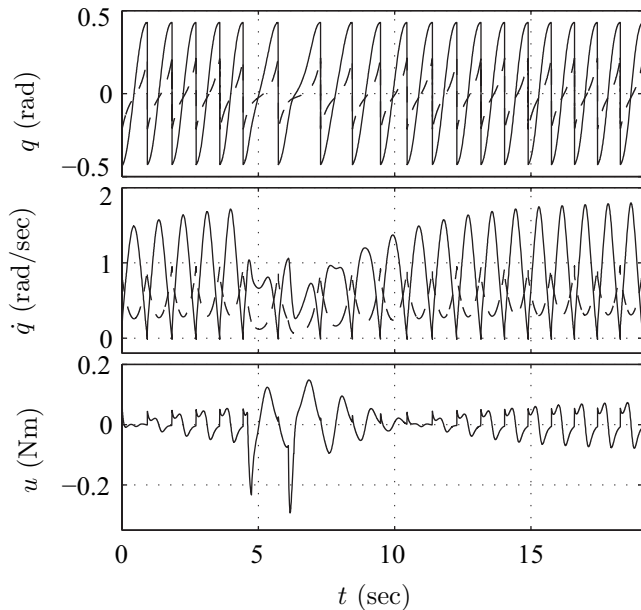


Figure 6.24. Plots illustrating the effect of perturbations. Curves corresponding to q_1 and q_2 are solid and dashed, respectively.

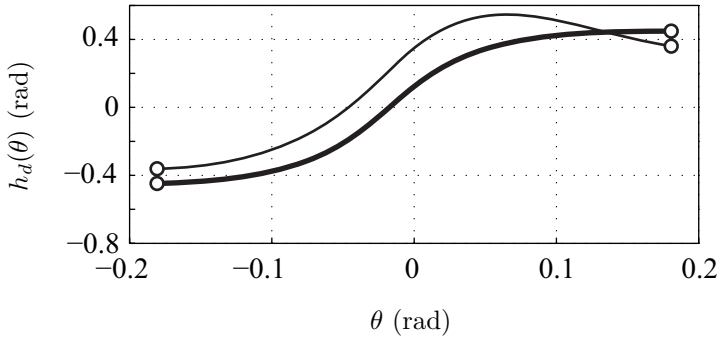


Figure 6.25. Passive motion (bold line) and augmented passive motion (thin line) as a function of θ . Enforcement of the augmented motion results in a closed-loop system that is capable of walking on flat ground.

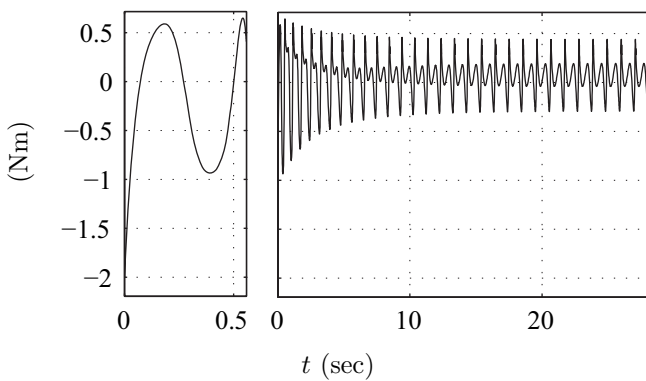


Figure 6.26. Torque evolution for a simulation of thirty (30) steps on zero slope using a sample-based HZD controller. Torque evolution over first step is left and the torque evolution over all steps is right. The peak torque is -2.0 Nm .

Systematic Design of Event-Based Feedback Controllers for Walking

The previous chapter has addressed the problem of designing controllers that induce exponentially stable, periodic walking motions at a given fixed rate for a planar, bipedal robot with one degree of underactuation in single support. This chapter provides two additional control features: (i) the ability to serially compose such controllers in order to obtain walking at several discrete walking rates with guaranteed stability during the transitions and (ii) the ability to regulate the robot's average walking rate to a continuum of values, while rejecting modest disturbances. Taken together, these two features afford the construction of a feedback controller that takes the robot from a standing position, through a range of walking rates, and back to a standing position, while providing local stabilization and disturbance rejection. The key technical tool is the Poincaré map of the closed-loop robot model.

The method used here for serially composing two controllers is motivated by a switching idea presented in [30]: controllers were first designed to accomplish the individual tasks of juggling, catching, and palming a ping-pong ball by a robot arm; these controllers were then sequentially composed via switching to accomplish the complex task of maneuvering the ping-pong ball in a three-dimensional workspace with an obstacle. The regions of attraction of each controller were first empirically estimated within the full state space of the robot. Switching from one controller to another without loss of stability was then accomplished by comparing the current state of the robot to the region of attraction of the controller for the next desired task. The problem faced in this chapter is more challenging in that the domains of attraction of any two of the individual controllers may have empty intersection, and hence a transition controller will be required to steer the robot from the region of attraction of one controller into the region of attraction of a second, “nearby” controller. A feedback schematic of the controller is depicted in Fig. 7.1.

The second result is an event-based PI controller that is able to regulate average walking rate to a continuum of values, to reject the effect of moderate disturbances on average walking rate, and to hasten convergence of average walking rate to its steady state value. The event-based controller provides PI-action to adjust the parameters of a within-stride controller that, for fixed parameter values, induces an exponentially stable, periodic orbit. Parameter adjustment takes place just after impact (swing leg touching the ground). A

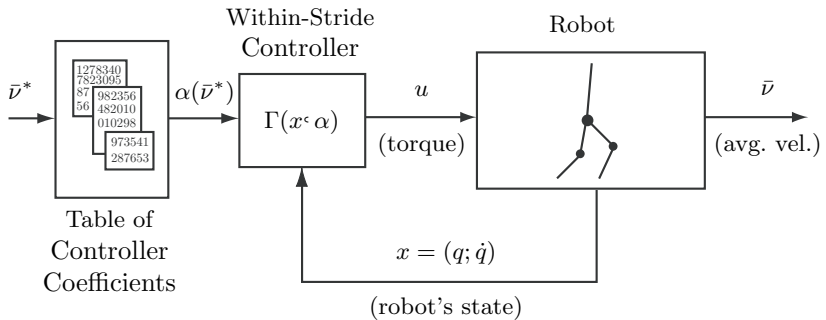


Figure 7.1. Feedback diagram showing a family of controllers parameterized by α , where each set of parameters has been designed so that the corresponding within-stride controller $\Gamma(x, \alpha)$ yields walking at a different desired speed. More generally, each parameter could represent a controller that is appropriate for a particular set of walking conditions, such as flat ground with a high coefficient of friction, flat ground with a low coefficient of friction, walking up a slope of a given grade, walking down a slope with a given grade, etc.

feedback schematic of the controller is depicted in Fig. 7.2. This idea is most closely related to the work of [7].

7.1 Overview of Key Facts

This section summarizes some notation and results from Chapters 3, 5, and 6 that are used extensively in the present chapter. The configuration coordinates of the robot in single support (also commonly called the swing phase) are denoted by $q = (q_1; \dots; q_N) \in \mathcal{Q}$, the state space is denoted by $T\mathcal{Q}$, and a control is applied at each connection of two links, but not at the contact point with the ground (i.e., no ankle torque), for a total of $(N - 1)$ controls. The hybrid model of the robot (single support phase Lagrangian dynamics plus impact map) is expressed as a nonlinear system with impulse effects

$$\Sigma : \begin{cases} \dot{x} = f(x) + g(x)u & x^- \notin \mathcal{S} \\ x^+ = \Delta(x^-) & x^- \in \mathcal{S}, \end{cases} \quad (7.1)$$

with $x = (q; \dot{q})$. The impact or walking surface, \mathcal{S} , is defined as

$$\mathcal{S} := \{(q, \dot{q}) \in T\mathcal{Q} \mid p_2^v(q) = 0, p_2^h(q) > 0\}, \quad (7.2)$$

where p_2^v and p_2^h are the Cartesian coordinates of the swing leg end (see Fig. 3.2(a)). The impact map $\Delta : \mathcal{S} \rightarrow T\mathcal{Q}$ computes the value of the state

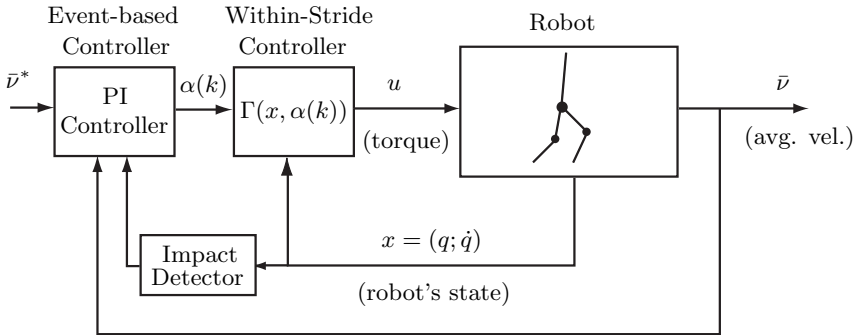


Figure 7.2. Feedback diagram showing an event-based PI-controller for regulating average walking speed to a desired value, $\bar{\nu}^*$. The parameters of the within-stride controller are updated at each impact event, in other words, on a stride-to-stride basis. Hence, the overall feedback controller, consisting of the within-stride control action and the stride-to-stride control action, is hybrid, just like the underlying biped model.

just after impact with \mathcal{S} , $x^+ = (q^+; \dot{q}^+)$, from the value of the state just before impact, $x^- = (q^-; \dot{q}^-)$. Since the configuration coordinates necessarily involve the specification of which of the two legs is in contact with the ground, the coordinates must be relabeled after each step to take into account the successive changing of the support leg. This is reflected in the impact map via a constant, invertible matrix R , $q^+ := Rq^-$.

The control design involves the choice of a set of holonomic constraints that are asymptotically imposed on the robot via feedback control. This is accomplished by interpreting the constraints as output functions depending only on the configuration variables of the robot, and designing a controller that drives the outputs to zero sufficiently fast; see [Section 5.5](#). The outputs $y \in \mathbb{R}^{N-1}$ are chosen as

$$y = h(q, \alpha) = H_0 q - h_d(\theta(q), \alpha), \quad (7.3)$$

with terms defined as follows:

1. H_0 is an $(N-1) \times N$ matrix of real coefficients specifying what is to be controlled.
2. $\theta(q) := cq$, where c is a $1 \times N$ row vector of real coefficients, is a scalar function of the configuration variables and should be chosen so that it is monotonically increasing along a periodic orbit of the robot ($\theta(q)$ replaces time as a means of parameterizing a periodic walking motion). Define $\theta^+ = cq^+$ and $\theta^- = cq^-$ to be the initial and final values of θ , respectively, along a step.

3. Normalization of θ to take values between zero and one,

$$s(q) := \frac{\theta(q) - \theta^+}{\theta^- - \theta^+}. \quad (7.4)$$

4. Bézier polynomials of degree $M \geq 3$

$$b_i(s) := \sum_{k=0}^M \alpha_k^i \frac{M!}{k!(M-k)!} s^k (1-s)^{M-k}. \quad (7.5)$$

5. For α_k^i as above, define a $(N-1) \times 1$ column vector $\alpha_k := (\alpha_k^1; \dots; \alpha_k^{N-1})$ and a $(N-1) \times (M+1)$ matrix $\alpha := [\alpha_0, \dots, \alpha_M]$.

6.

$$h_d(\theta(q), \alpha) := \begin{bmatrix} b_1 \circ s(q) \\ \vdots \\ b_{N-1} \circ s(q) \end{bmatrix}, \quad (7.6)$$

where the dependence on α is implicit through b_i ; see (7.5).

The matrix of parameters α is said to be a *regular parameter* of output (7.3) if the output satisfies Hypotheses HH1–HH5 of Chapter 5, which together imply the invertibility of the decoupling matrix and the existence of a two-dimensional, smooth, zero dynamics associated with the swing phase of the robot. Let $\mathcal{A} \subset \mathbb{R}^{(N-1) \times (M+1)}$ be the set of regular parameters; then \mathcal{A} is open because Hypotheses HH2, HH3, and HH5 are rank conditions and because condition HH4 requires a zero of a function depending continuously on α to remain in an open set.

Let \mathcal{Z}_α be the swing phase zero dynamics manifold. Let Γ_α be any feedback satisfying the conditions of Theorem 5.4 or Theorem 5.5 so that \mathcal{Z}_α is invariant under the swing phase dynamics in closed loop with Γ_α and is locally (finite-time or sufficiently exponentially quickly) attractive otherwise. It follows that $\Gamma_\alpha|_{\mathcal{Z}_\alpha} = -(L_g L_f h(\cdot, \alpha))^{-1} L_f^2 h(\cdot, \alpha)$ [127], and thus (i) $\Gamma_\alpha|_{\mathcal{Z}_\alpha}$ is uniquely determined by the choice of parameters used in the output and is completely independent of the choice of feedback used to drive the constraints asymptotically to zero; and (ii) even though Γ_α is not necessarily smooth, $\Gamma_\alpha|_{\mathcal{Z}_\alpha}$ is as smooth as the robot model.

For a regular parameter value α of output (7.3), a very simple characterization of $\mathcal{S} \cap \mathcal{Z}_\alpha$, the configuration and velocity of the robot at the end of a phase of single support, can be given. Define

$$q_\alpha^- := H^{-1} \begin{bmatrix} \alpha_M \\ \theta_\alpha^- \end{bmatrix} \quad (7.7a)$$

$$\omega_\alpha^- := H^{-1} \begin{bmatrix} \frac{M}{\theta_\alpha^- - \theta_\alpha^+} (\alpha_M - \alpha_{M-1}) \\ 1 \end{bmatrix}, \quad (7.7b)$$

where $H := [H_0; c]$, and the initial and final values of θ corresponding to this output are denoted by θ_α^+ and θ_α^- , respectively. Then

$$\mathcal{S} \cap \mathcal{Z}_\alpha = \{(q_\alpha^-, \dot{q}_\alpha^-) \mid \dot{q}_\alpha^- = a \omega_\alpha^-, a \in \mathbb{R}\} \quad (7.8)$$

and is determined by the *last two columns* of the parameter matrix α . In a similar fashion, $\Delta(\mathcal{S} \cap \mathcal{Z}_\alpha)$, which gives the configuration, q_α^+ , and velocity, \dot{q}_α^+ , of the robot at the beginning of a subsequent phase of single support, may be simply characterized and is determined by the *first two columns* of the parameter matrix α . From Corollary 6.1,

$$\begin{bmatrix} \alpha_0 \\ \theta_\alpha^+ \end{bmatrix} = HRH^{-1} \begin{bmatrix} a_M \\ \theta_\alpha^- \end{bmatrix} \quad (7.9)$$

implies $h(\cdot, \alpha) \circ \Delta|_{(\mathcal{S} \cap \mathcal{Z}_\alpha)} = 0$, while, if $\dot{q}_\alpha^+ := \Delta_{\dot{q}}(q_\alpha^-) \omega_\alpha^-$, results in $c\dot{q}_\alpha^+ \neq 0$, then

$$\alpha_1 = \frac{\theta_\alpha^- - \theta_\alpha^+}{Mc\dot{q}_\alpha^+} H_0 \dot{q}_\alpha^+ + \alpha_0 \quad (7.10)$$

implies $L_f h(\cdot, \alpha) \circ \Delta|_{(\mathcal{S} \cap \mathcal{Z}_\alpha)} = 0$. The key thing to note is that these two conditions involve, once again, only the *first two columns* of the parameter matrix α . In a similar fashion the *last two columns* of the parameter matrix α may be chosen so that $h(\cdot, \alpha)|_{(\mathcal{S} \cap \mathcal{Z}_\alpha)} = 0$ and $L_f h(\cdot, \alpha)|_{(\mathcal{S} \cap \mathcal{Z}_\alpha)} = 0$.

Conditions (7.9) and (7.10) imply that $\Delta(\mathcal{S} \cap \mathcal{Z}_\alpha) \subset \mathcal{Z}_\alpha$, in which case \mathcal{Z}_α is then controlled-invariant for the full hybrid model of the robot. The resulting restriction dynamics is called the *hybrid zero dynamics*. Corollary 5.1 provides necessary and sufficient conditions for the hybrid zero dynamics to admit an exponentially stable, periodic orbit transversal to \mathcal{S} , \mathcal{O}_α . When these conditions are met, the matrix of parameters α is said to give rise to an exponentially stable walking motion. When Γ_α is designed according to Theorem 5.4 or Theorem 5.5, the exponentially stable orbit in the hybrid zero dynamics is also exponentially stable in the full-dimensional model, (7.1). The domain of attraction of \mathcal{O}_α in the full-dimensional model cannot be easily estimated; however, its domain of attraction intersected with $\mathcal{S} \cap \mathcal{Z}_\alpha$, that is, the domain of attraction of the associated fixed-point of the restricted Poincaré map, $\rho_\alpha : \mathcal{S} \cap \mathcal{Z}_\alpha \rightarrow \mathcal{S} \cap \mathcal{Z}_\alpha$, is computed analytically in Theorem 5.3.

7.2 Transition Control

Let α and β be two regular sets of parameters of output (7.3), with corresponding swing phase zero dynamics manifolds, \mathcal{Z}_α and \mathcal{Z}_β . Suppose that $\Delta(\mathcal{S} \cap \mathcal{Z}_\alpha) \subset \mathcal{Z}_\alpha$ and $\Delta(\mathcal{S} \cap \mathcal{Z}_\beta) \subset \mathcal{Z}_\beta$, and that there exist exponentially sta-

ble periodic orbits,¹ $\mathcal{O}_\alpha \subset \mathcal{Z}_\alpha$ and $\mathcal{O}_\beta \subset \mathcal{Z}_\beta$, both transversal to \mathcal{S} ; denote the corresponding controllers by Γ_α and Γ_β . The goal is to be able to transition from \mathcal{O}_α to \mathcal{O}_β without the robot falling (i.e., with stability guaranteed). If it were known that the domains of attraction of the two orbits had a nonempty intersection, then the method of [30] could be applied directly. Numerically evaluating the domains of attraction on the full-dimensional model is unpleasant, so another means of ensuring a stable transition is sought that is based on easily computable quantities, the domains of attraction of the restricted Poincaré maps associated with Γ_α and Γ_β .

Since in general $\mathcal{Z}_\alpha \cap \mathcal{Z}_\beta = \emptyset$, the method for providing a stable transition from \mathcal{Z}_α and \mathcal{Z}_β will be to introduce a one-step transition controller $\Gamma_{(\alpha \rightarrow \beta)}$ whose (swing phase) zero dynamics manifold $\mathcal{Z}_{(\alpha \rightarrow \beta)}$ connects the zero dynamics manifolds \mathcal{Z}_α and \mathcal{Z}_β ; this is conceptually illustrated in Fig. 7.3. More precisely, switching will be synchronized with impact events and the zero dynamics manifold $\mathcal{Z}_{(\alpha \rightarrow \beta)}$ will be chosen to map exactly from the one-dimensional manifold $\Delta(\mathcal{S} \cap \mathcal{Z}_\alpha)$ (i.e., the state of the robot just after impact with \mathcal{S} under controller Γ_α) to the one-dimensional manifold $\mathcal{S} \cap \mathcal{Z}_\beta$ (i.e., the state of the robot just before impact with \mathcal{S} under controller Γ_β). The one-step transition controller $\Gamma_{(\alpha \rightarrow \beta)}$ differs from a deadbeat controller in that $\Gamma_{(\alpha \rightarrow \beta)}$ takes *all points* in a subset of manifold $\Delta(\mathcal{S} \cap \mathcal{Z}_\alpha)$ into a subset of the manifold $\mathcal{S} \cap \mathcal{Z}_\beta$ as opposed to a deadbeat controller that would map a subset of $\Delta(\mathcal{S} \cap \mathcal{Z}_\alpha)$ to a *point* in $\mathcal{S} \cap \mathcal{Z}_\beta$. The design of multistep transition controllers is also possible but is not addressed here.

By Lemmas 6.1 and 6.2, any zero dynamics manifold $\mathcal{Z}_{(\alpha \rightarrow \beta)}$ with parameters

$$\begin{aligned} (\alpha \rightarrow \beta)_0 &= \alpha_0 \\ (\alpha \rightarrow \beta)_1 &= \frac{M_\alpha}{M_{(\alpha \rightarrow \beta)}} \frac{\theta_\beta^- - \theta_\alpha^+}{\theta_\alpha^- - \theta_\alpha^+} (\alpha_1 - \alpha_0) + \alpha_0 \\ (\alpha \rightarrow \beta)_{M_{(\alpha \rightarrow \beta)}-1} &= \frac{M_\beta}{M_{(\alpha \rightarrow \beta)}} \frac{\theta_\beta^- - \theta_\alpha^+}{\theta_\beta^- - \theta_\beta^+} (\beta_{M_\beta-1} - \beta_{M_\beta}) + \beta_{M_\beta} \\ (\alpha \rightarrow \beta)_{M_{(\alpha \rightarrow \beta)}} &= \beta_{M_\beta} \\ \theta_{(\alpha \rightarrow \beta)}^+ &= \theta_\alpha^+ \\ \theta_{(\alpha \rightarrow \beta)}^- &= \theta_\beta^- \end{aligned} \quad (7.11)$$

satisfies

$$\mathcal{Z}_{(\alpha \rightarrow \beta)} \cap \Delta(\mathcal{S} \cap \mathcal{Z}_\alpha) = \Delta(\mathcal{S} \cap \mathcal{Z}_\alpha) \quad (7.12a)$$

¹In this presentation, it is implicitly assumed that these would correspond to walking at different average walking rates, but they could correspond to walking on surfaces with different slopes, for example.

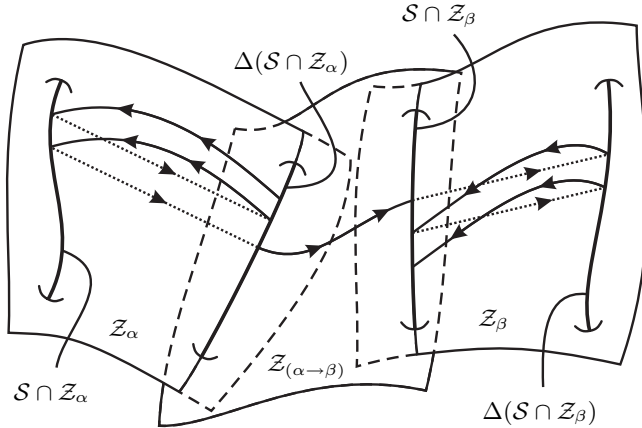


Figure 7.3. Composition of two controllers Γ_α and Γ_β via transition controller $\Gamma_{(\alpha \rightarrow \beta)}$. Under the action of Γ_α the dynamics evolve on Z_α . Switching to $\Gamma_{(\alpha \rightarrow \beta)}$ when the state enters $\Delta(\mathcal{S} \cap Z_\alpha)$ causes the dynamics to evolve along $Z_{(\alpha \rightarrow \beta)}$ to $\mathcal{S} \cap Z_\beta$. Switching to Γ_β when the state enters $\mathcal{S} \cap Z_\beta$ causes the dynamics to evolve on Z_β .

$$\Delta(\mathcal{S} \cap Z_{(\alpha \rightarrow \beta)}) = \Delta(\mathcal{S} \cap Z_\beta); \quad (7.12b)$$

see once again Fig. 7.3. The intermediate parameter values, $(\alpha \rightarrow \beta)_i$, $i = 2, \dots, M_{(\alpha \rightarrow \beta)} - 2$, affect the walking motion, and one could choose their values through optimization, for example, to minimize the torques required to evolve along the surface $Z_{(\alpha \rightarrow \beta)}$. However, the simple choice

$$(\alpha \rightarrow \beta)_i = (\alpha_i + \beta_i)/2, \quad i = 2, \dots, M_{(\alpha \rightarrow \beta)} - 2, \quad (7.13)$$

has proven effective in practice. The reason for this seems to be intimately linked the use of Bézier polynomials in the design of h_d .

Assume that the parameter matrix given in (7.11) and (7.13) is regular and let $\Gamma_{(\alpha \rightarrow \beta)}$ be an associated controller; then $\Gamma_{(\alpha \rightarrow \beta)}|_{Z_{(\alpha \rightarrow \beta)}}$ is uniquely determined by the matrix of parameters $(\alpha \rightarrow \beta)$. The goal now is to determine under what conditions $\Gamma_{(\alpha \rightarrow \beta)}$ will effect a transition from the region of attraction (in $\mathcal{S} \cap Z_\alpha$) of \mathcal{O}_α to the region of attraction (in $\mathcal{S} \cap Z_\beta$) of \mathcal{O}_β .

Let $P_{(\alpha \rightarrow \beta)} : \mathcal{S} \rightarrow \mathcal{S}$ be the Poincaré return map of the model (7.1) in closed loop with $\Gamma_{(\alpha \rightarrow \beta)}$ and consider $P_{(\alpha \rightarrow \beta)}|_{(\mathcal{S} \cap Z_\alpha)}$. By construction of $Z_{(\alpha \rightarrow \beta)}$, $\Delta(\mathcal{S} \cap Z_\alpha) \subset Z_{(\alpha \rightarrow \beta)}$. Since $Z_{(\alpha \rightarrow \beta)}$ is invariant under $\Gamma_{(\alpha \rightarrow \beta)}$, it follows that $P_{(\alpha \rightarrow \beta)}(\mathcal{S} \cap Z_\alpha) \subset \mathcal{S} \cap Z_{(\alpha \rightarrow \beta)}$. But by construction, $\mathcal{S} \cap Z_{(\alpha \rightarrow \beta)} = \mathcal{S} \cap Z_\beta$. Thus, the restriction of the Poincaré return map to $\mathcal{S} \cap Z_\alpha$ induces a (partial) map

$$\rho_{(\alpha \rightarrow \beta)} : \mathcal{S} \cap Z_\alpha \rightarrow \mathcal{S} \cap Z_\beta. \quad (7.14)$$

In Section 5.4.1, a closed-form expression for $\rho_{(\alpha \rightarrow \beta)}$ is computed on the basis of the two-dimensional zero dynamics associated with $Z_{(\alpha \rightarrow \beta)}$.

Let $\mathcal{D}_\alpha \subset \mathcal{S} \cap \mathcal{Z}_\alpha$ and $\mathcal{D}_\beta \subset \mathcal{S} \cap \mathcal{Z}_\beta$ be the domains of attraction of the restricted Poincaré maps $\rho_\alpha : \mathcal{S} \cap \mathcal{Z}_\alpha \rightarrow \mathcal{S} \cap \mathcal{Z}_\alpha$ and $\rho_\beta : \mathcal{S} \cap \mathcal{Z}_\beta \rightarrow \mathcal{S} \cap \mathcal{Z}_\beta$ associated with the orbits \mathcal{O}_α and \mathcal{O}_β , respectively.² It follows that $\rho_{(\alpha \rightarrow \beta)}^{-1}(\mathcal{D}_\beta)$ is precisely the set of states in $\mathcal{S} \cap \mathcal{Z}_\alpha$ that can be steered into the domain of attraction of \mathcal{O}_β under the control law $\Gamma_{(\alpha \rightarrow \beta)}$. In general, from stability considerations, one is more interested in $\mathcal{D}_\alpha \cap \rho_{(\alpha \rightarrow \beta)}^{-1}(\mathcal{D}_\beta)$, the set of states in the domain of attraction of \mathcal{O}_α that can be steered into the domain of attraction of \mathcal{O}_β in one step under the control law $\Gamma_{(\alpha \rightarrow \beta)}$ (see Fig. 7.3).

Theorem 7.1 (Serial Composition of Stable Walking Motions)

Assume that α and β are regular parameters of output (7.3), and that $(\alpha \rightarrow \beta)$ defined by (7.11) and (7.13) is also regular. Suppose furthermore that

1. $\Delta(\mathcal{S} \cap \mathcal{Z}_\alpha) \subset \mathcal{Z}_\alpha$ and $\Delta(\mathcal{S} \cap \mathcal{Z}_\beta) \subset \mathcal{Z}_\beta$;
2. there exist exponentially stable, periodic orbits \mathcal{O}_α and \mathcal{O}_β in \mathcal{Z}_α and \mathcal{Z}_β , respectively, both transversal to \mathcal{S} , so that the domains of attraction $\mathcal{D}_\alpha \subset \mathcal{S} \cap \mathcal{Z}_\alpha$ and $\mathcal{D}_\beta \subset \mathcal{S} \cap \mathcal{Z}_\beta$ of the associated restricted Poincaré maps are nonempty and open;
3. $\Gamma_{(\alpha \rightarrow \beta)}$ satisfies the conditions of Theorem 5.4 so that $\mathcal{Z}_{(\alpha \rightarrow \beta)}$ is invariant under the swing phase dynamics in closed loop with $\Gamma_{(\alpha \rightarrow \beta)}$.

Then the set of states in \mathcal{D}_α that can be steered into \mathcal{D}_β in one step under the control law $\Gamma_{(\alpha \rightarrow \beta)}$ is equal to $\mathcal{D}_\alpha \cap \rho_{(\alpha \rightarrow \beta)}^{-1}(\mathcal{D}_\beta)$.

Proof This follows directly from the definition of $\rho_{(\alpha \rightarrow \beta)}$; see Proposition 4.3.

An example is given in the next chapter. The above result also holds for feedbacks Γ_α , Γ_β , and $\Gamma_{(\alpha \rightarrow \beta)}$ designed according to Theorem 5.5. One has to be aware, however, that the state of the closed-loop system does not reach \mathcal{Z}_α in finite time, and hence the switching conditions given in the theorem can only be approximately met.

²Since the existence of exponentially stable, periodic orbits has been assumed, these domains are nonempty and open.

7.3 Event-Based PI-Control of the Average Walking Rate

The goal of this section is to design an *event-based controller*³ that adjusts the parameters in the output (7.3) so as to achieve walking at a *continuum* of rates instead of some finite set of rates, as would be achieved with the switching design of the previous section. The key idea is to view the numerical parameters⁴ α in the virtual constraints as control parameters in the Poincaré map. Let Γ_α be a controller satisfying the hypotheses of Section 7.1 and denote the closed-loop system formed with (7.1) by

$$\Sigma_\alpha : \begin{cases} \dot{x} = f_{cl}(x, \alpha) & x^- \notin \mathcal{S} \\ x^+ = \Delta(x^-) & x^- \in \mathcal{S}, \end{cases} \quad (7.15)$$

where $f_{cl}(x, \alpha) := f(x) + g(x)\Gamma_\alpha(x)$. The closed-loop system is then a collection of systems with impulse effects, indexed by the parameter matrix α ; see for example, [Section 4.6](#). Varying α at each impact event of the walking cycle, and holding it constant during the swing phase, will provide a means to vary the average walking rate.

Three controller designs will be presented. Each of them is based on the Poincaré map of (7.15), with α viewed as a control variable. The first two controller designs exploit the hybrid zero dynamics. Consequently, the computations associated with their design involve restricted Poincaré maps and are often relatively easy to perform on practical examples. In addition, for these two methods, the feedback controller Γ_α can be based on either the finite-time controller of Theorem 5.4 or the input-output linearizing controller of Theorem 5.5. The third design will be based directly on the Poincaré return map of (7.15) and to effectively carry out the required computations, the closed-loop system must be continuously differentiable. This restricts the validity to feedback controllers Γ_α designed according to Theorem 5.5.

7.3.1 Average Walking Rate

Define the average walking rate over a step⁵ to be step length divided by the elapsed time of a step. For a controller Γ_α satisfying the hypotheses of Section 7.1, the average walking rate is computed from the model (7.15) as follows. Let $P_\alpha : \mathcal{S} \rightarrow \mathcal{S}$ be the Poincaré return map and let $T_{I,\alpha} : T\mathcal{Q} \rightarrow \mathbb{R} \cup \{\infty\}$ be the time-to-impact function. The average walking rate is formally

³That is, a controller that acts step-to-step with updates occurring at impacts.

⁴For this section, it is assumed that the degrees of the Bézier polynomials in h_d are *fixed*.

⁵A step starts with the swing leg on the ground and behind the robot and ends with the swing leg on the ground and in front of the robot.

defined as a (partial) map $\bar{\nu}_\alpha : \mathcal{S} \rightarrow \mathbb{R}_{\geq 0}$ by

$$\bar{\nu}_\alpha := \frac{p_2^h \circ P_\alpha}{T_{I,\alpha} \circ \Delta}, \quad (7.16)$$

where, p_2^h , when evaluated on \mathcal{S} , computes step length (see Fig. 3.2(a)).

On the open subset $\tilde{\mathcal{S}} \subset \mathcal{S}$ where $0 < T_{I,\alpha} \circ \Delta < \infty$ and the associated impacts are transversal to \mathcal{S} , both P_α and $T_{I,\alpha} \circ \Delta$ are well-defined and continuous in the case of Γ_α satisfying the hypotheses of Theorem 5.4, and well-defined and continuously differentiable in the case of Γ_α satisfying the hypotheses of Theorem 5.5. It follows that $\bar{\nu}_\alpha$ restricted to $\tilde{\mathcal{S}}$ is also continuous in the first case and continuously differentiable in the second. However, for later use, note that if α is a regular parameter value of output (7.3) giving rise to a hybrid zero dynamics, that is, $\Delta(\mathcal{S} \cap \mathcal{Z}_\alpha) \subset \mathcal{Z}_\alpha$, then $\bar{\nu}_\alpha$ restricted to $\tilde{\mathcal{S}} \cap \mathcal{Z}_\alpha$ depends smoothly on the states and the parameter values α used to define the outputs, (7.3), for both types of feedback controllers.

7.3.2 Design and Analysis Based on the Hybrid Zero Dynamics

Two sets of assumptions are investigated for completing the controller design on the basis of the hybrid zero dynamics. In the first case, the parameters are varied in such a way that they affect the gait of the robot only in the “interior” of a step, while leaving the state of the robot at the boundary of a step, that is, at beginning and end of a step, unchanged. A modification to the height of the swing leg at the midpoint of the gait would satisfy this restriction, for example, but a parametric change to step length would not be permitted. In the second case, more general parameter variations are allowed that will encompass changes at the boundary of the step. The two designs are presented separately because the first one is simpler and easier to follow. The results are based on Theorems 4.8 and 4.9, respectively.

Case I: For any regular parameter value $\alpha \in \mathcal{A}$ of output (7.3) satisfying $\Delta(\mathcal{S} \cap \mathcal{Z}_\alpha) \subset \mathcal{Z}_\alpha$, the corresponding restricted Poincaré map has been denoted $\rho_\alpha : \mathcal{S} \cap \mathcal{Z}_\alpha \rightarrow \mathcal{S} \cap \mathcal{Z}_\alpha$. To emphasize the dependence on α , for $z \in \mathcal{S} \cap \mathcal{Z}_\alpha$, let $\rho(z, \alpha) := \rho_\alpha(z)$; similarly, let $\bar{\nu}(z, \alpha) := \bar{\nu}_\alpha(z)$.

Let $\bar{\alpha}$ be a given regular value of α such that $\rho_{\bar{\alpha}} : \mathcal{S} \cap \mathcal{Z}_{\bar{\alpha}} \rightarrow \mathcal{S} \cap \mathcal{Z}_{\bar{\alpha}}$ has an exponentially stable fixed point transversal to \mathcal{S} , and denote the fixed point by $z_{\bar{\alpha}}^*$. Let $\delta\alpha \in \mathbb{R}^{(N-1) \times (M+1)}$ be such that $\delta\alpha \neq 0$ and

$$(\delta\alpha)_0 = (\delta\alpha)_1 = (\delta\alpha)_{M-1} = (\delta\alpha)_M = 0. \quad (7.17)$$

Then, for $w \in \mathbb{R}$ sufficiently small in magnitude, each value of the one-parameter curve $\bar{\alpha} + w\delta\alpha \in \mathbb{R}^{(N-1) \times (M+1)}$ is also regular. From (7.17),

$$\mathcal{S} \cap \mathcal{Z}_{\bar{\alpha} + w\delta\alpha} = \mathcal{S} \cap \mathcal{Z}_{\bar{\alpha}} \quad (7.18a)$$

$$\Delta(\mathcal{S} \cap \mathcal{Z}_{\bar{\alpha} + w\delta\alpha}) = \Delta(\mathcal{S} \cap \mathcal{Z}_{\bar{\alpha}}). \quad (7.18b)$$

Thus, $\rho_{\bar{\alpha}+w\delta\alpha} : \mathcal{S} \cap \mathcal{Z}_{\bar{\alpha}} \rightarrow \mathcal{S} \cap \mathcal{Z}_{\bar{\alpha}}$, and the following single-input, single-output dynamic system can be defined,

$$\begin{aligned} z[k+1] &= \rho(z[k], \bar{\alpha} + w[k]\delta\alpha) \\ \eta[k+1] &= \bar{\nu}(z[k], \bar{\alpha} + w[k]\delta\alpha) \\ y_{\text{vel}}[k] &= \eta[k], \end{aligned} \quad (7.19)$$

with two-dimensional state space $\mathcal{S} \cap \mathcal{Z}_{\bar{\alpha}} \times \mathbb{R}$, input $w \in \mathbb{R}$ and output equal to average walking rate, $y_{\text{vel}} \in \mathbb{R}$. Its linearization is

$$\begin{aligned} \delta z[k+1] &= a_{11}\delta z[k] + b_1\delta w[k] \\ \delta \eta[k+1] &= a_{21}\delta z[k] + b_2\delta w[k] \\ \delta y_{\text{vel}}[k] &= \delta \eta[k], \end{aligned} \quad (7.20)$$

where⁶

$$\begin{aligned} a_{11} &:= \left. \frac{\partial \rho}{\partial z}(z, \bar{\alpha} + w\delta\alpha) \right|_{\substack{z=z_{\bar{\alpha}}^* \\ w=0}} \quad b_1 := \left. \frac{\partial \rho}{\partial w}(z, \bar{\alpha} + w\delta\alpha) \right|_{\substack{z=z_{\bar{\alpha}}^* \\ w=0}} \\ a_{21} &:= \left. \frac{\partial \bar{\nu}}{\partial z}(z, \bar{\alpha} + w\delta\alpha) \right|_{\substack{z=z_{\bar{\alpha}}^* \\ w=0}} \quad b_2 := \left. \frac{\partial \bar{\nu}}{\partial w}(z, \bar{\alpha} + w\delta\alpha) \right|_{\substack{z=z_{\bar{\alpha}}^* \\ w=0}}. \end{aligned} \quad (7.21)$$

The linearized system (7.20) is exponentially stable if, and only if, $|a_{11}| < 1$. An easy computation shows that its DC-gain is nonzero if, and only if,

$$a_{21}b_1 + b_2(1 - a_{11}) \neq 0. \quad (7.22)$$

Theorem 7.2 (Event-Based PI Control Applied to the Hybrid Zero Dynamics, Case-I)

Let $\bar{\alpha}$ be a regular parameter value of the output (7.3) such that $\Delta(\mathcal{S} \cap \mathcal{Z}_{\bar{\alpha}}) \subset \mathcal{S} \cap \mathcal{Z}_{\bar{\alpha}}$ and assume there exists an exponentially stable periodic orbit in $\mathcal{Z}_{\bar{\alpha}}$ transversal to \mathcal{S} . Denote the corresponding fixed point of the restricted Poincaré return map by $z_{\bar{\alpha}}^*$. Assume there exists $\delta\alpha$ satisfying (7.17) and such that the nonzero DC-gain condition, (7.22), holds. Then average walking rate can be regulated via PI control. In particular, there exist $\epsilon^* > 0$, and scalars \bar{K}_P and \bar{K}_I such that for all η^* satisfying $|\eta^* - \bar{\nu}(z_{\bar{\alpha}}^*, \bar{\alpha})| < \epsilon^*$, the system consisting of (7.19) in closed loop with the proportional plus integral controller⁷

$$\begin{aligned} e[k+1] &= e[k] + (\eta^* - \eta[k]) \\ w[k] &= \bar{K}_P(\eta^* - \eta[k]) + \bar{K}_Ie[k] \end{aligned} \quad (7.23)$$

⁶We have abused notation and not made the distinction between z as a point in TQ that lies in $\mathcal{S} \cap \mathcal{Z}_{\bar{\alpha}}$ and z as a coordinate on $\mathcal{S} \cap \mathcal{Z}_{\bar{\alpha}}$. Note that TQ has dimension $2N$ and $\mathcal{S} \cap \mathcal{Z}_{\bar{\alpha}}$ has dimension one.

⁷The state $e[k]$ is the integral of the error between the desired average velocity and the current average velocity of the robot.

has an exponentially stable equilibrium, and thus, when initialized sufficiently near the equilibrium, $\lim_{k \rightarrow \infty} (\eta^* - \eta[k]) = 0$.

Proof The linear system (7.20) is exponentially stable because the exponential stability of the fixed-point $z_{\bar{\alpha}}^*$ implies that $|a_{11}| < 1$. This, combined with the DC-gain being nonzero, implies the existence of a PI controller of the form

$$\begin{aligned}\delta e[k+1] &= \delta e[k] + (\delta \eta^* - \delta \eta[k]) \\ \delta w[k] &= \bar{K}_P(\delta \eta^* - \delta \eta[k]) + \bar{K}_I \delta e[k]\end{aligned}\quad (7.24)$$

such that the closed-loop system (7.20) with (7.24) is exponentially stable and satisfies $\lim_{k \rightarrow \infty} (\delta \eta^* - \delta \eta[k]) = 0$, where $\delta \eta^* := \eta^* - \bar{\nu}(z_{\bar{\alpha}}^*, \bar{\alpha})$. Since the closed loop of (7.20) with (7.24) is the linearization of (7.19) in closed loop with (7.23), the result follows.

The PI controller in (7.23) is realized on the full-hybrid model of the robot as

$$\left. \begin{array}{l} \dot{x} = f(x) + g(x)\Gamma_{\bar{\alpha}+w\delta\alpha} \\ \dot{e} = 0 \\ \dot{w} = 0 \\ \dot{\eta} = 0 \\ x^+ = \Delta(x^-) \\ e^+ = e^- + (\eta^* - \eta^-) \\ w^+ = \bar{K}_P(\eta^* - \eta^-) + \bar{K}_I e^- \\ \eta^+ = \bar{\nu}(x^-, \bar{\alpha} + w^+ \delta\alpha) \end{array} \right\} \begin{array}{l} x^- \notin \mathcal{S} \\ \\ \\ \\ \\ x^- \in \mathcal{S} \end{array} \quad (7.25)$$

where the extra states are used to store past values of $\bar{\nu}$ and w , and to implement the difference equation in the PI controller. The existence of an exponentially stable orbit is analyzed next.

Theorem 7.3 (Event-Based PI Control Applied to the Full Model, Case-I)

Assume the hypotheses of Theorem 7.2 and for a regular parameter α let Γ_α be any feedback satisfying the hypotheses of either Theorem 5.4 or Theorem 5.5, so that \mathcal{Z}_α is invariant under the swing phase dynamics in closed loop with Γ_α and is locally (finite-time or sufficiently exponentially quickly) attractive otherwise. Assume that \bar{K}_P and \bar{K}_I have been chosen so that (7.19) in closed loop with (7.23) has an exponentially stable equilibrium. Then the hybrid model (7.25) possesses an exponentially stable orbit and $\lim_{t \rightarrow \infty} (\eta^* - \eta(t)) = 0$.

Remark 7.1 An alternative realization of (7.25) can be given. Since from (7.17) the step length is fixed for all values of w , the average walking rate can be computed directly from its definition: step length divided by elapsed time

for a step. This leads to

$$\left. \begin{array}{l} \dot{x} = f(x) + g(x)\Gamma_{\bar{\alpha}+w\delta\alpha} \\ \dot{t} = 1 \\ \dot{e} = 0 \\ \dot{w} = 0 \\ x^+ = \Delta(x^-) \\ t^+ = 0 \\ e^+ = e^- + (\eta^* - \frac{p_2^h(q_{\bar{\alpha}}^-)}{t^-}) \\ w^+ = \bar{K}_P(\eta^* - \frac{p_2^h(q_{\bar{\alpha}}^-)}{t^-}) + \bar{K}_I e^- \end{array} \right\} \begin{array}{l} x^- \notin \mathcal{S} \\ x^- \in \mathcal{S} \end{array} \quad (7.26)$$

where $p_2^h(q_{\bar{\alpha}}^-)$ computes step length.

Remark 7.2 Exponential stability of the nominal orbit gives $|a_{11}| < 1$, which implies that $1 - a_{11} > 0$. From (5.71a) and (5.75), it can be assumed that $a_{21} > 0$. Hence, a sufficient condition for the DC-gain (7.22) to be nonzero is $b_1 > 0$ and $b_2 > 0$. Thus, PI control of average walking speed is possible if one can find $\delta\alpha$ satisfying (7.17) and

$$\sum_{i=1}^{N-1} \sum_{k=2}^{M-2} \delta\alpha_k^i \frac{\partial \rho(z, \alpha)}{\partial \alpha_k^i} \Big|_{z_{\bar{\alpha}}^*} > 0 \quad (7.27a)$$

$$\sum_{i=1}^{N-1} \sum_{k=2}^{M-2} \delta\alpha_k^i \frac{\partial \bar{\nu}(z, \alpha)}{\partial \alpha_k^i} \Big|_{z_{\bar{\alpha}}^*} > 0. \quad (7.27b)$$

Therefore, it is enough to find one pair of indices (k, i) , with $2 \leq k \leq M - 2$, and $1 \leq i \leq N - 1$, such that

$$\frac{\partial \rho(z, \alpha)}{\partial \alpha_k^i} \Big|_{z_{\bar{\alpha}}^*} \quad \text{and} \quad \frac{\partial \bar{\nu}(z, \alpha)}{\partial \alpha_k^i} \Big|_{z_{\bar{\alpha}}^*} \quad (7.28)$$

are both nonzero and have the same sign. This condition will be verified on the example of Section 7.4.

Remark 7.3 What if the nominal orbit is not exponentially stable (i.e., $|a_{11}| \geq 1$)? If (7.20) is stabilizable, then the nonzero DC-gain condition (7.22) is equivalent to stabilizability of (7.20) augmented with the integrator of (7.24). Exponentially stable regulation can be achieved therefore with a slight extension to the PI controller:

$$e[k+1] = e[k] + (\eta^* - \eta[k]) \quad (7.29)$$

$$w[k] = \bar{K}_P(\eta^* - \eta[k]) + \bar{K}_I e[k] + \bar{K}_Z(z[k] - z_{\alpha}^*[k]).$$

Remark 7.4 The PI-controller (7.23) was constructed on the basis of a one-parameter curve $\alpha_w := \bar{\alpha} + w\delta\alpha \in \mathcal{A}$. The same procedure can be extended to a multi-parameter curve, $\alpha_w := \bar{\alpha} + \sum_{i=1}^k w_i \delta\alpha_i \in \mathcal{A}$, where each $\delta\alpha_i$ satisfies (7.17) and $w = (w_1; \dots; w_k)$. This extension is used in [Chapter 9](#).

Case II: A control design is now presented that relaxes the conditions (7.17) so that parameter updates that change the posture of the robot at the end of the step are permitted. This will allow step length to be varied as well as torso lean angle, for example. Mathematically speaking, the additional complication is that the state space of $z[k+1] = \rho(z[k], \alpha[k])$, which is the step boundary $\mathcal{S} \cap \mathcal{Z}_\alpha$, also depends on the parameters. The solution, as given in Theorem 4.9, is to use dynamic extension and a form of “transition control” to account for the parameter dependence.

Let $\bar{\alpha}$ be a regular parameter value of the output (7.3) such that $\Delta(\mathcal{S} \cap \mathcal{Z}_{\bar{\alpha}}) \subset \mathcal{S} \cap \mathcal{Z}_{\bar{\alpha}}$ and $\rho_{\bar{\alpha}} : \mathcal{S} \cap \mathcal{Z}_{\bar{\alpha}} \rightarrow \mathcal{S} \cap \mathcal{Z}_{\bar{\alpha}}$ has an exponentially stable fixed point transversal to \mathcal{S} . Denote the fixed point by $z_{\bar{\alpha}}^*$. Let $\delta\alpha \in \mathbb{R}^{(N-1) \times (M+1)}$ be such that $\delta\alpha \neq 0$ and

$$(\delta\alpha)_0 = (\delta\alpha)_1 = 0. \quad (7.30)$$

Then, for $w \in \mathbb{R}$ sufficiently small in magnitude, each value of the one-parameter curve

$$\bar{\alpha}_w := \bar{\alpha} + w\delta\alpha \in \mathbb{R}^{(N-1) \times (M+1)} \quad (7.31)$$

is also regular. However, in general, $\Delta(\mathcal{S} \cap \mathcal{Z}_{\bar{\alpha}_w}) \not\subset \mathcal{S} \cap \mathcal{Z}_{\bar{\alpha}_w}$, which means the controller design cannot be carried out on the restriction map of the hybrid zero dynamics, as in Case-I. This lack of invariance, which arises from the weaker conditions on $\delta\alpha$ in (7.30), as opposed to (7.17), makes the analysis and design of the controller more involved.

Based on Theorem 6.1, for sufficiently small real values v and w , define

$$a_0(\bar{\alpha}, v) := H_0 R H^{-1} \begin{bmatrix} (\bar{\alpha}_v)_{M_{\bar{\alpha}}} \\ \theta_{\bar{\alpha}_v}^- \end{bmatrix} \quad (7.32)$$

and

$$\begin{aligned} a_1(\bar{\alpha}, v, w) &:= H_0 \Delta_{\dot{q}} H^{-1} \\ &\cdot \begin{bmatrix} M_{\bar{\alpha}} \\ \theta_{\bar{\alpha}_v}^- - \theta_{\bar{\alpha}_v}^+ ((\bar{\alpha}_v)_{M_{\bar{\alpha}}} - (\bar{\alpha}_v)_{M_{\bar{\alpha}}-1}) \\ 1 \end{bmatrix} \\ &\cdot \frac{\theta_{\bar{\alpha}_w}^- - \theta_{\bar{\alpha}_w}^+}{M_{\bar{\alpha}}} c \Delta_{\dot{q}} \omega_{\bar{\alpha}_v}^- + a_0(\bar{\alpha}, v); \end{aligned} \quad (7.33)$$

in addition, set

$$a(\bar{\alpha}, v, w) := [a_0(\bar{\alpha}, v), a_1(\bar{\alpha}, v, w), (\bar{\alpha})_2, \dots, (\bar{\alpha})_{M_{\bar{\alpha}}}] + w\delta\alpha. \quad (7.34)$$

Theorem 6.1 implies that for all $\bar{v}, v, w \in \mathbb{R}$ sufficiently small,

$$\Delta(\mathcal{S} \cap \mathcal{Z}_{a(\bar{\alpha}, \bar{v}, v)}) \subset \mathcal{Z}_{a(\bar{\alpha}, v, w)}. \quad (7.35)$$

Because $\mathcal{S} \cap \mathcal{Z}_\alpha$ only depends on the last two columns of the parameter matrix α , it follows that by construction of a ,

$$\mathcal{S} \cap \mathcal{Z}_{a(\bar{\alpha}, \bar{v}, v)} = \mathcal{S} \cap \mathcal{Z}_{\bar{\alpha}_v} \quad \text{and} \quad \mathcal{S} \cap \mathcal{Z}_{a(\bar{\alpha}, v, w)} = \mathcal{S} \cap \mathcal{Z}_{\bar{\alpha}_w}. \quad (7.36)$$

Hence, $P_{a(\bar{\alpha}, v, w)} : \mathcal{S} \cap \mathcal{Z}_{\bar{\alpha}_v} \rightarrow \mathcal{S} \cap \mathcal{Z}_{\bar{\alpha}_w}$.

To construct the equivalent of (7.19), denote the restriction map by

$$\bar{\rho}_{v,w} := P_{a(\bar{\alpha}, v, w)}|_{\mathcal{S} \cap \mathcal{Z}_{\bar{\alpha}_v}}, \quad (7.37)$$

and define a single-input, single-output dynamic system on

$$\{(\mathcal{S} \cap \mathcal{Z}_{\bar{\alpha}_v}, v) \mid v \in \mathbb{R}\} \times \mathbb{R} \quad (7.38)$$

by

$$\begin{aligned} z[k+1] &= \bar{\rho}(z[k], v[k], w[k]) \\ v[k+1] &= w[k] \\ \eta[k+1] &= \bar{\nu}(z[k], a(\bar{\alpha}, v[k], w[k])) \\ y_{\text{vel}}[k] &= \eta[k] \end{aligned} \quad (7.39)$$

with input $w \in \mathbb{R}$, output $y_{\text{vel}} \in \mathbb{R}$ equal to the average walking rate, and $\bar{\rho}(z, v, w) := \bar{\rho}_{v,w}(z)$. Its linearization is

$$\begin{aligned} \delta z[k+1] &= a_{11} \delta z[k] + a_{12} \delta v[k] + b_1 \delta w[k] \\ \delta v[k+1] &= \delta w[k] \\ \delta \eta[k+1] &= a_{21} \delta z[k] + a_{22} \delta v[k] + b_2 \delta w[k] \\ \delta y_{\text{vel}}[k] &= \delta \eta[k] \end{aligned} \quad (7.40)$$

where

$$\begin{aligned} a_{11} &:= \frac{\partial \bar{\rho}}{\partial z}(z, v, w) & a_{12} &:= \frac{\partial \bar{\rho}}{\partial v}(z, v, w) \\ a_{21} &:= \frac{\partial \bar{\nu}}{\partial z}(z, v, w) & a_{22} &:= \frac{\partial \bar{\nu}}{\partial v}(z, v, w) \\ b_1 &:= \frac{\partial \bar{\rho}}{\partial w}(z, v, w) & b_2 &:= \frac{\partial \bar{\nu}}{\partial w}(z, v, w), \end{aligned} \quad (7.41)$$

and the right-hand sides of (7.41) are evaluated at $z = z_{\bar{\alpha}}^*$, $v = 0$, and $w = 0$. The linearized system (7.40) is exponentially stable if, and only if, $|a_{11}| < 1$. The DC-gain is nonzero if, and only if,

$$a_{21}(b_1 + a_{12}) + (a_{22} + b_2)(1 - a_{11}) \neq 0. \quad (7.42)$$

Theorem 7.4 (Event-Based PI Control Applied to the Hybrid Zero Dynamics, Case-II)

Let $\bar{\alpha}$ be a regular parameter value of the output (7.3) such that $\Delta(\mathcal{S} \cap \mathcal{Z}_{\bar{\alpha}}) \subset \mathcal{S} \cap \mathcal{Z}_{\bar{\alpha}}$ and assume there exists an exponentially stable periodic orbit in $\mathcal{Z}_{\bar{\alpha}}$ transversal to \mathcal{S} . Denote the corresponding fixed point of the restricted Poincaré return map by $z_{\bar{\alpha}}^*$. Assume there exists $\delta\alpha$ satisfying (7.30) and such that the nonzero DC-gain condition (7.42) holds. Then average walking rate can be regulated via PI control. In particular, there exist $\epsilon^* > 0$, and scalars \bar{K}_P and \bar{K}_I such that for all η^* satisfying $|\eta^* - \bar{\nu}(z_{\bar{\alpha}}^*, \bar{\alpha})| < \epsilon^*$, the system consisting of (7.39) in closed loop with the proportional plus integral controller

$$\begin{aligned} e[k+1] &= e[k] + (\eta^* - \eta[k]) \\ w[k] &= \bar{K}_P(\eta^* - \eta[k]) + \bar{K}_Ie[k] \end{aligned} \quad (7.43)$$

has an exponentially stable equilibrium, and thus, when initialized sufficiently near the equilibrium, $\lim_{k \rightarrow \infty}(\eta^* - \eta[k]) = 0$.

Proof The linear system (7.40) is exponentially stable because the exponential stability of the fixed-point $z_{\bar{\alpha}}^*$ implies that $|a_{11}| < 1$. This, combined with the DC-gain being nonzero, implies the existence of a PI controller of the form

$$\begin{aligned} \delta e[k+1] &= \delta e[k] + (\delta\eta^* - \delta\eta[k]) \\ \delta w[k] &= \bar{K}_P(\delta\eta^* - \delta\eta[k]) + \bar{K}_I\delta e[k] \end{aligned} \quad (7.44)$$

such that the closed-loop system (7.40) with (7.44) is exponentially stable and satisfies $\lim_{k \rightarrow \infty}(\delta\eta^* - \delta\eta[k]) = 0$, where $\delta\eta^* := (\eta^* - \bar{\nu}(z_{\bar{\alpha}}^*, \bar{\alpha}))$. Because the closed loop of (7.40) with (7.44) is the linearization of (7.39) in closed loop with (7.43), the result follows.

The realization of the controller on the full-dimensional model proceeds as in Case-I, as does the corresponding stability analysis. The details are left to the reader.

7.3.3 Design and Analysis Based on the Full-Dimensional Model

For a regular value α of output (7.3), let Γ_α be an input-output linearizing controller constructed as in Theorem 5.5, and let $P_\alpha : \mathcal{S} \rightarrow \mathcal{S}$ denote the Poincaré return map of the closed-loop system (7.15). As before, to emphasize the dependence on α , for $x \in \mathcal{S}$, let $P(x, \alpha) := P_\alpha(x)$; similarly, let $\bar{\nu}(x, \alpha) := \bar{\nu}_\alpha(x)$.

Let $\bar{\alpha}$ be a fixed regular value of α such that $P_{\bar{\alpha}} : \mathcal{S} \rightarrow \mathcal{S}$ has an exponentially stable fixed point transversal to \mathcal{S} and denote the fixed point by $x_{\bar{\alpha}}^*$. Let $\delta\alpha \in \mathbb{R}^{(N-1) \times (M+1)}$ be nonzero. Then, for $w \in \mathbb{R}$ sufficiently small in magnitude, each value of the one-parameter curve $\bar{\alpha} + w\delta\alpha \in \mathbb{R}^{(N-1) \times (M+1)}$ is also

regular. Because $P_{\bar{\alpha}+w\delta\alpha} : \mathcal{S} \rightarrow \mathcal{S}$, the following single-input, single-output dynamic system can be defined,

$$\begin{aligned} x[k+1] &= P(x[k], \bar{\alpha} + w[k]\delta\alpha) \\ \eta[k+1] &= \bar{\nu}(x[k], \bar{\alpha} + w[k]\delta\alpha) \\ y_{\text{vel}}[k] &= \eta[k], \end{aligned} \quad (7.45)$$

with $2N$ -dimensional state space $\mathcal{S} \times \mathbb{R}$, input $w \in \mathbb{R}$, and output equal to average walking rate, $y_{\text{vel}} \in \mathbb{R}$. Its linearization is

$$\begin{aligned} \delta x[k+1] &= \bar{A}_{11}\delta x[k] + \bar{B}_1\delta w[k] \\ \delta\eta[k+1] &= \bar{A}_{21}\delta x[k] + \bar{B}_2\delta w[k] \\ \delta y_{\text{vel}}[k] &= \delta\eta[k], \end{aligned} \quad (7.46)$$

where⁸

$$\begin{aligned} \bar{A}_{11} &:= \frac{\partial P}{\partial x}(x, \bar{\alpha} + w\delta\alpha) \Big|_{\substack{x=x^*_\alpha \\ w=0}} & \bar{B}_1 &:= \frac{\partial P}{\partial w}(x, \bar{\alpha} + w\delta\alpha) \Big|_{\substack{x=x^*_\alpha \\ w=0}} \\ \bar{A}_{21} &:= \frac{\partial \bar{\nu}}{\partial x}(x, \bar{\alpha} + w\delta\alpha) \Big|_{\substack{x=x^*_\alpha \\ w=0}} & \bar{B}_2 &:= \frac{\partial \bar{\nu}}{\partial w}(x, \bar{\alpha} + w\delta\alpha) \Big|_{\substack{x=x^*_\alpha \\ w=0}}. \end{aligned} \quad (7.47)$$

The linearized system (7.46) is exponentially stable if, and only if, all of the eigenvalues of \bar{A}_{11} have magnitude less than one. An easy computation shows that its DC-gain is nonzero if, and only if,

$$\bar{A}_{21} (I_{(2N-1) \times (2N-1)} - \bar{A}_{11})^{-1} \bar{B}_1 + \bar{B}_2 \neq 0. \quad (7.48)$$

Theorem 7.5 (Event-Based PI Control Designed on the Full-Dimensional Model)

Let $\bar{\alpha}$ a given regular value of α such that $P_{\bar{\alpha}} : \mathcal{S} \rightarrow \mathcal{S}$ has an exponentially stable fixed point transversal to \mathcal{S} and denote the fixed point by $x^*_{\bar{\alpha}}$. Let $\delta\alpha \in \mathbb{R}^{(N-1) \times (M+1)}$ be such that the nonzero DC-gain condition, (7.48), is met. Then average walking rate can be regulated via PI control. In particular, there exist $\epsilon^* > 0$, and scalars \bar{K}_P and \bar{K}_I such that for all η^* satisfying $|\eta^* - \bar{\nu}(z^*_{\bar{\alpha}}, \bar{\alpha})| < \epsilon^*$, the system consisting of (7.45) in closed loop with the proportional plus integral controller

$$\begin{aligned} e[k+1] &= e[k] + (\eta^* - \eta[k]) \\ w[k] &= \bar{K}_P(\eta^* - \eta[k]) + \bar{K}_Ie[k] \end{aligned} \quad (7.49)$$

⁸We have abused notation and not made the distinction between x as a point in $T\mathcal{Q}$ that lies in \mathcal{S} and x as a coordinate on \mathcal{S} . Note that $T\mathcal{Q}$ has dimension $2N$ and \mathcal{S} has dimension $2N - 1$.

has an exponentially stable equilibrium, and thus, when initialized sufficiently near the equilibrium, $\lim_{k \rightarrow \infty} (\eta^* - \eta[k]) = 0$.

Proof The matrix \bar{A}_{11} is the Jacobian of $P_{\bar{\alpha}}$ evaluated at $x_{\bar{\alpha}}^*$. Hence, by Corollary 4.1, the exponential stability of the fixed-point $x_{\bar{\alpha}}^*$ implies that the eigenvalues of \bar{A}_{11} have magnitude less than one, proving that the linear system (7.46) is exponentially stable. This property combined with the DC-gain being nonzero implies the existence of a PI controller of the form

$$\begin{aligned}\delta e[k+1] &= \delta e[k] + (\delta\eta^* - \delta\eta[k]) \\ \delta w[k] &= \bar{K}_P(\delta\eta^* - \delta\eta[k]) + \bar{K}_I\delta e[k]\end{aligned}\quad (7.50)$$

such that the closed-loop system (7.46) with (7.50) is exponentially stable and satisfies $\lim_{k \rightarrow \infty} (\delta\eta^* - \delta\eta[k]) = 0$, where $\delta\eta^* := \eta^* - \bar{\nu}(z_{\bar{\alpha}}^*, \alpha)$. Because the closed loop of (7.46) with (7.50) is the linearization of (7.45) in closed loop with (7.49), the result follows.

Remark 7.5 If $\bar{\alpha}$ in Theorem 7.5 is such that $\Delta(\mathcal{S} \cap \mathcal{Z}_{\bar{\alpha}}) \subset \mathcal{S} \cap \mathcal{Z}_{\bar{\alpha}}$, then the stability of the fixed point can be checked on the basis of the restricted Poincaré map.

7.4 Examples

An example is presented that shows how an event-based PI-controller can induce walking at a continuum of rates while providing stabilization and a modest amount of robustness to disturbances, to parameter mismatch between the design model and the actual robot, and to structural mismatch between the design model and the actual robot. The results are illustrated via three simulations on the five-link model studied in Section 6.6.2, with a controller verifying the assumptions of Case-I. An example using Case-II is given in the next chapter.

7.4.1 Choice of $\delta\alpha$

For the following three examples, finite differences were used to verify the sufficient condition shown in (7.27) for several values of i and k . In this way, it was determined that adjusting the angle of the swing leg femur during mid-step would have a sufficiently strong effect on the average walking speed (this corresponded to $i = 2$ and $k = 3$). Hence, $\delta\alpha$ was chosen to be all zeros with the exception of $\delta\alpha_3^2$ which was set to 1.

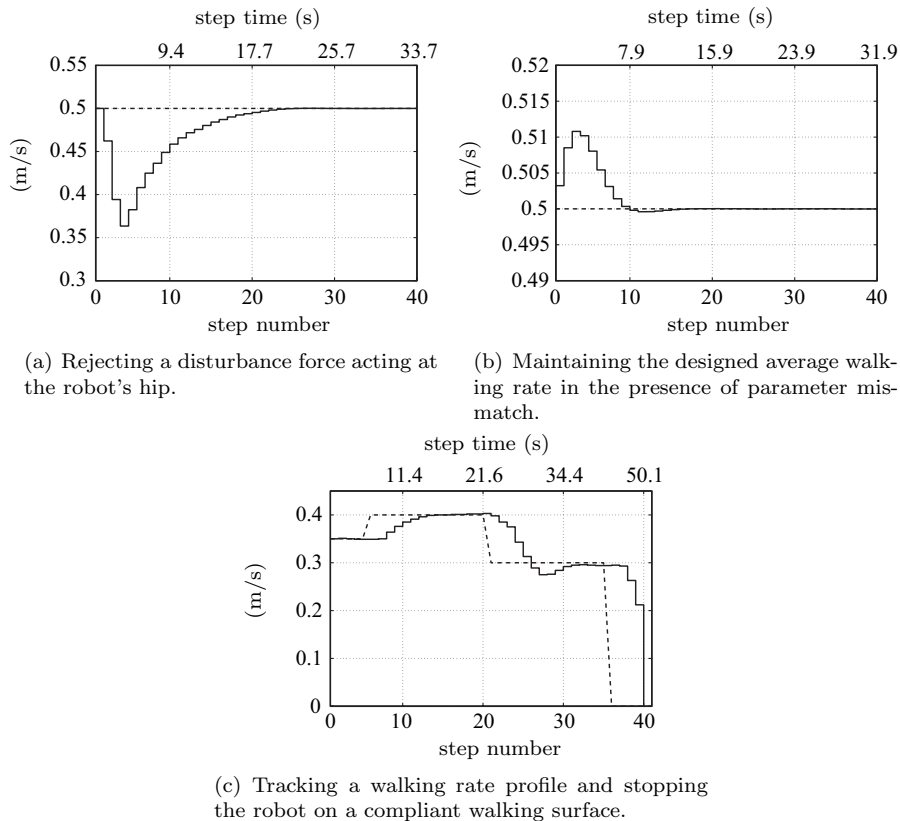


Figure 7.4. Illustration of an event-based PI control to handle a constant disturbance, parameter mismatch, and model mismatch. Commanded (dashed) versus actual (solid) average walking rate.

7.4.2 Robustness to Disturbances

This example will illustrate robustness to disturbances by simulation of the robot with an external force acting on the hips. Event-based PI control is used to reject a 3 N external force acting horizontally at the robot's hip opposite to the direction of walking.

The robot is initialized at the fixed point of a controller with average walking rate equal to 0.50 m/s. Event-based PI control with gains $\bar{K}_P = 5$ and $\bar{K}_I = 2$ and set-point $\eta^* = 0.5$ is applied starting on the second step coincident with the application of a constant 3 N force acting at the hips. [Figure 7.4\(a\)](#) depicts the actual walking rate versus the commanded value of 0.50 m/s. The peak torque for this example is 70.1 Nm, about half of the 150 Nm that is possible with the motors and gearing of RABBIT.

Without application of event-based PI control, the 3 N force slows the robot to a stop; i.e., the average walking rate slows from 0.50 m/s to 0 m/s.

7.4.3 Robustness to Parameter Mismatch

For this example, event-based PI control is used to maintain the designed average walking rate in the presence of parameter mismatch between the design model and the actual model. The actual model's torso mass, torso inertia, tibia mass and tibia inertia were set to 110 percent of the design model's values while the actual model's femur mass and femur inertia were set to 90 percent of those of the design model. The robot is initialized at the fixed point of a controller whose average walking rate corresponds to 0.50 m/s. Event-based PI control with gains $\bar{K}_P = 5$ and $\bar{K}_I = 2$ and set-point $\eta^* = 0.5$ is applied starting on the first step. Figure 7.4(b) illustrates the actual walking rate versus the commanded rate of 0.50 m/s. The peak torque for this example is 53.8 Nm, about one third of the 150 Nm possible.

Without application of event-based PI control, the parameter mismatch changes the robot's average walking rate from 0.50 m/s to 0.54 m/s.

7.4.4 Robustness to Structural Mismatch

This example will illustrate robustness to structural mismatch between the design model and the evaluation model. In addition, the robot will be commanded to track a walking rate profile and then slow to a stop using a single within-stride controller in conjunction with event-based PI control.

The robot model of the previous two examples is used, except that instead of assuming a rigid impact, the *compliant impact model* with dynamic friction of [176] is used.⁹ A nominal controller was designed on the basis of the rigid contact model to have an average walking rate of 0.30 m/s. When

⁹See also [Section 9.6.1](#).

implemented on the robot with the compliant model, this yielded an average walking rate of 0.35 m/s.

In the simulation, the robot is initialized near a periodic orbit of the compliant model. Event-based PI control with gains $\bar{K}_P = 0.3$ and $\bar{K}_I = 0.03$ is applied starting on the sixth step with set-point $\eta^* = 0.40$. On the twenty-first step the set-point is changed to $\eta^* = 0.30$. To transition from walking to a stable standing position, on the thirty-sixth step the set-point of the event-based PI control was set to $\eta^* = 0$. Using this technique slowed the robot until it did not have enough energy to make a step, thus stopping the robot.¹⁰

The peak torque for this example is 52 Nm, about one third of the 150 Nm possible. [Figure 7.4\(c\)](#) gives the commanded versus actual average walking rate.

¹⁰The robot will, in fact, continue to rock back and forth, alternating impacts with each leg, and decreasing the kinetic energy of the robot with each impact.

Experimental Results for Walking

This chapter presents the results of applying the theory of [Chapters 6 and 7](#) to RABBIT, a bipedal robot that was described in Section 2.1 (see [Fig. 8.1](#)), and the result of applying the theory of Chapter 6 to ERNIE, a bipedal robot that was described in detail in Section 2.2 (see [Fig. 8.3](#)). Recall that for both RABBIT and ERNIE five links are connected by revolute joints to form two symmetric legs and a torso. Actuators supply torque at each of the four internal joints: an actuator at each knee and an actuator at each connection of the torso and a femur. RABBIT’s actuators are identical and capable of producing peak torque of 150 Nm each. ERNIE’s actuators are also identical and capable of producing peak torque of 28 Nm each (see [Section 2.2.6](#) for a comment on ERNIE’s motor and gearhead pairs). To prevent motions in the frontal plane, RABBIT and ERNIE were constructed with booms attached at the hip. Both robots have no feet and no means of supplying actuation between their stance leg ends and the ground.

In addition to reporting the results of the walking experiments, this chapter provides further details on certain aspects of RABBIT’s and ERNIE’s experimental setups that are relevant to control design and are not captured by the model presented in [Chapter 3](#). The chapter begins with a discussion of the experimental issues. The actual implementation of the control algorithms follows. The chapter concludes with a discussion of experiments.

8.1 Implementation Issues

8.1.1 RABBIT’s Implementation Issues

This subsection presents three important aspects of RABBIT that are not addressed by the model given in Section 3.4, namely, the additional dynamics introduced by the boom used to constrain RABBIT’s motions to be planar, RABBIT’s gear reducers, and the irregular, nonrigid surface on which RABBIT walks. These effects are accommodated in the controller designs for the experiments presented in Section 8.3 so that the experimental, closed-loop performance will more closely match the design specifications.

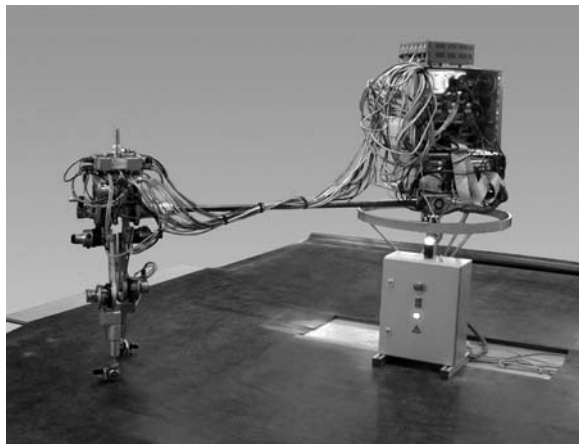


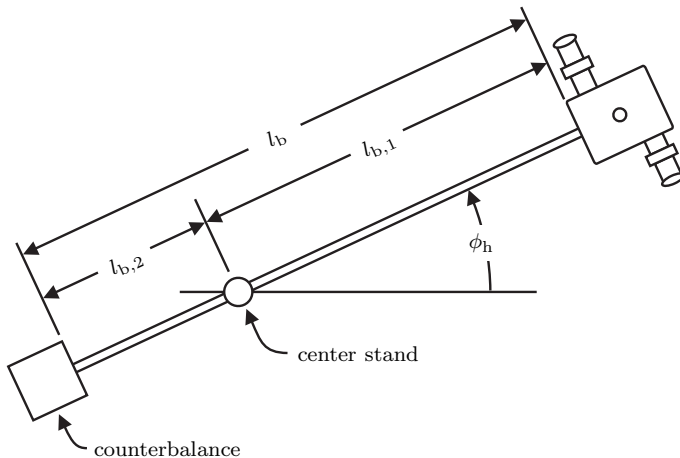
Figure 8.1. The biped prototype RABBIT’s experimental setup.

8.1.1.1 Modeling the Boom

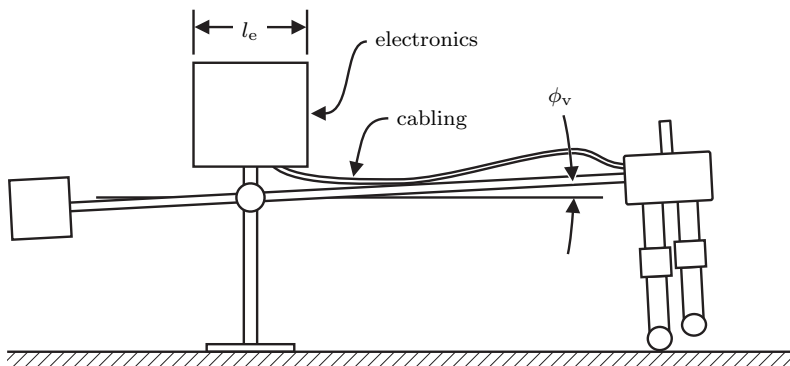
The boom attached to the hip constrains RABBIT’s motions to a “sagittal plane” that is tangent to a sphere centered at the universal joint that connects the boom to the center stand (see Figs. 2.3, 8.1, and 8.2). The boom system consists of the boom, center stand, counterbalance, and cabling. “Training wheels,” were attached to the boom to provide a measure of safety. The post of the training wheels has a prismatic joint with a stop to prevent the robot’s hip from dropping so low that the knees could strike the ground, but otherwise does not support the robot’s weight. The boom system also includes two encoders at the universal joint to measure horizontal and vertical angular displacement of the boom about the center stand.

An important consideration with a boom system is how to connect power and communications cabling between the robot and the support electronics. Unless a slip ring is used, cabling connected to the support electronics will become twisted or wound as the robot circles the center stand. Unfortunately, a slip ring was not installed at the time when the experiments reported here were performed, and the cables had to be unwound after each experiment.

The inertia of the boom system is significant enough to require incorporation into RABBIT’s model. The inertia has four components due to (i) the boom connecting RABBIT, the center stand, and the counterbalance, (ii) the counterbalance, (iii) the cabling connecting RABBIT to the support electronics, and (iv) the support electronics (see Figs. 8.1 and 8.2). Since the training wheels are not always used, and since they are relatively light, their inertia is



(a) Overhead view of RABBIT's experimental setup. For clarity, the electronics are not drawn.



(b) Side view of RABBIT's experimental setup.

Figure 8.2. Various dimensions of RABBIT's experimental setup.

not included. The inertia may be approximated as

$$I_s = \underbrace{\frac{1}{3} \frac{m_b}{l_b} (l_{b,1}^3 + l_{b,2}^3)}_{\text{boom}} + \underbrace{m_w l_{b,2}^2}_{\text{counterbalance}} + \underbrace{\frac{1}{3} m_c l_{b,1}^2}_{\text{cabling}} \quad (8.1)$$

$$I_e = \frac{1}{12} m_e l_e^2. \quad (8.2)$$

This results in additional kinetic energy,

$$K_a = \frac{1}{2} I_s (\dot{\phi}_h^2 + \dot{\phi}_v^2) + \frac{1}{2} I_e \dot{\phi}_h^2, \quad (8.3)$$

where ϕ_h and ϕ_v are the horizontal and vertical angular displacements of RABBIT about the center stand (see Fig. 8.2). The angles ϕ_h and ϕ_v may be approximated by

$$\phi_h \approx \frac{p_H^h(q) - p_H^h(q_0)}{l_{b,1}} \quad \text{and} \quad \phi_v \approx \frac{p_H^v(q) - p_H^v(q_0)}{l_{b,1}}, \quad (8.4)$$

where q_0 is RABBIT's configuration at the beginning of a step and p_H^h and p_H^v are the horizontal and vertical positions of the hip.

There is also additional potential energy due to the boom, the counterbalance, and the cabling,

$$V_a = \underbrace{\frac{1}{2} g_0 \frac{m_b}{l_b} (l_{b,1}^2 - l_{b,2}^2) \sin(\phi_v)}_{\text{boom}} - \underbrace{g_0 m_w l_{b,2} \sin(\phi_v)}_{\text{counterbalance}} + \underbrace{\frac{1}{2} g_0 m_c l_{b,1} \sin(\phi_v)}_{\text{cabling}}. \quad (8.5)$$

Note that the counterbalance mass may be chosen to negate the potential energy due to the boom and cabling. In the experiments described in Section 8.3, no counterbalance was used; the required counterbalance of 52 kg could not be securely fastened to the boom because of the short length of $l_{b,2}$.

The controllers used for the experiments reported in Section 8.3 were designed using equations of motion which included a model of the boom mass and inertia. These equations of motion were calculated by first forming an updated Lagrangian—the planar model's Lagrangian with the kinetic energy K_a added and the potential energy V_a subtracted—and then using the method of Lagrange. Table 8.1 gives the parameter values for the boom system setup used for the experiments.

Aside from the ability to counterbalance the boom, the choice of boom length has other important considerations. The longer the boom, the better the approximation of RABBIT as a planar mechanical system; however, the

Table 8.1. RABBIT's experimental platform parameters.

| Model Parameter | Units | Label | Value |
|--------------------------|-------|-----------|-------|
| Boom length | m | l_b | 1.5 |
| Hip to stand distance | m | $l_{b,1}$ | 1.4 |
| Stand height | m | l_s | 1.4 |
| Boom mass | kg | m_b | 5.0 |
| Cable mass | kg | m_c | 2.0 |
| Counterbalance mass | kg | m_w | 0.0 |
| Support electronics mass | kg | m_e | 20.0 |

longer the boom, the greater the dynamic effects of the additional kinetic (8.3) and potential (8.5) energies, and the greater the flexibility of the boom. Boom flexibility was found to be of great significance experimentally. The boom was initially chosen to be 3 m in length. Flexing of the tubular steel boom resulted in forces on RABBIT's hip large enough to cause foot slippage. Consequently, the 3 m boom was swapped for a 1.5 m boom, and the foot slippage problem was solved.

8.1.1.2 Gear Reducers and Joint Friction

To allow smaller, lighter-weight motors to be used, RABBIT has gear reducers between its motors and links. The gear reducers have two important effects on RABBIT's dynamics. The first effect is to add significant joint friction, which effectively eliminates all passive motions of the joints. The second effect is to approximately decouple the robot's dynamics, leaving reflected rotor inertia as the only significant inertial load on the motor. Both effects were taken into consideration in the control implementation described in Section 8.2.

The joint friction was modeled by viscous and static friction terms,

$$F(q, \dot{q}) := F_v \dot{q} + F_s \operatorname{sgn}(\dot{q}), \quad (8.6)$$

where

$$F_v = \operatorname{diag}(F_{v,H}, F_{v,H}, F_{v,K}, F_{v,K}, 0) \quad (8.7a)$$

$$F_s = \operatorname{diag}(F_{s,H}, F_{s,H}, F_{s,K}, F_{s,K}, 0). \quad (8.7b)$$

The identified values of RABBIT's frictional parameters are given in [Table 6.3](#). Note that both the viscous and static friction values are substantial; at the hip, the static friction is approximately ten percent of the motor/gear reducer system's peak available torque of 150 Nm.

Another, in some ways desirable, effect of gear reducers is to scale the inertial load experienced by the motors. This scaling approximately decouples the robot's actuated dynamics so that the only significant dynamic terms are

the inertia of the motors' rotors and the unactuated dynamics. Writing the model in motor coordinates makes this evident.

Define the motor shaft coordinates $\bar{q} := N_g q$ where

$$N_g = \text{diag}(n_g, n_g, n_g, n_g) \quad (8.8)$$

and n_g are the gear reducers' gear ratio (the four gear reducers are identical). Since the absolute angle, q_5 , is unactuated, $(N_g)_{55} = 1$. When the motors' rotor inertias and the gear ratios are included in RABBIT's swing phase model, (3.8), and the model is written in the motor shaft coordinates, the equations of motion become

$$\begin{bmatrix} \frac{1}{n_g^2} D_{1,1} + I_a I_{4 \times 4} & \frac{1}{n_g} D_{1,2} \\ \frac{1}{n_g} D'_{1,2} & (D)_{5,5} \end{bmatrix} \ddot{\bar{q}} + \begin{bmatrix} \frac{1}{n_g^2} C_{1,1} & \frac{1}{n_g} C_{1,2} \\ \frac{1}{n_g} C'_{1,2} & (C)_{5,5} \end{bmatrix} \dot{\bar{q}} + N_g^{-1} G - N_g^{-1} F = B \bar{u} \quad (8.9)$$

where $\bar{u} := (\bar{u}_1; \bar{u}_2; \bar{u}_3; \bar{u}_4)$ is the vector of torques supplied at the output shafts of the motors and I_a is the motors' rotor inertia (the four motors are identical). The result is that the actuated dynamics are approximately decoupled and the block of actuated dynamics is approximately decoupled from the unactuated dynamics. The motors' rotor inertia and gear ratio are given in [Table 6.3](#).

8.1.1.3 The Walking Surface

The floor on which RABBIT walks is concrete with 30 cm wide cabling access trenches covered with 4 mm steel plates. In preliminary experiments, it was found that after stepping on one of the four plates crossing RABBIT's path, RABBIT would slow significantly. Since the gait—change in the shape over a step—was the same, this indicated that the energy dissipation due to impacting the concrete surface is less than the energy dissipation due to impacting the steel plates. To help make the walking surface uniform, the floor was covered with 1.5 cm particle board, which was then covered with a layer of 3 mm rubber (see [Fig. 8.1](#)). An added benefit was an increased coefficient of friction for the walking surface. It was also hoped that the rubber layer would extend the life of RABBIT by providing a modest amount of compliance.

8.1.2 ERNIE's Implementation Issues

Some of the aspects of ERNIE that are not captured by the model presented in Section 3.4 are shared with RABBIT, and one is unique to ERNIE. The aspects that are shared with RABBIT are the boom dynamics and the approximate decoupling effect of the robot's dynamics due to the gear reducers; the other two aspects associated with RABBIT, joint friction and walking

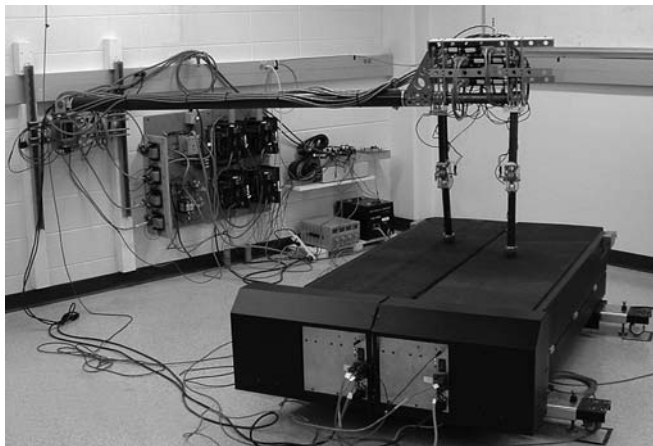


Figure 8.3. The biped prototype ERNIE's experimental setup.

surface uniformity, do not apply to ERNIE since its joint friction is small and since it walks on a treadmill, which has a uniform walking surface. The aspect that is unique to ERNIE is the dynamics of the robot-treadmill interaction. These aspects impacted the controller designs for the experiments presented in Section 8.3.

ERNIE's parameters, which are given in [Table 8.2](#), were determined from the 3D solid modeling software used in its design. Since ERNIE's joint friction was found empirically to be small, it was not identified and assumed to be zero in implementation; see [\(8.15\)](#). The measurement conventions of the parameters are the same as RABBIT's; see [Fig. 6.14](#). [Table 8.3](#) gives the parameter values for the boom system setup used for the experiments.

8.1.2.1 Robot-Treadmill Interaction

Lateral compliance of ERNIE's treadmill's belts provides a restorative torque that helps to stabilize the average position of ERNIE on the treadmill when walking. Consider [Fig. 8.4](#) which depicts a top view of ERNIE walking on its treadmill with the inner leg as the stance leg. The desired average value of ϕ_h over a step is zero. That is, the desired average orientation of the robot's sagittal plane over a step is parallel to the treadmill's direction of progression. Since the leg ends do not readily slip on the treadmill's surface, when $\phi_h \neq 0$ the lateral compliance of the treadmill's belts provides a restorative torque that may be approximated as follows.

Assume the treadmill's belts have a lateral stiffness of k_{belt} . The force experienced at the stance leg in the lateral direction of the treadmill may be approximated as

$$F_{\text{belt}} \approx k_{\text{belt}}d = k_{\text{belt}}l_{b,1}(1 - \cos(\phi_h)). \quad (8.10)$$

Table 8.2. Identified link parameters for ERNIE. The friction parameters were not identified.

| Model Parameter | Units | Label | Value |
|---------------------|-------------------|-----------|-------|
| Mass | kg | M_T | 13.6 |
| | | M_f | 1.5 |
| | | M_t | 1.0 |
| Length | m | l_T | 0.28 |
| | | l_f | 0.36 |
| | | l_t | 0.36 |
| Inertia | kg·m ² | I_T | 0.09 |
| | | I_f | 0.02 |
| | | I_t | 0.02 |
| Mass center | m | p_T^M | 0.14 |
| | | p_f^M | 0.13 |
| | | p_t^M | 0.12 |
| Viscous friction | Ns | $F_{v,H}$ | - |
| | | $F_{v,K}$ | - |
| Static friction | Nm | $F_{s,H}$ | - |
| | | $F_{s,K}$ | - |
| Gear ratio | - | n_g | 91 |
| Motor rotor inertia | kg·m ² | I_a | 0.02 |

Thus, the restorative torque may be approximated as

$$\tau_{\text{belt}} \approx F_{\text{belt}} l_{b,1} \sin(\phi_h) = k_{\text{belt}} l_{b,1}^2 \sin(\phi_h)(1 - \cos(\phi_h)). \quad (8.11)$$

This torque acts to stabilize average position of the robot when walking on the treadmill.

8.2 Control Algorithm Implementation: Imposing the Virtual Constraints

The swing phase zero dynamics, (5.40) or (5.47), is independent of the feedback used to zero the associated output. The feedback introduced in Section 5.5.1, a computed torque prefeedback plus finite-time converging controllers, is one possible feedback controller. The input-output linearizing

Table 8.3. ERNIE's experimental platform parameters.

| Model Parameter | Units | Label | Value |
|--------------------------|-------|-----------|-------|
| Boom length | m | l_b | 2.2 |
| Hip to stand distance | m | $l_{b,1}$ | 2.2 |
| Stand height | m | l_s | 0.99 |
| Boom mass | kg | m_b | 2.7 |
| Cable mass | kg | m_c | 2.2 |
| Counterbalance mass | kg | m_w | N/A |
| Support electronics mass | kg | m_e | N/A |

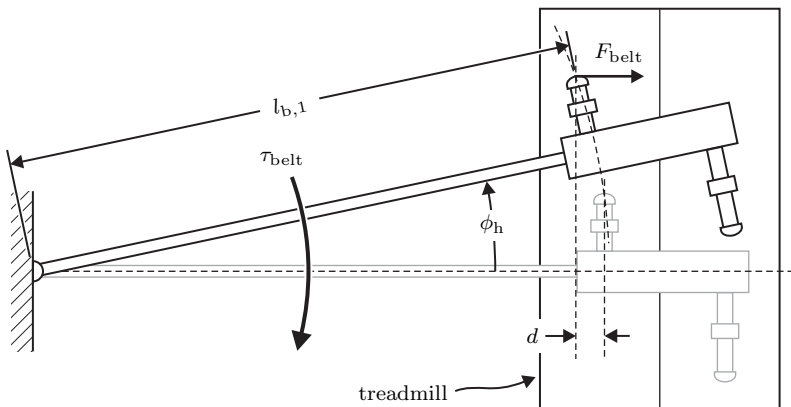


Figure 8.4. Top view of ERNIE's experimental setup. Lateral compliance in the treadmill belts provides a restorative torque that tends to keep the robot's sagittal plane aligned with the treadmill. The position of ERNIE when $\phi_h = 0$ is depicted in gray.

prefeedback (5.88) decouples the output dynamics, resulting in a chain of four double integrators. In light of the decoupling effect of the gear reducers (see Section 8.1.1.2) and the likely inaccuracy of the parameter identification, high-gain decoupled PD controllers were used instead to impose the virtual constraints on RABBIT and ERNIE. It was found that this control was able to zero the outputs sufficiently well to induce walking with dynamic characteristics very similar to the theoretical design.

As in the example of Section 6.6.2.1, for the experiments involving RABBIT and ERNIE, outputs of the form (6.3), with $h_0(q)$ and $\theta(q)$ as in (6.4), were used with

$$H_0 = [I \ 0] \quad (8.12a)$$

$$c = [-1 \ 0 \ -1/2 \ 0 \ -1], \quad (8.12b)$$

which results in the output

$$y = (q_1; q_2; q_3; q_4) - h_d \circ \theta(q). \quad (8.13)$$

[Fig. 6.13\(b\)](#) gives $\theta(q)$ corresponding to this choice of c . The Bézier polynomial degree, M , was chosen to be 6, which left five free parameters to be chosen for each output component (two parameters per output component are used to impose invariance; see [Remark 6.1](#)). This implied a total of 20 output function parameters to be chosen via optimization. The optimization problem was posed as described in Section 6.3 to choose the 20 free parameters of h_d by approximately minimizing the cost

$$J(\alpha) := \frac{1}{p_2^h(q^-)} \int_0^{T_I(\xi_2^-)} \|u_\alpha^*(t)\|_2^2 dt, \quad (8.14)$$

where $q^- \in \mathcal{S} \cap \mathcal{Z}$, $T_I(\xi_2^-)$ corresponds to the step duration, $p_2^h(q_0^-)$ corresponds to step length, and $u_\alpha^*(t)$ is the result of evaluating (5.35) along the periodic solution of the hybrid zero dynamics.

The tradeoff between the energy dissipation due to impacts and the energy gained through shape change (cf. [Theorem 5.3](#) and [Fig. 6.7](#)) determines the closed-loop system's average walking rate and stability. Uncertainty in the model parameters and unmodeled dynamics during the swing phase affect the energy gained through shape change. Imperfections in the impact model change the amount of energy dissipated. To study the latter, RABBIT was simulated using a compliant ground contact model described in [176]. It was found that stability was preserved, but the steady-state average walking rate differed from the average walking rate designed assuming rigid impacts. This was also observed experimentally.

For RABBIT walking on the wood and rubber walking surface, it was found that in the design of walking motions, the amount of energy dissipated at impact had to be scaled to be less than the value predicted by the rigid model at low walking speeds and greater at higher walking speeds. This was accomplished by scaling δ_{zero} (see (5.67) for its definition) by a constant a . A series of controllers over a range of values of a were generated and then evaluated using the procedure described in Section 8.3 to determine their steady-state average walking rates. The value of a resulting in a controller that induced the desired average walking rate, $\bar{\nu}$, was recorded. [Figure 8.5](#) gives a plot of these values of a versus the corresponding average walking rate. Surprisingly, the relationship is approximately linear; the least squares fit is $a(\bar{\nu}) = 1.296 - 0.425\bar{\nu}$. The corresponding map has not yet been generated for ERNIE.

To zero the output resulting from optimization on the hybrid zero dynamics (suitably updated to accommodate the implementation issues), the decoupled,

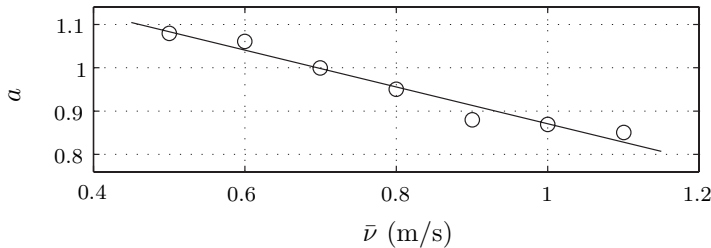


Figure 8.5. Average walking rate of RABBIT versus impact map scaling constant a . The solid line is a least squares fit to empirically determined impact scalings (indicated by circles). This apparently linear relationship between average walking rate and impact scaling is reminiscent of the classical coefficient of restitution relation, $e = 1 - av_0$, where e is the coefficient of restitution, a is some material-dependent constant, and v_0 is the impacting velocity [89, p. 258]. It is hypothesized that this approximately linear relation will hold for other walking surfaces, suggesting it as a means of identifying the surface to determine how the rigid impact model, i.e., δ_{zero} , should be modulated as a function of $\bar{\nu}$.

Table 8.4. RABBIT's experiment control parameter values.

| Control Parameter | Units | Label | Value |
|--------------------|-------|-----------|-------|
| Proportional gains | N | $K_{P,H}$ | 2000 |
| | | $K_{P,K}$ | 1500 |
| Derivative gains | Ns | $K_{D,H}$ | 10 |
| | | $K_{D,K}$ | 10 |

PD controller with friction compensation¹

$$u = -K_P e - K_D \dot{e} + F_v h_d \circ \hat{\theta}(\hat{q}) + F_s \operatorname{sgn}(e) \quad (8.15)$$

was used, where the terms $F_v h_d \circ \hat{\theta}(q)$ and² $F_s \operatorname{sgn}(e)$ correspond to feed-forward viscous and static friction compensation terms and

$$K_P = \operatorname{diag}(K_{P,H}, K_{P,H}, K_{P,K}, K_{P,K}) \quad (8.16a)$$

$$K_D = \operatorname{diag}(K_{D,H}, K_{D,H}, K_{D,K}, K_{D,K}) \quad (8.16b)$$

are the proportional and derivative gains given in Tables 8.4 and 8.5.

¹The friction compensation terms are due to C. Canudas de Wit.

²As is commonly done to circumvent the difficulties associated with the discontinuity of the signum function, in implementation, a scaled arctangent function was used in its place, i.e., for large τ , $\operatorname{sgn}(x) \approx 2/\pi \tan^{-1}(\tau x)$.

Table 8.5. ERNIE's experiment control parameter values.

| Control Parameter | Units | Label | Value |
|--------------------|-------|-----------|-------|
| Proportional gains | N | $K_{P,H}$ | 50 |
| | | $K_{P,K}$ | 50 |
| Derivative gains | Ns | $K_{D,H}$ | 1 |
| | | $K_{D,K}$ | 1 |

The error signals are defined as

$$e := H_0 \hat{q} - h_d \circ \hat{\theta}(\hat{q}) \quad \text{and} \quad \dot{e} := H_0 \dot{\hat{q}} - \frac{\partial h_d}{\partial \theta} \hat{\theta}(\hat{q}), \quad (8.17)$$

where $(\hat{q}; \dot{\hat{q}})$ is the robot's state with relabeling,

$$(\hat{q}; \dot{\hat{q}}) := \begin{cases} (q; \dot{q}), & \text{if stance leg is right leg} \\ (\Delta_q q; \Delta_q \dot{q}), & \text{if stance leg is left leg.} \end{cases} \quad (8.18)$$

A state machine was used to determine the current stance leg as required by (8.18). Since h_d is only designed for³ $0 \leq (\theta(q) - \theta^+)/(\theta^- - \theta^+) \leq 1$, where $\theta^- := \theta(q^-)$ and $\theta^+ := \theta \circ \Delta_q(q^-)$, $q^- \in \mathcal{S} \cap \mathcal{Z}$, the scalar function of the robot's state $\theta(q)$ was saturated,

$$(\hat{\theta}(q); \dot{\hat{\theta}}(q)) := \begin{cases} (\theta(q); \dot{\theta}(\hat{q})), & 0 < \frac{\theta(q) - \theta^+}{\theta^- - \theta^+} < 1 \\ (\theta^-; 0), & \frac{\theta(q) - \theta^+}{\theta^- - \theta^+} > 1 \\ (\theta^+; 0), & \frac{\theta(q) - \theta^+}{\theta^- - \theta^+} < 0. \end{cases} \quad (8.19)$$

The velocities were estimated using a five-point numerical differentiator described in [65] and applied to the encoder outputs.

The PD-based feedback (8.15) provided surprisingly good joint-level tracking (see, for example, Fig. 8.7). Because of this, other options were not explored.

The feedback controller (8.15)–(8.19) was implemented on the dSPACE DS1103 systems running with a sample period of 1.5 ms (667 Hz). A state machine was used to implement high-level control actions, such as which low-level continuous controller to run and when to switch among controllers. The implementations also have safety mechanisms which set the commanded control signals to zero in the event of an anomalous condition, such as a joint exceeding a position limit, or upon user request.

³The parameterization of Bézier polynomials is such that they are only defined on the unit interval.

8.3 Experiments

8.3.1 Experimental Validation Using RABBIT

This section describes six experiments that highlight the capabilities and robustness of controllers designed via the theoretical framework given in Chapters 6 and 7. The experiments reported were performed during a three week period, from February 24 through March 14, 2003. At this time, RABBIT had just been installed into its permanent location, pictured in Fig. 8.1, where about 6 to 7 laps about the center stand, or 200 steps, are possible; the limit on the number of laps is due to the winding of the power and Ethernet cabling about the center stand. During this period, many small details had to be addressed in regards to improving the experimental platform before evaluation of the controllers could begin.

The experiments were conducted as follows: each experiment began with the robot suspended in the air, lifted by an experimenter. After an encoder calibration phase, the robot was servoed to a configuration $(q; \dot{q}) = (q_0; 0) \in \Delta(\mathcal{S} \cap \mathcal{Z})$ and then placed on the ground. Once on the ground, data collection was initiated and the control was switched to the virtual constraint based feedback controller (8.15)–(8.19). This was possible because $(q; \dot{q}) = (q_0; 0) \in \Delta(\mathcal{S} \cap \mathcal{Z})$ is an asymptotically stable point under the hybrid zero dynamics based controller. To initiate walking, an experimenter pushed the robot’s torso—temporarily fully actuating the robot’s underactuated dynamics—supplying the energy required to land the robot’s state in the basin of attraction of the Poincaré return map. Once in motion, the robot reached steady-state walking within ten to twenty steps. To stop the robot, an experimenter grabbed the torso—again, fully actuating the robot’s dynamics—slowing the robot to a stop in double support. This ability to interact with the robot’s dynamics by pushing on the robot is a consequence of the zero dynamics’ parameterization by $\theta(q)$. Through mechanical coupling, forces on the robot drive $\theta(q)$ which, in turn, determine the evolution of the robot’s actuated DOF. Figure 8.6 gives video frames of RABBIT taking a step for a typical walking motion. Videos of these experiments are available at [239, 240].

8.3.1.1 Walking at a Fixed Rate

These first two experiments illustrate the performance of controllers designed via the theoretical framework presented in Sections 6.1–6.3.

Experiment 1: Walking at 0.7 m/s: In this first experiment, a feedback controller was designed to induce stable walking at an average rate of 0.7 m/s. The experiment lasted approximately 93 seconds during which RABBIT took 170 steps. Figures 8.7–8.12 are plots of various quantities of interest over a



Figure 8.6. Video frames of RABBIT taking a step. The interval between frames is 120 ms. Note the safety cable attached to the boom to provide a measure of safety.

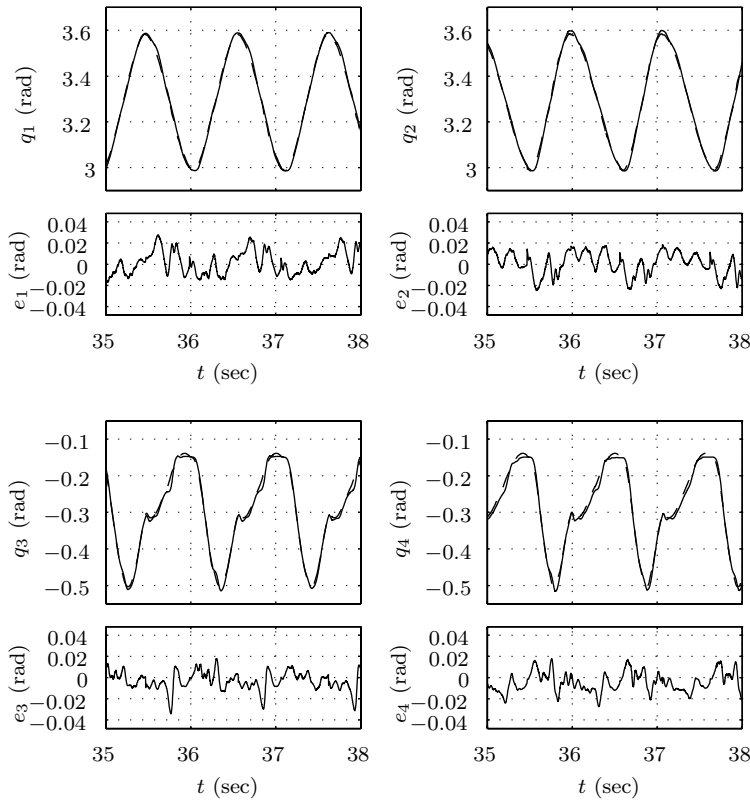


Figure 8.7. RABBIT walking at 0.7 m/s: joint angles q_i and errors $e_i = q_i - h_{d,i}$, $i = 1$ to 4, versus time. Actual joint trajectories are solid and $h_{d,i}$ for $i = 1, \dots, 4$ are dashed.

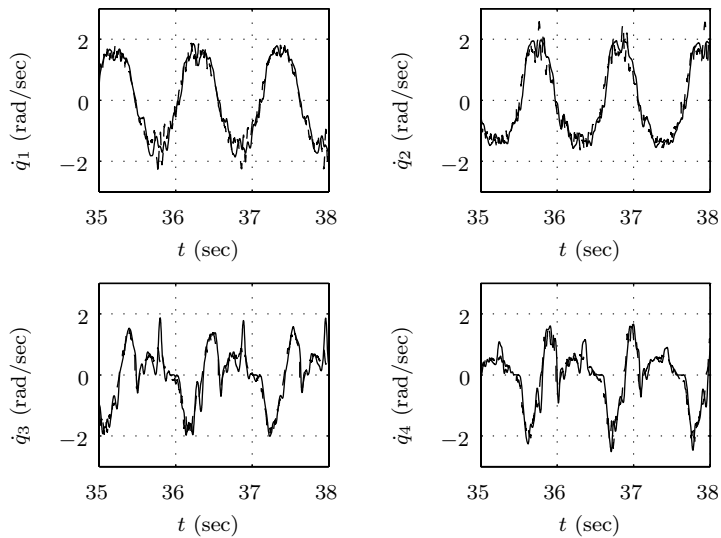


Figure 8.8. RABBIT walking at 0.7 m/s: joint velocities versus time. Actual joint trajectories are solid and $(\partial h_{d,i}/\partial \dot{\theta})\dot{\theta}$ for $i = 1, \dots, 4$ are dashed.

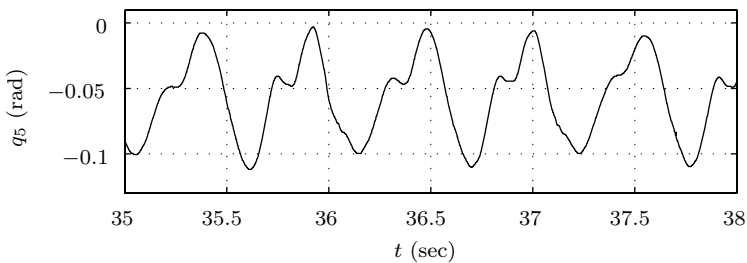


Figure 8.9. RABBIT walking at 0.7 m/s: q_5 versus time.

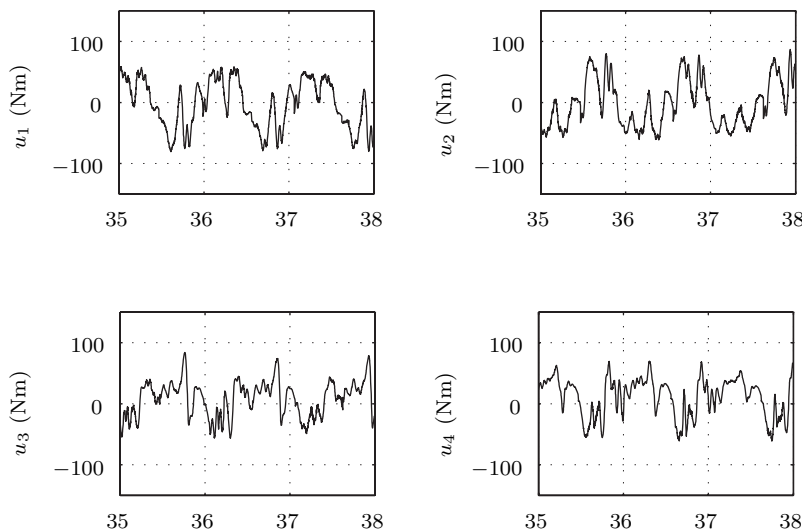


Figure 8.10. RABBIT walking at 0.7 m/s: control signals versus time.

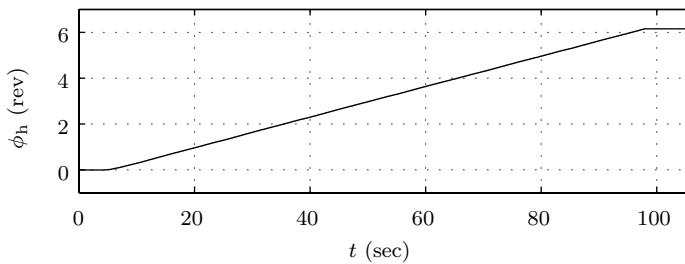


Figure 8.11. RABBIT walking at 0.7 m/s: horizontal boom angle, ϕ_h , versus time.

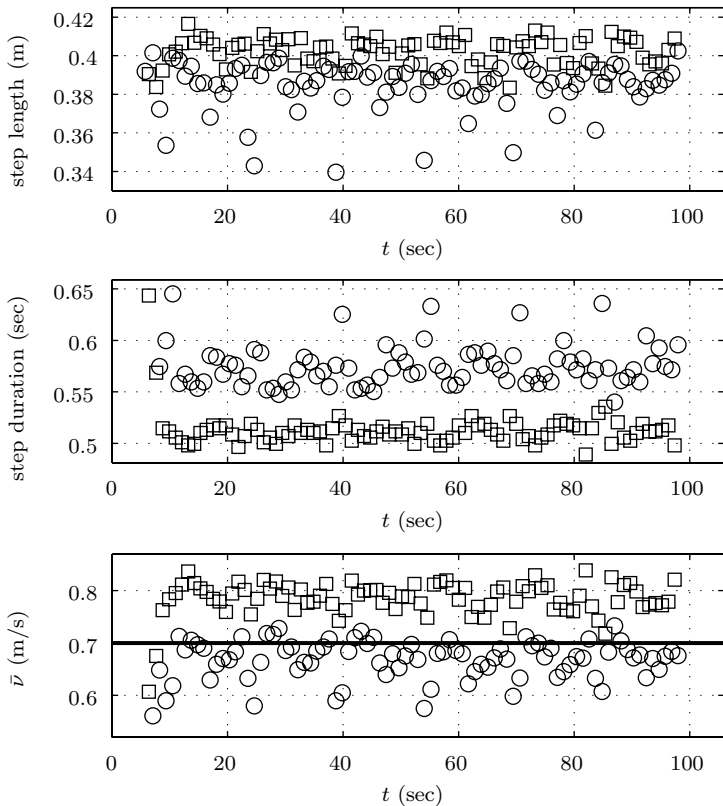


Figure 8.12. RABBIT walking at 0.7 m/s: step length, step duration, and average walking rate versus time. Circles represent steps taken by the outer leg, squares represent steps taken by the inner leg.

representative time interval containing approximately five steps. Figures 8.7 and 8.8 give the tracking performance. Figure 8.10 gives the commanded control signals. The peak commanded torque is less than 100 Nm, two thirds of the actuators' 150 Nm maximum. Figure 8.9 gives the trace of the torso angle. Note the torso angle is not a directly controlled quantity. Figure 8.11 gives the trace of the horizontal angular displacement of the boom, ϕ_h . As indicated by Fig. 8.11, the robot took approximately six laps about the center stand to complete the 170 steps. Note the constant slope and monotonicity of the trace of ϕ_h indicating smooth, horizontal motion of the hip. Figure 8.12 gives the step length, step duration, and the ratio of step length to step duration, step rate. The data points of Fig. 8.12 were calculated upon swing foot touchdown declaration. The step lengths given in Fig. 8.12 were calculated using the measured joint angles and the robot's identified link lengths. In each plot of Fig. 8.12, squares indicate data points corresponding to the inner leg—the leg closest to the center stand—and circles indicate data points corresponding to the outer leg—the leg farthest from the center stand. Labeling the data points in this way reveals differences between the inner and outer legs in step length, step duration, and step rate. Since the two legs are, to within close approximation, identical, the difference is likely due to the non-sagittal plane dynamics created by the boom system. Aside from the differences between the inner and outer legs, the variations in step length and step duration may be attributed to several factors. The ones believed to be most significant are nonuniformity in the walking surface, variability in the declaration of leg touchdown, and flexibility in the robot's joints. Careful comparison of Fig. 8.12 with Fig. 8.11 reveals that the step rate is periodic in ϕ_h . The periodic change with ϕ_h is due to nonuniformity in the walking surface: one section of the wood and rubber walking surface was not firmly lying on the ground because of unevenness in the underlying concrete floor.

Experiment 2: Demonstration of Robustness to Perturbations: The second experiment demonstrates the robustness of controllers designed via the method of Sections 6.1–6.3. Two types of perturbations were applied to RABBIT while it was being feedback controlled to walk at 0.9 m/s. The first perturbation was a 10 kg mass added to the torso, which resulted in a shift of the average walking rate from 0.9 m/s to 1.0 m/s. (In the fifth experiment, described in Section 8.3.1.2, it will be demonstrated that the designed walking rate may be recovered through the use of event-based integral control.) In addition to the sizable perturbation to the robot's model (the robot's nominal mass is 32 kg), the second perturbation was aperiodic, short duration forces applied to the RABBIT's torso by an experimenter in both the forward and reverse directions. Despite these significant perturbations, RABBIT did not fall; the experiment lasted approximately 74 seconds during which RABBIT took 164 steps.

Figures 8.13 and 8.14 are plots of the actual and desired joint trajectories

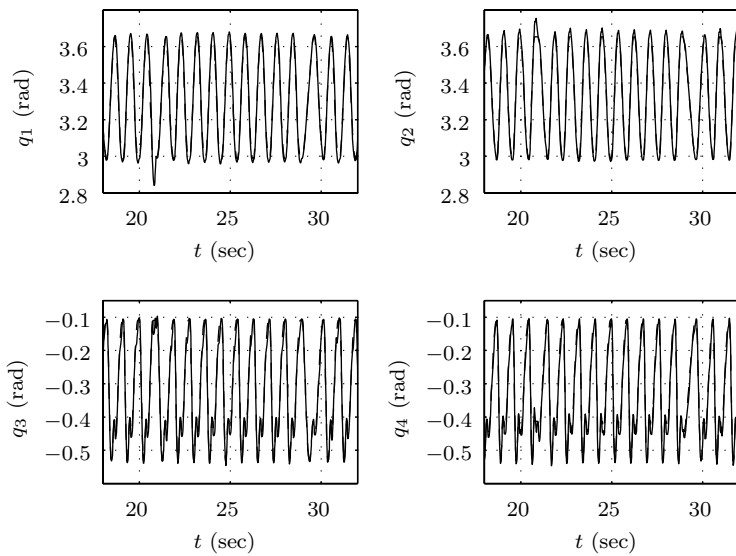


Figure 8.13. RABBIT robustness demonstration: joint angles versus time. Actual joint trajectories are solid and $h_{d,i}$ for $i = 1, \dots, 4$ are dashed.

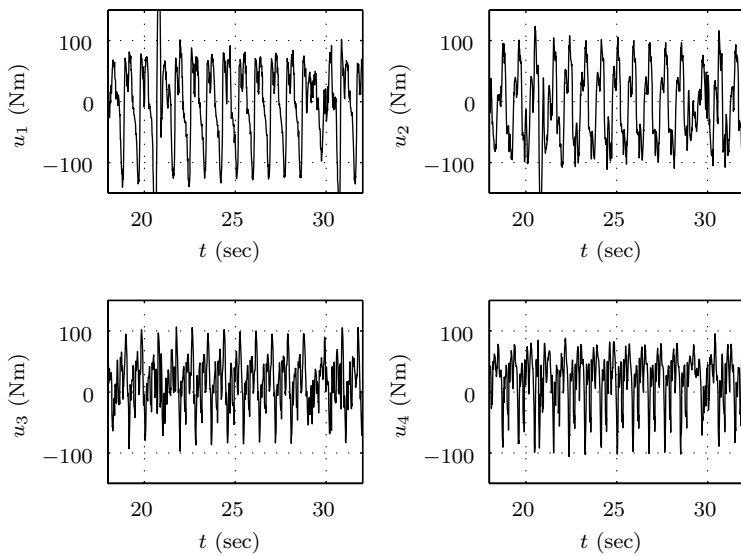


Figure 8.14. RABBIT robustness demonstration: control signals versus time.

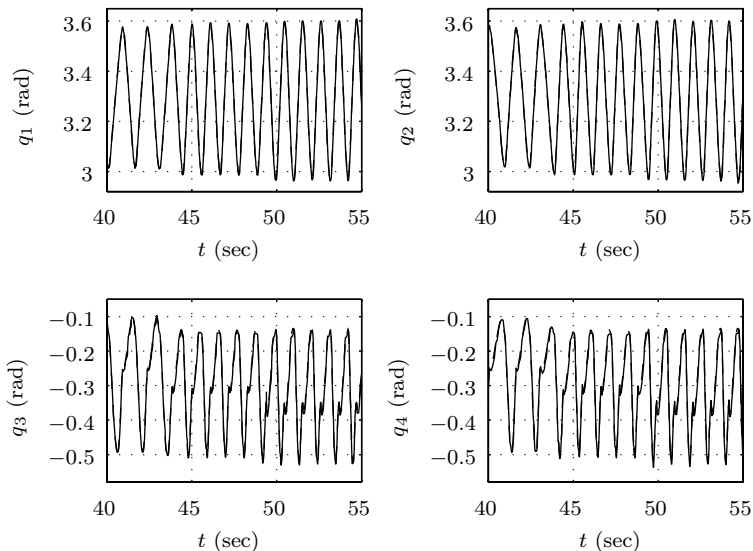


Figure 8.15. RABBIT transitioning: joint angles versus time. Actual joint trajectories are solid and $h_{d,i}$ for $i = 1, \dots, 4$ are dashed.

and the commanded control signals over a representative time interval in which the robot was pushed in the forward direction (at approximately 20.5 seconds) and in the reverse direction (at approximately 29 seconds). Note that the change in the reference motion, h_d , during the application of these forces. The commanded control signals are within the actuators' limits, except during the force perturbations when they saturate (see Fig. 8.14).

8.3.1.2 Transitioning and Event-Based Within-Stride Control

The four experiments below illustrate the transition controller developed in Section 7.2 and the event-based controller developed in Section 7.3. Both techniques exploit freedom in the output function parameter choice while respecting invariance of the associated zero dynamics manifold.

Experiment 3: Transitioning Between Controllers: The third experiment demonstrates the use of the one-step transition controllers presented in Section 7.2. A transition controller designed according to Theorem 7.1 is able to effect a transition from the region of attraction of one walking controller to another by steering the state of the system using the same technical machinery used to render the zero dynamics invariant. The application of the transition controller is synchronized with swing leg touchdown.

For the experiment, a set of controllers was designed for walking at constant speeds of 0.5 m/s to 0.8 m/s, at increments of 0.1 m/s. The transition

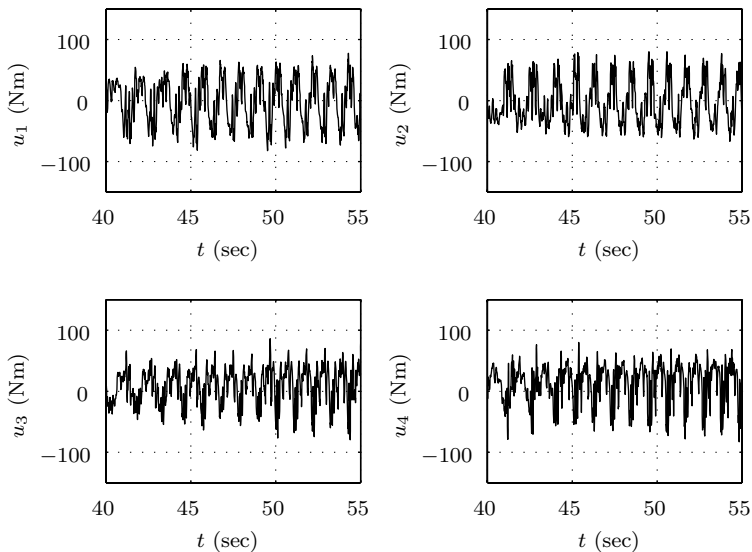


Figure 8.16. RABBIT transitioning: control signals versus time.

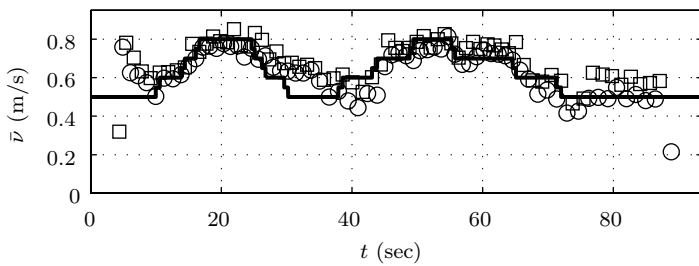


Figure 8.17. RABBIT transitioning: average walking rate versus time. Circles represent steps taken by the outer leg, squares represent steps taken by the inner leg. The desired walking rate is indicated by a solid line.

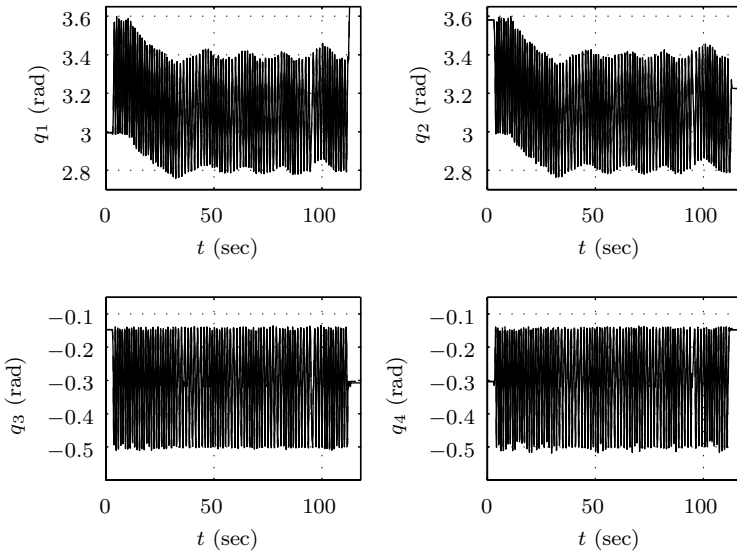


Figure 8.18. Using I-control to change fixed point of RABBIT’s walking rate: joint angles versus time. Actual joint trajectories are solid and $h_{d,i}$ for $i = 1, \dots, 4$ are dashed.

controller methodology was then employed to vary the commanded walking speed from 0.5 m/s to 0.8 m/s, by 0.1 m/s increments, and then from 0.8 m/s to 0.5 m/s, in 0.1 m/s decrements, after which, this entire sequence was repeated (see Fig. 8.17). The transition controllers were designed according to (7.11) and (7.13). The experiment lasted approximately 86 seconds during which RABBIT took 139 steps.

Figures 8.15 and 8.16 are plots of the actual and desired joint trajectories and the commanded control signals over a representative time interval of approximately twenty-six steps where the control was transitioned from 0.6 m/s to 0.8 m/s. Note that changes in the reference motion, $h_{d,i}$, occur with no visible difference in error, or in commanded control signal.

Experiment 4: Using Event-Based Integral Control to Modify the Fixed Point: In this fourth experiment, the same feedback used in the first experiment to induce walking at 0.7 m/s was applied with the addition of an event-based PI control, developed in Section 7.3, to modify the steady-state average walking rate from 0.7 m/s to 0.6 m/s. The event-based control acts through modifications of the Bézier polynomial coefficients at double support events.

The event-based control was performed on the stance and swing leg relative angles, q_1 and q_2 , which results in a change of the torso angle; see Fig. 6.13(a).

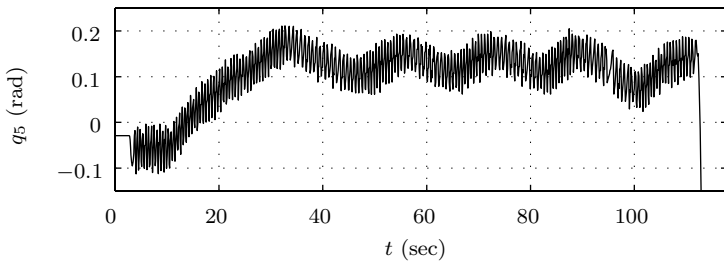


Figure 8.19. Using I-control to change fixed point of RABBIT's walking rate: q_5 versus time.

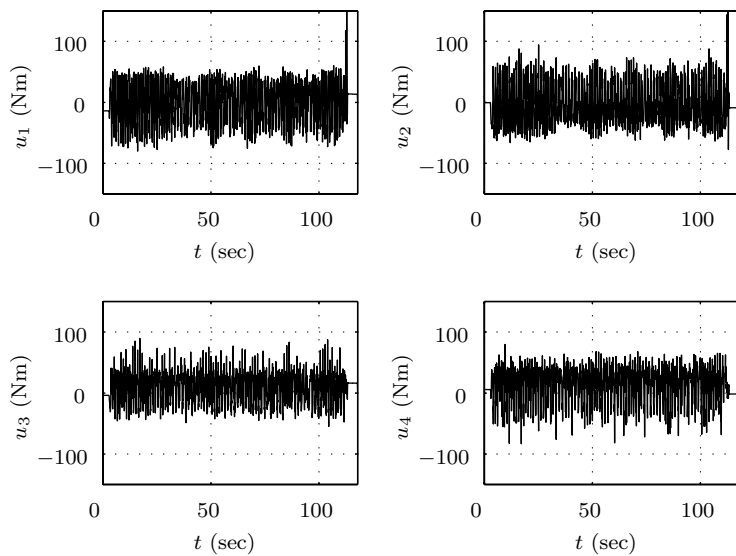


Figure 8.20. Using I-control to change fixed point of RABBIT's walking rate: control signals versus time.

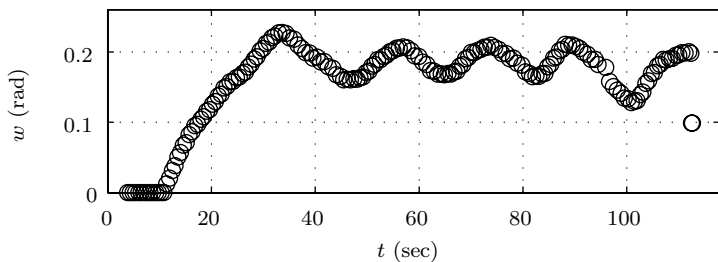


Figure 8.21. Using I-control to change fixed point of RABBIT's walking rate: w versus time.

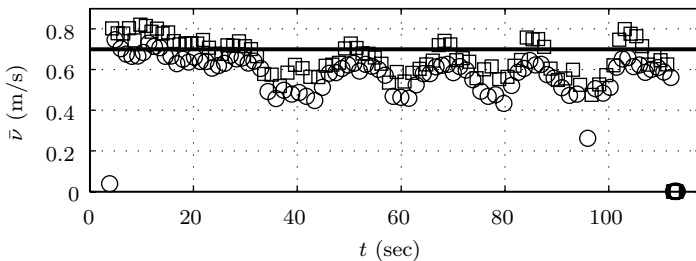


Figure 8.22. Using I-control to change fixed point of RABBIT's walking rate: average walking rate versus time. Circles represent steps taken by the outer leg, squares represent steps taken by the inner leg.

This was accomplished by setting $\delta\alpha$ to zero except for

$$\delta\alpha_j^i = 1, \text{ for } i = 1, 2 \quad \text{and} \quad j = 2, \dots, M. \quad (8.20)$$

The controller (7.23) with set-point $\eta^* = 0.6$ and control gains $K_I = 0.06$ and $K_P = 0$ was applied on the 15th step (at approximately 11 seconds). The proportional gain, K_P , was set to zero because of the noise introduced by the variance in step rate. The experiment lasted approximately 110 seconds during which RABBIT took 181 steps. Figure 8.21 gives the value of w given in (7.23) versus time. Note that the ringing in w and, consequently, in average walking rate is likely due to the integral gain being set too high; see Fig. 8.22. Yet, if that is indeed the case, it still took over 50 steps for the average walking rate to converge to 0.6 m/s.

Figures 8.18–8.20 are plots of various quantities of interest for the entire experiment. Note the change in the reference motion, h_d , for q_1 and q_2 with no visible difference (in particular, no spikes) in commanded control signal. Figure 8.19 gives the torso angle change resulting from the changing of q_1 and q_2 (see the measurement conventions given in Fig. 6.13(a)).

Experiment 5: Using Event-Based Integral Control to Reject a Perturbation: In the fifth experiment, the same feedback used in the first experiment to induce walking at 0.7 m/s was applied and a 10 kg mass was attached to the torso. This perturbation resulted in a shift of the average walking rate from 0.7 m/s to approximately 0.85 m/s (the change in average walking rate was determined in a separate experiment not reported here). The average walking rate of 0.7 m/s was recovered using the event-based integral control described in the previous experiment, but with $K_I = 0.04$ and $\eta^* = 0.7$ applied on the 14th step (at approximately 11 seconds). The experiment lasted approximately 95 seconds during which RABBIT took 164 steps.

Figure 8.24 gives the value of w given in (7.23) versus time. Again, note that the ringing in w and, consequently, in average walking rate (see Fig. 8.25) is

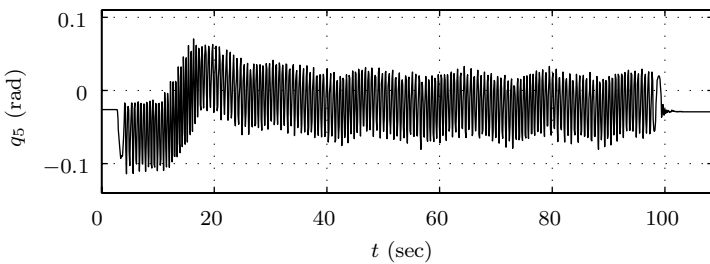


Figure 8.23. Using I-control to reject a perturbation for RABBIT: q_5 versus time.

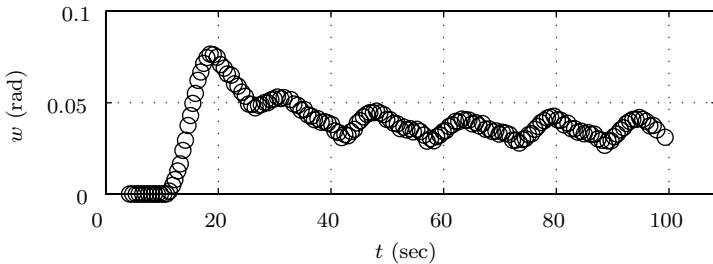


Figure 8.24. Using I-control to reject a perturbation for RABBIT: w versus time.

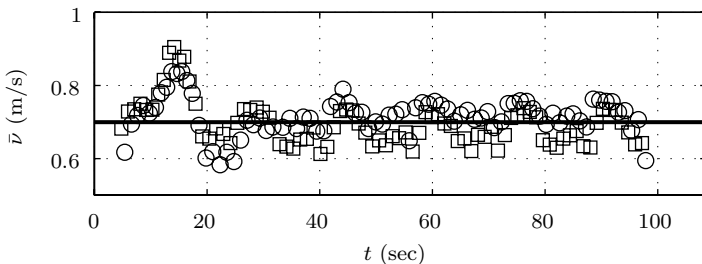


Figure 8.25. Using I-control to reject a perturbation for RABBIT: average walking rate versus time. Circles represent steps taken by the outer leg, squares represent steps taken by the inner leg.

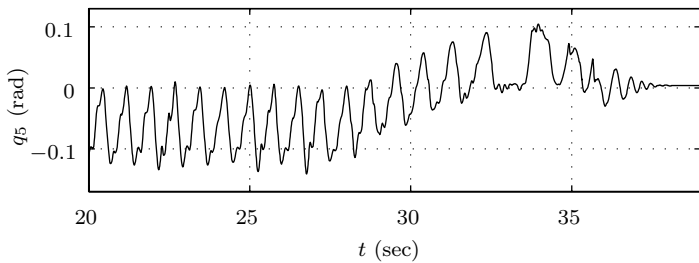


Figure 8.26. Using I-control to stop RABBIT: q_5 versus time.

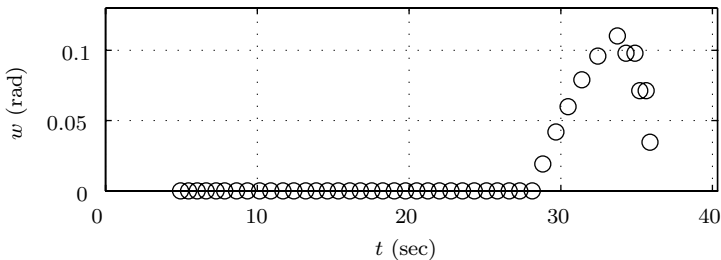


Figure 8.27. Using I-control to stop RABBIT: w versus time.

likely due to the integral gain being too large. The torso angle trace reflecting the action of the event-based integral control is given in Fig. 8.23. This regulation of the torso angle by integral control was able to recover the 0.7 m/s average walking rate (see Fig. 8.25).

Experiment 6: Using Event-Based Integral Control to Stop the Robot: In the sixth and final experiment, event-based integral control was used to bring RABBIT from a steady-state average walking rate of 0.5 m/s to a stop. This was achieved by slowing the average walking rate of RABBIT to where it no longer had enough kinetic energy to successfully complete a step; for further explanation, see Fig. 6.7, which provides a graphical interpretation of (5.79) and (5.80). The integral control described in the fourth experiment (based on Section 8.3.1.2) with $K_I = 0.04$ and $\eta^* = 0$ was applied on the 34th step (at approximately 29 seconds) and RABBIT stopped advancing by the 39th step (at approximately 34 seconds); see Fig. 8.28. After “stopping,” RABBIT rocked back and forth until its remaining kinetic energy was dissipated.

Figure 8.26 is a plot of the torso angle for a time interval including a portion of the steady-state walking cycle and the stopping of RABBIT. The increase

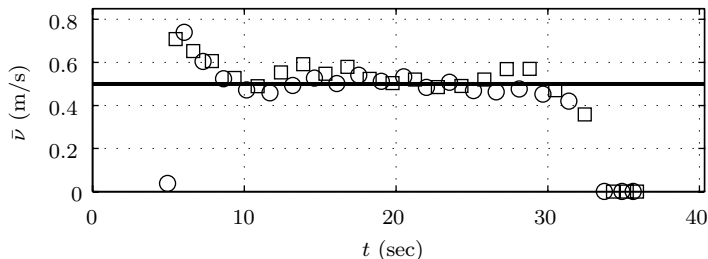


Figure 8.28. Using I-control to stop RABBIT: average walking rate versus time. Circles represent steps taken by the outer leg, squares represent steps taken by the inner leg.

in the torso angle⁴ reflects the action of the integral control; see Figs. 8.26 and 8.27.

8.3.1.3 Further Experimental Work on RABBIT

Further experimental work on RABBIT has been carried out by Sabourin⁵ et al. [198]. Successful walking is demonstrated with ground height variations from 0 to 15 mm. Robustness to impulsive forces was confirmed as in Experiment 2 of Section 8.3.1.1, and the regulation of walking speed through control of the torso angle was confirmed as in Experiment 4 of Section 8.3.1.1. Finally, the ability of the robot to walk backward under a constant applied force was confirmed, just as in [43] (see *A nice bonus: reverse is built into the controller*).

The control algorithm used in [198] is also based on virtual constraints, with the evolution of the joints tied to the absolute orientation of the stance leg.⁶ The controller is implemented using a neural network. The virtual constraints as learned by the neural network do not necessarily create a hybrid zero dynamics, so this work is more closely related to the control design illustrated in Section 6.6.1, which is based on [98], than the results of Chapter 5, which are based on [245].

⁴An increase means the torso becomes more upright or leans back; see Fig. 6.13(a).

⁵On p. 843 of [198], it is stated that the hybrid zero dynamics cannot be applied to robots with feet. This is incorrect as seen in Chapter 10 and [54]. On the same page, it is stated that “[the hybrid zero dynamics] is based on a simplified mechanical model and does not, for instance, take into account the realistic characteristics of the footground contact,” which is also incorrect. The hybrid zero dynamics is exactly an invariant subsystem of the robot under closed-loop control. No approximations are involved. The model of the foot-ground contact as captured by the hybrid zero dynamics is just as accurate as the model used in the full-dimensional robot model.

⁶In this work, in the single support phase, the angle of the stance knee is regulated to a constant value, hence the angle of the stance leg makes sense.

8.3.2 Experimental Validation Using ERNIE

This section describes two experiments that demonstrate the use of controllers designed via the theoretical framework given in [Chapter 6](#). The experiments confirm that walking with springs in parallel with the knee joints increases the energetic efficiency of walking [5].

The experiments were conducted in a similar fashion to those conducted on RABBIT; see [Section 8.3.1](#). The primary difference was in the initiation of the walking experiment. Once ERNIE's encoders had been calibrated, it was placed on the treadmill and the controller was switched to the virtual constraint based feedback controller, (8.15)–(8.19), with the treadmill at zero speed. To initiate walking, an experimenter held the robot's boom stationary while the treadmill's speed was ramped up. As a consequence of the zero dynamics' parameterization by forward progression—which is relative to a frame fixed to the treadmill's belt—the robot's gait naturally synchronized with the treadmill. Once the treadmill's speed matched that of the gait design, the experimenter then let go of the boom. To stop the robot, the experimenter grabbed the boom, holding it stationary, and the treadmill's speed was ramped down. Videos of these experiments are available at [239, 240].

8.3.2.1 Experiment 1: Walking at a Fixed Rate

For this first experiment, a feedback controller was designed to induce stable walking at an average rate of 0.32 m/s. Using this gait, ERNIE is able to walk indefinitely on the treadmill. Approximately 60 seconds of data during which ERNIE took 87 steps are presented here.

[Figures 8.29–8.31](#) are plots of various quantities of interest over a representative time interval containing approximately ten steps. Figure 8.29 gives the tracking performance. Note that the measurement conventions of ERNIE's coordinates are the same as RABBIT's; see [Fig. 6.13\(a\)](#). [Figure 8.30](#) gives the evolution of the torso angle. Figure 8.31 gives the commanded control signals. The peak commanded torque is 42 Nm. Note the torso angle is not a directly controlled quantity. [Figure 8.32](#) gives the trace of the horizontal displacement of the hips with respect to a frame fixed to the treadmill's belt. Note the constant slope and monotonicity of the trace of hip position, indicating smooth, horizontal motion. [Figure 8.33](#) gives the step length, step duration, and the ratio of step length to step duration, step rate. The data points of Fig. 8.33 were calculated upon swing foot touchdown declaration. The step lengths given in Fig. 8.33 were calculated using the measured joint angles and the robot's designed link lengths. In each plot of Fig. 8.33, squares indicate data points corresponding to the inner leg—the leg closest to the wall—and circles indicate data points corresponding to the outer leg—the leg farthest from the wall. Labeling the data points in this way reveals differences between the inner and outer legs in step length, step duration, and step rate. The differences are likely due to the non-sagittal plane kinematics created by the boom system.

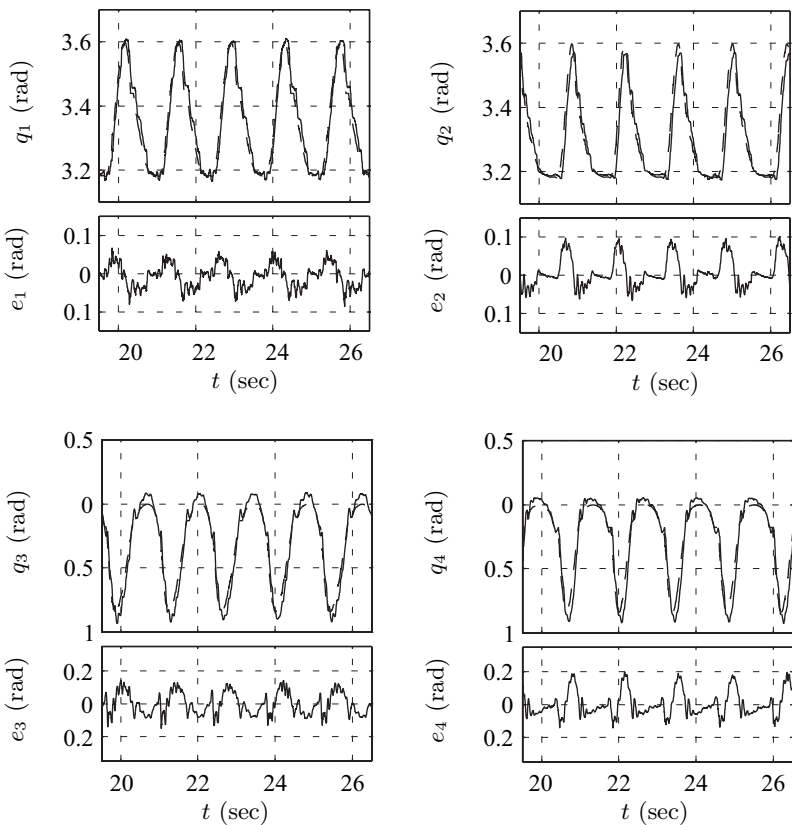


Figure 8.29. ERNIE walking at 0.32 m/s: joint angles q_i and errors $e_i = q_i - h_{d,i}$, $i = 1$ to 4, versus time. Actual joint trajectories are solid and $h_{d,i}$ for $i = 1, \dots, 4$ are dashed.

Using the commanded current (see Fig. 8.31) and joint velocity estimated from the measured joint angles (see Fig. 8.29), the average power consumed during the experiment by ERNIE's four actuators was estimated to be 10.1 W. Note that this estimate does not include estimates of any of the amplifier losses, the power consumed by the computers and sensors, etc. Although the estimate only provides a rough approximation of the power consumed, it allows us to compare with the case of walking at the same rate with springs in parallel with the knees; see the end of Section 8.3.2.2.

8.3.2.2 Experiment 2: Walking at a Fixed Rate with Springs in Parallel with the Knees

For the second experiment, a feedback controller was designed to induce stable walking at an average rate of 0.32 m/s using a model of the robot that included

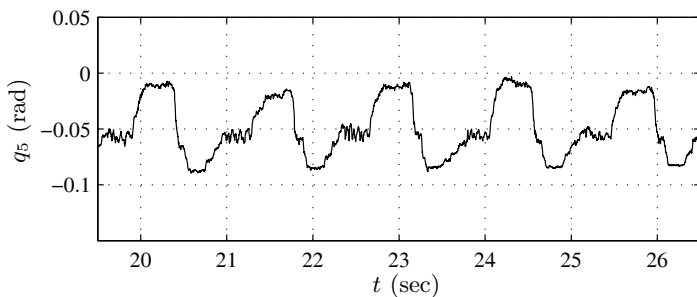


Figure 8.30. ERNIE walking at 0.32 m/s: q_5 versus time.

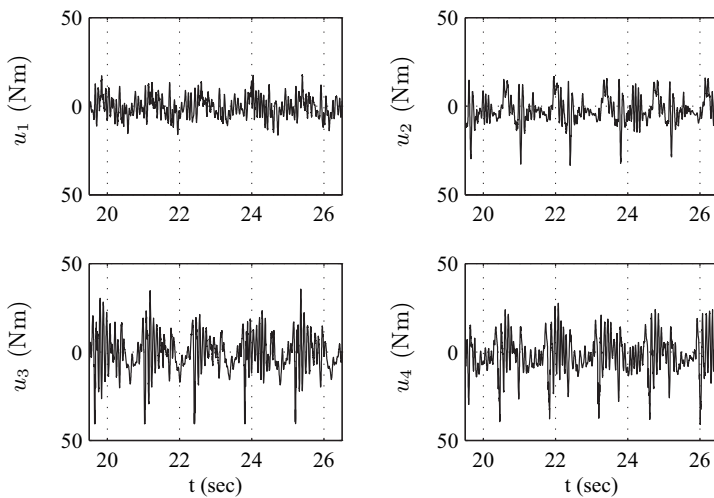


Figure 8.31. ERNIE walking at 0.32 m/s: control signals versus time.

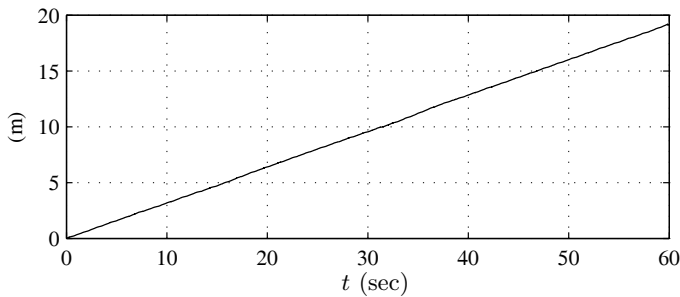


Figure 8.32. ERNIE walking at 0.32 m/s: hip horizontal displacement with respect to a frame fixed to the treadmill's belt versus time.

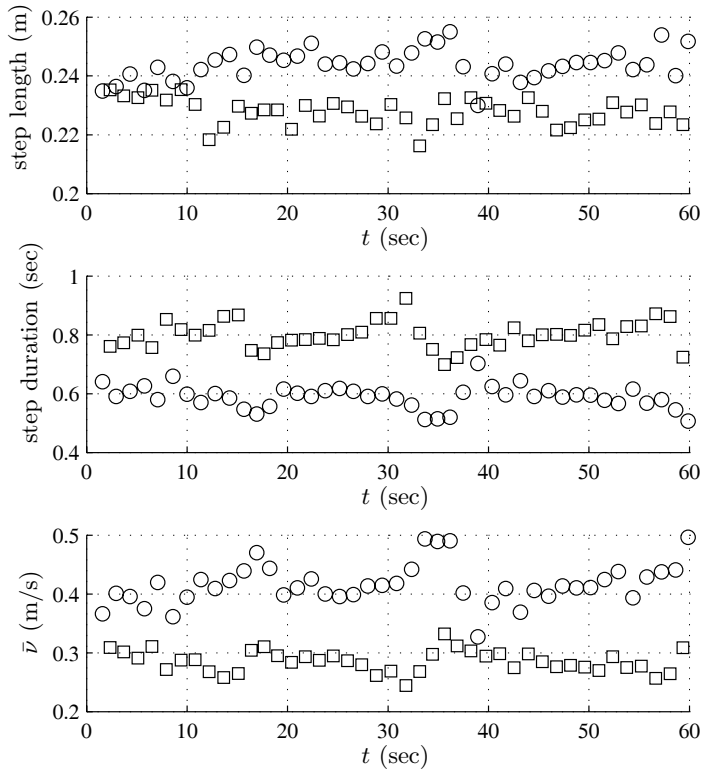


Figure 8.33. ERNIE walking at 0.32 m/s: step length, step duration, and average walking rate versus time. Circles represent steps taken by the outer leg, squares represent steps taken by the inner leg.

springs in parallel with the knee joints. The stiffness of each knee's spring was 16 Nm/rad and the springs' rest positions corresponded to $q_3 = q_4 = -0.06$ rad (-3.4 deg). As in the previous experiment, using this gait, ERNIE is able to walk indefinitely on the treadmill. Approximately 60 seconds of data during which ERNIE took 88 steps are presented here.

Figures 8.34–8.36 are plots of various quantities of interest over a representative time interval containing approximately ten steps. Figure 8.34 gives the tracking performance. Figure 8.35 gives the evolution of the torso angle. Figure 8.36 gives the commanded control signals. The peak commanded torque is 41 Nm. Figure 8.37 gives the trace of the horizontal displacement of the hips. Note the constant slope and monotonicity of the trace of hip position indicating smooth, horizontal motion. Figure 8.38 gives the step length, step duration, and the ratio of step length to step duration, step rate.

Using the same method as in the previous experiment, the average power consumed during the experiment by ERNIE's four actuators was estimated to be 8.9 W, which is 88% of the average power consumed when walking without springs; see Section 8.3.2.1. Investigations into the energetic benefits of (parallel joint) compliance are ongoing at The Ohio State University and a host of other places around the world [58, 159, 162, 231].

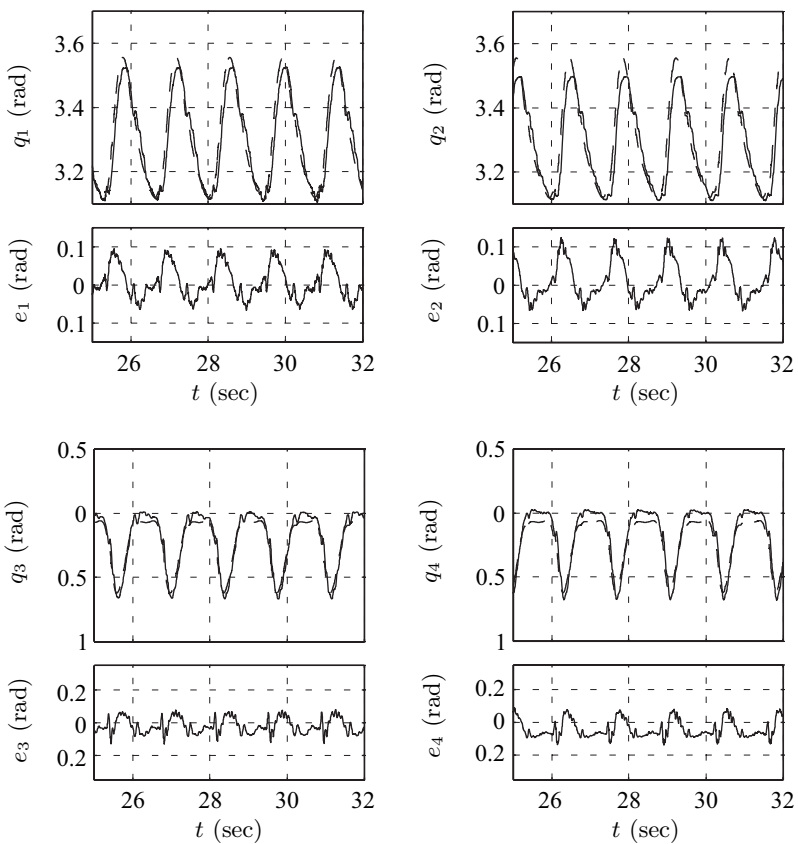


Figure 8.34. ERNIE walking at 0.32 m/s with springs in parallel with the knee joints: joint angles q_i and errors $e_i = q_i - h_{d,i}$, $i = 1$ to 4, versus time. Actual joint trajectories are solid and $h_{d,i}$ for $i = 1, \dots, 4$ are dashed.

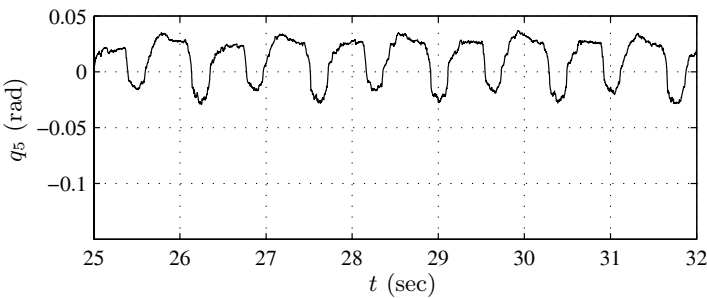


Figure 8.35. ERNIE walking at 0.32 m/s with springs in parallel with the knee joints: q_5 versus time.

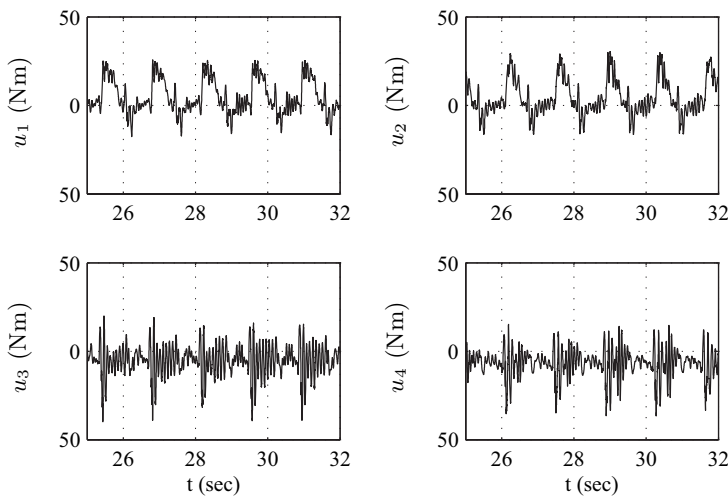


Figure 8.36. ERNIE walking at 0.32 m/s with springs in parallel with the knee joints: control signals versus time.

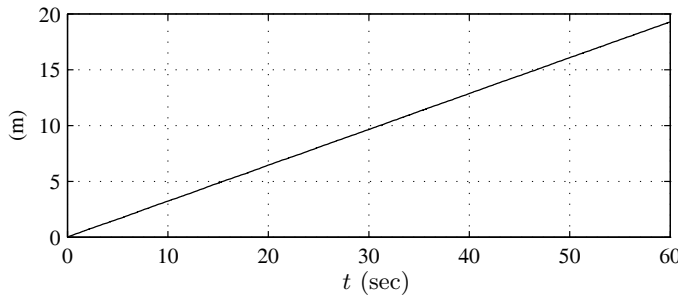


Figure 8.37. ERNIE walking at 0.32 m/s with springs in parallel with the knee joints: hip horizontal displacement with respect to a frame fixed to the treadmill's belt versus time.

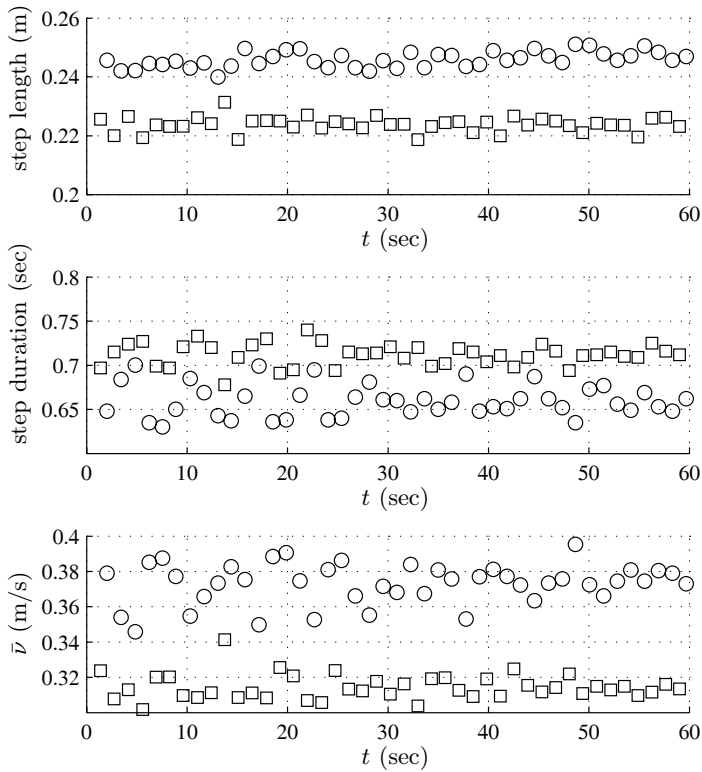


Figure 8.38. ERNIE walking at 0.32 m/s with springs in parallel with the knee joints: step length, step duration, and average walking rate versus time. Circles represent steps taken by the outer leg, squares represent steps taken by the inner leg.

Running with Point Feet

This chapter addresses the design and analysis of asymptotically stable running gaits for planar bipedal robots with point feet. Here, running is defined loosely as *forward motion* with alternation of *single support* (one leg on the ground) and *flight* (no contact with the ground). Without forward motion, the robot would be jumping in place, or “jogging” in place. The principal objective is to present a time-invariant feedback controller that yields provably asymptotically stable periodic running motions. One of the keys to accomplishing this objective will be to design the feedback controller on the basis of virtual constraints, as was done in [Chapter 6](#) for walking. This will lead to the notion of a *hybrid zero dynamics for running*, and to the closed-form computation of the restricted Poincaré return map.

A first set of experiments to use the theory of running developed in this chapter is presented in Section 9.9. In these experiments, RABBIT executed six running steps on multiple occasions, but a steady-state running gait was not achieved. The observed gait was remarkably human-like, having long stride lengths (approx. 50 cm or 36% of body length), flight phases of significant duration (approx. 100 ms or 25% of step duration), an upright posture, and an average forward rate of 0.6 m/s.

The detailed hypotheses on the class of robots and the class of running gaits to which the results apply were given in [Chapter 3](#). In particular, Section 3.5 used the method of Lagrange to derive dynamic models of the stance, flight, and impact phases. These models were assembled into an overall hybrid model of running in Section 3.5.4, which for convenience is repeated here:

$$\Sigma_f : \begin{cases} \mathcal{X}_f = T\mathcal{Q}_f \\ \mathcal{F}_f : (\dot{x}_f) = f_f(x_f) + g_f(x_f)u \\ \mathcal{S}_f^s = \{x_f \in \mathcal{X}_f \mid H_f^s(x_f) = 0\} \\ \mathcal{T}_f^s : x_s^+ = \Delta_f^s(x_f^-) \end{cases} \quad (9.1)$$

$$\Sigma_s : \begin{cases} \mathcal{X}_s = T\mathcal{Q}_s \\ \mathcal{F}_s : (\dot{x}_s) = f_s(x_s) + g_s(x_s)u \\ \mathcal{S}_s^f = \{x_s \in \mathcal{X}_s \mid H_s^f(x_s) = 0\} \\ \mathcal{T}_s^f : x_f^+ = \Delta_s^f(x_s^-) \end{cases}$$

where \mathcal{F}_f is the flow on state manifold \mathcal{X}_f , \mathcal{S}_f^s is the switching hyper-surface for

transitions between \mathcal{X}_f and \mathcal{X}_s , and $T_f^s : \mathcal{S}_f^s \rightarrow \mathcal{X}_s$ is the transition function applied when $x_f \in \mathcal{S}_f^s$. The symbol “f” denotes the flight phase and the symbol “s” denotes the stance phase. The superscripts “+” and “−” define the beginning and end of a phase respectively. When they are applied to a variable that is only defined for a single phase, such as θ_s , then there is no ambiguity, and hence, for example, θ_s^+ will be used instead of θ_s^{s+} . For a variable such as \mathbf{x}_{cm} , which is used in both flight and stance phases, the notation \mathbf{x}_{cm}^{s+} , \mathbf{x}_{cm}^{s-} , \mathbf{x}_{cm}^{f+} , and \mathbf{x}_{cm}^{f-} is used. The superscript “*” occasionally is used to denote the value of a variable on a periodic orbit; an exception is u^* , which denotes a feedback control rendering a zero dynamics manifold invariant.

In this chapter, angles are measured with a clockwise convention so that in the stance phase the angular momentum of the robot’s center of mass about the contact point with the ground is positive when the robot is moving left to right.

9.1 Related Work

In the early 1980s, Raibert proposed an elegant conceptualization of running in terms of a one-legged, prismatic-kneed hopper [184, 185]. He decomposed his control actions into three parts—hopping height, foot touchdown angle, and body posture—and emphasized the role of symmetry in designing stable running motions. The remarkable success of Raibert’s control law motivated others to analytically characterize its stability [76, 139], and to further investigate the role of passive elements in achieving efficient running with a hopper [4]. Raibert’s control scheme has been augmented with leg-coordination logic to achieve running in prismatic-kneed bipeds and quadrupeds [116, 185].

Various attempts have been made to extend a Raibert-style controller to a robot with revolute joints. Building on the ideas of Koditschek et al. [27, 81, 165, 188], a spring-loaded inverted-pendulum model—essentially a prismatic-kneed hopper with a radially symmetric body and a massless leg—was approximately embedded into a one-legged, revolute-jointed robot with an ankle, knee, and hip [201, 202]. With this approach, the center of mass of the robot could be nicely controlled. However, there was no natural “posture principle” to specify the evolution of the remaining degrees of freedom of the robot; also, the ballistic phase was difficult to address, due to underactuation and the non-holonomic constraint arising from conservation of angular momentum. Various methods for controlling the attitude of bodies undergoing ballistic motion have been studied; see [48, 88, 141, 158, 199] and references therein.

In late 2003, both Iguana Robotics and Sony announced (separate) exper-

imental demonstrations of running for bipedal robots with revolute knees. In early 2004, running was announced for another humanoid robot, HRP-2LR [132]. In December 2004, Honda's robot, ASIMO, achieved running at 3 km/hr (0.8 m/s) with a 50 ms flight phase using a controller based on "posture control." A year later, ASIMO ran at a new top speed of 6 km/hr. The reader is invited to seek videos of these robots on the web. The controller of Sony's robot was based on the ZMP, that of Iguana Robotics is based on central pattern generators (CPGs), and HRP-2LR uses "resolved momentum." To our best knowledge, only two other bipeds with revolute knees have been designed to perform running—Johnnie in Munich, Germany [175] and RABBIT in Grenoble, France [26, 43].

The computation of optimal running trajectories has been studied in [77]. Trajectory tracking for running was investigated on a simulation model of the Honda biped, ASIMO, [131]. A nominal trajectory was computed offline, and then during the ballistic phase, an online trajectory modification was made to allow Raibert-like control of foot placement. A control strategy for running that does not rely on trajectory tracking was studied in [126], where a Raibert-like controller was used on a planar robot with a torso and two prismatic-kneed legs. The control action sought to excite natural passive solutions of the dynamics by restoring energy lost at touchdown.

9.2 Qualitative Discussion of the Control Law Design

This section describes in qualitative terms a control law design for planar bipedal running that is presented in detail in Section 9.3, analyzed in Section 9.4, and illustrated via simulations on RABBIT in Section 9.5. An important difference with respect to the control law designs presented for walking in [Chapters 5 and 6](#) is that running has two continuous-time phases, stance and flight, and discrete transitions between them. Moreover, the flight phase presents more complications for controller design than does the stance phase: the flight phase has two additional degrees of freedom and angular momentum about the center of mass is conserved.

9.2.1 Analytical Tractability through Invariance, Attractivity, and Configuration Determinism at Transitions

Above all, the control strategy is constructed to facilitate the stability analysis of the closed-loop hybrid system consisting of the robot, the running surface, and the feedback controller. As in walking, the philosophy is that if stability analysis can be rendered sufficiently simple, then it becomes possible to ex-

plore efficiently a large set of asymptotically stable running gaits in order to find one that meets additional performance objectives, such as minimum energy consumption per distance traveled for a given average speed, or minimum peak-actuator power demand.

The controller will be hybrid, with continuous-time feedback signals applied in the stance and the flight phases, and discrete (or event-based) updates of controller parameters performed at the transitions between phases. The design of the controller uses two principles that are ubiquitous in nonhybrid systems, namely invariance and attractivity, with the notion of invariance being extended to hybrid systems so as to include the discrete transitions as well as the continuous flow of the Lagrangian dynamics. Hybrid invariance will lead to the creation of a low-dimensional hybrid subsystem of the full-dimensional closed-loop system. The low-dimensional hybrid subsystem is called the hybrid zero dynamics of running. Attractivity will mean that trajectories of the full-dimensional closed-loop system converge locally and sufficiently rapidly to those of the hybrid zero dynamics so that existence and stability of periodic running motions can be restricted to the study of the hybrid zero dynamics. The Poincaré return map for the hybrid zero dynamics will turn out to be one-dimensional. When transitions between phases in the hybrid zero dynamics occur at known configurations of the robot—this is called *configuration determinism* at transitions—it will turn out that the Poincaré return map can be computed in closed form, thereby rendering stability analysis of the closed-loop system tractable.

9.2.2 Desired Geometry of the Closed-Loop System

The objective of the control law design is to achieve the internal structure of the closed-loop system that is depicted in Fig. 9.1. The vertical surfaces \mathcal{S}_s^f and \mathcal{S}_f^s represent the points in the state space where the transitions from stance to flight and from flight to stance occur, respectively; see (9.1). The surface on the left, \mathcal{Z}_s , is created by the stance-phase controller; it is designed to be invariant in the usual sense that if the system is initialized in \mathcal{Z}_s , the solution of the stance-phase differential equation remains in \mathcal{Z}_s until it intersects \mathcal{S}_s^f , at which time the flight phase is initiated. The family of surfaces on the right, \mathcal{Z}_{f,a_f} , (shown for two values of a_f , namely, $a_{f,1}$ and $a_{f,4}$) is created by the flight-phase controller; each surface is designed to be invariant in the usual sense that if the system is initialized in \mathcal{Z}_{f,a_f} , the solution of the flight-phase differential equation remains in \mathcal{Z}_{f,a_f} until it intersects \mathcal{S}_f^s , at which time the stance phase is reinitialized through the impact map, Δ_f^s . The value of the parameter a_f is selected at each transition from stance to flight as a function of the angular momentum of the robot about the stance leg end, σ_1^{s-} , in such a way that evolution along the surface $\mathcal{Z}_{f,a_f(\sigma_1^{s-})}$ will cause the robot to land on \mathcal{Z}_s with a predetermined configuration. This brings out a second form of invariance that is related to the hybrid nature of the system: the parameter

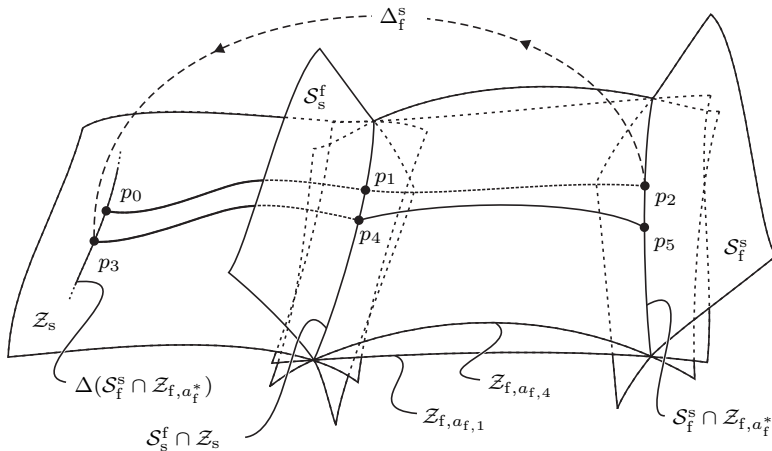


Figure 9.1. Geometry of the closed-loop system that is achieved with the controller presented in this chapter. Under the action of the feedback controller, the state of the system evolves on the low-dimensional surfaces \mathcal{Z}_s and \mathcal{Z}_{f,a_f} . Consider two strides of a running cycle initiated at the beginning of stance (at p_0). The robot's state evolves in \mathcal{Z}_s throughout stance until the state enters \mathcal{S}_s^f (at p_1), when two discrete events occur: the robot lifts off to begin the flight phase; and the controller selects a value of a_f that will be held constant throughout the flight phase. The value of the parameter, call it $a_{f,1}$, is determined as a function of the angular momentum about the stance leg end at transition into flight in such a way that the robot will land in a predetermined configuration. During the flight phase, the state of the robot evolves in $\mathcal{Z}_{f,a_f,1}$ until it enters \mathcal{S}_f^s (at p_2). The impact mapping Δ_f^s is then applied and the next stance phase is begun (at p_3) and the process repeats. If the robot terminates the ensuing stance phase (at p_4) with an angular momentum that is different than what it had on the previous stride (at p_1), due to conservation of angular momentum about the center of mass in the flight phase, the robot must evolve on a different surface in the flight phase this time in order to land in the same configuration it had on the previous landing. The required change in flight-phase evolution is accomplished by appropriate selection of $a_{f,4}$, which specifies $\mathcal{Z}_{f,a_f,4}$. By design, the rule for selecting a_f results in $\mathcal{S}_f^s \cap \mathcal{Z}_{f,a_f,1} = \mathcal{S}_f^s \cap \mathcal{Z}_{f,a_f,4}$. This common set has been denoted by $\mathcal{S}_f^s \cap \mathcal{Z}_{f,a_f^*}$, where a_f^* is the parameter value corresponding to a periodic orbit.

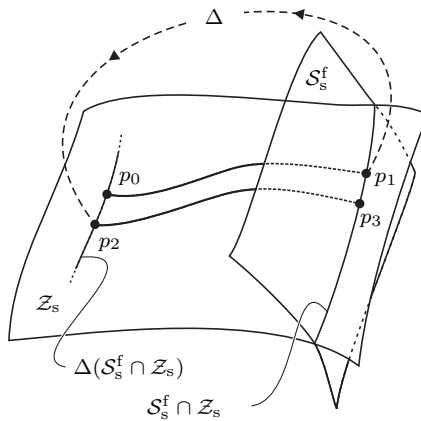


Figure 9.2. Geometry of the closed-loop system when the flight phase and the impact map Δ_s^s are composed to form a generalized impact map Δ that maps $S_s^f \cap Z_s$ to Z_s . This is analogous to the geometry that has been designed into walking in previous chapters. The analogy becomes exact if the robot's configuration at the initiation of the stance phase is the same for all points in $S_s^f \cap Z_s$.

a_f is selected so that the composition of the flight-phase dynamics with the impact map Δ_s^s maps $S_s^f \cap Z_s$ back to Z_s . This is shown in Fig. 9.1 with an arrow looping from the end of the flight phase back to the initiation of the stance phase, and more succinctly in Fig. 9.2, where a generalized impact map Δ is used to represent the composition of the flight-phase dynamics with Δ_s^s .

Not shown in either figure is the behavior of the robot off the hybrid zero dynamics. This is where attractivity comes into play. In addition to creating the invariant surfaces, the feedback controller must also ensure that trajectories that start off the surfaces converge to the surfaces. Both the creation of the invariant surfaces and their attractivity are accomplished with the use of virtual constraints.

9.3 Control Law Development

Separate state-variable control strategies are developed for the stance and flight phases of the running cycle. The controller for each phase is formulated as an output zeroing problem resulting in nontrivial zero dynamics. For the flight phase, it will be advantageous to allow the control to depend also on the initial value of the flight state or, equivalently, the final value of the stance state.

9.3.1 Stance Phase Control

As in Section 6.4, define the output

$$y_s = h_s(q) := q_b - h_{d,s} \circ \theta_s(q) \quad (9.2)$$

on the stance phase of (9.1), where the three times continuously differentiable function $h_{d,s} : \mathbb{R} \rightarrow \mathbb{R}^{N-1}$ encodes the stance-phase gait. It is assumed that the associated decoupling matrix, $L_{g_s} L_{f_s} h_s$, is invertible, $\Phi_s(q) := [h_s; \theta_s]$ is a global diffeomorphism on \mathcal{Q}_s ,

$$\mathcal{Z}_s := \{x_s \in T\mathcal{Q}_s \mid h_s(x_s) = 0, L_{f_s} h_s(x_s) = 0\} \quad (9.3)$$

is an embedded two-dimensional submanifold of $T\mathcal{Q}_s$, and $\mathcal{S}_s^f \cap \mathcal{Z}_s$ is an embedded one-dimensional submanifold of $T\mathcal{Q}_s$; see Fig. 9.1.

The feedback control is chosen to render \mathcal{Z}_s invariant under the closed-loop dynamics as well as attractive (either in finite time as in Theorem 5.4 or sufficiently exponentially rapidly, as in Theorem 5.5):

$$u_s(x_s) = (L_{g_s} L_{f_s} h_s(x_s))^{-1} (v(h_s(x_s), L_{f_s} h_s(x_s)) - L_{f_s}^2 h_s(x_s)), \quad (9.4)$$

where v renders the origin of

$$\ddot{y}_s = v(y_s, \dot{y}_s) \quad (9.5)$$

globally exponentially stable. The closed-loop system is denoted

$$f_{cl,s}(x_s) := f_s(x_s) + g_s(x_s) u_s(x_s). \quad (9.6)$$

The feedback control

$$u_s^*(x_s) = -(L_{g_s} L_{f_s} h_s(x_s))^{-1} L_{f_s}^2 h_s(x_s) \quad (9.7)$$

renders \mathcal{Z}_s invariant under the stance-phase dynamics; that is, for every $z \in \mathcal{Z}_s$,

$$f_{zero}(z) := f_s(z) + g_s(z) u_s^*(z) \in T_z \mathcal{Z}_s. \quad (9.8)$$

\mathcal{Z}_s is called the *stance-phase zero dynamics manifold* and $\dot{z} = f_{zero}(z)$ is called the *stance-phase zero dynamics*. Following the development in Chapter 5 and Section 6.4, $(\theta_s; \sigma_1)$ is a valid set of local coordinates for \mathcal{Z}_s and in these coordinates the zero dynamics has the form

$$\begin{aligned} \dot{\theta}_s &= \frac{1}{\mathbf{I}(\theta_s)} \sigma_1, \\ \dot{\sigma}_1 &= m_{tot} g_0 \mathbf{x}_{cm}(\theta_s), \end{aligned} \quad (9.9)$$

where $\mathbf{I}(\theta_s)$ is the virtual inertia defined in (6.73). Moreover, in these coordinates, $\mathcal{S}_s^f \cap \mathcal{Z}_s$ is given by

$$\{(q_0^{s-}; \dot{q}^{s-}) \mid q_0^{s-} = \Phi_s^{-1}(0, \theta_{s,0}^-), \dot{q}^{s-} = \dot{q}_0^{s-} \sigma_1^{s-}, \sigma_1^{s-} \in \mathbb{R}\}, \quad (9.10)$$

where $\theta_{s,0}^-$ is the value of θ_s on $\mathcal{S}_s^f \cap \mathcal{Z}_s$ and

$$\dot{q}_0^{s-} = \left[\begin{array}{c} \frac{\partial h_s}{\partial q} \\ A_N \end{array} \right]^{-1} \left|_{q_0^{s-}} \right. \begin{bmatrix} 0_{(N-1) \times 1} \\ 1 \end{bmatrix}, \quad (9.11)$$

where A_N was defined in Section 3.5.5.

For later use in computing a Poincaré return map on the zero dynamics, it is noted that (9.9) has Lagrangian¹ $\mathcal{L}_{s,\text{zero}} := K_{s,\text{zero}} - V_{s,\text{zero}}$, where

$$K_{s,\text{zero}} := \frac{1}{2}(\sigma_1)^2 \quad (9.12)$$

$$V_{s,\text{zero}}(\theta_s) := - \int_{\theta_s^+}^{\theta_s} \mathbf{I}(\xi) m_{\text{tot}} g_0 \mathbf{x}_{\text{cm}}(\xi) d\xi; \quad (9.13)$$

the choice of the lower limit θ_s^+ is arbitrary and will be made later. Also for later use, define

$$\begin{bmatrix} \lambda_x(q_0^{s-}) \\ \lambda_y(q_0^{s-}) \end{bmatrix} := \frac{\partial \mathbf{f}_{\text{cm}}(q_0^{s-})}{\partial q} \dot{q}_0^{s-}, \quad (9.14)$$

so that

$$\begin{bmatrix} \dot{\mathbf{x}}_{\text{cm}}^{s-} \\ \dot{\mathbf{y}}_{\text{cm}}^{s-} \end{bmatrix} \Big|_{\mathcal{S}_s^f \cap \mathcal{Z}_s} = \begin{bmatrix} \lambda_x(q_0^{s-}) \\ \lambda_y(q_0^{s-}) \end{bmatrix} \sigma_1^{s-}. \quad (9.15)$$

9.3.2 Flight Phase Control

The overall goal of the flight-phase controller is to land the robot in a favorable manner for continuing with the stance phase. It will turn out that a particularly interesting objective is the following: if the robot enters the flight phase from the stance-phase zero dynamics manifold, \mathcal{Z}_s , control the robot so that it lands on \mathcal{Z}_s in a *fixed* configuration. The analytical motivation for this objective will be made clear in Section 9.4. The feasibility of landing in a fixed configuration will be illustrated in Section 9.5 with a feedback controller that depends on x_f and the final value of the state of the preceding stance phase. To realize such a controller as a state-variable feedback, the flight-state vector is augmented with dummy variables a_f whose values can be set at the transition from stance to flight. Let $a_f \in \mathcal{A} := \mathbb{R}^p$, $p \in \mathbb{N}$.

In other regards, paralleling the development of the stance phase controller, define the output

$$y_f = h_f(q_f, a_f) := q_b - h_{d,f}(\mathbf{x}_{\text{cm}}, a_f), \quad (9.16)$$

where $h_{d,f}$ is at least three-times differentiable. Then, the following can be easily shown: for any value of a_f ,

¹See Corollary 5.2.

1. the decoupling matrix, $L_{g_f} L_{f_f} h_f$, is everywhere invertible;
2. $\Phi_f := [h_f; q_N; \mathbf{x}_{cm}; \mathbf{y}_{cm}]$ is a global diffeomorphism on \mathcal{Q}_f ;
3. the flight-phase zero-dynamics manifold

$$\mathcal{Z}_{f,a_f} := \{x_f \in T\mathcal{Q}_f \mid h_f(x_f, a_f) = 0, L_{f_f} h_f(x_f, a_f) = 0\} \quad (9.17)$$

- is a six-dimensional embedded submanifold of $T\mathcal{Q}_f$;
4. $\mathcal{S}_f^s \cap \mathcal{Z}_{f,a_f}$ is a five-dimensional embedded submanifold of $T\mathcal{Q}_f$;
 5. $(q_N; \mathbf{x}_{cm}; \mathbf{y}_{cm}; \sigma_{cm}; \dot{\mathbf{x}}_{cm}; \dot{\mathbf{y}}_{cm})$ is a set of global coordinates for \mathcal{Z}_{f,a_f} ; and
 6. the flight-phase zero dynamics has the form

$$\dot{q}_N = \kappa_{1,f}(\sigma_{cm}, \mathbf{x}_{cm}, \dot{\mathbf{x}}_{cm}, a_f) \quad (9.18a)$$

$$\dot{\sigma}_{cm} = 0 \quad (9.18b)$$

$$\ddot{\mathbf{x}}_{cm} = 0 \quad (9.18c)$$

$$\ddot{\mathbf{y}}_{cm} = -g_0, \quad (9.18d)$$

where (9.18a) arises from evaluating

$$\dot{q}_N = \frac{\sigma_{cm}}{A_{N,N}(q_b)} - \sum_{i=1}^{N-1} \frac{A_{N,i}(q_b)}{A_{N,N}(q_b)} \dot{q}_i \quad (9.19)$$

on \mathcal{Z}_{f,a_f} . Note that in Fig. 9.1, only a two-dimensional projection of \mathcal{Z}_{f,a_f} could be shown and $\mathcal{S}_f^s \cap \mathcal{Z}_{f,a_f}$ was represented as a one-dimensional projection.

The feedback controller is defined as

$$u_f(x_f, a_f) := -(L_{g_f} L_{f_f} h_f(x_f, a_f))^{-1} \left(K_p h_f(x_f, a_f) + K_d L_{f_f} h_f(x_f, a_f) + L_{f_f}^2 h_f(x_f, a_f) \right), \quad (9.20)$$

where $\ddot{y}_f + K_d \dot{y}_f + K_p y_f = 0$ has $y_f = 0$ as an exponentially stable equilibrium point. Let $\bar{x}_f := (x_f; a_f)$ and denote the right-hand side of (3.85) (i.e., the flight phase dynamics of (9.1)) and the trivial parameter dynamics $\dot{a}_f = 0$ in closed loop with (9.20) by

$$f_{cl,f}(\bar{x}_f) := \begin{bmatrix} f_f(x_f) + g_f(x_f) u_f(\bar{x}_f) \\ 0 \end{bmatrix}. \quad (9.21)$$

9.3.3 Closed-Loop Hybrid Model

The closed-loop hybrid model is

$$\begin{aligned} \Sigma_{f,cl} : & \left\{ \begin{array}{l} \bar{\mathcal{X}}_f = T\mathcal{Q}_f \times \mathcal{A} \\ \bar{\mathcal{F}}_{cl,f} : (\dot{x}_f) = f_{cl,f}(\bar{x}_f) \\ \bar{\mathcal{S}}_f^s = \{(x_f; a_f) \in \bar{\mathcal{X}}_f \mid H_f^s(x_f) = 0\} \\ \bar{T}_f^s : x_s^+ = \bar{\Delta}_f^s(\bar{x}_f^-) := \Delta_f^s(x_f^-) \end{array} \right. \\ \Sigma_{s,cl} : & \left\{ \begin{array}{l} \mathcal{X}_s = T\mathcal{Q}_s \\ \mathcal{F}_{cl,s} : (\dot{x}_s) = f_{cl,s}(x_s) \\ \mathcal{S}_s^f = \{x_s \in \mathcal{X}_s \mid H_s^f(x_s) = 0\} \\ \bar{T}_s^f : x_f^+ = \Delta_s^f(x_s^-), \quad a_f^+ = w_s^f(x_s^-), \end{array} \right. \end{aligned} \quad (9.22)$$

where the parameter update law w_s^f is at least continuously differentiable. The internal geometry of the closed-loop system is shown in Fig. 9.1.

9.4 Existence and Stability of Periodic Orbits

This section exploits the internal geometric structure of the closed-loop system (9.22) to obtain a low-dimensional, closed-form characterization of asymptotically stable, periodic running motions. Following Section 4.3, Section 9.4.1 develops the Poincaré section and the Poincaré return map that will be used for analyzing periodic orbits of (9.22). The analytical results based on restriction dynamics—that is, the hybrid zero dynamics of Fig. 9.2—are developed in Section 9.4.2.

9.4.1 Definition of the Poincaré Return Map

A periodic running motion corresponds to a periodic orbit in the closed-loop model. A fixed point of the Poincaré return map is equivalent to a periodic orbit. Because running consists of two phases, the Poincaré return map is naturally viewed as the composition of two maps: $P := P_s \circ P_f$, as in Fig. 9.3, where $P_s : \bar{\mathcal{S}}_f^s \rightarrow \mathcal{S}_s^f$ follows a solution of the closed-loop model from the impact event at the end of flight to just before the end of stance, and $P_f : \mathcal{S}_s^f \rightarrow \bar{\mathcal{S}}_f^s$ follows a solution from the end-of-stance event to just before the end of flight. Because not every landing will result in the completion of a stance phase (for example, the robot may not have sufficient speed), P_s is only a partial map. And, because not every transition out of stance results in a successful flight phase followed by a successful stance phase, P_f is a partial map. Hence, the

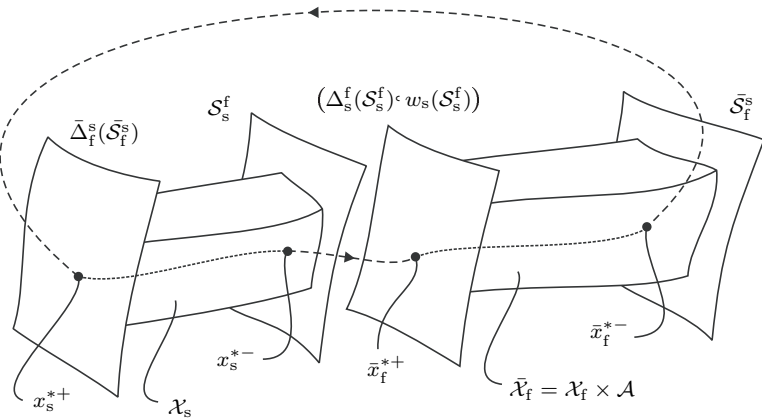


Figure 9.3. Poincaré maps for the closed-loop system. Conceptually, $P_s : \bar{\mathcal{S}}_f^s \rightarrow \mathcal{S}_s^f$, and is determined by following the flow of the closed-loop stance model from the impact at the end of flight up to, and not including, the transition from stance to flight. Similarly, $P_f : \mathcal{S}_s^f \rightarrow \bar{\mathcal{S}}_f^s$ is determined by following the flow of the closed-loop flight model augmented with the trivial parameter dynamics, $\dot{a}_f = 0$, from the transition at the end of stance up to, and not including, the impact event at the end of flight. The composite Poincaré map is $P : \mathcal{S}_s^f \rightarrow \mathcal{S}_s^f$, where $P := P_s \circ P_f$. A periodic orbit corresponds to a fixed point of P , namely, $x_s^{*-} = P(x_s^{*-+})$.

domains where these maps are well defined should be identified, which will give rise to the subsets $\tilde{\mathcal{S}}_s^f \subset \mathcal{S}_s^f$ and $\tilde{\mathcal{S}}_f^s \subset \bar{\mathcal{S}}_f^s$.

As in walking, define the *stance-time-to-impact function*,² $T_{I,s} : x_0 \in \mathcal{X}_s \rightarrow \mathbb{R} \cup \{\infty\}$, by

$$T_{I,s} := \begin{cases} \inf\{t \geq 0 \mid \varphi_{cl,s}(t, x_0) \in \mathcal{S}_s^f\} & \text{if } \exists t \text{ s.t. } \varphi_{cl,s}(t, x_0) \in \mathcal{S}_s^f \\ \infty & \text{otherwise,} \end{cases} \quad (9.23)$$

where $\varphi_{cl,s}(t, x_0)$ is an integral curve of (9.6) corresponding to $\varphi_{cl,s}(0, x_0) = x_0$. From Lemma C.1 in [Appendix C.1](#), $T_{I,s}$ is continuous at points x_0 where $0 < T_{I,s}(x_0) < \infty$ and the intersection with \mathcal{S}_s^f is transversal.³ Hence, $\tilde{\mathcal{X}}_s := \{x_s \in \mathcal{X}_s \mid 0 < T_{I,s}(x_s) < \infty, L_{f_{cl,s}} H_s^f(\varphi_{cl,s}(T_{I,s}(x_s), x_s)) \neq 0\}$ is open, and consequently, $\tilde{\mathcal{S}}_f^s := \bar{\Delta}_f^{s,-1}(\tilde{\mathcal{X}}_s)$ is an open subset of $\bar{\mathcal{S}}_f^s$. It follows that the

²Flows from one surface to another are sometimes called impact maps or impact functions. $T_{I,s}$ could also be called the *time-to-flight function*.

³Transversality guarantees nonzero vertical leg end velocity at impact; that is, the foot does not just scuff the ground.

generalized Poincaré stance map $P_s : \tilde{\mathcal{S}}_s^s \rightarrow \mathcal{S}_s^f$ defined by

$$P_s(\bar{x}_f) := \varphi_{cl,s}(T_{I,s}(\bar{\Delta}_f^s(\bar{x}_f)), \bar{\Delta}_f^s(\bar{x}_f)), \quad (9.24)$$

is well defined and continuous (the terminology of a *generalized-Poincaré map* follows Appendix D of [173]).

Similarly, the generalized Poincaré flight map $P_f : \tilde{\mathcal{S}}_s^f \rightarrow \tilde{\mathcal{S}}_s^s$, is defined by

$$P_f(x_s) := \varphi_{cl,f}(T_{I,f}(\Delta_s^f(x_s), w_s^f(x_s)), \Delta_s^f(x_s), w_s^f(x_s)), \quad (9.25)$$

where, $T_{I,f} : \bar{x}_0 \in \tilde{\mathcal{X}}_f \rightarrow \mathbb{R} \cup \{\infty\}$ by

$$T_{I,f} := \begin{cases} \inf\{t \geq 0 \mid \varphi_{cl,f}(t, \bar{x}_0) \in \tilde{\mathcal{S}}_s^s\} & \text{if } \exists t \text{ s.t. } \varphi_{cl,f}(t, \bar{x}_0) \in \tilde{\mathcal{S}}_s^s \\ \infty & \text{otherwise,} \end{cases} \quad (9.26)$$

and

$$\begin{aligned} \tilde{\mathcal{S}}_s^f = \{x_s \in \mathcal{S}_s^f \mid 0 < T_{I,f}(\Delta_s^f(x_s), w_s^f(x_s)) < \infty, \\ L_{f_{cl,f}} H_f^s(\varphi_{cl,f}(T_{I,f}(\Delta_s^f(x_s), w_s^f(x_s)), \Delta_s^f(x_s), w_s^f(x_s))) \neq 0\}. \end{aligned} \quad (9.27)$$

In [173, Appendix D], it is proved that P_f is continuously differentiable.

The Poincaré return map $P : \tilde{\mathcal{S}}_s^f \rightarrow \mathcal{S}_s^f$ for (9.22) is defined by

$$P := P_s \circ P_f; \quad (9.28)$$

see [Section 4.3.3](#).

9.4.2 Analysis of the Poincaré Return Map

The following theorem demonstrates that the closed-loop model for running that results from the developed control structure has the same form as the models for walking.

Theorem 9.1 (Connecting Running to Walking)

Let P be as (9.28), and let $\mathcal{S} := \mathcal{S}_s^f$, and $\tilde{\mathcal{S}} := \tilde{\mathcal{S}}_s^f$. Then P is also the Poincaré return map for the system with impulse effects

$$\Sigma_{cl} : \begin{cases} \dot{x}_s(t) = f_{cl,s}(x_s(t)) & x_s^-(t) \notin \mathcal{S} \\ x_s^+(t) = \Delta(x_s^-(t)) & x_s^-(t) \in \mathcal{S}, \end{cases} \quad (9.29)$$

where $\Delta := \bar{\Delta}_f^s \circ P_f$.

Proof See [Theorem 4.3](#).

Note that the system with impulse effects (9.29) has the same form as the models studied in previous chapters for walking gaits. The association of running with walking indicates how results developed for walking, such as closed-form stability analysis on the basis of a restricted Poincaré map, may be extended to running. In this section and the next, several results along this line of reasoning are developed and illustrated on an asymptotically stable running gait.

Suppose that $\Delta(\tilde{\mathcal{S}} \cap \mathcal{Z}_s) \subset \mathcal{Z}_s$, where \mathcal{Z}_s is the stance-phase zero dynamics manifold. Then, from Chapter 5, (9.29) has a hybrid zero dynamics, which may be called the *hybrid zero dynamics of running*:

$$\begin{aligned}\dot{z} &= f_{\text{zero}}(z) & z^- \notin \mathcal{S} \cap \mathcal{Z}_s \\ z^+ &= \Delta_{\text{zero}}(z^-) & z^- \in \mathcal{S} \cap \mathcal{Z}_s,\end{aligned}\quad (9.30)$$

where the restricted impact map is $\Delta_{\text{zero}} := \Delta|_{\tilde{\mathcal{S}} \cap \mathcal{Z}_s}$ and f_{zero} is given by (9.8). The key properties in walking gaits that led to a rich analytic theory were \mathcal{Z}_s -*invariance*, $\Delta(\tilde{\mathcal{S}} \cap \mathcal{Z}_s) \subset \mathcal{Z}_s$, and what will be called *configuration determinism at transition*: $\pi \circ \Delta(\tilde{\mathcal{S}} \cap \mathcal{Z}_s)$ consists of a single point, where $\pi : T\mathcal{Q}_s \rightarrow \mathcal{Q}_s$ is the canonical projection. How to achieve these conditions for $\Delta = \bar{\Delta}_f^s \circ P_f$ through design of the flight-phase controller will be detailed in Section 9.5.

Let q_0^{s-} be as defined in (9.10) and define $q_0^{s+} := \pi \circ \Delta(q_0^{s-}, *)$. Use (3.86) to define the positions of the center of mass at the beginning of the stance phase, $(\mathbf{x}_{\text{cm}}^{s+}; \mathbf{y}_{\text{cm}}^{s+})$, and the end of the stance phase, $(\mathbf{x}_{\text{cm}}^{s-}; \mathbf{y}_{\text{cm}}^{s-})$. In the following, it is assumed that the center of mass is behind the stance leg at the beginning of the stance phase, and thus $\mathbf{x}_{\text{cm}}^{s+} < 0$.

Theorem 9.2 (Characterization of Restricted Impact Map)

Suppose that $\Delta(\tilde{\mathcal{S}} \cap \mathcal{Z}_s) \subset \mathcal{Z}_s$ and $\pi \circ \Delta(\tilde{\mathcal{S}} \cap \mathcal{Z}_s) = \{q_0^{s+}\}$. In the coordinates $(\theta_s; \sigma_1)$ for \mathcal{Z}_s , the restricted impact map is given by

$$\Delta_{\text{zero}}(\theta_{s,0}^-, \sigma_1^{s-}) = \begin{bmatrix} \theta_{s,0}^+ \\ \delta(\sigma_1^{s-}) \end{bmatrix}, \quad (9.31)$$

where

$$\theta_{s,0}^+ = \theta_s(q_0^{s+}) \quad (9.32a)$$

$$\delta(\sigma_1^{s-}) = \chi\sigma_1^{s-} - \sqrt{(\beta\sigma_1^{s-})^2 + \alpha}, \quad (9.32b)$$

and

$$\alpha = -2m_{\text{tot}}^2 g_0 (\mathbf{x}_{\text{cm}}^{s+})^2 (\mathbf{y}_{\text{cm}}^{s+} - \mathbf{y}_{\text{cm}}^{s-}) \quad (9.33a)$$

$$\beta = m_{\text{tot}} \mathbf{x}_{\text{cm}}^{s+} \lambda_y(q_0^{s-}) \quad (9.33b)$$

$$\chi = 1 + m_{\text{tot}} \mathbf{x}_{\text{cm}}^{s-} \lambda_y(q_0^{s-}) + m_{\text{tot}} (\mathbf{y}_{\text{cm}}^{s+} - \mathbf{y}_{\text{cm}}^{s-}) \lambda_x(q_0^{s-}). \quad (9.33c)$$

The proof is given in [Appendix C.5.1](#).

Remark 9.1

1. $\chi < 0$ would imply a sign change in the angular momentum at impact, which would be incompatible with the definition of running as forward motion with a flight phase.
2. If $\mathbf{x}_{\text{cm}}^{\text{s}+} < 0$ is not assumed, the general expression for (9.32b) is

$$\delta(\sigma_1^{\text{s}-}) = \chi\sigma_1^{\text{s}-} + \text{sgn}(\mathbf{x}_{\text{cm}}^{\text{s}+})\sqrt{(\beta\sigma_1^{\text{s}-})^2 + \alpha}, \quad (9.34)$$

where $\text{sgn}(x)$ is the sign of x .

3. When $\alpha = 0$, that is, the center of mass has the same height at the beginning and end of the stance phase,

$$\delta(\sigma_1^{\text{s}-}) = (\chi - |\beta|)\sigma_1^{\text{s}-} \quad (9.35)$$

is linear, exactly as in walking; indeed, $\delta_{\text{zero}} = (\chi - |\beta|)$.

4. In terms of the coordinates $(\theta_{s,0}^-; \zeta := \frac{1}{2}(\sigma_1^{\text{s}-})^2)$ for $\tilde{\mathcal{S}} \cap \mathcal{Z}_s$, where the (generalized) kinetic energy of the stance-phase zero dynamics is used instead of the angular momentum, (9.32b) becomes

$$\delta_e(\zeta) = (\chi^2 + \beta^2)\zeta - \chi\sqrt{2\alpha\zeta + (2\beta\zeta)^2} + \frac{\alpha}{2}. \quad (9.36)$$

5. Implicit in the construction of $\tilde{\mathcal{S}}$ is the condition $2\alpha\zeta + (2\beta\zeta)^2 \geq 0$. Also a part of the construction of $\tilde{\mathcal{S}}$ is the condition that $T_{I,f}$ is a positive real number; under the assumptions made on Δ , this is equivalent to checking that $\mathbf{y}_{\text{cm}}^{\text{s}+} > \mathbf{y}_{\text{cm}}^{\text{s}-}$ and $\lambda_y(q_0^{\text{s}-}) < 0$ do not simultaneously occur.

Let $P : \tilde{\mathcal{S}} \rightarrow \mathcal{S}$ be the Poincaré return map for (9.29), and hence, also for (9.22), and suppose that $\Delta(\tilde{\mathcal{S}} \cap \mathcal{Z}_s) \subset \mathcal{Z}_s$, as in [Fig. 9.2](#). Then $P(\tilde{\mathcal{S}} \cap \mathcal{Z}_s) \subset \mathcal{S} \cap \mathcal{Z}_s$, and the restriction map $\rho : \tilde{\mathcal{S}} \cap \mathcal{Z}_s \rightarrow \mathcal{S} \cap \mathcal{Z}_s$,

$$\rho := P|_{\tilde{\mathcal{S}} \cap \mathcal{Z}_s}, \quad (9.37)$$

is well defined. The restricted Poincaré return map ρ is important because it is scalar and, by Theorem 5.4 and Theorem 5.5, asymptotically stable fixed points of it correspond to asymptotically stable periodic orbits of the hybrid model (9.29), and hence, to asymptotically stable running gaits.

Theorem 9.3 (Closed-form for ρ)

Suppose that $\Delta(\tilde{\mathcal{S}} \cap \mathcal{Z}_s) \subset \mathcal{Z}_s$ and $\pi \circ \Delta(\tilde{\mathcal{S}} \cap \mathcal{Z}_s) = \{q_0^{s+}\}$. Let $(\theta_{s,0}^-; \sigma_1^{s-}) \in \tilde{\mathcal{S}} \cap \mathcal{Z}_s$, and set $\zeta := \frac{1}{2}(\sigma_1^{s-})^2$. Then

$$\rho(\zeta) = \delta_e(\zeta) - V_{s,\text{zero}}(\theta_{s,0}^-), \quad (9.38)$$

with domain of definition

$$\mathcal{D}_\rho := \left\{ \zeta > 0 \mid \delta_e(\zeta) - V_{s,\text{zero}}^{\max} > 0, \quad 2\alpha\zeta + (2\beta\zeta)^2 \geq 0 \right\}, \quad (9.39)$$

where δ_e is defined in (9.36), and

$$V_{s,\text{zero}}^{\max} := \max_{\theta_{s,0}^+ \leq \theta_s \leq \theta_{s,0}^-} V_{s,\text{zero}}(\theta_s). \quad (9.40)$$

Moreover, the first derivative of the restricted Poincaré return map is

$$\frac{d\rho}{d\zeta}(\zeta) = \frac{d\delta_e}{d\zeta}(\zeta) = (\chi^2 + \beta^2) - \chi \frac{\alpha + 4\beta^2\zeta}{\sqrt{2\alpha\zeta + (2\beta\zeta)^2}}. \quad (9.41)$$

The proof is given in [Appendix C.5.2](#).

Remark 9.2

1. Computing a fixed point of (9.38) is easily reduced to solving a quadratic equation. If its discriminant Υ is non-negative, where

$$\begin{aligned} \Upsilon := 4\chi^2 &\left(\chi^2 \alpha^2 \right. \\ &\left. + (-2V_{s,\text{zero}}(\theta_{s,0}^-) + \alpha) (-\alpha\chi^2 + \alpha - 2\beta^2 V_{s,\text{zero}}(\theta_{s,0}^-)) \right), \end{aligned} \quad (9.42)$$

the fixed point can be explicitly calculated as

$$\zeta^* = \frac{(\chi^2 + \beta^2 - 1)(2V_{s,\text{zero}}(\theta_{s,0}^-) - \alpha) + 2\chi^2\alpha - \sqrt{\Upsilon}}{2((\chi + \beta)^2 - 1)((\chi - \beta)^2 - 1)}. \quad (9.43)$$

2. As in walking, the restricted Poincaré map can be interpreted in terms of energy transfer; see [Fig. 9.4](#).

The following two corollaries are immediate.

Corollary 9.1 (Exponentially Stable Fixed Points)

Suppose that $\zeta^* \in \mathcal{D}_\rho$ is a fixed point of ρ . Then it is exponentially stable if, and only if,

$$\mu := (\chi^2 + \beta^2) - \chi \frac{\alpha + 4\beta^2\zeta^*}{\sqrt{2\alpha\zeta^* + (2\beta\zeta^*)^2}} \quad (9.44)$$

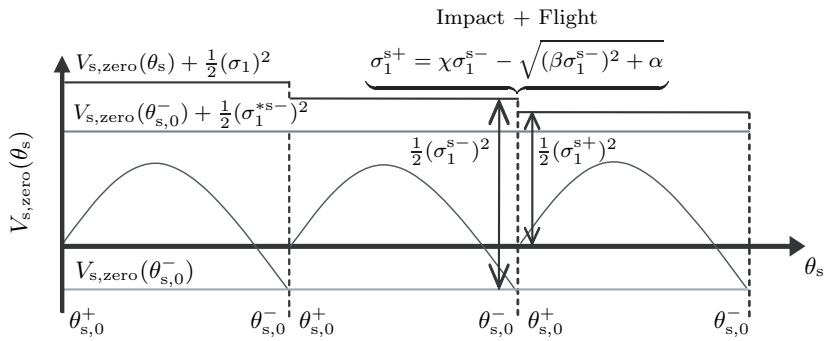


Figure 9.4. The stance phase zero dynamics is Lagrangian, and thus throughout the stance phase, the corresponding total energy $V_{s,zero}(\theta_s) + \frac{1}{2}(\sigma_1)^2$ is constant. Over the impact-plus-flight phase, the change in total energy depends on the angular momentum through $\delta(\sigma_1^{s-})$ and the potential energy through $V_{s,zero}(\theta_{s,0}^-)$. The total energy corresponding to the periodic orbit is $V_{s,zero}(\theta_{s,0}^-) + \frac{1}{2}(\sigma_1^{*s-})^2$.

satisfies $|\mu| < 1$.

Corollary 9.2 (Qualitative Analysis of ρ)

The following statements are true:

- (a) $\lim_{\zeta \searrow 0} \frac{d\rho}{d\zeta}(\zeta) = -\infty$, for $\chi > 0$ and $\alpha \geq 0$;
- (b) $\lim_{\zeta \searrow \frac{-\alpha}{2\beta^2}} \frac{d\rho}{d\zeta}(\zeta) = -\infty$, for $\chi > 0$ and $\alpha < 0$;
- (c) $\lim_{\zeta \rightarrow \infty} \frac{d\rho}{d\zeta}(\zeta) = \chi - |\beta|^2$; and
- (d) $\frac{d^2\rho}{d\zeta^2}(\zeta) = \chi \frac{\alpha^2}{(2\alpha\zeta + 4\beta^2\zeta^2)^{3/2}}$ does not change sign.

Figure 9.5 provides a graphical depiction of ρ for $\chi > 0$, $\alpha \geq 0$, and $\frac{\alpha}{2} - V_{s,zero}(\theta_{s,0}^-) > 0$. Similar figures could be drawn for other cases. The next result shows that these qualitative features of the Poincaré return map lead to a large region of attraction for an exponentially stable fixed-point.

Theorem 9.4 (Nonlocal Convergence in the HZD)

Consider $\rho : \mathcal{D}_\rho \rightarrow \mathbb{R}$, and suppose that

1. $(\chi - |\beta|)^2 < 1$,
2. $\chi > 0$,
3. and there exists $\zeta^* \in \mathcal{D}_\rho$ such that $\rho(\zeta^*) = \zeta^*$ and $\frac{d\rho}{d\zeta}(\zeta^*) > 0$.

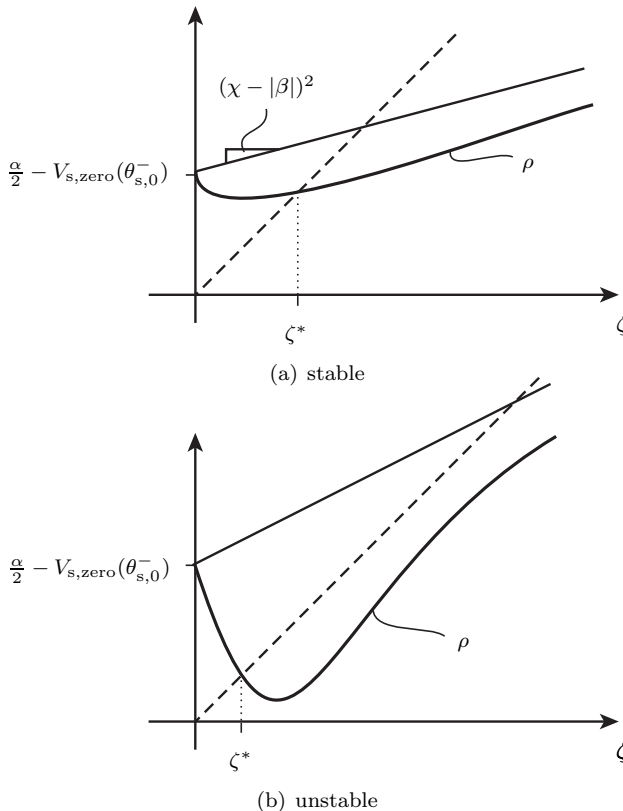


Figure 9.5. Qualitatively different Poincaré maps that may occur in running. The dashed line is the identity map and the bold line is a sketch of the restricted Poincaré return map. In (a), the fixed point is exponentially stable because the intersection with the identity line occurs with a positive slope less than 1.0. In (b), the fixed point is unstable because the intersection with the identity line occurs with a negative slope less than -1.0 .

Then, the following statements are true:

(a) ζ^* is the unique fixed-point of ρ ;

(b) the set

$$\tilde{\mathcal{D}}_\rho = \left\{ \zeta \in \mathcal{D}_\rho \mid \frac{d\rho}{d\zeta}(\zeta) > 0 \right\} \quad (9.45)$$

is unbounded and connected; and

(c) ζ^* is locally exponentially stable and every solution of $\zeta(k+1) = \rho(\zeta(k))$ initialized in $\tilde{\mathcal{D}}_\rho$ converges monotonically to ζ^* .

The proof is given in [Appendix C.5.3](#). This result shows that once the motion of the robot has settled near the hybrid zero dynamics, the domain of attraction of the periodic orbit is quite large. The analysis in Theorem 9.4 has not accounted for the peak torque of the actuators and the allowed friction cone at the support leg end. This theorem should thus be viewed as stating that such physical considerations will determine the limits on the region of attraction, and that the semi-global convergence of the control loop *per se* is not the key limiting factor.

For all of the examples worked by the authors, if an exponentially stable fixed point was found, hypotheses (1), (2) and (3) of Theorem 9.4 have always held as well. In particular, μ was always greater than 0.4 and $\tilde{\mathcal{D}}_\rho$ equalled \mathcal{D}_ρ , that is, the Poincaré map was always strictly increasing on the region of interest. In the case of Raibert’s hopper, the Poincaré map was shown to be unimodal—and thus not strictly increasing on the domain of interest [139]. Nevertheless, semi-global stability was established using a more powerful analysis method due to Singer [209] and Guckenheimer [101].

9.5 Example: Illustration on RABBIT

The analytical results of Section 9.4 make it straightforward to determine if a control law of the kind specified in Section 9.3 leads to the existence of a stable periodic orbit. However, proposing specific values for the output functions so that the evolution of the robot is energetically efficient, while respecting actuator limits, the friction cone at the contact point of the leg end, and liftoff at the beginning of the flight phase, is nearly impossible to do by intuition. Here, the feedback designs will be based on optimization.

Using the method proposed in [44], time-trajectories of (9.1), corresponding to average running speeds varying from 0.5 m/s to 2.75 m/s and parameter values given in [Table 6.3](#), were determined for RABBIT (see [Chapter 2](#) for details on the planar, bipedal robot, RABBIT). The running trajectories satisfy

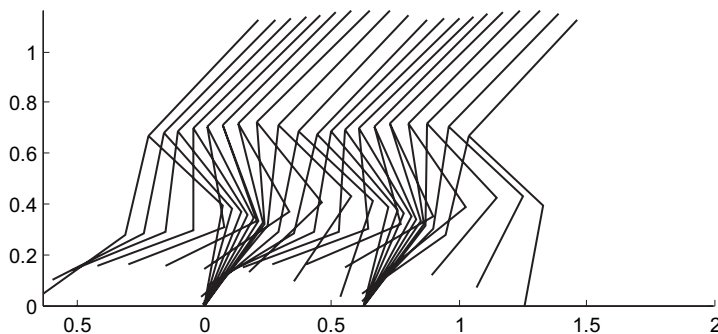


Figure 9.6. Stick diagram for a running trajectory with average speed 1.5 m/s.

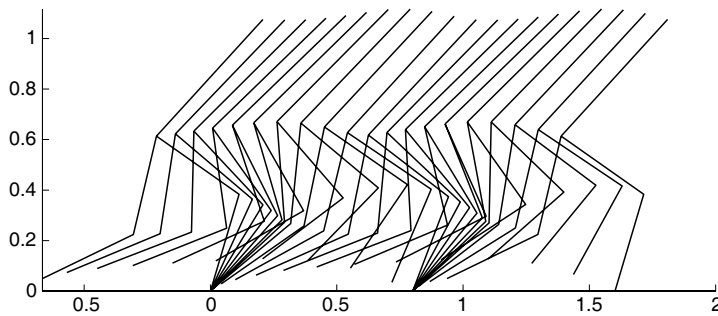


Figure 9.7. Stick diagram for a running trajectory with average speed 2.5 m/s.

$\ddot{y}_1 > 0$ at the beginning of the flight phase, the duration of the flight phase is at least 25% of the duration of a stride, and the required coefficient of friction is less than $2/3$. Stick-figure diagrams corresponding to the running motions of 1.5 m/s and 2.5 m/s are given in Fig. 9.6 and Fig. 9.7.

Denote by \mathcal{O} the path traced out in the state spaces of the hybrid model of the robot by any one of these running trajectories. It was checked that $\bar{\mathcal{O}}$, the closure of \mathcal{O} , intersects \mathcal{S}_s^f and \mathcal{S}_s^s exactly once; define $x_f^{-*} = \mathcal{O} \cap \mathcal{S}_f^s$ and $x_s^{-*} = \bar{\mathcal{O}} \cap \mathcal{S}_s^f$. The goal is to design a time-invariant state-feedback controller à la Section 9.3 that has \mathcal{O} as its asymptotically stable periodic orbit. Recall that designing the controller is equivalent to specifying the output functions in (9.2) and (9.16) and the parameter update-law in (9.22).

9.5.1 Stance Phase Controller Design

On the basis of x_f^{-*} and x_s^{-*} , the values of q_0^{s+} (the initial configuration in stance on the periodic orbit), q_0^{s-} (the final configuration in stance on the

periodic orbit), \dot{q}_0^{s+} (the normalized initial velocity in stance on the periodic orbit; see (9.11)), and \dot{q}_0^{s-} (the normalized final velocity in stance on the periodic orbit⁴) are easily deduced, which in turn give the initial and final values of θ_s on the periodic orbit, $\theta_{s,0}^+$ and $\theta_{s,0}^-$.

As in Section 6.5 (see also [176]), an output $y_s = h_s(q) := q_b - h_{d,s} \circ \theta_s(q)$ was designed so that it satisfied the boundary conditions and vanishes (nearly) along the stance phase of the periodic orbit, and thus the orbit is an integral curve of the stance-phase zero dynamics. For this, the function $h_{d,s}$ was selected to be a degree four polynomial in θ_s . The design method in [44] that is used to compute the periodic orbit essentially guarantees that the technical conditions of Section 9.3 are satisfied for h_s ; nevertheless, the conditions were formally verified. Once h_s is known, so is \mathcal{Z}_s , and, by construction, $\mathcal{O} \cap T\mathcal{Q}_s \subset \mathcal{Z}_s$.

9.5.2 Stability of the Periodic Orbits

The data required to determine the restricted Poincaré map ρ in Theorem 9.3 and Theorem 9.4 can be computed directly from $h_{d,s}$. This was carried out for each of the running trajectories studied in this chapter. The numerical values are summarized in Table 9.1. In each case, $\mu < 1$ and hence if a flight-phase controller can be determined to meet the conditions of Theorem 9.3, the corresponding orbit will be asymptotically stable. Note that slower running speeds yield smaller values of μ . So, for fast running, the convergence toward the periodic orbit will be slow. A plot of the restricted Poincaré map is provided in Fig. 9.8 for the trajectory corresponding to an average speed of 1.5 m/s.

9.5.3 Flight Phase Controller Design

The flight phase controller, $y_f = h_f(q_f, a_f) := q_b - h_{d,f}(\mathbf{x}_{cm}, a_f)$, $a_f = w_s^f(x_s^-)$, is to be designed so that trajectories of the closed-loop system that takeoff from the stance-phase zero dynamics manifold, \mathcal{Z}_s , land on \mathcal{Z}_s ; moreover, the landing configuration should be independent of the robot's takeoff velocity from \mathcal{Z}_s . Since from Section 9.5.1 the initial stance-phase configuration of the robot on the periodic orbit is equal to q_0^{s+} , these two conditions become

$$\Delta(\tilde{\mathcal{S}} \cap \mathcal{Z}_s) \subset \mathcal{Z}_s \quad (9.46)$$

$$\pi \circ \Delta(\tilde{\mathcal{S}} \cap \mathcal{Z}_s) = q_0^{s+}, \quad (9.47)$$

where, as before, $\pi : T\mathcal{Q}_s \rightarrow \mathcal{Q}_s$ is the canonical projection. The design of the controller can now be broken down into several steps. First, (9.46) and (9.47) will be translated from boundary conditions on configuration and velocity at the *beginning* of the (next) stance phase, into boundary conditions

⁴In (9.11), replace evaluation at q_0^{s-} with q_0^{s+} .

Table 9.1. Stability analysis of various running motions. If $\zeta > \zeta_{min}$, then $\zeta \in \mathcal{D}_\rho$.

| Average Velocity | $V_{zero}(\theta_s^-)$ | $V_{s,zero}^{\max}$ | \mathbf{x}_{cm}^{s+} (cm) | \mathbf{y}_{cm}^{s+} (cm) | \mathbf{x}_{cm}^{s-} (cm) | \mathbf{y}_{cm}^{s-} (cm) | $\lambda_x(q_0^{s-})$ (10^{-2}) |
|------------------|------------------------|---------------------|--------------------------------|--------------------------------|--------------------------------|--------------------------------|--|
| 0.50 m/s | -66 | 21 | -6.8 | 62.4 | 14.0 | 69.8 | 3.74 |
| 0.75 m/s | -114 | 36 | -8.8 | 62.1 | 18.4 | 68.8 | 3.83 |
| 1.00 m/s | -168 | 54 | -10.9 | 61.5 | 22.6 | 67.5 | 3.95 |
| 1.25 m/s | -219 | 74 | -12.9 | 60.5 | 26.4 | 65.7 | 4.09 |
| 1.50 m/s | -258 | 100 | -15.1 | 59.3 | 29.6 | 63.8 | 4.27 |
| 1.75 m/s | -274 | 134 | -17.7 | 58.1 | 32.3 | 61.7 | 4.48 |
| 2.00 m/s | -285 | 167 | -20.1 | 56.7 | 34.6 | 59.7 | 4.69 |
| 2.25 m/s | -306 | 123 | -17.5 | 55.6 | 34.0 | 59.1 | 4.78 |
| 2.50 m/s | -309 | 81 | -14.4 | 54.7 | 32.5 | 59.0 | 4.85 |
| 2.75 m/s | -260 | 70 | -13.2 | 55.2 | 29.8 | 58.6 | 4.91 |

| Average Velocity | $\lambda_y(q_0^{s-})$ (10^{-3}) | α | β (10^{-2}) | χ | ζ_{min} | ζ^* | μ | $\chi - \beta $ |
|------------------|--|----------|--------------------------|--------|---------------|-----------|-------|------------------|
| 0.50 m/s | 5.4 | 9.12 | -1.37 | 0.926 | 53 | 151 | 0.695 | 0.832 |
| 0.75 m/s | 3.3 | 14.26 | -1.07 | 0.926 | 88 | 275 | 0.708 | 0.838 |
| 1.00 m/s | 2.3 | 19.04 | -0.92 | 0.931 | 125 | 434 | 0.729 | 0.850 |
| 1.25 m/s | 2.0 | 23.34 | -0.96 | 0.940 | 164 | 615 | 0.754 | 0.866 |
| 1.50 m/s | 2.3 | 27.33 | -1.29 | 0.955 | 206 | 801 | 0.785 | 0.887 |
| 1.75 m/s | 3.0 | 30.84 | -1.99 | 0.976 | 253 | 982 | 0.826 | 0.914 |
| 2.00 m/s | 3.3 | 32.77 | -2.47 | 0.990 | 294 | 1162 | 0.856 | 0.932 |
| 2.25 m/s | 3.9 | 29.56 | -2.52 | 0.986 | 231 | 1327 | 0.859 | 0.922 |
| 2.50 m/s | 5.0 | 23.69 | -2.66 | 0.984 | 161 | 1503 | 0.870 | 0.916 |
| 2.75 m/s | 5.0 | 15.91 | -2.45 | 0.994 | 127 | 1729 | 0.908 | 0.940 |

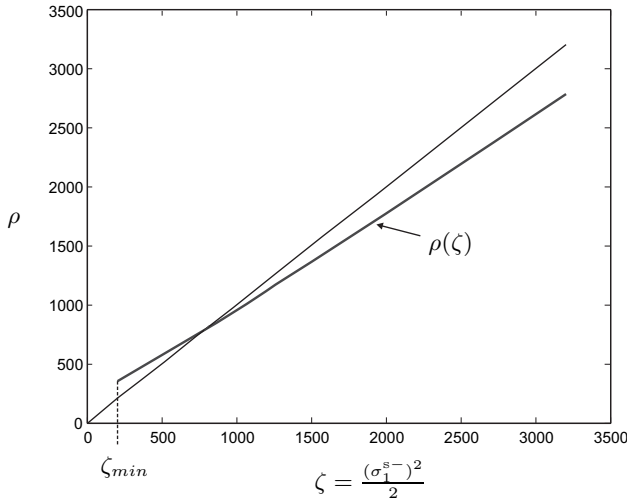


Figure 9.8. Running at 1.5 m/s. The restricted Poincaré map (bold) associated with the closed-loop system. The fixed point occurs where the graph of ρ intersects the graph of the identity map (thin line).

at the *end* of the (current) flight phase. This will result in control objectives for the configuration and velocity of the body coordinates and for the overall orientation of the robot at landing. In a second step, because the body coordinates q_b are directly actuated, it is straightforward to design a family of functions $h_{d,f}(\mathbf{x}_{cm}, a_f)$ that achieve the boundary conditions on the body-coordinate configuration and velocity, once the flight duration is determined from the ballistic motion of the robot's center of mass. The final step is more difficult because it is indirect: adjust the evolution of the body coordinates as a function of the takeoff velocity so as to achieve a desired orientation q_5 of the robot at landing.

To begin the first step, observe that because $(q_0^{s+}; \dot{q})$ is in $\pi^{-1}(q_0^{s+}) \cap \mathcal{Z}_s$ if, and only if, $\dot{q} = \dot{q}_0^{s+}\sigma_1^{s+}$ for some $\sigma_1^{s+} \in \mathbb{R}$, and $(q_0^{s-}; \dot{q})$ is in $\tilde{\mathcal{S}} \cap \mathcal{Z}_s$ if, and only if, $\dot{q} = \dot{q}_0^{s-}\sigma_1^{s-}$ for some $\sigma_1^{s-} \in \mathbb{R}$, conditions (9.46) and (9.47) are equivalent to

$$\forall \sigma_1^{s-}, \exists \sigma_1^{s+} \text{ s.t. } \Delta(q_0^{s-}, \dot{q}_0^{s-}\sigma_1^{s-}) = (q_0^{s+}; \dot{q}_0^{s+}\sigma_1^{s+}). \quad (9.48)$$

From Theorem 9.2, it follows that $\sigma_1^{s+} = \delta(\sigma_1^{s-})$, and hence (9.48) is equivalent to

$$\Delta(q_0^{s-}, \dot{q}_0^{s-}\sigma_1^{s-}) = (q_0^{s+}; \dot{q}_0^{s+}\delta(\sigma_1^{s-})), \quad (9.49)$$

which gives specific boundary conditions, just *after* impact, to be met by the design of the flight phase controller. In particular, recalling that $q = (q_b; q_5)$, it is seen that (9.49) places constraints on the body configuration variables and their derivatives, and on the overall orientation of the robot, q_5 , while

the constraint on \dot{q}_5 is equivalent to $\sigma_1^{s+} = \delta(\sigma_1^{s-})$, if the other constraints are met.

For the purpose of computation, it is convenient to transform (9.49) to conditions in the flight-phase state space, $T\mathcal{Q}_f$, instead of the stance-phase state space, $T\mathcal{Z}_s$. This is done as follows: the boundary conditions (9.49) specify the height of the center of mass at impact, and from this information, the flight time, t_f , is computed for any initial condition in $\tilde{\mathcal{S}} \cap \mathcal{Z}_s$; see (C.58) in [Appendix C.5.1](#). Using (C.59) and (9.15), the velocity of the center of mass can be expressed as a function of σ_1^{s-} ,

$$\begin{bmatrix} \dot{\mathbf{x}}_{cm}^{f-} \\ \dot{\mathbf{y}}_{cm}^{f-} \end{bmatrix} = \begin{bmatrix} \lambda_x(q_0^{s-})\sigma_1^{s-} \\ -\sqrt{(\lambda_y(q_0^{s-})\sigma_1^{s-})^2 - 2g_0(\mathbf{y}_{cm}^{s+} - \mathbf{y}_{cm}^{s-})} \end{bmatrix}. \quad (9.50)$$

The impact model (3.98), can be rewritten to define the angular velocity at the end of flight satisfying (9.49):

$$\dot{q}^{f-} = A^{-1} \left(A + m_{tot} \frac{\partial \mathbf{f}_2}{\partial q} \frac{\partial \mathbf{f}_2}{\partial q} \right) R^{-1} \dot{q}_0^{s+} \delta(\sigma_1^{s-}) + m_{tot} A^{-1} \frac{\partial \mathbf{f}_2}{\partial q} \begin{bmatrix} \dot{\mathbf{x}}_{cm}^{f-} \\ \dot{\mathbf{y}}_{cm}^{f-} \end{bmatrix}. \quad (9.51)$$

These last two equations define a function $\dot{q}_0(q_0^{s+}, \sigma_1^{s-})$ such that (9.49) is equivalent to

$$\begin{aligned} q_0^{f-} &= R^{-1} q_0^{s+} \\ \dot{q}^{f-} &= \dot{q}_0(q_0^{s+}, \sigma_1^{s-}). \end{aligned} \quad (9.52)$$

In summary, the objective of the flight-phase controller is to meet the boundary conditions given in (9.52). Meeting these two conditions will ensure that invariance of \mathcal{Z}_s under the composition of the flight phase and impact model is achieved, (9.46), and that configuration determinism at transition, (9.47), is also met; see [Figs. 9.1](#) and [9.2](#).

The design of $h_{d,f}$ can now be given in two more steps. First, define⁵

$$\tau(\mathbf{x}_{cm}, \sigma_1^{s-}) = \frac{\mathbf{x}_{cm} - \mathbf{x}_{cm}^{f+}}{t_f \dot{\mathbf{x}}_{cm}^{f+}} = \frac{\mathbf{x}_{cm} - \mathbf{x}_{cm}^{f+}}{t_f \lambda_x(q_0^{s-})\sigma_1^{s-}}; \quad (9.53)$$

the real-valued function τ varies between 0 and 1 and can be used to parameterize trajectories from $\tilde{\mathcal{S}} \cap \mathcal{Z}_s$ to $\pi^{-1}(q_0^{s+}) \cap \mathcal{Z}_s$ in a neighborhood of the periodic orbit. Choose a function $\text{fcn}(a_1, \dots, a_5) : [0, 1] \rightarrow \mathbb{R}^4$ such that

$$\begin{aligned} \text{fcn}(a_1, \dots, a_5)(0) &= a_1 \\ \frac{d\text{fcn}}{d\tau}(a_1, \dots, a_5)(0) &= a_2 \\ \text{fcn}(a_1, \dots, a_5)(1) &= a_3 \\ \frac{d\text{fcn}}{d\tau}(a_1, \dots, a_5)(1) &= a_4, \end{aligned} \quad (9.54)$$

⁵Note that $\overline{\mathbf{x}_{cm}^{f+}} = \mathbf{x}_{cm}^{s-}$.

and there exist a_1^*, \dots, a_5^* for which $q_b - \text{fcn}(a_1^*, \dots, a_5^*)(\tau)$ (nearly) vanishes on \mathcal{O} . Here, this was accomplished with a degree four polynomial. Off the orbit, use (9.54) to solve for a_1, \dots, a_4 as functions of σ_1^{s-} so that $q_b(\tau) = \text{fcn}(a_1, \dots, a_5)(\tau)$ satisfies the constraints on the body coordinates imposed by (9.52). Specifically, set $a_1 = (q_0^{s-})_b$, $a_3 = (R^{-1}q_0^{s+})_b$, $a_2 = (q_0^{s-}\sigma_1^{s-})_b$, and $a_4 = (\dot{q}_0(q_0^{s+}, \sigma_1^{s-}))_b$. Define

$$h_{d,f}(\mathbf{x}_{cm}, \sigma_1^{s-}, a_5) := \text{fcn}(a_1, \dots, a_5)(\tau) \quad (9.55)$$

with $a_i(\sigma_1^{s-})$, $i = 1, \dots, 4$ and $\tau(\mathbf{x}_{cm}, \sigma_1^{s-})$ as determined above. Define $q_5(0) = (q_0^{s-})_5$ and $q_{5,d} = (R^{-1}q_0^{s+})_5$.

In the final step, the goal is to select a_5 as a function of σ_1^{s-} so that the q_5 -component—the overall orientation of the robot—satisfies the landing constraint. This is done as follows. The output (9.55) satisfies all of the conditions of Section 9.3, and hence the evolution of q_5 in the flight-phase zero dynamics is given by $\dot{q}_5 = \kappa_{1,f}(\sigma_{cm}, \mathbf{x}_{cm}, \dot{\mathbf{x}}_{cm}, \sigma_1^{s-}, a_5)$. In the flight phase, σ_{cm} and $\dot{\mathbf{x}}_{cm}$ are constant and can be substituted by their values from $\tilde{\mathcal{S}} \cap \mathcal{Z}_s$. In addition, $\mathbf{x}_{cm}(t) = \mathbf{x}_{cm}^{s-} + t\lambda_x(q_0^{s-})\sigma_1^{s-}$. Hence, $\dot{q}_5 = \tilde{\kappa}_{1,f}(t, \sigma_1^{s-}, a_5)$. Letting σ_1^{*s-} denote the value of σ_1^{s-} on the orbit, \mathcal{O} , $q_{5,d} = q_5(0) + \int_0^{t_f} \tilde{\kappa}_{1,f}(t, \sigma_1^{*s-}, a_5^*) dt$ is satisfied because, by construction of the output, the orbit corresponds to an integral curve of the flight-phase zero dynamics. Finally, it is verified (numerically) that

$$\frac{\partial}{\partial a_5} \left(q_{5,d} - q_5(0) - \int_0^{t_f} \tilde{\kappa}_{1,f}(t, \sigma_1^{*s-}, a_5) dt \right) \Big|_{a_5=a_5^*} \neq 0, \quad (9.56)$$

and thus by the implicit function theorem, there exists an open subset about σ_1^{*s-} and a differentiable function \tilde{w}_s^f such that $\tilde{w}_s^f(\sigma_1^{*s-}) = a_5^*$ and

$$q_{5,d} = q_5(0) + \int_0^{t_f} \tilde{\kappa}_{1,f}(t, \sigma_1^{s-}, \tilde{w}_s^f(\sigma_1^{s-})) dt. \quad (9.57)$$

Since (9.57) is scalar while a_5 has four components, there exist an infinite number of solutions for \tilde{w}_s^f . Hence, a numerical optimization was performed to find, for each point in a neighborhood of σ_1^{*s-} , a value of a_5 that steers q_5 to $q_{5,d}$, while minimizing⁶ $\|a_5 - a_5^*\|$. The flight-phase control design is completed by formally defining $h_{d,f}(q_f, a_f)$, $a_f := (\sigma_1^{s-}; a_5)$, and $w_s^f(x_s^-) := (\sigma_1^{s-}; \tilde{w}_s^f(\sigma_1^{s-}))$.

9.5.4 Simulation without Modeling Error

The control law developed above has been simulated on a model of RABBIT for the various running motions. Assuming no modeling error and initializing

⁶Other criteria could be used, such as minimization of the torques in the flight phase. This latter criterion requires the computation of the torques via the dynamic model, and hence is costly in calculation time.

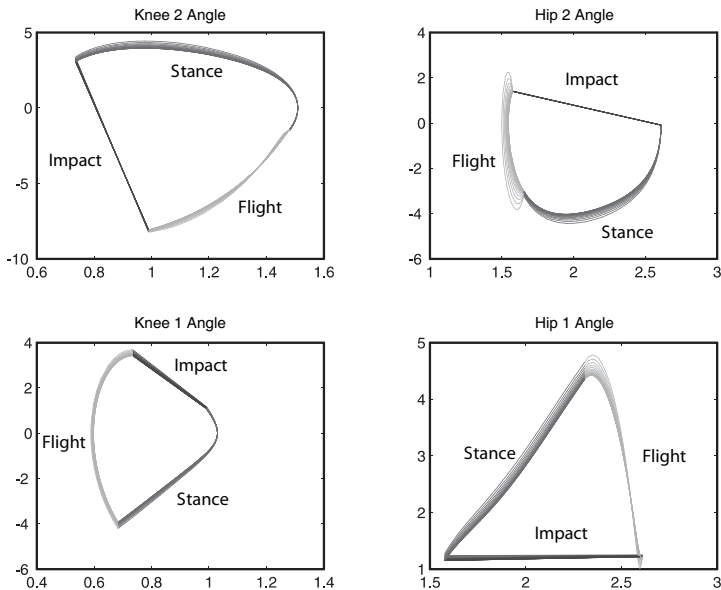


Figure 9.9. Running at 1.5 m/s. The four graphs depict the relative joint angles in radians (x-axis) versus their velocities in rad/sec (y-axis) in the stance, flight, and impact phases. The swing knee angle is the knee of leg-2, the swing hip angle is the hip of leg-2, the stance knee angle is the knee of leg-1, and the stance hip angle is the hip of leg-1. At impact, the roles of the limbs are exchanged as a consequence the configuration angles change at impact; see (3.101). Notice that the robot has the same configuration at each transition between phases. The plots indicate that a limit cycle is achieved.

the closed-loop system off the periodic orbit—with the initial velocity 10% higher than the value on the periodic orbit—the simulation data presented in Figs. 9.9–9.16 are obtained for the running motions of 1.5 m/s and 2.5 m/s.

For a running speed of 1.5 m/s (resp., 2.5 m/s) Figs. 9.9 and 9.10 (resp., Figs. 9.13 and 9.14) show the phase-plane evolution of the configuration variables. The convergence to the periodic orbit is clear. By the design of the controller, the stance-phase evolution of the configuration variables does not change stride-to-stride; only the velocities change. In the flight phase, (most notably, for the hips and the torso when running at 1.5 m/s), the path traced out is modified so that the robot lands in the desired state.

Figures 9.11 and 9.15 depict the torques for running at 1.5 m/s and 2.5 m/s, respectively. As the motion converges to the periodic orbit, the torques correspond to their optimal values, and hence are within the capabilities of the actuators. Off the periodic orbit, the torques are significantly higher in the flight phase. For the slower 1.5 m/s-orbit, the torque increase occurs principally in the hips. For the faster 2.5 m/s-orbit, the torque increase is more

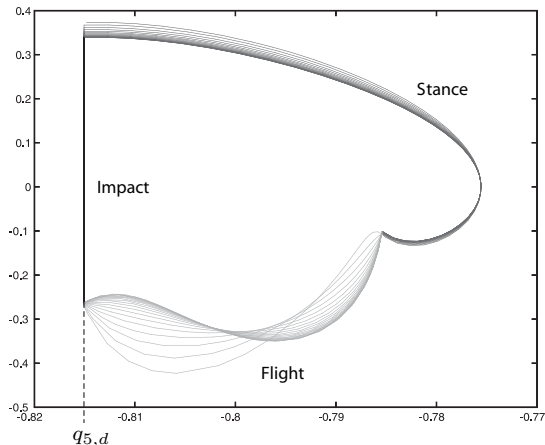


Figure 9.10. Running at 1.5 m/s. The graph depicts torso angle in radians (x-axis) versus its velocity in rad/sec (y-axis) in the stance and flight phases. Notice that the flight-phase controller has regulated the torso angle to its desired value of $q_{5,d}$ at impact. The plot indicates that a limit cycle is achieved.

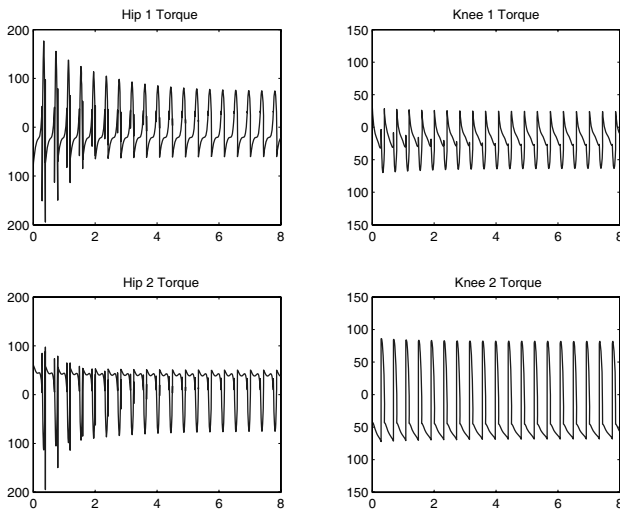


Figure 9.11. Running at 1.5 m/s. The four graphs depict the joint torques in Newton-meters (y-axis) versus time in seconds (x-axis) in the stance and flight phases. Upon convergence to the periodic orbit, the achieved torques are very close to their optimal values. The torque is higher in the flight phase away from the periodic orbit, especially in the hips.

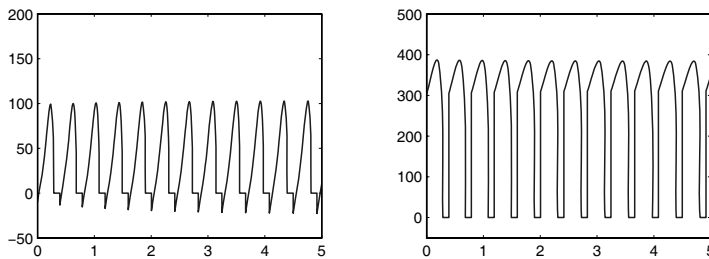


Figure 9.12. Running at 1.5 m/s. The left graph depicts leg-1 (stance leg) horizontal force in Newtons (y-axis) versus time in seconds (x-axis) in the stance and flight phases. The right graph depicts vertical force (y-axis) versus time (x-axis) in the stance and flight phases. The impulsive forces existing during impact are not presented.

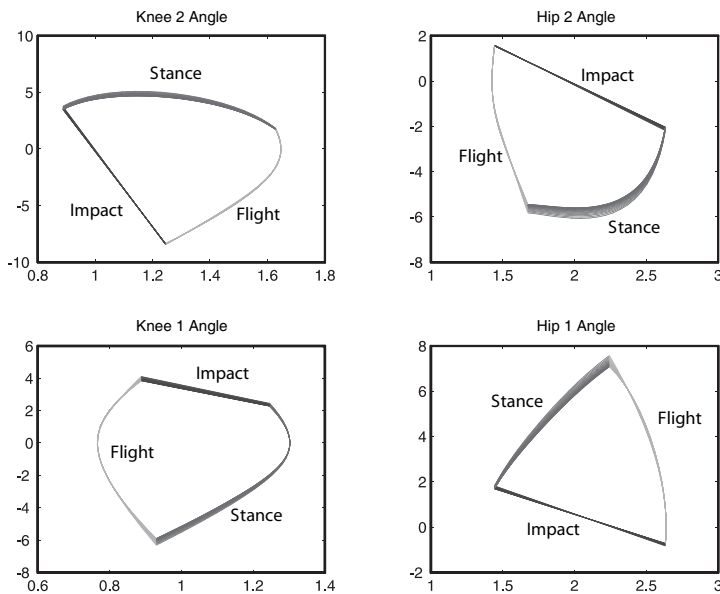


Figure 9.13. Running at 2.5 m/s. The four graphs depict the relative joint angles in radians (x-axis) versus their velocities in rad/sec (y-axis) in the stance, flight, and impact phases. The swing knee angle is the knee of leg-2, the swing hip angle is the hip of leg-2, the stance knee angle is the knee of leg-1, and the stance hip angle is the hip of leg-1. At impact, the roles of the limbs are exchanged as a consequence the configuration angles change at impact; see (3.101). Notice that the robot has the same configuration at each transition between phases. The plots indicate that a limit cycle is achieved.

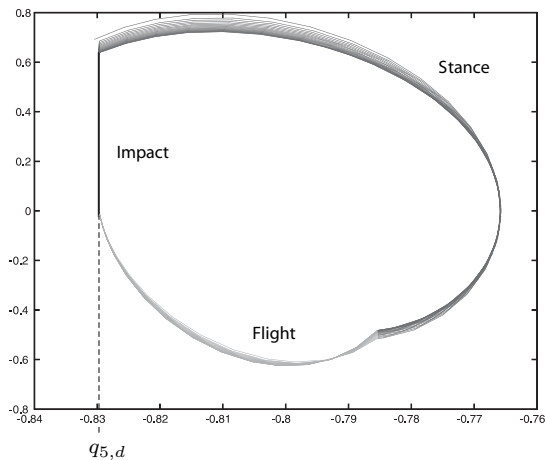


Figure 9.14. Running at 2.5 m/s. The graph depicts torso angle in radians (x-axis) versus its velocity in rad/sec (y-axis) in the stance and flight phases. Notice that the flight-phase controller has regulated the torso angle to its desired value of $q_{5,d}$ at impact. The plot indicates that a limit cycle is achieved.

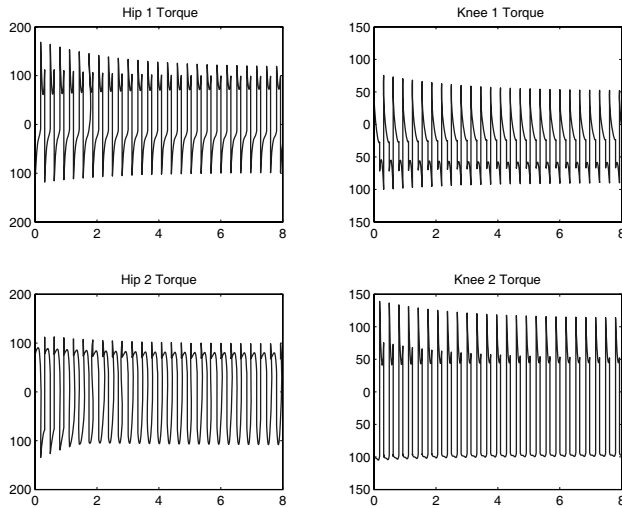


Figure 9.15. Running at 2.5 m/s. The four graphs depict the joint torques in Newton-meters (y-axis) versus time in seconds (x-axis) in the stance and flight phases. Upon convergence to the periodic orbit, the achieved torques are very close to their optimal values. The torque is higher in the flight phase away from the periodic orbit, especially in the hips.

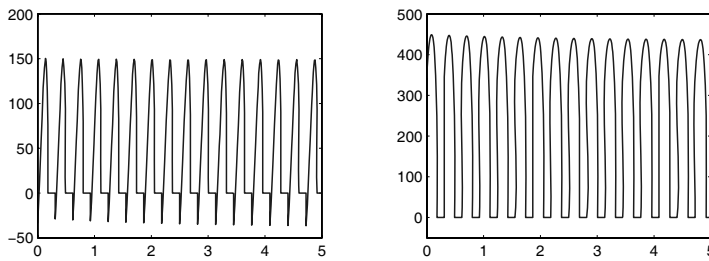


Figure 9.16. Running at 2.5 m/s. The left graph depicts leg-1 (stance leg) horizontal force in Newtons (y-axis) versus time in seconds (x-axis) in the stance and flight phases. The right graph depicts vertical force (y-axis) versus time (x-axis) in the stance and flight phases. The impulsive forces existing during impact are not presented.

evenly divided among the four actuators and is smaller in magnitude; the corresponding modification to the path in the flight phase is also smaller; see Figs. 9.13 and 9.14.

The reaction forces on leg-1 are provided in Figs. 9.12 and 9.16. These graphs show the alternating phases of single support and flight. The robot will not slip for a coefficient of friction greater than 0.5. The vertical force during the single support phase is very close to the weight of the robot (from Table 6.3, its mass is 32 kg).

9.6 A Partial Robustness Evaluation

The purpose of this section is to show that the proposed control strategy may still yield an attractive limit cycle even if the hypotheses made in the modeling of the robot, the control law's construction, and the analysis and simulation of the closed-loop system are not met exactly. The model of Section 3.5 assumed a rigid contact between the leg end and the ground. Here, a *compliant contact model* will be used [176]. This has several consequences. First, the seven DOF model of Section 3.5.1 will be used in the stance phase, with the position of the leg end with respect to the ground evolving freely as a function of the reaction forces provided by the compliant contact model. Second, the robot will enter the flight phase when the reaction forces at the leg end go to zero. Finally, the impact forces at touch down will be computed by the compliant model as well. In addition to these changes, parameter error will be introduced in the robot model.

Table 9.2. Compliant contact model parameters.

| Parameter | Value | Parameter | Value |
|---------------|-----------------|---------------|------------------|
| λ^a | 9×10^6 | ϑ^a | 260 |
| λ^b | 0.3 | ϑ^b | 0.6 |
| ϑ^c | 0.18 | n | 1.5 |
| ϑ^d | 0.3 | k | 25×10^5 |
| | | ϑ^e | 0.285 |

9.6.1 Compliant Contact Model

In the experimental platform of RABBIT, see [Sections 2.1](#), [6.6.2.1](#), and [8.1.1](#), the contact between the ends of the robot's legs and the ground is compliant and the ends of the legs may slip. A model that more closely reflects these points is summarized here. A more detailed discussion is available in [176] and the references therein.

The dynamic model consists of the full 7-DOF model of the biped (3.84) with the computation of the forces acting on the leg end being given by

$$\begin{aligned} F_n &= -\lambda^a |\mathbf{z}|^n \dot{\mathbf{z}} - \lambda^b |\mathbf{z}|^n \operatorname{sgn}(\dot{\mathbf{z}}) \sqrt{|\dot{\mathbf{z}}|} + k |\mathbf{z}|^n \\ F_t &= (\vartheta^a d + \vartheta^b \dot{d} + \vartheta^c \mathbf{v} + \vartheta^d \operatorname{sgn}(\dot{\mathbf{v}}) \sqrt{|\dot{\mathbf{v}}|}) |F_n| \\ \dot{d} &= \mathbf{v} - |\mathbf{v}| \frac{\vartheta^a}{\vartheta^e} d, \end{aligned} \quad (9.58)$$

where $\mathbf{z} \leq 0$ is the penetration depth (if $\mathbf{z} \leq 0$, the leg is in contact with the ground, if $\mathbf{z} > 0$, the leg is not in contact with the ground and the contact forces equal zero) and \mathbf{v} is the relative velocity of the end of the leg with respect to the ground. This model supposes that the interface between the two contacting surfaces is a contact between bristles; the average deflection d of the bristles is an internal state used to model dynamic friction. The numerical values used in the simulation, given in Table 9.2, were adjusted for a nominal penetration of approximately 3 mm and to avoid rebound of the leg during the stance phase.

Together, the models (3.84) and (9.58) describe the robot's evolution in all phases of motion: flight, stance, and impact. The robot's dynamics are then described by ordinary (nonhybrid) differential equations over the entire stride, even during the impact, which will now have a nonzero duration. With this model, contact forces at the leg end are continuous, which means in particular that they will not experience an instantaneous jump to zero at the transition from stance to flight as supposed in the development of the control law.

9.6.2 Simulation with Modeling Error

In addition to the structural change in the contact model, parametric modeling error is included. A deviation of $\pm 20\%$ in the masses and inertias was introduced between the robot's design model and the simulation model; symmetry of the two legs was preserved. It is important to note that one consequence of parametric error is that there will be an error in the state of the robot at landing; because the flight-phase controller does not correspond to the simulation model, it will not correctly account for the conservation of angular momentum. Finally, saturation of ± 150 Nm was introduced on the torques to take into account the limitations of the actuators of RABBIT.

Despite all of the differences between the simulation model and the model used to design the controller, the feedback controller illustrated in Section 9.5 is able to induce a stable running motion. This is shown in Figs. 9.17–9.20 for a nominal speed of 1.5 m/s. In the simulations, the controller was switched from the stance phase to flight phase when $\theta_s(q)$ attained θ_s^- , and it was switched from flight phase to stance phase when the penetration of the leg end into the compliant surface exceeded 2 mm. Due to the differences in the design and simulation models, the limit cycle does not correspond exactly to the theoretical prediction. The value of ζ^* calculated from the simulation data and the model parameters is 829, whereas the value predicted with the rigid model and perfectly known parameters was 801 (see Table 9.1). The average running speed was calculated to be 1.54 m/s, compared to the design's value of 1.50 m/s.

Figures 9.17 and 9.18 show the evolution of the configuration variables in the phase plane; the convergence to a limit cycle is clear. At touchdown, the roles of the legs are swapped, as when the rigid contact model was used. At the beginning of the stance phase, the impact causes an abrupt change in the robot's velocities. At the moment of contact, the robot's velocities still correspond to their values from the flight phase. The control law sees this as a large set-point error and consequently applies a large torque, resulting in saturation; see Fig. 9.19. Once past the impact, the evolution of the relative angles is quite close to what was predicted with the rigid impact model; see Fig. 9.9 and Fig. 9.10. The perturbations during the flight phase are small because the initial condition of the simulation lies on the periodic orbit corresponding to the rigid contact model and no parametric modeling error.

The reaction forces on leg-1 are provided in Fig. 9.20. These graphs show the alternating phases of single support and flight. Except during impact, which is no longer instantaneous, the forces are close to the values predicted by the earlier simulation; see Fig. 9.12. The penetration of the stance leg end stabilizes at approximately 3 mm. These two plots show clearly the very rapid liftoff of the stance leg to initiate the flight phase. Consequently, for the purposes of modeling, feedback design, and analysis, it is as reasonable to suppose an instantaneous transition to the flight phase as it is to suppose an instantaneous impact.

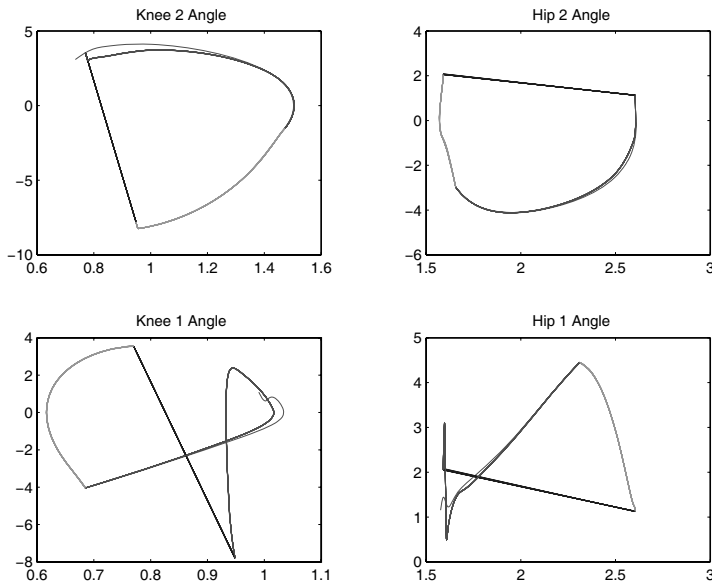


Figure 9.17. Running at 1.5 m/s with the compliant contact model and parametric modeling error. The four graphs depict the relative joint angles in radians (x-axis) versus their velocities in rad/sec (y-axis) in the stance, flight, and impact phases. The swing knee angle is the knee of leg-2, the swing hip angle is the hip of leg-2, the stance knee angle is the knee of leg-1, and the stance hip angle is the hip of leg-1. At impact, the roles of the limbs are exchanged. Notice the abrupt change in the velocities at impact, especially in the stance leg. The plots indicate that a limit cycle is achieved.

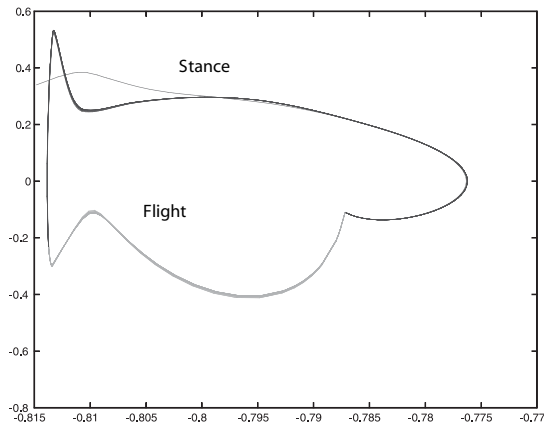


Figure 9.18. Running at 1.5 m/s with the compliant contact model and parametric modeling error. The graph depicts torso angle in radians (x-axis) versus its velocity in rad/sec (y-axis) in the stance and flight phases. Notice that the flight-phase controller has approximately regulated the torso angle to its desired value of $q_{5,d}$ at impact. The plot indicates that a limit cycle is achieved.

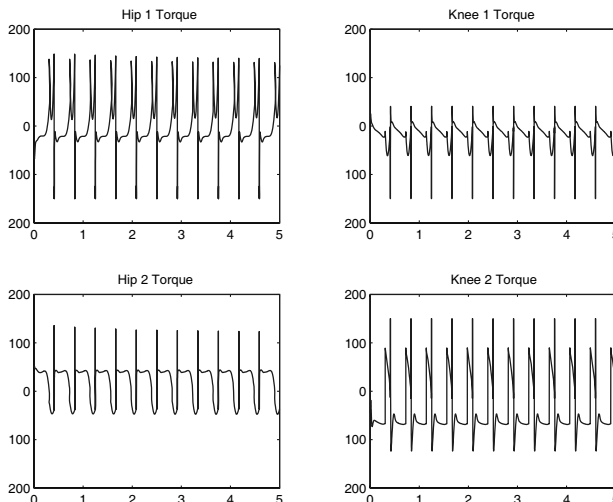


Figure 9.19. Running at 1.5 m/s with the compliant contact model and parametric modeling error. The four graphs depict the joint torques in Newton-meters (y-axis) versus time in seconds (x-axis) in the stance and flight phases. The torques are limited to ± 150 Nm. Upon convergence to the periodic orbit, the achieved torques are close to their optimal values. Prior to convergence, note the larger torques in the beginning of the stance phase due to a combination of modeling error and landing in the wrong state.

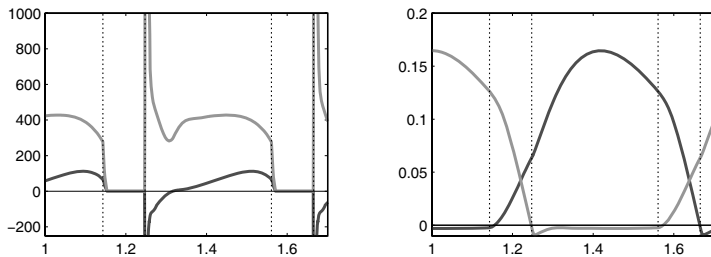


Figure 9.20. Running at 1.5 m/s with the compliant contact model and parametric modeling error. The left graph depicts leg-1 (stance leg) horizontal and vertical force components in Newtons (y-axis) versus time in seconds (x-axis) in the stance and flight phases. Large forces occur at touchdown; the maximal vertical force is close to 8000 N and the maximal horizontal force is close to -4000 N with the compliant contact model. The vertical lines show the instant of transition between the control law phases. The right graph depicts the vertical position of the leg end in meters (y-axis) versus time in seconds (x-axis) in the stance and flight phases. Notice that the flight control law induces the stance leg to lift off quickly and the reaction forces to go to zero.

9.7 Additional Event-Based Control for Running

Each of the feedback designs illustrated in Section 9.5 resulted in a nominally exponentially stable running motion. Indeed, this has been the case for all of the periodic orbits computed using the techniques in [44]. From Table 9.1, it is seen that the rate of convergence to the periodic orbit decreases as the average running speed increases (that is, μ becomes closer to 1.0). The aim of this section is to illustrate how an additional event-based control action introduced in Chapter 7 can be profitably used to increase the rate of convergence to the periodic orbit. It will also be shown that the additional feedback action can be used to reduce the magnitude of the torques that are used in the flight phase to attain the desired landing state.

Remark 9.3 In Section 9.6.2, it was seen that modeling error alters the average running speed. As in Chapter 7, event-based control could also be used to attenuate the effects of modeling error on average running speed. In addition, it could be used to stabilize a periodic orbit that was nominally unstable under the feedback designs proposed so far.

9.7.1 Deciding What to Control

Based on the approach taken in [185], it is natural to conjecture that modification of the target landing configuration stride-to-stride can be used to improve the rate of convergence to the orbit and the peak torques in the flight phase. In particular, the horizontal distance between the center of mass and the stance leg has a strong effect⁷ on μ . This suggests modifying the landing configuration in the direction $[0; 0; 1; 0; 0]$. On the other hand, the action of modifying the flight trajectory to obtain the correct orientation of the torso at landing is what leads to the higher torques. This suggests modifying the landing configuration in the direction $[0; 0; 0; 0; 1]$.

9.7.2 Implementing Stride-to-Stride Updates of Landing Configuration

Let $q_0^{\text{f}^-}$ denote the nominal landing configuration for one of the running motions of Section 9.5; see (9.52). Set the desired landing configuration at the k th stride to be

$$q_{0,d}^{\text{f}^-}(k) = q_0^{\text{f}^-} + [0; 0; w_1(k); 0; w_2(k)], \quad (9.59)$$

where the scalars $w_1(k)$ and $w_2(k)$ are to be updated at the end of each stance phase. Through the impact map (3.101), a change in the desired landing configuration needs to be accompanied by a corresponding change in the desired initial stance configuration. Both of these changes entail stride-to-stride parameter updates to the stance and flight controllers of Section 9.3. As a result, the restricted Poincaré map is now a function of $w_1(k)$ and $w_2(k)$ and can be viewed as a discrete-time control system

$$\zeta(k+1) = \rho(\zeta(k), w_1(k), w_2(k)) \quad (9.60)$$

with state space $\tilde{\mathcal{S}} \cap \mathcal{Z}_s$ and inputs $(w_1; w_2) \in \mathbb{R}^2$; see Chapters 4 and 7 for details. Linearizing (9.60) about the nominal fixed-point ζ^* corresponding to $w_1 = 0$ and $w_2 = 0$ results in

$$\delta\zeta(k+1) = \mu\delta\zeta(k) + b_1\delta w_1(k) + b_2\delta w_2(k). \quad (9.61)$$

The value of μ is determined from Corollary 9.1; the sensitivities b_1 and b_2 are more easily determined numerically through a simulation of the model.

Linear state variable feedback $\delta w_1(k) = k_1\delta\zeta(k)$, $\delta w_2(k) = k_2\delta\zeta(k)$ can then be used to tradeoff peak torques and the rate of convergence to the fixed point. For the running motion with average speed of 1.5 m/s, it was

⁷When the heights of the center of mass at the beginning and end of the stance phase are the same, $\mu = (\chi - |\beta|)$, which is a function only of the horizontal position of the center of mass with respect to the stance leg end; see (9.33).

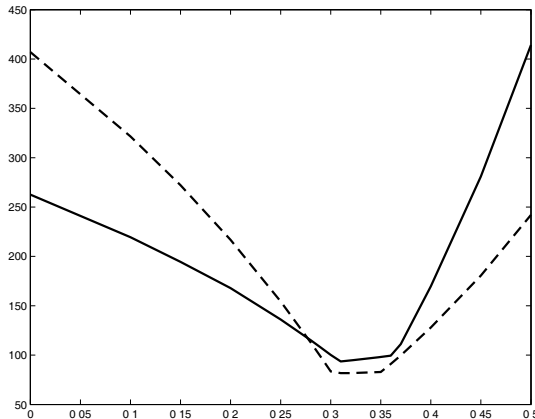


Figure 9.21. A one-parameter search to minimize peak torque. Let $k_2 = ak_1$. The graph depicts the maximal torque in Newton-meters (y-axis) versus the parameter a (x-axis) for an initial velocity of the robot equal to $\pm 10\%$ of its value on the periodic orbit (the solid line corresponds to $+10\%$ and the dashed line corresponds to -10%). The best choice of parameter a is $0.3 < a < 0.35$ to minimize the peak torque.

arbitrarily decided to place the closed-loop eigenvalue at $\mu_d = 2/3$. A one-parameter search was then performed to minimize the torques in the flight phase when the velocity upon entering the flight phase differed from the value on the periodic orbit by $\pm 10\%$, subject to $\mu + k_1 b_1 + k_2 b_2 = 2/3$; see Fig. 9.21. This resulted in $k_1 = 7.8 \times 10^{-5}$ and $k_2 = 2.6 \times 10^{-5}$. It is important to note that transient performance has been optimized subject to a stability constraint.

9.7.3 Simulation Results

Assuming no modeling error and initializing the closed-loop system off the periodic orbit—with the initial velocity 10% higher than its value on the periodic orbit—yields the simulation data presented in Figs. 9.22–9.24. The landing configuration is being modified at each stride. The orientation of the support hip and the torso vary slightly stride-to-stride under the event-based feedback. The deviation in the flight phase trajectory—compare Figs. 9.22 and 9.23 to Figs. 9.9 and 9.10—is clearly much less under the event-based control action. Consequently, the torques during the flight phase are noticeably reduced; see Fig. 9.24.

The evolution of ζ from stride-to-stride over the course of the simulation is presented in Fig. 9.25. The desired convergence rate has been achieved.

The evolution of the event-based control action w_1 is presented in Fig. 9.26. The induced variation in the landing configuration is rather small. Despite

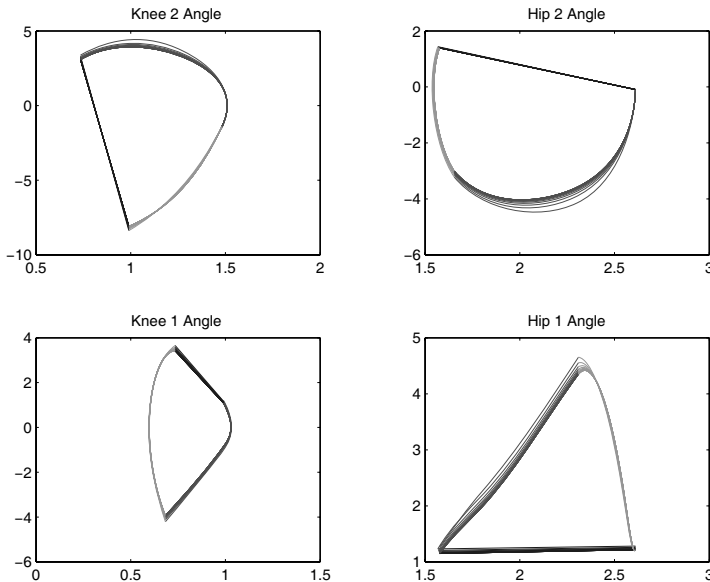


Figure 9.22. Running at 1.5 m/s with event-based control of the landing configuration. The four graphs depict the relative joint angles in radians (x-axis) versus their velocities in rad/sec (y-axis) in the stance, flight, and impact phases. The swing knee angle is the knee of leg-2, the swing hip angle is the hip of leg-2, the stance knee angle is the knee of leg-1, and the stance hip angle is the hip of leg-1. At impact, the roles of the limbs are exchanged as a consequence the configuration angles change at impact; see (3.101). Notice that the robot no longer has the same configuration at each transition between phases. The plots indicate that a limit cycle is achieved.

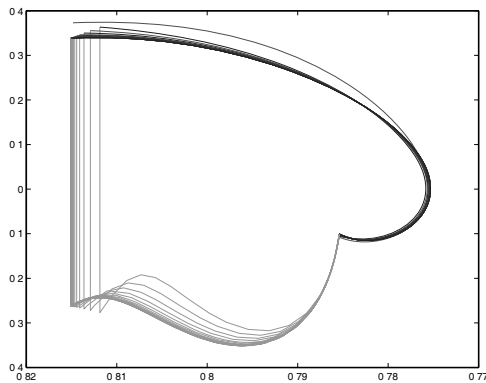


Figure 9.23. Running at 1.5 m/s with event-based control of the landing configuration. The graph depicts torso angle in radians (x-axis) versus its velocity in rad/sec (y-axis) in the stance and flight phases. Notice that the torso angle at the end of the flight phase varies stride-to-stride. The plot indicates that a limit cycle is achieved.

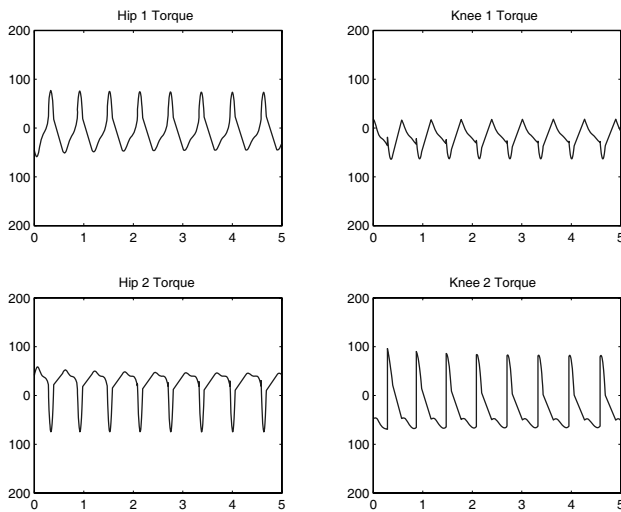


Figure 9.24. Running at 1.5 m/s with event-based control of the landing configuration. The four graphs depict the joint torques in Newton-meters (y-axis) versus time in seconds (x-axis) in the stance and flight phases. Modifying the landing configuration stride-to-stride has resulted in much smaller torques when the robot is off the periodic orbit.

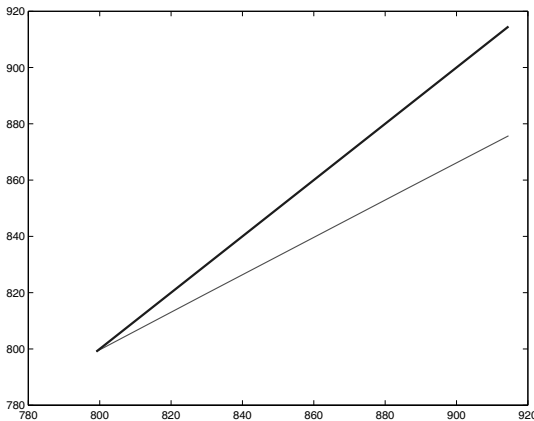


Figure 9.25. Running at 1.5 m/s with event-based control of the landing configuration. The graph's thick line depicts the value of ζ at step $k+1$ (y-axis) versus its value at step k (x-axis) as obtained directly from the simulation. The desired modification in the slope of the Poincaré map has been obtained without changing the fixed point: slope ≈ 0.66 and $\zeta^* \approx 800$. The thin line is the identity map. The fixed point is at the intersection of the two lines.

this, there are significant improvements in the rate of convergence to the periodic orbit and the reduction in peak torque.

9.8 Alternative Control Law Design

Up to this point, in order to achieve invariance of the zero dynamics manifold at landing, a deadbeat action has been incorporated in the flight phase controller to steer the robot to land in a predetermined configuration, while respecting conservation of angular momentum about the robot's center of mass. This action of the hybrid controller is key to creating a hybrid zero dynamics that allows the stability of a running motion to be analyzed in closed form on the basis of a restricted Poincaré map. In this section, the hypotheses on the landing configuration are slightly relaxed, leading to a controller that is easier to design, but which still lends the closed-loop system to a reduced-dimension stability test. To account for the changing configuration of the robot at touchdown, a form of the transition controller of Section 7.2 is adopted.⁸ Key points of the stability analysis are highlighted in Section 9.8.1.7.

⁸Caveat: the transition controller used here takes into account the joint angles of the robot at touchdown but not the joint angular velocities. As a result, a true HZD of running is not created, and the stability analysis of the closed-loop system must be modified accordingly.

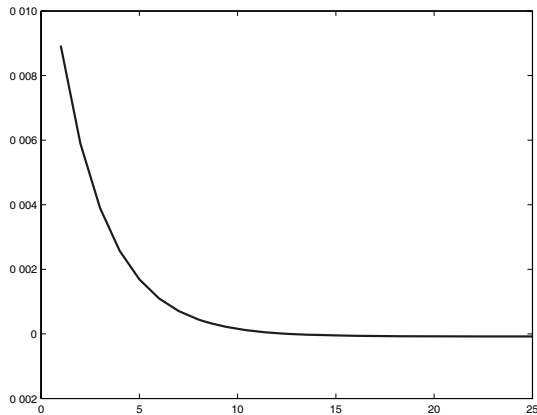


Figure 9.26. Running at 1.5 m/s with event-based control of the landing configuration. The graph depicts w_1 (y-axis) versus step number (x-axis) as obtained in the simulation. Note that $w_2 = (k_2/k_1)w_1$.

9.8.1 Controller Design

The discrete and continuous actions of the modified hybrid control law are now discussed in detail.

9.8.1.1 Virtual Constraints

Since RABBIT has four independent actuators (two at the hips and two at the knees), four virtual constraints may be imposed in both the stance and flight phases. For purposes of design, the virtual constraints are parameterized as in Chapter 6. The parameter sets of the stance phase and flight phase virtual constraints are distinguished by a_s and a_f , respectively, taking values in $\mathcal{A}_s := \mathbb{R}^{n_s}$ and $\mathcal{A}_f := \mathbb{R}^{n_f}$. The parameter may be updated at takeoff and landing events but are otherwise constant. With this notation, the virtual constraints for stance and flight are, respectively,

$$y = q_b - h_{d,s}[a_s](\theta_s(q_s)) \quad (9.62a)$$

$$y = q_b - h_{d,f}[a_f](\theta_f[a_f](q_f)). \quad (9.62b)$$

9.8.1.2 Stance Phase Control

The controller for the stance phase acts by updating the parameters a_s and by enforcing the virtual constraints (9.62a). Apart from different boundary conditions that will be introduced on the virtual constraints, this control is identical to the controller developed in Section 9.3.1. The stance phase parameter vector, a_s , may be expressed as

$$a_s := (a_{s,0}; a_{s,1}; \dots; a_{s,m_s-1}; a_{s,m_s}; \theta_s^-; \theta_s^+), \quad (9.63)$$

where $m_s \geq 3$, $a_{s,i} \in \mathbb{R}^4$ for $i \in \{0, 1, \dots, m_s - 1, m_s\}$, and $\theta_s^-, \theta_s^+ \in \mathbb{R}$. Note that $n_s = 4(m_s + 1) + 2$. The terms θ_s^- and θ_s^+ are the values of the function $\theta_s(q_s)$ evaluated at the end and the beginning of the stance phase. Instead of Bézier polynomials, suppose that a slightly different class of polynomials⁹ are used such that:

$$\begin{aligned} h_{d,s}[a_s](\theta_s^+) &= a_{s,0} & \frac{d}{d\theta_s} h_{d,s}[a_s](\theta_s^-) &= a_{s,m_s-1} \\ \frac{d}{d\theta_s} h_{d,s}[a_s](\theta_s^+) &= a_{s,1} & h_{d,s}[a_s](\theta_s^-) &= a_{s,m_s}. \end{aligned} \quad (9.64)$$

The stance-phase virtual constraints are imposed on the dynamics by using a control $u_s : \mathcal{X}_s \times \mathcal{A}_s \rightarrow \mathbb{R}^4$ that drives (9.62a) to zero *in finite time*. The specific conditions are as in Theorem 5.4.

9.8.1.3 Flight Phase Control

The development of the flight-phase controller is similar to that of the stance-phase controller. The key difference is the choice of θ_f in (9.62b) to be a function of the position of the center of mass. The flight-phase parameter vector, a_f , is defined as

$$a_f := (a_{f,0}; a_{f,1}; \dots; a_{f,m_f-1}; a_{f,m_f}; x_{cm,f}^+; \dot{x}_{cm,f}^+; T_f), \quad (9.65)$$

where $m_f \geq 3$, $a_{f,i} \in \mathbb{R}^4$ for $i \in \{0, 1, \dots, m_f - 1, m_f\}$, and $x_{cm,f}^+, \dot{x}_{cm,f}^+, T_f \in \mathbb{R}$. Note that $n_f = 4(m_f + 1) + 3$. The terms $x_{cm,f}^+$, $\dot{x}_{cm,f}^+$, and T_f are, respectively, the horizontal position of the center of mass at the beginning of the flight phase, the horizontal velocity of the center of mass at the beginning of the flight phase, and the estimated¹⁰ duration of the flight phase. The flight phase virtual constraints (9.62b) are given by

$$\theta_f[a_f](q_f) := \frac{1}{T_f} \left(\frac{x_{cm} - x_{cm,f}^+}{\dot{x}_{cm,f}^+} \right), \quad (9.66)$$

and $h_{d,f}[a_f]$, which, as in the stance phase, is a smooth, vector-valued function that satisfies

$$\begin{aligned} h_{d,f}[a_f](0) &= a_{f,0} & \frac{d}{d\theta_f} h_{d,f}[a_f](1) &= a_{f,m_f-1} \\ \frac{d}{d\theta_f} h_{d,f}[a_f](0) &= a_{f,1} & h_{d,f}[a_f](1) &= a_{f,m_f}. \end{aligned} \quad (9.67)$$

For a given stride, let t_f denote the elapsed time within the flight phase. By conservation of linear momentum, $\dot{x}_{cm,f}^+$ is constant during flight, which

⁹Any class of smooth functions satisfying these properties may be used to define virtual constraints.

¹⁰Calculation of T_f requires the height of the center of mass at landing, $y_{cm,f}^-$, to be known *a priori*, which is only possible if the virtual constraints are exactly enforced throughout the flight phase.

implies $t_f = (x_{cm} - x_{cm,f}^+)/\dot{x}_{cm,f}^+$. As a result, $\theta_f = t_f/T_f$ is a valid substitute for (9.66), and for this reason, the given flight phase virtual constraints are said to be *time scaled*. Flight phase virtual constraints are enforced using any smooth state-feedback controller $u_f : \mathcal{X}_f \times \mathcal{A}_f \rightarrow \mathbb{R}^4$ that drives (9.62b) to zero exponentially quickly.

9.8.1.4 Transition Control: Landing

In the event that landing occurs with the state of the robot not satisfying the virtual constraints, the control parameters of the subsequent stance phase, a_s , are updated to ensure that the configuration of the robot satisfies $q_b - h_{d,s}[a_s](\theta_s^+) = 0$. The parameter updates are governed by the differentiable function $w_f^s : \mathcal{S}_f^s \rightarrow \mathcal{A}_s$, such that for $a_s = w_f^s(x_f^-)$,

$$\begin{aligned} a_{s,0} &= q_b^+ \\ a_{s,1} &= a_{s,1}^* & \theta_s^+ &= \theta_s(q_s^+) \\ &\vdots & \theta_s^- &= \theta_s^{-*} \\ a_{s,m_s-1} &= a_{s,m_s-1}^* \\ a_{s,m_s} &= a_{s,m_s}^*. \end{aligned} \tag{9.68}$$

In the above, q_s^+ is calculated using $\Delta_f^s(x_f^-)$, and the terms θ_s^{-*} and $a_{s,i}^* \in \mathbb{R}^4$, $i \in \{1, \dots, m_s - 1, m_s\}$ are constant parameters chosen during design.

If the stance phase finite-time controller can satisfy the virtual constraints (9.62a) before the liftoff event occurs, and the parameter updates obey (9.68), then the stance phase will terminate with $q_b - h_{d,s}[a_s](\theta_s^-) = 0$, or equivalently, with $q^- = q^{-*}$.

9.8.1.5 Transition Control: Takeoff

At takeoff, the parameters of the flight phase virtual constraints, a_f , are updated so that the duration of the planned motion of the robot is equal to the estimated flight time. Parameter updates are governed by a continuously differentiable function $w_s^f : \mathcal{S}_s^f \rightarrow \mathcal{A}_f$, such that for $a_f = w_s^f(x_s^-)$,

$$\begin{aligned} a_{f,0} &= a_{f,0}^* \\ a_{f,1} &= a_{f,1}^* & x_{cm,f}^+ &= (f_{cm}(q_s^-))_1 \\ &\vdots & \dot{x}_{cm,f}^+ &= \left(\frac{\partial f_{cm}}{\partial q_s}(q_s^-) \dot{q}_s^- \right)_1 \\ a_{f,m_f-1} &= a_{f,m_f-1}^* \\ a_{f,m_f} &= a_{f,m_f}^* \\ T_f &= \frac{\dot{y}_{cm,f}^+}{g_0} + \frac{\sqrt{(\dot{y}_{cm,f}^+)^2 - 2g_0(y_{cm,f}^{-*} - y_{cm,f}^+)}}{g_0}, \end{aligned} \tag{9.69}$$

where $y_{\text{cm},f}^{-*}$ is the height of the center of mass at the end of the flight phase on the limit cycle. The terms $a_{f,i}^* \in \mathbb{R}^4, i \in \{0, 1, \dots, m_f - 1, m_f\}$ are parameters chosen during design. As before, initiation of the takeoff event is a control decision, designated to occur when $\theta_s(q) = \theta_s^-$. In the closed-loop model, the switching hypersurface is $\mathcal{S}_s^f = \{(x_s, a_s) \in \mathcal{X}_s \times \mathcal{A}_s \mid H_s^f(x_s, a_s) = 0\}$ where $H_s^f(x_s, a_s) := \theta_s(q) - \theta_s^-$.

9.8.1.6 Closed-Loop Hybrid Model

The closed-loop hybrid model is defined as before. Define the augmented state spaces $\bar{\mathcal{X}}_f := T\mathcal{Q}_f \times \mathcal{A}_f$ and $\bar{\mathcal{X}}_s := T\mathcal{Q}_s \times \mathcal{A}_s$ with elements given by $\bar{x}_f := (q_f; \dot{q}_f; a_f)$ and $\bar{x}_s := (q; \dot{q}; a_s)$. The closed-loop dynamics may then be written as

$$\bar{f}_f(\bar{x}_f) := \begin{bmatrix} f_f(x_f) + g_f(x_f)u_f(x_f, a_f) \\ 0_{n_f \times 1} \end{bmatrix} \quad (9.70a)$$

$$\bar{f}_s(\bar{x}_s) := \begin{bmatrix} f_s(x_s) + g_s(x_s)u_s(x_s, a_s) \\ 0_{n_s \times 1} \end{bmatrix}. \quad (9.70b)$$

The vectors of zeros correspond to the fact that the virtual constraint parameters do not change during the continuous phases of running. The impact maps in which the parameters are updated are modified to include the parameter update laws w_f^s and w_s^f :

$$\bar{\Delta}_f^s(\bar{x}_f^-) := \begin{bmatrix} \Delta_f^s(x_f^-) \\ w_f^s(x_f^-) \end{bmatrix} \quad (9.71a)$$

$$\bar{\Delta}_s^f(\bar{x}_s^-) := \begin{bmatrix} \Delta_s^f(x_s^-) \\ w_s^f(x_s^-) \end{bmatrix}. \quad (9.71b)$$

The closed-loop hybrid model is then

$$\Sigma_{cl,f} : \left\{ \begin{array}{l} \bar{\mathcal{X}}_f = T\mathcal{Q}_f \times \mathcal{A}_f \\ \bar{\mathcal{F}}_f : (\dot{\bar{x}}_f) = \bar{f}_f(\bar{x}_f) \\ \bar{S}_f^s = \{(x_f; a_f) \in \bar{\mathcal{X}}_f \mid H_f^s(x_f) = 0\} \\ \bar{T}_f^s : \bar{x}_f^+ = \bar{\Delta}_f^s(\bar{x}_f^-) \end{array} \right. \quad (9.72a)$$

$$\Sigma_{cl,s} : \left\{ \begin{array}{l} \bar{\mathcal{X}}_s = T\mathcal{Q}_s \times \mathcal{A}_s \\ \bar{\mathcal{F}}_s : (\dot{\bar{x}}_s) = \bar{f}_s(\bar{x}_s) \\ \bar{S}_s^f = \{(x_s; a_s) \in \bar{\mathcal{X}}_s \mid H_s^f(x_s, a_s) = 0\} \\ \bar{T}_s^f : \bar{x}_s^+ = \bar{\Delta}_s^f(\bar{x}_s^-). \end{array} \right. \quad (9.72b)$$

9.8.1.7 Existence and Stability of Periodic Orbits

The Poincaré return map is formed as in (9.28). Theorem 9.1 still holds, but its application cannot be further simplified via the restricted Poincaré map of Theorem 9.3, because the zero dynamics manifold of the stance phase is *not* invariant under the impact map. The analysis of the existence and stability of periodic orbits proceeds, instead, with Theorem 4.4, which uses a different restricted Poincaré map; see (4.23).

9.8.2 Design of Running Motions with Optimization

The parameter optimization method of Section 6.3 can be modified to search the parameter spaces \mathcal{A}_s and \mathcal{A}_f for a set of parameters resulting in a desirable gait. Optimization is performed directly on the parameters of the virtual constraints in order to *simultaneously* determine a periodic running motion and a controller that achieves it. This is in contrast with the approach of Section 9.5 where the virtual constraints were designed by regression against optimal, precomputed, periodic trajectories. As in Section 6.3, constraints are incorporated into the search to address actuator limits, allowable joint space, and unilateral ground-contact forces. The constraints are also selected to ensure steady-state running at a desired speed. The cost function is selected to achieve overall efficiency of the gait.

A periodic orbit is sought on which the virtual constraints are identically satisfied. This has two consequences: first, the integration of the closed-loop system dynamics can be performed using the stance and flight phase zero dynamics (see [Section 9.3](#) for details), resulting in short computation times; and second, the virtual constraint parameters a_s and a_f are not completely independent. Once the independent parameters have been identified (i.e., once the dependent parameters are eliminated), standard numerical optimization routines may be used to search for desirable gaits. The implementation of such a procedure is outlined next.

9.8.2.1 Boundary Conditions of the Virtual Constraints

The transition maps of takeoff and landing can be used to identify redundancies between the virtual constraint parameter vectors a_s and a_f . Given the state corresponding to the limit-cycle stance phase end, $x_s^{-*} = (q_s^{-*}; \dot{q}_s^{-*})$, the state at the beginning of the subsequent flight phase may be computed as $x_f^{+*} = (q_f^{+*}; \dot{q}_f^{+*}) = \Delta_s^f(x_s^{-*})$. For both x_s^{-*} and x_f^{+*} to satisfy the virtual constraints of their respective phases, the following relations must hold,

$$\begin{aligned} a_{s,m_s-1}^* &= \dot{q}_{b,s}^{-*}/\dot{\theta}_s^{-*} & a_{f,0}^* &= q_{b,f}^{+*} \\ a_{s,m_s}^* &= q_{b,s}^{-*} & a_{f,1}^* &= \dot{q}_{b,f}^{+*} T_f^*, \end{aligned} \tag{9.73}$$

which are derived by applying (9.64), (9.66), (9.67), and (9.69) to (9.62). These are the boundary conditions associated with the liftoff event of the

periodic orbit. The state of the robot at the beginning of the stance phase, $x_s^{+*} = (q_s^{+*}; \dot{q}_s^{+*})$, can be related to the state at the end of the previous flight phase, $x_f^{-*} = (q_f^{-*}; \dot{q}_f^{-*})$, by the landing map $x_s^{+*} = \Delta_f^s(x_f^{-*})$ to yield the following additional design constraints,

$$\begin{aligned} a_{s,0}^* &= q_{b,s}^{+*} & a_{f,m_f-1}^* &= \dot{q}_{b,f}^{-*} T_f^* \\ a_{s,1}^* &= \dot{q}_{b,s}^{+*} / \dot{\theta}_s^{+*} & a_{f,m_f}^* &= q_{b,f}^{-*}. \end{aligned} \quad (9.74)$$

The update law presented here enforces fewer boundary conditions than the update law of Section 9.5. The extra boundary conditions associated with takeoff are already satisfied by (9.73), but those of landing are not met by (9.74); they are more difficult to satisfy due to conservation of angular momentum in the flight phase. The main theoretical result of this section is that invariance of the flight and stance phase constraint surfaces over the landing event is not a necessary condition for achieving provably stable running. As noted earlier, relaxing this condition makes running motions significantly easier to design.

9.8.2.2 Optimization Algorithm Details

Trial gaits for the running experiments were generated using the constrained nonlinear optimization routine `fmincon` of MATLAB's Optimization Toolbox. Three quantities are involved in optimization: J , a scalar cost function to be minimized on the periodic orbit, EQ , a vector of equality constraints, and $INEQ$, a vector of inequality constraints. The following is a description of the optimization procedure that was implemented. The independent and dependent terms¹¹ of optimization are given in [Table 9.3](#). Note that when the optimizer terminates with the constraints satisfied, x_s^{+*} will be a point located on a closed-loop periodic orbit and the virtual constraints will be parameterized by (9.63) and (9.65).

9.8.2.3 Algorithm

1. Select the state corresponding to the end of the flight phase, $x_f^{-*} = (q_f^{-*}; \dot{q}_f^{-*})$.
2. Using the flight-to-stance transition function Δ_f^s calculate the state corresponding to the beginning of the subsequent stance phase, $x_s^{+*} = (q_s^{+*}; \dot{q}_s^{+*})$.
3. Calculate θ_s^{+*} by (9.68) and $a_{s,0}^*$, $a_{s,1}^*$ by (9.74).

¹¹“Terms” is used to describe those variables used in optimization; these are different from the *parameters* of the virtual constraints.

Table 9.3. Independent and dependent terms used in optimization. The choice of the independent terms is nonunique and depends on the specific optimization procedure. The terms below correspond to the algorithm in Section 9.8.2.3, which is one straightforward method to ensure boundary conditions on the virtual constraints in order to ensure periodicity of an orbit satisfying the virtual constraints.

| Terms of Optimization | |
|--|--|
| Independent | Dependent |
| $x_f^{-*} \in \mathbb{R}^{14}$ | $\theta_s^{+*} \in \mathbb{R}$ |
| $a_{s,2}^*, \dots, a_{s,m_s}^* \in \mathbb{R}^4$ | $a_{s,0}^*, a_{s,1}^* \in \mathbb{R}^4$ |
| $\theta_s^{-*} \in \mathbb{R}$ | $x_s^{+*} \in \mathbb{R}^{10}$ |
| $a_{f,2}^*, \dots, a_{f,m_f-2}^* \in \mathbb{R}^4$ | $a_{f,0}^*, a_{f,1}^* \in \mathbb{R}^4$ |
| | $a_{f,m_f-1}^*, a_{f,m_f}^* \in \mathbb{R}^4$ |
| | $x_{cm,f}^{+*}, \dot{x}_{cm,f}^{+*}, T_f^* \in \mathbb{R}$ |
| | $x_f^- \in \mathbb{R}^{14}$ |

4. Select $a_{s,2}^*, \dots, a_{s,m_s}^*$, and θ_s^{-*} to complete the stance phase parameter vector a_s .
5. Using parameters a_s and the initial condition x_s^{+*} , integrate the equations of motion of stance and apply the stance-to-flight transition operator Δ_s^f to obtain $x_f^{+*} = (q_f^{+*}; \dot{q}_f^{+*})$.
6. Calculate $a_{f,0}^*$, $a_{f,1}^*$ by (9.73); a_{f,m_f-1}^* , a_{f,m_f}^* by (9.74); and $x_{cm,f}^{+*}$, $\dot{x}_{cm,f}^{+*}$, and T_f^* by (9.69).
7. Select $a_{f,2}^*, \dots, a_{f,m_f-2}^*$ to complete the flight phase parameter vector a_f .
8. Using parameters a_f and initial condition x_f^{+*} , integrate the equations of motion of flight to obtain x_f^- .
9. Evaluate J , EQ , and $INEQ$.
10. Iterate Steps 1 to 9 until J is (approximately) minimized, each entry of EQ is zero, and each entry of $INEQ$ is less than zero.

9.8.2.4 An Example Running Motion

A sample running gait designed by the above algorithm is now presented. A stick diagram of this motion is given in Fig. 9.27(a). The stability analysis outlined in Section 9.8.1.7 was applied to the resulting running motion. Figure 9.27(b) gives the restricted Poincaré map, which indicates that the motion is locally exponentially stable. The gait was designed to minimize the integral of torque squared per distance traveled, with the following constraints:

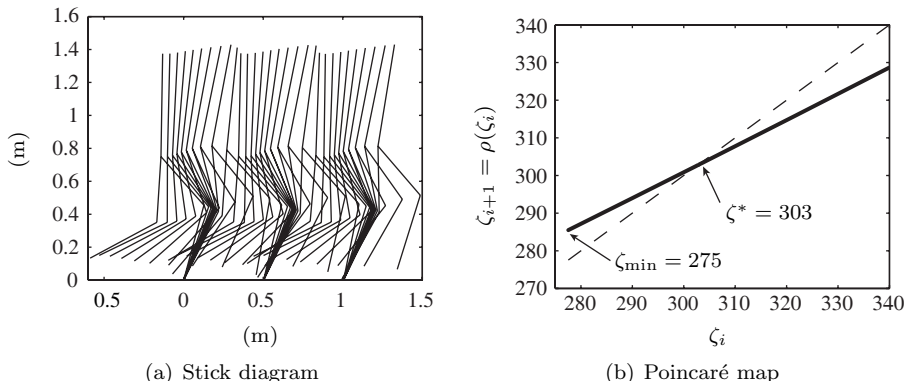


Figure 9.27. Stick diagram and Poincaré map for the example running motion (rate 0.58 m/s). Poincaré map constructed by evaluating $\zeta := (\sigma_{s,1}^-)^2/2$ at the end of successive stance phases, where $\sigma_{s,1}^-$ is the angular momentum about the stance leg end just before liftoff. The fixed point, $\zeta^* = 303$, is located at the intersection of ρ and the identity map and corresponds to an equilibrium running rate of 0.58 m/s. The slope of the graph at ζ^* is $d\rho/d\zeta \approx 0.67$, indicating exponential stability.

Equality constraints, EQ:

- error associated with finding a fixed point $\|x_f^- - x_f^{-*}\|$
- deviation from the desired running rate
- required frictional forces at the leg ends are zero just before takeoff and just after landing (to prevent slipping at these transitions)

Inequality constraints, INEQ:

- magnitude of the required torque at each joint less than 100 Nm
- knee angles to lie in $(0^\circ, -70^\circ)$ and hip angles to lie in $(130^\circ, 250^\circ)$ (see Fig. 6.13 for measurement conventions)
- minimum height of the swing foot during stance greater than 7 cm
- required coefficient of friction of the stance phase less than 0.7
- flight time greater than or equal to 25% of the total gait duration
- landing foot impacts the ground at an angle of approach less than 45° from vertical
- joint angular velocities less than 5 rad/sec.

9.9 Experiment

This section summarizes a first attempt to experimentally validate the theory of stable running developed in this chapter. The controller used was the one of Section 9.8 because its implementation was easier than that of the one reported in Section 9.3. In the set of experiments RABBIT executed six running steps on multiple occasions, but a steady-state running gait was not achieved. The observed gait was remarkably human-like, having long stride lengths (approx. 50 cm or 36% of body length), flight phases of significant duration (approx. 100 ms or 25% of step duration), an upright posture, and an average forward rate of 0.6 m/s. A video is available at [96, 239, 240].

9.9.1 Hardware Modifications to RABBIT

Prior to the experiment reported here, only walking experiments had been performed with RABBIT. To prepare for the task of running, four hardware modifications were made.

The first modification was the inclusion of prosthetic shock absorbers in the shanks. It was speculated that with shock absorbers the landing would cause less wear and tear on the harmonic drive gear reducers that form RABBIT's hip and knee joints. The inclusion of shock absorbers added approximately 5 cm to each shank.

The second modification was the installation of force sensitive resistors into RABBIT's point feet. These devices allowed for more accurate measurement of the touchdown time than did the previously installed mechanical contact switches. Since these sensors suffer from significant drift, their signals were numerically differentiated to make easier the detection of impact events.

The last two modifications were the bolting of aluminum u-channel stock along each thigh and the widening of the hips. Both of these changes were made to help prevent flexing of the legs in the frontal plane. Significant flexing was witnessed during the first several experimental trials of running. This problem was more pronounced in running than in walking because of the greater impact forces associated with landing. On several occasions RABBIT "tripped itself" during a stance phase of running when the swing leg passed by the stance leg (the legs knocked against each other). This came about because RABBIT was designed to have its legs close together to better approximate a planar biped.

9.9.2 Result: Six Running Steps

After completing the hardware modifications and successfully reproducing previous walking experiments, running experiments were conducted. A num-

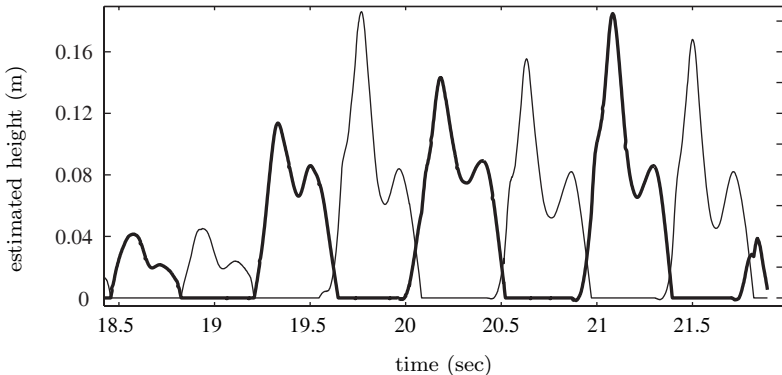


Figure 9.28. Estimated height of the feet (i.e., leg ends) with RABBIT's left foot indicated in bold. Flight phases occur when neither foot is at zero height.

ber of experimental trials resulted in RABBIT taking several human-like¹² running steps. One such trial, which was an implementation of the example running motion of Section 9.8.2.4, will be discussed here.

For this experiment, motion was initiated by an experimenter who pushed the robot forward, into the basin of attraction of a walking controller that induced walking with an average forward walking rate of 0.8 m/s. RABBIT then achieved stable walking, followed by a transition to running in a single step, followed by 6 running steps. After the sixth step, the experiment was terminated by the control software when the tracking error limit of 0.3 radians was exceeded for the stance knee angle. Examination of collected data suggests that tracking error resulted from actuator saturation.¹³ Data also show the swing leg extremely close to the ground at the moment the experiment was terminated, suggesting the swing leg may have, in fact, struck the ground contributing additional tracking error.

A plot of estimated¹⁴ foot height is given in Fig. 9.28. Average stride duration for the steps was 431 ms. Flight times, observed as those portions of Fig. 9.28 where neither leg is at zero height, lasted an average of 107 ms (25% of the stride). Videos of the experiment and many additional data plots are available at [96, 239, 240].

¹²A human-like gait is considered to be characterized by an upright posture, a torso leaning slightly forward, and a long step length.

¹³See Section 8.2 for a description of the PD controllers used to enforce the virtual constraints.

¹⁴When RABBIT is in flight, there is no accurate way to determine hip height. A sensor was mounted to record boom pitch angle, but due to flexing of the boom, these data were inaccurate. During the stance phase, this lack of sensing does not pose a problem because the end of the stance leg is always at zero height.

9.9.3 Discussion

Several drawbacks related to RABBIT's hardware did not appear until running was attempted. (For a discussion of general implementation issues of walking, including unmodeled effects of the boom, gear reducers, and an uneven walking surface, see [Section 8.1.1](#).) Future running experiments—whether on RABBIT or another, similar mechanism—should take into account the following issues.

9.9.3.1 Boom Dynamics

The perturbing effects of the boom were found to be much more significant during flight phases than during stance phases. When RABBIT is modeled as a planar system, an analysis of the three-dimensional mechanics shows that the contribution of the boom to the center of mass dynamics is significant. Specifically, q_5 is no longer, in general, a cyclic variable during flight. However, if boom masses are appropriately distributed, the parabolic motion of the center of mass, as modeled in a planar system, is recovered. Unfortunately, this special mass distribution was impossible because RABBIT does not have a counterweight system.

9.9.3.2 Walking Surface

The walking surface was also a source of problems. This surface—consisting of rubber over elevated plywood supported on the edges by a wood frame—was originally built to provide a uniform, level surface. Although the surface appears uniform, walking experiments demonstrated otherwise. It was found that the surface has “fast” and “slow” areas corresponding to varying floor stiffness and coefficient of friction.

9.9.3.3 Limited Joint Space

For safety, RABBIT's joints have hard stops that limit its joint space, which, for example, prevent the shank from contacting the thigh. Although the available joint space was sufficient for walking, it became a significantly limiting factor in the design of running gaits. These hard stops prevented the swing leg from being folded close to the hip, which is a natural and desirable motion that minimizes the leg's rotational inertia.

Part III

Walking with Feet

10

Walking with Feet and Actuated Ankles

The stance foot plays an important role in human walking since it contributes to forward progression, vertical support, and initiation of the lifting of the swing leg from the ground [155, 166]. Working with a mechanical model, Kuo showed in [144] that plantarflexion of the ankle, which initiates heel rise and toe roll, is the most efficient method to reduce energy loss at the subsequent impact of the swing leg. This motion is also necessary for the *aesthetics* of mechanical walking.

The present chapter addresses the modeling and control of planar bipedal robots with nontrivial feet, with emphasis on a walking motion that allows *anthropomorphic foot action* [203] as depicted in Fig. 10.1. The studied robot model is planar, bipedal, and fully actuated in the sense that it has revolute, actuated ankles that are attached to feet of nonzero length. The desired walking motion is assumed to consist of three successive phases: a fully actuated phase where the stance foot is flat on the ground, an underactuated phase where the stance heel lifts from the ground and the stance foot rotates about the toe, and an instantaneous double support phase where leg exchange takes place. The main objective is to show how the feedback design methodology presented for robots with point feet can be extended to obtain a provably asymptotically stabilizing controller that integrates the fully actuated and underactuated phases of walking. By comparison, existing humanoid robots, such as Asimo, use only the fully actuated phase (i.e., they only execute flat-footed walking), while RABBIT and ERNIE use only the underactuated

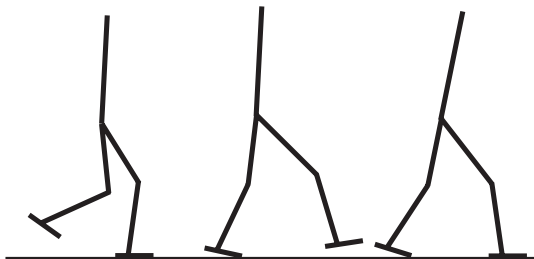


Figure 10.1. The three phases of walking modeled in this chapter: (left) fully actuated phase where the stance foot is flat on the ground, (center) underactuated phase where the stance heel rises from the ground and the stance foot rotates about the stance toe, and (right) double-support phase where the swing foot impacts the ground.

phase (i.e., they have no feet and hence walk as if on stilts). The controller proposed here is organized around the hybrid zero dynamics of [Chapter 5](#) in order that the stability analysis of the closed-loop system may be reduced to a one-dimensional Poincaré map that can be computed in closed form.

10.1 Related Work

A stability analysis of a flat-footed walking gait for a five-link biped with an actuated ankle was carried out numerically in [120, 121], using the Poincaré return map. The control law used feedback linearization to maintain the robot's posture and advance the swing leg; trajectory tracking was only used in the limited sense that the horizontal component of the center of mass was commanded to advance at a constant rate. The unilateral constraints due to foot contact were carefully presented. Motivated by energy efficiency, elegant work in [216, 217] has shown how to realize a passive walking gait in a fully actuated bipedal robot walking on a flat surface. Stability of the resulting walking motion has been rigorously established. The main drawback, however, is that the assumption of full actuation once again restricts the foot motion to flat-footed walking.

For walking gaits that include foot rotation, various *ad hoc* control solutions have been proposed in the literature [160, 171, 203, 207, 223, 251], but none of them can guarantee stability in the presence of the underactuation that occurs during heel roll or toe roll. The previous work presented in Chapters 5–7 on the control of robots with point feet is well suited to handle this underactuation; indeed, conceptually, a point foot corresponds to continuous rotation about the toe throughout the entire stance phase (e.g., walking like a ballerina or as if on stilts). In this chapter, the analysis of walking with point feet is extended to design a controller that provides asymptotically stable walking with an anthropomorphic foot motion. To underline that the ZMP criterion alone is not sufficient for the stability of a walking gait, the results of this chapter are used to construct a periodic orbit on which *the ZMP criterion is satisfied at each point of the gait, but yet the orbit is unstable.*

10.2 Robot Model

A hybrid model of walking with feet is developed for a planar bipedal robot satisfying all of the hypotheses of [Chapter 3](#), with the addition of nontrivial rigid feet with actuated revolute ankles. In particular, the robot is assumed

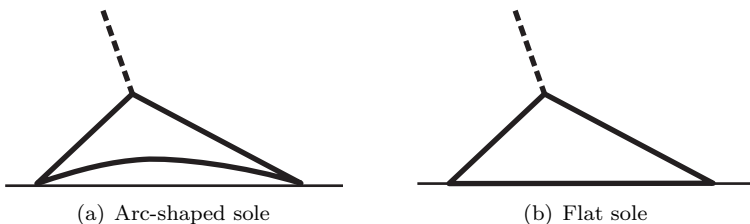


Figure 10.2. Examples of foot shapes. In both cases, the ground contact forces can be resolved into a force vector and a torque.

to consist of $N \geq 4$ rigid links connected by ideal (frictionless) revolute joints to form a tree structure (no closed kinematic chains). It is assumed to have two identical open chains called “legs” that are connected at a point called the “hips.” The link at the extremity of each leg is called a “foot” and the joint between the foot and the remainder of the leg is called an “ankle.” The feet are assumed to be “forward facing.” The forward end of each foot is called a “toe” and the back end is called a “heel.” Each revolute joint is assumed to be independently actuated. It is assumed that walking consists of three successive phases, a fully actuated phase, an underactuated phase, and a double-support phase; see Fig. 10.1.

During the double-support phase, the swing foot impacts the ground. For simplicity, it is assumed that the swing foot is parallel to the ground at impact. It is also assumed that the feet are arc shaped so that the only contact points with the ground are the heel and the toe; see Fig. 10.2. Due to the impacts, impulsive forces are applied at the toe and the heel simultaneously, which cause discontinuous changes in the velocities; however, the position states are assumed to remain continuous [124].

10.2.1 Robot and Gait Hypotheses

For clarity, the explicit hypotheses on the robot, gait and impact are listed here. The robot is assumed to be:

- HR1.F) comprised of N rigid links connected by $(N - 1)$ ideal revolute joints (i.e., rigid and frictionless) to form a single open kinematic chain; furthermore, each link has nonzero mass and a nonzero moment of inertia about at least one of its joints.
 - HR2.F) planar, with motion constrained to the sagittal plane;
 - HR3.F) bipedal, with two symmetric legs connected at a common point called the hip, and both leg ends are terminated in forward-facing feet of nonzero length;
 - HR4.F) independently actuated at each of the $(N - 1)$ ideal revolute joints; in particular, the ankles are actuated.

Feedback controller design will be carried out to achieve the following properties consistent with the simplest form of an anthropomorphic walking gait.

HGW1.F) Walking consists of three successive phases: a fully actuated phase, an underactuated phase, and a double-support phase.

HGW2.F) During the fully actuated phase, the stance foot remains flat on the ground and does not slip.

HGW3.F) Throughout the fully actuated phase, the angular momentum about the stance ankle is never zero.

HGW4.F) Throughout the underactuated phase, the stance toe acts as a pivot.

HGW5.F) The double support phase is instantaneous and the associated impact can be modeled as a rigid contact [124].

HGW6.F) The positions and velocities are continuous across the transition from the fully actuated phase to the underactuated phase.

HGW7.F) In each step, the swing leg starts from strictly behind the stance leg and is placed strictly in front of the stance leg at impact.

HGW8.F) In steady state, the motion is symmetric with respect to the two legs.

HGW9.F) Walking is from left to right and takes place on a level surface.

The impact hypotheses are listed next.

HI1.F) An impact results from the contact of the swing leg foot with the ground.

HI2.F) The impact is instantaneous.

HI3.F) At impact, the heel and toe of the swing foot touch the ground simultaneously. The impact results in no rebound and no slipping of the swing foot, and the angular velocity of the foot is zero immediately after impact.

HI4.F) At the moment of impact, the stance foot lifts from the ground without interaction.

HI5.F) The external forces during the impact can be represented by impulses.

HI6.F) The actuators cannot generate impulses and hence can be ignored during impact.

HI7.F) The impulsive forces may result in an instantaneous change in the robot's velocities, but there is no instantaneous change in the configuration.

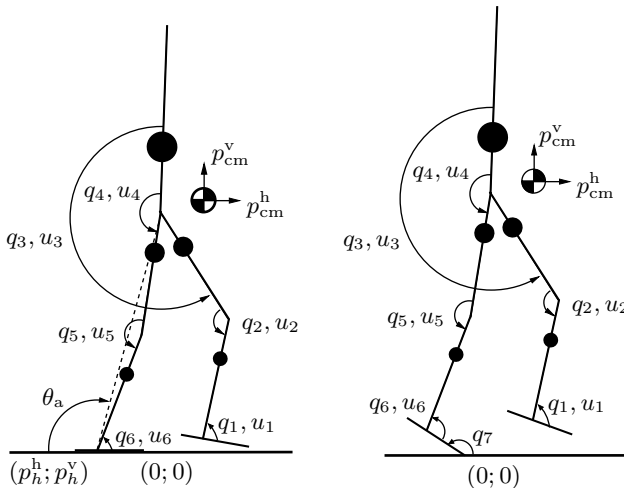


Figure 10.3. Model of a 7-link robot with coordinate convention. θ_u is not shown. It is defined as $\theta_u = \pi - q_7 + \theta_a$. In general, for an N -link robot, it is assumed that q_{N-1} is the angle between the stance foot and the stance tibia and q_N is the angle between the ground and the sole of the stance foot. The toe of the stance foot is taken as the origin, $(0; 0)$. The Cartesian position of the heel of the stance foot is denoted $p_h = (p_h^h; p_h^v)$ and the Cartesian position of the ankle of the stance foot is denoted as $p_a = (p_a^h; p_a^v)$.

10.2.2 Coordinates

A representative robot is shown in Fig. 10.3 along with a coordinate convention. For purposes of modeling, generalized coordinates are chosen as $N - 1$ relative angles, q_1, \dots, q_{N-1} , and one absolute angle, q_N , with a counter-clockwise measuring convention. In particular, q_N is the angle of the stance foot with respect to the walking surface and q_{N-1} is the relative angle of the stance tibia with respect to the stance foot. Note that during the fully actuated phase, when the stance foot is fixed with respect to the ground, the angle of the stance tibia, q_{N-1} , can then be considered as referenced to the inertial frame, and hence becomes an absolute angle.

10.2.3 Underactuated Phase

The underactuated phase is when the stance heel of the robot rises from the ground and the robot begins to roll over the stance toe; this condition is characterized by the foot rotation indicator (FRI) point of [92] being strictly in front of the stance foot. The stance toe is assumed to act as a pivot; this condition is characterized by the forces at the toe lying within the allowed friction cone. Both of these conditions (i.e., foot rotation and nonslip) are

constraints that must be imposed in the final controller design phase, which is discussed in Section 10.5.

Since there is no actuation between the stance toe and the ground, the dynamics of the robot in this phase is equivalent to an N -DOF robot with unactuated point feet and identical legs, as modeled in [Chapter 3](#). Define the generalized coordinates as $q_u = (q_1; \dots; q_N) \in \mathcal{Q}_u$, where \mathcal{Q}_u is a simply connected open subset of¹ \mathbb{T}^N . The dynamics are obtained using the method of Lagrange, yielding

$$D_u(q_u)\ddot{q}_u + C_u(q_u, \dot{q}_u)\dot{q}_u + G_u(q_u) = B_u u_u, \quad (10.1)$$

where $u_u = (u_1; \dots; u_{N-1})$ is the vector of torques applied at the joints. The dynamic equation in state-variable form is expressed as

$$\dot{x}_u = f_u(x_u) + g_u(x_u)u_u, \quad (10.2)$$

where $x_u = (q_u; \dot{q}_u)$.

10.2.4 Fully Actuated phase

During the fully actuated phase, the stance foot is assumed to remain flat on the ground without slipping. The ankle of the stance leg is assumed to act as an actuated pivot. Since the stance foot is motionless during this phase, the dynamics of the robot during the fully actuated phase is equivalent to an $N - 1$ DOF robot without the stance foot and with actuation at the stance ankle, as studied in [11]. Let $q_a = (q_1; \dots; q_{N-1}) \in \mathcal{Q}_a$ be the configuration variables, where q_1, \dots, q_{N-2} denote the relative angles of the joints except the stance ankle, q_{N-1} denotes the angle of the stance ankle joint, and \mathcal{Q}_a is a simply connected open subset of \mathbb{T}^{N-1} ; see [Fig. 10.3](#). Note that because the stance foot remains on the ground, q_{N-1} is now an absolute angle (i.e., it is referenced to the inertial frame).

The dynamics for the fully actuated phase are derived using the method of Lagrange, yielding a model of the form

$$D_a(q_a)\ddot{q}_a + C_a(q_a, \dot{q}_a)\dot{q}_a + G_a(q_a) = B_{a1}u_b + B_{a2}u_A, \quad (10.3)$$

where \dot{q}_a are the velocities, $u_A = u_{N-1}$ is the input at the ankle joint, and $u_b = (u_1; \dots; u_{N-2})$ is the vector of inputs applied at the remaining joints. The state is taken as $x_a = (q_a; \dot{q}_a) \in T\mathcal{Q}_a$ and the dynamic equation is given

¹Recall that for $k \geq 1$, $\mathbb{T}^k = \underbrace{\mathbb{S} \times \dots \times \mathbb{S}}_{k-\text{times}}$.

by²

$$\dot{x}_a = \begin{bmatrix} \dot{q}_a \\ D_a^{-1}(-C_a \dot{q}_a - G_a + B_{a2} u_A) \end{bmatrix} + \begin{bmatrix} 0 \\ D_a^{-1} B_{a1} u_b \end{bmatrix} \quad (10.4a)$$

$$=: f_a(x_a, u_A) + g_a(x_a) u_b. \quad (10.4b)$$

Note that, to satisfy the condition that the stance foot is flat on the ground, the FRI point needs to be kept strictly within the support region of the foot.³ This constraint must be imposed in the final controller design stage; see [Section 10.5](#).

10.2.5 Double-Support Phase

The development of the impact model for the instantaneous double-support phase involves the reaction forces at the leg ends and thus requires an (N+2)-DOF model (e.g., N DOF for the joints and 2 DOF for the position of the center of mass); see [Section 3.4.2](#). Adding Cartesian coordinates, $(p_{cm}^h; p_{cm}^v)$, to the center of mass of the robot gives $q_d = (q_u; p_{cm}^h; p_{cm}^v)$ and $\dot{q}_d = (\dot{q}_u; \dot{p}_{cm}^h; \dot{p}_{cm}^v)$; see [Fig. 10.3](#). Since the swing heel and the swing toe are assumed to land on the ground at the same time, there are two ground reaction forces, which can be modeled as a resultant force and torque acting on the swing foot at the ankle. Let $\Upsilon_a^F(q_d)$ denote the Cartesian coordinates of the swing ankle and let $\Upsilon_a^\tau(q_d)$ denote the absolute angle of the swing foot. The method of Lagrange yields the dynamical model⁴

$$D_d(q_d)\ddot{q}_d + C_d(q_d, \dot{q}_d)\dot{q}_d + G_d(q_d) = B_d u + E_d^F \delta F + E_d^\tau \delta \tau, \quad (10.5)$$

where $u = (u_b; u_A)$, $E_d^F = \frac{\partial \Upsilon_a^F(q_d)}{\partial q_d}$, $E_d^\tau = \frac{\partial \Upsilon_a^\tau(q_d)}{\partial q_d}$, and δF and $\delta \tau$ denote the resultant reaction force and torque at the swing ankle, respectively, when forces are applied at the heel and toe.

Under the Hypotheses HI6.F (the actuators are not impulsive) and HI3.F (the stance foot neither rebounds nor slips), following the procedure in [Section 3.4.2](#) gives

$$\begin{aligned} x_a^+ &= \begin{bmatrix} [R \ 0_{N-1 \times 2}] q_d^- \\ [R \ 0_{N-1 \times 5}] \Pi \begin{bmatrix} D_d \dot{q}_d^- \\ 0_{3 \times 1} \end{bmatrix} \end{bmatrix} \\ &=: \begin{bmatrix} \Delta_{q,u}^a(q_u^-) \\ \Delta_{\dot{q},u}^a(q_u^-) \dot{q}_u^- \end{bmatrix} =: \Delta_u^a(x_u^-), \end{aligned} \quad (10.6)$$

²Note that the ankle torque is included in $f_a(x_a, u_A)$; the reason for this will be clear in [Section 10.3](#).

³Equivalently, the CoP is strictly within the support region of the foot.

⁴The model is equivalent to the flight phase of running.

where R is a relabeling matrix⁵ to reflect the swapping of the roles of the legs and

$$\Pi := \begin{bmatrix} D_d & -(E_d^F)' & -(E_d^T)' \\ E_d^F & 0_{2 \times 2} & 0_{2 \times 1} \\ E_d^T & 0_{1 \times 2} & 0_{1 \times 1} \end{bmatrix}^{-1}. \quad (10.7)$$

Note that, because the stance toe acts as a pivot just before the impact, $x_d^- = (q_d^-; \dot{q}_d^-)$ is uniquely determined by x_u^- . The size of the relabeling matrix R is $N - 1 \times N$ so that x_a^+ , which does not include the degree of freedom of the stance foot, is uniquely defined. Since the stance foot is constrained to remain on the ground during the fully actuated phase, the configuration of the robot is uniquely determined.

10.2.6 Foot Rotation, or Transition from Full Actuation to Underactuation

The transition from a flat foot to rotation about the toe can be initiated by causing the angular acceleration about the stance toe to become negative. To characterize the motion of the stance foot, or equivalently, when the robot transitions from full actuation—foot is flat on the ground—to underactuation—foot rotates about the toe—the FRI is used [92]. By enforcing that the FRI point is strictly in front of the stance foot, the transition is initiated. If torque discontinuities⁶ are allowed—as they are assumed to be here—when to allow foot rotation becomes a control decision. In view of simplifying the analysis of periodic orbits in Section 10.4, the transition is assumed to occur at a prespecified point in the fully actuated phase.⁷ Hence, $H_a^u = \theta_a(q_a) - \theta_{a,0}^-$, where $\theta_a(q_a)$ is the angle of the hips with respect to the stance ankle (see Fig. 10.3) and $\theta_{a,0}^-$ is a constant to be determined.

The positions and the velocities remain continuous with a step-change in torque. The ensuing initial value of the underactuated phase, x_u^+ , is defined so as to achieve continuity in the position and velocity variables:

$$x_u^+ = \begin{bmatrix} q_u^+ \\ \dot{q}_u^+ \end{bmatrix} = \begin{bmatrix} q_a^- \\ \pi \\ \dot{q}_a^- \\ 0 \end{bmatrix} =: \Delta_a^u(x_a^-). \quad (10.8)$$

⁵See Section 3.4.2, where a relabeling matrix was first used. Note that here R is not square due to the different number of configuration variables in the two phases.

⁶This is a modeling decision. In practice, the torque is continuous due to actuator dynamics. It is assumed here that the actuator time constant is small enough that it need not be modeled.

⁷When the transition condition is met, namely, $\theta_a = \theta_{a,0}^-$, a jump in the torque is made to achieve $\dot{q}_N < 0$. This moves the FRI point in front of the foot.

Continuity of the torques is not imposed, and hence neither is continuity of the accelerations. It is assumed that the control law in the underactuated phase will be designed so that the FRI point is in front of the toe.

Remark 10.1 For a foot of nonzero height, q_N is the angle of the sole of the stance foot with respect to the ground. Hence the value of π in (10.8).

10.2.7 Overall Hybrid Model

As in Section 3.5.4, where a hybrid model for running was presented, the overall model for walking with feet can be expressed as a nonlinear hybrid system containing two state manifolds (called “charts” in [103]):

$$\Sigma_a : \begin{cases} \mathcal{X}_a &= T\mathcal{Q}_a \\ \mathcal{F}_a : \dot{x}_a &= f_a(x_a, u_A) + g_a(x_a)u_b \\ \mathcal{S}_a^u &= \{x_a \in T\mathcal{Q}_a \mid H_a^u(x_a) = 0\} \\ \mathcal{T}_a^u : x_a^+ &= \Delta_a^u(x_a^-) \end{cases} \quad (10.9)$$

$$\Sigma_u : \begin{cases} \mathcal{X}_u &= T\mathcal{Q}_u \\ \mathcal{F}_u : \dot{x}_u &= f_u(x_u) + g_u(x_u)u_u \\ \mathcal{S}_u^a &= \{x_u \in T\mathcal{Q}_u \mid H_u^a(x_u) = 0\} \\ \mathcal{T}_u^a : x_u^+ &= \Delta_u^a(x_u^-) \end{cases}$$

where, for example, \mathcal{F}_a is the flow on state manifold \mathcal{X}_a , \mathcal{S}_a^u is the switching hyper-surface for transitions between \mathcal{X}_a and \mathcal{X}_u , $\mathcal{T}_a^u : \mathcal{S}_a^u \rightarrow \mathcal{X}_u$ is the transition function applied when $x_a \in \mathcal{S}_a^u$.

The transition from the underactuated phase to the fully actuated phase occurs when the swing foot impacts the ground. Hence, $H_u^a(x_u) = \Upsilon_h^v(x_u)$, where $\Upsilon_h^v(x_u)$ denotes the vertical coordinate (height) of the swing heel; see Fig. 10.4.

Remark 10.2 \mathcal{S}_a^u is read as the switching surface *from* the fully actuated phase, denoted a , *to* the underactuated phase, denoted u .

10.2.8 Comments on the FRI Point and Angular Momentum

The FRI point is defined in [92] as “the point on the foot/ground contact surface, within or outside the convex hull of the foot-support area, at which the resultant moment of the force/torque impressed on the foot is normal to the surface.” A few remarks will be made on the properties of the FRI point and angular momentum during the fully actuated and double-support phases.

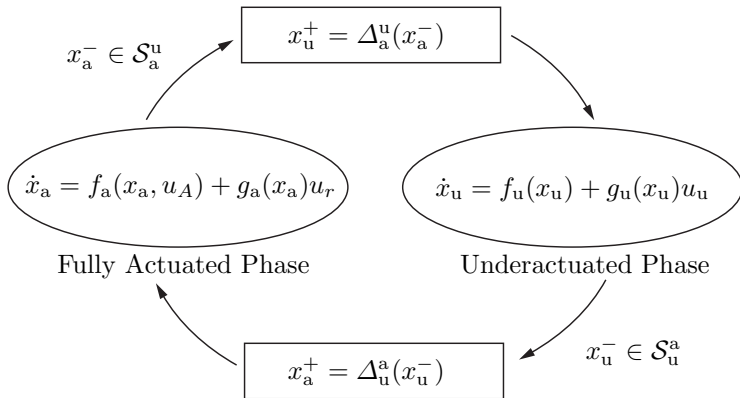


Figure 10.4. Diagram of hybrid system model for walking with a fully actuated (flat-footed) phase and an underactuated (toe-roll) phase.

Fully Actuated phase: Suppose that the Hypotheses HR1.F, HR2.F and HGW2.F of Section 10.2 are satisfied, and the coordinates are as in Section 10.2.2; see Fig. 10.5. The origin $(0; 0)$ is assumed to be located at the toe of the stance foot. Let $(p_{cm}^h; p_{cm}^v)$ be the Cartesian coordinates of the robot's center of the mass and let $(p_a^h; p_a^v)$ be the Cartesian coordinates of the stance ankle. Let $(p_{FRI}^h; 0)$ be the FRI point on the ground and $F_{FRI} = (F_{FRI}^T; F_{FRI}^N)$ be the ground reaction force at the FRI point. Let \vec{r}_1 be a vector from the stance toe to the center of mass, \vec{r}_2 represent the vector from the stance toe to the stance ankle, and let \vec{r}_3 denote the vector from the stance ankle to the center of mass, respectively. Let \vec{R} be the vector from the stance toe to the FRI point. Finally, let K_u and V_u be the kinetic energy and potential energy for the robot, respectively, expressed in terms of the variables of the underactuated phase,⁸ and denote the Lagrangian as

$$\mathcal{L}_u = K_u - V_u. \quad (10.10)$$

In terms of the center of mass, the potential energy of the robot is given as

$$V_u = m_{\text{tot}}g_0 p_{cm}^v. \quad (10.11)$$

Due to the choice of coordinates, the following relations are obtained⁹:

$$\frac{\partial V_u}{\partial q_N} = m_{\text{tot}}g_0 p_{cm}^h, \quad (10.12)$$

⁸Using this Lagrangian allows the ground reaction forces to be analyzed, and hence the position of the FRI point can be studied.

⁹See Proposition B.8 and Proposition B.9.

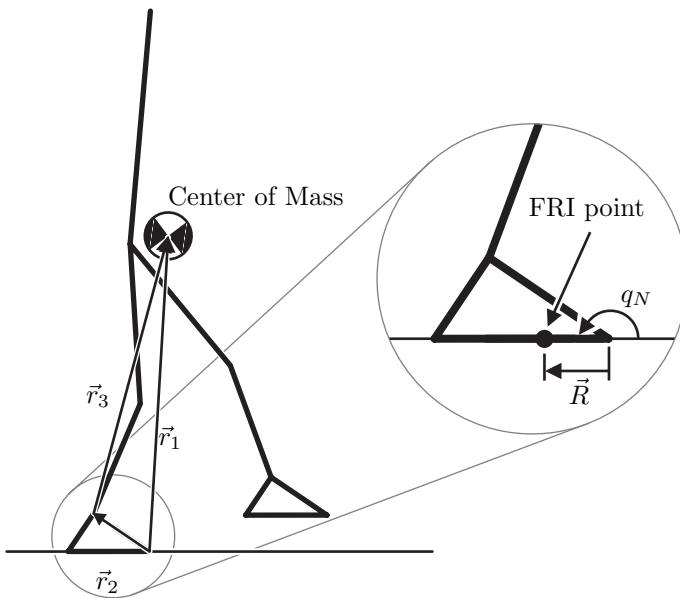


Figure 10.5. Definition of parameters and measurement conventions for a biped with feet. With the origin established at the toe of the stance foot, $\vec{r}_1 = p_{cm}$, $\vec{r}_2 = p_a$, $\vec{r}_3 = p_{cm} - p_a$, and $\vec{R} = (p_{FRI}^h; 0)$. The angle q_N is the (absolute) angle of the sole of the stance foot with respect to the ground, measured with a counterclockwise convention.

$$\frac{\partial \mathcal{L}_u}{\partial q_N} = \frac{\partial K_u}{\partial q_N} - \frac{\partial V_u}{\partial q_N} = -\frac{\partial V_u}{\partial q_N} = -m_{tot}g_0 p_{cm}^h, \quad (10.13)$$

(because q_N is a cyclic variable of K_u , that is, $\partial K_u / \partial q_N = 0$), and

$$\sigma_u := \bar{\sigma}_N = \frac{\partial \mathcal{L}_u}{\partial \dot{q}_N}, \quad (10.14)$$

where σ_u denotes the angular momentum about the stance toe. Because $\vec{r}_1 = \vec{r}_2 + \vec{r}_3$,

$$\sigma_u = \sigma_a + \vec{r}_2 \wedge m_{tot} \dot{p}_{cm}, \quad (10.15)$$

where σ_a denotes the angular momentum about the stance ankle and \dot{p}_{cm} is the velocity of the center of mass. Substituting $\vec{r}_2 = (p_a^h; p_a^v)$, (10.14) and (10.15) imply

$$\frac{d}{dt} \frac{\partial \mathcal{L}_u}{\partial \dot{q}_N} = \frac{d}{dt} (\sigma_a + \vec{r}_2 \wedge m_{tot} \dot{p}_{cm}) = \dot{\sigma}_a + m_{tot} p_a^h \ddot{p}_{cm}^v - m_{tot} p_a^v \ddot{p}_{cm}^h. \quad (10.16)$$

Since there is no actuation at the stance toe, the only torque applied is from the ground reaction force, and thus the method of Lagrange yields

$$\frac{d}{dt} \frac{\partial \mathcal{L}_u}{\partial \dot{q}_N} - \frac{\partial \mathcal{L}_u}{\partial q_N} = \vec{R} \wedge F_{FRI} = p_{FRI}^h F_{FRI}^N, \quad (10.17)$$

which, together with (10.13) and (10.16), implies

$$\dot{\sigma}_a + m_{\text{tot}} p_a^h \ddot{p}_{\text{cm}}^v - m_{\text{tot}} p_a^v \ddot{p}_{\text{cm}}^h + m_{\text{tot}} g_0 p_{\text{cm}}^h = p_{\text{FRI}}^h F_{\text{FRI}}^N. \quad (10.18)$$

During the fully actuated phase, the position of the supporting ankle is stationary. Therefore, applying the angular momentum balance theorem to the robot about the supporting ankle yields

$$\dot{\sigma}_a = -m_{\text{tot}} g_0 (p_{\text{cm}}^h - p_a^h) + (\vec{R} - \vec{r}_2) \wedge F_{\text{FRI}}. \quad (10.19)$$

Furthermore, from the equilibrium in rotation of the supporting foot about the ankle,

$$0 = -u_A + (\vec{R} - \vec{r}_2) \wedge F_{\text{FRI}} - m_{\text{foot}} g_0 (p_{\text{foot,cm}}^h - p_a^h), \quad (10.20)$$

where m_{foot} is the mass of the foot and $p_{\text{foot,cm}}$ is the position of the center of mass of the foot, because the foot does not rotate and the external moments are $-u_A$, the moment of the ground reaction force applied at the FRI point, and the moment of the gravity force; see Fig. 10.6. These last two equations give

$$\dot{\sigma}_a = -m_{\text{tot}} g_0 (p_{\text{cm}}^h - p_a^h) + m_{\text{foot}} g_0 (p_{\text{foot,cm}}^h - p_a^h) + u_A, \quad (10.21)$$

which with (10.18) implies

$$\begin{aligned} p_{\text{FRI}}^h F_{\text{FRI}}^N &= -m_{\text{tot}} g_0 (p_{\text{cm}}^h - p_a^h) + m_{\text{foot}} g_0 (p_{\text{foot,cm}}^h - p_a^h) + u_A \\ &\quad + m_{\text{tot}} p_a^h \ddot{p}_{\text{cm}}^v - m_{\text{tot}} p_a^v \ddot{p}_{\text{cm}}^h + m_{\text{tot}} g_0 p_{\text{cm}}^h, \end{aligned} \quad (10.22)$$

and therefore,

$$p_{\text{FRI}}^h F_{\text{FRI}}^N = m_{\text{tot}} g_0 p_a^h + m_{\text{tot}} p_a^h \ddot{p}_{\text{cm}}^v - m_{\text{tot}} p_a^v \ddot{p}_{\text{cm}}^h + m_{\text{foot}} g_0 (p_{\text{foot,cm}}^h - p_a^h) + u_A. \quad (10.23)$$

Since $F_{\text{FRI}}^N = m_{\text{tot}} g_0 + m_{\text{tot}} \ddot{p}_{\text{cm}}^v$, (10.23) yields the location of the FRI point as a function of the applied ankle torque

$$p_{\text{FRI}}^h = p_a^h + \frac{-m_{\text{tot}} p_a^v \ddot{p}_{\text{cm}}^h + m_{\text{foot}} g_0 (p_{\text{foot,cm}}^h - p_a^h) + u_A}{m_{\text{tot}} g_0 + m_{\text{tot}} \ddot{p}_{\text{cm}}^v}. \quad (10.24)$$

A similar conclusion can be also obtained by considering the equilibrium of the supporting foot as shown in Fig. 10.6, because $F_{\text{FRI}}^T = m_{\text{tot}} \ddot{p}_{\text{cm}}^h$.

The position of the FRI point can also be related to terms in the dynamics of the robot that do not directly involve the control input, u . Indeed, from (10.18), using $F_{\text{FRI}}^N = m_{\text{tot}} g_0 + m_{\text{tot}} \ddot{p}_{\text{cm}}^v$ yields

$$\dot{\sigma}_a + m_{\text{tot}} (p_a^h - p_{\text{FRI}}^h) \ddot{p}_{\text{cm}}^v - m_{\text{tot}} p_a^v \ddot{p}_{\text{cm}}^h = -m_{\text{tot}} g_0 (p_{\text{cm}}^h - p_{\text{FRI}}^h). \quad (10.25)$$

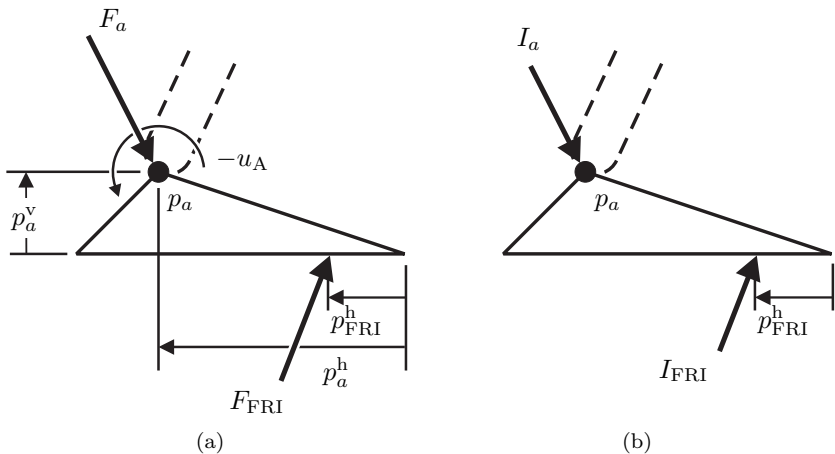


Figure 10.6. Free-body diagrams of the supporting foot with forces, torques, and impulsive forces indicated. Because the ankle and FRI point are located to the left of the toe, p_a^h and p_{FRI}^h are negative. Not indicated are the mass of the foot m_{foot} , the position of the center of mass of the foot, $p_{\text{foot,cm}}$, and the moment of inertia of the foot about its center of mass, J_{foot} .

Using the angular momentum transfer theorem, since by definition the vertical component of the FRI point is identically zero, the angular momentum about the FRI point is

$$\sigma_{\text{FRI}} = \sigma_a + (\vec{r}_2 - \vec{R}) \wedge m_{\text{tot}} \dot{p}_{\text{cm}} \quad (10.26a)$$

$$= \sigma_a + m_{\text{tot}}(p_a^h - p_{\text{FRI}}^h) \dot{p}_{\text{cm}}^v - m_{\text{tot}} p_a^v \dot{p}_{\text{cm}}^h. \quad (10.26b)$$

Equation (10.25) can be rewritten as

$$\dot{\sigma}_{\text{FRI}} = -m_{\text{tot}} g_0(p_{\text{cm}}^h - p_{\text{FRI}}^h) - m_{\text{tot}} \dot{p}_{\text{FRI}}^h \dot{p}_{\text{cm}}^v, \quad (10.27)$$

where \dot{p}_{FRI} is the velocity of the FRI point. When the position of the FRI point is constant, the above simplifies to

$$\dot{\sigma}_{\text{FRI}} = -m_{\text{tot}} g_0(p_{\text{cm}}^h - p_{\text{FRI}}^h). \quad (10.28)$$

Double-support phase: Attention is now turned to the impacting foot during the double-support phase. The fact that the foot neither slips, rebounds, nor rotates after impact will be used.

The effect of the ground reaction force at the moment of impact can be expressed as an external impulsive force with intensity I_{FRI} applied at the CoP of the impacting foot, that is, at the (instantaneous) FRI point. At the moment of impact of the (former swing) foot with the ground, a linear

momentum balance of the robot gives

$$I_{\text{FRI}} = m_{\text{tot}}(\dot{p}_{\text{cm}}^+ - \dot{p}_{\text{cm}}^-). \quad (10.29)$$

The impulsive forces acting on the foot consist of the force applied at the ankle by the shin, I_a , and the force applied at the CoP by the ground, I_{FRI} . A linear momentum balance of the foot at the moment of impact gives

$$I_{\text{FRI}} + I_a = m_{\text{foot}}(\dot{p}_{\text{foot,cm}}^+ - \dot{p}_{\text{foot,cm}}^-), \quad (10.30)$$

where m_{foot} is the mass of the foot and $p_{\text{foot,cm}}$ is the position of the center of mass of the foot. Thus I_a is given by

$$I_a = -I_{\text{FRI}} + m_{\text{foot}}(\dot{p}_{\text{foot,cm}}^+ - \dot{p}_{\text{foot,cm}}^-). \quad (10.31)$$

By performing an angular momentum balance about the center of mass of the foot, the equilibrium of the foot at impact gives

$$J_{\text{foot}}(\omega_{\text{foot}}^+ - \omega_{\text{foot}}^-) = (p_{\text{FRI}} - p_{\text{foot,cm}}) \wedge I_{\text{FRI}} + (p_a - p_{\text{foot,cm}}) \wedge I_a, \quad (10.32)$$

where J_{foot} is the inertia of the swing foot about its center of mass and ω_{foot} is the absolute angular velocity of the swing foot. Using (10.29) and (10.31) yields

$$\begin{aligned} J_{\text{foot}}(\omega_{\text{foot}}^+ - \omega_{\text{foot}}^-) &= (p_{\text{FRI}} - p_a) \wedge m_{\text{tot}}(\dot{p}_{\text{cm}}^+ - \dot{p}_{\text{cm}}^-) \\ &\quad + (p_a - p_{\text{foot,cm}}) \wedge m_{\text{foot}}(\dot{p}_{\text{foot,cm}}^+ - \dot{p}_{\text{foot,cm}}^-). \end{aligned} \quad (10.33)$$

By the angular momentum transfer theorem,

$$\sigma_{\text{FRI}} = \sigma_a + (p_a - p_{\text{FRI}}) \wedge m_{\text{tot}} \dot{p}_{\text{cm}}. \quad (10.34)$$

Hence, (10.33) can be rewritten as

$$\begin{aligned} J_{\text{foot}}(0 - \omega_{\text{foot}}^-) &= (\sigma_a - \sigma_{\text{FRI}})^+ - (\sigma_a - \sigma_{\text{FRI}})^- \\ &\quad + (p_a - p_{\text{foot,cm}}) \wedge m_{\text{foot}}(0 - \dot{p}_{\text{foot,cm}}^-), \end{aligned} \quad (10.35)$$

where $\omega_{\text{foot}}^+ = 0$, Hypothesis HI3.F and $\dot{p}_{\text{foot,cm}}^+ = 0$ have been used. During the impact, the resultant ground reaction force I_{FRI} is applied at the FRI point.¹⁰ As a consequence, the angular momentum about the FRI point is conserved at impact,

$$\sigma_{\text{FRI}}^+ = \sigma_{\text{FRI}}^-, \quad (10.36)$$

¹⁰Recall, I_{FRI} is applied at the (instantaneous) CoP of the impacting foot. But because the foot is assumed not to rotate after impact, the CoP must be strictly within the support polygon of the foot, and hence the CoP and the FRI point coincide.

and the change in angular momentum about the ankle of the impacting foot is therefore given by

$$\sigma_a^+ = \sigma_a^- - J_{foot} \omega_{foot}^- + m_{foot} (p_a - p_{foot,cm}) \wedge \dot{p}_{foot,cm}^- \quad (10.37)$$

Remark 10.3 If the inertia and the mass of the foot are neglected, then (10.37) implies that the angular momentum about the ankle of the impacting foot is unchanged during impact.

Remark 10.4 From (10.33) and the fact that $p_{FRI}^V = 0$, the position of the FRI point at impact can be deduced to be

$$p_{FRI}^h = p_a^h - p_a^v \frac{\dot{p}_{cm}^{h+} - \dot{p}_{cm}^{h-}}{\dot{p}_{cm}^{v+} - \dot{p}_{cm}^{v-}} + \frac{m_{foot} (p_a - p_{foot,cm}) \wedge \dot{p}_{foot,cm}^- - J_{foot} \omega_{foot}^-}{m_{tot} (\dot{p}_{cm}^{v+} - \dot{p}_{cm}^{v-})} \quad (10.38)$$

10.3 Creating the Hybrid Zero Dynamics

In a certain sense, the basic idea of the control law design is quite straightforward. Following the developments in [Part II](#) of the book, we use the method of virtual constraints to create a two-dimensional zero dynamics manifold \mathcal{Z}_u in the $2N$ -dimensional state space of the underactuated phase. This requires the use of the full complement of $N - 1$ actuators on the robot. In the fully actuated phase, we have one less degree of freedom because the stance foot is motionless and flat on the ground. Consequently, we use $N - 2$ actuators—all actuators except the ankle of the stance foot—to create a two-dimensional zero dynamics manifold \mathcal{Z}_a —that is compatible with \mathcal{Z}_u in the sense that the following invariance conditions hold: $\Delta_a^u(\mathcal{S}_a^u \cap \mathcal{Z}_a) \subset \mathcal{Z}_u$ and $\Delta_u^a(\mathcal{S}_u^a \cap \mathcal{Z}_u) \subset \mathcal{Z}_a$. The actuation authority at the ankle is subsequently employed for stability and efficiency augmentation, and for enforcing the nonrotation of the foot. The invariance conditions guarantee the existence of a hybrid zero dynamics for the closed-loop hybrid model. As in the analysis of running in [Chapter 9](#), the stability analysis methods of [Chapter 4](#) are then adapted to compute the Poincaré map of the closed-loop system in closed form. Precise stability conditions then follow.

10.3.1 Control Design for the Underactuated Phase

The greatest difficulties in control design and analysis involve the underactuated phase of the motion. Since the stance toe acts as a pivot and there is no actuation at the stance toe, the feedback design proceeds as in [Chapter 6](#)

on the control of walking with point feet. Let $y_u = h_u(x_u)$ be an $(N - 1) \times 1$ vector of output functions satisfying Hypotheses HH1–HH5 of pages 119 and 126. For convenience, these are rewritten here as:

- HH1.u) The output function $h_u(x_u)$ depends only on the configuration variables;
- HH2.u) The decoupling matrix $L_{g_u} L_{f_u} h_u$ is invertible for an open set $\tilde{\mathcal{Q}}_u \subset \mathcal{Q}_u$;
- HH3.u) There exists a smooth real-valued function $\theta_u(q_u)$ such that

$$[h_u(q_u); \theta_u(q_u)] : \tilde{\mathcal{Q}}_u \rightarrow \mathbb{R}^N \quad (10.39)$$

is a diffeomorphism onto its image;

- HH4.u) There exists a point in $\tilde{\mathcal{Q}}_u$ where h_u vanishes.

- HH5.u) There exists a unique point $q_{u,0}^- \in \tilde{\mathcal{Q}}_u$ such that $(h_u(q_u^-); \Upsilon_a^v(q_u^-)) = (0; 0)$, $\Upsilon_t^h(q_u^-) > 0$ and the rank of $[h_u; \Upsilon_a^v]$ at $q_{u,0}^-$ equals N , where $\Upsilon_t^h(x_u)$ denotes the horizontal coordinate of the swing toe.

Then, as in [Chapter 5](#), there exists a smooth manifold

$$\mathcal{Z}_u = \{x_u \in T\mathcal{Q}_u \mid h_u(x_u) = 0, L_{f_u} h_u(x_u) = 0\}, \quad (10.40)$$

called the underactuated-phase zero dynamics manifold, and $\mathcal{S}_u^a \cap \mathcal{Z}_u$ is smooth; moreover $\mathcal{S}_u^a \cap \mathcal{Z}_u$ is one-dimensional if $\mathcal{S}_u^a \cap \mathcal{Z}_u \neq \emptyset$. Differentiating the output y_u twice yields,

$$\ddot{y}_u = \nu_u \quad (10.41a)$$

$$= L_{f_u}^2 h_u(x_u) + L_{g_u} L_{f_u} h_u(x_u) u_u. \quad (10.41b)$$

Since the decoupling matrix $L_{g_u} L_{f_u} h_u(x_u)$ is invertible, the feedback control

$$u_u^* := -(L_{g_u} L_{f_u} h_u(x_u))^{-1} L_{f_u}^2 h_u(x_u) \quad (10.42)$$

renders the zero dynamics manifold forward invariant. The underactuated phase zero dynamics in the coordinates $z_u := (\theta_u; \sigma_u)$ can be written as

$$\dot{\theta}_u = \kappa_{1u}(\theta_u) \sigma_u \quad (10.43a)$$

$$\dot{\sigma}_u = \kappa_{2u}(\theta_u), \quad (10.43b)$$

where σ_u is the angular momentum about the stance toe during the underactuated phase. Equations (10.43a) and (10.43b) are written as $\dot{z}_u = f_{\mathcal{Z}_u}(z_u)$. Note that by the choice of coordinates, $\sigma_u = \bar{\sigma}_N = d_u(q_u) \dot{q}_u$, where d_u is the last row of D_u .

10.3.2 Control Design for the Fully Actuated Phase

Since the stance foot is motionless and acting as a base during this phase, the model only has $N - 1$ DOF. Consequently, the robot is fully actuated, opening up many feedback design possibilities. For example, we could design for an empty zero dynamics, *though we would run a high risk of requiring so much ankle torque that the foot would rotate, thereby causing underactuation.* Instead, we follow a design where, in principle, the ankle torque could be used exclusively for ensuring that the foot does not rotate, but in most cases, it can also be used to augment stability and efficiency of the overall walking cycle.

$N - 2$ virtual constraints are used to create a two-dimensional zero dynamics for the fully actuated phase that is driven by the ankle torque. Let $y_a = h_a(x_a)$ be a $(N - 2) \times 1$ vector of output functions. Let the output function y_a satisfy Hypotheses HH1–HH5 of pages 119 and 126. For convenience, these are rewritten here as:

- HH1.a) The output function $h_a(x_a)$ depends only on the configuration variables of the fully actuated phase;
- HH2.a) For $u_A = 0$, the decoupling matrix $L_{g_a} L_{f_a} h_a$ is invertible for an open set $\tilde{\mathcal{Q}}_a \subset \mathcal{Q}_a$;
- HH3.a) There exists a smooth real-valued function $\theta_a(q_a)$ such that

$$[h_a(q_a); \theta_a(q_a)] : \tilde{\mathcal{Q}}_a \rightarrow \mathbb{R}^{N-1} \quad (10.44)$$

is a diffeomorphism onto its image;

- HH4.a) There exists a point in $\tilde{\mathcal{Q}}_a$ where h_a vanishes;
- HH5.a) There exists a unique point $q_{a,0}^- \in \tilde{\mathcal{Q}}_a$ such that $y_a = h_a(q_{a,0}^-) = 0$, $H_a^u(q_{a,0}^-) = 0$ and $[h_a; H_a^u]$ has full rank.

Then, as in [Chapter 5](#), there exists a smooth manifold

$$\mathcal{Z}_a = \{x_a \in T\mathcal{Q}_a \mid h_a(x_a) = 0, L_{f_a} h_a(x_a) = 0\}, \quad (10.45)$$

called the fully actuated-phase zero dynamics manifold, and $\mathcal{S}_a^u \cap \mathcal{Z}_a$ is smooth; moreover, $\mathcal{S}_a^u \cap \mathcal{Z}_a$ is one-dimensional if $\mathcal{S}_a^u \cap \mathcal{Z}_a \neq \emptyset$.

Differentiating twice the output y_a for the fully actuated phase gives

$$\ddot{y}_a = L_{f_a}^2 h_a(x_a, u_A) + L_{g_a} L_{f_a} h_a(x_a) u_b. \quad (10.46)$$

Since $L_{g_a} L_{f_a} h_a$ is invertible, the feedback control

$$u_b^* = -(L_{g_a} L_{f_a} h_a(x_a))^{-1} L_{f_a}^2 h_a(x_a, u_A) \quad (10.47)$$

renders forward invariant the zero dynamics manifold of the fully actuated phase.

In the coordinates $z_a := (\theta_a; \sigma_a)$ for the zero dynamics manifold and using (10.21), the fully actuated phase zero dynamics can be written as

$$\dot{\theta}_a = \kappa_{1a}(\theta_a)\sigma_a \quad (10.48a)$$

$$\dot{\sigma}_a = \kappa_{2a}(\theta_a) + u_A, \quad (10.48b)$$

where u_A is the torque applied at the stance ankle and σ_a is the angular momentum about the stance ankle during the fully actuated phase. Equations (10.48a) and (10.48b) are written as $\dot{z}_a = f_{\mathcal{Z}_a}(z_a, u_A)$. Due to the choice of coordinates, $\sigma_a = \bar{\sigma}_{N-1} = d_a(q_a)\dot{q}_a$, where d_a is the last row of D_a ,

10.3.3 Transition Map from the Fully Actuated Phase to the Underactuated Phase

The transition map from the fully actuated phase to the underactuated phase on the zero dynamics becomes

$$\theta_u^+ = \theta_u \circ \begin{bmatrix} q_a^- \\ \pi \end{bmatrix} \quad (10.49a)$$

$$\sigma_u^+ = \delta_a^u \sigma_a^-, \quad (10.49b)$$

where δ_a^u is a constant that can be calculated as in Section 5.3. Even though the values of the joint positions and velocities are continuous at the transition between the fully actuated and underactuated phases, and hence the angular momentum is also continuous, the point where the angular momentum is calculated changes. We have

$$\sigma_u^+ = \sigma_a^- + \vec{r}_2 \wedge m_{\text{tot}} \dot{p}_{\text{cm}}^-, \quad (10.50)$$

where \vec{r}_2 , the position of the ankle relative to the toe, is defined as in Fig. 10.5, m_{tot} is total mass, and \dot{p}_{cm} is the velocity of the center of mass. On the zero dynamics, all of the joint velocities are proportional to σ_a and thus the velocity of the center of mass can be written as in (9.15), namely,

$$\dot{p}_{\text{cm}}^-|_{\mathcal{S}_a^u \cap \mathcal{Z}_a} = \begin{bmatrix} \lambda_x^a(q_a^-) \\ \lambda_y^a(q_a^-) \end{bmatrix} \sigma_a^-. \quad (10.51)$$

Hence, using $p_a = \vec{r}_2$,

$$\begin{aligned} \delta_a^u &= 1 + \vec{r}_2 \wedge m_{\text{tot}} \begin{bmatrix} \lambda_x^a(q_a^-) \\ \lambda_y^a(q_a^-) \end{bmatrix} \\ &= 1 + m_{\text{tot}} p_a^h \lambda_y^a(q_a^-) - m_{\text{tot}} p_a^v \lambda_x^a(q_a^-). \end{aligned} \quad (10.52)$$

10.3.4 Transition Map from the Underactuated Phase to the Fully Actuated Phase

The transition map from the underactuated phase to the fully actuated phase on the hybrid zero dynamics becomes

$$\theta_a^+ = \theta_a(Rq_u^-), \quad (10.53a)$$

$$\sigma_a^+ = \delta_u^a \sigma_u^-, \quad (10.53b)$$

where δ_u^a is a constant that can be calculated as in Section 5.3. At impact, the variation of the angular momentum about the ankle of the impacting leg is known from (10.37). To determine δ_u^a it is sufficient use the principle of angular momentum transfer in order to calculate the angular momentum around the ankle of the impacting leg just before the impact, namely¹¹

$$\sigma_a^- = \sigma_u^- - (\vec{d} + \vec{r}_2) \wedge m_{\text{tot}} \dot{p}_{\text{cm}}^-, \quad (10.54)$$

where \vec{d} is the vector *from* the toe of the (former) stance foot *to* the toe of the impacting foot, at the moment of impact. If the ground is horizontal $\vec{d} = (d; 0)$, $d > 0$. Hence, from (10.37),

$$\begin{aligned} \sigma_a^+ = \sigma_u^- - (\vec{d} + \vec{r}_2) \wedge m_{\text{tot}} \dot{p}_{\text{cm}}^- \\ - J_{\text{foot}} \omega_{\text{foot}}^- + m_{\text{foot}}(p_a - p_{\text{foot,cm}}) \wedge \dot{p}_{\text{foot,cm}}^-. \end{aligned} \quad (10.55)$$

On the zero dynamics manifold, all of the joint velocities are proportional to σ_u , and thus the velocity of the center of mass can be written as in (9.15), namely,

$$\dot{p}_{\text{cm}}^-|_{S_u^a \cap \mathcal{Z}_u} = \begin{bmatrix} \lambda_x^u(q_u^-) \\ \lambda_y^u(q_u^-) \end{bmatrix} \sigma_u^-, \quad (10.56)$$

the velocity of the center of mass of the feet can be written as :

$$\dot{p}_{\text{foot,cm}}^-|_{S_u^a \cap \mathcal{Z}_u} = \begin{bmatrix} \lambda_{fx}^u(q_u^-) \\ \lambda_{fy}^u(q_u^-) \end{bmatrix} \sigma_u^-, \quad (10.57)$$

and the absolute velocity of the swing (i.e., impacting) foot can be expressed as

$$\omega_{\text{foot}}^-|_{S_u^a \cap \mathcal{Z}_u} = \omega_0(q_u^-) \sigma_u^-. \quad (10.58)$$

¹¹Note that on flat ground, $\vec{d} + \vec{r}_2 = (d + p_a^h; p_a^v)$.

It follows that

$$\delta_u^a = 1 - (\vec{d} + \vec{r}_2) \wedge m_{\text{tot}} \begin{bmatrix} \lambda_x^u(q_u^-) \\ \lambda_y^u(q_u^-) \end{bmatrix} - J_{foot}\omega_0(q_u^-) + \\ (p_a - p_{foot,cm}) \wedge m_{foot} \begin{bmatrix} \lambda_{fx}^u(q_u^-) \\ \lambda_{fy}^u(q_u^-) \end{bmatrix} \quad (10.59a)$$

$$= 1 - m_{\text{tot}}(d + p_a^h)\lambda_y^u(q_u^-) + m_{\text{tot}}p_a^v\lambda_x^u(q_u^-) - J_{foot}\omega_0(q_u^-) + \\ m_{foot}(p_a^h - p_{foot,cm}^h)\lambda_{fy}^u(q_u^-) - m_{foot}(p_a^v - p_{foot,cm}^v)\lambda_{fx}^u(q_u^-). \quad (10.59b)$$

10.3.5 Hybrid Zero Dynamics

Let \mathcal{Z}_a be the zero dynamics manifold of the fully actuated phase and $\dot{z}_a = f_{\mathcal{Z}_a}(z_a, u_A)$ be the associated zero dynamics driven by u_A . Let Δ_a^u be the transition map from the fully actuated phase to the underactuated phase. Let \mathcal{Z}_u be the zero dynamics manifold of the underactuated phase and $\dot{z}_u = f_u(z_u)$ be the associated zero dynamics. Let Δ_u^a be the transition map from the underactuated phase to the fully actuated phase. If $\forall z_a \in \mathcal{S}_a^u \cap \mathcal{Z}_a$, $\Delta_a^u(z_a) \in \mathcal{Z}_u$ and $\forall z_u \in \mathcal{S}_u^a \cap \mathcal{Z}_u$, $\Delta_u^a(z_u) \in \mathcal{Z}_a$, then

$$\begin{cases} \dot{z}_a = f_{\mathcal{Z}_a}(z_a, u_A), z_a^- \notin \mathcal{S}_a^u \cap \mathcal{Z}_a, u_A \in \mathbb{R} \\ z_u^+ = \Delta_a^u(z_a), z_a^- \in \mathcal{S}_a^u \cap \mathcal{Z}_a \\ \dot{z}_u = f_{\mathcal{Z}_u}(z_u), z_u^- \notin \mathcal{S}_u^a \cap \mathcal{Z}_u \\ z_a^+ = \Delta_u^a(z_u), z_u^- \in \mathcal{S}_u^a \cap \mathcal{Z}_u \end{cases} \quad (10.60)$$

is an invariant hybrid subsystem of the full-dimensional hybrid model. The system (10.60) is called the *hybrid zero dynamics* and \mathcal{Z}_a and \mathcal{Z}_u are hybrid zero dynamics manifolds.

Remark 10.5 By definition, the manifolds \mathcal{Z}_a and \mathcal{Z}_u are impact invariant if, and only if, $\forall z_a^- \in \mathcal{S}_a^u \cap \mathcal{Z}_a$,

$$h_u \circ \Delta_a^u(z_a^-) = 0, \quad (10.61a)$$

$$L_{f_u} h_u \circ \Delta_a^u(z_a^-) = 0, \quad (10.61b)$$

and $\forall z_u^- \in \mathcal{S}_u^a \cap \mathcal{Z}_u$ and $u_A = 0$,

$$h_a \circ \Delta_u^a(z_u^-) = 0, \quad (10.62a)$$

$$L_{f_a} h_a \circ \Delta_u^a(z_u^-) = 0. \quad (10.62b)$$

How to achieve these conditions is developed in Section 10.5.

10.4 Ankle Control and Stability Analysis

Due to the ankle torque that appears in the zero dynamics for the fully actuated phase in (10.48b), the robot's center of mass can move backward as well as forward during a step. In other words, the angular momentum about the stance ankle can be zero before entering the underactuated phase. We assume here, however, that the angular momentum is never zero during a step; see HGW3.F in [Section 10.2](#). One can think of this hypothesis as a difference between walking and dancing.¹² During the underactuated phase, the angular momentum about the toe is never zero, if the robot completes a step; see [Proposition 5.1](#).

The ankle torque provides additional design freedom in the fully actuated phase, which can be used for various purposes. In this chapter, two possible uses of the ankle torque are suggested: changing the walking speed of the robot through potential-energy shaping; and affecting the convergence rate to the periodic orbit. In [Chapter 11](#), a third use is suggested: directly controlling the position of the FRI point. The stability of the robot on the hybrid zero dynamics is analyzed with a Poincaré map for the overall system, which is obtained by composing the Poincaré maps for each phase.

10.4.1 Analysis on the Hybrid Zero Dynamics for the Underactuated Phase

For the underactuated phase, the zero dynamics is equivalent to the robot with unactuated point feet. If the robot completes a step, the angular momentum during the underactuated phase is never zero. Therefore, $\zeta_u = \sigma_u^2/2$ is a valid coordinate transformation, where σ_u is the angular momentum. Let $z_u^- = (\theta_u^-, \sigma_u^-) \in \mathcal{S}_u^a \cap \mathcal{Z}_u$ and let θ_u^+ be defined as in (10.49a). If $\zeta_u^+ - V_{\mathcal{Z}_u}^{max} > 0$, then applying the procedure of Section 5.4.1 to (10.43a) and (10.43b) gives

$$\frac{1}{2}(\sigma_u^-)^2 - \frac{1}{2}(\sigma_u^+)^2 = \zeta_u^- - \zeta_u^+ = -V_{\mathcal{Z}_u}(\theta_u^-), \quad (10.63)$$

where

$$V_{\mathcal{Z}_u}(\theta_u) = - \int_{\theta_u^+}^{\theta_u^-} \frac{\kappa_{2u}(\xi)}{\kappa_{1u}(\xi)} d\xi, \quad (10.64a)$$

$$V_{\mathcal{Z}_u}^{max} = \max_{\theta_u^+ \leq \theta_u \leq \theta_u^-} V_{\mathcal{Z}_u}(\theta_u). \quad (10.64b)$$

Anticipating the coordinate change, $\zeta_a = \sigma_a^2/2$, of the next section, the restricted Poincaré map for the underactuated phase of the hybrid zero dynam-

¹²In dancing, the body's center of mass frequently moves forward and backward.

ics $\rho_u : \mathcal{S}_a^u \cap \mathcal{Z}_a \rightarrow \mathcal{S}_u^a \cap \mathcal{Z}_u$ is defined with (10.49b) as $\zeta_a^- \rightarrow \zeta_u^-$ by

$$\rho_u(\zeta_a^-) = (\delta_a^u)^2 \zeta_a^- - V_{\mathcal{Z}_u}(\theta_u^-). \quad (10.65)$$

10.4.2 Analysis on the Hybrid Zero Dynamics for the Fully Actuated Phase with Ankle Torque Used to Change Walking Speed

An ankle torque control strategy that is useful for modifying the walking speed is proposed. The restricted Poincaré map for the fully actuated phase is then calculated, and the Poincaré map for the overall reduced system is determined for stability analysis of the robot on the hybrid zero dynamics.

Since the angular momentum of the robot during the fully actuated phase, σ_a , is not zero, $\zeta_a = \sigma_a^2/2$ is a valid coordinate transformation. For the purpose of potential-energy shaping, the ankle torque during the fully actuated phase, u_A , is assumed to be a function of θ_a only. Then, (10.48a) and (10.48b) become

$$d\zeta_a = \sigma_a d\sigma_a = \frac{\kappa_{2a}(\theta_a)}{\kappa_{1a}(\theta_a)} + \frac{u_A(\theta_a)}{\kappa_{1a}(\theta_a)} d\theta_a. \quad (10.66)$$

Let $z_a^- = (\theta_a^-; \sigma_a^-) \in \mathcal{S}_a^u \cap \mathcal{Z}_a$ and θ_a^+ be defined as in (10.53a). For $\theta_a^+ \leq \theta_a \leq \theta_a^-$, define

$$V_{\mathcal{Z}_a}^{u_A}(\theta_a) = - \int_{\theta_a^+}^{\theta_a} \frac{\kappa_{2a}(\xi)}{\kappa_{1a}(\xi)} + \frac{u_A(\xi)}{\kappa_{1a}(\xi)} d\xi, \quad (10.67a)$$

$$V_{\mathcal{Z}_a}^{u_A, max} = \max_{\theta_a^+ \leq \theta_a \leq \theta_a^-} V_{\mathcal{Z}_a}^{u_A}(\theta_a). \quad (10.67b)$$

If $\zeta_a^+ - V_{\mathcal{Z}_a}^{u_A, max} > 0$, then (10.66) can be integrated, which results in

$$\frac{1}{2}(\sigma_a^-)^2 - \frac{1}{2}(\sigma_a^+)^2 = \zeta_a^- - \zeta_a^+ = -V_{\mathcal{Z}_a}^{u_A}(\theta_a^-). \quad (10.68)$$

With (10.53b), the Poincaré map for the fully actuated phase on the hybrid zero dynamics, $\rho_a : \mathcal{S}_a^u \cap \mathcal{Z}_u \rightarrow \mathcal{S}_a^u \cap \mathcal{Z}_a$, is defined as $\zeta_u^- \rightarrow \zeta_a^-$ by

$$\rho_a(\zeta_u^-) = (\delta_a^u)^2 \zeta_u^- - V_{\mathcal{Z}_a}^{u_A}(\theta_a^-). \quad (10.69)$$

Hence, the Poincaré map for the overall reduced system in $(\theta_u; \zeta_u)$ coordinates, $\rho : \mathcal{S}_u^a \cap \mathcal{Z}_u \rightarrow \mathcal{S}_u^a \cap \mathcal{Z}_u$, is defined as the composition of (10.65) and (10.69) as follows:

$$\begin{aligned} \rho(\zeta_u^-) &= \rho_u \circ \rho_a(\zeta_u^-) \\ &= (\delta_a^u)^2 (\delta_u^a)^2 \zeta_u^- - (\delta_a^u)^2 V_{\mathcal{Z}_a}^{u_A}(\theta_a^-) - V_{\mathcal{Z}_u}(\theta_u^-), \end{aligned} \quad (10.70)$$

with domain of definition

$$\begin{aligned} \mathcal{D} &= \{ \zeta_u^- > 0 \mid (\delta_u^a)^2 \zeta_u^- - V_{\mathcal{Z}_a}^{u_A, max} > 0, \\ &\quad (\delta_a^u)^2 (\delta_u^a)^2 \zeta_u^- - (\delta_a^u)^2 V_{\mathcal{Z}_a}^{u_A}(\theta_a^-) - V_{\mathcal{Z}_u}^{max} > 0 \}. \end{aligned} \quad (10.71)$$

Theorem 10.1

Assume Hypotheses HR1.F–HR4.F for the robot, HGW1.F–HGW9.F for its gait, and HI1.F–HI7.F for the impact model. If virtual constraints are selected to satisfy Hypotheses HH1.a–HH5.a, and HH1.u–HH5.u, then

$$\zeta_u^* = -\frac{(\delta_a^u)^2 V_{Z_a}^{u_A}(\theta_a^-) + V_{Z_u}(\theta_u^-)}{1 - (\delta_a^u)^2 (\delta_u^a)^2} \quad (10.72)$$

is an exponentially stable fixed point of (10.70) if, and only if,

$$0 < (\delta_a^u)^2 (\delta_u^a)^2 < 1, \quad (10.73a)$$

$$\frac{(\delta_a^u)^2 (\delta_u^a)^2 V_{Z_u}(\theta_u^-) + (\delta_a^u)^2 V_{Z_a}^{u_A}(\theta_a^-)}{1 - (\delta_a^u)^2 (\delta_u^a)^2} + V_{Z_u}^{max} < 0, \quad (10.73b)$$

$$\frac{(\delta_u^a)^2 (\delta_a^u)^2 V_{Z_a}^{u_A}(\theta_a^-) + (\delta_u^a)^2 V_{Z_u}(\theta_u^-)}{1 - (\delta_a^u)^2 (\delta_u^a)^2} + V_{Z_a}^{u_A,max} < 0. \quad (10.73c)$$

Proof \mathcal{D} is nonempty if, and only if, $(\delta_a^u)^2 (\delta_u^a)^2 > 0$. If there exists $\zeta_u^* \in \mathcal{D}$ satisfying $\rho(\zeta_u^*) = (\delta_a^u)^2 (\delta_u^a)^2 \zeta_u^* - (\delta_a^u)^2 V_{Z_a}^{u_A}(\theta_a^-) - V_{Z_u}(\theta_u^-)$, then ζ_u^* is an exponentially stable fixed point if, and only if, $0 < (\delta_a^u)^2 (\delta_u^a)^2 < 1$, and in this case, (10.72) is the value of the fixed point. Finally, (10.73b) and (10.73c) are the necessary and sufficient conditions for (10.72) to be in \mathcal{D} .

Remark 10.6 The stability of the reduced model is not affected by the choice of $u_A(\theta_a)$ since δ_a^u does not depend on u_A . However, the existence and value of the fixed point ζ_u^* are affected by u_A through the modification of $V_{Z_a}^{u_A,max}$.

10.4.3 Analysis on the Hybrid Zero Dynamics for the Fully Actuated Phase with Ankle Torque Used to Affect Convergence Rate

It is now shown how the ankle torque can be used to affect the stability of the robot on the hybrid zero dynamics. In particular, the ankle torque is used to affect convergence rate. For the analysis, the Poincaré map for the fully actuated phase is calculated and then composed with the Poincaré map of the underactuated phase to provide the Poincaré map of the overall reduced system.

Because the angular momentum about the stance ankle is assumed to be nonzero during the fully actuated phase, $\zeta_a = \sigma_a^2/2$ is a valid coordinate transformation. Define the ankle torque u_A to be

$$u_A = -\kappa_{2a}(\theta_a) + \kappa_{1a}(\theta_a) \left(k_a(\zeta_a - \zeta_a^*(\theta_a)) + \frac{d\zeta_a^*(\theta_a)}{d\theta_a} \right), \quad (10.74)$$

where k_a is a (negative) constant, $\zeta_a^*(\theta_a)$ is a differentiable, positive function of θ_a specifying the desired path of ζ_a during the fully actuated phase, and $\kappa_{1a}(\theta_a)$ and $\kappa_{2a}(\theta_a)$ are from (10.48a) and (10.48b), respectively. Then, the zero dynamics becomes

$$\dot{\theta}_a = \kappa_{1a}(\theta_a)\sigma_a \quad (10.75a)$$

$$\dot{\sigma}_a = \kappa_{1a}(\theta_a) \left(k_a(\zeta_a - \zeta_a^*(\theta_a)) + \frac{d\zeta_a^*(\theta_a)}{d\theta_a} \right). \quad (10.75b)$$

In the coordinates $(\theta_a; \zeta_a)$, combining (10.75a) and (10.75b) yields

$$\frac{d\zeta_a}{d\theta_a} = k_a(\zeta_a - \zeta_a^*(\theta_a)) + \frac{d\zeta_a^*(\theta_a)}{d\theta_a}. \quad (10.76)$$

Define $\eta = \zeta_a - \zeta_a^*(\theta_a)$. Then, with (10.76), differentiating η gives

$$\frac{d\eta}{d\theta_a} = \frac{d\zeta_a}{d\theta_a} - \frac{d\zeta_a^*(\theta_a)}{d\theta_a} \quad (10.77a)$$

$$= k_a(\zeta_a - \zeta_a^*(\theta_a)) = k_a\eta, \quad (10.77b)$$

which can be solved over the interval $\theta_a^+ \leq \theta_a \leq \theta_a^-$ to give

$$\eta(\theta_a) = e^{k_a(\theta_a - \theta_a^+)}\eta(\theta_a^+), \quad (10.78)$$

as long as $\zeta_a(\theta_a)$ remains positive. It follows that

$$\zeta_a(\theta_a) = \zeta_a^*(\theta_a) + e^{k_a(\theta_a - \theta_a^+)}(\zeta_a^+ - \zeta_a^*(\theta_a^+)) \quad (10.79a)$$

$$= e^{k_a(\theta_a - \theta_a^+)} (\zeta_a^+ - \bar{V}_{\mathcal{Z}_a}(\theta_a)), \quad (10.79b)$$

where

$$\bar{V}_{\mathcal{Z}_a}(\theta_a) := \zeta_a^*(\theta_a^+) - e^{-k_a(\theta_a - \theta_a^+)}\zeta_a^*(\theta_a); \quad (10.80)$$

moreover, $\zeta_a(\theta_a) > 0$ for $\theta_a^+ \leq \theta_a \leq \theta_a^-$ if, and only if,

$$\zeta_a^+ > \bar{V}_{\mathcal{Z}_a}^{max}, \quad (10.81)$$

where

$$\bar{V}_{\mathcal{Z}_a}^{max} := \max_{\theta_a^+ \leq \theta_a \leq \theta_a^-} \bar{V}_{\mathcal{Z}_a}(\theta_a). \quad (10.82)$$

Because $\theta_a = \theta_a^-$ at the transition from the fully actuated phase to the underactuated phase,

$$\zeta_a^- = e^{k_a(\theta_a^- - \theta_a^+)} (\zeta_a^+ - \bar{V}_{\mathcal{Z}_a}(\theta_a^-)). \quad (10.83)$$

The Poincaré map for the fully actuated phase, $\rho_a : \mathcal{S}_u^a \cap \mathcal{Z}_u \rightarrow \mathcal{S}_a^u \cap \mathcal{Z}_a$, is therefore given as $\zeta_u^- \rightarrow \zeta_a^-$ by

$$\rho_a(\zeta_u^-) = e^{k_a(\theta_a^- - \theta_a^+)} ((\delta_u^a)^2 \zeta_u^- - \bar{V}_{\mathcal{Z}_a}(\theta_a^-)). \quad (10.84)$$

Combining (10.65) and (10.84) gives the Poincaré map for the overall reduced system. In the coordinates $(\theta_u; \zeta_u)$, $\rho = \rho_u \circ \rho_a : \mathcal{S}_u^a \cap \mathcal{Z}_u \rightarrow \mathcal{S}_u^a \cap \mathcal{Z}_u$, is given as follows:

$$\rho(\zeta_u^-) = (\delta_a^u)^2 e^{k_a(\theta_a^- - \theta_a^+)} ((\delta_u^a)^2 \zeta_u^- - \bar{V}_{\mathcal{Z}_a}(\theta_a^-)) - V_{\mathcal{Z}_u}(\theta_u^-), \quad (10.85)$$

with domain of definition

$$\mathcal{D} = \{\zeta_u^- \in \mathbb{R} \mid (\delta_a^u)^2 \rho_a(\zeta_u^-) - V_{\mathcal{Z}_u}^{max} > 0, (\delta_u^a)^2 \zeta_u^- - \bar{V}_{\mathcal{Z}_a}^{max} > 0\}. \quad (10.86)$$

Theorem 10.2

Assume Hypotheses HR1.F–HR4.F for the robot, HGW1.F–HGW9.F for its gait, and HI1.F–HI7.F for the impact model, as well as the Hypotheses HH1.a–HH5.a and HH1.u–HH5.u for the virtual constraints. Let ζ^* be a differentiable function of θ_a satisfying the following condition

$$\zeta_a^*(\theta_a) > 0, \quad \forall \theta_a \in [\theta_a^+, \theta_a^-]. \quad (10.87)$$

Then,

$$\zeta_u^* = -\frac{(\delta_a^u)^2 e^{k_a(\theta_a^- - \theta_a^+)} \bar{V}_{\mathcal{Z}_a}(\theta_a^-) + V_{\mathcal{Z}_u}(\theta_u^-)}{1 - (\delta_u^a)^2 (\delta_a^u)^2 e^{k_a(\theta_a^- - \theta_a^+)}} \quad (10.88a)$$

$$= \frac{(\delta_u^a)^2 \zeta_a^*(\theta_a^-) - (\delta_a^u)^2 e^{k_a(\theta_a^- - \theta_a^+)} \zeta_a^*(\theta_a^+) - V_{\mathcal{Z}_u}(\theta_u^-)}{1 - (\delta_u^a)^2 (\delta_a^u)^2 e^{k_a(\theta_a^- - \theta_a^+)}} \quad (10.88b)$$

is an exponentially stable fixed point of (10.85) if, and only if,

$$0 < (\delta_u^a)^2 (\delta_a^u)^2 e^{k_a(\theta_a^- - \theta_a^+)} < 1 \quad (10.89)$$

and

$$(\delta_a^u)^2 e^{k_a(\theta_a^- - \theta_a^+)} \frac{(\delta_u^a)^2 V_{\mathcal{Z}_u}(\theta_u^-) + \bar{V}_{\mathcal{Z}_a}(\theta_a^-)}{1 - (\delta_u^a)^2 (\delta_a^u)^2 e^{k_a(\theta_a^- - \theta_a^+)}} + V_{\mathcal{Z}_u}^{max} < 0, \quad (10.90a)$$

$$(\delta_u^a)^2 \frac{(\delta_a^u)^2 e^{k_a(\theta_a^- - \theta_a^+)} \bar{V}_{\mathcal{Z}_a}(\theta_a^-) + V_{\mathcal{Z}_u}(\theta_u^-)}{1 - (\delta_u^a)^2 (\delta_a^u)^2 e^{k_a(\theta_a^- - \theta_a^+)}} + \bar{V}_{\mathcal{Z}_a}^{max} < 0. \quad (10.90b)$$

Proof The domain of definition, \mathcal{D} , is nonempty if, and only if, $0 < (\delta_u^a)^2 (\delta_a^u)^2 e^{k_a(\theta_a^- - \theta_a^+)}$ is satisfied. If there exists $\zeta_u^* \in \mathcal{D}$ satisfying $\zeta_u^* = \rho(\zeta_u^*)$, where ρ is the Poincaré map defined in (10.85), then, ζ_u^* is an exponentially fixed point if, and only if, (10.89) is satisfied, in which case the value of the fixed point is given as (10.88). Finally, the two inequalities in (10.90) are the necessary and sufficient conditions for ζ_u^* given in (10.88) to be in \mathcal{D} .

Remark 10.7 The convergence rate of the solution to the limit cycle can be altered by the ankle torque, u_A , through choice of k_a , as long as the constraint

on the FRI point remaining within the foot support region during the fully actuated phase is satisfied.

Remark 10.8 Suppose that (10.85) has a fixed point. Then $\zeta_a^*(\theta_a)$ lies on the periodic orbit if, and only if,

$$(\delta_u^a)^2 (\delta_a^u)^2 \zeta_a^*(\theta_a^-) - \zeta_a^*(\theta_a^+) = (\delta_u^a)^2 V_{Z_u}(\theta_u^-). \quad (10.91)$$

10.4.4 Stability of the Robot in the Full-Dimensional Model

Using the material of [Chapter 4](#) and following the development in Section 5.5, it is straightforward to prove that exponentially stable periodic orbits of the hybrid zero dynamics are *exponentially stabilizable* in the full-dimensional model.

10.5 Designing the Virtual Constraints

To render the analytical results in the previous section useful for feedback design, a convenient finite parametrization of the virtual constraints must be introduced, as in Section 6.2. This introduces free parameters into the hybrid zero dynamics, (10.60). A minimum cost criterion can then be posed and parameter optimization applied to the hybrid zero dynamics to design a provably stable, closed-loop system with satisfied design constraints, such as walking at a prescribed average speed, the forces on the support leg lying in the allowed friction cone, and the foot rotation indicator is point within the convex hull of the foot during the fully actuated phase and strictly in front of the foot in the underactuated phase.

10.5.1 Parametrization Using Bézier polynomials

For the parametrization of the output function for each phase, Bézier polynomials are used. Let

$$b_a^i(s_a) := \sum_{k=0}^{M_a} \alpha_k^i \frac{M_a!}{k!(M_a-k)!} s_a^k (1-s_a)^{M_a-k}, \quad (10.92a)$$

$$b_u^i(s_u) := \sum_{k=0}^{M_u} \beta_k^i \frac{M_u!}{k!(M_u-k)!} s_u^k (1-s_u)^{M_u-k}, \quad (10.92b)$$

where $M_a > 3$, $M_u > 3$, $s_a(\theta_a) = \frac{\theta_a - \theta_a^+}{\theta_a^- - \theta_a^+}$ and $s_u(\theta_u) = \frac{\theta_u - \theta_u^+}{\theta_u^- - \theta_u^+}$. Note that $s_a = 0$, $s_a = 1$, $s_u = 0$, and $s_u = 1$ represent the beginning and the end of

the fully actuated phase and the beginning and the end of the underactuated phase, respectively. Define the output function for each phase, satisfying the output Hypotheses HH1.a–HH5.a and HH1.u–HH5.u, as in Section 10.3 , to be

$$y_a = h_a(q_a) = h_a^t(q_a) - h_a^d \circ \theta_a(q_a) \quad (10.93a)$$

$$y_u = h_u(q_u) = h_u^t(q_u) - h_u^d \circ \theta_u(q_u), \quad (10.93b)$$

where h_a^t is a vector with $N - 2$ elements specifying independent values to be controlled during the fully actuated phase, h_u^t is a vector containing $N - 1$ independent values to be controlled during the underactuated phase, $h_a^d(\theta_a)$ and $h_u^d(\theta_u)$ are the desired curves for the controlled elements to track during each phase. The desired curves, $h_a^d(\theta_a)$ and $h_u^d(\theta_u)$, are defined as follows:

$$h_a^d(\theta_a) = \begin{bmatrix} b_a^1 \circ s_a(\theta_a) \\ \dots \\ b_a^{N-2} \circ s_a(\theta_a) \end{bmatrix}, \quad (10.94a)$$

$$h_u^d(\theta_u) = \begin{bmatrix} b_u^1 \circ s_u(\theta_u) \\ \dots \\ b_u^{N-1} \circ s_u(\theta_u) \end{bmatrix}. \quad (10.94b)$$

Note that due to the properties of the Bézier polynomials, the desired output function at the beginning of each phase is

$$h_a^d(s_a)|_{s_a=0} = \alpha_0 \quad (10.95a)$$

$$\frac{\partial h_a^d(s_a)}{\partial s_a} \Big|_{s_a=0} = M_a(\alpha_1 - \alpha_0) \quad (10.95b)$$

$$h_u^d(s_u)|_{s_u=0} = \beta_0 \quad (10.95c)$$

$$\frac{\partial h_u^d(s_u)}{\partial s_u} \Big|_{s_u=0} = M_u(\beta_1 - \beta_0), \quad (10.95d)$$

and, similarly, at the end of each phase is

$$h_a^d(s_a)|_{s_a=1} = \alpha_{M_a} \quad (10.96a)$$

$$\frac{\partial h_a^d(s_a)}{\partial s_a} \Big|_{s_a=1} = M_a(\beta_{M_a} - \beta_{M_a-1}) \quad (10.96b)$$

$$h_u^d(s_u)|_{s_u=1} = \beta_{M_u} \quad (10.96c)$$

$$\frac{\partial h_u^d(s_u)}{\partial s_u} \Big|_{s_u=1} = M_u(\beta_{M_u} - \beta_{M_u-1}), \quad (10.96d)$$

where

$$\alpha_i = \begin{bmatrix} \alpha_i^1 \\ \vdots \\ \alpha_i^{N-2} \end{bmatrix}, \quad i = 0, \dots, M_a \quad (10.97a)$$

$$\beta_j = \begin{bmatrix} \beta_j^1 \\ \vdots \\ \beta_j^{N-1} \end{bmatrix}, \quad j = 0, \dots, M_u. \quad (10.97b)$$

When the ankle torque is used to affect the stability as explained in Section 10.4.3, the desired path of the angular momentum also needs to be designed. Since the angular momentum during the fully actuated phase is never zero, $\zeta^* = (\sigma^*)^2/2$ is parameterized instead of the desired angular momentum, σ^* , which is given by

$$\zeta^* \circ s_a(\theta_a) := \sum_{k=0}^m \gamma_k \frac{m!}{k!(m-k)!} s_a^k (1 - s_a)^{m-k}, \quad (10.98)$$

where $m > 1$. By the properties of Bézier polynomials,

$$\zeta^*(s_a)|_{s_a=0} = \gamma_0 \quad (10.99a)$$

$$\zeta^*(s_a)|_{s_a=1} = \gamma_m. \quad (10.99b)$$

10.5.2 Achieving Impact Invariance of the Zero Dynamics Manifolds

To achieve the invariance, the output function for each phase needs to be designed such that the invariance conditions (10.61a), (10.61b), (10.62a), and (10.62b) are satisfied. Since y_a and y_u satisfy HH3.a and HH3.u, respectively, $[h_a(q_a); \theta_a(q_a)]$ and $[h_u(q_u); \theta_u(q_u)]$ are invertible maps. Using (10.93), we obtain that

$$H_a(q_a) := \begin{bmatrix} h_a^t(q_a) \\ \theta_a(q_a) \end{bmatrix} \quad (10.100)$$

and

$$H_u(q_u) := \begin{bmatrix} h_u^t(q_u) \\ \theta_u(q_u) \end{bmatrix} \quad (10.101)$$

are also invertible maps. By definition, on the zero dynamics manifold for each phase, the output function satisfies the following conditions.

$$y_a = h_a(q_a) = h_a^t(q_a) - h_a^d \circ \theta_a(q_a) = 0, \quad (10.102a)$$

$$y_u = h_u(q_u) = h_u^t(q_u) - h_u^d \circ \theta_u(q_u) = 0. \quad (10.102b)$$

Since $H_a(q_a)$ and $H_u(q_u)$ are invertible, the condition for the position states after the transition to remain in the zero dynamics manifold for the underactuated phase is derived as

$$\begin{bmatrix} \beta_0 \\ \theta_u(q_u^+) \end{bmatrix} = H_u \circ \begin{bmatrix} H_a^{-1} \circ \begin{bmatrix} \alpha_{M_a} \\ \theta_a(q_a^-) \end{bmatrix} \\ \pi \end{bmatrix}. \quad (10.103)$$

Similarly, the condition for the position states to be in the zero dynamics manifold for the fully actuated phase after the transition from the underactuated phase to the fully actuated can be obtained to be

$$\begin{bmatrix} \alpha_0 \\ \theta_a(q_a^+) \end{bmatrix} = H_a \circ \left(R \left(H_u^{-1} \circ \begin{bmatrix} \beta_{M_u} \\ \theta_u(q_u^-) \end{bmatrix} \right) \right), \quad (10.104)$$

where R is the relabeling matrix. Since $\dot{y}_a = 0$ and $\dot{y}_u = 0$ on the zero dynamics manifold for each phase,

$$\dot{y}_a = \frac{\partial h_a^t(q_a)}{\partial q_a} \dot{q}_a - \frac{\partial h_a^d}{\partial s_a} \frac{\partial s_a}{\partial \theta_a} \dot{\theta}_a = 0, \quad (10.105a)$$

$$\dot{y}_u = \frac{\partial h_u^t(q_u)}{\partial q_u} \dot{q}_u - \frac{\partial h_u^d}{\partial s_u} \frac{\partial s_u}{\partial \theta_u} \dot{\theta}_u = 0. \quad (10.105b)$$

Since $H_a(q_a)$ and $H_u(q_u)$ are invertible, the condition for the velocity states after the transition from the fully actuated phase to the underactuated phase to be in the zero dynamics manifold for the underactuated phase can be obtained from the transition map (10.8) as

$$\beta_1 = \frac{\theta_u^- - \theta_u^+}{M_u} \frac{\partial h_u^t}{\partial q_u} \Lambda \frac{\kappa_{1a}(\theta_a^-)}{\kappa_{1u}(\theta_u^+) \delta_a^u} + \beta_0, \quad (10.106)$$

where

$$\Lambda := \begin{bmatrix} \frac{\partial H_a}{\partial q_a}^{-1} & \begin{bmatrix} \frac{M_a(\alpha_{M_a} - \alpha_{M_a-1})}{\theta_a^- - \theta_a^+} \\ 1 \end{bmatrix} \\ 0_{1 \times 1} & \end{bmatrix}. \quad (10.107)$$

Similarly, the condition for the velocity states to be in the zero dynamics manifold for the fully actuated after the transition can be obtained as

$$\alpha_1 = \frac{\theta_a^- - \theta_a^+}{M_a} \frac{\partial h_a^t}{\partial q_a} \Delta_{\dot{q}, u}^a(q_u^-) \frac{\partial H_u}{\partial q_u}^{-1} \Xi \frac{\kappa_{1u}(\theta_u^-)}{\kappa_{1a}(\theta_a^+) \delta_u^a} + \alpha_0, \quad (10.108)$$

where

$$\Xi := \begin{bmatrix} \frac{M_u(\beta_{M_u} - \beta_{M_u-1})}{\theta_u^- - \theta_u^+} \\ 1 \end{bmatrix}. \quad (10.109)$$

When the ankle torque is controlled to affect the stability, the desired path of the angular momentum during the fully actuated phase, $\zeta_a^*(s_a)$, needs to satisfy (10.87), which is essentially equivalent to the nonzero angular momentum hypothesis HGW3.F, and (10.91) for periodicity. Since $\zeta_a^*(\theta_a^+) = \gamma_0$ and $\zeta_a^*(\theta_a^-) = \gamma_m$, the condition for γ_0 is given by

$$\gamma_0 = (\delta_a^u)^2 (\delta_a^a)^2 \gamma_m - (\delta_a^u)^2 V_{Z_u}(\theta_a^-), \quad (10.110)$$

from (10.91).

10.5.3 Specifying the Remaining Free Parameters

There are free coefficients in the Bézier polynomials after meeting the invariance conditions and they can be used to satisfy constraints for stability, ground reaction forces being within the friction cone to avoid slipping, anthropomorphic gait, average walking speed, etc. This section explains the various constraints.

Equality constraint:

EC1) Average walking speed is constant. The walking speed of the robot, which is defined as step length divided by time duration of a step, is given by

$$v = \frac{L_s}{T_s}, \quad (10.111)$$

where L_s is the step length and T_s is the time elapsed for the step.

Inequality constraints:

IEC1) The stability condition (10.89) is satisfied;

IEC2) The nonslipping assumption is satisfied. In each phase, the foot will not slip if the ratio of the tangential reaction force and the normal reaction force from the ground are within the friction cone, which can be formulated as

$$\left| \frac{F_T}{F_N} \right| \leq \mu_s, \quad (10.112)$$

where μ_s is the Coulomb friction coefficient of the surface, F_T is the tangential force, and F_N is the normal reaction force;

IEC3) The normal reaction force from the ground is positive. This is due to the fact that the ground reaction force is unilateral. In other words, the ground is not sticky;

IEC4) The height of the swing foot is positive between impacts;

IEC5) The FRI point is within the stance footprint (i.e., the convex hull of the foot) during the fully actuated phase and strictly in front of the stance foot at the beginning of the underactuated phase;

IEC6) The stance foot leaves the ground after the double support;

IEC7) The angles of the knees and ankles are limited to produce an anthropomorphic gait;

IEC8) The torque applied at each joint is limited to a physically realizable value.

The desired output functions and the desired angular momentum during a step need to be determined, subject to the invariance condition and the constraints being satisfied. This can be formulated as an numerical optimization problem. The cost function used here is defined as

$$J = \frac{1}{L_s} \int_{T_I^+}^{T_I^-} \sum_{k=1}^N |\dot{q}_k u_k| dt, \quad (10.113)$$

where L_s is the step length, T_I^+ and T_I^- are the time of beginning and end of the step, respectively.

10.6 Simulation

For purpose of illustration, a planar bipedal robot with seven links is used. See Fig. 10.3 for the detailed coordinate conventions. The degrees of the polynomials used in the desired output functions and desired angular momentum for both phases are set to be $M_a = 6$, $M_u = 6$, and $m = 5$. The parameters used for the simulation are given in Table 10.1. The parameters are defined as shown in Fig. 10.7. A stick figure diagram of the walking motion over one step is depicted in Fig. 10.8.

Figures 10.9 and 10.10 show the position and velocity states of the robot. During the underactuated phase, the angle of the stance foot decreases, which implies that the robot rolls over the stance toe.

Let $(0; 0)$ be the Cartesian coordinate of the stance toe and let $(p_h^h; 0)$ be the location of the stance heel during the fully actuated phase; see Fig. 10.3. In order for the stance foot not to rotate, the location of the FRI point, $(p_{\text{FRI}}^h; 0)$ needs to satisfy

$$p_h^h < p_{\text{FRI}}^h < 0. \quad (10.114)$$

The validity of this condition is illustrated in Fig. 10.11, confirming that the stance foot remains flat on the ground during the fully actuated phase.

Table 10.1. Parameters for simulation. Note that ankle height is zero.

| Model Parameter | Units | Link | Label | Value |
|-----------------|-------------------|-------|-------------|--------|
| Mass | kg | Torso | M_{Torso} | 36.044 |
| | | Femur | M_{Femur} | 9.149 |
| | | Tibia | M_{Tibia} | 3.000 |
| | | Foot | M_{Foot} | 0.200 |
| Length | m | Torso | L_{Torso} | 0.625 |
| | | Femur | L_{Femur} | 0.400 |
| | | Tibia | L_{Tibia} | 0.400 |
| | | Toe | L_{Toe} | 0.100 |
| | | Heel | L_{Heel} | 0.060 |
| Inertia | kg·m ² | Torso | J_{Torso} | 5.527 |
| | | Femur | J_{Femur} | 0.331 |
| | | Tibia | J_{Tibia} | 0.149 |
| | | Foot | J_{Foot} | 0.100 |
| Center of Mass | m | Torso | l_{Torso} | 0.200 |
| | | Femur | l_{Femur} | 0.163 |
| | | Tibia | l_{Tibia} | 0.137 |
| | | Foot | l_{Foot} | 0.030 |

The applied torques are shown in Fig. 10.12. Note that the torques have a discontinuity at the transition from the fully actuated phase to the underactuated phase, which is allowed in this study.

10.7 Special Case of a Gait without Foot Rotation

The previous analysis can be specialized to a gait without foot rotation, in other words, to a gait with only flat-footed walking. This allows the differences with the ZMP criterion to be highlighted in the next section.

The stability conditions can be derived by specializing the calculations in Section 10.4 to this case, the Poincaré map of the hybrid zero dynamics is

$$\rho(\zeta_a^-) = (\delta_a^a)^2 \zeta_a^- - V_{Z_a}^{u_A}(\theta_a^-), \quad (10.115)$$

where $V_{Z_a}^{u_A}$, the potential energy, is given in (10.67a), and, based on Sec-

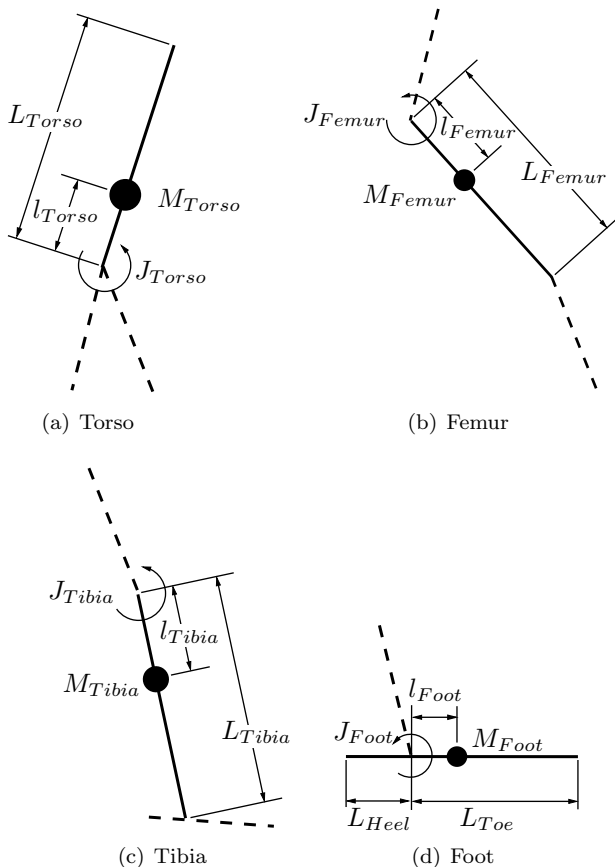


Figure 10.7. Parameter definitions for each link. Note that ankle height is zero; that is, $p_a^v = 0$.

tions 10.3.3 and 10.3.4,

$$\begin{aligned}\delta_a^a &= 1 - \vec{d} \wedge m_{\text{tot}} \begin{bmatrix} \lambda_x^a(q_a^-) \\ \lambda_y^a(q_a^-) \end{bmatrix} - J_{foot} \omega_0(q_a^-) \\ &= 1 - m_{\text{tot}} d \lambda_y^a(q_a^-) - J_{foot} \omega_0(q_a^-)\end{aligned}\quad (10.116)$$

on flat ground.

The stability theorem becomes the following.

Corollary 10.1

Under the Hypotheses HR1.F–HR4.F, HGW1.F–HGW9.F, HI1.F–HI7.F, and

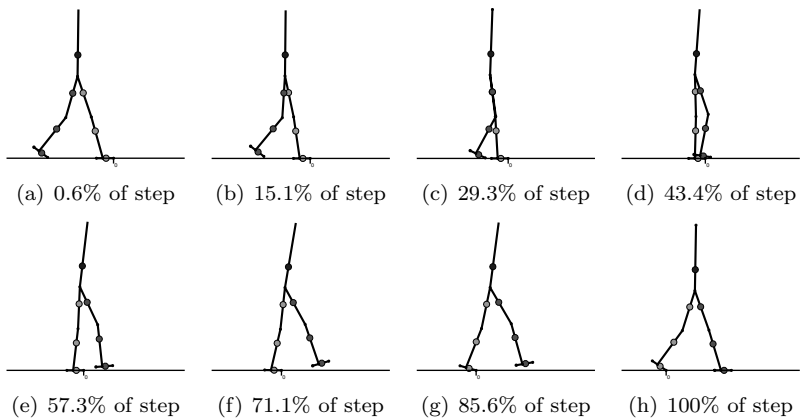


Figure 10.8. Stick diagram of the robot during one step of the stable gait of Section 10.6.

HH1.a–HH5.a,

$$\zeta_a^* = -\frac{V_{Z_a}^{u_A}(\theta_a^-)}{1 - (\delta_a^a)^2} \quad (10.117)$$

is an exponentially stable fixed point of (10.115) if, and only if,

$$0 < (\delta_a^a)^2 < 1, \quad (10.118a)$$

$$\frac{(\delta_a^a)^2 V_{Z_a}^{u_A}(\theta_a^-)}{1 - (\delta_a^a)^2} + V_{Z_a}^{u_A, max} < 0. \quad (10.118b)$$

These conditions are the same as in Theorem 5.3 for point-feet, with the exception that the potential energy term $V_{Z_a}^{u_A}$ can be shaped by choice of the ankle torque, u_A ; see second term in (10.67a).

10.8 ZMP and Stability of an Orbit

The ZMP has been widely used as an indication of balance of a bipedal robot [114, 117, 147, 207, 214, 233, 235]. The ZMP being within the stance footprint is a sufficient and necessary condition for the stance foot not to rotate, but it does not mean the resulting walking motion corresponds to an asymptotically stable periodic orbit. In this section, the special case of flat-footed walking is considered in order to illustrate that the ZMP criterion alone is not sufficient for the stability of the robot.

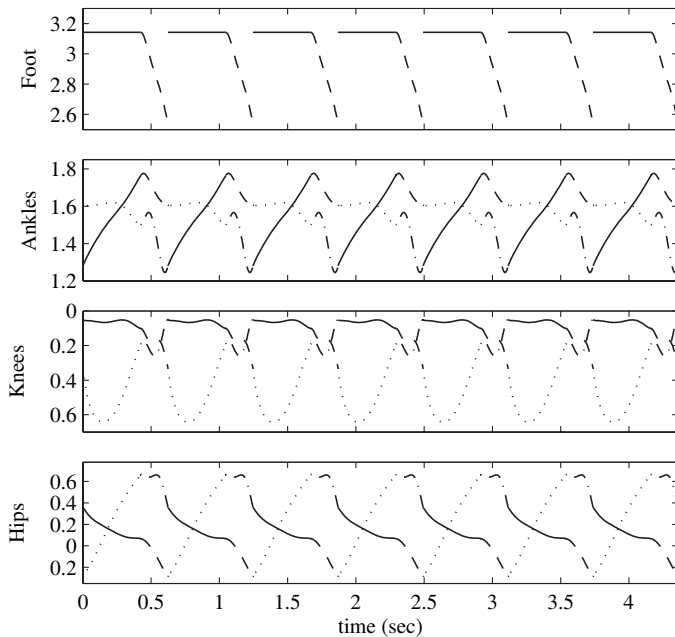


Figure 10.9. Joint angles (rad) of the robot on the HZD. The robot is walking at 1 m/s with a stable gait. Curves corresponding to the stance and swing legs during the fully actuated phase are solid and dotted, respectively. Curves corresponding to the stance and swing legs during the underactuated phase are dashed and dash-dotted, respectively.

Consider a planar bipedal robot and a gait consisting only of the fully actuated phase followed by an instantaneous double-support phase. The method of Section 10.5 was used to design a periodic orbit of the robot such that: (i) the FRI point is within the stance footprint during the fully actuated phase in order for the stance foot to remain flat on the ground and (ii) $(\delta_a^a)^2$ in (10.115) is greater than one; see Table 10.2. Note that if the stance foot does not rotate, the FRI point is equivalent to the ZMP. The ankle torque is used for shaping the potential energy in this illustration.

Figure 10.13 shows the FRI point during the fully actuated phase. Since the location of the FRI point satisfies (10.114), the stance foot does not rotate and the ZMP criterion would “predict” stability. The gait, however, is not stable. Table 10.2 shows the Poincaré analysis of the unstable gait. Since $\delta_a^a = 1.266$, the condition (10.118a) is not satisfied, which causes instability. The lack of stability is manifested by the walking speed diverging when there is a small error in the velocity states at the initial conditions as shown in Fig. 10.14. In this simulation, the velocity initial conditions are set to 99.5% of their value on the periodic orbit.

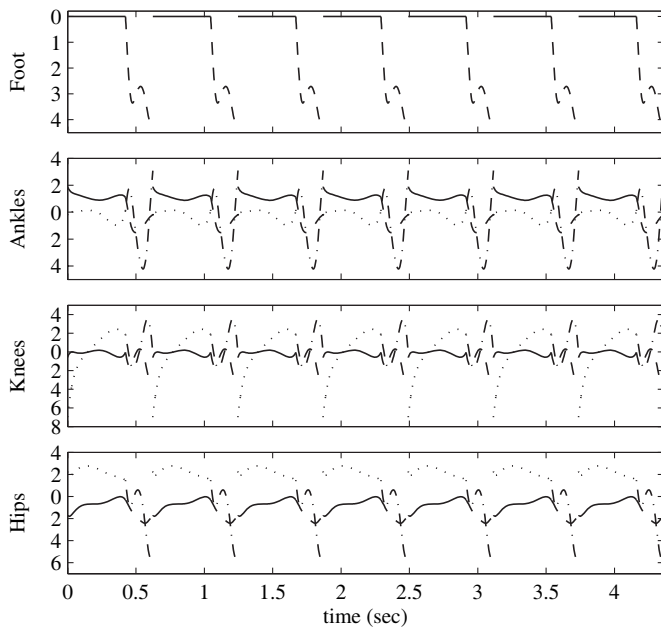


Figure 10.10. Joint velocities (rad/s) of the robot on the HZD. The robot is walking at 1 m/s with a stable gait. Curves corresponding to the stance and swing legs during the fully actuated phase are solid and dotted, respectively. Curves corresponding to the stance and swing legs during the underactuated phase are dashed and dash-dotted, respectively.

Even with the unstable gait, the hybrid zero dynamics is invariant. [Figure 10.15](#) shows the phase portrait of the absolute angle of the robot. The point A represents the initial condition. The gait of the robot diverges from the limit cycle, which implies that the periodic orbit is not stable.

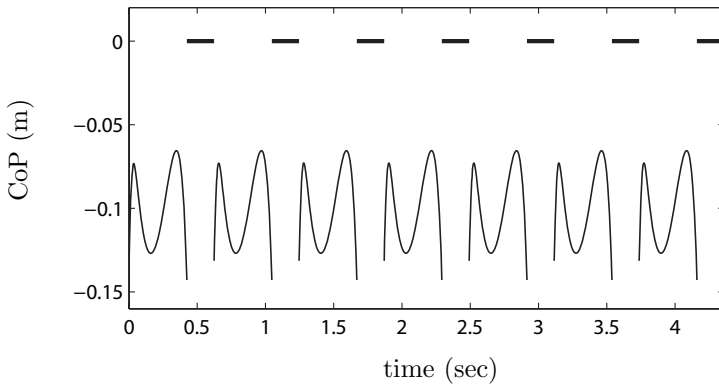


Figure 10.11. Location of the CoP while walking at 1 m/s with a stable gait. The CoP validates the conditions for the respective phases. Namely, it is located at the toe during the underactuated phase (bold line) and it is strictly within the footprint, $-0.16 < p_{\text{FRI}}^{\text{h}} < 0$, during the fully actuated phase, when it is therefore equal to the FRI point. The discontinuity in the location of the CoP is due to the discontinuity in the torque at each transition.

Table 10.2. Quantities of the Poincaré return map of the hybrid zero dynamics for an unstable gait.

| δ_a^a | $V_{Z_a}^{u_A}(\theta_a^-)$ (kgm^2/s) ² | $V_{Z_a}^{u_A,max}$ (kgm^2/s) ² | ζ_a^* (kgm^2/s) ² |
|--------------|---|---|---|
| 1.266 | 505 | 1050 | 1678 |

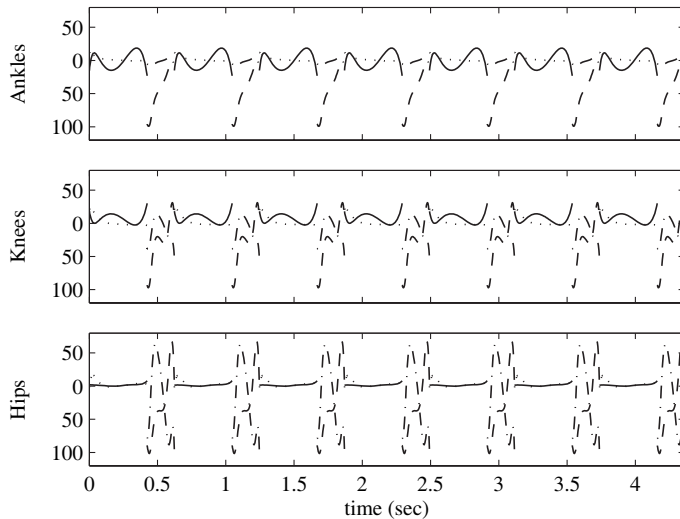


Figure 10.12. Joint torques (Nm) of the robot when walking at 1 m/s with a stable gait. Curves corresponding to the stance and swing legs during the fully actuated phase are solid and dotted, respectively. Curves corresponding to the stance and swing legs during the underactuated phase are dashed and dash-dotted, respectively.

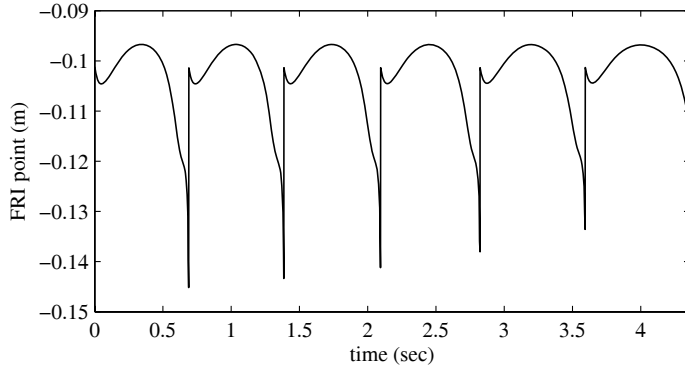


Figure 10.13. Location of FRI point for an unstable, flat-footed gait. The FRI point remains strictly within the stance footprint, $-0.16 < p_{\text{FRI}}^{\text{h}} < 0$, and hence the ZMP criterion is satisfied.

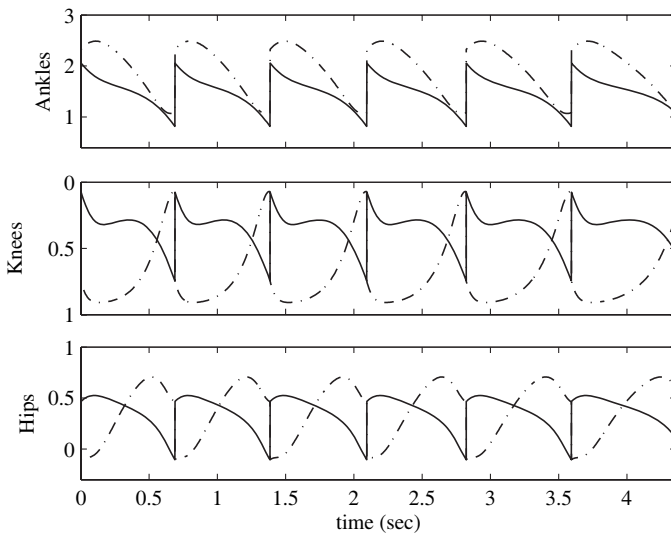


Figure 10.14. Divergence of the joint angles (rad) of the robot with an unstable gait that satisfies the ZMP criterion. The velocity states are initialized at 99.5% of their values on the periodic orbit. Curves corresponding to the stance and the swing legs are solid and dash-dotted, respectively.

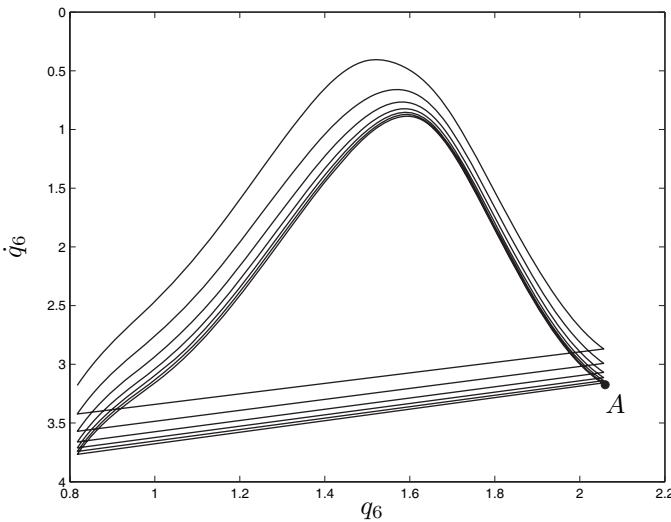


Figure 10.15. Phase portrait of the absolute angle of the robot for an unstable gait that satisfies the ZMP criterion. The point A represents the initial condition, selected so that the joint velocities are 99.5% of their values on the periodic orbit. The robot's motion clearly diverges from the periodic orbit, commensurate with $\delta_a^a > 1$ in Table 10.2.

11

Directly Controlling the Foot Rotation Indicator Point

The majority of robot control policies are built around the notion of controlling the FRI point.¹ In particular, most of the control strategies are decomposed into a low-level controller and a high-level controller, where the low-level controller ensures the tracking of the reference motion for each joint, and the high-level controller modifies the reference motion in order to ensure that the FRI point remains within the convex hull of the foot support region; see Fig. 1.8. The previous chapter concluded, however, by emphasizing that the existence and stability of an orbit depend on much more than just the position of the FRI point: It is quite possible to have gaits where the FRI point is within the convex hull of the foot support region and where the robot remains upright, but yet the gait is not periodic, or it is periodic, but is not asymptotically stable. This chapter addresses the direct control of the FRI point in the context of the tools associated with the hybrid zero dynamics framework. In particular, control of the FRI point is achieved along with a guarantee of the existence and exponential stability of a periodic walking motion.

11.1 Introduction

In human walking, one observes heel strike, followed by rotation of the foot about the heel, followed by the foot being in full contact with the ground, and then rotation about the toe just before the heel strike on the opposite foot. It is therefore natural to assume that the center of pressure moves forward from heel to toe throughout a step via progressive flexing of the

¹Recall that as long as the FRI point remains inside the convex hull of the foot support region, $\text{CoP} = \text{ZMP} = \text{FRI}$ and the supporting foot does not rotate. Recall also that the center of pressure or CoP is a standard notion in mechanics that was renamed the zero moment point or ZMP by Vukobratovic and coworkers [233, 235]. The FRI point of Goswami is a more general notion because it is defined when the foot is in rotation with respect to the walking surface [92].

foot.² In human walking, the rotation about the heel occurs during the non-instantaneous double-support phase, which is not considered in the current study where the double support phase is assumed to be instantaneous. Hence, as in the analysis of the preceding chapter, the rotation about the heel is neglected and the impact is assumed to take place with the foot parallel to the ground. In order for the supporting foot to remain flat on the ground, the FRI point must never reach the limits of the convex hull of the foot support region. Direct control of the position of the FRI point is a way to prevent this from occurring.

The control strategy presented here is based on using the stance ankle torque to obtain a desired evolution of the FRI position during the fully actuated phase. For the underactuated phase, the control strategy given in Section 10.4.1 is used.

For robots with point feet (i.e., without feet), Part II of the book demonstrated that the angular momentum about the stance leg end was an important variable for studying the zero dynamics. When controlling the position of the FRI point during the fully actuated phase, it is straightforward to use the angular momentum about the FRI point in order to study the zero dynamics. We assume here that the angular momentum around the FRI is never zero during a step. In particular, Hypothesis HGW3.F of Section 10.2.1 is replaced with the following³:

-
- HGW10.F) Throughout the fully actuated phase, the angular momentum about the FRI point is nonzero.

11.2 Using Ankle Torque to Control FRI Position During the Fully Actuated Phase

An ankle-torque control strategy is proposed for regulating the FRI position, p_{FRI}^h . The analysis of Section 10.4.2 is modified to reflect this new objective. The counterclockwise angular measurement convention is used in the theoretical development. *In the simulations reported in Sections 11.4 and 11.6, a clockwise angular measurement convention is used so that forward motion corresponds to positive angular momentum.*

²For mechanical walking, the CoP can evolve in an arbitrary manner during the flat-footed phase, as long as it stays strictly within the convex hull of the footprint. In human walking, the heel strikes first, meaning the CoP is at the heel, then the foot rolls about the heel contact until the foot is flat on the ground. At the end of the step, ankle flexion forces the CoP to the toe in order to initiate toe roll. Hence, at the beginning of ground contact, the CoP is at the back of the foot and at the end of the step, the CoP is at the front of the foot. A reasonable conjecture is that it advances monotonically in between.

³It will be seen that HGW10.F implies HGW3.F.

11.2.1 Ability to Track a Desired Profile of the FRI Point

The desired position of the FRI during the fully actuated phase is assumed here to be a function of θ_a only: $p_{\text{FRI}}^{\text{h,d}}(\theta_a)$. It is now shown that under Hypothesis HGW10.F, the ankle torque u_A can be chosen to achieve a desired evolution of the FRI point.

Let $y_a = h_a(x_a)$ be an $(N - 2) \times 1$ vector of output functions satisfying Hypotheses HH1.a–HH5.a. On the corresponding zero dynamics of the fully actuated phase, the position of the center of mass can be expressed as a function of θ_a . It follows that on the zero dynamics, the velocity of the center of mass is proportional to the angular momentum about the stance ankle via:

$$\dot{p}_{\text{cm}} = \begin{bmatrix} \lambda_x^a(\theta_a) \\ \lambda_y^a(\theta_a) \end{bmatrix} \sigma_a, \quad (11.1)$$

and its acceleration is

$$\ddot{p}_{\text{cm}}^{\text{h}} = \lambda_x^a(\theta_a)\dot{\sigma}_a + \dot{\lambda}_x^a(\theta_a)\sigma_a \quad (11.2a)$$

$$\ddot{p}_{\text{cm}}^{\text{v}} = \lambda_y^a(\theta_a)\dot{\sigma}_a + \dot{\lambda}_y^a(\theta_a)\sigma_a. \quad (11.2b)$$

Using (10.48a) and (10.48b), the acceleration of the center of mass is related to u_A by

$$\ddot{p}_{\text{cm}}^{\text{h}} = \lambda_x^a(\theta_a)\kappa_{2a}(\theta_a) + \lambda_x^a(\theta_a)u_A + \frac{\partial \lambda_x^a(\theta_a)}{\partial \theta_a}\kappa_{1a}(\theta_a)\sigma_a^2 \quad (11.3a)$$

$$\ddot{p}_{\text{cm}}^{\text{v}} = \lambda_y^a(\theta_a)\kappa_{2a}(\theta_a) + \lambda_y^a(\theta_a)u_A + \frac{\partial \lambda_y^a(\theta_a)}{\partial \theta_a}\kappa_{1a}(\theta_a)\sigma_a^2. \quad (11.3b)$$

Substituting the above into (10.24) and rearranging terms yields

$$\gamma_2(\theta_a)u_A = \gamma_0(\theta_a) + \gamma_1(\theta_a)\sigma_a^2, \quad (11.4)$$

where

$$\begin{aligned} \gamma_0(\theta_a) &= (p_{\text{FRI}}^{\text{h,d}}(\theta_a) - p_a^{\text{h}})m_{\text{tot}}(g_0 + \lambda_y^a(\theta_a)\kappa_{2a}(\theta_a)) + \\ &\quad p_a^{\text{v}}m_{\text{tot}}\lambda_x^a(\theta_a)\kappa_{2a}(\theta_a) - (p_{\text{foot,cm}}^{\text{h}} - p_a^{\text{h}})m_{\text{foot}}g_0 \end{aligned} \quad (11.5a)$$

$$\begin{aligned} \gamma_1(\theta_a) &= (p_{\text{FRI}}^{\text{h,d}}(\theta_a) - p_a^{\text{h}})m_{\text{tot}}\frac{\partial \lambda_y^a(\theta_a)}{\partial \theta_a}\kappa_{1a}(\theta_a) + \\ &\quad p_a^{\text{v}}m_{\text{tot}}\frac{\partial \lambda_x^a(\theta_a)}{\partial \theta_a}\kappa_{1a}(\theta_a) \end{aligned} \quad (11.5b)$$

$$\gamma_2(\theta_a) = 1 + (p_a^{\text{h}} - p_{\text{FRI}}^{\text{h,d}}(\theta_a))m_{\text{tot}}\lambda_y^a(\theta_a) - p_a^{\text{v}}m_{\text{tot}}\lambda_x^a(\theta_a). \quad (11.5c)$$

Therefore, we can solve for u_A as a function of the desired FRI position if, and only if,

$$\gamma_2(\theta_a) \neq 0. \quad (11.6)$$

On the zero dynamics, however, (10.26b) becomes

$$\sigma_{\text{FRI}} = (1 + m_{\text{tot}}(p_a^{\text{h}} - p_{\text{FRI}}^{\text{h}})\lambda_y^{\text{a}}(\theta_{\text{a}}) - m_{\text{tot}}p_a^{\text{v}}\lambda_x^{\text{a}}(\theta_{\text{a}}))\sigma_{\text{a}}, \quad (11.7)$$

and hence Hypothesis HGW10.F implies (11.6), showing that the stance ankle torque, u_{A} , can indeed be used to regulate the FRI position. The required control is then

$$u_{\text{A}} = \frac{\gamma_0(\theta_{\text{a}})}{\gamma_2(\theta_{\text{a}})} + \frac{\gamma_1(\theta_{\text{a}})}{\gamma_2(\theta_{\text{a}})}\sigma_{\text{a}}^2. \quad (11.8)$$

11.2.2 Analyzing the Zero Dynamics

Using the coordinates $(\theta_{\text{a}}; \sigma_{\text{a}})$ for the zero dynamics manifold and substituting (11.8) into (10.48a) and (10.48b), the zero dynamics of the fully actuated phase can be written as

$$\dot{\theta}_{\text{a}} = \kappa_{1\text{a}}(\theta_{\text{a}})\sigma_{\text{a}} \quad (11.9\text{a})$$

$$\dot{\sigma}_{\text{a}} = \kappa_{3\text{a}}(\theta_{\text{a}}) + \kappa_{4\text{a}}(\theta_{\text{a}})\sigma_{\text{a}}^2, \quad (11.9\text{b})$$

where

$$\kappa_{3\text{a}}(\theta_{\text{a}}) := \kappa_{2\text{a}}(\theta_{\text{a}}) + \frac{\gamma_0(\theta_{\text{a}})}{\gamma_2(\theta_{\text{a}})}, \text{ and} \quad (11.10\text{a})$$

$$\kappa_{4\text{a}}(\theta_{\text{a}}) := \frac{\gamma_1(\theta_{\text{a}})}{\gamma_2(\theta_{\text{a}})}. \quad (11.10\text{b})$$

In a similar manner, using the coordinates $(\theta_{\text{a}}; \sigma_{\text{FRI}})$, where σ_{FRI} is the angular momentum about the FRI point, the zero dynamics can be written as

$$\dot{\theta}_{\text{a}} = \kappa_{1\text{FRI}}(\theta_{\text{a}})\sigma_{\text{FRI}} \quad (11.11\text{a})$$

$$\dot{\sigma}_{\text{FRI}} = \kappa_{2\text{FRI}}(\theta_{\text{a}}) + \kappa_{3\text{FRI}}(\theta_{\text{a}})\sigma_{\text{FRI}}^2, \quad (11.11\text{b})$$

where, from (10.26b), (10.27), and (11.7),

$$\kappa_{1\text{FRI}}(\theta_{\text{a}}) := \frac{\kappa_{1\text{a}}(\theta_{\text{a}})}{\gamma_2(\theta_{\text{a}})} \quad (11.12\text{a})$$

$$\kappa_{2\text{FRI}}(\theta_{\text{a}}) := -m_{\text{tot}}g_0(p_{\text{cm}}^{\text{h}}(\theta_{\text{a}}) - p_{\text{FRI}}^{\text{h,d}}(\theta_{\text{a}})) \quad (11.12\text{b})$$

$$\kappa_{3\text{FRI}}(\theta_{\text{a}}) := -m_{\text{tot}} \frac{\partial p_{\text{FRI}}^{\text{h,d}}(\theta_{\text{a}})}{\partial \theta_{\text{a}}} \lambda_y^{\text{a}}(\theta_{\text{a}}) \kappa_{1\text{a}}(\theta_{\text{a}}) \left(\frac{1}{\gamma_2(\theta_{\text{a}})} \right)^2. \quad (11.12\text{c})$$

On the zero dynamics manifold, the fully actuated phase begins with $\theta_{\text{a}} = \theta_{\text{a}}^+$ and finishes with $\theta_{\text{a}} = \theta_{\text{a}}^-$. Under HGW10.F, σ_{FRI} is nonzero throughout the fully actuated phase, which leads to

$$\frac{d\sigma_{\text{FRI}}}{d\theta_{\text{a}}} = \frac{\kappa_{2\text{FRI}}(\theta_{\text{a}})}{\kappa_{1\text{FRI}}(\theta_{\text{a}})} \frac{1}{\sigma_{\text{FRI}}} + \frac{\kappa_{3\text{FRI}}(\theta_{\text{a}})}{\kappa_{1\text{FRI}}(\theta_{\text{a}})} \sigma_{\text{FRI}}. \quad (11.13)$$

Doing the now-familiar change of coordinates $\zeta_{\text{FRI}} = (\sigma_{\text{FRI}})^2/2$ results in

$$\frac{d\zeta_{\text{FRI}}}{d\theta_a} = \frac{\kappa_{2\text{FRI}}(\theta_a)}{\kappa_{1\text{FRI}}(\theta_a)} + 2\frac{\kappa_{3\text{FRI}}(\theta_a)}{\kappa_{1\text{FRI}}(\theta_a)}\zeta_{\text{FRI}}. \quad (11.14)$$

The above is a linear in ζ_{FRI} , θ_a -varying ODE and has the explicit solution

$$\zeta_{\text{FRI}}(\theta_a) = (\delta_{\text{FRI}}(\theta_a))^2 \zeta_{\text{FRI}}^+ - V_{Z_a}^{\text{FRI}}(\theta_a), \quad (11.15)$$

where

$$\delta_{\text{FRI}}(\theta_a) = \exp \left(\int_{\theta_a^+}^{\theta_a} \frac{\kappa_{3\text{FRI}}(\tau_1)}{\kappa_{1\text{FRI}}(\tau_1)} d\tau_1 \right) \quad (11.16a)$$

$$V_{Z_a}^{\text{FRI}}(\theta_a) = - \int_{\theta_a^+}^{\theta_a} \exp \left(2 \int_{\tau_2}^{\theta_a} \frac{\kappa_{3\text{FRI}}(\tau_1)}{\kappa_{1\text{FRI}}(\tau_1)} d\tau_1 \right) \frac{\kappa_{2\text{FRI}}(\tau_2)}{\kappa_{1\text{FRI}}(\tau_2)} d\tau_2. \quad (11.16b)$$

Note that if the desired FRI point is selected to be constant during this phase, then $\kappa_{3\text{FRI}}(\theta_a) \equiv 0$ and $\delta_{\text{FRI}}(\theta_a) \equiv 1$, and hence the result simplifies to the case of point feet; see [Section 5.4.1](#). Equation (11.15) has been obtained using hypothesis HGW10.F, thus the condition $\zeta_{\text{FRI}}(\theta_a) > 0$ must be satisfied for θ_a between θ_a^- and θ_a^+ , yielding the condition

$$\zeta_{\text{FRI}}^+ > \bar{V}^{\max}, \quad (11.17)$$

with

$$\bar{V}^{\max} := \max_{\theta_a^+ \leq \theta_a \leq \theta_a^-} \frac{V_{Z_a}^{\text{FRI}}(\theta_a)}{(\delta_{\text{FRI}}(\theta_a))^2}. \quad (11.18)$$

In order to obtain the Poincaré map for the fully actuated phase on the hybrid zero dynamics, $\rho_a : S_u^a \cap Z_u \rightarrow S_a^u \cap Z_a$, the relation between ζ_u^- and ζ_{FRI}^+ and between ζ_a^- and ζ_{FRI}^+ have to be defined. At θ_a^+ , using the principle of angular momentum transfer,⁴

$$\sigma_{\text{FRI}}^+ = \sigma_a^+ + m_{\text{tot}}(p_a^h - p_{\text{FRI}}^{h,d}(\theta_a^+))\dot{p}_{cm}^v - m_{\text{tot}}p_a^v\dot{p}_{cm}^h. \quad (11.19)$$

In combination with (11.1) and (10.53b), we obtain a linear relation between σ_{FRI}^+ and σ_u^- , written as

$$\sigma_{\text{FRI}}^+ = \delta_u^{\text{FRI}}\sigma_u^-. \quad (11.20)$$

At θ_a^- , using the principle of angular momentum transfer,

$$\sigma_{\text{FRI}}^- = \sigma_a^- + m_{\text{tot}}(p_a^h - p_{\text{FRI}}^{h,d}(\theta_a^-))\dot{p}_{cm}^v - m_{\text{tot}}p_a^v\dot{p}_{cm}^h. \quad (11.21)$$

Using (11.1), we obtain a linear relation between σ_{FRI}^- and σ_a^- , written as

$$\sigma_a^- = \delta_a^{\text{FRI}}\sigma_{\text{FRI}}^-. \quad (11.22)$$

⁴Note that the angular momentum about the FRI point is conserved during impact, but the position of the FRI point can be different before impact, at impact and after impact.

Thus the Poincaré map for the fully actuated phase on the hybrid zero dynamics, $\rho_a : \mathcal{S}_u^a \cap \mathcal{Z}_u \rightarrow \mathcal{S}_u^a \cap \mathcal{Z}_a$, becomes

$$\rho_a(\zeta_u^-) = (\delta_{\text{FRI}}^a)^2 (\delta_{\text{FRI}}(\theta_a^-))^2 (\delta_u^{\text{FRI}})^2 \zeta_u^- - (\delta_{\text{FRI}}^a)^2 V_{\mathcal{Z}_a}^{\text{FRI}}(\theta_a^-). \quad (11.23)$$

The Poincaré map $\rho(\zeta_u^-) : \mathcal{S}_u^a \cap \mathcal{Z}_u \rightarrow \mathcal{S}_u^a \cap \mathcal{Z}_u$ for the overall reduced system is defined as the composition of (10.65) and (11.23). In coordinates $(\theta_u; \zeta_u)$,

$$\rho(\zeta_u^-) = \rho_u \circ \rho_a(\zeta_u^-) \quad (11.24a)$$

$$= (\delta_a^u)^2 (\delta_{\text{FRI}}^a)^2 (\delta_{\text{FRI}}(\theta_a^-))^2 (\delta_u^{\text{FRI}})^2 \zeta_u^- \\ - (\delta_a^u)^2 (\delta_{\text{FRI}}^a)^2 V_{\mathcal{Z}_a}^{\text{FRI}}(\theta_a^-) - V_{\mathcal{Z}_u}(\theta_u^-), \quad (11.24b)$$

with domain of definition

$$\mathcal{D} = \{ \zeta_u^- > 0 \mid (\delta_u^{\text{FRI}})^2 \zeta_u^- - \bar{V}^{\max} > 0, \\ (\delta_a^u)^2 (\delta_{\text{FRI}}^a)^2 (\delta_{\text{FRI}}(\theta_a^-))^2 (\delta_u^{\text{FRI}})^2 \zeta_u^- - (\delta_a^u)^2 (\delta_{\text{FRI}}^a)^2 V_{\mathcal{Z}_a}^{\text{FRI}}(\theta_a^-) - V_{\mathcal{Z}_u}^{\max} > 0 \}. \quad (11.25)$$

Theorem 11.1

Assume the Hypotheses HR1.F–HR4.F on the robot, HGW1.F–HGW10.F on its gait, and HI1.F–HI7.F on the impact model. If virtual constraints are selected to satisfy Hypotheses HH1.a–HH5.a and HH1.u–HH5.u, then

$$\zeta_u^* = -\frac{(\delta_a^u)^2 (\delta_{\text{FRI}}^a)^2 V_{\mathcal{Z}_a}^{\text{FRI}}(\theta_a^-) + V_{\mathcal{Z}_u}(\theta_u^-)}{1 - (\delta_a^u)^2 (\delta_{\text{FRI}}^a)^2 (\delta_{\text{FRI}}(\theta_a^-))^2 (\delta_u^{\text{FRI}})^2} \quad (11.26)$$

is an exponentially stable fixed point of (11.24a) if, and only if,

$$0 < (\delta_a^u)^2 (\delta_{\text{FRI}}^a)^2 (\delta_{\text{FRI}}(\theta_a^-))^2 (\delta_u^{\text{FRI}})^2 < 1, \quad (11.27a)$$

$$\frac{(\delta_u^{\text{FRI}})^2 (\delta_a^u)^2 (\delta_{\text{FRI}}^a)^2 V_{\mathcal{Z}_a}^{\text{FRI}} + (\delta_u^{\text{FRI}})^2 V_{\mathcal{Z}_u}(\theta_u^-)}{1 - (\delta_a^u)^2 (\delta_{\text{FRI}}^a)^2 (\delta_{\text{FRI}}(\theta_a^-))^2 (\delta_u^{\text{FRI}})^2} + \bar{V}^{\max} < 0, \quad (11.27b)$$

$$\frac{(\delta_a^u)^2 (\delta_{\text{FRI}}^a)^2 (\delta_{\text{FRI}}(\theta_a^-))^2 (\delta_u^{\text{FRI}})^2 V_{\mathcal{Z}_u}(\theta_u^-) + (\delta_a^u)^2 (\delta_{\text{FRI}}^a)^2 V_{\mathcal{Z}_a}^{\text{FRI}}(\theta_a^-)}{1 - (\delta_a^u)^2 (\delta_{\text{FRI}}^a)^2 (\delta_{\text{FRI}}(\theta_a^-))^2 (\delta_u^{\text{FRI}})^2} \\ + V_{\mathcal{Z}_u}^{\max} < 0. \quad (11.27c)$$

Proof \mathcal{D} is nonempty if, and only if, $(\delta_a^u)^2 (\delta_{\text{FRI}}^a)^2 (\delta_{\text{FRI}}(\theta_a^-))^2 (\delta_u^{\text{FRI}})^2 > 0$. If there exists $\zeta_u^* \in \mathcal{D}$ satisfying $\rho(\zeta_u^*) = \zeta_u^*$, then it is an exponentially stable fixed point if, and only if, $0 < (\delta_a^u)^2 (\delta_{\text{FRI}}^a)^2 (\delta_{\text{FRI}}(\theta_a^-))^2 (\delta_u^{\text{FRI}})^2 < 1$, and in this case, (11.26) is the value of ζ_u^* . Finally, (11.27b) and (11.27c) are the necessary and sufficient conditions for (11.26) to be in \mathcal{D} .

Remark 11.1 The selection of the desired evolution of the FRI point affects both the periodic motion and the convergence rate to the periodic motion. The position of the FRI point weakly affects the term $\kappa_{1\text{FRI}}$, which represents the inertia of the robot about the FRI point and is always positive. The shape of $p_{\text{FRI}}^{\text{h,d}}(\theta_a)$, as characterized by $\partial p_{\text{FRI}}^{\text{h,d}}(\theta_a)/\partial\theta_a$, affects the term $\kappa_{3\text{FRI}}$ and thus the convergence rate to the periodic orbit of the zero dynamics. To accelerate convergence, the term $(\delta_{\text{FRI}}(\theta_a^-))^2$ must be as small as possible, and thus $\kappa_{3\text{FRI}}$ must be negative. It follows that increasing $\partial p_{\text{FRI}}^{\text{h,d}}(\theta_a)/\partial\theta_a$ when the velocity of the center of mass is directed upward decreases the convergence rate while increasing $\partial p_{\text{FRI}}^{\text{h,d}}(\theta_a)/\partial\theta_a$ when the velocity of the center of mass is directed downward increases the convergence rate. The mean value of $p_{\text{FRI}}^{\text{h,d}}(\theta_a)$ mainly affects $\kappa_{2\text{FRI}}$. Moving the FRI point toward the toe decreases the fixed point, ζ_u^* , and consequently, the average walking speed. If the FRI point is moved sufficiently near the toe, a periodic solution may cease to exist because either condition (11.27b) or (11.27c) is no longer satisfied.

11.3 Special Case of a Gait without Foot Rotation

The previous analysis can be specialized to a gait without foot rotation, in other words, to a gait with only flat-footed walking. The development parallels Section 10.8 and is only sketched. To obtain the Poincaré map for the fully actuated phase on the hybrid zero dynamics, $\rho_a : S_a^a \cap \mathcal{Z}_a \rightarrow S_a^a \cap \mathcal{Z}_a$, the relation between ζ_{FRI}^- and ζ_{FRI}^+ from one step to the next has to be determined. This variation is due to the impact. During the impact, the evolution of the angular momentum around the new stance ankle is known from (10.37). By transfer of the angular momentum at θ_a^- from the FRI position to the stance ankle,

$$\sigma_a^- = \sigma_{\text{FRI}}^- - m_{\text{tot}}(p_a^h - p_{\text{FRI}}^{\text{h,d}}(\theta_a^-))\dot{p}_{\text{cm}}^v + m_{\text{tot}}p_a^v\dot{p}_{\text{cm}}^h. \quad (11.28)$$

The transfer of angular momentum at θ_a^+ from the stance ankle to the FRI position after impact is given by (11.19). The combination of the three equations (10.37), (11.19), and (11.28) yields a linear relation between σ_{FRI}^+ and σ_{FRI}^- of the form

$$\sigma_{\text{FRI}}^+ = \delta_{\text{FRI}}^{\text{FRI}}\sigma_{\text{FRI}}^-. \quad (11.29)$$

Thus the Poincaré map of the hybrid zero dynamics, $\rho_a : S_a^a \cap \mathcal{Z}_a \rightarrow S_a^a \cap \mathcal{Z}_a$, is

$$\rho_a(\zeta_{\text{FRI}}^-) = (\delta_{\text{FRI}}(\theta_a^-))^2(\delta_{\text{FRI}}^{\text{FRI}})^2\zeta_{\text{FRI}}^- - V_{\mathcal{Z}_a}^{\text{FRI}}(\theta_a^-). \quad (11.30)$$

The stability theorem becomes the following.

Corollary 11.1

Assume the Hypotheses HR1.F–HR4.F on the robot, HGW1.F–HGW10.F on its gait, and HI1.F–HI7.F on the impact model. If virtual constraints are selected to satisfy Hypotheses HH1.a–HH5.a, then

$$\zeta_{\text{FRI}}^* = -\frac{V_{\mathcal{Z}_a}^{\text{FRI}}(\theta_a^-)}{1 - (\delta_{\text{FRI}}(\theta_a^-))^2(\delta_{\text{FRI}}^{\text{FRI}})^2} \quad (11.31)$$

is an exponentially stable fixed point of (11.30) if, and only if,

$$0 < (\delta_{\text{FRI}}(\theta_a^-))^2(\delta_{\text{FRI}}^{\text{FRI}})^2 < 1 \quad (11.32)$$

and

$$\frac{(\delta_{\text{FRI}}^{\text{FRI}})^2 V_{\mathcal{Z}_a}^{\text{FRI}}(\theta_a^-)}{1 - (\delta_{\text{FRI}}(\theta_a^-))^2(\delta_{\text{FRI}}^{\text{FRI}})^2} + \bar{V}^{\max} < 0. \quad (11.33)$$

11.4 Simulations

The control law of Section 11.2 is evaluated here for the periodic motion depicted in the stick-diagram of Fig. 11.1. This trajectory includes only the fully actuated and double support phases, and has been designed using [69]. Polynomials of degree 4 were used. The trajectory was optimized for a robot *without feet*, namely RABBIT, and will be applied to a robot with massless feet and all other parameters the same as RABBIT. The feet are 28 cm long, and taking the toe as the origin, they have the following dimensions: $p_a^h = -20$ cm, $p_a^v = 8$ cm (ankle position) and $p_h^h = -28$ cm (heel position). Various desired evolutions of the FRI point will be imposed and sensitivity to modeling error will be assessed. *Recall that in the simulations reported here and in Section 11.6, a clockwise angular measurement convention is used so that forward motion corresponds to positive angular momentum.*

11.4.1 Nominal Controller

The evolution of the FRI position is chosen to be a linear function of θ_a . As θ_a varies from θ_a^+ to θ_a^- , $p_{\text{FRI}}^{h,d}(\theta_a)$ will vary from -0.23 m to -0.08 m. The control law imposes the virtual constraints $h_a(x_a) = 0$ and $p_{\text{FRI}}^h = p_{\text{FRI}}^{h,d}(\theta_a)$, all of which are determined by regression against the nominal periodic walking motion, as in Section 9.5. The zero dynamics that results from imposing these constraints on the system are described by θ_a , σ_{FRI} and (11.11a) and (11.11b). These equations along with the constraints describe completely the behavior of the system on the zero dynamics manifold.

The single support phase begins with $\theta_a = \theta_a^+ = -0.247$ rad and finishes with $\theta_a = \theta_a^- = 0.346$ rad, thus the behavior of the system can be described in

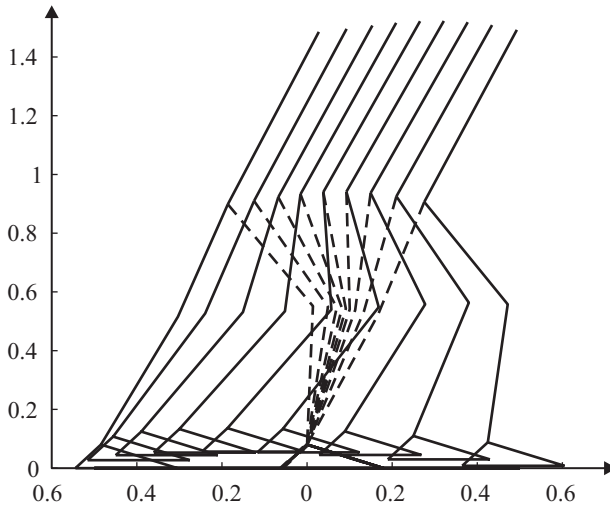


Figure 11.1. The stick diagram of the desired gait. The stance leg is dotted. Axes' units are meters.

a phase-plane plot of $(\theta_a; \sigma_{\text{FRI}})$, with θ_a initialized at θ_a^+ and different initial values for σ_{FRI} , as shown in Fig. 11.2. For sufficiently high initial values of σ_{FRI} , the robot completes a step. For sufficiently low initial values, in fact, for $\sigma_{\text{FRI}} < \sigma_{\text{FRI}}^m = \sqrt{2V^{\max}}$, the angular momentum σ_{FRI} crosses zero and the robot falls backward.

The evolution of $\delta_{\text{FRI}}^2(\theta_a)$ and $V_{Z_a}^{\text{FRI}}(\theta_a)$ are given in Fig. 11.3. Their final values, $V_{Z_a}^{\text{FRI}}(\theta_a^-) = -224.8$ and $\delta_{\text{FRI}}^2(\theta_a^-) = 1.0008$, are useful for constructing the Poincaré map presented in Fig. 11.4. The behavior of ζ_{FRI} during the impact is defined by $(\delta_{\text{FRI}}^{\text{FRI}})^2$, which is equal to 0.6914 for this example. The minimal value of ζ_{FRI}^- for which a step can be achieved is $\bar{V}^{\max}/(\delta_{\text{FRI}}^{\text{FRI}})^2 = 197.45$. The upper bound ζ_{FRI}^M corresponds to the value of ζ_{FRI}^- for which the normal of the ground reaction force vanishes.

The periodic motion occurs at the intersection of the Poincaré return map and the identity map, as given by (11.31). For this example, the fixed point occurs at $\zeta_{\text{FRI}}^* \approx 730$. The corresponding average walking speed is 0.945 m/s. The slope of the Poincaré return map ρ_a is $(\delta_{\text{FRI}}^{\text{FRI}})^2(\delta_{\text{FRI}}^{\text{FRI}})^2 = 0.692$, and because it is less than 1, the corresponding periodic walking motion is exponentially stable. The stability arises from the effect of the impact because $(\delta_{\text{FRI}}^{\text{FRI}})^2$ is close to 1.

A simulation was done for ten steps, assuming no modeling error and initializing the state of the robot off the periodic orbit, with an initial velocity 47% greater than its value on the periodic orbit; see Fig. 11.5. Convergence toward a periodic motion was obtained for each of the five joints of the robot. As an illustration, the evolution of the angle of the torso is depicted in Fig. 11.5(a).

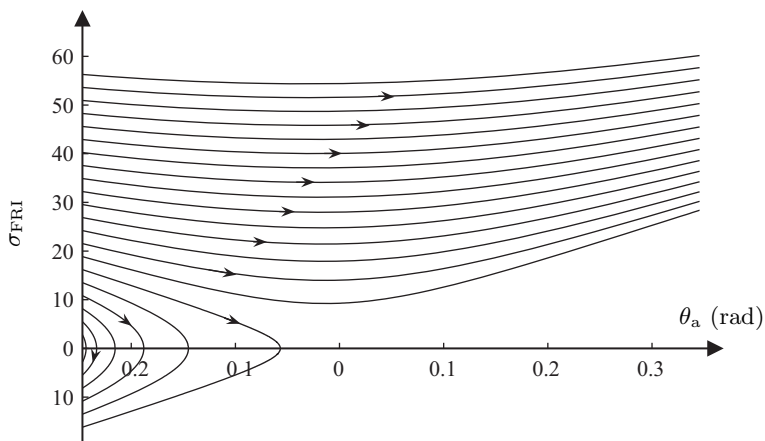


Figure 11.2. The phase plane for the zero dynamics of the nominal controller of Section 11.4.1. A clockwise angular measurement convention is being used, and consequently, when $\sigma_{\text{FRI}} < 0$, the robot is falling backward.

The same convergence is also evident in the evolution of the position of the FRI point with respect to time in Fig. 11.5(b); for each step, its evolution is linear from -0.23 m to -0.08 m , though the duration of the step varies: at the beginning, the steps are faster and then a periodic behavior is obtained asymptotically. Figure 11.5(c) presents the evolution of σ_{FRI} with respect to time; it clearly converges toward a periodic motion.

11.4.2 With Modeling Errors

In practice, the robot's parameters are not perfectly known. We assume here that there are mass errors of $+10\%$ in each of the thighs, $+30\%$ for the shins, and $+50\%$ for the torso. In addition, there is an error of $+30\%$ in the position of the center of mass of the torso. These errors have the following consequences:

- because the virtual constraints are designed with an incorrect model of the robot, the velocity after impact is not the expected value, and hence impact invariance is lost for the zero dynamics manifold;
- because the position of the FRI point is calculated on the basis of an incorrect dynamic model, the evolution of the FRI point will not be exactly as planned.

With the state of the robot initialized at the same value as in the previous example, the resulting behavior of the robot over 10 steps is presented in Fig. 11.6. Tracking errors were observed in the virtual constraints, most particularly at the beginning of each step, due to the effect of the impacts, but

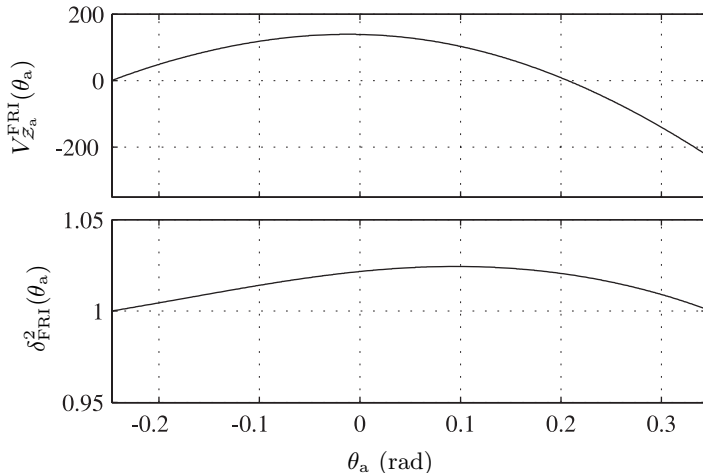


Figure 11.3. The evolution of ζ_{FRI} during the fully actuated phase, under the nominal controller of Section 11.4.1, s characterized by $V_{Z_a}^{\text{FRI}}(\theta_a)$ and $\delta_{\text{FRI}}^2(\theta_a)$. The position of the FRI point is being controlled to increase linearly, from back to front. Because the vertical component of the velocity of the center of mass is directed upward at the beginning of the step and then downward, $\delta_{\text{FRI}}(\theta_a)$ increases at the beginning of the step and then decreases.

the tracking errors in angular velocity were very nearly periodic. Convergence to an approximately periodic motion was observed, as depicted for the phase-plane evolution of the torso in Fig. 11.6(a). Convergence is also seen in the evolution of σ_{FRI} with respect to time in Fig. 11.6(c). The resulting periodic motion is not the nominal motion. Because the real robot is heavier than the model used for control design, the ground reaction forces are greater, and consequently, even though the actual evolution of the FRI point p_{FRI}^h shown in Fig. 11.6(b) is nearly linear, its upper and lower limits are smaller than on the nominal orbit. In this particular case, the change in the evolution of the FRI point does not cause a problem because the required constraints on the equilibrium of the supporting foot are always satisfied. On the other hand, if the real robot were lighter than the modeled robot, the FRI point could be outside the foot support region and the equilibrium constraints on the supporting foot could be violated. Hence, a safety margin is necessary when the minimum and the maximum values for $p_{\text{FRI}}^{h,d}(\theta_a)$ are defined.

11.4.3 Effect of FRI Evolution on the Walking Gait

The evolution of the FRI point throughout the step affects the existence and stability of the periodic motion obtained with the proposed control law. To illustrate this point, we consider various linear evolutions of the position of

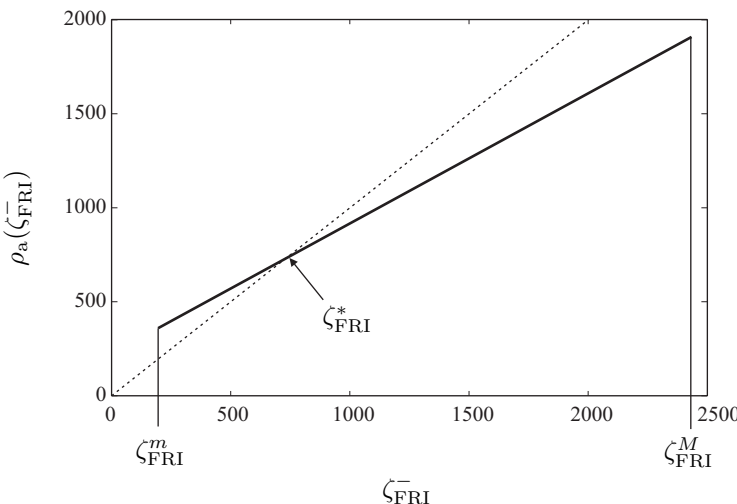


Figure 11.4. The Poincaré map of the hybrid zero dynamics for the gait of Fig. 11.1 when the nominal controller of Section 11.4.1 is applied.

the FRI point with different average values, $\frac{1}{2}(p_{\text{FRI}}^{\text{h,d}}(\theta_a^+) + p_{\text{FRI}}^{\text{h,d}}(\theta_a^-))$, while holding constant the net change in the position of the FRI point, $p_{\text{FRI}}^{\text{h,d}}(\theta_a^-) - p_{\text{FRI}}^{\text{h,d}}(\theta_a^+) = 15 \text{ cm}$.

Table 11.1 presents the main properties of the periodic motion and of the control law with respect to the variation of the average value of the FRI position during one step. Placing the average position of the FRI closer to the toe leads to larger values of δ_{FRI} and smaller values of ζ_{FRI}^* and average walking speed. When the center of mass is in front of the FRI point, the torque due to gravity speeds up the motion. When the center of mass is behind the FRI point, the torque due to gravity slows down the motion. When the average position of the FRI is moved forward, the portion of the step where gravity speeds up the motion decreases, and thus the average walking speed decreases.

In the last row of Table 11.1, the value of ζ_{FRI}^* is less than the minimum value necessary to complete a step (i.e., it does not satisfy (11.33)), and consequently a walking motion cannot be produced.

The choice of $p_{\text{FRI}}^{\text{h,d}}(\theta_a)$ does not affect the geometric (kinematic) behavior of the robot, but only its temporal evolution. For the geometric evolution depicted in Fig. 11.1, which, we recall, was designed for a robot without feet, the walking speed is 1.0 m/s. The same average walking speed can be achieved with various choices of $p_{\text{FRI}}^{\text{h,d}}(\theta_a)$ on the robot with feet.

Table 11.2, which is for constant walking speed, summarizes the main stability properties of the hybrid zero dynamics for various linear evolutions of $p_{\text{FRI}}^{\text{h,d}}(\theta_a)$, with increasing variation of $p_{\text{FRI}}^{\text{h,d}}(\theta_a)$. It is observed that the fixed

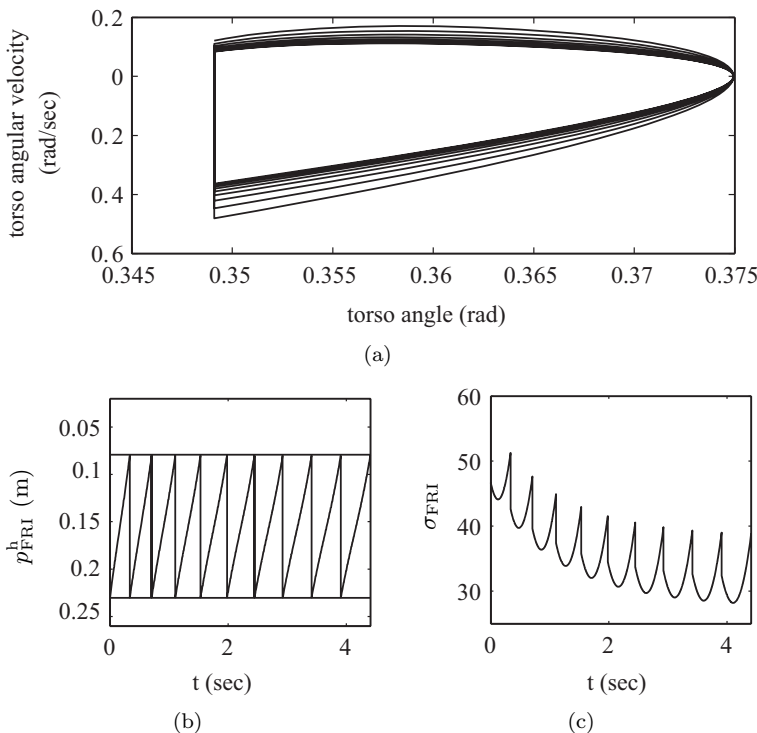


Figure 11.5. As predicted by the Poincaré map, the convergence to a periodic motion is observed in simulation with the nominal control law of Section 11.4.1 when there is no modeling error.

point ζ_{FRI}^* is not strongly affected by the presence of feet, and, in particular, it seems insensitive to variation in the evolution of the FRI point. The relative size of the basin of attraction is more sensitive to the evolution of the FRI point, with a larger excursion of p_{FRI}^h yielding a larger basin of attraction. The angular momentum about the ankle varies due to gravity, just as in an inverted pendulum. At the beginning of the step, the center of mass is behind the ankle and the torque due to gravity decreases the magnitude of the angular momentum, slowing down the robot. In the later part of the step, the center of mass is in front of the ankle and the torque due to gravity increases the magnitude of the angular momentum, accelerating the robot. The vertical component of the ground reaction force is directed upward throughout the step. Its horizontal component is directed backward at the beginning of single support and forward at the end. Thus, if the FRI point is behind the ankle at the beginning of step and in front of the ankle at the end, the ankle torque u_A is opposite to the torque due to gravity. Consequently, the angular momentum has less variation throughout the step. This particularity appears

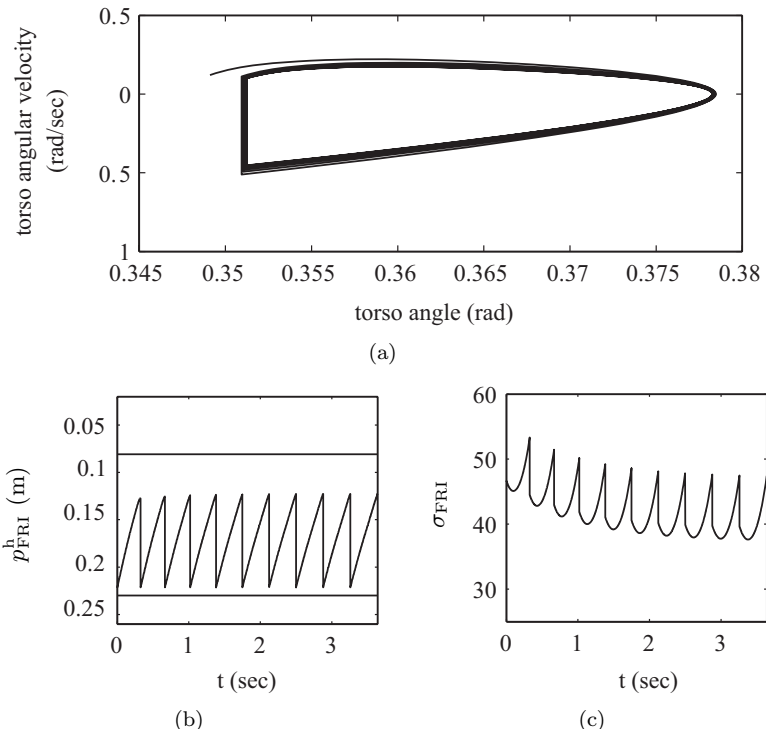


Figure 11.6. The convergence to a (nearly) periodic motion is still observed in simulation with the nominal control law of Section 11.4.1 when there is modeling error.

to widen the basin of attraction.

When the evolution of the FRI point is linear, it has almost no effect on the stability of the fixed point because $\delta_{\text{FRI}}^2(\theta_a^-)$ is close to 1 (see Fig. 11.7(a)). It seems attractive to decrease this term by choosing a parabolic evolution of the FRI point

$$p_{\text{FRI}}^{h,d}(\theta_a) = p_{\text{FRI}}^{h,\min} + 4(p_{\text{FRI}}^{h,\max} - p_{\text{FRI}}^{h,\min}) \left(\theta_a - \frac{\theta_a^- + \theta_a^+}{2} \right)^2 \quad (11.34)$$

in order that a backward motion of the FRI point occurs for an upward evolution of the center of mass, and vice-versa. The evolution of $p_{\text{FRI}}^{h,d}(\theta_a)$ and of $\delta_{\text{FRI}}^2(\theta_a)$ are presented in Fig. 11.7(b) for such a case. The value $\delta_{\text{FRI}}^2(\theta_a^-)$ does decrease, but because the position of the FRI point changes in the forward direction just after impact, the value $\delta_{\text{FRI}}^{\text{FRI}}$ increases, with the net result that their product is nearly constant. Another method to decrease $\delta_{\text{FRI}}^2(\theta_a^-)$ without changing the initial or final positions of the FRI point is proposed in Fig. 11.7(c). The forward motion of the FRI position linearly

Table 11.1. Effect of $p_{\text{FRI}}^{\text{h,d}}(\theta_a)$ on the walking motion, for a similar kinematic evolution of the robot. The evolution of the FRI point is linear with respect to θ_a , the amplitude of the displacement of the FRI point is 15 cm, and its average position varies. This change dramatically affects the average walking speed of the robot.

| $\frac{p_{\text{FRI}}^{\text{h,d}}(\theta_a^+) + p_{\text{FRI}}^{\text{h,d}}(\theta_a^-)}{2}$ | Periodic Motion | | | |
|---|-----------------|------------------------|---------------------------|--|
| | speed | ζ_{FRI}^* | $(\delta_{\text{FRI}})^2$ | $(\delta_{\text{FRI}}^{\text{FRI}})^2$ |
| -17.5 cm | 1.185 m/s | 1042 | 1.001 | 0.676 |
| -16.5 cm | 1.076 m/s | 890 | 1.0009 | 0.683 |
| -15.5 cm | 0.945 m/s | 730 | 1.0008 | 0.691 |
| -14.5 cm | 0.781 m/s | 561 | 1.0007 | 0.700 |
| -13.5 cm | 0.545 m/s | 384 | 1.0006 | 0.708 |
| -12.5 cm | | 196 | 1.0005 | 0.716 |

| $\frac{p_{\text{FRI}}^{\text{h,d}}(\theta_a^+) + p_{\text{FRI}}^{\text{h,d}}(\theta_a^-)}{2}$ | Basin of Attraction | | | |
|---|------------------------|--|------------------------|--|
| | ζ_{FRI}^m | $\frac{\zeta_{\text{FRI}}^* - \zeta_{\text{FRI}}^m}{\zeta_{\text{FRI}}^*}$ | ζ_{FRI}^M | $\frac{\zeta_{\text{FRI}}^M - \zeta_{\text{FRI}}^*}{\zeta_{\text{FRI}}^*}$ |
| -17.5 cm | 143 | 86 % | 2365 | 127 % |
| -16.5 cm | 169 | 81 % | 2383 | 168 % |
| -15.5 cm | 197 | 73 % | 2438 | 234 % |
| -14.5 cm | 227 | 59 % | 2456 | 338 % |
| -13.5 cm | 258 | 32 % | 2474 | 544 % |
| -12.5 cm | no periodic motion | | | |

increases in the last portion of the step, when the velocity of the center of mass is directed downward, but in the initial part of the step, the FRI point is held constant.

11.5 A Variation on FRI Position Control

Instead of controlling the exact position of the FRI point throughout a step, it is possible to use the ankle torque to fulfill other control objectives while maintaining the FRI point in a desired region, $(p_{\text{FRI}}^{\text{h min}}, p_{\text{FRI}}^{\text{h max}})$. As an example, consider the control law of Section 10.4.3, which was designed to increase

Table 11.2. Effect of $p_{\text{FRI}}^{\text{h,d}}(\theta_a)$ on the stability properties of the hybrid zero dynamics for the same geometric evolution of the robot and the same average walking speed. The first line corresponds to the robot without feet, the five following lines correspond to different choices of $p_{\text{FRI}}^{\text{h,d}}(\theta_a)$ for the robot with feet.

| $\frac{p_{\text{FRI}}^{\text{h,d}}(\theta_a^+) + p_{\text{FRI}}^{\text{h,d}}(\theta_a^-)}{2}$ | $p_{\text{FRI}}^{\text{h,d}}(\theta_a^-) - p_{\text{FRI}}^{\text{h,d}}(\theta_a^+)$ | Periodic Motion | | |
|---|---|------------------------|---------------------------|--|
| | | ζ_{FRI}^* | $(\delta_{\text{FRI}})^2$ | $(\delta_{\text{FRI}}^{\text{FRI}})^2$ |
| -20.79 cm | 0 cm | 1473 | 1 | 0.63 |
| -20.3 cm | 5 cm | 1416 | 1.0005 | 0.64 |
| -19.82 cm | 10 cm | 1361 | 1.0009 | 0.65 |
| -19.35 cm | 15 cm | 1307 | 1.0012 | 0.66 |
| -18.9 cm | 20 cm | 1255 | 1.0015 | 0.67 |

| $\frac{p_{\text{FRI}}^{\text{h,d}}(\theta_a^+) + p_{\text{FRI}}^{\text{h,d}}(\theta_a^-)}{2}$ | Basin of Attraction | | | |
|---|------------------------|--|------------------------|--|
| | ζ_{FRI}^m | $\frac{\zeta_{\text{FRI}}^* - \zeta_{\text{FRI}}^m}{\zeta_{\text{FRI}}^*}$ | ζ_{FRI}^M | $\frac{\zeta_{\text{FRI}}^M - \zeta_{\text{FRI}}^*}{\zeta_{\text{FRI}}^*}$ |
| -20.79 cm | 204 | 86 % | 2493 | 69 % |
| -20.3 cm | 167 | 88 % | 2436 | 72 % |
| -19.82 cm | 132 | 90 % | 2380 | 73 % |
| -19.35 cm | 99 | 92 % | 2280 | 74 % |
| -18.9 cm | 68 | 94 % | 2235 | 78 % |

the rate of convergence to a periodic walking motion. In place of (10.74), let

$$u_A = -\kappa_{2a}(\theta_a) + \kappa_{1a}(\theta_a) \left(\chi(\theta_a, \zeta_a) + \frac{d\zeta_a^*(\theta_a)}{d\theta_a} \right), \quad (11.35)$$

where σ_a is the angular momentum about the ankle in the fully actuated phase, $\sigma_a^*(\theta_a)$ is the value of the angular momentum about the ankle on the periodic orbit, $\zeta_a = \sigma_a^2/2$, $\zeta_a^*(\theta_a) = (\sigma_a^*(\theta_a))^2/2$ and $\chi(\theta_a, \zeta_a)$ is to be determined. Note that with this choice of u_A , (10.77b) becomes

$$\frac{d(\zeta_a - \zeta_a^*(\theta_a))}{d\theta_a} = \chi(\theta_a, \zeta_a), \quad (11.36)$$

and hence with appropriate choice of $\chi(\theta_a, \zeta_a)$, the error $\zeta_a - \zeta_a^*(\theta_a)$ will tend to zero, yielding convergence to the periodic orbit.

Based on (11.4) and (11.35), χ can be related to the FRI position by an expression of the form

$$\chi(\theta_a, \zeta_a) = \frac{\gamma_3(\theta_a, \zeta_a) + \gamma_4(\theta_a, \zeta_a)p_{\text{FRI}}^{\text{h}}}{\gamma_5(\theta_a) + \gamma_6(\theta_a)p_{\text{FRI}}^{\text{h}}}, \quad (11.37)$$

from which it is possible to compute upper and lower bounds on $\chi(\theta_a, \zeta_a)$ so that $p_{\text{FRI}}^h \in (p_{\text{FRI}}^{h \min}, p_{\text{FRI}}^{h \max})$. Denote these bounds by $\chi(\theta_a, \zeta_a)^{\min}$ and $\chi(\theta_a, \zeta_a)^{\max}$, respectively. A *linear controller with saturation* would then be an obvious candidate to speed up convergence to the periodic orbit while maintaining the FRI point in a safe region to avoid foot rotation:

$$\chi(\theta_a, \zeta_a) := \begin{cases} \chi(\theta_a, \zeta_a)^{\max} & \text{if } K_z(\zeta_a - \zeta_a^*(\theta_a)) \geq \chi(\theta_a, \zeta_a)^{\max} \\ \chi(\theta_a, \zeta_a)^{\min} & \text{if } K_z(\zeta_a - \zeta_a^*(\theta_a)) \leq \chi(\theta_a, \zeta_a)^{\min} \\ K_z(\zeta_a - \zeta_a^*(\theta_a)) & \text{otherwise,} \end{cases} \quad (11.38)$$

though many other controllers suggest themselves as well.

11.6 Simulations

The ankle control law defined by (11.35) and (11.38) was evaluated on the reference trajectory described in Section 11.4.1. The desired evolution of $\sigma_a^*(\theta_a)$ is selected to be the periodic motion arising from the ankle control strategy (11.8), with $p_{\text{FRI}}^{h,d}(\theta_a) = -23 + 15 \frac{\theta_a - \theta_a^+}{\theta_a^- - \theta_a^+}$ measured in units of centimeters. In (11.38), the upper and lower bounds on the FRI point are taken as $p_{\text{FRI}}^{h \min} = -26$ cm and $p_{\text{FRI}}^{h \max} = -2$ cm.

The evolution of the zero dynamics is shown in Fig. 11.8, in terms of the variables $(\theta_a; \dot{\theta}_a)$, for $K_z = 4$. For initial angular velocities varying from 0.7 to 3.2 rad/sec, the final angular velocity is close to the desired periodic velocity, which explains the relatively flat portion of the Poincaré map in Fig. 11.9. The basin of attraction is larger (for lower velocities) than for the first control law, as can be seen in Fig. 11.9.

The action of the control strategy is more fully illustrated through the evolution of p_{FRI}^h for various initial velocities $\dot{\theta}_a$ in Fig. 11.10. When the actual motion of the biped is slower than the nominal motion, the position of the FRI is moved backward to accelerate the motion until the limit $p_{\text{FRI}}^{h \min}$ is reached. When the actual motion of the biped is faster than the nominal motion, the position of the FRI is moved forward to decelerate the motion until the limit $p_{\text{FRI}}^{h \max}$ is reached.

The Poincaré return map corresponding to the second control law is presented in the Fig. 11.9, along with the Poincaré return map of the first control law. The second controller was designed to have the same fixed point as the first controller. The differences in the performance of the two controllers are clear: when the initial velocity is far from the fixed point, the constraint on p_{FRI}^h limits the rate of convergence to the orbit so that it is compatible with keeping the foot flat on the ground, and when the initial velocity is near the fixed point, the saturated, high-gain linear control action enhances the convergence rate.

Assuming no modeling error and initializing the state of the robot off the periodic orbit (with an initial velocity 47% higher than the periodic value), the results of 10 walking steps of the robot are depicted in Fig. 11.11. The convergence toward a periodic motion is observed, as shown for the trunk via a phase plot in Fig. 11.11(a). The periodic motion is almost reached in two steps. This convergence is also illustrated via the evolution of the position of the FRI point with respect to time in Fig. 11.11(b). To decelerate the motion over the first step, the position of the FRI stays on the front limit $p_{\text{FRI}}^{\text{h max}}$. For the ensuing steps, its evolution is linear from -0.23 m to -0.08 m , with a behavior corresponding to the nominal periodic trajectory. Figure 11.11(c) presents the evolution of $\dot{\theta}_a$ with respect to θ_a ; it clearly converges to a periodic motion.

In order to illustrate some robustness properties of this control law, the same modeling errors as in Section 11.4.2 are used. A simulation of 10 walking steps is presented in Fig. 11.12. The biped's initial state is chosen to be 47% higher than the fixed point. The convergence toward a periodic motion is illustrated via a phase-plane plot of the torso in Fig. 11.12(a); errors can be observed at the impact times. Convergence toward a periodic motion is also shown in Fig. 11.12(b) via the evolution of the FRI point with respect to time. The evolution of the FRI point is different than its nominal evolution even though $\dot{\theta}_a$ nearly converges to the nominal motion by the end of the second step, as shown in Fig. 11.12(c). In the presence of modeling error, the terms $\chi(\theta_a, \zeta_a)^{\text{min}}$ and $\chi(\theta_a, \zeta_a)^{\text{max}}$ do not correspond exactly to $p_{\text{FRI}}^{\text{h min}} = p_{\text{FRI}}^{\text{h min}}$ and $p_{\text{FRI}}^{\text{h max}} = p_{\text{FRI}}^{\text{h max}}$, thus a safety margin must be taken into account to ensure that the foot does not rotate: the values of $p_{\text{FRI}}^{\text{h min}}$ and $p_{\text{FRI}}^{\text{h max}}$ must be strictly within the convex hull of the foot support region.

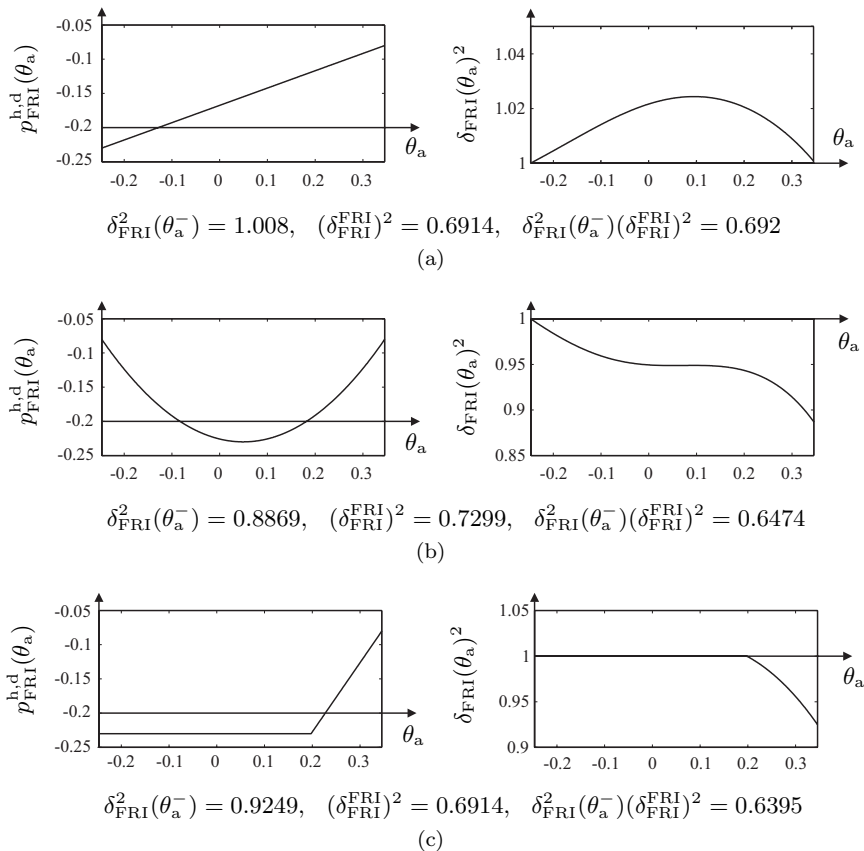


Figure 11.7. The evolution of $p_{\text{FRI}}^{\text{h},\text{d}}(\theta_a)$ can be chosen in order to decrease the value $\delta_{\text{FRI}}(\theta_a^-)$ and to increase the convergence rate. In the first case (top pair), a linear evolution is considered as reference. In the second case (middle pair), a parabolic evolution is chosen, and it is observed that even though $\delta_{\text{FRI}}(\theta_a^-)$ decreases, because $\delta_{\text{FRI}}^{\text{FRI}}$ increases, their product is only slightly decreased. The movement of the FRI point at the beginning of the step, from the toe toward the heel, seems unnatural and inefficient because $\delta_{\text{FRI}}^{\text{FRI}}$ increases. This unnatural evolution of the FRI point is avoided in the third case (bottom pair); the initial and final values of $p_{\text{FRI}}^{\text{h},\text{d}}(\theta_a)$ are designed to be the same as in the first case, in order to have the same value for $\delta_{\text{FRI}}^{\text{FRI}}$. The chosen piecewise-linear evolution for $p_{\text{FRI}}^{\text{h},\text{d}}(\theta_a)$ does improve the convergence rate.

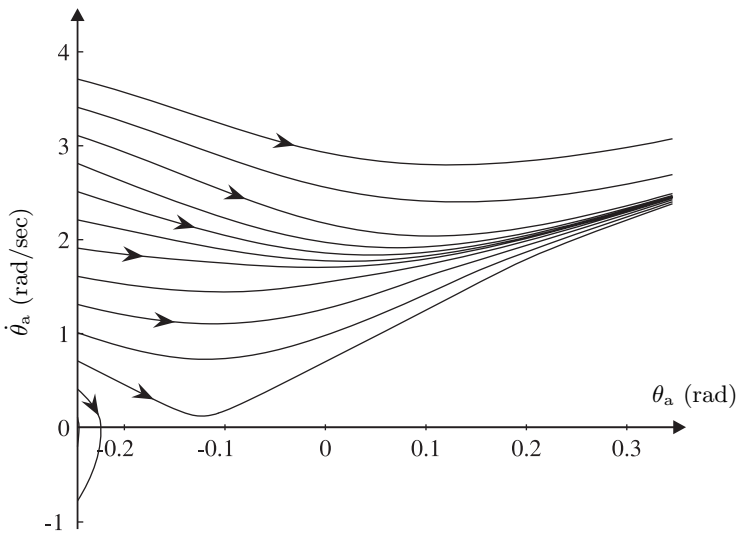


Figure 11.8. Evolution of the zero dynamics in its phase plane $(\theta_a; \dot{\theta}_a)$, for the control law (11.35)–(11.38). When $\dot{\theta}_a < 0$, the robot is falling backward.

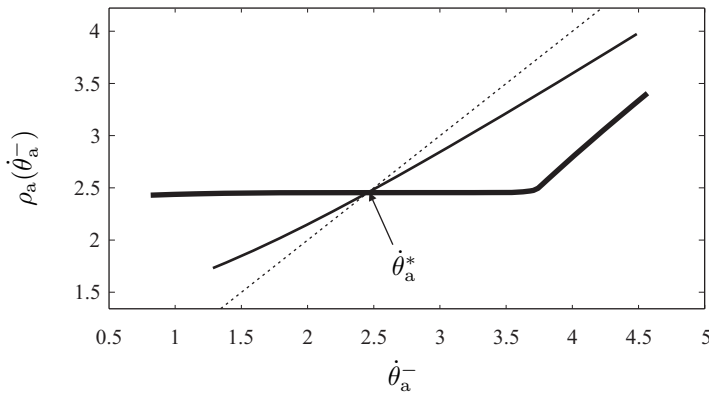


Figure 11.9. Comparison of the Poincaré maps for the two ankle control laws of this chapter, presented in terms of $\dot{\theta}_a$. The first control law induces a uniform forward progression of the FRI point (the Poincaré map is indicated with a normal-weight line). The second control law actively varies the FRI point in order to increase convergence rate, subject to the FRI point remaining within predetermined bounds that guarantee nonrotation of the stance foot (the Poincaré map is indicated with a bold line). The identity map is indicated with a dashed line. Units are rad/sec.

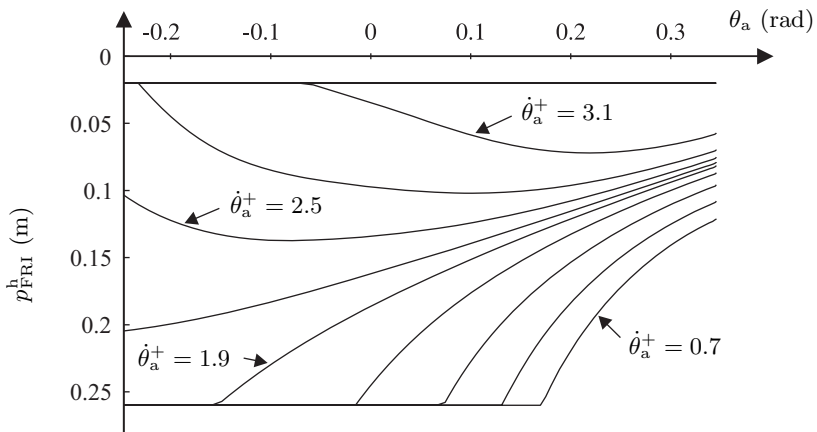


Figure 11.10. The evolution of the position of the FRI point for various initial velocities $\dot{\theta}_a$ measured in rad/sec.

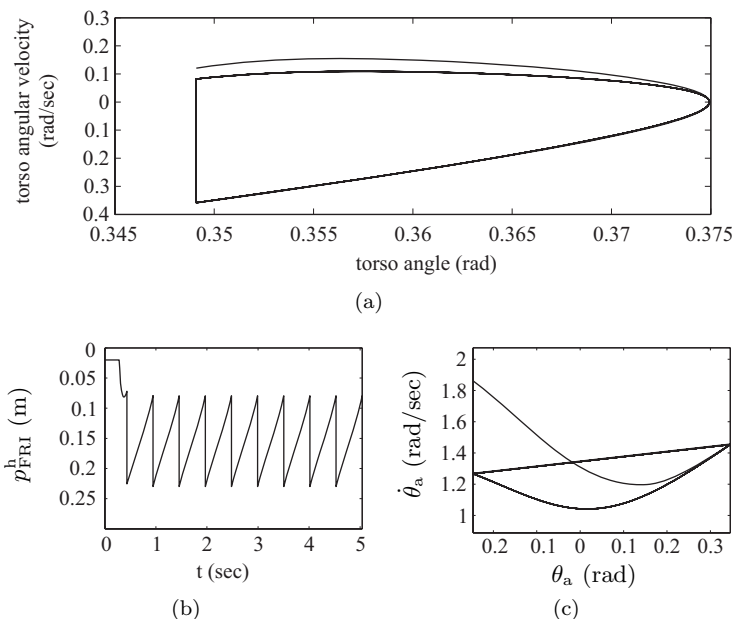


Figure 11.11. As predicted by the Poincaré map, the convergence to a periodic motion is observed in simulation with the second control law, without modeling error.

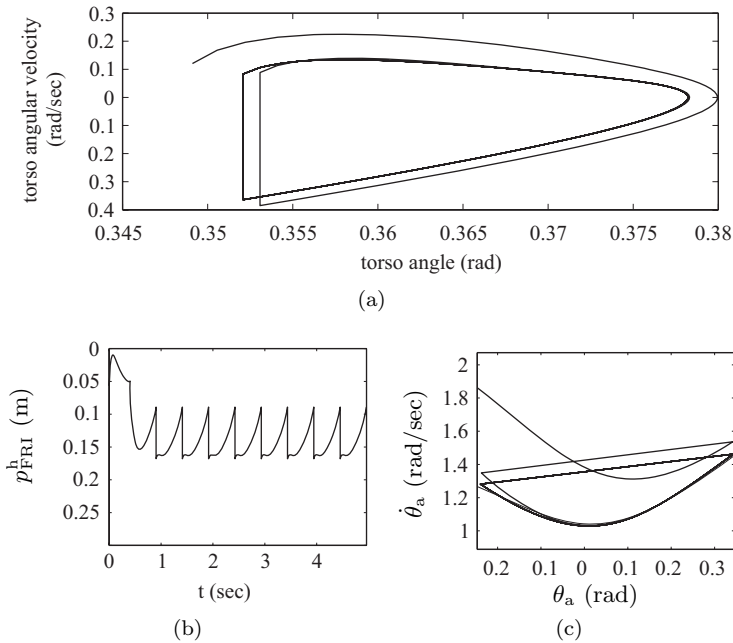


Figure 11.12. The convergence toward a periodic motion is still observed in simulation with the second control law, with modeling error.

A

Getting Started

For those readers who do not wish to read the book from cover to cover, this appendix summarizes two possible routes through the material. In the first case, it is assumed that the reader is a graduate student and the objective is to master the essentials of [Chapter 3](#) through [Chapter 6](#), with the presumption that once this material is assimilated, the remaining chapters should not be overly difficult. This program is based on our experience in teaching this material. In the second case, the reader is assumed to be a professional researcher and the objective is to ascertain if the methods of this book have anything to offer an *existing* biped project. Here, we can only suggest what we would try if we were brought into the project. Our suggestions are untested and may be naive.

A.1 Graduate Student

A detailed program is provided for working through the first half of the book. The initial steps are quite detailed in order to assure success. Subsequent steps demand progressively more initiative from the student. The philosophy is to work through the book with an example at hand because most of the notions are more manageable when reduced to special cases.

1. There are two rather simple models treated in the text.
 - (a) A two-link walker (a.k.a. the Acrobot or the compass biped) is given in Section 3.4.6.1. This robot has two legs without knees or feet. The legs are connected at a point called a hip. The robot does not have a torso. There is one actuator to control the angle between the two legs.
 - (b) A three-link walker is given in Section 3.4.6.2. This robot is the two-link walker with the addition of a torso attached at the hip. Two actuators are used to control the relative angles between the torso and each leg. Because the position of the COM can be varied by changing the lean angle of the torso, it is easier to vary the walking speed of this robot than the two-link robot. Because the robot

has two actuators, it is more representative of the multivariable feedback control designs used for more general robots.

- (c) It will be assumed in the following that the reader uses the three-link walker for all of the examples. However, whenever a particular step presents difficulties, it is suggested to return to the two-link robot and work out the difficulties there before returning to the three-link robot. Numerous graduate students have succeeded in getting the three-link robot to walk, using the parameter values and controllers suggested in the book. When things don't work, the first place to look is your own code!
2. As needed, review Lagrange's method for obtaining the equations of motion for a planar mechanical system comprised of rigid links and revolute joints; see [Appendix B.4](#).
 3. Use Lagrange's method to derive the equations of motion of the three-link robot in single support. First use the absolute coordinates of [Fig. 3.5-\(a\)](#). Then derive the equations of motion in the coordinates of Fig. 3.5-(b), using first the method of Lagrange, and then, starting with the model in the coordinates of Fig. 3.5-(a), re-derive the dynamic model using the coordinate transformations given in (3.72) and (3.73). While all of this can be done by hand, it will be very tedious. It is suggested to use a symbolic manipulation package. This becomes more crucial at each successive step of working one's way through the book.
 4. Derive the impact model. Initially, it is enough to do this in the coordinates of Fig. 3.5-(a). Before including leg swapping, set the parameter values as in [Table 3.2](#) and verify that when

$$\begin{bmatrix} \theta_1 \\ \theta_2 \\ \theta_3 \end{bmatrix} = \begin{bmatrix} \pi/8 \\ -\pi/8 \\ \pi/6 \end{bmatrix},$$

the impact model transforms the velocity vector as follows

$$\begin{bmatrix} \dot{\theta}_1 \\ \dot{\theta}_2 \\ \dot{\theta}_3 \end{bmatrix} = \begin{bmatrix} 1.5 \\ -1.5 \\ 0 \end{bmatrix} \rightarrow \begin{bmatrix} -0.258 \\ 0.878 \\ 1.905 \end{bmatrix}.$$

After leg swapping has been included in the impact model, verify that

$$\begin{bmatrix} \theta_1 \\ \theta_2 \\ \theta_3 \end{bmatrix} = \begin{bmatrix} \pi/8 \\ -\pi/8 \\ \pi/6 \end{bmatrix} \rightarrow \begin{bmatrix} -\pi/8 \\ \pi/8 \\ \pi/6 \end{bmatrix},$$

and

$$\begin{bmatrix} \dot{\theta}_1 \\ \dot{\theta}_2 \\ \dot{\theta}_3 \end{bmatrix} = \begin{bmatrix} -0.258 \\ 0.878 \\ 1.905 \end{bmatrix} \rightarrow \begin{bmatrix} 0.878 \\ -0.258 \\ 1.905 \end{bmatrix}.$$

This will provide confidence that the impact model has been correctly computed.

5. It is now important to simulate the hybrid model, (3.30). This is most easily done when the system is under closed-loop control. With this in mind, read Section 6.6.1. Before doing anything, it is important to understand the issue of leg scuffing in walking models without knees; refer, as necessary, to the literature in order to become comfortable with this issue. The impact or switching surface is defined in (6.88) and a simple feedback law is presented in (6.90) and (6.101). Note that the necessary background in order to understand the Lie derivative notation is given in [Appendix B](#); see in particular [Definition B.7](#) and the definition of the decoupling matrix in (B.70). Applying the feedback (6.90) with the suggested parameter values and with the initial conditions

$$\begin{bmatrix} \theta_1 \\ \theta_2 \\ \theta_3 \end{bmatrix} = \begin{bmatrix} \pi/8 \\ -\pi/8 \\ \pi/6 \end{bmatrix} \quad \text{and} \quad \begin{bmatrix} \dot{\theta}_1 \\ \dot{\theta}_2 \\ \dot{\theta}_3 \end{bmatrix} = \begin{bmatrix} 1.60 \\ -1.60 \\ 0 \end{bmatrix} \quad (\text{end of step}),$$

or, equivalently,

$$\begin{bmatrix} \theta_1 \\ \theta_2 \\ \theta_3 \end{bmatrix} = \begin{bmatrix} -\pi/8 \\ \pi/8 \\ \pi/6 \end{bmatrix} \quad \text{and} \quad \begin{bmatrix} \dot{\theta}_1 \\ \dot{\theta}_2 \\ \dot{\theta}_3 \end{bmatrix} = \begin{bmatrix} 0.94 \\ -0.28 \\ 2.04 \end{bmatrix} \quad (\text{start of step})$$

will quickly converge to a periodic solution. It is a good idea to do a stick figure animation of the motion in addition to looking at angular position and velocity traces. Using trial and error, explore the basin of attraction of the controller. Compute the contact forces at the stance foot during the swing phase and compute the impulsive forces at impact.

6. Optional (easy): Apply an input-output linearizing controller as in (5.96) and repeat the above. Explore the effects of varying the proportional and derivative gains.
7. Return to [Chapter 3](#) and read Section 3.1 through Section 3.4.6. Scan the informal treatment of the method of Poincaré return maps given in [Appendix B.3](#). With this as background, read Sections 4.1, 4.2, and 4.4. Apply Theorem 4.4 to the three-link model in closed loop with the feedback (6.101). Verify that the fixed point of the restricted Poincaré map correctly identifies the periodic orbit.

8. Optional (challenging): Apply Corollary 4.1 to the three-link robot model in closed loop with an input-output linearizing controller. It will be necessary to numerically evaluate the Poincaré first return map, $P : \mathcal{S} \rightarrow \mathcal{S}$. More precisely, using symmetric differences, estimate the Jacobian of the Poincaré map and compute its eigenvalues. It may be wise to gain experience on the two-link model walking on a shallow slope and with the control set to zero. Armed with this experience, estimating the Jacobian of the Poincaré map for the three-link walker will be easier. In order to apply Corollary 4.1, it is easier to “estimate” the Jacobian as a 6×6 matrix instead of a 5×5 matrix; see [173] in order to understand this better and for help on interpreting the results. In the above, you have probably taken advantage of the fact that you already knew the fixed point of the Poincaré map. If so, try to find the fixed point using the Poincaré map and without using your a priori knowledge of the fixed point; hints on how to do this are available in the literature. Based on analyzing the Jacobian of the Poincaré map, find a value of ϵ in (5.96) for which the closed-loop system no longer has a stable periodic orbit.
9. It is now time to move on to the hybrid zero dynamics. Read [Chapter 5](#), with referral as necessary to [Appendix B.2](#). Be sure to work out the details of the examples in Sections 5.1.1 and 5.1.2. Then read Section 6.4, which presents results on the hybrid zero dynamics when the output is specialized to a simplified form. The next objective is to obtain for the three-link robot an output in the form (6.60) that will satisfy all of the hypotheses of Theorem 5.1. This will be accomplished using Theorem 6.2. Implement a feedback controller based on the outputs given in (6.108) and the optimized parameter values given in [Table 6.2](#). You will notice that less torque is required. Run the simulation long enough so that the periodic orbit is well identified. Over the periodic orbit, record the configuration variables, θ_1 , θ_2 , and θ_3 , and the torques u_1 and u_2 . Referring to [Fig. 3.5](#) and (3.73), determine q_1 and q_2 on the orbit and plot them versus θ_1 . For each of q_1 and q_2 , regress a seventh-degree polynomial $h_{d,i}(\theta_1)$ against θ_1 so that on the periodic orbit, $q_1 - h_{d,1}(\theta_1) \equiv 0$ and $q_2 - h_{d,2}(\theta_1) \equiv 0$. To the extent that your regression “accurately” represents the functional dependence of q_1 and q_2 on θ_1 along the periodic orbit, Theorem 6.2 guarantees that the output

$$y_1 = q_1 - h_{d,1}(\theta_1) \tag{A.1a}$$

$$y_2 = q_2 - h_{d,2}(\theta_1) \tag{A.1b}$$

will yield a hybrid zero dynamics. Note that in the θ -coordinates, the output is

$$y_1 = \theta_1 - \theta_3 + \pi - h_{d,1}(\theta_1) \tag{A.2a}$$

$$y_2 = \theta_2 - \theta_3 + \pi - h_{d,2}(\theta_1). \tag{A.2b}$$

Compute the swing phase zero dynamics, following either the procedure suggested in Section 5.2 or Section 6.4 (you may find this easier to do in the coordinates of [Fig. 3.5-\(b\)](#)). Then determine δ_{zero} per (5.67) or (6.81), or directly from the periodic orbit using (6.84) (see the proof of [Theorem 6.2](#)). The functions κ_1 and κ_2 in (5.47) will appear very complicated when computed symbolically; it is suggested to plot them versus θ_1 to understand better their structure. It is important to observe that the swing phase zero dynamics can be computed without inverting the inertia matrix or the decoupling matrix.

10. Once the hybrid zero dynamics has been determined, compute its solutions via simulation and map them onto solutions of the full-dimensional model via $q_i = h_{d,i}(\theta_1)$, $\dot{q}_i = \frac{dh_{d,i}(\theta_1)}{d\theta_1}\dot{\theta}_1$, for $i = 1, 2$ and $u = u^*$ in (5.35). If the regression was done well, on the periodic orbit, u^* should be (nearly) equal to the torque that you recorded in Step 9, based on the outputs given in (6.108). Determine the Poincaré map of the hybrid zero dynamics and compare it to the result obtained by applying [Theorem 4.4](#), just as you did in Step 7; because the zero dynamics model is invariant for the closed-loop system, it will not matter whether you are applying a feedback of the form (5.95) or (5.96). Compute the equivalent of [Fig. 6.7](#). Verify [Theorem 5.5](#) through a simulation study.
11. The exercises so far have provided you with some facility in computing the hybrid zero dynamics and in interpreting what the various terms mean. Fundamentally, up to this point, however, your ability to control the robot has not been advanced through the use of the hybrid zero dynamics. The objective of the next two steps is to understand the power of this approach.
12. Consider again the outputs given in (6.108), but this time, do not plug in the parameters of [Table 6.2](#). Instead, compute a feedback controller of the form (5.95) or (5.96) as a function of the parameters in the output (6.108). Set up a cost function similar to (6.43) and use a parameter optimization algorithm to minimize the cost function along a periodic orbit of the closed-loop system, subject to the robot walking no slower than it does with the optimized parameters of Table 6.2. Note that you will be obliged to compute solutions using the full-(six)-dimensional model. Note also that for each new value of the parameters, finding a periodic orbit is time consuming. Initialize your search from the “original values” given in Table 6.2. Be prepared for a lot of frustration.
13. This time, apply the approach of Sections 6.1–6.3. Follow the example in Section 6.6.2. It is suggested to initialize the coefficients of the Bézier polynomials so that the output “approximates” (6.90) away from the endpoints of the step. This time you will be computing solutions with a

two-dimensional model. In addition, for a given parameter value, determining if a periodic orbit exists is very straightforward; see [Theorem 5.3](#). This completes the introduction to [Chapters 4–6](#).

14. (Optional) Design an event-based controller that uses the torso lean angle to regulate the walking speed.
-

A.2 Professional Researcher

It is assumed that the reader has a *planar* bipedal robot on which he wishes to evaluate the methods of this book. It will be assumed initially that the robot does not have feet; comments on the case of robots with feet will be made toward the end of the section. Two general cases will be considered:

1. The reader has already a controller that induces an acceptable stable, periodic walking gait. The objective is therefore to improve the efficiency or robustness of the gait.
2. The reader does not have a controller that induces a walking gait. The design of a controller must therefore start from scratch.

In order to guarantee that the methods of the book will produce a feedback controller resulting in a stable walking gait for a robot without feet, the robot needs to satisfy hypotheses HR1–HR5 of Section 3.2. The desired gait of the robot needs to satisfy HGW1–HGW7 of Section 3.2. For a robot with feet, the hypotheses are given in [Chapters 10](#) and [11](#). A key assumption in each case is that the double support phase is essentially instantaneous. To have an idea of just how closely all of these conditions must be met in practice, read about the bipedal robots RABBIT and ERNIE in [Chapters 2](#) and [8](#).

A.2.1 Reader Already Has a Stabilizing Controller

The objective here is to take advantage of the fact that a stable walking gait is already available in order to short cut the design process of the virtual constraints. Indeed, the initial controller will not be determined analytically, as in Sections 6.1–6.3. Instead, an existing walking motion of the robot will be used to generate numerically a set of virtual constraints that will be used for feedback control, as in Section 6.5, similar to the first example of Section 6.6.3.2. This short cut will permit the reader to experiment with the methods of this book with the least amount of initial effort.

1. Read Sections 1.4, 5.1.2, and 6.6.1 in order to learn about the concept of *virtual constraints* and how the notion of using feedback to impose

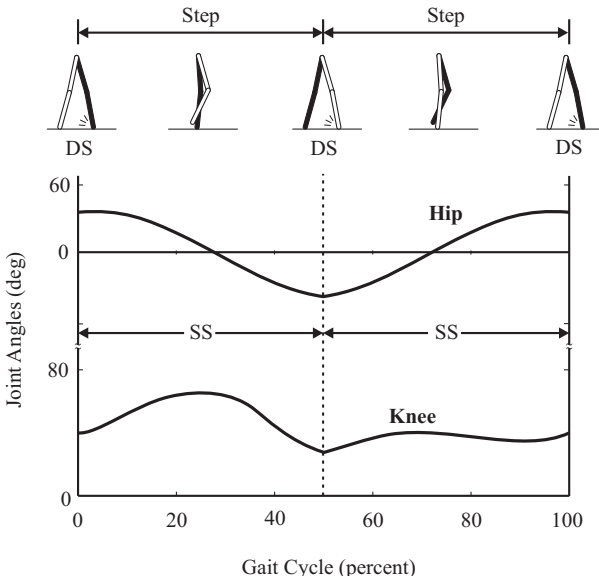


Figure A.1. Joint angles for a four-link walker over a complete gait cycle, that is, two steps. The gait cycle consists of two phases each of double support (DS) and single support (SS). Depicted are the relative hip angle and the knee angle of the leg drawn in white. The first single support phase can be thought of as a graph of (A.3) for the relative angles of the hip and knee during the swing phase, and the second single support phase is a graph of (A.3) for the relative angles of the hip and knee during the stance phase. The angle θ in (A.3) can be taken as the angle of the hip with respect to the ground contact point of the stance leg.

virtual constraints leads to the design of feedback controllers for stable walking gaits. The underlying idea is that any attempt to describe walking, even something as simple as the difference between human-like walking (knees bent forward) and bird-like walking (knees bent backward), inevitably leads to a description of the *posture* or *shape* of the robot over a step. In other words, a description of walking involves at least a partial specification of the path followed in the configuration space of the biped; see Fig. A.1. To express this mathematically, let $q_b = (q_1; \dots; q_{N-1})$ be a set of *body* coordinates for the robot and let θ be the angle of some point of the robot with respect to an inertial frame, and assume moreover that θ has been chosen so that it is strictly monotonic throughout the step. Then the path of the robot in the configuration space can be expressed as

$$0 = q_b - h_d(\theta). \quad (\text{A.3})$$

A natural objective is therefore: determine a feedback controller that drives asymptotically to zero the output function

$$y = h(q) := q_b - h_d(\theta). \quad (\text{A.4})$$

The relation (A.3) is called a *virtual constraint* because it is being imposed by feedback; see again [Section 1.4](#). For reassurance that a relatively simple feedback controller can often be used to (approximately) impose the virtual constraints, see [Section 8.2](#).

2. It is suggested to assign body coordinates as the relative angles of the actuated joints; see [Fig. 3.6-\(a\)](#). Determine a variable $\theta(q)$ that can be used to parameterize the position of the robot *within* a step; θ must be strictly monotonic over a step, and thus, after scaling, it can be used as the horizontal-axis in [Fig. A.1](#). Typically, θ would be synthesized from angular measurements, an inclinometer, or a combination of these; see Figs. 3.6 and [6.13\(b\)](#) for possible choices of θ .
3. Using your existing controller, put your biped into a periodic walking motion and record the values of q_b and θ over several cycles (optionally, record the torque commands u as well). Then, take the data and form a plot analogous to Fig. A.1. Use regression and your favorite set of regressors (such as polynomials) to determine virtual constraints as in (A.3); an alternative approach using splines is explained in Section 6.5. (Optionally, apply the same technique to determine the nominal torque commands over a periodic orbit, $u^{nom}(\theta)$.) In the book, it has been assumed that the robot is *symmetric*, that is, the “left” and “right” legs are identical to one another. In this case, it is only necessary to determine the virtual constraints over a single step, with say the left leg as the stance leg, and use coordinate relabeling to determine the virtual constraints when the right leg is the stance leg. If your robot has asymmetry, then you need to determine two sets of virtual constraints, one for each leg as the stance leg. In principle, different functions θ can be used for each set of constraints.
4. If your current control system consists of decentralized PD controllers at the joints set up to do tracking of time-based trajectories, then the virtual constraints can be imposed as in (8.15), where $e = y$; in other words, a decentralized PD-controller, “tracking-based” architecture can be maintained:

$$u = -K_P y - K_D \dot{y} + \text{optional friction compensation}, \quad (\text{A.5})$$

or,

$$u = u^{nom}(\theta) - K_P y - K_D \dot{y} + \text{optional friction compensation}. \quad (\text{A.6})$$

Note that a finite state machine is needed to keep track of which leg is in stance and therefore which set of virtual constraints is to be applied on the left and right legs. Tuning the PD-gains such that the virtual constraints are well applied while avoiding resonances in the drivetrain can be challenging.¹ *It is assumed that the user will already have in place safety mechanisms of the type discussed in Chapter 8.* These are crucial.

Remark A.1 (Closed-Loop Stability) Theorem 6.2 and (6.78)–(6.81) imply that, as long as the virtual constraints are well imposed,² the closed-loop system will have an exponentially stable periodic orbit if, and only if, the vertical component of the velocity of the center of mass of the robot is *negative* just before impact. The latter is solely a property of the user’s nominal periodic orbit that was used in building the virtual constraints.

5. The effectiveness of (A.5) or (A.6) in applying the virtual constraints can be tested by rocking the robot back and forth on the stance leg and noting that the swing leg moves forward and retracts as appropriate. The correctness of the finite state machine can be tested by guiding the robot through a few steps, forward and backward, and noting that leg exchange takes place properly; see videos at [239, 240]. A walking experiment can be initiated by pushing the robot forward with enough initial velocity that it enters the basin of attraction of the controller. Alternatively, the user’s existing controller can be used and when the robot is near the nominal periodic orbit, switch to the virtual constraint-based controller.
6. If the robot has a torso, then it is relatively easy to alter the position of the center of mass of the robot over a step without altering the relative posture of the legs. In this case, event-based PI control can be easily implemented to vary the walking speed of the robot; see Chapter 7 and Experiment 4 on RABBIT in Section 8.3.1.2.
7. If the user can produce nominal walking gaits of several different speeds, it is easy to design virtual constraint-based controllers and switch among them. For this, it is best if Bézier polynomials were used as the regressors

¹As an alternative to a PD-controller, see (5.96); its computation requires the use of a model.

²For virtual constraints computed on the basis of predetermined periodic orbits, the associated decoupling matrix will be invertible on the periodic as long as the angular momentum of the robot about the stance leg end is nonzero on the periodic orbit; see the proof of Theorem 6.2.

when building the virtual constraints; see [Section 7.2](#) and Experiment 3 on RABBIT in [Section 8.3.1.2](#).

8. Sections 6.5.2 and 6.6.3.2 illustrate how to take an initial controller based on virtual constraints and modify it in order to improve the gait (in the example, a gait designed to work on a downward slope was modified to work on flat ground). The same idea can be used to improve energy efficiency, for example, or to reduce peak torque requirements. In principle, carrying this out requires a good model of the robot, but it may be possible to use reinforcement learning to tune the parameters in an augmentation function online [227].

A.2.2 Controller Design Must Start from Scratch

When constructing the robot, the reader may have verified that periodic walking motions existed which respect the power limitations of the actuators and the workspace constraints of the mechanism. If so, the reader may use one of the previously computed periodic walking motions and essentially repeat the steps of Section A.2.1. Otherwise, it is suggested that the reader work through (an abridged version of) Section A.1, skipping those exercises that pertain to skills that the reader has already mastered through past experience. Even for robots of the complexity of RABBIT and ERNIE, the authors found it essential to have worked through simpler examples before tackling these bipeds.

A.2.3 Walking with Feet

This section suggests modifications to Section A.2.1 to take into account the presence of feet. For simplicity, it is assumed that flat-footed walking is desired, though walking with foot rotation is treated thoroughly in [Chapters 10](#) and [11](#).

1. The ankle control strategy of Section 10.4.2 can be very easily implemented. Using the reader's existing controller, record the torque of the stance ankle over a periodic walking cycle and regress it against θ to determine $u_A(\theta)$. All other joints are treated as in Step 3 of Section A.2.1, including the ankle of the swing leg. The controller is implemented as in Step 4 of Section A.2.1, *with the stance ankle torque set equal to $u_A(\theta)$* . If the CoP (equivalently, ZMP or FRI point) is *strictly within* the foot support region on the periodic orbit used for building the virtual constraints, then the stability analysis of Remark A.1 still applies; see [Corollary 10.1](#). The remaining steps of Section A.2.1 can be carried out with no significant changes.
2. If force sensors or some other means is available to estimate the CoP of the stance foot, equivalently, the ZMP or FRI point, then the control law

of Section 11.2 can be applied. Using the reader’s existing controller, record the FRI position (optionally, the torque as well) of the stance ankle over a periodic walking cycle and regress it against θ to determine $p_{\text{FRI}}^{\text{h,d}}(\theta)$ (optionally, $u_A(\theta)$ as well). All other joints are treated as in Step 3 of Section A.2.1, including the ankle of the swing leg. The controller is implemented as in Step 4 of Section A.2.1, *with the stance ankle torque set equal to*

$$u_A = -K_P(p_{\text{FRI}}^{\text{h}} - p_{\text{FRI}}^{\text{h,d}}(\theta)) + \text{optional friction compensation}, \quad (\text{A.7})$$

or,

$$u = u_A^{\text{nom}}(\theta) - K_P(p_{\text{FRI}}^{\text{h}} - p_{\text{FRI}}^{\text{h,d}}(\theta)) + \text{optional friction compensation}. \quad (\text{A.8})$$

If the CoP (equivalently, ZMP or FRI point) is *strictly within* the foot support region on the periodic orbit used for building the virtual constraints, then the stability analysis of Remark A.1 still applies; see [Corollary 11.1](#). The remaining steps of Section A.2.1 can be carried out with no significant changes.

A.2.4 3D Robot

The extension of the work presented in the book to 3D robots is an open issue. Some nice results have been reported in [80], where, using the notion of virtual constraints and zero dynamics (called interlocking dynamics in their paper), the control of a 3D mechanism has been demonstrated experimentally. In addition, we can report that Prof. Ching-Long Shih, Department of Electrical Engineering, National Taiwan University of Science and Technology, spent six months as a visiting professor at the University of Michigan. After working through the program suggested in Section A.1, he applied the method of virtual constraint-based control to a 30 cm tall 3D robot with feet. He was able to obtain stable walking with about two weeks of effort. This work is not yet published.

B

Essential Technical Background

This appendix provides background information on various aspects of mechanics and nonlinear control. The level of presentation is elementary, and in some sense the material here serves primarily to establish a common vocabulary. The reader will find material on differential geometry (embedded manifolds, coordinate charts, diffeomorphisms, tangent spaces, vector fields, invariant manifolds, restriction dynamics, Lie derivatives, Lie brackets, involutive distributions), geometric nonlinear control (relative degrees, decoupling matrices, zero dynamics, I-O linearization), the method of Poincaré sections (periodic orbits, transversal sections, Poincaré maps, fixed points), and Lagrangian mechanics in the plane (kinematic chains, absolute and relative angles, generalized coordinates, potential energy and kinetic energy, linear and angular momentum, Lagrange-Euler equation). Our modest objective is make the book more widely accessible, knowing that it will not be self-contained. The [End Notes](#) provide references for further reading.

A brief comment on notation is in order before beginning the overview. Traditionally, coordinates on a smooth surface are expressed as n -tuples of scalars (x_1, x_2, \dots, x_n) , with $x_i \in \mathbb{R}$, and whenever necessary, the n -tuple is identified with the column vector

$$\begin{bmatrix} x_1 \\ x_2 \\ \vdots \\ x_n \end{bmatrix} \tag{B.1}$$

in order to write down a differential equation or to perform operations such as the chain rule in vector form. Tradition will be respected in [Appendix B.1](#), but elsewhere in the appendix and the book, coordinates are immediately identified with the column vector (B.1) and written in-line as $(x_1; x_2; \dots; x_n)$. See also the remarks in [Section 3.3](#). The arguments of a multivariable function will continue to be separated by a comma.

B.1 Smooth Surfaces and Associated Notions

The objective of this section is to provide an elementary introduction to a few concepts in differential geometry. For the purposes of this book, it is enough to identify smooth manifolds with smooth surfaces in \mathbb{R}^n , and with this in mind, we will take a simplified¹ approach to the subject based on level sets of smooth functions from \mathbb{R}^n to \mathbb{R}^{n-m} . It is assumed that the reader is familiar with the concepts of open and closed sets, continuity, and differentiability, all in \mathbb{R}^n . The topics covered are embedded submanifolds, coordinate charts, diffeomorphisms, tangent spaces, vector fields on manifolds, invariant submanifolds, restriction dynamics, Lie derivatives, Lie brackets, and involutive distributions.

B.1.1 Manifolds and Embedded Submanifolds

The idea of an m -dimensional manifold is to define an object that locally looks like an open subset of \mathbb{R}^m and its local pieces can be glued together smoothly. The model to have in mind is an idealized representation of the surface of the earth as a sphere, which when viewed locally, is indistinguishable from \mathbb{R}^2 . We begin by defining the notion of a “smooth surface” in \mathbb{R}^n . Let $\|\cdot\|$ be any norm on \mathbb{R}^n , such as the Euclidean norm, and let $B_r(p)$ denote the *open ball* of radius r centered at p , namely, the set $\{x \in \mathbb{R}^n \mid \|x - p\| < r\}$.

Definition B.1 (Embedded submanifold of \mathbb{R}^n) *Let M be a nonempty subset of \mathbb{R}^n and let $1 \leq m \leq n$ and $k \geq 1$. M is an m -dimensional, C^k -embedded submanifold of \mathbb{R}^n if $\forall p \in M$ there exists $r > 0$ and a function $F : B_r(p) \rightarrow \mathbb{R}^{n-m}$ such that*

1. $M \cap B_r(p) = \{x \in B_r(p) \mid F(x) = 0\}$,

2. F is k -times differentiable, and

3. $\forall \bar{x} \in M \cap B_r(p)$, $\text{rank } \frac{\partial F}{\partial x} \Big|_{\bar{x}} = n - m$.

¹A more correct treatment of the concept of a differentiable manifold and its attendant structures is based on the concept of an atlas of coordinate charts and requires basic notions of topology, namely, homeomorphisms and Hausdorff spaces. We will avoid these complications by working with smooth surfaces in \mathbb{R}^n . In places, our development is not as coherent as the traditional approach. The interested reader can see the [End Notes](#) for references to a mathematically detailed approach to the subject.

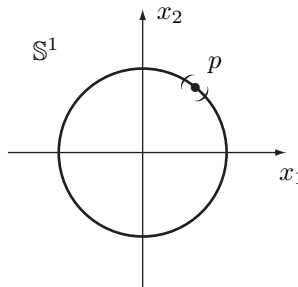


Figure B.1. The unit circle embedded in \mathbb{R}^2 .

The degree of smoothness is determined by k . If the function F is infinitely differentiable at points of M , then one commonly says that the submanifold is *smooth*, though sometimes this just means that it is C^k for some $k \geq 1$.

Example B.1 (Unit circle embedded in \mathbb{R}^2)

The circle of radius one, \mathbb{S}^1 (see Fig. B.1), is a 1-dimensional smooth embedded submanifold of \mathbb{R}^2 . To show this, let $F : \mathbb{R}^2 \rightarrow \mathbb{R}$ by

$$F(x_1, x_2) = x_1^2 + x_2^2 - 1. \quad (\text{B.2})$$

Verifying the first two parts of Definition B.1 is trivial since F is clearly infinitely differentiable, and \mathbb{S}^1 is equal to the set of points where F vanishes. To verify the rank condition specified in the third part of the definition, note that for $(\bar{x}_1, \bar{x}_2) \in \mathbb{S}^1$, $\text{rank } (\partial F / \partial x)|_{(\bar{x}_1, \bar{x}_2)} = \text{rank } [2\bar{x}_1 \ 2\bar{x}_2] = 1$, because $(\bar{x}_1, \bar{x}_2) \in \mathbb{S}^1$ implies at least one of \bar{x}_1 and \bar{x}_2 is nonzero.

Remark B.1 One of the drawbacks of the simplified approach we are taking to defining a manifold is that it is not clear that a manifold can be defined in an intrinsic manner independent of the particular embedding into \mathbb{R}^n , for some n . For example, the unit circle could also be viewed as an 1-dimensional smooth embedded submanifold of \mathbb{R}^3 by choosing

$$F(x_1, x_2, x_3) = \begin{bmatrix} x_1^2 + x_2^2 + x_3^2 - 1 \\ x_1 \end{bmatrix}, \quad (\text{B.3})$$

which leads one to wonder if a unit circle in \mathbb{R}^2 is intrinsically different from a unit circle in \mathbb{R}^3 , or \mathbb{R}^{17} for that matter? The answer is no and the development of the definition of a manifold in terms of coordinate atlases eliminates any such doubts. On the other hand, a famous theorem from the 1930s due to Whitney states that every m -dimensional manifold can be embedded in \mathbb{R}^n , for some $n \leq 2m + 1$. Hence, the simplified definition we have given does not exclude any manifolds.

For the purposes of this book, the terms *manifold* and *embedded submanifold of \mathbb{R}^n* are taken to be synonymous. That is, a set M is an m -dimensional C^k -manifold if for some n , it is an m -dimensional, C^k -embedded submanifold of \mathbb{R}^n . By taking F in Definition B.1 to be identically zero, we trivially have that \mathbb{R}^n is a smooth n -dimensional submanifold of itself, and hence is a smooth n -dimensional manifold. More generally, any open subset of \mathbb{R}^n is a smooth n -dimensional manifold. Other common examples include circles, spheres, and tori. A set consisting of isolated points² in \mathbb{R}^n for some $n \geq 1$, will be called a zero-dimensional manifold. Consistent with this definition of a manifold, M , we can formally define an embedded submanifold of M in the following manner.

Definition B.2 (Embedded submanifold) Let M be m -dimensional, C^k -manifold of \mathbb{R}^n , with $r > 0$ and $F : B_r(p) \rightarrow \mathbb{R}^{n-m}$ satisfying the conditions of Definition B.1. A nonempty subset $\tilde{N} \subset M$ is a C^k \tilde{n} -dimensional embedded submanifold of M if $\forall p \in \tilde{N}$ there exists $\tilde{r} > 0$ and a function $\tilde{F} : B_{\tilde{r}}(p) \rightarrow \mathbb{R}^{m-\tilde{n}}$ such that

1. $\tilde{N} \cap B_{\tilde{r}}(p) = \{x \in M \cap B_{\tilde{r}}(p) \mid \tilde{F}(x) = 0\},$

2. \tilde{F} is k -times differentiable, and

3. $\forall \tilde{x} \in \tilde{N} \cap B_{\tilde{r}}(p),$

$$\text{rank} \begin{bmatrix} \frac{\partial F}{\partial x} \Big|_{\tilde{x}} \\ \frac{\partial \tilde{F}}{\partial x} \Big|_{\tilde{x}} \end{bmatrix} = n - \tilde{n}. \quad (\text{B.4})$$

Remark B.2 With this definition, the unit circle is easily shown to be an embedded submanifold of the unit sphere.

B.1.2 Local Coordinates and Smooth Functions

It is convenient to locally parameterize points in an m -dimensional manifold by a list of m numbers, called local coordinates. Let M be an m -dimensional C^k -embedded submanifold of \mathbb{R}^n and let $p \in M$. Suppose that $r > 0$ and $F : B_r(p) \rightarrow \mathbb{R}^{n-m}$ satisfy the conditions of Definition B.1. Let (x_1, x_2, \dots, x_n)

²A collection of points in $A \subset \mathbb{R}^n$ is isolated if there exists $\epsilon > 0$ such that for every pair of points $p, q \in A$, $B_\epsilon(p) \cap B_\epsilon(q) = \emptyset$.

be a set of coordinates on \mathbb{R}^n , and without loss of generality, suppose that

$$\text{rank} \begin{bmatrix} \frac{\partial F_1(p)}{\partial x_{m+1}} & \frac{\partial F_1(p)}{\partial x_{m+2}} & \cdots & \frac{\partial F_1(p)}{\partial x_n} \\ \vdots & \vdots & \ddots & \vdots \\ \frac{\partial F_{n-m}(p)}{\partial x_{m+1}} & \frac{\partial F_{n-m}(p)}{\partial x_{m+2}} & \cdots & \frac{\partial F_{n-m}(p)}{\partial x_n} \end{bmatrix} = n - m \quad (\text{B.5})$$

By the Implicit Function Theorem [127], there exist $0 < \bar{r} \leq r$ and C^k functions $g_i(x_1, x_2, \dots, x_m)$, $m + 1 \leq i \leq n$, such that for $(x_1, x_2, \dots, x_n) \in B_{\bar{r}}(p)$,

$$F(x_1, \dots, x_m, g_{m+1}(x_1, \dots, x_m), \dots, g_n(x_1, \dots, x_m)) = 0. \quad (\text{B.6})$$

It follows that

$$\begin{aligned} M \cap B_{\bar{r}}(p) = \{(x_1, x_2, \dots, x_n) \in B_{\bar{r}}(p) \mid \\ x_{m+1} = g_{m+1}(x_1, \dots, x_m), \dots, x_n = g_n(x_1, \dots, x_m)\}, \end{aligned} \quad (\text{B.7})$$

and hence points in M are locally parameterized by (x_1, \dots, x_m) . The m -tuple (x_1, \dots, x_m) is called at set of *local coordinates* for M , and the pair $((x_1, \dots, x_m), B_{\bar{r}}(p) \cap M)$ is called a *local coordinate chart* for M . More generally, a set of m C^k -functions $\lambda_i : B_{\bar{r}}(p) \rightarrow \mathbb{R}$, $1 \leq i \leq m$, such that

$$\text{rank} \begin{bmatrix} \frac{\partial \lambda_1(p)}{\partial x_1} & \cdots & \frac{\partial \lambda_1(p)}{\partial x_n} \\ \vdots & & \vdots \\ \frac{\partial \lambda_m(p)}{\partial x_1} & \cdots & \frac{\partial \lambda_m(p)}{\partial x_n} \\ \frac{\partial F_1(p)}{\partial x_1} & \cdots & \frac{\partial F_1(p)}{\partial x_n} \\ \vdots & & \vdots \\ \frac{\partial F_{n-m}(p)}{\partial x_1} & \cdots & \frac{\partial F_{n-m}(p)}{\partial x_n} \end{bmatrix} = n \quad (\text{B.8})$$

define local coordinates on M . Indeed, the rank condition (B.8) guarantees that

$$\begin{bmatrix} \tilde{x}_1 \\ \vdots \\ \tilde{x}_m \\ \tilde{x}_{m+1} \\ \vdots \\ \tilde{x}_n \end{bmatrix} = \begin{bmatrix} \lambda_1(x) \\ \vdots \\ \lambda_m(x) \\ F_1(x) \\ \vdots \\ F_{n-m}(x) \end{bmatrix} \quad (\text{B.9})$$

define a set of local coordinates on \mathbb{R}^n about p . In these coordinates, (B.5) holds, which yields

$$M \cap B_{\bar{r}}(p) = \{(\tilde{x}_1, \tilde{x}_2, \dots, \tilde{x}_n) \in B_{\bar{r}}(p) \mid \tilde{x}_{m+1} = 0, \dots, \tilde{x}_n = 0\}, \quad (\text{B.10})$$

and hence the m -tuple $(\tilde{x}_1 = \lambda_1, \dots, \tilde{x}_m = \lambda_m)$ parameterizes M .

Example B.2 (Coordinates on the circle embedded in \mathbb{R}^2)

Continuing Example B.1, let $p = (0, 1)$, let $\|(x_1, x_2)\| = \max\{|x_1|, |x_2|\}$ be the max-norm, and take $r = 1$. Then an easy calculation gives that

$$\mathbb{S}^1 \cap B_r(p) = \{(x_1, x_2) \in B_r(p) \mid x_2 = \sqrt{1 - x_1^2}\} \quad (\text{B.11a})$$

$$= \{(x_1, x_2) \in \mathbb{R}^2 \mid |x_1| < 1, x_2 = \sqrt{1 - x_1^2}\}, \quad (\text{B.11b})$$

and hence in a neighborhood of $p = (0, 1)$, $(x_1, \mathbb{S}^1 \cap B_r(p))$ is a local coordinate chart on \mathbb{S}^1 . For $p = (-1, 0)$, we have

$$\mathbb{S}^1 \cap B_r(p) = \{(x_1, x_2) \in B_r(p) \mid x_1 = -\sqrt{1 - x_2^2}\} \quad (\text{B.12a})$$

$$= \{(x_1, x_2) \in \mathbb{R}^2 \mid |x_2| < 1, x_1 = -\sqrt{1 - x_2^2}\}, \quad (\text{B.12b})$$

and hence in a neighborhood of $p = (-1, 0)$, $(x_2, \mathbb{S}^1 \cap B_r(p))$ is a local coordinate chart on \mathbb{S}^1 .

Let M_1 and M_2 be embedded submanifolds of \mathbb{R}^{n_1} and \mathbb{R}^{n_2} , respectively. A function $\gamma : M_1 \rightarrow M_2$ is C^k at $p \in M_1$ if it is the local restriction of a function from \mathbb{R}^{n_1} to \mathbb{R}^{n_2} which is C^k at p ; that is, there exists $r > 0$ and $\hat{\gamma} : B_r(p) \rightarrow \mathbb{R}^{n_2}$ such that $\forall x \in B_r(p)$, $\gamma(x) = \hat{\gamma}(x)$, and $\hat{\gamma}$ is k -times continuously differentiable at p . It follows that $\gamma : M_1 \rightarrow M_2$ is C^k at p if its representation in local coordinates is C^k at p , that is, if for each $p \in M$, and local coordinate chart $((x_1, \dots, x_{m_1}), M_1 \cap B_{\bar{r}_1}(p))$ and $((x_1, \dots, x_{m_2}), M_2 \cap B_{\bar{r}_2}(\gamma(p)))$, $\gamma(x_1, \dots, x_{m_1})$ is C^k .

$\gamma : M_1 \rightarrow M_2$ is a C^k -diffeomorphism if it is invertible (i.e., one-to-one and onto) and both γ and γ^{-1} are C^k . Two manifolds M_1 and M_2 are diffeomorphic if there exists a diffeomorphism $\gamma : M_1 \rightarrow M_2$. The function $\gamma : M_1 \rightarrow M_2$ is a C^k -local diffeomorphism at $p \in M_1$ if there exists $\bar{r}_1 > 0$ such that $\gamma : M_1 \cap B_{\bar{r}_1}(p) \rightarrow M_2$ is a C^k -diffeomorphism onto its image. From the Inverse Function Theorem (or the Rank Theorem) this is true if, and only if,

$$m_1 = m_2 = \text{rank } \frac{\partial \gamma}{\partial x} \Big|_p. \quad (\text{B.13})$$

B.1.3 Tangent Spaces and Vector Fields

A tangent space of an m -dimensional C^k -manifold at a point p is an m -dimensional vector space, which is thought of as a linear approximation to the surface at p . A precise definition follows.

Definition B.3 (Tangent space) Let M be an m -dimensional C^k -embedded submanifold of \mathbb{R}^n and let $p \in M$. Suppose that $r > 0$ and that $F : B_r(p) \rightarrow$

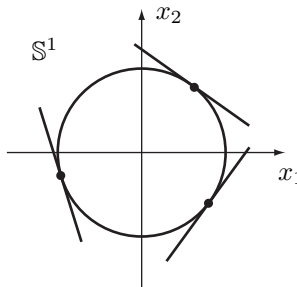


Figure B.2. The unit circle embedded in \mathbb{R}^2 with tangent spaces at three distinct points.

\mathbb{R}^{n-m} is a C^k -function satisfying the conditions of Definition B.1. The tangent space at p , denoted $T_p M$, is equal to the nullspace of $\frac{\partial F}{\partial x}(p)$; that is,

$$T_p M := \left\{ v \in \mathbb{R}^n \mid \frac{\partial F}{\partial x}(p) v = 0 \right\}. \quad (\text{B.14})$$

The tangent bundle of M is $TM := \bigcup_{p \in M} T_p M$, the union of the tangent spaces.

By construction, the tangent space at a point is always a vector space with the same dimension as the underlying manifold. It is useful to note that the tangent bundle of an m -dimensional C^k -manifold, $k \geq 2$, is a $2m$ -dimensional C^{k-1} -manifold in general. To see this point, let $(p, v_0) \in TM$, that is, $p \in M$ and $v_0 \in T_p M$, and let r and F be as in Definition B.1. For the open subset of $\mathbb{R}^n \times \mathbb{R}^n$ we take $B_r(p) \times \mathbb{R}^n$, and for the function whose level set locally defines TM , we take $F_* : B_r(p) \times \mathbb{R}^n \rightarrow \mathbb{R}^{n-m} \times \mathbb{R}^{n-m}$, by

$$F_*(\bar{x}, \bar{v}) := \begin{bmatrix} F(\bar{x}) \\ \frac{\partial F}{\partial x} \Big|_{\bar{x}} \bar{v} \end{bmatrix}. \quad (\text{B.15})$$

Then the first and second properties of Definition B.1 are clearly satisfied due to the definition of the tangent bundle in Definition B.3. To verify the third property, we note that

$$\left. \frac{\partial F_*}{\partial(x, v)} \right|_{(\bar{x}, \bar{v})} = \begin{bmatrix} \frac{\partial F}{\partial x} \Big|_{\bar{x}} & 0 \\ * & \frac{\partial F}{\partial x} \Big|_{\bar{x}} \end{bmatrix} \quad (\text{B.16})$$

is lower triangular and hence its rank is equal³ to $2(n - m)$ as required.

³ $\overline{\text{rank } \frac{\partial F_*}{\partial(x, v)} \Big|_{(\bar{x}, \bar{v})}} = 2 \text{ rank } \frac{\partial F}{\partial x} \Big|_{\bar{x}}$

Example B.3 (Tangent space of the unit circle embedded in \mathbb{R}^2)

Continuing Example B.1, the tangent space of the unit circle at a point $p = (p_1, p_2) \in \mathbb{S}^1$ is obtained by applying Definition B.3. This yields a one-dimensional vector space

$$T_p \mathbb{S}^1 = \left\{ \begin{bmatrix} v_1 \\ v_2 \end{bmatrix} \in \mathbb{R}^2 \mid [2p_1 \ 2p_2] \begin{bmatrix} v_1 \\ v_2 \end{bmatrix} = 0 \right\} \quad (\text{B.17a})$$

$$= \left\{ \alpha \begin{bmatrix} -p_2 \\ p_1 \end{bmatrix} \mid \alpha \in \mathbb{R} \right\}. \quad (\text{B.17b})$$

Figure B.2 gives a sketch of $T_p \mathbb{S}^1$ for three distinct points in \mathbb{S}^1 , from which one may extrapolate a conceptual picture of $T \mathbb{S}^1$. One must keep in mind that even though $T \mathbb{S}^1$ is a two-dimensional manifold, it cannot be drawn in \mathbb{R}^2 .

To see why $T_p M$ is called a tangent space, consider a differentiable curve $c(t)$ passing through a point $p \in M$, that is, consider a differentiable function $c : (t_0, t_2) \rightarrow M$ and a point $t_1 \in (t_0, t_2)$, with $p = c(t_1)$. Then, for $|t_0 - t_1| + |t_1 - t_2|$ sufficiently small, $F \circ c$ is well-defined and identically zero, and therefore

$$\frac{d}{dt} F \circ c \Big|_{t_1} = \frac{\partial F}{\partial x} \Big|_p \frac{dc}{dt} \Big|_{t_1} = 0. \quad (\text{B.18})$$

It follows that $\frac{dc}{dt} \Big|_{t_1} \in T_p M$. Hence, just as the derivative of a curve lies along the line tangent to the curve, $T_p M$ is tangent to M . Similarly, just as the line tangent to a curve is a local approximation of the curve, the tangent space of M can be thought of as a local approximation of M .

Definition B.4 (Vector field on a manifold) Let M be a C^k , m -dimensional manifold. A vector field f on M is an assignment to each point $p \in M$ of a vector $f(p) \in T_p M$. The vector field is C^k if f is a C^k function on M .

Example B.4 (Vector field on the unit circle embedded in \mathbb{R}^2)

Continuing Example B.1, recall that Example B.3 established that the tangent space at a point $p = (p_1, p_2) \in \mathbb{S}^1$ is given by (B.17a). Hence, a vector field f on \mathbb{S}^1 is given by

$$f(p) = f(p_1, p_2) = \alpha(p_1, p_2) \begin{bmatrix} -p_2 \\ p_1 \end{bmatrix} \in T_p \mathbb{S}^1, \quad (\text{B.19})$$

where $\alpha : \mathbb{S}^1 \rightarrow \mathbb{R}$. The vector field is depicted in Fig. B.3 for α constant.

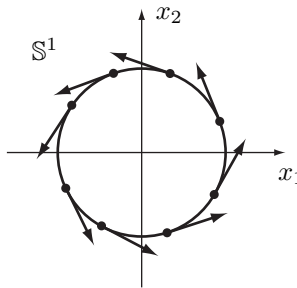


Figure B.3. A vector field on the unit circle embedded in \mathbb{R}^2 .

B.1.4 Invariant Submanifolds and Restriction Dynamics

Definition B.5 (Integral curve of a vector field) Let M be a C^k , m -dimensional manifold and f a vector field on M . A differentiable curve $c : (t_0, t_f) \rightarrow M$ such that

$$\frac{dc(t)}{dt} = f(c(t)) \quad (\text{B.20})$$

for all $t \in (t_0, t_f)$ is an integral curve of f .

For obvious reasons, the curve is often denoted by $x(t)$ and (B.20) is written suggestively as

$$\dot{x} = f(x). \quad (\text{B.21})$$

Moreover, the time interval is often assumed to be closed on the left, $[t_0, t_f]$. In this case, if in addition the integral curve satisfies $x(t_0) = x_0$ for some $x_0 \in M$, then $x : [t_0, t_f] \rightarrow M$ is the solution of f with initial condition x_0 at time t_0 . By abuse of notation, this is commonly denoted $x(t, t_0, x_0)$, or simply $x(t, x_0)$ when t_0 is taken as 0.

Definition B.6 (Invariant submanifold) Let M be a manifold and f a locally Lipschitz continuous vector field on M . $\tilde{N} \subset M$ is an invariant submanifold of f if

1. \tilde{N} is an embedded submanifold of M , and
2. for all $x_0 \in \tilde{N}$, $\exists t_1 > 0$ and an integral curve of f , $x : [0, t_1] \rightarrow M$, such that $x(0) = x_0$ and $\forall t \in (0, t_1)$, $x(t) \in \tilde{N}$.

One also says that \tilde{N} is *forward invariant* or more simply, *invariant* under f , or that \tilde{N} is an *integral submanifold* of f . When \tilde{N} is an invariant submanifold of f , then in particular, \tilde{N} is a manifold and hence its tangent space can be

defined. If f is at least locally Lipschitz continuous, then standard results on existence and uniqueness of solutions to differential equations can be used to provide a test of the invariant submanifold property that does not rely on computing the solution.

Proposition B.1 (Invariant Submanifold Test)

Let M be a manifold and f a locally Lipschitz continuous vector field on M . $\tilde{N} \subset M$ is an invariant submanifold of f if

1. \tilde{N} is an embedded submanifold of M , and

2. for all $p \in \tilde{N}$, $f(p) \in T_p \tilde{N}$.

Example B.5 (The unit circle as an invariant submanifold of \mathbb{R}^2)

Continuing Example B.1, consider the vector field on \mathbb{R}^2 given by

$$f(x) = f(x_1, x_2) = \begin{bmatrix} -x_2 \\ x_1 \end{bmatrix}, \quad (\text{B.22})$$

and let $x_0 = (x_{0,1}, x_{0,2}) \in \mathbb{S}^1$. Then, the solution of $\dot{x} = f(x)$, $x(0) = x_0$ is

$$x(t) = \exp \left(\begin{bmatrix} 0 & -1 \\ 1 & 0 \end{bmatrix} t \right) \begin{bmatrix} x_{0,1} \\ x_{0,2} \end{bmatrix} \quad (\text{B.23a})$$

$$= \begin{bmatrix} \cos(t) & -\sin(t) \\ \sin(t) & \cos(t) \end{bmatrix} \begin{bmatrix} x_{0,1} \\ x_{0,2} \end{bmatrix} \quad (\text{B.23b})$$

$$= \begin{bmatrix} x_{0,1} \cos(t) - x_{0,2} \sin(t) \\ x_{0,1} \sin(t) + x_{0,2} \cos(t) \end{bmatrix}. \quad (\text{B.23c})$$

It is easily checked that $F(x(t)) = 0$ for all $t \geq 0$. Therefore, \mathbb{S}^1 is an invariant submanifold of f .

In general, it is not possible to compute the solution of a differential equation in closed-form in order to apply Definition B.6, and hence applying Proposition B.1 is much easier. Since f is smooth and Example B.3 immediately establishes that $f(p) \in T_p \mathbb{S}^1$ for all $p \in \mathbb{S}^1$, it is concluded that \mathbb{S}^1 is an invariant submanifold of f with no further computations.

From Proposition B.1, if \tilde{N} is an invariant submanifold of a Lipschitz continuous vector field f on M , then $f|_{\tilde{N}}$, which is read f restricted to \tilde{N} and defined by

$$\forall p \in \tilde{N}, f|_{\tilde{N}}(p) = f(p), \quad (\text{B.24})$$

is a vector field on \tilde{N} (that is, $f|_{\tilde{N}}(p) \in T_p \tilde{N}$). The corresponding differential equation on \tilde{N} is called the *restriction dynamics*, $\dot{x} = f|_{\tilde{N}}(x)$. The importance of this concept is that it corresponds to a lower-dimensional differential

equation, since in general $\tilde{n} < m$. To see this, suppose that $p \in \tilde{N} \subset M$ and that $((x_1, \dots, x_m), B_r(p) \cap M)$ is a coordinate chart for M about p in which $B_r(p) \cap \tilde{N} = \{(x_1, \dots, x_m) \in B_r(p) \cap M \mid x_{\tilde{n}+1} = \tilde{g}_{\tilde{n}+1}(x_1, \dots, x_{\tilde{n}}), \dots, x_m = \tilde{g}_m(x_1, \dots, x_{\tilde{n}})\}$. Then $((x_1, \dots, x_{\tilde{n}}), B_r(p) \cap \tilde{N})$ is a coordinate chart for \tilde{N} about p , and the restriction dynamics is given by

$$\begin{bmatrix} \dot{x}_1 \\ \vdots \\ \dot{x}_{\tilde{n}} \end{bmatrix} = \begin{bmatrix} f_1(x_1, \dots, x_{\tilde{n}}, \tilde{g}_{\tilde{n}+1}(x_1, \dots, x_{\tilde{n}}), \dots, \tilde{g}_m(x_1, \dots, x_{\tilde{n}})) \\ \vdots \\ f_{\tilde{n}}(x_1, \dots, x_{\tilde{n}}, \tilde{g}_{\tilde{n}+1}(x_1, \dots, x_{\tilde{n}}), \dots, \tilde{g}_m(x_1, \dots, x_{\tilde{n}})) \end{bmatrix}. \quad (\text{B.25})$$

Example B.6 (Restriction dynamics on the unit circle)

By Example B.5, \mathbb{S}^1 is invariant under the vector field (B.22). Using the coordinate chart about $p = (0, 1)$ given in Example B.2, the restriction dynamics is computed to be

$$\dot{x}_1 = -\sqrt{1 - x_1^2}. \quad (\text{B.26})$$

The change of coordinates $x_1 = \sin(\theta)$ results in

$$\dot{\theta} = -1. \quad (\text{B.27})$$

It is an easy exercise to verify that if in Example B.2 we had started in polar coordinates on \mathbb{R}^2 , then we would have obtained this result directly. Similarly, using the coordinate chart about $p = (-1, 0)$ given in Example B.2, the restriction dynamics is computed to be

$$\dot{x}_2 = -\sqrt{1 - x_2^2}. \quad (\text{B.28})$$

B.1.5 Lie Derivatives, Lie Brackets, and Involutive Distributions

Definition B.7 (Lie derivative) Let M be a C^k , m -dimensional manifold, f a vector field on M , and $h : M \rightarrow \mathbb{R}$ a differentiable real-valued function. The Lie derivative of h with respect to f is the real-valued function $L_f h : M \rightarrow \mathbb{R}$ by

$$\forall p \in M, L_f h(p) := \frac{\partial h}{\partial x}(p)f(p). \quad (\text{B.29})$$

If $h : M \rightarrow \mathbb{R}^n$ is vector valued and differentiable, then applying the above definition component-wise results in

$$L_f h(p) := \begin{bmatrix} \frac{\partial h_1}{\partial x}(p)f(p) \\ \vdots \\ \frac{\partial h_n}{\partial x}(p)f(p) \end{bmatrix} = \frac{\partial h}{\partial x}(p)f(p), \quad (\text{B.30})$$

in which case, $L_f h : M \rightarrow \mathbb{R}^n$.

Some useful properties and notation are briefly summarized. In order to see that $L_f h$ is a directional derivative, suppose that c is an integral curve of f such that $c(t_1) = p$. Then

$$\frac{d}{dt} (h \circ c) \Big|_{t_1} = \frac{\partial h}{\partial x} \Big|_p \frac{dc}{dt} \Big|_{t_1} \quad (\text{B.31a})$$

$$= \frac{\partial h}{\partial x} \Big|_p f(p) \quad (\text{B.31b})$$

$$= L_f h(p). \quad (\text{B.31c})$$

In general, if h is k_1 -times differentiable and f is k_2 -times differentiable, then $L_f h$ is at least $\min\{k_1 - 1, k_2\}$ -times differentiable. When h and f are sufficiently many times differentiable, $L_f^2 h = L_f(L_f h)$, and the symbol $L_f^k h$ means applying L_f k -times. If g is another vector field on M , then $L_g(L_f h)$ is simply denoted as $L_g L_f h$, and similarly for $L_f L_g h$. In general $L_g L_f h \neq L_f L_g h$. By convention, if $k = 0$, $L_f^k h = h$.

Example B.7 (Lie derivative)

Continuing Example B.1, consider the vector field (B.22) on \mathbb{R}^2 and define $h : \mathbb{R}^2 \rightarrow \mathbb{R}$ by $h(x_1, x_2) = x_1^2 + x_2^2 - 1$. Then

$$L_f h(x) = [2x_1, 2x_2] \begin{bmatrix} -x_2 \\ x_1 \end{bmatrix} \quad (\text{B.32a})$$

$$\equiv 0, \quad (\text{B.32b})$$

which means that h is constant along integral curves (i.e., solutions) of f , as is easily seen.

Definition B.8 (Lie bracket) Let M be a C^∞ , m -dimensional manifold, and let f and g be C^∞ vector fields on M . The Lie bracket of f and g is the vector field on M defined by

$$\forall p \in M, [f, g](p) := \frac{\partial g}{\partial x}(p)f(p) - \frac{\partial f}{\partial x}(p)g(p). \quad (\text{B.33})$$

Definition B.9 (Involutive distribution) Let M be a C^∞ , m -dimensional manifold. A distribution is a specification at each point of M of a subspace of $T_p M$; the distribution is commonly denoted $\Delta(p)$. The distribution Δ is constant dimensional if $\dim \Delta(p)$ does not vary with $p \in M$; it is C^∞ (or smooth) if about each $p \in M$ there exist $r > 0$ and a finite set of C^∞ vector fields X_1, \dots, X_k on $B_r(p) \cap M$ such that $\forall x \in B_r(p) \cap M$, $\Delta(x) =$

$\text{span}\{X_1(x), \dots, X_k(x)\}$. A vector field X belongs to Δ if $X(p) \in \Delta(p)$ for all $p \in M$. Finally, a C^∞ distribution Δ is involutive if X and Y belong to Δ , then so does their Lie bracket, $[X, Y]$.

A famous theorem of Frobenius states that if a C^∞ distribution is constant dimensional and involutive, then in the neighborhood of any point, there exists local coordinates in which the distribution can be expressed as the span of constant vector fields.

Example B.8 (Distribution)

Let $M = \mathbb{R}^3$ and consider the vector fields

$$X_1(x) = \begin{bmatrix} -x_2 \\ x_1 \\ 0 \end{bmatrix} \quad \text{and} \quad X_2(x) = \begin{bmatrix} x_1 \\ x_2 \\ x_1 x_3^2 \end{bmatrix}. \quad (\text{B.34})$$

Then,

$$[X_1, X_2](x) = \begin{bmatrix} 0 \\ 0 \\ -x_2 x_3^2 \end{bmatrix}. \quad (\text{B.35})$$

Define a distribution by $\Delta(x) = \text{span}\{X_1(x), X_2(x)\}$. Then the dimension of the distribution is easily checked to be two for all $x \neq 0$. However, the distribution is not involutive because for $x = (1, 1, 1)$, the vector field $[X_1, X_2](x) \notin \Delta(x)$. Indeed, $[X_1, X_2](x)$ is linearly independent of $X_1(x)$, $X_2(x)$ at the point $x = (1, 1, 1)$ because the matrix

$$\begin{bmatrix} -1 & 1 & 0 \\ 1 & 1 & 0 \\ 0 & 1 & -1 \end{bmatrix} \quad (\text{B.36})$$

has rank three.

B.2 Elementary Notions in Geometric Nonlinear Control

The objective of this section is to provide an elementary introduction to a few concepts in nonlinear geometric control, including the relative degree, the decoupling matrix, the zero dynamics, and static I-O linearization. For simplicity, it is assumed that the state space is an open subset of \mathbb{R}^n and that the system is C^∞ . Single-input single-output (SISO) control systems are

treated first and then the simplest multiple-input multiple-output (MIMO) extensions are noted.

B.2.1 SISO Nonlinear Affine Control System

Consider a SISO control system

$$\begin{aligned}\dot{x} &= f(x) + g(x)u \\ y &= h(x),\end{aligned}\tag{B.37}$$

defined on \mathcal{X} , an open subset of \mathbb{R}^n . It is assumed that the vector fields f and g are C^∞ and the output $h : \mathcal{X} \rightarrow \mathbb{R}$ is C^∞ . Because \dot{x} is affine in $u \in \mathbb{R}$, the system is said to be *affine*. Though not considered here, \mathcal{X} could in general be an n -dimensional manifold and (B.37) would be the representation of the control system in a local coordinate chart.

B.2.1.1 Relative Degree

The system (B.37) is said to have *relative degree* r at $x_0 \in \mathcal{X}$ if

- a) for all $0 \leq k < r - 1$, $L_g L_f^k h(x) = 0$ for all x in an open set about x_0 , and
- b) $L_g L_f^{r-1} h(x_0) \neq 0$.

The interpretation of this definition is the following. By the chain rule, the derivative of the output of (B.37) computed along a solution of the model is

$$\dot{y} = \frac{\partial h}{\partial x} (f + gu) = L_f h + L_g h u.\tag{B.38}$$

The relative degree is $r = 1$ if, and only if, $L_g h(x_0)$ is nonzero, which implies that the first derivative of the output is directly affected by the input, at least near x_0 . If however $L_g h \equiv 0$, then computing the second derivative gives

$$\ddot{y} = \frac{\partial L_f h}{\partial x} (f + gu) = L_f^2 h + L_g L_f h u.\tag{B.39}$$

The relative degree is then $r = 2$ if, and only if, $L_g L_f h(x_0)$ is nonzero, which implies that the second derivative of the output is directly affected by the input, etc.

Proposition B.2 (Independence Condition)

If (B.37) has relative degree r at x_0 , then on a neighborhood of x_0 , the functions $\{h, L_f h, \dots, L_f^{r-1} h\}$ are independent, that is,

$$\text{rank} \begin{bmatrix} \frac{\partial h}{\partial x}(x_0) \\ \frac{\partial L_f h}{\partial x}(x_0) \\ \vdots \\ \frac{\partial L_f^{r-1} h}{\partial x}(x_0) \end{bmatrix} = r. \quad (\text{B.40})$$

The above fact is proven in [127, Chap. 4] and shows in particular that if the relative degree at x_0 exists, then $r \leq n$.

B.2.1.2 Zero Dynamics

Suppose now that the relative degree of (B.37) exists at each point of \mathcal{X} and is constant, denoted r . Let $y^{(k)}(t) = \frac{d^k}{dt^k}y(t)$. Then,

$$y^{(r)} = L_f^r h + L_g L_f^{r-1} h u, \quad (\text{B.41})$$

and for all $x \in \mathcal{X}$, $L_g L_f^{r-1} h(x) \neq 0$. Define a state variable feedback $u^* : \mathcal{X} \rightarrow \mathbb{R}$ by

$$L_f^r h + L_g L_f^{r-1} h u^* \equiv 0, \quad (\text{B.42})$$

and set $f^* := f + g u^*$; that is, $\forall x \in \mathcal{X}$,

$$\begin{aligned} u^*(x) &:= -\frac{L_f^r h(x)}{L_g L_f^{r-1} h(x)} \\ f^*(x) &:= f(x) + g(x)u^*(x) = f(x) - g(x)\frac{L_f^r h(x)}{L_g L_f^{r-1} h(x)}. \end{aligned} \quad (\text{B.43})$$

The *zero dynamics manifold* is defined to be

$$\mathcal{Z} = \{x \in \mathcal{X} \mid h(x) = 0, \dots, L_f^{r-1} h(x) = 0\}. \quad (\text{B.44})$$

By Proposition B.2, when \mathcal{Z} is nonempty, it is a C^∞ , $(n - r)$ -dimensional embedded submanifold of \mathcal{X} . Indeed,

$$\mathcal{Z} = \{x \in \mathcal{X} \mid F(x) = 0\}, \quad (\text{B.45})$$

where

$$F = \begin{bmatrix} h \\ \vdots \\ L_f^{r-1} h \end{bmatrix}, \quad (\text{B.46})$$

and Proposition B.2 establishes the key rank condition of Definition B.1. By the definition of f^* , it follows that for all $0 \leq k \leq r$, $L_{f^*}^k h \equiv 0$, which implies that $\frac{\partial F}{\partial x} f^* \equiv 0$. It follows from Proposition B.1, therefore, that \mathcal{Z} is invariant under f^* . The restriction dynamics $f^*|_{\mathcal{Z}}$ is called the *zero dynamics* of (B.37).

When the dimension of \mathcal{Z} is at least one, it is interesting to develop this in local coordinates.

Proposition B.3 (Local Coordinates for the Zero Dynamics)

If (B.37) has relative degree $r < n$ at x_0 , then on a neighborhood of x_0 , there exist C^∞ functions $\{\phi_{r+1}, \dots, \phi_n\}$ such that

$$\text{rank} \begin{bmatrix} \frac{\partial h}{\partial x}(x_0) \\ \vdots \\ \frac{\partial L_f^{r-1} h}{\partial x}(x_0) \\ \frac{\partial \phi_{r+1}}{\partial x}(x_0) \\ \vdots \\ \frac{\partial \phi_n}{\partial x}(x_0) \end{bmatrix} = n \quad (\text{B.47})$$

and for $r + 1 \leq k \leq n$,

$$L_g \phi_k \equiv 0. \quad (\text{B.48})$$

The above fact is proven in [127, Chap. 4]. In the new coordinates (η, z) given by

$$\begin{bmatrix} \eta \\ z \end{bmatrix} = \begin{bmatrix} \eta_1 \\ \vdots \\ \eta_r \\ z_1 \\ \vdots \\ z_{n-r} \end{bmatrix} = \begin{bmatrix} h(x) \\ \vdots \\ L_f^{r-1} h(x) \\ \phi_{r+1}(x) \\ \vdots \\ \phi_n(x) \end{bmatrix} \quad (\text{B.49})$$

the zero dynamics manifold is given by

$$\mathcal{Z} = \{(\eta, z) \mid \eta = 0\}. \quad (\text{B.50})$$

Letting \tilde{f} (resp. \tilde{g} , \tilde{h}) denote f (resp. g , h) in the new coordinates, it can be

shown that (B.37) has the form

$$\frac{d}{dt} \begin{bmatrix} \eta_1 \\ \vdots \\ \eta_{r-1} \\ \eta_r \\ z_1 \\ \vdots \\ z_{n-r} \end{bmatrix} = \begin{bmatrix} \eta_2 \\ \vdots \\ \eta_r \\ \tilde{f}_r(\eta, z) \\ \tilde{f}_{r+1}(\eta, z) \\ \vdots \\ \tilde{f}_n(\eta, z) \end{bmatrix} + \begin{bmatrix} 0 \\ \vdots \\ 0 \\ \tilde{g}_r(\eta, z) \\ 0 \\ \vdots \\ 0 \end{bmatrix} u \quad (\text{B.51})$$

$$y = \tilde{h}(\eta, z) = \eta_1.$$

Letting \tilde{f}^* denote f^* in the new coordinates, it follows that

$$\tilde{f}^*(\eta, z) = \begin{bmatrix} \eta_2 \\ \vdots \\ \eta_r \\ 0 \\ \tilde{f}_{r+1}(\eta, z) \\ \vdots \\ \tilde{f}_n(\eta, z) \end{bmatrix}, \quad (\text{B.52})$$

which gives

$$\tilde{f}^*|_{\mathcal{Z}}(z) = \begin{bmatrix} \tilde{f}_{r+1}(0, z) \\ \vdots \\ \tilde{f}_n(0, z) \end{bmatrix}. \quad (\text{B.53})$$

Remark B.3 Without the condition (B.48), then (B.51) becomes

$$\frac{d}{dt} \begin{bmatrix} \eta_1 \\ \vdots \\ \eta_{r-1} \\ \eta_r \\ z_1 \\ \vdots \\ z_{n-r} \end{bmatrix} = \begin{bmatrix} \eta_2 \\ \vdots \\ \eta_r \\ \tilde{f}_r(\eta, z) \\ \tilde{f}_{r+1}(\eta, z) \\ \vdots \\ \tilde{f}_n(\eta, z) \end{bmatrix} + \begin{bmatrix} 0 \\ \vdots \\ 0 \\ \tilde{g}_r(\eta, z) \\ \tilde{g}_{r+1}(\eta, z) \\ \vdots \\ \tilde{g}_n(\eta, z) \end{bmatrix} u \quad (\text{B.54})$$

$$y = \tilde{h}(\eta, z) = \eta_1,$$

and then, using (B.43), (B.53) becomes

$$\tilde{f}^*|_{\mathcal{Z}}(z) = \begin{bmatrix} \tilde{f}_{r+1}(0, z) \\ \vdots \\ \tilde{f}_n(0, z) \end{bmatrix} - \begin{bmatrix} \tilde{g}_{r+1}(0, z) \\ \vdots \\ \tilde{g}_n(0, z) \end{bmatrix} \frac{\tilde{f}_r(0, z)}{\tilde{g}_r(0, z)}. \quad (\text{B.55})$$

B.2.1.3 Input-Output Linearization

Consider the SISO affine system (B.37) and suppose that its relative degree r exists at each point of \mathcal{X} and is constant, so that (B.41) holds everywhere on \mathcal{X} . Applying the state variable feedback

$$u = \frac{1}{L_g L_f^{r-1} h} (-L_f^r h + v), \quad (\text{B.56})$$

$v \in \mathbb{R}$, results in

$$y^{(r)} = v. \quad (\text{B.57})$$

The system (B.37) has been *input-output linearized*. Taking $v = -k_{r-1} L_f^{r-1} h - \dots - k_1 L_f h - k_0 h$, that is,

$$u = \frac{1}{L_g L_f^{r-1} h} \left(-L_f^r h - k_{r-1} L_f^{r-1} h - \dots - k_1 L_f h - k_0 h \right), \quad (\text{B.58})$$

results in

$$y^{(r)} + k_{r-1} y^{(r-1)} + \dots + k_0 y = 0. \quad (\text{B.59})$$

To understand the effect of this feedback on the evolution of the state of the system, apply (B.58) to (B.51), yielding

$$\frac{d}{dt} \begin{bmatrix} \eta_1 \\ \vdots \\ \eta_{r-1} \\ \eta_r \\ z_1 \\ \vdots \\ z_{n-r} \end{bmatrix} = \begin{bmatrix} \eta_2 \\ \vdots \\ \eta_r \\ -k_0\eta_1 - \cdots - k_{r-1}\eta_r \\ \tilde{f}_{r+1}(\eta, z) \\ \vdots \\ \tilde{f}_n(\eta, z) \end{bmatrix}. \quad (\text{B.60})$$

Hence, if the coefficients k_{r-1}, \dots, k_0 are assigned so that $y(t)$ asymptotically tends to zero, then $\eta_1(t)$ through $\eta_r(t)$ asymptotically tend to zero and the state “converges” to a solution of the zero dynamics.

Regular feedback: A state variable feedback of the form

$$u = \alpha(x) + \beta(x)v, \quad (\text{B.61})$$

$v \in \mathbb{R}$, is *regular* for (B.37) if $\forall x \in \mathcal{X}, \beta(x) \neq 0$. The closed-loop system is denoted

$$\begin{aligned} \dot{x} &= f_{cl}(x) + g_{cl}(x)v \\ y &= h(x), \end{aligned} \quad (\text{B.62})$$

where

$$\begin{aligned} f_{cl}(x) &= f(x) + g(x)\alpha(x) \\ g_{cl}(x) &= g(x)\beta(x). \end{aligned} \quad (\text{B.63})$$

A regular state variable feedback does not change the relative degree of an output. Indeed, the following is true:

Proposition B.4 (Feedback and Relative Degree)

Suppose that (B.37) has relative degree r at x_0 . Then in a neighborhood of x_0 , for all $1 \leq k < r$, $L_{g_{cl}}^k h(x) = L_f^k h(x)$ and

$$L_{g_{cl}} L_{f_{cl}}^k h(x) = \begin{cases} 0 & k \leq r-2 \\ L_g L_f^{(r-1)} h(x) \beta(x) & k = r-1. \end{cases} \quad (\text{B.64})$$

Hence, if the feedback is regular, (B.37) and (B.62) have the same relative degree.

B.2.2 MIMO Nonlinear Affine Control System

This section quickly summarizes elementary extensions of Appendix B.2.1 to the case of *square nonlinear systems*, that is, systems with the same number of inputs as outputs. In general, dynamic state variable feedbacks are useful for understanding the zero dynamics and for achieving input-output linearization of MIMO systems. Here, we will limit ourselves to a particular case where static feedback is sufficient, namely, an invertible decoupling matrix will be assumed.

Consider a square MIMO affine control system

$$\begin{aligned}\dot{x} &= f(x) + \sum_{i=1}^m g_i(x)u_i \\ y &= \begin{bmatrix} h_1(x) \\ \vdots \\ h_m(x) \end{bmatrix}\end{aligned}\tag{B.65}$$

defined on \mathcal{X} , an open subset of \mathbb{R}^n . It is assumed that the vector fields f and g_i , $1 \leq i \leq m$, are C^∞ and the output functions $h_i : \mathcal{X} \rightarrow \mathbb{R}$, $1 \leq i \leq m$, are C^∞ . Because \dot{x} is affine in $u_i \in \mathbb{R}$, the system is said to be *affine*. Though not considered here, \mathcal{X} could in general be an n -dimensional manifold and (B.65) would be the representation of the control system in a local coordinate chart. For brevity, affine control systems are often denoted simply by

$$\begin{aligned}\dot{x} &= f(x) + g(x)u \\ y &= h(x),\end{aligned}\tag{B.66}$$

where

$$g(x) = [g_1(x), \dots, g_m(x)],\tag{B.67}$$

and

$$h(x) = \begin{bmatrix} h_1(x) \\ \vdots \\ h_m(x) \end{bmatrix}, \quad u = \begin{bmatrix} u_1 \\ \vdots \\ u_m \end{bmatrix}, \quad y = \begin{bmatrix} y_1 \\ \vdots \\ y_m \end{bmatrix}.\tag{B.68}$$

B.2.2.1 Vector Relative Degree

The system (B.65) is said to have *vector relative degree* (r_1, \dots, r_m) at $x_0 \in \mathcal{X}$ if

- a) for all $1 \leq j \leq m$, $1 \leq i \leq m$, $0 \leq k < r_i - 1$,

$$L_{g_j} L_f^k h_i(x) = 0\tag{B.69}$$

for all x in an open set about x_0 , and

b) the $m \times m$ -matrix (called the *decoupling matrix*)

$$A(x) = \begin{bmatrix} L_{g_1} L_f^{r_1-1} h_1(x) & \cdots & L_{g_m} L_f^{r_1-1} h_1(x) \\ \vdots & \ddots & \vdots \\ L_{g_1} L_f^{r_m-1} h_m(x) & \cdots & L_{g_m} L_f^{r_m-1} h_m(x) \end{bmatrix} \quad (\text{B.70})$$

is nonsingular at x_0 .

For each component of the output of (B.65), the interpretation of this definition is similar to the SISO case; in particular, r_i is the lowest derivative of y_i that is directly affected by at least one of the input components:

$$y_i^{(r_i)} = L_f^{r_i} h_i(x) + L_{g_1} L_f^{r_i-1} h_i(x) u_1 + \cdots + L_{g_m} L_f^{r_i-1} h_i(x) u_m, \quad (\text{B.71})$$

and at least one of the terms $L_{g_j} L_f^{r_i-1} h_i$ is nonzero at x_0 . Hence, the r_i are the natural notion of a relative degree defined line-by-line. Writing this out in vector form gives

$$\begin{bmatrix} y_1^{(r_1)} \\ \vdots \\ y_m^{(r_m)} \end{bmatrix} = \begin{bmatrix} L_f^{r_1} h_1(x) \\ \vdots \\ L_f^{r_m} h_m(x) \end{bmatrix} + A(x)u. \quad (\text{B.72})$$

Remark B.4 In general, the decoupling matrix will not be invertible at x_0 . It is emphasized that when the decoupling matrix is not invertible at x_0 , the vector relative degree is not defined at x_0 . When the decoupling matrix is singular, a dynamic feedback is often useful for input-output linearization and other feedback control problems. This topic is not treated here.

Proposition B.5 (Independence Condition (MIMO))

If (B.65) has a vector relative degree (r_1, \dots, r_m) at x_0 , then on a neighborhood of x_0 , the functions $\{h_1, \dots, L_f^{r_1-1} h_1, \dots, h_m, \dots, L_f^{r_m-1} h_m\}$ are independent, that is,

$$\text{rank} \begin{bmatrix} \frac{\partial h_1}{\partial x}(x_0) \\ \vdots \\ \frac{\partial L_f^{r_1-1} h_1}{\partial x}(x_0) \\ \vdots \\ \frac{\partial h_m}{\partial x}(x_0) \\ \vdots \\ \frac{\partial L_f^{r_m-1} h_m}{\partial x}(x_0) \end{bmatrix} = r_1 + \cdots + r_m. \quad (\text{B.73})$$

The above fact is proven in [127, Chap. 5] and shows in particular that if the vector relative degree at x_0 exists, then $r_1 + \dots + r_m \leq n$.

B.2.2.2 Zero Dynamics

Suppose now (B.65) has a vector relative degree at each point of \mathcal{X} and that the vector relative degree is constant and equal to (r_1, \dots, r_m) . Then,

$$\begin{bmatrix} y_1^{(r_1)} \\ \vdots \\ y_m^{(r_m)} \end{bmatrix} = \begin{bmatrix} L_f^{r_1} h_1 \\ \vdots \\ L_f^{r_m} h_m \end{bmatrix} + Au, \quad (\text{B.74})$$

and for all $x \in \mathcal{X}$, $A(x)$ is invertible. Define a state variable feedback $u^* : \mathcal{X} \rightarrow \mathbb{R}^m$ by

$$\begin{bmatrix} L_f^{r_1} h_1 \\ \vdots \\ L_f^{r_m} h_m \end{bmatrix} + Au^* \equiv 0, \quad (\text{B.75})$$

and set $f^* := f + gu^*$; that is, $\forall x \in \mathcal{X}$,

$$u^*(x) := -A(x)^{-1} \begin{bmatrix} L_f^{r_1} h_1(x) \\ \vdots \\ L_f^{r_m} h_m(x) \end{bmatrix} \quad (\text{B.76})$$

$$f^*(x) := f(x) + g(x)u^*(x).$$

The *zero dynamics manifold* is defined to be

$$\mathcal{Z} = \{x \in \mathcal{X} \mid h_1(x) = 0, \dots, L_f^{r_1-1} h_1(x) = 0, \dots, h_m(x) = 0, \dots, L_f^{r_m-1} h_m(x) = 0\}. \quad (\text{B.77})$$

By Proposition B.5, when \mathcal{Z} is nonempty, it is a C^∞ , $(n - r)$ -dimensional embedded submanifold of \mathcal{X} , where $r = r_1 + \dots + r_m$, and just as in the case of SISO systems, \mathcal{Z} is invariant under f^* . The restriction dynamics $f^*|_{\mathcal{Z}}$ is called the *zero dynamics* of (B.65).

When the dimension of \mathcal{Z} is at least one, it is interesting to develop this in local coordinates.

Proposition B.6 (Local Coordinates for the Zero Dynamics (MIMO))

If (B.65) has vector relative degree (r_1, \dots, r_m) at x_0 , and $r = r_1 + \dots + r_m < n$, then on a neighborhood of x_0 , there exist C^∞ functions $\{\phi_{r+1}, \dots, \phi_n\}$ such

that

$$\text{rank} \begin{bmatrix} \frac{\partial \eta_1}{\partial x}(x_0) \\ \vdots \\ \frac{\partial \eta_m}{\partial x}(x_0) \\ \frac{\partial \phi_{r+1}}{\partial x}(x_0) \\ \vdots \\ \frac{\partial \phi_n}{\partial x}(x_0) \end{bmatrix} = n, \quad (\text{B.78})$$

where

$$\eta_j = \begin{bmatrix} \eta_{j,1} \\ \vdots \\ \eta_{j,r_j} \end{bmatrix} = \begin{bmatrix} h_j \\ \vdots \\ L_f^{r_j-1} h_j \end{bmatrix}. \quad (\text{B.79})$$

Moreover, if the distribution $\text{span}\{g_1, \dots, g_m\}$ is involutive⁴ in a neighborhood of x_0 , then it is possible to choose the additional functions such that for $r+1 \leq k \leq n$, $1 \leq j \leq m$

$$L_{g_j} \phi_k \equiv 0. \quad (\text{B.80})$$

In the new coordinates $(\eta; z)$ defined by

$$\eta = \begin{bmatrix} \eta_1 \\ \vdots \\ \eta_m \end{bmatrix}, \quad z = \begin{bmatrix} \phi_{r+1} \\ \vdots \\ \phi_n \end{bmatrix}, \quad (\text{B.81})$$

the zero dynamics manifold is given by

$$\mathcal{Z} = \{(\eta; z) \mid \eta = 0\}, \quad (\text{B.82})$$

whether or not the involutivity condition holds, and hence whether or not the coordinates satisfy (B.80). However, without the involutivity condition, the determination of the zero dynamics becomes considerably more complicated, just as in (B.55). When (B.80) is not met, see [127, Chap. 5].

Assume therefore that (B.80) holds. Let \tilde{f}^* (resp. \tilde{f}) denote f^* (resp. f) in

⁴The invertibility of the decoupling matrix implies that the distribution has constant dimension.

the new coordinates. It can be shown that that

$$\tilde{f}^*(\eta, z) = \begin{bmatrix} \tilde{f}_1^*(\eta_1) \\ \vdots \\ \tilde{f}_m^*(\eta_m) \\ \tilde{f}_{r+1}(\eta, z) \\ \vdots \\ \tilde{f}_r(\eta, z) \end{bmatrix}, \quad (\text{B.83})$$

where

$$\tilde{f}_j^*(\eta_j) = \begin{bmatrix} \eta_{j,2} \\ \vdots \\ \eta_{j,r_j} \\ 0 \end{bmatrix}. \quad (\text{B.84})$$

Hence,

$$\tilde{f}^*|_{\mathcal{Z}}(z) = \begin{bmatrix} \tilde{f}_{r+1}(0, z) \\ \vdots \\ \tilde{f}_r(0, z) \end{bmatrix}, \quad (\text{B.85})$$

just as in the SISO case.

B.2.2.3 Input-Output Linearization

Consider the MIMO affine system (B.65) and suppose that it has a vector relative degree at each point of \mathcal{X} that it is constant and equal to (r_1, \dots, r_m) , so that (B.74) holds everywhere on \mathcal{X} , with the decoupling matrix being invertible. Applying the state variable feedback

$$u = A^{-1}(x) \left(v - \begin{bmatrix} L_f^{r_1} h_1 \\ \vdots \\ L_f^{r_m} h_m \end{bmatrix} \right), \quad (\text{B.86})$$

with $v \in \mathbb{R}^m$, results in

$$\begin{bmatrix} y_1^{(r_1)} \\ \vdots \\ y_m^{(r_m)} \end{bmatrix} = \begin{bmatrix} v_1 \\ \vdots \\ v_m \end{bmatrix}. \quad (\text{B.87})$$

The system (B.65) has been *input-output linearized*. If v is then chosen so that $y(t)$ asymptotically tends to zero, the state of the closed-loop system “converges” to the zero dynamics. Note that when $v = 0$, (B.86) corresponds to u^* .

Regular feedback: A state variable feedback of the form

$$u = \alpha(x) + \beta(x)v, \quad (\text{B.88})$$

$v \in \mathbb{R}^m$, is *regular* for (B.65) if $\forall x \in \mathcal{X}$, $\det(\beta(x)) \neq 0$. The closed-loop system is denoted

$$\begin{aligned} \dot{x} &= f_{cl}(x) + g_{cl}(x)v \\ y &= h(x), \end{aligned} \quad (\text{B.89})$$

where

$$\begin{aligned} f_{cl}(x) &= f(x) + g(x)\alpha(x) \\ g_{cl}(x) &= g(x)\beta(x). \end{aligned} \quad (\text{B.90})$$

A regular state variable feedback does not modify the vector relative degree of an output. Indeed, the following is true:

Proposition B.7 (Feedback and Vector Relative Degree)

Suppose that (B.65) has vector relative degree (r_1, \dots, r_m) at x_0 . Then in a neighborhood of x_0 ,

- a) for all $1 \leq j \leq m$, $1 \leq i \leq m$, $0 \leq k < r_i - 1$,

$$L_{g_{cl,j}} L_{f_{cl}}^k h_i(x) = 0, \quad (\text{B.91})$$

and

- b) the $m \times m$ decoupling matrix of the closed-loop system satisfies

$$A_{cl}(x) := \begin{bmatrix} L_{g_{cl,1}} L_{f_{cl}}^{r_1-1} h_1(x) & \cdots & L_{g_{cl,m}} L_{f_{cl}}^{r_1-1} h_1(x) \\ \vdots & \ddots & \vdots \\ L_{g_{cl,1}} L_{f_{cl}}^{r_m-1} h_m(x) & \cdots & L_{g_{cl,m}} L_{f_{cl}}^{r_m-1} h_m(x) \end{bmatrix} = A(x)\beta(x). \quad (\text{B.92})$$

Hence, if the feedback is regular, the decoupling matrix of (B.65) is invertible if, and only if, the decoupling matrix of (B.89) is invertible, and in this case, the two systems have the same vector relative degree.

B.3 Poincaré's Method of Determining Limit Cycles

The method of Poincaré sections and return maps is widely used to determine the existence and stability of periodic orbits in a broad range of system models, such as time-invariant and periodically-time-varying ordinary differential

equations [102, 173], hybrid systems consisting of several time-invariant ordinary differential equations linked by event-based switching mechanisms and reinitialization rules [98, 167], differential-algebraic equations [115], and relay systems with hysteresis [91], to name just a few. While the analytical details may vary significantly from one class of models to another, on a conceptual level, the method of Poincaré is consistent and straightforward: sample the solution of a system according to an event-based or time-based rule, and then evaluate the stability properties of equilibrium points (also called fixed points) of the sampled system, which is called the Poincaré return map. Fixed points of the Poincaré map correspond⁵ to *periodic orbits* of the underlying system. Roughly speaking, if the solutions of the underlying system depend continuously on the initial conditions, then equilibrium points of the Poincaré map are stable (asymptotically stable) if, and only if, the corresponding orbit is stable (asymptotically stable), and if the solutions are Lipschitz continuous in the initial conditions, then the equivalence extends to exponential stability.

This section provides an informal understanding of Poincaré's method for determining the existence and stability properties of periodic solutions of differential equations. While the method is applicable to ordinary differential equations in \mathbb{R}^n , here, the essential ideas are illustrated on a time-invariant system in the plane.

Consider the *van der Pol oscillator*

$$\begin{aligned}\dot{x}_1 &= x_2 \\ \dot{x}_2 &= -x_1 + \epsilon(1 - x_1^2)x_2\end{aligned}\tag{B.93}$$

evolving on \mathbb{R}^2 . This equation is well known to have a limit cycle.⁶ For $\epsilon = +1$, the limit cycle is asymptotically stable and for $\epsilon = -1$, the limit cycle is unstable; see Fig. B.4. These facts can be verified by simulation, or more systematically, through the method of Poincaré sections.

B.3.1 Poincaré Return Map

The method of Poincaré sections provides a systematic method for testing whether or not a limit cycle exists in a given region of state space. In the case of the van der Pol oscillator, suppose we suspect that a limit cycle passes through the x_2 -axis for⁷ $1 < x_2 < 3$. Define a hyper surface $\mathcal{S} := \{(x_1; x_2) \in \mathbb{R}^2 \mid x_1 = 0, 1 < x_2 < 3\}$, as depicted in Fig. B.4(a); \mathcal{S} is called a *Poincaré section*. The *Poincaré return map* $P : \mathcal{S} \rightarrow \mathcal{S}$ is constructed as follows: take a point $x \in \mathcal{S}$ and view it as an initial condition for the van der Pol oscillator.

⁵Fixed points of $P^k = P \circ \dots \circ P$ k -times also correspond to periodic orbits. The associated analysis problems for $k > 1$ are essentially the same as for $k = 1$ and are not discussed here.

⁶There is no known closed form expression for the limit cycle. Asymptotically exact approximations are discussed in [138].

⁷The Poincaré section could be taken as $(0, \infty)$, of course. However, since in general the map must be computed numerically, in practice, one often starts with a smaller choice.

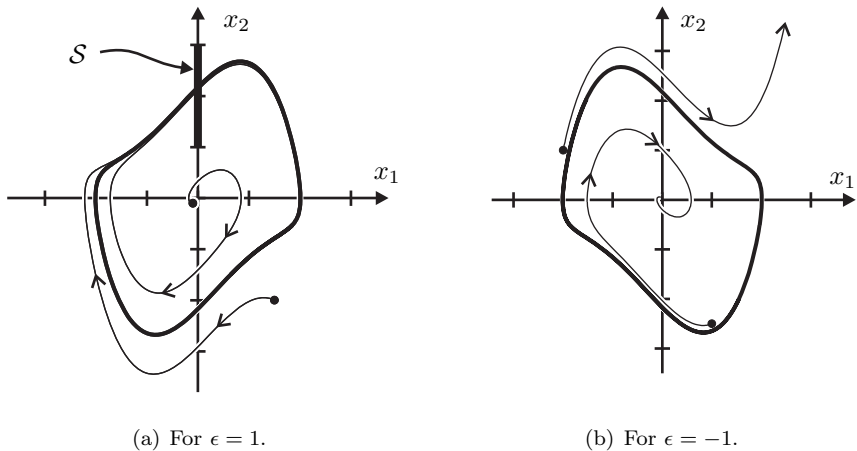


Figure B.4. Limit cycles in a van der Pol oscillator. The initial conditions are indicated by dots. In (a), for all initial conditions except the origin, the solution converges to the limit cycle and one says the limit cycle is asymptotically stable. In (b), the solutions diverge from the limit cycle, and one says the limit cycle is unstable. One possible choice for a Poincaré section is shown in (a).

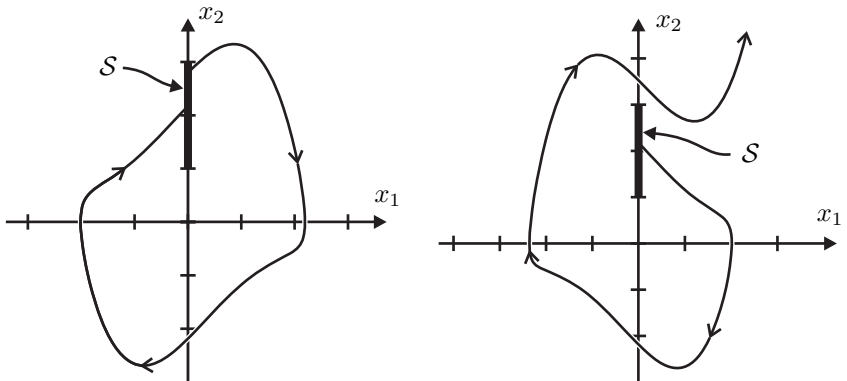
Suppose the resulting solution $\phi(t, x)$ eventually intersects \mathcal{S} (on the opposite side) for the first time at $t = T_I(x)$. Then the Poincaré map is defined to be $P(x) := \phi(T_I(x), x)$. If, on the other hand, the solution never intersects \mathcal{S} , then the Poincaré map is not well defined at that point. These cases are illustrated in Fig. B.5.

B.3.2 Fixed Points and Periodic Orbits

A point $x^* \in \mathcal{S}$ such that $P(x^*) = x^*$ is called a *fixed point*. By the definition of P , this means that when (B.93) is initialized at x^* , the solution returns to x^* in $T_I(x^*)$ seconds, meaning the solution $\phi(t, x^*)$ is periodic with period $T = T_I(x^*)$. The set of points in the plane traced out by the periodic solution is called the *periodic orbit*, or less formally, the *limit cycle*. We see that there is a one-to-one correspondence of fixed points of the Poincaré map and periodic orbits. Indeed, fixed points correspond to the intersection of the periodic orbit with \mathcal{S} , or, said another way, fixed points correspond to initial conditions on \mathcal{S} for which the corresponding solution of the van der Pol oscillator traces out a periodic orbit.

Since $x \in \mathcal{S}$ always has $x_1 = 0$, the Poincaré return map can be written as

$$P : \begin{bmatrix} 0 \\ x_2 \end{bmatrix} \rightarrow \begin{bmatrix} 0 \\ P_2(x_2) \end{bmatrix}. \quad (\text{B.94})$$



(a) A point at which the return map is well defined: a solution of the differential equation exists that starts on one side of \mathcal{S} and ends on the opposite side.

(b) A point at which the return map is not well defined: a solution of the differential equation initialized on \mathcal{S} never intersects \mathcal{S} again.

Figure B.5. Defining the Poincaré return map.

Thus, finding a fixed point is equivalent to finding x_2^* such that $x_2^* = P_2(x_2^*)$; this is the same as the graph of P_2 crossing the graph of the identity function, $x_2 \rightarrow x_2$. Figures B.6 and B.7 depicts plots of the Poincaré return map of the van der Pol oscillator for $\epsilon = \pm 1$, and shows the associated fixed points.

Take a point $x_0 \in \mathcal{S}$ and use it as an initial condition of the van der Pol oscillator. Consider the resulting solution, $\phi(t, x_0)$, and denote by t_1 the time of its first intersection with \mathcal{S} , and in general, by t_k the time of its k -th intersection with \mathcal{S} ; see Fig. B.8. Denote the point in \mathcal{S} at which the solution impacted at time t_k by $x[k] := x(t_k) := \phi(t_k, x_0)$. Then by definition of the Poincaré map, $x[k+1] = P(x[k])$, which is a discrete-time system that evolves on the Poincaré section, \mathcal{S} . Since x_1 is constant on \mathcal{S} , the discrete-time system on \mathcal{S} is equivalent to the scalar discrete-time system $x_2[k+1] = P_2(x_2[k])$ on the interval $(1, 3) \subset \mathbb{R}$; see (B.94). Analyzing the stability of this later equation is straightforward on the basis of the graphs in Figs. B.6 and B.7. Consider first Fig. B.6, and take an initial point $x_2[0]$ to the left of x_2^* . Then $x_2[0] < x_2[1] = P_2(x_2[0]) < x_2^*$. By induction, $x_2[k] < x_2[k+1] = P_2(x_2[k]) < x_2^*$. Hence, the sequence $x_2[k]$ is monotonically increasing and bounded from above, and thus has a limit point that is, moreover, a fixed point of P_2 . Since inspection of Fig. B.6 shows there is only one fixed point, $\lim_{k \rightarrow \infty} x_2[k] = x_2^*$. The same argument can be repeated for $x_2[0]$ to the right of x_2^* , and hence x_2^* is an attractive equilibrium point of $x_2[k+1] = P_2(x_2[k])$, and because the convergence is monotonic, it is also stable in the sense of Lyapunov. Therefore, x_2^* is an asymptotically stable equilibrium point of $x_2[k+1] = P_2(x_2[k])$, in agreement with the phase portrait shown in Fig. B.4(a).

Consider next Fig. B.7, and take any point x_2 to the right of x_2^* . Then

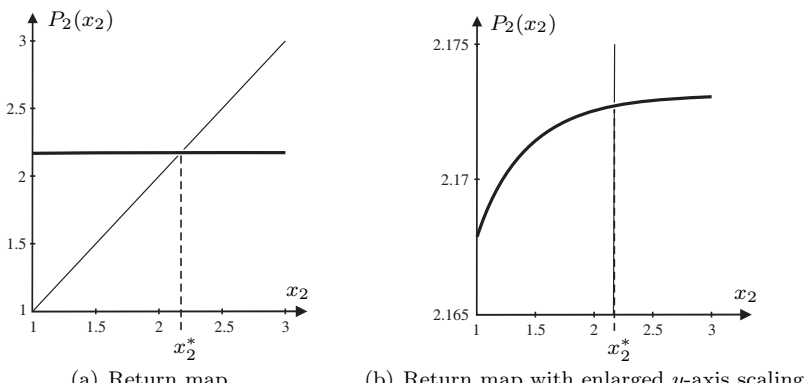


Figure B.6. Poincaré return map for the van der Pol oscillator (thick lines) with an asymptotically stable limit cycle. A fixed point corresponds to the intersection of the Poincaré map with the identity map (thin lines) and is denoted by x_2^* . Since the x_1 component is constant on the Poincaré section, the actual fixed point is $x^* = (0; x_2^*)$. The return map is shown in (a) and (b) with different scales, due to the very rapid convergence of the van der Pol oscillator for $\epsilon = +1$.

$x_2^* < x_2 < P_2(x_2)$ easily follows, which leads to the estimate $|P(x_2) - x_2^*| > |x_2 - x_2^*|$. Hence the equilibrium point is unstable, in agreement with the phase portrait shown in Fig. B.4(b).

In summary, the Poincaré return map $P : \mathcal{S} \rightarrow \mathcal{S}$ converts the problem of finding limit cycles (i.e., periodic orbits) of the van der Pol differential equation into one of finding equilibrium points for a discrete-time system evolving on the Poincaré section, namely, $x[k+1] = P(x[k])$, $x[0] \in \mathcal{S}$. Since the Poincaré section is a hyper surface, it has dimension one less than the dimension of the state space of the differential equation. In addition, the stability of the limit cycle can be determined by the analyzing the stability of the corresponding equilibrium point, $x^* = P(x^*)$. In the particular case of the van der Pol equation, this meant that the existence and stability of a limit cycle could be determined by analyzing a scalar map.

B.3.3 Utility of the Poincaré Return Map

Computing the return map requires the solution of the differential equation, for which numerical computations are needed, that is, numerical simulations of the differential equation. So why even bother with the method of Poincaré sections? Why not just simulate the differential equation to find the limit cycle? Mathematical rigor is always a good reason. The method of Poincaré sections provides necessary and sufficient conditions for the existence of asymptotically stable periodic orbits. Nevertheless, in the planar case, the practical advan-

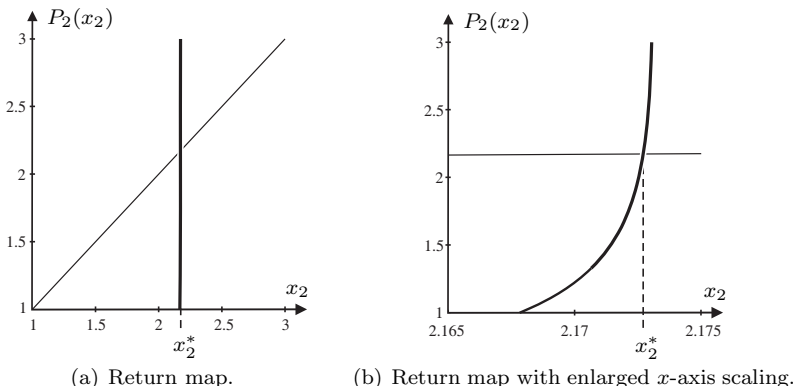


Figure B.7. Poincaré return map for the van der Pol oscillator (thick lines) with an unstable stable limit cycle. A fixed point corresponds to the intersection of the Poincaré map with the identity map (thin lines) and is denoted by x_2^* . Since the x_1 component is constant on the Poincaré section, the actual fixed point is $x^* = (0; x_2^*)$. The return map is shown in (a) and (b) with different scales, due to the very rapid divergence of the van der Pol oscillator for $\epsilon = -1$.

tages of the Poincaré return map are sometimes hard to see. Clearly, finding the asymptotically stable limit cycle of the van der Pol equation for $\epsilon = +1$ is very easy to do with a simulation because the limit cycle is “globally” attractive in the sense that the solution for every nonzero initial condition converges to it. No matter how disorganized your search is, you can’t help but find the limit cycle! When $\epsilon = -1$, with probability one, random initialization and forward simulation will never find the unstable limit cycle, whereas Poincaré’s method works in this case with no more difficulty than in the (stable) case of $\epsilon = +1$. This appears to be a plus for Poincaré’s method. However, since a simple time-reversal renders the unstable limit cycle stable, the advantage of Poincaré’s method for the van der Pol equation is still debatable.

Therefore, other than mathematical rigor, why bother with the method of Poincaré sections? If the rate of convergence to a limit cycle is slow, if the domain of attraction is small, or if the goal is to establish that a system does not possess a limit cycle in a given region of its state space, then, even in the case of planar systems, Poincaré’s method is superior to brute force simulation with random initialization. The power of Poincaré’s method is more evident in higher-dimensional systems of differential equations because it suggests bringing in additional numerical tools to the problem of finding periodic orbits and determining if they are stable. As shown in Fig. B.9, Poincaré’s method is conceptually unchanged by increasing the dimension of the system: the Poincaré section \mathcal{S} is defined by placing a hyper surface transversal to a suspected periodic orbit, and the Poincaré return map P :

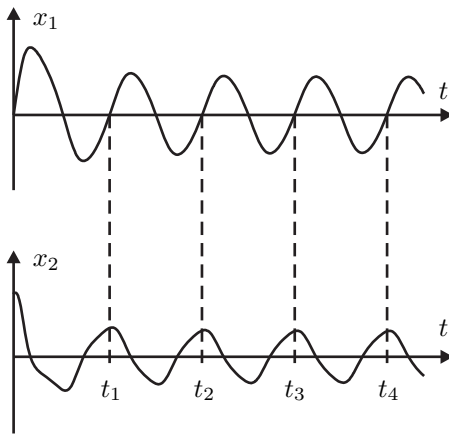


Figure B.8. Sequence of impact times, $\{t_k\}_{k=1}^{\infty}$. When used as event-based sampling times of the solution of the van der Pol oscillator, they generate a discrete-time system on \mathcal{S} , denoted $x[k+1] = P(x[k])$, where $x[k] := x(t_k) := \phi(t_k, x_0)$.

$\mathcal{S} \rightarrow \mathcal{S}$ is defined by initializing the differential equation in \mathcal{S} and following the resulting solution until its first intersection with \mathcal{S} on the opposite side; if no such intersection occurs, the Poincaré return map is not defined at that point. Since periodic orbits of the differential equation correspond to fixed points of the Poincaré map, they correspond to finding roots of $P(x) - x = 0$, a problem for which many numerical algorithms exist. Applying a Newton-Raphson algorithm to the Poincaré return map can significantly accelerate the search for periodic orbits. Once a fixed point has been found, the equivalence between fixed points and equilibrium points of the discrete-time system $x[k+1] = P(x[k])$, $x[0] \in \mathcal{S}$, can be exploited to test for stability or instability of an

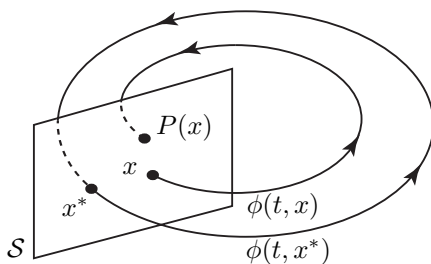


Figure B.9. Geometric interpretation of a Poincaré return map $P : \mathcal{S} \rightarrow \mathcal{S}$ for an ordinary differential equation (nonhybrid) as event-based sampling of the solution near a periodic orbit. The Poincaré section, \mathcal{S} , may be any hyper (codimension one) C^1 -surface that is transversal to the periodic orbit.

orbit by analyzing the eigenvalues of the Jacobian linearization about the equilibrium. Practical numerical algorithms for these computations are one of the subjects of the book [173].

All of these ideas have been applied to the problem of finding stable walking motions in bipeds. The most significant success stories have clearly been in passive robots (i.e., no actuators) [74, 93, 115, 118, 228], particularly, the surprising discovery of asymptotically stable limit cycles in a three-dimensional passive bipedal robot [59]. So far, there are only a few reported cases where Poincaré’s method has been used as a basis for tuning controller parameters so as to create an asymptotically stable limit cycle in an actuated bipedal robot [143, 169, 170].

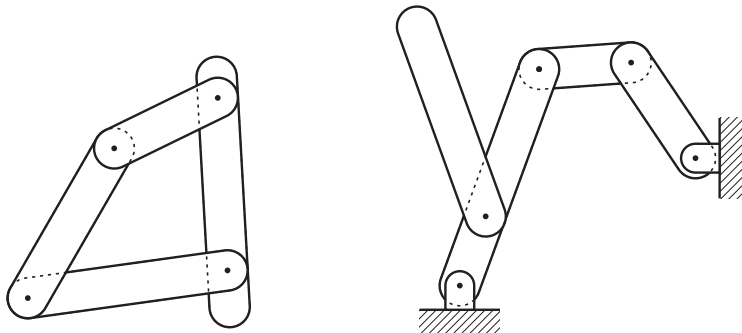
B.4 Planar Lagrangian Dynamics

This section provides a very selective overview of Lagrangian dynamics as used to compute dynamic models of planar bipedal robots. Much more general treatments are available in most textbooks dealing with robotic manipulator dynamics and some recent monographs on model-based animation of human figures. The topics reviewed include open versus closed kinematic chains, computing the kinetic and potential energies of a single link and multiple links in common situations, absolute versus relative angles, generalized coordinates, the Lagrangian and Lagrange’s equation (also called the Euler-Lagrange equation), angular momentum, body coordinates, shape variables, cyclic coordinates, and holonomic constraints. Familiarity with center of mass and moment of inertia is assumed; see [Appendix B.4.10](#) and [Appendix D](#).

B.4.1 Kinematic Chains

The robots treated in this book will be modeled as connections of rigid links through revolute joints, with all links lying in a common plane and the axes of rotation of the joints being normal to the plane. Each joint connects two links and only two links. If $m > 2$ links are connected at a common point, then the connection uses $m - 1$ joints. In this review of mechanics, each joint is further assumed to be *ideal*, meaning that the connection is rigid⁸ and frictionless. Finally, links are implicitly assumed to be *noninterfering*, meaning that, magically, individual links can assume arbitrary positions and orientations without contacting one another. Mechanisms can be designed to be noninterfering, cf. [RABBIT](#) or [ERNIE](#) in Chapter 2.

⁸That is, the joint is not flexible as is the case, for example, in robots with actuator transmission compliance.



(a) The closed-loop involves only links.

(b) The loop involves the inertial frame through the two pivots.

Figure B.10. Closed kinematic chains.

A collection of links is called a *kinematic chain* if it cannot be separated into two disjoint sets of links without a common joint. A kinematic chain is *open* if it does not contain any loops. As in Fig. B.10, if at least one link in the chain is connected to a rigid base called the ground, then the ground must be included when determining if a chain contains a loop or not. A loop is also called a *closed kinematic chain*. Recalling our convention that a joint can connect only two links, an open kinematic chain with N links has $N - 1$ joints. An open kinematic chain is called a *serial chain* if each link has at most two joints and the joints are not colocated; otherwise, it is a *tree structure*; see Fig. B.11.

A *pivot* is an ideal revolute joint whose axis of revolution has a fixed position with respect to the inertial frame; in other words, it functions as a base. A kinematic chain where exactly one link is connected to a pivot is said to be *pinned*; see Fig. B.11. In a tree structure, the pivot may be colocated with a revolute joint of the chain. If no point on a kinematic chain is constrained with respect to the inertial frame, the chain is said to be *free* or *freely evolving*.

Remark B.5 We will assume that individual links have nonzero mass, length, and moment of inertia about their center of mass. While the nonzero mass and moment of inertia assumptions are not strictly necessary on every link in order to arrive at a “well defined” mechanical model, they rule out certain trivial cases that we would otherwise have to carefully delineate. We leave it to the interested reader to include this extra generality.

The connection of links through prismatic joints is also not considered. The interested reader should have no trouble extending the results to include robots with prismatic knees, for example.

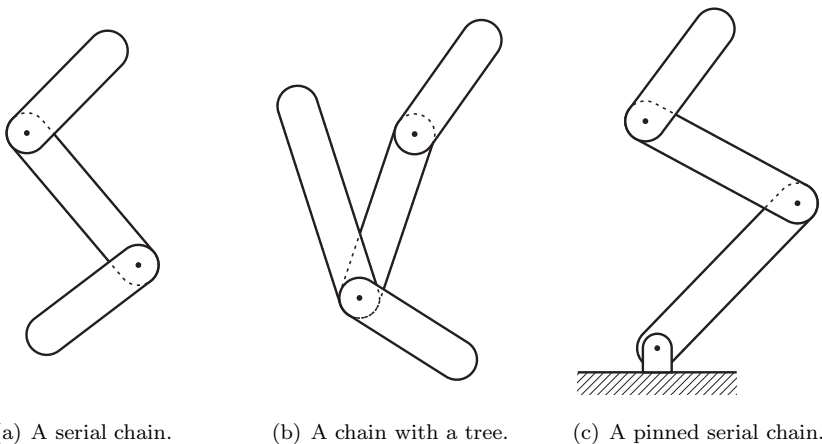


Figure B.11. Open kinematic chains.

B.4.2 Kinetic and Potential Energy of a Single Link

The kinetic and potential energies of a collection of N -links are formed from the sums of the kinetic and potential energies of each individual link. Hence, consider first a single, free, link of mass m_i as depicted in Fig. B.12. A means must be established on the link for situating the relative positions of one or more revolute joints, the center of mass, and, possibly, the end of the link. Typically, measurements are made relative to a joint or to a link end. Formally, this establishes a *coordinate frame on the link*, with the origin at some point of interest, typically a joint or link end.⁹ With respect to the link coordinate frame, a point will be denoted by $(\ell^h; \ell^v)$.

As in Fig. B.13, let $p_i = (p_i^h; p_i^v) \in \mathbb{R}^2$ denote the Cartesian position of the origin of the coordinate frame of link- i with respect to a fixed coordinate frame, called a *world frame* or an *inertial frame*, and let θ_i^{abs} be an element in \mathbb{S} , the circle,¹⁰ denote its orientation with respect to the inertial frame. The angle θ_i^{abs} is called the *absolute orientation* or the *absolute angle* of link- i since it references the link's orientation to the inertial frame. We will assume that all angles are positive in the *counterclockwise direction*, more precisely, we are assuming that all angles are measured such that they are increasing in the counterclockwise direction. The consequences of using the opposite sign convention are spelled out explicitly in Appendix B.4.9.

The *configuration space* of the link is $\mathcal{Q}_{\text{link}} := \mathbb{S} \times \mathbb{R}^2$. Referring again to Fig. B.13, any point $(\bar{\ell}_i^h; \bar{\ell}_i^v)$ in the link frame can be mapped to its Cartesian

⁹See Appendix D for a more general treatment.

¹⁰We identify the circle with \mathbb{R} modulo 2π so that the difference of two values in \mathbb{S} makes sense.

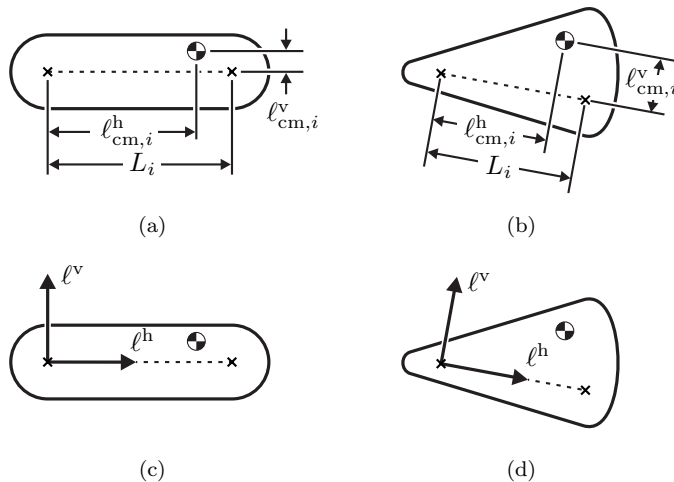


Figure B.12. Establishing local coordinates on a link. Typically, measurements are presented relative to a joint or to a link end, as shown in (a) and (b). Formally, this establishes a coordinate axis on the link, as shown in (c) and (d).

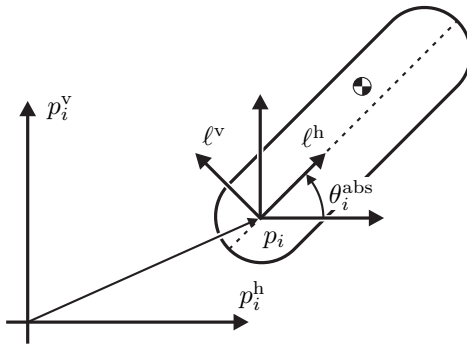


Figure B.13. Configuration of a link. Let $p_i = (p_i^h; p_i^v)$ be the position of the origin of the link coordinate frame with respect to the inertial frame. This point is most correctly denoted by the arrow directed from the origin of the inertial frame to the origin of the link frame, but, most commonly on a figure, it is shown by translating the inertial frame to the origin of the link frame. An advantage of the latter convention is that the absolute orientation of the link with respect to the inertial frame, θ_i^{abs} , is easily indicated. Note that angles are positive in the counterclockwise direction.

coordinates $(\bar{p}_i^h; \bar{p}_i^v)$ in the inertial frame using $(\theta_i^{\text{abs}}; p_i^h; p_i^v) \in \mathcal{Q}_{\text{link}}$:

$$\begin{bmatrix} \bar{p}_i^h \\ \bar{p}_i^v \end{bmatrix} = \begin{bmatrix} p_i^h \\ p_i^v \end{bmatrix} + \mathbf{R}(\theta_i^{\text{abs}}) \begin{bmatrix} \bar{\ell}_i^h \\ \bar{\ell}_i^v \end{bmatrix}, \quad (\text{B.95})$$

where

$$\mathbf{R}(\theta_i^{\text{abs}}) := \begin{bmatrix} \cos(\theta_i^{\text{abs}}) & -\sin(\theta_i^{\text{abs}}) \\ \sin(\theta_i^{\text{abs}}) & \cos(\theta_i^{\text{abs}}) \end{bmatrix}. \quad (\text{B.96})$$

The velocity of the link in the inertial frame is given by

$$\begin{bmatrix} \dot{\bar{p}}_i^h \\ \dot{\bar{p}}_i^v \end{bmatrix} = \begin{bmatrix} \dot{p}_i^h \\ \dot{p}_i^v \end{bmatrix} + \begin{bmatrix} 0 & -1 \\ 1 & 0 \end{bmatrix} \mathbf{R}(\theta_i^{\text{abs}}) \begin{bmatrix} \bar{\ell}_i^h \\ \bar{\ell}_i^v \end{bmatrix} \dot{\theta}_i^{\text{abs}}, \quad (\text{B.97})$$

where $\dot{\theta}_i^{\text{abs}}$ is the (absolute) angular velocity, and we have used the fact that

$$\frac{d}{d\theta} \mathbf{R}(\theta) = \begin{bmatrix} 0 & -1 \\ 1 & 0 \end{bmatrix} \mathbf{R}(\theta), \quad (\text{B.98})$$

that is,

$$\frac{d}{d\theta} \begin{bmatrix} \cos(\theta) & -\sin(\theta) \\ \sin(\theta) & \cos(\theta) \end{bmatrix} = \begin{bmatrix} 0 & -1 \\ 1 & 0 \end{bmatrix} \begin{bmatrix} \cos(\theta) & -\sin(\theta) \\ \sin(\theta) & \cos(\theta) \end{bmatrix}. \quad (\text{B.99})$$

When the link is free, its configuration and velocity can take on any value in $T\mathcal{Q}_{\text{link}}$ and one says that the link has *three degrees of freedom*¹¹ (DOF).

The position of the center of mass of link- i in the world frame can be expressed as

$$\begin{bmatrix} p_{\text{cm},i}^h \\ p_{\text{cm},i}^v \end{bmatrix} = \begin{bmatrix} p_i^h \\ p_i^v \end{bmatrix} + \mathbf{R}(\theta_i^{\text{abs}}) \begin{bmatrix} \ell_{\text{cm},i}^h \\ \ell_{\text{cm},i}^v \end{bmatrix}, \quad (\text{B.100})$$

and its velocity is given by

$$\begin{bmatrix} \dot{p}_{\text{cm},i}^h \\ \dot{p}_{\text{cm},i}^v \end{bmatrix} = \begin{bmatrix} \dot{p}_i^h \\ \dot{p}_i^v \end{bmatrix} + \begin{bmatrix} 0 & -1 \\ 1 & 0 \end{bmatrix} \mathbf{R}(\theta_i^{\text{abs}}) \begin{bmatrix} \ell_{\text{cm},i}^h \\ \ell_{\text{cm},i}^v \end{bmatrix} \dot{\theta}_i^{\text{abs}}. \quad (\text{B.101})$$

The position and velocity of the center of mass will now be used to determine the potential energy and kinetic energy of the link.

We assume now that gravity is directed downward along the vertical axis of the inertial frame. With this assumption, the *potential energy* of the link is

$$V_i = m_i g_0 p_{\text{cm},i}^v, \quad (\text{B.102})$$

¹¹Recall that we are assuming that a link has nonzero mass, length, and moment of inertia about the center of mass. These assumptions rule out a point mass, which only has two degrees of freedom because its orientation and angular velocity would not be defined.

where g_0 is the gravitational constant. The *kinetic energy* of the link is given by

$$K_i = \frac{1}{2}m_i \left((\dot{p}_{cm,i}^h)^2 + (\dot{p}_{cm,i}^v)^2 \right) + \frac{1}{2}J_{cm,i} \left(\dot{\theta}_i^{\text{abs}} \right)^2, \quad (\text{B.103})$$

where $J_{cm,i}$ is the moment of inertia about the center of mass of link- i . In many cases, one has at hand instead the moment of inertia about the origin of the link's coordinate frame. In this case, substituting (B.101) into (B.103) allows the kinetic energy to be computed as

$$\begin{aligned} K_i &= \frac{1}{2}m_i \left((\dot{p}_i^h)^2 + (\dot{p}_i^v)^2 \right) + \frac{1}{2}J_i \left(\dot{\theta}_i^{\text{abs}} \right)^2 \\ &\quad + m_i \begin{bmatrix} \dot{p}_i^v \\ -\dot{p}_i^h \end{bmatrix}' \mathbf{R}(\theta_i^{\text{abs}}) \begin{bmatrix} \ell_{cm,i}^h \\ \ell_{cm,i}^v \end{bmatrix} \dot{\theta}_i^{\text{abs}}, \end{aligned} \quad (\text{B.104})$$

where

$$J_i = J_{cm,i} + m_i((\ell_{cm,i}^h)^2 + (\ell_{cm,i}^v)^2) \quad (\text{B.105})$$

is the moment of inertia about the origin of the link's coordinate frame. This fact is often called the *parallel axis theorem*.

Remark B.6 The kinetic energy of a free single link is a positive definite function of the velocities when we assume that the mass is nonzero and the moment of inertia about the center of mass is nonzero. Indeed, (B.103) can be rewritten as

$$K_i = \frac{1}{2} \begin{bmatrix} \dot{\theta}_i^{\text{abs}} \\ \dot{p}_{cm,i}^h \\ \dot{p}_{cm,i}^v \end{bmatrix}' \begin{bmatrix} J_{cm,i} & 0 & 0 \\ 0 & m_i & 0 \\ 0 & 0 & m_i \end{bmatrix} \begin{bmatrix} \dot{\theta}_i^{\text{abs}} \\ \dot{p}_{cm,i}^h \\ \dot{p}_{cm,i}^v \end{bmatrix}. \quad (\text{B.106})$$

Similarly, (B.104) can be rewritten as

$$K_i = \frac{1}{2} \begin{bmatrix} \dot{\theta}_i^{\text{abs}} \\ \dot{p}_i^h \\ \dot{p}_i^v \end{bmatrix}' \begin{bmatrix} J_i & d_{12} & d_{13} \\ d_{12} & m_i & 0 \\ d_{13} & 0 & m_i \end{bmatrix} \begin{bmatrix} \dot{\theta}_i^{\text{abs}} \\ \dot{p}_i^h \\ \dot{p}_i^v \end{bmatrix}, \quad (\text{B.107})$$

where

$$d_{12} = -\frac{m_i}{2} (\ell_{cm,i}^h \sin(\theta_i^{\text{abs}}) + \ell_{cm,i}^v \cos(\theta_i^{\text{abs}})) \quad (\text{B.108})$$

$$d_{13} = -\frac{m_i}{2} (\ell_{cm,i}^v \sin(\theta_i^{\text{abs}}) - \ell_{cm,i}^h \cos(\theta_i^{\text{abs}})). \quad (\text{B.109})$$

Using (B.105), (B.107) can be shown to be positive definite.

In the case of N links, we simply sum up (B.102) and (B.103) for $i = 1, \dots, N$ to compute the *total potential energy* and the *total kinetic energy*,

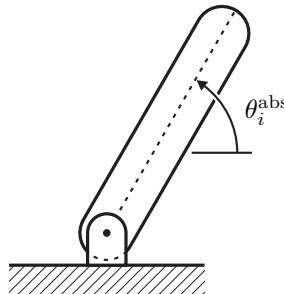


Figure B.14. A single pinned link. Its configuration can be specified with a single number, the absolute orientation, θ_i^{abs} .

respectively, in terms of the $3N$ configuration coordinates $(\theta_i^{\text{abs}}; p_{i_0}^{\text{h}}; p_{i_0}^{\text{v}})$, $i = 1, \dots, N$, and the $3N$ velocities, $(\dot{\theta}_i^{\text{abs}}; \dot{p}_{i_0}^{\text{h}}; \dot{p}_{i_0}^{\text{v}})$. When the links are free (no joints), there is nothing more to it as the coordinates are independent. However, joints clearly impose constraints on the configurations and velocities, and consequently, the configurations and velocities can be parameterized with fewer coordinates. Developing this idea leads to the important notion of generalized coordinates.

The basic idea of a *generalized coordinate* can be seen in a pinned single link, as in Fig. B.14. For simplicity, assume that the link coordinate frame and the inertial frame are both located at the pivot so that the constraints imposed by the pivot become particularly simple: $(p_i^{\text{h}}; p_i^{\text{v}}) = (0; 0)$ and $(\dot{p}_i^{\text{h}}; \dot{p}_i^{\text{v}}) = (0; 0)$. Consequently, the allowed configuration and velocity of the link can be expressed in terms of a single coordinate and derivative, $(\theta_i^{\text{abs}}; \dot{\theta}_i^{\text{abs}}) \in \mathbb{T}\mathbb{S}$. The link is said to have one DOF. The potential and kinetic energies can obviously be expressed in terms of θ_i^{abs} and $\dot{\theta}_i^{\text{abs}}$. The coordinate θ_i^{abs} is a special case of a generalized coordinate.

B.4.3 Free Open Kinematic Chains

Consider a free N -link open kinematic chain as depicted in Figs. B.11(a) and B.11(b). Number the links one through N , and let $p_i = (p_i^{\text{h}}; p_i^{\text{v}}) \in \mathbb{R}^2$ denote the Cartesian position of the origin of the coordinate frame of link- i with respect to an inertial frame, and let $\theta_i^{\text{abs}} \in \mathbb{S}$ denote the link's absolute orientation (i.e., its orientation with respect to the inertial frame). Number the joints one through $N - 1$, and denote by $a(j)$ and $b(j)$ the two links connected by the j -th joint. Denote the position of joint- j on link- $a(j)$ (resp. link- $b(j)$) by $(\ell_{a(j),j}^{\text{h}}; \ell_{a(j),j}^{\text{v}})$ (resp. $(\ell_{b(j),j}^{\text{h}}; \ell_{b(j),j}^{\text{v}})$). The constraints imposed

by the joints yield $2(N - 1)$ equations:

$$\begin{bmatrix} p_{a(j)}^h \\ p_{a(j)}^v \end{bmatrix} + \mathbf{R}(\theta_{a(j)}^{\text{abs}}) \begin{bmatrix} \ell_{a(j),j}^h \\ \ell_{a(j),j}^v \end{bmatrix} - \begin{bmatrix} p_{b(j)}^h \\ p_{b(j)}^v \end{bmatrix} - \mathbf{R}(\theta_{b(j)}^{\text{abs}}) \begin{bmatrix} \ell_{b(j),j}^h \\ \ell_{b(j),j}^v \end{bmatrix} = \begin{bmatrix} 0 \\ 0 \end{bmatrix}, \quad (\text{B.110})$$

for $j = 1, \dots, N - 1$.

For an open kinematic chain, the set of equations (B.110) is always consistent (i.e., there always exist solutions) for arbitrary values of the absolute angles. Moreover, for any $i_0 \in \{1, \dots, N\}$, the set of all solutions can be written in the form¹²

$$\begin{bmatrix} p_i^h \\ p_i^v \end{bmatrix} = \begin{bmatrix} p_{i_0}^h \\ p_{i_0}^v \end{bmatrix} + \begin{bmatrix} \check{\Upsilon}_{i_0,i}^h(\theta_1^{\text{abs}}, \dots, \theta_N^{\text{abs}}) \\ \check{\Upsilon}_{i_0,i}^v(\theta_1^{\text{abs}}, \dots, \theta_N^{\text{abs}}) \end{bmatrix}, \quad (\text{B.111})$$

for $i \in \{1, \dots, N\}$, $i \neq i_0$, where $\check{\Upsilon}_{i_0,i}^h$ and $\check{\Upsilon}_{i_0,i}^v$ are affine in $\cos(\theta_j^{\text{abs}})$ and $\sin(\theta_j^{\text{abs}})$. In other words, the $(N + 2)$ -variables $(\theta_1^{\text{abs}}, \dots, \theta_N^{\text{abs}}, p_{i_0}^h; p_{i_0}^v)$ parameterize all configurations that are compatible with the joint constraints (B.110). This is another example of generalized coordinates.

Generalized coordinates: The configuration space of N free links in the plane is the Cartesian product of the individual configuration spaces, $\mathcal{Q}_{\text{link}}^N := \mathcal{Q}_{\text{link}} \times \dots \times \mathcal{Q}_{\text{link}}$ (N -times), and consequently has dimension $3N$. The subset of configurations compatible with the constraints is

$$\mathcal{Q}_f := \{(\theta_1^{\text{abs}}, p_1^h, p_1^v; \dots; \theta_N^{\text{abs}}, p_N^h, p_N^v) \in \mathcal{Q}_{\text{link}}^N \mid (\text{B.110}) \text{ holds } \forall \text{ joints}\}. \quad (\text{B.112})$$

For a free open kinematic chain, \mathcal{Q}_f is an $(N + 2)$ -dimensional embedded submanifold¹³ of $\mathcal{Q}_{\text{link}}^N$, and moreover, $(\theta_1^{\text{abs}}, \dots, \theta_N^{\text{abs}}, p_{i_0}^h; p_{i_0}^v)$ is a set of local

¹²Proving this for a serial chain is a recommended and straightforward exercise.

¹³This can be shown as follows. Note that (B.110) defines a smooth mapping $F_j : \mathcal{Q}_{\text{link}}^N \rightarrow \mathbb{R}^2$, and an easy calculation shows that it has rank two. Define next $F : \mathcal{Q}_{\text{link}}^N \rightarrow \mathbb{R}^{2(N-1)}$ by

$$F = \begin{bmatrix} F_1 \\ \vdots \\ F_{N-1} \end{bmatrix} \quad (\text{B.113})$$

so that

$$\mathcal{Q}_f := \left\{ (\theta_1^{\text{abs}}, p_1^h, p_1^v; \dots; \theta_N^{\text{abs}}, p_N^h, p_N^v) \in \mathcal{Q}_{\text{link}}^N \mid \begin{aligned} & F(\theta_1^{\text{abs}}, p_1^h, p_1^v, \dots, \theta_N^{\text{abs}}, p_N^h, p_N^v) = 0 \end{aligned} \right\}. \quad (\text{B.114})$$

The definition of an open kinematic chain is equivalent to rank of F equals $2(N - 1)$, establishing that \mathcal{Q}_f has the claimed properties. Alternatively, (B.111) can be used to express F_j in an explicit manner which simplifies the computation of the rank of F . Equation (B.111) shows that $(\theta_1^{\text{abs}}, \dots, \theta_N^{\text{abs}}, p_{i_0}^h; p_{i_0}^v)$ is a set of local coordinates on \mathcal{Q}_f

coordinates for \mathcal{Q}_f . Local coordinates for \mathcal{Q}_f are called *generalized coordinates*; they will be denoted by $q_f = (q_1; \dots; q_{N+2})$.

A few specific examples of generalized coordinates are discussed. They are obtained by applying simple diffeomorphisms to the generalized coordinates just identified.

The *center of mass* of any collection of N links is related to the center of mass of the individual links by

$$\begin{bmatrix} p_{cm}^h \\ p_{cm}^v \end{bmatrix} = \sum_{i=1}^N \frac{m_i}{m_{tot}} \begin{bmatrix} p_{cm,i}^h \\ p_{cm,i}^v \end{bmatrix}, \quad (B.115)$$

where $m_{tot} := \sum_{i=1}^N m_i$ is the total mass. Using (B.100) and (B.111), this can be written as

$$\begin{bmatrix} p_{cm}^h \\ p_{cm}^v \end{bmatrix} = \begin{bmatrix} p_{i_0}^h \\ p_{i_0}^v \end{bmatrix} + \begin{bmatrix} \tilde{\Upsilon}_{i_0}^h(\theta_1^{abs}, \dots, \theta_N^{abs}) \\ \tilde{\Upsilon}_{i_0}^v(\theta_1^{abs}, \dots, \theta_N^{abs}) \end{bmatrix}, \quad (B.116)$$

where

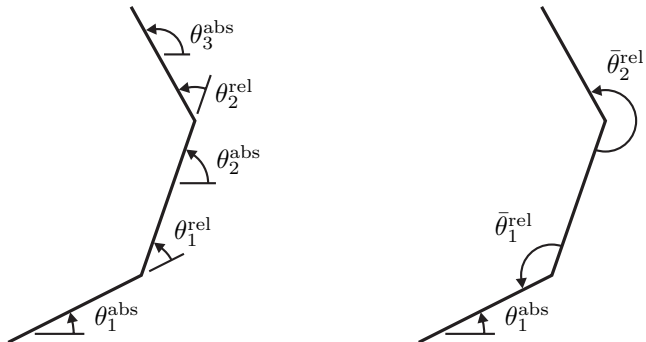
$$\begin{bmatrix} \tilde{\Upsilon}_{i_0}^h(\theta_1^{abs}, \dots, \theta_N^{abs}) \\ \tilde{\Upsilon}_{i_0}^v(\theta_1^{abs}, \dots, \theta_N^{abs}) \end{bmatrix} = \sum_{i=1}^N \frac{m_i}{m_{tot}} \left(\begin{bmatrix} \tilde{\Upsilon}_{i_0,i}^h(\theta_1^{abs}, \dots, \theta_N^{abs}) \\ \tilde{\Upsilon}_{i_0,i}^v(\theta_1^{abs}, \dots, \theta_N^{abs}) \end{bmatrix} + \mathbf{R}(\theta_i^{abs}) \begin{bmatrix} \bar{\ell}_i^h \\ \bar{\ell}_i^v \end{bmatrix} \right). \quad (B.117)$$

Hence, $q_f = (\theta_1^{abs}; \dots; \theta_N^{abs}; p_{cm}^h; p_{cm}^v)$ is a set of generalized coordinates for a free, open kinematic chain.

Define the *relative angle*¹⁴ between links $a(i)$ and $b(i)$ at joint- i by $\theta_i^{rel} = \theta_{b(i)}^{abs} - \theta_{a(i)}^{abs}$. Then $q_f = (\theta_1^{rel}; \dots; \theta_{N-1}^{rel}; \theta_{j_0}^{abs}; p_{i_0}^h; p_{i_0}^v)$, for any $1 \leq j_0 \leq N$ and $1 \leq i_0 \leq N$, is a set of generalized coordinates. To show this for a tree structure requires notation that we do not need elsewhere, so it is skipped. In the special case of a serial chain, suppose that the links and joints are numbered consecutively from one end to the other in such a manner that $a(i) = i$ and $b(i) = i+1$. Then it is easy to show that $(\theta_1^{rel}; \dots; \theta_{N-1}^{rel}; \theta_1^{abs}; p_1^h; p_1^v)$ are generalized coordinates because $\theta_{j+1}^{abs} = \theta_1^{abs} + \theta_1^{rel} + \dots + \theta_j^{rel}$, for $j \in \{1, \dots, N-1\}$. The general result follows similar reasoning.

Remark B.7 More generally, at joint- i , the difference between any two absolute angles for links $a(i)$ and $b(i)$ will be called a *relative angle*. See Fig. B.15. Absolute and relative angles are invariant under translations of the inertial frame. Relative angles are also invariant under rotations of the

¹⁴Recall that we are assuming that all angles are positive in the counterclockwise direction, and thus, in particular, $\theta_{b(i)}^{abs}$ and $\theta_{a(i)}^{abs}$ have the same orientation.



(a) Here $\theta_2^{\text{abs}} = \theta_1^{\text{abs}} + \theta_1^{\text{rel}}$ and $\theta_3^{\text{abs}} = \theta_2^{\text{abs}} + \theta_2^{\text{rel}}$. (b) Here $\theta_2^{\text{abs}} = \theta_1^{\text{abs}} - \bar{\theta}_1^{\text{rel}} + \pi$ and $\theta_3^{\text{abs}} = \theta_3^{\text{abs}} + \bar{\theta}_1^{\text{rel}} - \pi$.

Figure B.15. Different choices of relative angles. There is no uniformly accepted convention for assigning relative angles.

inertial frame. In fact, relative angles give the shape of the kinematic chain, independent of its orientation and position in the plane. For this reason, $(\theta_1^{\text{rel}}, \dots; \theta_{N-1}^{\text{rel}})$ are sometimes called *shape variables* or *shape coordinates*; see also the definition of *body coordinates* introduced later.

Kinetic and potential energy: Given a set of generalized coordinates, $q_f = (q_1; \dots; q_{N+2})$, it is always possible¹⁵ to express $(\theta_i^{\text{abs}}; p_i^h; p_i^v)$ as functions of q_f . We abuse notation and write this simply as

$$\begin{bmatrix} \theta_i^{\text{abs}} \\ p_i^h \\ p_i^v \end{bmatrix} = \begin{bmatrix} \theta_i^{\text{abs}}(q_f) \\ p_i^h(q_f) \\ p_i^v(q_f) \end{bmatrix}. \quad (\text{B.118})$$

Via the chain rule, the corresponding velocities are computed as

$$\begin{bmatrix} \dot{\theta}_i^{\text{abs}}(q_f, \dot{q}_f) \\ \dot{p}_i^h(q_f, \dot{q}_f) \\ \dot{p}_i^v(q_f, \dot{q}_f) \end{bmatrix} = \left(\frac{\partial}{\partial q_f} \begin{bmatrix} \theta_i^{\text{abs}}(q_f) \\ p_i^h(q_f) \\ p_i^v(q_f) \end{bmatrix} \right) \dot{q}_f. \quad (\text{B.119})$$

For later use, note that

$$\frac{\partial}{\partial \dot{q}_i} \begin{bmatrix} \dot{\theta}_i^{\text{abs}}(q_f, \dot{q}_f) \\ \dot{p}_i^h(q_f, \dot{q}_f) \\ \dot{p}_i^v(q_f, \dot{q}_f) \end{bmatrix} = \frac{\partial}{\partial q_i} \begin{bmatrix} \theta_i^{\text{abs}}(q_f) \\ p_i^h(q_f) \\ p_i^v(q_f) \end{bmatrix}. \quad (\text{B.120})$$

¹⁵Indeed, by definition of local coordinates of Q_f , it is possible to express each of $\theta_1^{\text{abs}}, \dots, \theta_N^{\text{abs}}, p_{i_0}^h$, and $p_{i_0}^v$ as functions of q_f , and then, (B.111) completes the job.

Substituting (B.118) and (B.119) into (B.102) and (B.103) yields

$$V_i(q_f) = m_i g_0 p_{cm,i}^v(q_f), \quad (B.121)$$

where m_i is the mass of the link and g_0 is the gravitational constant, and

$$\begin{aligned} K_i(q_f, \dot{q}_f) &= \frac{1}{2} m_i \left((\dot{p}_{cm,i}^h(q_f, \dot{q}_f))^2 + (\dot{p}_{cm,i}^v(q_f, \dot{q}_f))^2 \right) \\ &\quad + \frac{1}{2} J_{cm,i} \left(\dot{\theta}_i^{abs}(q_f, \dot{q}_f) \right)^2, \end{aligned} \quad (B.122)$$

where $J_{cm,i}$ is the moment of inertia about the center of mass of link- i . Alternatively, (B.104) is used to compute the kinetic energy. We note that K_i is a quadratic, positive semi-definite function of \dot{q}_f since

$$K_i = \frac{1}{2} \dot{q}_f' \left[m_i \left(\frac{\partial p_{cm,i}}{\partial q_f} \right)' \left(\frac{\partial p_{cm,i}}{\partial q_f} \right) + J_{cm,i} \left(\frac{\partial \theta_i^{abs}}{\partial q_f} \right)' \left(\frac{\partial \theta_i^{abs}}{\partial q_f} \right) \right] \dot{q}_f \quad (B.123)$$

The *total potential energy* is then

$$V_f(q_f) := \sum_{i=1}^N V_i(q_f) = m_{tot} g_0 p_{cm}^v, \quad (B.124)$$

and the *total kinetic energy* is

$$K_f(q_f, \dot{q}_f) := \sum_{i=1}^N K_i(q_f, \dot{q}_f). \quad (B.125)$$

The total kinetic energy is always a positive definite,¹⁶ quadratic function of the generalized velocities, and can be written as

$$K_f(q_f, \dot{q}_f) =: \frac{1}{2} \dot{q}_f' D_f(q_f) \dot{q}_f, \quad (B.126)$$

where $D_f(q_f)$ is $(N+2) \times (N+2)$ and positive definite for each $q_f \in \mathcal{Q}_f$. The matrix $D_f(q_f)$ is called the *mass-inertia matrix*.

B.4.4 Pinned Open Kinematic Chains

Consider the free N -link open kinematic chain of the previous section, along with the established notation. Suppose now that the chain is pinned as depicted in Fig. B.11(c). Denote the position of the pivot in the inertial frame by $(p_0^h; p_0^v)$. Assume that link- i_0 is connected to the pivot, and denote the

¹⁶See Remark B.10.

position of the axis of the pivot in the link frame by $(\ell_{i_0,0}^h; \ell_{i_0,0}^v)$. The two constraints imposed by the pivot are

$$\begin{bmatrix} p_{i_0}^h \\ p_{i_0}^v \end{bmatrix} + \begin{bmatrix} \cos(\theta_{i_0}^{\text{abs}}) & -\sin(\theta_{i_0}^{\text{abs}}) \\ \sin(\theta_{i_0}^{\text{abs}}) & \cos(\theta_{i_0}^{\text{abs}}) \end{bmatrix} \begin{bmatrix} \ell_{i_0,0}^h \\ \ell_{i_0,0}^v \end{bmatrix} - \begin{bmatrix} p_0^h \\ p_0^v \end{bmatrix} = \begin{bmatrix} 0 \\ 0 \end{bmatrix}. \quad (\text{B.127})$$

The constraints imposed by the joints are as before, (B.110). For a pinned open kinematic chain, the combined set of constraint equations, (B.110) and (B.127), is always consistent (i.e., there always exist solutions) for arbitrary values of the absolute angles. Moreover, the set of all solutions can be written in the form

$$\begin{bmatrix} p_i^h \\ p_i^v \end{bmatrix} = \begin{bmatrix} p_0^h \\ p_0^v \end{bmatrix} + \begin{bmatrix} \bar{T}_i^h(\theta_1^{\text{abs}}, \dots, \theta_N^{\text{abs}}) \\ \bar{T}_i^v(\theta_1^{\text{abs}}, \dots, \theta_N^{\text{abs}}) \end{bmatrix}, \quad (\text{B.128})$$

for $i = 1, \dots, N$, where $\bar{T}_{i_0,i}^h$ and $\bar{T}_{i_0,i}^v$ are linear in $\cos(\theta_j^{\text{abs}})$ and $\sin(\theta_j^{\text{abs}})$. In other words, the N -variables $(\theta_1^{\text{abs}}; \dots; \theta_N^{\text{abs}})$ (minimally) parameterize all configurations that are compatible with the combined joint and pivot constraints, and thus constitute a set of *generalized coordinates* for a pinned open kinematic chain.

Generalized coordinates: The subset of configurations compatible with the constraints is

$$\mathcal{Q}_s := \{(\theta_1^{\text{abs}}; p_1^h; p_1^v; \dots; \theta_N^{\text{abs}}; p_N^h; p_N^v) \in \mathcal{Q}_{\text{link}}^N \mid (\text{B.110}) \text{ and } (\text{B.127}) \text{ hold } \forall \text{ joints}\}. \quad (\text{B.129})$$

By (B.128), \mathcal{Q}_s is an N -dimensional embedded submanifold and moreover, $(\theta_1^{\text{abs}}; \dots; \theta_N^{\text{abs}})$ is a set of local coordinates. By construction,

$$\mathcal{Q}_s := \{(\theta_1^{\text{abs}}; p_1^h; p_1^v; \dots; \theta_N^{\text{abs}}; p_N^h; p_N^v) \in \mathcal{Q}_f \mid (\text{B.127}) \text{ holds}\}. \quad (\text{B.130})$$

Thus, \mathcal{Q}_s is also an N -dimensional embedded submanifold of \mathcal{Q}_f .

Remark B.8 The single support or stance phase of a walking or running bipedal robot will be modeled with a pinned open kinematic chain. Hence, instead of using “ p ” for pinned, the subscript “ s ” is being used in anticipation of \mathcal{Q}_s denoting the configuration manifold for the single support phase of walking or running. The flight phase of running will be modeled with a free open kinematic chain. The subscript “ f ” serves handily the dual purpose of denoting free and flight.

Local coordinates $q_s = (q_1; \dots; q_N)$ for \mathcal{Q}_s are called *generalized coordinates*. Specific examples include $(\theta_1^{\text{abs}}; \dots; \theta_N^{\text{abs}})$ and $(\theta_1^{\text{rel}}; \dots; \theta_{N-1}^{\text{rel}}; \theta_{j_0}^{\text{abs}})$, for any $j_0 \in \{1, \dots, N\}$.

Kinetic and potential energy: Given a set of generalized coordinates, $q_s = (q_1; \dots; q_N)$, we abuse notation and write

$$\begin{bmatrix} \theta_i^{\text{abs}} \\ p_{\text{cm},i}^{\text{h}} \\ p_{\text{cm},i}^{\text{v}} \end{bmatrix} = \begin{bmatrix} \theta_i^{\text{abs}}(q_s) \\ p_{\text{cm},i}^{\text{h}}(q_s) \\ p_{\text{cm},i}^{\text{v}}(q_s) \end{bmatrix}. \quad (\text{B.131})$$

Via the chain rule, the corresponding velocities are computed

$$\begin{bmatrix} \dot{\theta}_i^{\text{abs}}(q_s, \dot{q}_s) \\ \dot{p}_{\text{cm},i}^{\text{h}}(q_s, \dot{q}_s) \\ \dot{p}_{\text{cm},i}^{\text{v}}(q_s, \dot{q}_s) \end{bmatrix} = \left(\frac{\partial}{\partial q_s} \begin{bmatrix} \theta_i^{\text{abs}}(q_s) \\ p_{\text{cm},i}^{\text{h}}(q_s) \\ p_{\text{cm},i}^{\text{v}}(q_s) \end{bmatrix} \right) \dot{q}_s. \quad (\text{B.132})$$

Substituting (B.131) and (B.132) into (B.102) and (B.103) yields

$$V_i(q_s) = m_i g_0 p_{\text{cm},i}^{\text{v}}(q_s), \quad (\text{B.133})$$

where m_i is the mass of the link and g_0 is the gravitational constant, and

$$\begin{aligned} K_i(q_s, \dot{q}_s) &= \frac{1}{2} m_i \left((\dot{p}_{\text{cm},i}^{\text{h}}(q_s, \dot{q}_s))^2 + (\dot{p}_{\text{cm},i}^{\text{v}}(q_s, \dot{q}_s))^2 \right) \\ &\quad + \frac{1}{2} J_{\text{cm},i} \left(\dot{\theta}_i^{\text{abs}}(q_s, \dot{q}_s) \right)^2, \end{aligned} \quad (\text{B.134})$$

where $J_{\text{cm},i}$ is the moment of inertia about the center of mass of link- i . Alternatively, (B.104) can be used to compute the kinetic energy. Just as in (B.123), we note that K_i is a quadratic, positive semi-definite function of \dot{q}_s :

$$K_i = \frac{1}{2} \dot{q}_s' \left[m_i \left(\frac{\partial p_{\text{cm},i}}{\partial q_s} \right)' \left(\frac{\partial p_{\text{cm},i}}{\partial q_s} \right) + J_{\text{cm},i} \left(\frac{\partial \theta_i^{\text{abs}}}{\partial q_s} \right)' \left(\frac{\partial \theta_i^{\text{abs}}}{\partial q_s} \right) \right] \dot{q}_s. \quad (\text{B.135})$$

The *total potential energy* is then

$$V_s(q_s) := \sum_{i=1}^N V_i(q_s) = m_{\text{tot}} g_0 p_{\text{cm}}^{\text{v}}(q_s), \quad (\text{B.136})$$

and the *total kinetic energy* is

$$K_s(q_s, \dot{q}_s) := \sum_{i=1}^N K_i(q_s, \dot{q}_s). \quad (\text{B.137})$$

The total kinetic energy is always a positive definite (see Remark B.9), quadratic function of the generalized velocities, and can be written as

$$K_s(q_s, \dot{q}_s) =: \frac{1}{2} \dot{q}_s' D_s(q_s) \dot{q}_s, \quad (\text{B.138})$$

where $D_s(q_s)$ is $N \times N$ and positive definite for each $q_s \in \mathcal{Q}_s$. The matrix $D_s(q_s)$ is called the *mass-inertia matrix*.

Remark B.9 Note that if $J_{cm,i} > 0$, then

$$\text{rank} \sum_{i=1}^N \left[J_{cm,i} \frac{\partial \theta_i^{\text{abs}}(q_s)}{\partial q_s} \frac{\partial \theta_i^{\text{abs}}(q_s)}{\partial q_s} \right] = \text{rank} \begin{bmatrix} \frac{\partial \theta_1^{\text{abs}}(q_s)}{\partial q_s} \\ \vdots \\ \frac{\partial \theta_N^{\text{abs}}(q_s)}{\partial q_s} \end{bmatrix} = N, \quad (\text{B.139})$$

and thus $m_i > 0$ and $J_{cm,i} > 0$ are sufficient conditions for the mass-inertia matrix to be positive definite. This explains the assumptions made in Remark B.5.

B.4.5 The Lagrangian and Lagrange's Equations

Let \bar{N} equal N or $(N+2)$, and let \mathcal{Q} equal \mathcal{Q}_s or \mathcal{Q}_f . Let $q = (q_1; \dots; q_{\bar{N}}) \in \mathcal{Q}$ be a set of generalized coordinates, and let $V : \mathcal{Q} \rightarrow \mathbb{R}$ and $K : T\mathcal{Q} \rightarrow \mathbb{R}$ be the total potential energy and total kinetic energy, respectively.

The *Lagrangian* is the real-valued function $\mathcal{L} : T\mathcal{Q} \rightarrow \mathbb{R}$ given by the total kinetic energy minus the total potential energy,

$$\mathcal{L}(q, \dot{q}) := K(q, \dot{q}) - V(q). \quad (\text{B.140})$$

Lagrange's equation is

$$\frac{d}{dt} \frac{\partial \mathcal{L}}{\partial \dot{q}} - \frac{\partial \mathcal{L}}{\partial q} = \Gamma, \quad (\text{B.141})$$

where Γ is the vector of generalized torques and forces. If the kinetic energy is quadratic, that is,

$$K(q, \dot{q}) = \frac{1}{2} \dot{q}' D(q) \dot{q}, \quad (\text{B.142})$$

then (B.141) results in the second-order differential equation

$$D(q) \ddot{q} + C(q, \dot{q}) \dot{q} + G(q) = \Gamma, \quad (\text{B.143})$$

where $G(q) = \frac{\partial V(q)}{\partial q}$, and $C(q, \dot{q}) \dot{q} = \left(\frac{\partial}{\partial q} (D(q) \dot{q}) \right) \dot{q} - \frac{1}{2} \left(\frac{\partial}{\partial q} (D(q) \dot{q}) \right)' \dot{q}$. The matrix function C is not uniquely defined, but it is traditional to choose

$$C_{kj} = \sum_{i=1}^{\bar{N}} \frac{1}{2} \left(\frac{\partial D_{kj}}{\partial q_i} + \frac{\partial D_{ki}}{\partial q_j} - \frac{\partial D_{ij}}{\partial q_k} \right) \dot{q}_i, \quad (\text{B.144})$$

where $1 \leq k, j \leq \bar{N}$ and C_{kj} is the kj entry of the matrix C .

B.4.6 Generalized Forces and Torques

The right-hand side of (B.141), Γ , is the sum of the external generalized forces and torques (moments) acting on the kinematic chain. The computation of the generalized forces and torques is presented for three cases encountered in this book. These formulas follow from what is known as the *principle of virtual work* or d'Alembert's principle.

Force acting at a point: Suppose that a force $F = (F_T; F_N)$ is acting on a kinematic chain at a point $p_i = (p_i^h; p_i^v)$. Then

$$\Gamma_i = \left(\frac{\partial p_i}{\partial q} \right)' F. \quad (\text{B.145})$$

Torque acting on a single link: Suppose that a torque τ is acting on a single link- i of a kinematic chain, that is, the torque is acting between the link and the inertial frame. Let θ_i^{abs} denote the absolute orientation of the link. Then

$$\Gamma_i = \left(\frac{\partial \theta_i^{\text{abs}}}{\partial q} \right)' \tau. \quad (\text{B.146})$$

Torque acting at a revolute connection of two links: Suppose that a torque τ is applied at a revolute joint connecting two links and let θ_j^{rel} be the associated relative angle. Then

$$\Gamma_j = \left(\frac{\partial \theta_j^{\text{rel}}}{\partial q} \right)' \tau. \quad (\text{B.147})$$

B.4.7 Angular Momentum

The objective here is to summarize a few results on angular momentum for an N -link open kinematic chain that is either free or pinned. To fulfill this objective, we need a planar version of the cross product.

Define the *wedge product* of two vectors $x := (x_1; x_2)$ and $y := (y_1; y_2)$ in \mathbb{R}^2 as

$$x \wedge y := x_1 y_2 - x_2 y_1. \quad (\text{B.148})$$

This is a skew symmetric product and is related to the usual cross product¹⁷ in \mathbb{R}^3 as follows: if $\{e_1, e_2, e_3\}$ are the natural basis vectors in \mathbb{R}^3 , then $x \wedge y =$

¹⁷In \mathbb{R}^3 , the cross product of two vectors is another vector, and in particular, the cross product of two vectors in $\text{span}\{e_1, e_2\}$ lies in $\text{span}\{e_3\}$. The wedge product computes the coefficient of the vector in $\text{span}\{e_3\}$.

$[(x_1e_1 + x_2e_2) \times (y_1e_1 + y_2e_2)] \cdot e_3$. For later use, we also note that

$$x \wedge y = \begin{bmatrix} x_1 \\ x_2 \end{bmatrix}' \begin{bmatrix} 0 & 1 \\ -1 & 0 \end{bmatrix} \begin{bmatrix} y_1 \\ y_2 \end{bmatrix}. \quad (\text{B.149})$$

Let p_a be a point in the plane. The *angular momentum* of link- i about the point p_a is

$$\sigma_{a,i} := m_i(p_{cm,i} - p_a) \wedge \dot{p}_{cm,i} + J_{cm,i}\dot{\theta}_i^{\text{abs}}, \quad (\text{B.150})$$

and the *total angular momentum about a generic point p_a* is

$$\sigma_a := \sum_{i=1}^N \sigma_{a,i} \quad (\text{B.151a})$$

$$= \sum_{i=1}^N m_i(p_{cm,i} - p_a) \wedge \dot{p}_{cm,i} + J_{cm,i}\dot{\theta}_i^{\text{abs}} \quad (\text{B.151b})$$

$$= \sum_{i=1}^N \left(m_i p_{cm,i} \wedge \dot{p}_{cm,i} + J_{cm,i}\dot{\theta}_i^{\text{abs}} \right) - m_{\text{tot}} p_a \wedge \dot{p}_{cm}. \quad (\text{B.151c})$$

Taking $p_a = p_{cm}$ yields the *total angular momentum about the center of mass*,

$$\sigma_{cm} := \sum_{i=1}^N \left(m_i p_{cm,i} \wedge \dot{p}_{cm,i} + J_{cm,i}\dot{\theta}_i^{\text{abs}} \right) - m_{\text{tot}} p_{cm} \wedge \dot{p}_{cm}. \quad (\text{B.152})$$

For later use, we note a few more facts. Let σ_b be the total angular momentum about a point p_b . Then,

$$\sigma_a - \sigma_b = m_{\text{tot}}(p_b - p_a) \wedge \dot{p}_{cm}, \quad (\text{B.153})$$

or equivalently,

$$\sigma_a = \sigma_b + m_{\text{tot}}(p_b - p_a) \wedge \dot{p}_{cm}, \quad (\text{B.154})$$

which is sometimes called the *angular momentum transfer formula*. Taking $p_b = p_{cm}$ in (B.153) yields

$$\sigma_a - \sigma_{cm} = m_{\text{tot}}(p_{cm} - p_a) \wedge \dot{p}_{cm}. \quad (\text{B.155})$$

B.4.8 Further Remarks on Lagrange's Method

The following results can be found in many books on robotics and mechanics. They are given here in a form that will help in the computation of the impact map and the zero dynamics of a mechanical system.

Free chain in coordinates for \mathcal{Q}_s and the center of mass: Let q_s be any generalized coordinates for \mathcal{Q}_s such that $q_f = (q_s; p_{cm}^h; p_{cm}^v)$ is a set of generalized coordinates for \mathcal{Q}_f . Because q_s are generalized coordinates for \mathcal{Q}_s , we can write $\theta_i^{abs}(q_s)$. Use (B.100) and (B.111), or (B.116), to write the center of mass of each link as

$$p_{cm,i} = p_{cm} + \Upsilon_i(q_s). \quad (\text{B.156})$$

From (B.115), it follows that

$$\sum_{i=1}^N m_i \Upsilon_i(q_s) = 0, \quad (\text{B.157})$$

which in turn yields

$$\sum_{i=1}^N m_i \dot{\Upsilon}_i(q_s) = 0, \quad (\text{B.158})$$

where $\dot{\Upsilon}_i(q_s) = \frac{\partial \Upsilon_i(q_s)}{\partial q_s} \dot{q}_s$.

We now compute the total kinetic energy, using expression (B.103) for the kinetic energy of an individual link:

$$K = \frac{1}{2} \sum_{i=1}^N \left[m_i \dot{p}_{cm}' \dot{p}_{cm} + 2m_i \dot{p}_{cm}' \frac{\partial \Upsilon_i(q_s)}{\partial q_s} \dot{q}_s + \dot{q}_s' m_i \frac{\partial \Upsilon_i(q_s)'}{\partial q_s} \frac{\partial \Upsilon_i(q_s)}{\partial q_s} \dot{q}_s + J_{cm,i} \dot{q}_s' \frac{\partial \theta_i^{abs}(q_s)'}{\partial q_s} \frac{\partial \theta_i^{abs}(q_s)}{\partial q_s} \dot{q}_s \right], \quad (\text{B.159})$$

which, using (B.158), simplifies to

$$K = \frac{1}{2} m_{tot} \dot{p}_{cm}' \dot{p}_{cm} + \frac{1}{2} \dot{q}_s' \sum_{i=1}^N \left[m_i \frac{\partial \Upsilon_i(q_s)'}{\partial q_s} \frac{\partial \Upsilon_i(q_s)}{\partial q_s} + J_{cm,i} \frac{\partial \theta_i^{abs}(q_s)'}{\partial q_s} \frac{\partial \theta_i^{abs}(q_s)}{\partial q_s} \right] \dot{q}_s. \quad (\text{B.160})$$

Hence, in the chosen coordinates, the mass-inertia matrix is block diagonal

$$D_f(q_f) = \begin{bmatrix} A(q_s) & 0 \\ 0 & m_{tot} I_{2 \times 2} \end{bmatrix}, \quad (\text{B.161})$$

where

$$A(q_s) := \sum_{i=1}^N \left[m_i \frac{\partial \Upsilon_i(q_s)'}{\partial q_s} \frac{\partial \Upsilon_i(q_s)}{\partial q_s} + J_{cm,i} \frac{\partial \theta_i^{abs}(q_s)'}{\partial q_s} \frac{\partial \theta_i^{abs}(q_s)}{\partial q_s} \right]. \quad (\text{B.162})$$

Using (B.156), the total angular momentum about a generic point p_a can be expressed as

$$\sigma_a = m_{\text{tot}}(p_{\text{cm}} - p_a) \wedge \dot{p}_{\text{cm}} + \sum_{i=1}^N m_i \Upsilon_i \wedge \dot{\Upsilon}_i + J_{\text{cm},i} \dot{\theta}_i^{\text{abs}}. \quad (\text{B.163})$$

Taking $p_a = p_{\text{cm}}$ yields the total angular momentum about the center of mass,

$$\sigma_{\text{cm}} := \sum_{i=1}^N m_i \Upsilon_i \wedge \dot{\Upsilon}_i + J_{\text{cm},i} \dot{\theta}_i^{\text{abs}}. \quad (\text{B.164})$$

Remark B.10 Recall that we have assumed $m_i > 0$ and $J_{\text{cm},i} > 0$. It follows that

$$\text{rank} \sum_{i=1}^N \left[J_{\text{cm},i} \frac{\partial \theta_i^{\text{abs}}(q_s)}{\partial q_s} \frac{\partial \theta_i^{\text{abs}}(q_s)}{\partial q_s} \right] = \text{rank} \begin{bmatrix} \frac{\partial \theta_1^{\text{abs}}(q_s)}{\partial q_s} \\ \vdots \\ \frac{\partial \theta_N^{\text{abs}}(q_s)}{\partial q_s} \end{bmatrix} = N, \quad (\text{B.165})$$

which shows that A is positive definite, and hence D_f is also positive definite.

Body coordinates and cyclic variables: Consider an N -link open kinematic chain, pinned or free. If a point on the “body” (i.e., the kinematic chain) is represented with respect to a Cartesian coordinate frame attached to one of the links instead of the inertial frame, then the resulting coordinate representation is invariant under translations and rotations of the inertial frame, which is equivalent to being invariant under changes in the position and orientation of the body with respect to the inertial frame. Developing this idea by repeating the development followed for generalized coordinates yields what are called *body coordinates*. We will take a short cut and use the following definition: $q_b = (q_1; \dots; q_{N-1})$ is a set of body coordinates with respect to a coordinate frame attached to link- i_0 of an N -link open kinematic chain if any point \bar{p} on the chain can be expressed in the form

$$\begin{bmatrix} \bar{p}^h \\ \bar{p}^v \end{bmatrix} = \begin{bmatrix} p_{i_0}^h \\ p_{i_0}^v \end{bmatrix} + \mathbf{R}(\theta_{i_0}^{\text{abs}}) \begin{bmatrix} \bar{\ell}_{i_0}^h(q_b) \\ \bar{\ell}_{i_0}^v(q_b) \end{bmatrix}, \quad (\text{B.166})$$

and $q_s = (q_b; \theta_{i_0}^{\text{abs}})$ is a set of generalized coordinates for \mathcal{Q}_s . The last requirement is equivalent to $q_f = (q_b; \theta_{i_0}^{\text{abs}}; p_{i_0}^h; p_{i_0}^v)$ is a set of generalized coordinates for \mathcal{Q}_f .

As long as the absolute angles θ_i^{abs} , $1 \leq i \leq N$ are defined with the same orientation, the set of $N - 1$ differences $\theta_i^{\text{abs}} - \theta_{i_0}^{\text{abs}}$, $1 \leq i \leq N$, $i \neq i_0$, form a set of body coordinates associated with link- i_0 . The relative angles $(\theta_1^{\text{rel}}; \dots; \theta_{N-1}^{\text{rel}})$ form a set of body coordinates with respect to any link- i_0 .

Some important properties associated with body coordinates are summarized next.

Proposition B.8

Let q_b be a set of body coordinates associated with link- i_0 of an N -link open kinematic chain. Let $q_s = (q_b; \theta_{i_0}^{\text{abs}})$ and $q_f = (q_b; \theta_{i_0}^{\text{abs}}; p_{i_0}^h; p_{i_0}^v)$. Let q stand for q_s or q_f . The following statements hold:

$$(a) \frac{\partial}{\partial q_N} \theta_i^{\text{abs}}(q) \equiv 1, \text{ for } i \in \{1, \dots, N\};$$

(b) Any point p on the kinematic chain satisfies

$$\frac{\partial}{\partial q_N} \begin{bmatrix} (p^h - p_{i_0}^h)(q) \\ (p^v - p_{i_0}^v)(q) \end{bmatrix} = \begin{bmatrix} 0 & -1 \\ 1 & 0 \end{bmatrix} \begin{bmatrix} (p^h - p_{i_0}^h)(q) \\ (p^v - p_{i_0}^v)(q) \end{bmatrix}, \quad (\text{B.167})$$

(c) and hence, the centers of mass satisfy

$$\frac{\partial}{\partial q_N} \begin{bmatrix} (p_{cm,i}^h - p_{i_0}^h)(q) \\ (p_{cm,i}^v - p_{i_0}^v)(q) \end{bmatrix} = \begin{bmatrix} 0 & -1 \\ 1 & 0 \end{bmatrix} \begin{bmatrix} (p_{cm,i}^h - p_{i_0}^h)(q) \\ (p_{cm,i}^v - p_{i_0}^v)(q) \end{bmatrix}, \quad (\text{B.168})$$

for $i \in \{1, \dots, N\}$, and

$$\frac{\partial}{\partial q_N} \begin{bmatrix} (p_{cm}^h - p_{i_0}^h)(q) \\ (p_{cm}^v - p_{i_0}^v)(q) \end{bmatrix} = \begin{bmatrix} 0 & -1 \\ 1 & 0 \end{bmatrix} \begin{bmatrix} (p_{cm}^h - p_{i_0}^h)(q) \\ (p_{cm}^v - p_{i_0}^v)(q) \end{bmatrix}; \quad (\text{B.169})$$

(d) The mass-inertia matrix for the pinned chain satisfies $\frac{\partial}{\partial q_N} D_s(q_s) \equiv 0$, and hence, D_s depends only on q_b .

If the generalized coordinates are chosen instead as $q_f = (q_b; \theta_{i_0}^{\text{abs}}; p_{cm}^h; p_{cm}^v)$, where q_b are body coordinates associated with link- i_0 , then (a), (b) and (c) still hold, and moreover,

(e) the mass-inertia matrix for the free chain, D_f , has the block-diagonal form given in (B.161), with $\frac{\partial}{\partial q_N} A(q_s) \equiv 0$; in other words, both D_f and A depend only on q_b .

Remark B.11 If all of the absolute angles do not have the same orientation, then (a) of Proposition B.8 must be modified to take into account sign differences. Recall that we assume all absolute angles are positive in the counterclockwise direction.

Proof For simplicity of notation in establishing (a), assume $i_0 = N$. Because $(\theta_1^{\text{abs}} - \theta_N^{\text{abs}}, \dots, \theta_{N-1}^{\text{abs}} - \theta_N^{\text{abs}})$ is a set of body coordinates, there locally

exists a function F such that

$$\begin{bmatrix} \theta_1^{\text{abs}} - \theta_N^{\text{abs}} \\ \vdots \\ \theta_{N-1}^{\text{abs}} - \theta_N^{\text{abs}} \end{bmatrix} = F(q_b), \quad (\text{B.170})$$

and hence

$$\begin{bmatrix} \theta_1^{\text{abs}} \\ \vdots \\ \theta_{N-1}^{\text{abs}} \end{bmatrix} = \begin{bmatrix} \theta_N^{\text{abs}} \\ \vdots \\ \theta_N^{\text{abs}} \end{bmatrix} + F(q_b). \quad (\text{B.171})$$

From this, part (a) is immediate. Part (b) is immediate from (B.166), and this gives (c) as well. If the definition of kinetic energy had been developed from fundamentals as in [Appendix D](#), part (d) would follow immediately from invariance of the Euclidean norm of the velocities under a rotation of the inertial frame, and part (e) would follow from invariance of the Euclidean norm of the velocities under a rotation of the inertial frame and a translation of the inertial frame. To prove these results using the formalism of this summary of planar Lagrangian dynamics, we first assume the chain is pinned at p_0 and use (B.166) to write

$$\begin{bmatrix} p_0^{\text{h}} \\ p_0^{\text{v}} \end{bmatrix} = \begin{bmatrix} p_{i_0}^{\text{h}} \\ p_{i_0}^{\text{v}} \end{bmatrix} + \mathbf{R}(\theta_{i_0}^{\text{abs}}) \begin{bmatrix} \tilde{\ell}_{i_0,0}^{\text{h}}(q_b) \\ \tilde{\ell}_{i_0,0}^{\text{v}}(q_b) \end{bmatrix}, \quad (\text{B.172})$$

where $p_0 = (p_0^{\text{h}}; p_0^{\text{v}})$ is the Cartesian position of the pivot, and hence (B.166) is equivalent to

$$\begin{bmatrix} \bar{p}^{\text{h}} \\ \bar{p}^{\text{v}} \end{bmatrix} = \begin{bmatrix} p_0^{\text{h}} \\ p_0^{\text{v}} \end{bmatrix} + \mathbf{R}(\theta_{i_0}^{\text{abs}}) \begin{bmatrix} \tilde{\ell}_{i_0}^{\text{h}}(q_b) \\ \tilde{\ell}_{i_0}^{\text{v}}(q_b) \end{bmatrix}, \quad (\text{B.173})$$

where

$$\begin{bmatrix} \tilde{\ell}_{i_0}^{\text{h}}(q_b) \\ \tilde{\ell}_{i_0}^{\text{v}}(q_b) \end{bmatrix} = \begin{bmatrix} \tilde{\ell}_{i_0}^{\text{h}}(q_b) \\ \tilde{\ell}_{i_0}^{\text{v}}(q_b) \end{bmatrix} - \begin{bmatrix} \tilde{\ell}_{i_0,0}^{\text{h}}(q_b) \\ \tilde{\ell}_{i_0,0}^{\text{v}}(q_b) \end{bmatrix}. \quad (\text{B.174})$$

Using (B.173) and the fact that the pivot is fixed, the velocity of the center of mass of link- i can be expressed in the form

$$\begin{bmatrix} \dot{p}_{cm,i}^{\text{h}} \\ \dot{p}_{cm,i}^{\text{v}} \end{bmatrix} = \mathbf{R}(\theta_{i_0}^{\text{abs}}) \left(\frac{\partial}{\partial q_b} \begin{bmatrix} \tilde{\ell}_{cm,i}^{\text{h}}(q_b) \\ \tilde{\ell}_{cm,i}^{\text{v}}(q_b) \end{bmatrix} \right) \dot{q}_b + \begin{bmatrix} 0 & -1 \\ 1 & 0 \end{bmatrix} \mathbf{R}(\theta_{i_0}^{\text{abs}}) \begin{bmatrix} \tilde{\ell}_{cm,i}^{\text{h}}(q_b) \\ \tilde{\ell}_{cm,i}^{\text{v}}(q_b) \end{bmatrix} \dot{\theta}_{i_0}^{\text{abs}}. \quad (\text{B.175})$$

Because

$$\begin{bmatrix} 0 & -1 \\ 1 & 0 \end{bmatrix} \mathbf{R}(\theta_{i_0}^{\text{abs}}) = \mathbf{R}(\theta_{i_0}^{\text{abs}}) \begin{bmatrix} 0 & -1 \\ 1 & 0 \end{bmatrix}, \quad (\text{B.176})$$

(B.175) yields

$$\begin{bmatrix} \dot{p}_{cm,i}^h \\ \dot{p}_{cm,i}^v \end{bmatrix} = \mathbf{R}(\theta_{i_0}^{abs}) \left(\left(\frac{\partial}{\partial q_b} \begin{bmatrix} \tilde{\ell}_{cm,i}^h(q_b) \\ \tilde{\ell}_{cm,i}^v(q_b) \end{bmatrix} \right) \dot{q}_b + \begin{bmatrix} 0 & -1 \\ 1 & 0 \end{bmatrix} \begin{bmatrix} \tilde{\ell}_{cm,i}^h(q_b) \\ \tilde{\ell}_{cm,i}^v(q_b) \end{bmatrix} \dot{\theta}_{i_0}^{abs} \right). \quad (\text{B.177})$$

Substituting this expression into (B.122) shows that the kinetic energy of link- i is independent of $q_N = \theta_{i_0}^{abs}$, hence the total kinetic energy is as well.

We now just sketch the proof of the second part of the proposition since it follows very closely the reasoning used above. In the coordinates $q_f = (q_b; \theta_{i_0}^{abs}; p_{cm}^h; p_{cm}^v)$ the proof of (a) is the same as above. Next, we use (B.166) to write

$$\begin{bmatrix} p_{cm}^h \\ p_{cm}^v \end{bmatrix} = \begin{bmatrix} p_{i_0}^h \\ p_{i_0}^v \end{bmatrix} + \mathbf{R}(\theta_{i_0}^{abs}) \begin{bmatrix} \bar{\ell}_{i_0,cm}^h(q_b) \\ \bar{\ell}_{i_0,cm}^v(q_b) \end{bmatrix}, \quad (\text{B.178})$$

and hence (B.166) is equivalent to

$$\begin{bmatrix} \bar{p}^h \\ \bar{p}^v \end{bmatrix} = \begin{bmatrix} p_{cm}^h \\ p_{cm}^v \end{bmatrix} + \mathbf{R}(\theta_{i_0}^{abs}) \begin{bmatrix} \bar{\ell}_{i_0}^h(q_b) \\ \bar{\ell}_{i_0}^v(q_b) \end{bmatrix}, \quad (\text{B.179})$$

where this time

$$\begin{bmatrix} \bar{\ell}_{i_0}^h(q_b) \\ \bar{\ell}_{i_0}^v(q_b) \end{bmatrix} = \begin{bmatrix} \bar{\ell}_{i_0}^h(q_b) \\ \bar{\ell}_{i_0}^v(q_b) \end{bmatrix} - \begin{bmatrix} \bar{\ell}_{i_0,cm}^h(q_b) \\ \bar{\ell}_{i_0,cm}^v(q_b) \end{bmatrix}. \quad (\text{B.180})$$

Parts (b) and (c) are immediate from (B.179). Part (e) is established using the reasoning employed in establishing (B.161).

Variables that do not appear in the mass-inertia matrix are called *cyclic variables*. When coordinates are chosen in the form $q_s = (q_b; \theta_{i_0}^{abs})$, then q_N is cyclic for a pinned open kinematic chain; this is just expressing the invariance of the kinetic energy under rotations of the inertial frame, or of the chain with respect to the inertial frame. Similarly, when coordinates are chosen in the form $q_f = (q_b; \theta_{i_0}^{abs}; p_{cm}^h; p_{cm}^v)$, then q_N , p_{cm}^h , and p_{cm}^v are cyclic for a free open kinematic chain; this is just expressing the invariance of the kinetic energy under rotations and translations of the inertial frame, or of the chain with respect to the inertial frame.

Conjugate momenta: As in [Appendix B.4.5](#), let \bar{N} equal N or $(N + 2)$, and let \mathcal{Q} equal \mathcal{Q}_s or \mathcal{Q}_f . Let $q = (q_1; \dots; q_{\bar{N}}) \in \mathcal{Q}$ be a set of generalized coordinates, and let $\mathcal{L}(q, \dot{q}) := K(q, \dot{q}) - V(q)$ be the Lagrangian. The *generalized conjugate momenta*, or just *conjugate momenta* for short, are

$$\bar{\sigma}_i := \frac{\partial}{\partial \dot{q}_i} \mathcal{L}(q, \dot{q}), \quad (\text{B.181})$$

for $i \in \{1, \dots, \bar{N}\}$. Since¹⁸ $\frac{\partial}{\partial \dot{q}_i} \mathcal{L}(q, \dot{q}) = \frac{\partial}{\partial \dot{q}_i} K(q, \dot{q})$, the conjugate momenta can also be computed as $\bar{\sigma}_i := \frac{\partial}{\partial \dot{q}_i} K(q, \dot{q})$, which is convenient because it corresponds to

$$\bar{\sigma}_i = d_i(q)\dot{q}, \quad (\text{B.182})$$

where d_i is the i -th row of D .

By Lagrange's equation, (B.141),

$$\frac{d}{dt} \bar{\sigma}_i = \frac{\partial \mathcal{L}(q, \dot{q})}{\partial q_i} + \gamma_i, \quad (\text{B.183})$$

where γ_i is the i -th row of Γ . If q_i is cyclic, this simplifies to

$$\frac{d}{dt} \bar{\sigma}_i = -\frac{\partial V(q)}{\partial q_i} + \gamma_i. \quad (\text{B.184})$$

Proposition B.9

Let q_b be a set of body coordinates associated with link- i_0 of an N -link open kinematic chain. Let $q_s = (q_b; \theta_{i_0}^{\text{abs}})$ and $q_f = (q_b; \theta_{i_0}^{\text{abs}}; p_{cm}^h; p_{cm}^v)$. Then the following statements hold:

- (a) if the chain is free, $\frac{\partial}{\partial \dot{q}_N} \mathcal{L}(q_f, \dot{q}_f) = \sigma_{cm}$, the angular momentum about the center of mass, and $\frac{d}{dt} \sigma_{cm} = \gamma_N$;
- (b) if the chain is pinned, $\frac{\partial}{\partial \dot{q}_N} \mathcal{L}(q_s, \dot{q}_s) = \sigma_0$, the angular momentum about the pivot,¹⁹ and

$$\frac{d}{dt} \sigma_0 = -m_{\text{tot}} g_0 (p_{cm}^h - p_0^h) + \gamma_N, \quad (\text{B.185})$$

where $p_0 = (p_0^h; p_0^v)$ is the Cartesian position of the pivot and γ_N is the external torque applied about the pivot.

Proof To prove (a) use (B.160) to compute

$$\bar{\sigma}_N = \sum_{i=1}^N \left(m_i \frac{\partial \Upsilon'_i}{\partial q_N} \dot{\Upsilon}_i + J_{cm,i} \dot{\theta}_i^{\text{abs}} \frac{\partial \theta_i^{\text{abs}}}{\partial q_N} \right). \quad (\text{B.186})$$

Then, using Proposition B.8, this can be written as

$$\bar{\sigma}_N = \sum_{i=1}^N \left(m_i \Upsilon'_i \begin{bmatrix} 0 & 1 \\ -1 & 0 \end{bmatrix} \dot{\Upsilon}_i + J_{cm,i} \dot{\theta}_i^{\text{abs}} \right). \quad (\text{B.187})$$

¹⁸This is because the potential energy is assumed to depend only upon the configuration variables and not the velocities.

¹⁹In (B.151a), take $p_a = p_0$, the pivot point.

Applying the definition of the wedge product yields,

$$\bar{\sigma}_N = \sum_{i=1}^N \left(m_i \Upsilon_i \wedge \dot{\Upsilon}_i + J_{cm,i} \dot{\theta}_i^{abs} \right), \quad (B.188)$$

which, when compared to (B.164), yields the result.

From (B.124), $\frac{\partial V(q_f)}{\partial q_N} = m_{tot} g_0 \frac{\partial p_{cm}^v}{\partial q_N} = 0$. Hence, $\frac{d}{dt} \sigma_{cm} = \frac{d}{dt} \bar{\sigma}_N = \gamma_N$.

To prove (b), we once again use (B.160), but this time with p_{cm} expressed as a function of q_s , to compute

$$\bar{\sigma}_N = m_{tot} \frac{\partial p_{cm}}{\partial q_N}' \dot{p}_{cm} + \sum_{i=1}^N \left(m_i \frac{\partial \Upsilon_i}{\partial q_N}' \dot{\Upsilon}_i + J_{cm,i} \dot{\theta}_i^{abs} \frac{\partial \theta_i^{abs}}{\partial q_N} \right). \quad (B.189)$$

Then, using Proposition B.8, this can be written as

$$\bar{\sigma}_N = m_{tot} (p_{cm} - p_0)' \begin{bmatrix} 0 & 1 \\ -1 & 0 \end{bmatrix} \dot{p}_{cm} + \sum_{i=1}^N \left(m_i \Upsilon_i' \begin{bmatrix} 0 & 1 \\ -1 & 0 \end{bmatrix} \dot{\Upsilon}_i + J_{cm,i} \dot{\theta}_i^{abs} \right). \quad (B.190)$$

Applying the definition of the wedge product yields,

$$\bar{\sigma}_N = m_{tot} (p_{cm} - p_0) \wedge \dot{p}_{cm} + \sum_{i=1}^N \left(m_i \Upsilon_i \wedge \dot{\Upsilon}_i + J_{cm,i} \dot{\theta}_i^{abs} \right). \quad (B.191)$$

Comparing (B.191) to (B.163) for $p_a = p_0$ yields $\bar{\sigma}_N = \sigma_0$.

From (B.136), $\frac{\partial V(q)}{\partial q_N} = m_{tot} g_0 \frac{\partial p_{cm}^v}{\partial q_N}$. Applying Proposition B.8 (c) with i_0 as the link attached to the pivot and $p_{i_0} = p_0$, this becomes $\frac{\partial V(q)}{\partial q_N} = m_{tot} g_0 (p_{cm}^h - p_0^h)$, which shows the result.

B.4.9 Sign Convention on Measuring Angles

The purpose of this section is to note the consequences of the sign convention used to measure angles. The standing assumption in this review of mechanics has been that angles are *positive* when measured in the *countrerclockwise*. This assumption was made because it is the most common.

The first remark is that sign convention is only important when speaking of quantities referenced to the inertial frame, such as absolute angles, absolute angular velocity, and angular momentum. For example, when angles are measured to increase in the countrerclockwise direction, the angular momentum of a link has been defined in (B.150) so that it is positive when the link is rotating countrerclockwise. In the following, the required changes for working with the *clockwise* convention of angle measurement are detailed. The most important changes involve angular momentum and its definition via the wedge product.

Angular position and velocity: Assume that angles increase in the clockwise direction. Then the rotation matrix in (B.96) should be defined as

$$\mathbf{R}(\theta_i^{\text{abs}}) := \begin{bmatrix} \cos(\theta_i^{\text{abs}}) & \sin(\theta_i^{\text{abs}}) \\ -\sin(\theta_i^{\text{abs}}) & \cos(\theta_i^{\text{abs}}) \end{bmatrix}. \quad (\text{B.192})$$

The velocity of a link in the inertial frame is then given by

$$\begin{bmatrix} \dot{\bar{p}}_i^{\text{h}} \\ \dot{\bar{p}}_i^{\text{v}} \end{bmatrix} = \begin{bmatrix} \dot{p}_i^{\text{h}} \\ \dot{p}_i^{\text{v}} \end{bmatrix} + \begin{bmatrix} 0 & 1 \\ -1 & 0 \end{bmatrix} \begin{bmatrix} \cos(\theta_i^{\text{abs}}) & \sin(\theta_i^{\text{abs}}) \\ -\sin(\theta_i^{\text{abs}}) & \cos(\theta_i^{\text{abs}}) \end{bmatrix} \begin{bmatrix} \bar{\ell}_i^{\text{h}} \\ \bar{\ell}_i^{\text{v}} \end{bmatrix} \dot{\theta}_i^{\text{abs}}, \quad (\text{B.193})$$

because

$$\frac{d}{d\theta} \begin{bmatrix} \cos(\theta) & \sin(\theta) \\ -\sin(\theta) & \cos(\theta) \end{bmatrix} = \begin{bmatrix} 0 & 1 \\ -1 & 0 \end{bmatrix} \begin{bmatrix} \cos(\theta) & \sin(\theta) \\ -\sin(\theta) & \cos(\theta) \end{bmatrix}. \quad (\text{B.194})$$

Because of (B.194), formulas (B.167), (B.168), and (B.169) in Proposition B.8 must be modified. For the convenience of the reader, the entire proposition is restated.

Proposition B.10

Let q_b be a set of body coordinates associated with link- i_0 of an N -link open kinematic chain. Let $q_s = (q_b; \theta_{i_0}^{\text{abs}})$, where $\theta_{i_0}^{\text{abs}}$ is measured so that it increases in the clockwise direction, and set $q_f = (q_b; \theta_{i_0}^{\text{abs}}; p_{i_0}^{\text{h}}; p_{i_0}^{\text{v}})$. Let q stand for q_s or q_f . The following statements hold:

(a) $\frac{\partial}{\partial q_N} \theta_i^{\text{abs}}(q) \equiv 1$, for $i \in \{1, \dots, N\}$;

(b) Any point p on the kinematic chain satisfies

$$\frac{\partial}{\partial q_N} \begin{bmatrix} (p^{\text{h}} - p_{i_0}^{\text{h}})(q) \\ (p^{\text{v}} - p_{i_0}^{\text{v}})(q) \end{bmatrix} = \begin{bmatrix} 0 & 1 \\ -1 & 0 \end{bmatrix} \begin{bmatrix} (p^{\text{h}} - p_{i_0}^{\text{h}})(q) \\ (p^{\text{v}} - p_{i_0}^{\text{v}})(q) \end{bmatrix}, \quad (\text{B.195})$$

(c) and hence, the centers of mass satisfy

$$\frac{\partial}{\partial q_N} \begin{bmatrix} (p_{\text{cm},i}^{\text{h}} - p_{i_0}^{\text{h}})(q) \\ (p_{\text{cm},i}^{\text{v}} - p_{i_0}^{\text{v}})(q) \end{bmatrix} = \begin{bmatrix} 0 & 1 \\ -1 & 0 \end{bmatrix} \begin{bmatrix} (p_{\text{cm},i}^{\text{h}} - p_{i_0}^{\text{h}})(q) \\ (p_{\text{cm},i}^{\text{v}} - p_{i_0}^{\text{v}})(q) \end{bmatrix}, \quad (\text{B.196})$$

for $i \in \{1, \dots, N\}$, and

$$\frac{\partial}{\partial q_N} \begin{bmatrix} (p_{\text{cm}}^{\text{h}} - p_{i_0}^{\text{h}})(q) \\ (p_{\text{cm}}^{\text{v}} - p_{i_0}^{\text{v}})(q) \end{bmatrix} = \begin{bmatrix} 0 & 1 \\ -1 & 0 \end{bmatrix} \begin{bmatrix} (p_{\text{cm}}^{\text{h}} - p_{i_0}^{\text{h}})(q) \\ (p_{\text{cm}}^{\text{v}} - p_{i_0}^{\text{v}})(q) \end{bmatrix}; \quad (\text{B.197})$$

(d) The mass-inertia matrix for the pinned chain satisfies $\frac{\partial}{\partial q_N} D_s(q_s) \equiv 0$, and hence, D_s depends only on q_b .

If the generalized coordinates are chosen instead as $q_f = (q_b; \theta_{i_0}^{\text{abs}}; p_{\text{cm}}^h; p_{\text{cm}}^v)$, where q_b are body coordinates associated with link- i_0 , then (a), (b) and (c) still hold, and moreover,

- (e) the mass-inertia matrix for the free chain, D_f , has the block-diagonal form given in (B.161), with $\frac{\partial}{\partial q_N} A(q_s) \equiv 0$; in other words, both D_f and A depend only on q_b .

Angular momentum: When angles are measured to increase in the clockwise direction, the sign on the definition of the *wedge product* of two vectors $x := (x_1; x_2)$ and $y := (y_1; y_2)$ in \mathbb{R}^2 is changed from (B.148) to read

$$x \wedge y := x_2 y_1 - x_1 y_2, \quad (\text{B.198})$$

that is,

$$x \wedge y = \begin{bmatrix} x_1 \\ x_2 \end{bmatrix}' \begin{bmatrix} 0 & -1 \\ 1 & 0 \end{bmatrix} \begin{bmatrix} y_1 \\ y_2 \end{bmatrix}. \quad (\text{B.199})$$

Hence, if $\{e_1, e_2, e_3\}$ are the natural basis vectors in \mathbb{R}^3 , then

$$x \wedge y = -[(x_1 e_1 + x_2 e_2) \times (y_1 e_1 + y_2 e_2)] \cdot e_3. \quad (\text{B.200})$$

With this modification to the wedge product, the defining equations for angular momentum and total angular momentum in (B.150) and (B.151a) remain unchanged and no alteration is necessary in the properties given in (B.152) through (B.155). A sign must be changed in (B.185) of Proposition B.9. For the convenience of the reader, the entire proposition is restated.

Proposition B.11

Let q_b be a set of body coordinates associated with link- i_0 of an N -link open kinematic chain. Let $q_s = (q_b; \theta_{i_0}^{\text{abs}})$, where $\theta_{i_0}^{\text{abs}}$ is measured so that it increases in the clockwise direction, and set $q_f = (q_b; \theta_{i_0}^{\text{abs}}; p_{\text{cm}}^h; p_{\text{cm}}^v)$. Then the following statements hold:

- (a) if the chain is free, $\frac{\partial}{\partial \dot{q}_N} \mathcal{L}(q_f, \dot{q}_f) = \sigma_{\text{cm}}$, the angular momentum about the center of mass, and $\frac{d}{dt} \sigma_{\text{cm}} = \gamma_N$;
- (b) if the chain is pinned, $\frac{\partial}{\partial \dot{q}_N} \mathcal{L}(q_s, \dot{q}_s) = \sigma_0$, the angular momentum about the pivot, and

$$\frac{d}{dt} \sigma_0 = m_{\text{tot}} g_0 (p_{\text{cm}}^h - p_0^h) + \gamma_N, \quad (\text{B.201})$$

where $p_0 = (p_0^h; p_0^v)$ is the Cartesian position of the pivot and γ_N is the external torque applied about the pivot (assumed to be measured with the same convention as $\theta_{i_0}^{\text{abs}}$).

B.4.10 Other Useful Facts

Canonical change of coordinates: Consider a mechanical system in generalized coordinates $(q; \dot{q}) \in T\mathcal{Q}$ with quadratic kinetic energy

$$K(q, \dot{q}) = \frac{1}{2} \dot{q}' D(q) \dot{q} \quad (\text{B.202})$$

and potential energy $V(q)$. Let $\bar{q} = F(q)$ be a local change of coordinates on \mathcal{Q} , that is, F is a local diffeomorphism. If the velocities are expressed as $\dot{\bar{q}} = \frac{\partial F}{\partial q} \dot{q}$, then the kinetic energy becomes

$$\bar{K}(\bar{q}, \dot{\bar{q}}) = \frac{1}{2} \dot{\bar{q}}' \bar{D}(\bar{q}) \dot{\bar{q}}, \quad (\text{B.203})$$

where

$$\bar{D}(\bar{q}) = \left. \frac{\partial F(q)}{\partial q}' D(q) \frac{\partial F(q)}{\partial q} \right|_{q=F^{-1}(\bar{q})}. \quad (\text{B.204})$$

The potential energy is

$$\bar{V}(\bar{q}) = V(q)|_{q=F^{-1}(\bar{q})}. \quad (\text{B.205})$$

The transformation

$$\begin{bmatrix} \bar{q} \\ \dot{\bar{q}} \end{bmatrix} = \begin{bmatrix} F(q) \\ \frac{\partial F(q)}{\partial q} \dot{q} \end{bmatrix} \quad (\text{B.206})$$

is called a *canonical change of coordinates*.

Workless holonomic constraints: A collection of N free links, a free open kinematic chain, and a pinned open kinematic chain are all special cases of a more general Lagrangian dynamical system called a *simple mechanical system*. Consider an n -dimensional manifold \mathcal{Q} with local coordinates $q \in \mathcal{Q}$ and tangent bundle $T\mathcal{Q}$. Suppose that $K : T\mathcal{Q} \rightarrow \mathbb{R}$ is quadratic in \dot{q} and positive definite, that is, $K = \frac{1}{2} \dot{q}' D(q) \dot{q}$, with D positive definite. Moreover, suppose that $V : \mathcal{Q} \rightarrow \mathbb{R}$. Then the dynamic system arising from $\mathcal{L} = K - V$ by

$$\frac{d}{dt} \frac{\partial \mathcal{L}}{\partial \dot{q}} - \frac{\partial \mathcal{L}}{\partial q} = \Gamma, \quad (\text{B.207})$$

where Γ is a set of generalized forces and torques, is called a *simple mechanical system*. The system is *simple* because the kinetic energy is quadratic and positive definite and the potential energy depends only on the configuration variables. From (B.143), if we set

$$x = \begin{bmatrix} x_1 \\ x_2 \end{bmatrix} = \begin{bmatrix} q \\ \dot{q} \end{bmatrix}, \quad (\text{B.208})$$

the system can be written in state variable form as

$$\begin{bmatrix} \dot{x}_1 \\ \dot{x}_2 \end{bmatrix} = \begin{bmatrix} x_2 \\ D^{-1}(x_1) (-C(x_1, x_2)x_2 - G(x_1) + \Gamma) \end{bmatrix}. \quad (\text{B.209})$$

A relation among the generalized coordinates that can be expressed in the form

$$q_2 = \lambda(q_1), \quad (\text{B.210})$$

where $(q_1; q_2)$ is a partition of q , is called a *holonomic constraint*. More generally, a relation of the form $F(q) = 0$ is also called a holonomic constraint. However, in a neighborhood of a point where F has constant rank, the Implicit Function Theorem ensures that a local representation of the form (B.210) exists, that is, $F(q_1, q_2) = 0$ if, and only if, $q_2 - \lambda(q_1) = 0$, so the more general form will not be considered here.

Consider the embedded submanifold of \mathcal{Q} defined by $\mathcal{Q}_r = \{(q_1; q_2) \in \mathcal{Q} \mid q_2 = \lambda(q_1)\}$. Then there exist generalized constraint forces of the form

$$\Gamma = \begin{bmatrix} -\frac{\partial \lambda(q_1)}{\partial q_1} \\ \mathbf{I} \end{bmatrix} u^*(q, \dot{q}), \quad (\text{B.211})$$

where $u^* : T\mathcal{Q} \rightarrow \mathbb{R}^m$, $m = \dim(q_2)$, such that $T\mathcal{Q}_r$ is invariant under solutions of

$$\begin{bmatrix} \dot{x}_1 \\ \dot{x}_2 \end{bmatrix} = \begin{bmatrix} x_2 \\ D^{-1}(x_1) \left(-C(x_1, x_2)x_2 - G(x_1) + \begin{bmatrix} -\frac{\partial \lambda(q_1)}{\partial q_1} \\ \mathbf{I} \end{bmatrix} u^*(x_1, x_2) \right) \end{bmatrix}. \quad (\text{B.212})$$

Moreover, the corresponding restriction dynamics is the simple mechanical system on $T\mathcal{Q}_r$ given by

$$\mathcal{L}_r(q_1, \dot{q}_1) = K_r(q_1, \dot{q}_1) - V_r(q_1) \quad (\text{B.213a})$$

$$V_r(q_r) = V(q_1, \lambda(q_1)) \quad (\text{B.213b})$$

$$K_r(q_1, \dot{q}_1) = \frac{1}{2} \dot{q}_1' D_r(q_1) \dot{q}_1 \quad (\text{B.213c})$$

$$\begin{aligned} D_r(q_1) &= D_{11}(q_1, \lambda(q_1)) + \left(\frac{\partial \lambda(q_1)}{\partial q_1} \right)' D_{22}(q_1, \lambda(q_1)) \frac{\partial \lambda(q_1)}{\partial q_1} \\ &\quad + \left(D_{12}(q_1, \lambda(q_1)) \frac{\partial \lambda(q_1)}{\partial q_1} \right)' + D_{12}(q_1, \lambda(q_1)) \frac{\partial \lambda(q_1)}{\partial q_1}, \end{aligned} \quad (\text{B.213d})$$

where

$$D(q_1, q_2) = \begin{bmatrix} D_{11}(q_1, q_2) & D_{12}(q_1, q_2) \\ D_{12}(q_1, q_2) & D_{22}(q_1, q_2) \end{bmatrix} \quad (\text{B.214})$$

is partitioned compatible with (q_1, q_2) . For obvious reasons, it is natural to write this as

$$\mathcal{L}_r = \mathcal{L}|_{T\mathcal{Q}_r}. \quad (\text{B.215})$$

The set of constraints (B.210) is said to be *workless* because the instantaneous power given by the inner product of the generalized constraint forces (B.211) and the velocity along the constraints,

$$\begin{bmatrix} -\frac{\partial \lambda(q_1)}{\partial q_1} \\ \mathbf{I} \end{bmatrix} \dot{q}_1, \quad (\text{B.216})$$

is zero.

Remark B.12 It is important to note that the restriction dynamics can be computed without determining the generalized constraint forces, (B.211).

Remark B.13 Let Γ be as in (B.211) and let $\tilde{\Gamma}$ be any set of generalized forces that do zero work on the constraints (B.210) *and* render $T\mathcal{Q}_r$ invariant. Then $\Gamma|_{T\mathcal{Q}_r} = \tilde{\Gamma}|_{T\mathcal{Q}_r}$.

Remark B.14 Let \mathcal{Q}_f be the configuration manifold of a free open kinematic chain and let $\mathcal{L}_f : T\mathcal{Q}_f \rightarrow \mathbb{R}$ be the corresponding Lagrangian. Consider the pinned open kinematic chain formed by attaching the free open kinematic chain to a pivot via (B.127). Then the configuration manifold of the pinned open kinematic chain is the embedded submanifold

$$\mathcal{Q}_s = \{q \in \mathcal{Q}_f \mid (\text{B.127}) \text{ holds}\} \quad (\text{B.217})$$

and its Lagrangian is

$$\mathcal{L}_s = \mathcal{L}_f|_{T\mathcal{Q}_s}. \quad (\text{B.218})$$

Accounting for motors and rigid gear trains: Consider an open kinematic chain with generalized coordinates q , kinetic energy $K(q, \dot{q})$ and potential energy $V(q)$. Consider also a motor of mass²⁰ M_{mot} and rotor inertia J_{rot} such that the motor housing is rigidly attached to link- i and the rotor is rigidly connected to an angle θ_j that is either a relative angle of the kinematic chain or the absolute angle of the pivot (of course, only if the chain is pinned). Because a motor is efficient at providing low torque at high speed and most robotic applications require high torque at low speed, suppose furthermore that the rotor is connected to θ_j through a gear ratio of R so that

$$\theta_{\text{rot}} = R\theta_j. \quad (\text{B.219})$$

²⁰The rotor mass is included.

Note that the absolute angle of the rotor is

$$\theta_{\text{rot}}^{\text{abs}}(q) = \theta_i^{\text{abs}}(q) + \theta_{\text{rot}} = \theta_i^{\text{abs}}(q) + R\theta_j(q). \quad (\text{B.220})$$

Let $p_{\text{mot}}(q)$ denote the Cartesian position of the motor center of mass, which is assumed to be independent of the position of the rotor (i.e., the rotor is symmetric).

The potential energy of the kinematic chain plus motor is simply

$$V_{\text{aug}}(q) = V(q) + g_0 M_{\text{mot}} p_{\text{mot}}^{\text{v}}(q). \quad (\text{B.221})$$

The kinetic energy of the kinematic chain plus motor is given by

$$\begin{aligned} K_{\text{aug}}(q, \dot{q}) &= K(q, \dot{q}) + \frac{1}{2} M_{\text{mot}} \left((\dot{p}_{\text{mot}}^{\text{h}}(q, \dot{q}))^2 + (\dot{p}_{\text{mot}}^{\text{v}}(q, \dot{q}))^2 \right) \\ &\quad + \frac{1}{2} J_{\text{rot}} \left(\dot{\theta}_{\text{rot}}^{\text{abs}}(q, \dot{q}) \right)^2, \end{aligned} \quad (\text{B.222})$$

which, when the last term is expanded, yields

$$\begin{aligned} K_{\text{aug}}(q, \dot{q}) &= K(q, \dot{q}) + \frac{1}{2} M_{\text{mot}} \left((\dot{p}_{\text{mot}}^{\text{h}}(q, \dot{q}))^2 + (\dot{p}_{\text{mot}}^{\text{v}}(q, \dot{q}))^2 \right) \\ &\quad + \frac{1}{2} J_{\text{rot}} \left(\dot{\theta}_i^{\text{abs}}(q, \dot{q}) \right)^2 + R J_{\text{rot}} \dot{\theta}_i^{\text{abs}}(q, \dot{q}) \dot{\theta}_j(q, \dot{q}) + \frac{1}{2} R^2 J_{\text{rot}} \left(\dot{\theta}_j(q, \dot{q}) \right)^2. \end{aligned} \quad (\text{B.223})$$

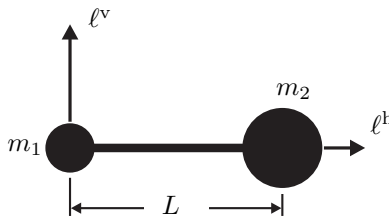
Remark B.15 The term $R^2 J_{\text{rot}}$ is called the *reflected rotor inertia*. In many practical situations, the gear ratio R is quite large, say 30 or more, in which case the reflected rotor inertia often exceeds the inertia of the link attached to the rotor. Note also that the moment of inertia of the motor housing about its center of mass has been assumed to be zero, that is, the motor housing has been modeled as a point mass.

Center of mass and moment of inertia: In a set of link coordinates, the center of mass of a rigid link with mass density $\rho(\ell^h, \ell^v)$ and point masses $\{m_1, \dots, m_k\}$ located at $(\ell_i^h; \ell_i^v)$ is defined by

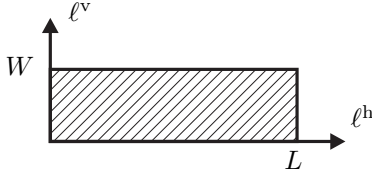
$$\begin{bmatrix} \ell_{\text{cm}}^h \\ \ell_{\text{cm}}^v \end{bmatrix} = \frac{1}{m_{\text{tot}}} \int \int_{\text{link}} \rho(\ell^h, \ell^v) \begin{bmatrix} \ell^h \\ \ell^v \end{bmatrix} d\ell^h d\ell^v + \frac{1}{m_{\text{tot}}} \sum_{i=1}^k m_i \begin{bmatrix} \ell_i^h \\ \ell_i^v \end{bmatrix}, \quad (\text{B.224})$$

where

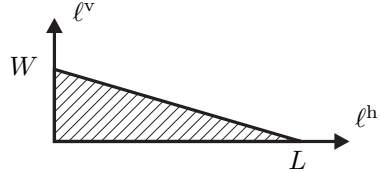
$$m_{\text{tot}} = \int \int_{\text{body}} \rho(\ell^h, \ell^v) d\ell^h d\ell^v + \sum_{i=1}^k m_i \quad (\text{B.225})$$



(a) Two point masses m_1 and m_2 joined by a massless bar of length L .



(b) A rectangular body of uniform density and total mass m_{tot} .



(c) A body of uniform density and triangular shape having total mass m_{tot} .

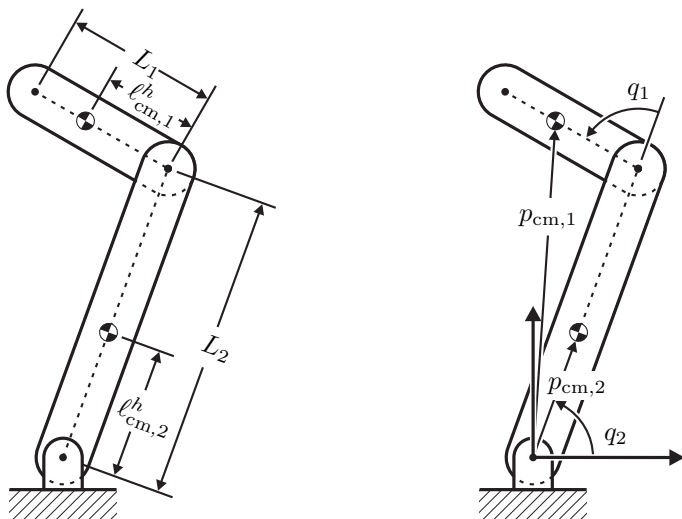
Figure B.16. Rigid bodies used to illustrate center of mass and moment of inertia.

is the total mass. For the link in Fig. B.16(a), the center of mass is $(\ell_{\text{cm}}^h; \ell_{\text{cm}}^v) = (\frac{m_2}{m_1+m_2}L; 0)$, in Fig. B.16(b), the center of mass is $(\ell_{\text{cm}}^h; \ell_{\text{cm}}^v) = (L/2; W/2)$, and Fig. B.16(c), the center of mass is $(\ell_{\text{cm}}^h; \ell_{\text{cm}}^v) = (L/3; W/3)$.

Let $\ell_0 = (\ell_0^h; \ell_0^v)$ be a fixed point in the link coordinates. The moment of inertia of the link about ℓ_0 is

$$\begin{aligned} J_0 &= \int \int_{\text{link}} \rho(\ell^h, \ell^v) ((\ell^h - \ell_0^h)^2 + (\ell^v - \ell_0^v)^2) d\ell^h d\ell^v \\ &\quad + \sum_{i=1}^k m_i ((\ell_i^h - \ell_0^h)^2 + (\ell_i^v - \ell_0^v)^2). \end{aligned} \quad (\text{B.226})$$

In Fig. B.16(a), the moment of inertia about the left end is $J_0 = m_2 L^2$ and the moment of inertia about the center of mass is $J_{\text{cm}} = \frac{m_1 m_2}{m_1 + m_2} L^2$. In Fig. B.16(b), the moment of inertia about the lower-left corner is $J_0 = \frac{m_{\text{tot}}}{3} (L^2 + W^2)$ and the moment of inertia about the center of mass is $J_{\text{cm}} = \frac{m_{\text{tot}}}{12} (L^2 + W^2)$. In Fig. B.16(c), the moment of inertia about the lower-left corner is $J_0 = \frac{m_{\text{tot}}}{6} (L^2 + W^2)$ and the moment of inertia about the center of mass is $J_{\text{cm}} = \frac{m_{\text{tot}}}{18} (L^2 + W^2)$.



(a) Measurement conventions for the link lengths and positions of the centers of mass. It is assumed that the center of mass of each link lies along the longitudinal axis of the link.

(b) The link measurement conventions. The origin or the world frame (inertial frame) is colocated with the pivot. The Cartesian positions of the centers of mass are also shown.

Figure B.17. Acrobot example.

B.4.11 Example: The Acrobot

The objective is to derive the model of a simple mechanical system. Consider the pinned two-link open kinematic chain shown in Fig. B.17, called the Acrobot, in which it is assumed that the relative angle between the two links is actuated. Figure B.17(a) depicts the link coordinates. Figure B.17(b) indicates that the origin of the world frame is colocated with the axis of the pivot,

$$\begin{bmatrix} p_0^h \\ p_0^v \end{bmatrix} = \begin{bmatrix} 0 \\ 0 \end{bmatrix}, \quad (\text{B.227})$$

and it also depicts the generalized coordinates q_1 and q_2 from which the absolute angles of the links are determined,

$$\begin{bmatrix} \theta_1^{\text{abs}} \\ \theta_2^{\text{abs}} \end{bmatrix} = \begin{bmatrix} q_1 + q_2 \\ q_2 \end{bmatrix}. \quad (\text{B.228})$$

Because the relative angle q_1 is a body coordinate and q_2 is an absolute angle, we know by Proposition B.8 that in the coordinates $(q_1; q_2)$, the mass-inertia matrix will only depend on q_1 , or in other words, q_2 is cyclic.

Denote the masses of the links by m_1 and m_2 , respectively, and let the inertias about the center of mass be $J_{\text{cm},1}$ and $J_{\text{cm},2}$, respectively. We now proceed to determine the Lagrangian of the system by computing its total potential energy and total kinetic energy. We begin by writing down the Cartesian positions of the center of mass of each link, and from this, we compute the center of mass of the kinematic chain:

$$\begin{bmatrix} p_{\text{cm},2}^{\text{h}} \\ p_{\text{cm},2}^{\text{v}} \end{bmatrix} = \mathbf{R}(\theta_2^{\text{abs}}) \begin{bmatrix} \ell_{\text{cm},2}^{\text{h}} \\ 0 \end{bmatrix} \quad (\text{B.229a})$$

$$= \begin{bmatrix} \ell_{\text{cm},2}^{\text{h}} \cos(q_2) \\ \ell_{\text{cm},2}^{\text{h}} \sin(q_2) \end{bmatrix} \quad (\text{B.229b})$$

$$\begin{bmatrix} p_{\text{cm},1}^{\text{h}} \\ p_{\text{cm},1}^{\text{v}} \end{bmatrix} = \mathbf{R}(\theta_2^{\text{abs}}) \begin{bmatrix} L_2 \\ 0 \end{bmatrix} + \mathbf{R}(\theta_1^{\text{abs}}) \begin{bmatrix} \ell_{\text{cm},1}^{\text{h}} \\ 0 \end{bmatrix} \quad (\text{B.229c})$$

$$= \begin{bmatrix} L_2 \cos(q_2) + \ell_{\text{cm},1}^{\text{h}} \cos(q_1 + q_2) \\ L_2 \sin(q_2) + \ell_{\text{cm},1}^{\text{h}} \sin(q_1 + q_2) \end{bmatrix} \quad (\text{B.229d})$$

$$\begin{bmatrix} p_{\text{cm}}^{\text{h}} \\ p_{\text{cm}}^{\text{v}} \end{bmatrix} = \frac{m_1}{m_1 + m_2} \begin{bmatrix} p_{\text{cm},1}^{\text{h}} \\ p_{\text{cm},1}^{\text{v}} \end{bmatrix} + \frac{m_2}{m_1 + m_2} \begin{bmatrix} p_{\text{cm},2}^{\text{h}} \\ p_{\text{cm},2}^{\text{v}} \end{bmatrix} \quad (\text{B.229e})$$

$$= \frac{1}{m_1 + m_2} \begin{bmatrix} (m_1 L_2 + m_2 \ell_{\text{cm},2}^{\text{h}}) \cos(q_2) + m_1 \ell_{\text{cm},1}^{\text{h}} \cos(q_1 + q_2) \\ (m_1 L_2 + m_2 \ell_{\text{cm},2}^{\text{h}}) \sin(q_2) + m_1 \ell_{\text{cm},1}^{\text{h}} \sin(q_1 + q_2) \end{bmatrix}. \quad (\text{B.229f})$$

Hence, by (B.136), the total potential energy is

$$V_s(q_1, q_2) = (m_1 + m_2) g_0 p_{\text{cm}}^{\text{v}}(q_1, q_2) \quad (\text{B.230a})$$

$$= (m_1 g_0 L_2 + m_2 g_0 \ell_{\text{cm},2}^{\text{h}}) \sin(q_2) + m_1 g_0 \ell_{\text{cm},1}^{\text{h}} \sin(q_1 + q_2). \quad (\text{B.230b})$$

To compute the total kinetic energy, we differentiate (B.228), (B.229b), and (B.229d) and then substitute the results into (B.134), (B.137), and (B.138) to obtain

$$K_s(q_1, \dot{q}_1, \dot{q}_2) =: \frac{1}{2} [\dot{q}_1 \quad \dot{q}_2] D_s(q_1) \begin{bmatrix} \dot{q}_1 \\ \dot{q}_2 \end{bmatrix}, \quad (\text{B.231})$$

where

$$(D_s(q_1))_{1,1} = m_1 (\ell_{\text{cm},1}^{\text{h}})^2 + J_{\text{cm},1} \quad (\text{B.232a})$$

$$(D_s(q_1))_{1,2} = m_1 \ell_{\text{cm},1}^{\text{h}} L_2 \cos(q_1) + m_1 (\ell_{\text{cm},1}^{\text{h}})^2 + J_{\text{cm},1} \quad (\text{B.232b})$$

$$(D_s(q_1))_{2,1} = m_1 \ell_{\text{cm},1}^{\text{h}} L_2 \cos(q_1) + m_1 (\ell_{\text{cm},1}^{\text{h}})^2 + J_{\text{cm},1} \quad (\text{B.232c})$$

$$(D_s(q_1))_{2,2} = 2m_1 \ell_{\text{cm},1}^{\text{h}} L_2 \cos(q_1) + m_1 L_2^2 + m_1 (\ell_{\text{cm},1}^{\text{h}})^2 + J_{\text{cm},1} + m_2 (\ell_{\text{cm},2}^{\text{h}})^2 + J_{\text{cm},2}. \quad (\text{B.232d})$$

From K_s and V_s , the dynamic model (B.143) is determined. The remaining terms are

$$(C_s(q_1, \dot{q}_1, \dot{q}_2))_{1,1} = 0 \quad (\text{B.233a})$$

$$(C_s(q_1, \dot{q}_1, \dot{q}_2))_{1,2} = m_1 \ell_{\text{cm},1}^{\text{h}} L_2 \sin(q_1) \dot{q}_2 \quad (\text{B.233b})$$

$$(C_s(q_1, \dot{q}_1, \dot{q}_2))_{2,1} = -m_1 \ell_{\text{cm},1}^{\text{h}} L_2 \sin(q_1) (\dot{q}_1 + \dot{q}_2) \quad (\text{B.233c})$$

$$(C_s(q_1, \dot{q}_1, \dot{q}_2))_{2,2} = -m_1 \ell_{\text{cm},1}^{\text{h}} L_2 \sin(q_1) \dot{q}_1, \quad (\text{B.233d})$$

$$(G_s(q_1, q_2))_1 = m_1 g_0 \ell_{\text{cm},1}^{\text{h}} \cos(q_1 + q_2) \quad (\text{B.234a})$$

$$\begin{aligned} (G_s(q_1, q_2))_2 = & m_1 g_0 L_2 \cos(q_1) + m_1 g_0 \ell_{\text{cm},1}^{\text{h}} \cos(q_1 + q_2) \\ & + m_2 g_0 \ell_{\text{cm},2}^{\text{h}} \cos(q_2), \end{aligned} \quad (\text{B.234b})$$

and

$$B_s = \begin{bmatrix} 1 \\ 0 \end{bmatrix}. \quad (\text{B.235})$$

Using either (B.151a) with $p_a = p_0$, the pivot point, or Proposition B.9, the total angular momentum about the pivot is computed to be

$$\sigma_0 = (D_s(q_1))_{2,1} \dot{q}_1 + (D_s(q_1))_{2,2} \dot{q}_2. \quad (\text{B.236})$$

From Proposition B.9 and the definition of the generalized conjugate momenta in (B.181), it follows that

$$\bar{\sigma}_2 = (D_s(q_1))_{2,1} \dot{q}_1 + (D_s(q_1))_{2,2} \dot{q}_2 = \sigma_0. \quad (\text{B.237})$$

Proofs and Technical Details

C.1 Proofs Associated with Chapter 4

C.1.1 Continuity of T_I

Lemma C.1

Suppose that Hypotheses HSH1–HSH3 hold. Then T_I is continuous at points x_0 where $0 < T_I(x_0) < \infty$ and $L_f H(\varphi^f(T_I(x_0), x_0)) \neq 0$.

Proof Let $\epsilon > 0$ be given. Define $\bar{x} := \varphi^f(T_I(x_0), x_0)$, and without loss of generality, suppose that $L_f H(\bar{x}) < 0$. Then, from the definition of T_I and HSH3, $H(\varphi^f(t, x_0)) > 0$ for all $0 \leq t < T_I(x_0)$. This in turn implies that, for any $0 < t_1 < T_I(x_0)$,

$$\mu(t_1) := \inf_{0 \leq t \leq t_1} \text{dist}(\varphi^f(t, x_0), \mathcal{S}) > 0, \quad (\text{C.1})$$

since: (a) $\varphi^f(t, x_0)$ is continuous in t ; (b) the interval $[0, t_1]$ is compact; and (c), by HSH3, \mathcal{S} is closed and equals the zero level set of H . By HSH2, there exists $\bar{\epsilon} > 0$ such that φ^f can be continued on $[0, T_I(x_0) + \bar{\epsilon}]$, [110]. Moreover, since $L_f H(\bar{x}) < 0$, for $\bar{\epsilon} > 0$ sufficiently small, $t_2 := T_I(x_0) + \bar{\epsilon}/2$ and $x_2 := \varphi^f(t_2, x_0)$, result in $H(x_2) < 0$. From $H(x_2) < 0$, it follows that $\text{dist}(x_2, \mathcal{S}) > 0$. If necessary, reduce $\bar{\epsilon}$ so that $0 < \bar{\epsilon} < \min\{\epsilon, T_I(x_0)\}$, and define $t_1 := T_I(x_0) - \bar{\epsilon}/2$ and $x_1 := \varphi^f(t_1, x_0)$. From (C.1), $\mu(t_1) > 0$. From HSH2, the solutions depend continuously on the initial conditions. Thus, there exists $\delta > 0$, such that, for all $x \in B_\delta(x_0)$, $\sup_{0 \leq t \leq t_2} \|\varphi^f(t, x) - \varphi^f(t, x_0)\| < \min\{\text{dist}(x_2, \mathcal{S}), \mu(t_1)/2\}$. Therefore, for $x \in B_\delta(x_0)$, $t_1 < T_I(x) < t_2$, which implies that $|T_I(x) - T_I(x_0)| < \epsilon$, establishing the continuity of T_I at x_0 .

C.1.2 Distance of a Trajectory to a Periodic Orbit

Recall that if \mathcal{O} is any periodic orbit that is transversal to \mathcal{S} , then $\mathcal{O} \subset \tilde{\mathcal{X}}$. For $x \in \tilde{\mathcal{X}}$, define

$$d(x) := \sup_{0 \leq t \leq T_I(x)} \text{dist}(\varphi^-(t, x), \mathcal{O}). \quad (\text{C.2})$$

Note that d vanishes on \mathcal{O} . Note also that for $0 < t \leq T_I(x)$, $\varphi^-(t, x) = \varphi^f(t, x)$, and hence

$$d(x) = \sup_{0 < t \leq T_I(x)} \text{dist}(\varphi^f(t, x), \mathcal{O}) = \sup_{0 \leq t \leq T_I(x)} \text{dist}(\varphi^f(t, x), \mathcal{O}). \quad (\text{C.3})$$

Note also that $\forall x, y \in \tilde{\mathcal{X}}$, $|\text{dist}(x, \mathcal{O}) - \text{dist}(y, \mathcal{O})| \leq \|x - y\|$.

Lemma C.2

Under HSH1–HSH3, $d : \tilde{\mathcal{X}} \rightarrow \mathbb{R}$ is well defined and continuous on $\tilde{\mathcal{X}}$.

Proof For any $x_0 \in \tilde{\mathcal{X}}$, $T_I(x_0)$ is finite, and $\varphi^f(t, x_0)$ is defined on the compact set $[0, T_I(x_0)]$. This and the continuity of $\varphi^f(t, x_0)$ with respect to t imply by the Heine-Borel Theorem that $d(x_0)$ is finite and well-defined. To show continuity, let $x_0 \in \tilde{\mathcal{X}}$ and $\epsilon > 0$ be given. By definition of T_I , $\bar{x} := \varphi^f(T_I(x_0), x_0) \in \mathcal{S}$. Without loss of generality, suppose that $L_f H(\bar{x}) < 0$. Let $\eta > 0$ be such that for all $0 < t < \eta$, $H(\varphi^f(t, \bar{x})) < 0$ and $\|\bar{x} - \varphi^f(t, \bar{x})\| < \epsilon$. Such an η exists because: (i) HSH2 implies there exists $\eta > 0$ such that φ^f can be continued on $[0, T_I(x_0) + \eta]$, [110]; (ii) $L_f H(\bar{x}) < 0$; and (iii) $\varphi^f(t, \bar{x})$ depends continuously on t . Define $t_3 := T_I(x_0) + \eta$. By HSH2 and Lemma C.1, there exists $\delta > 0$ such that for all $\tilde{x} \in B_\delta(x_0)$, $\sup_{0 \leq t \leq t_3} \|\varphi^f(t, x_0) - \varphi^f(t, \tilde{x})\| < \epsilon$ and $T_I(\tilde{x}) < t_3$. Hence,

$$\begin{aligned} |d(\tilde{x}) - d(x_0)| &= \left| \sup_{0 \leq t \leq T_I(\tilde{x})} \text{dist}(\varphi^f(t, \tilde{x}), \mathcal{O}) - \sup_{0 \leq t \leq T_I(x_0)} \text{dist}(\varphi^f(t, x_0), \mathcal{O}) \right| \\ &\leq \sup_{0 \leq t \leq t_3} |\text{dist}(\varphi^f(t, \tilde{x}), \mathcal{O}) - \text{dist}(\varphi^f(t, x_0), \mathcal{O})| \\ &\leq \sup_{0 \leq t \leq t_3} \|\varphi^f(t, \tilde{x}) - \varphi^f(t, x_0)\| \\ &\leq \epsilon. \end{aligned} \quad (\text{C.4})$$

C.1.3 Proof of Theorem 4.1

The first and second statements are immediate. Since the sufficiency portions of statements c) and d) are straightforward, only necessity is proved.

Stability and asymptotic stability are tackled first. Suppose that $P(x^*) = x^*$, and let \mathcal{O} be the periodic orbit of (4.1) corresponding to $\Delta(x^*)$. By b), the orbit is transversal to \mathcal{S} . Let $\epsilon > 0$ be given. Since x^* is stable in the sense of Lyapunov, for any $\bar{\epsilon} > 0$, there exists $\delta(\bar{\epsilon}) > 0$ such that, for all $k \geq 0$, $\bar{x} \in B_{\delta(\bar{\epsilon})}(x^*) \cap \mathcal{S}$, implies $P^k(\bar{x}) \in B_{\bar{\epsilon}}(x^*) \cap \mathcal{S}$, where P^k is P composed with itself k -times. In particular, this implies that for all $\bar{x} \in B_{\delta(\bar{\epsilon})}(x^*) \cap \mathcal{S}$, there exists a solution $\varphi(t)$ of (4.1) defined on $[0, \infty)$, such that $\varphi(0) = \Delta(\bar{x})$. Moreover, an upper bound on how far the solution φ wanders from the orbit \mathcal{O} is given by

$$\sup_{t \geq 0} \text{dist}(\varphi(t), \mathcal{O}) \leq \sup_{x \in B_{\bar{\epsilon}}(x^*) \cap \mathcal{S}} d \circ \Delta(x). \quad (\text{C.5})$$

By Lemma C.2, since \mathcal{O} is transversal to \mathcal{S} , and since $\Delta(x^*) \in \mathcal{O}$, $d \circ \Delta$ is continuous at x^* . Since $d \circ \Delta(x^*) = 0$, it follows that there exists $\bar{\epsilon} > 0$ such that $\sup_{x \in B_\epsilon(x^*) \cap \mathcal{S}} d \circ \Delta(x) < \epsilon$. This bound is valid for all initial conditions in $B_{\delta(\bar{\epsilon})}(x^*) \cap \mathcal{S}$. It remains to produce an open neighborhood of \mathcal{O} for which such a bound holds. But this is easily done by taking $\mathcal{V} := d^{-1}([0, \delta(\bar{\epsilon})))$, which completes the proof of c). Assume in addition that $\delta(\bar{\epsilon}) > 0$ was chosen sufficiently small so that $\lim_{k \rightarrow \infty} P^k(\bar{x}) = x^*$. Then by continuity of d and Δ , $\lim_{k \rightarrow \infty} d \circ \Delta(P^k(\bar{x})) = d \circ \Delta(x^*) = 0$, from which it easily follows that $\lim_{t \rightarrow \infty} \text{dist}(\varphi(t), \mathcal{O}) = 0$, proving d).

Attention is now turned to proving e). From HSH5, $T_I \circ \Delta(x^*) > 0$, and in combination with HSH2', it follows that there exists an open ball $\mathcal{B}_r(x^*)$, $r > 0$, and numbers T_* and T^* such that for every $x_0 \in \mathcal{B}_r(x^*) \cap \mathcal{S}$, $0 < T_* \leq T_I \circ \Delta(x_0) \leq T^* < \infty$, and $\forall x \in \Delta(\mathcal{B}_r(x^*))$, a solution to (4.2) exists on $[0, T^*]$.

Assume that \mathcal{O} is exponentially stable. Let $\delta > 0$ be such that $N e^{-\gamma T_*} \delta < r$ and $\mathcal{B}_\delta(x^*) \subset \mathcal{V}$ where N and γ are positive constants. Let $x_0 \in \mathcal{B}_\delta(x^*) \cap \mathcal{S}$ and define $x_{k+1} = P(x_k)$, $k \geq 1$. Then, by induction, $\|x_k - x^*\| \leq N e^{-k\gamma T_*} \text{dist}(x_0, \mathcal{O})$.

It is enough to show the converse for initial conditions in \mathcal{S} near x^* . Assume that x^* is exponentially stable. Since exponential stability of x^* implies stability i.s.L., by part c) of the theorem, \mathcal{O} is also stable i.s.L. Hence, there exists $\delta > 0$ such that $\text{dist}(x_0, \mathcal{O}) < \delta$ implies $\text{dist}(\varphi(t, x_0), \mathcal{O}) \leq r$, $t \geq 0$. Let $\mathcal{K} := \{x \in \mathcal{X} \mid \text{dist}(x, \mathcal{O}) \leq r\}$. Since \mathcal{K} is compact and f and Δ are differentiable, there exists a constant $\bar{L} < \infty$ such that $\|f(x) - f(\bar{x})\| \leq \bar{L}\|x - \bar{x}\|$, for all $x, \bar{x} \in \mathcal{K}$, and $\|\Delta(x) - \Delta(\bar{x})\| \leq \bar{L}\|x - \bar{x}\|$, for all $x, \bar{x} \in \mathcal{K} \cap \mathcal{S}$. Let $L := \bar{L}e^{\bar{L}T^*}$. Then, using standard bounds for the Lipschitz dependence of the solution of (4.2) with respect to its initial condition [138, Theorem 3.4, p. 96], it follows that for $x \in \mathcal{B}_\delta(x^*) \cap \mathcal{S}$,

$$\begin{aligned} \sup_{0 \leq t \leq T_I \circ \Delta(x)} \text{dist}(\varphi(t, \Delta(x)), \mathcal{O}) &\leq \sup_{0 \leq t \leq T^*} \|\varphi(t, \Delta(x)) - \varphi(t, \Delta(x^*))\| \\ &\leq L\|x - x^*\|. \end{aligned} \tag{C.6}$$

From this inequality, it follows easily that x^* being an exponentially stable fixed point of P implies the corresponding orbit is exponentially stable.

C.1.4 Proof of Proposition 4.1

If P is continuous at x , then P is necessarily well defined at x . Therefore, $T_I(x) < \infty$ and, by its definition, $P(x) = \varphi^f(T_I(\Delta(x)), \Delta(x))$. From the definition of $\tilde{\mathcal{S}}$ in (4.7),

$$\tilde{\mathcal{S}} := \{x \in \mathcal{X} \mid 0 < T_I(\Delta(x)) < \infty \text{ and } L_f H(\varphi^f(T_I(\Delta(x)), \Delta(x))) \neq 0\}, \tag{C.7}$$

which proves a). Part b) is immediate from the definition of stability of an equilibrium point in the sense of Lyapunov.

C.1.5 Proofs of Theorem 4.4 and Theorem 4.5

Only the last statement of Theorem 4.5 merits a comment as the other parts of both theorems either have been discussed in the main text or are immediate. Suppose that both $f|_{\mathcal{Z}}$ and $\Delta|_{\mathcal{Z}}$ in (4.24) are continuously differentiable. By HInv4, $\mathcal{O}(\Delta|_{\mathcal{Z}}(x^*))$ is an orbit of the full-model, and thus can also be denoted as $\mathcal{O}(\Delta(x^*))$; similarly, x^* is a fixed point of P . By HInv3, it follows easily that $\mathcal{O}(\Delta|_{\mathcal{Z}}(x^*))$ is exponentially stable in \mathcal{Z} if and only if $\mathcal{O}(\Delta(x^*))$ is exponentially stable in \mathcal{X} , and that x^* is an exponentially stable fixed point of ρ if and only if it is an exponentially stable fixed point of P . Then by part e) of Theorem 4.1, $x^* \in \hat{\mathcal{S}} \cap \mathcal{Z}$ is an exponentially stable equilibrium point of $x[k+1] = \rho(x[k])$ if, and only if, the orbit $\mathcal{O}(\Delta|_{\mathcal{Z}}(x^*))$ is exponentially stable within \mathcal{Z} .

C.1.6 Proof of Theorem 4.6

Throughout this proof, Hypotheses HSH1–HSH5 and HS1–HS6 are assumed to hold. The proof is based upon evaluating $\mathcal{D}P^\epsilon(x^*)$, the linearization of the Poincaré map about the fixed point, in a set of local coordinates. This is a commonly employed technique even for system with impulse effects [59, 93, 143, 228]. The new result here will be an expression for $\mathcal{D}P^\epsilon(x^*)$ that brings out its structure due to Hypotheses HS1–HS6.

C.1.6.1 Preliminaries

The usual approach to evaluating $\mathcal{D}P^\epsilon(x^*)$ is to view P^ϵ as a map from an open subset of \mathbb{R}^n to \mathbb{R}^n . The linearization is then an $n \times n$ matrix and it must subsequently be shown that one of its eigenvalues is always one and the remaining $n-1$ eigenvalues are those of $\mathcal{D}P^\epsilon(x^*) : T_{x^*}\mathcal{S} \rightarrow T_{x^*}\mathcal{S}$; see [115, 173]. Here, local coordinates on \mathcal{S} will be used so that $\mathcal{D}P^\epsilon(x^*)$ is computed directly as an $(n-1) \times (n-1)$ matrix.

In the coordinates $x = (z; \eta)$, HS4 implies that $x^* = (z^*, 0)$. Since $f_{k+1:n}^\epsilon(0) = 0$, HS5 is equivalent to $\frac{\partial H}{\partial z}(z^*, 0)f_{1:k}(z^*, 0) \neq 0$, which, writing $z = (z_1; \dots; z_k)$, is equivalent to $\sum_{i=1}^k \frac{\partial H}{\partial z_i}(z^*, 0)f_i(z^*, 0) \neq 0$. If necessary, the components of z can always be reordered so that

$$\frac{\partial H}{\partial z_1}(z^*, 0)f_1(z^*, 0) \neq 0; \quad (\text{C.8})$$

this will allow $(z_{2:k}; \eta)$, where $z_{2:k} = (z_2; \dots; z_k)$, to be used as coordinates for \mathcal{S} . Indeed, (C.8) implies that $\frac{\partial H}{\partial z_1}(z^*, 0) \neq 0$, and hence by the Implicit Function Theorem, there exists a continuously differentiable scalar function Γ on an open neighborhood of x^* such that

$$(z_1; z_{2:k}; \eta) \in \mathcal{S} \Leftrightarrow z_1 = \Gamma(z_{2:k}, \eta). \quad (\text{C.9})$$

It follows that

$$(z_1; z_{2:k}; \eta) \in \mathcal{S} \cap \mathcal{Z} \Leftrightarrow z_1 = \Gamma(z_{2:k}, 0) \text{ and } \eta = 0. \quad (\text{C.10})$$

Letting $\hat{\Delta}$ be the representation of Δ in local coordinates on \mathcal{S} gives

$$\hat{\Delta}(z_{2:k}, \eta) := \Delta(\Gamma(z_{2:k}, \eta), z_{2:k}, \eta). \quad (\text{C.11})$$

Defining the projection π by

$$\pi(z_1, z_{2:k}, \eta) = (z_{2:k}; \eta), \quad (\text{C.12})$$

then allows P^ϵ to be expressed in local coordinates $(z_{2:k}; \eta)$ on \mathcal{S} by

$$\hat{P}^\epsilon(z_{2:k}, \eta) := \pi \circ \phi^\epsilon \left(T_I^\epsilon \circ \hat{\Delta}(z_{2:k}, \eta), \hat{\Delta}(z_{2:k}, \eta) \right). \quad (\text{C.13})$$

Similarly, the restricted Poincaré map in local coordinates $z_{2:k}$ on $\mathcal{S} \cap \mathcal{Z}$ is given by

$$\hat{\rho}(z_{2:k}) := \pi_2 \circ \hat{P}^\epsilon \circ \mathcal{I}(z_{2:k}), \quad (\text{C.14})$$

where

$$\pi_2(z_{2:k}, \eta) = z_{2:k} \text{ and } \mathcal{I}(z_{2:k}) = (z_{2:k}; 0). \quad (\text{C.15})$$

C.1.6.2 Application of the Chain Rule

The proof is now broken down into three lemmas which together prove Theorem 4.6. The first involves the *trajectory sensitivity matrix* of $\dot{x} = f^\epsilon(x)$, which is defined by¹

$$\Phi^\epsilon(t, x_0) := \mathcal{D}_2 \phi^\epsilon(t, x_0) \quad (\text{C.16})$$

for t in the maximal domain of existence of $\phi^\epsilon(t, x_0)$. Partition $\Phi^\epsilon(t, x_0)$ compatible with $(z_1; z_{2:k}; \eta)$, viz.

$$\Phi^\epsilon(t, x_0) = \begin{bmatrix} \Phi_{11}^\epsilon(t, x_0) & \Phi_{12}^\epsilon(t, x_0) & \Phi_{13}^\epsilon(t, x_0) \\ \Phi_{21}^\epsilon(t, x_0) & \Phi_{22}^\epsilon(t, x_0) & \Phi_{23}^\epsilon(t, x_0) \\ \Phi_{31}^\epsilon(t, x_0) & \Phi_{32}^\epsilon(t, x_0) & \Phi_{33}^\epsilon(t, x_0) \end{bmatrix}. \quad (\text{C.17})$$

Lemma C.3

For all $x_0 \in \mathcal{Z}$, the entries of the sensitivity matrix $\Phi^\epsilon(t, x_0)$ satisfy:

- i) $\Phi_{31}^\epsilon(t, x_0) = \Phi_{32}^\epsilon(t, x_0) = 0$;

¹For a differentiable function $g(x_1, x_2, \dots, x_p)$, the notation $\mathcal{D}_i g(y_1, y_2, \dots, y_p)$ refers to $\partial g / \partial x_i$ evaluated at $(x_1; x_2; \dots; x_p) = (y_1; y_2; \dots; y_p)$. The argument x_i may be a vector. $\mathcal{D}g(y_1, y_2, \dots, y_p)$ is $(\partial g / \partial x_1, \partial g / \partial x_2, \dots, \partial g / \partial x_p)$ evaluated at $(x_1; x_2; \dots; x_p) = (y_1; y_2; \dots; y_p)$.

- ii) $\Phi_{11}^\epsilon(t, x_0)$, $\Phi_{21}^\epsilon(t, x_0)$, $\Phi_{12}^\epsilon(t, x_0)$, and $\Phi_{22}^\epsilon(t, x_0)$ are independent of ϵ ; and
iii) $\Phi_{33}^\epsilon(t, x_0) = e^{A(\epsilon)t}$.

Proof The trajectory sensitivity matrix may be calculated as follows [173]:

$$\begin{Bmatrix} \dot{x} \\ \dot{\Phi} \end{Bmatrix} = \begin{Bmatrix} f^\epsilon(x) \\ \mathcal{D}f^\epsilon(x)\Phi \end{Bmatrix} \text{ with i.c. } \begin{Bmatrix} x_0 \\ I \end{Bmatrix}. \quad (\text{C.18})$$

Hypothesis HS1 implies that for $i \in \{1, 2, 3\}$, $\mathcal{D}_i f_{1:k}^\epsilon(z_1, z_{2:k}, \eta)$ is independent of ϵ and that $\mathcal{D}_1 f_{k+1:n}^\epsilon(z_1, z_{2:k}, \eta) = 0$, $\mathcal{D}_2 f_{k+1:n}^\epsilon(z_1, z_{2:k}, \eta) = 0$, and $\mathcal{D}_3 f_{k+1:n}^\epsilon(z_1, z_{2:k}, \eta) = A(\epsilon)$. By the Peano-Baker formula, the trajectory sensitivity matrix satisfies

$$\begin{aligned} \Phi^\epsilon(t, x_0) &= I + \int_0^t K^\epsilon(\tau_1, x_0) d\tau_1 + \int_0^t \int_0^{\tau_1} K^\epsilon(\tau_1, x_0) K^\epsilon(\tau_2, x_0) d\tau_2 d\tau_1 \\ &\quad + \int_0^t \int_0^{\tau_1} \int_0^{\tau_2} K^\epsilon(\tau_1, x_0) K^\epsilon(\tau_2, x_0) K^\epsilon(\tau_3, x_0) d\tau_3 d\tau_2 d\tau_1 + \dots \end{aligned} \quad (\text{C.19})$$

where, since $x_0 \in \mathcal{Z}$, and \mathcal{Z} is invariant under the solution of $\dot{x} = f^\epsilon(x)$,

$$K^\epsilon(t, x_0) := \mathcal{D}f^\epsilon(x)|_{x=\phi_{\mathcal{Z}}(t, x_0)}. \quad (\text{C.20})$$

It is easily shown that

$$K^\epsilon(t, x_0) = \begin{bmatrix} K_{11}^\epsilon(t, x_0) & K_{12}^\epsilon(t, x_0) & K_{13}^\epsilon(t, x_0) \\ K_{21}^\epsilon(t, x_0) & K_{22}^\epsilon(t, x_0) & K_{23}^\epsilon(t, x_0) \\ K_{31}^\epsilon(t, x_0) & K_{32}^\epsilon(t, x_0) & K_{33}^\epsilon(t, x_0) \end{bmatrix}, \quad (\text{C.21})$$

where

- i) $K_{31}^\epsilon(t, x_0) = K_{32}^\epsilon(t, x_0) = 0$,
- ii) $K_{11}^\epsilon(t, x_0)$, $K_{21}^\epsilon(t, x_0)$, $K_{12}^\epsilon(t, x_0)$, and $K_{22}^\epsilon(t, x_0)$ are independent of ϵ , and
- iii) $K_{33}^\epsilon(t, x_0) = A(\epsilon)$.

Evaluating the expansion (C.19) term-by-term then verifies the lemma.

Lemma C.4

Let $(z_1^*; z_{2:k}^*; \eta^*) = x^*$ represent the fixed point and $t^* = T_I^\epsilon \circ \hat{\Delta}(z_{2:k}^*, \eta^*)$ be the fundamental period of the periodic orbit \mathcal{O} . Then,

$$\mathcal{D}\hat{P}^\epsilon(z_{2:k}^*, \eta^*) = \mathbf{C}(\mathbf{FT} + \mathbf{Q})\mathbf{R}, \quad (\text{C.22})$$

with matrices C, F, T, Q , and R as defined in (C.23); moreover, when partitioned compatibly with $(z_1; z_{2:k}; \eta)$, these matrices have the indicated structure²:

$$C := \mathcal{D}\pi(z_1^*, z_{2:k}^*, \eta^*) = \begin{bmatrix} 0 & I & 0 \\ 0 & 0 & I \end{bmatrix} \quad (\text{C.23a})$$

$$F := \mathcal{D}_1\phi^\epsilon(t^*, \hat{\Delta}(z_{2:k}^*, \eta^*)) = \begin{bmatrix} F_1 \\ F_2 \\ 0 \end{bmatrix} \quad (\text{C.23b})$$

$$T := \mathcal{D}T_I^\epsilon(\hat{\Delta}(z_{2:k}^*, \eta^*)) = [T_1 \ T_2 \ T_3^\epsilon] \quad (\text{C.23c})$$

$$Q := \Phi^\epsilon(t^*, \hat{\Delta}(z_{2:k}^*, \eta^*)) = \begin{bmatrix} Q_{11} & Q_{12} & Q_{13}^\epsilon \\ Q_{21} & Q_{22} & Q_{23}^\epsilon \\ 0 & 0 & e^{A(\epsilon)t^*} \end{bmatrix} \quad (\text{C.23d})$$

$$R := \mathcal{D}\hat{\Delta}(z_{2:k}^*, \eta^*) = \begin{bmatrix} R_{11} & R_{12} \\ R_{21} & R_{22} \\ 0 & R_{32} \end{bmatrix}. \quad (\text{C.23e})$$

Proof Equation (C.22) follows from the chain rule, using

$$\begin{aligned} (z_1^*; z_{2:k}^*; \eta^*) &= \phi^\epsilon(T_I^\epsilon \circ \hat{\Delta}(z_{2:k}^*, \eta^*), \hat{\Delta}(z_{2:k}^*, \eta^*)) \\ &= \phi_Z(T_{I,Z} \circ \hat{\Delta}(z_{2:k}^*, \eta^*), \hat{\Delta}(z_{2:k}^*, \eta^*)), \end{aligned} \quad (\text{C.24a})$$

$$t^* = T_I^\epsilon \circ \hat{\Delta}(z_{2:k}^*, \eta^*) = T_{I,Z} \circ \hat{\Delta}(z_{2:k}^*, \eta^*), \quad (\text{C.24b})$$

$$\Phi^\epsilon(t^*, \hat{\Delta}(z_{2:k}^*, \eta^*)) = \mathcal{D}_2\phi^\epsilon(t^*, \hat{\Delta}(z_{2:k}^*, \eta^*)). \quad (\text{C.24c})$$

The structure of C is immediate from the definition of π in (C.12). From [173, App. D], $F = f^\epsilon(z_1^*, z_{2:k}^*, \eta^*)$, leading to $F_3 = 0$ because $\eta^* = 0$. Also from [173, App. D], T_I^ϵ is differentiable due to the transversality condition HS5 with

$$\mathcal{D}T_I^\epsilon(\hat{\Delta}(z_{2:k}^*, \eta^*)) = -(L_{f^\epsilon}H(x^*))^{-1} \left(\frac{\partial H}{\partial x}(x^*) \right)^T \Phi^\epsilon(t^*, \hat{\Delta}(z_{2:k}^*, \eta^*)). \quad (\text{C.25})$$

The structure of Q is given by Lemma C.3, and the form of R follows from HS2, namely, (4.28).

²For a related decomposition, using a slightly different structure, see [57].

Lemma C.5

At the fixed point x^* , the linearization of the Poincaré map is

$$\mathcal{D}\hat{P}^\epsilon(z_{2:k}^*, \eta^*) = \begin{bmatrix} M_{11} & M_{12}^\epsilon \\ 0 & M_{22}^\epsilon \end{bmatrix}, \quad (\text{C.26})$$

and the linearization of the restricted Poincaré map is

$$\mathcal{D}\hat{\rho}(z_{2:k}^*) = M_{11}, \quad (\text{C.27})$$

where

$$M_{11} = (F_2 T_1 + Q_{21}) R_{11} + (F_2 T_2 + Q_{22}) R_{21} \quad (\text{C.28a})$$

$$M_{12}^\epsilon = (F_2 T_1 + Q_{21}) R_{12} + (F_2 T_2 + Q_{22}) R_{22} + (F_2 T_3^\epsilon + Q_{23}^\epsilon) R_{32} \quad (\text{C.28b})$$

$$M_{22}^\epsilon = e^{A(\epsilon)t^*} R_{32}. \quad (\text{C.28c})$$

Proof Multiplying out (C.22) and using the structure in (C.23) proves (C.28). The second part follows because the Poincaré map leaves $\mathcal{S} \cap \mathcal{Z}$ invariant. In local coordinates, direct calculation yields

$$\mathcal{D}\hat{\rho}(z_{2:k}^*) = \mathcal{D}\pi_2(z_{2:k}^*, \eta^*) \mathcal{D}\hat{P}^\epsilon(z_{2:k}^*, \eta^*) \mathcal{D}\mathcal{I}(z_{2:k}^*) \quad (\text{C.29a})$$

$$= [I \ 0] \begin{bmatrix} M_{11} & M_{12}^\epsilon \\ 0 & M_{22}^\epsilon \end{bmatrix} \begin{bmatrix} I \\ 0 \end{bmatrix} \quad (\text{C.29b})$$

$$= M_{11}. \quad (\text{C.29c})$$

C.1.6.3 Assembling all of the Pieces

The overall proof of Theorem 4.6 is completed as follows. Suppose that x^* is an exponentially stable fixed point of ρ . Then by (C.27), the eigenvalues of M_{11} have magnitude less than one. By HS6 and (C.28), $\lim_{\epsilon \searrow 0} M_{22}^\epsilon = \lim_{\epsilon \searrow 0} e^{A(\epsilon)t^*} R_{32} = 0$, and therefore, because eigenvalues depend continuously on the entries of the matrix, there exists $\bar{\epsilon} > 0$ such that for $0 < \epsilon < \bar{\epsilon}$, the eigenvalues of M_{22}^ϵ all have magnitude less than one, and hence, x^* is an exponentially stable fixed point of P^ϵ .

The other direction being trivial, the proof is complete.

C.1.7 Proof of Theorem 4.8

For clarity, first assume that $\mathcal{W} = \emptyset$ and consider

$$\Sigma_{aux} : \begin{cases} \begin{bmatrix} \dot{x}(t) \\ \dot{a}(t) \end{bmatrix} = f_{aux}(x(t), a(t)), & \begin{bmatrix} x^-(t) \\ a^-(t) \end{bmatrix} \notin \mathcal{S}_{aux} \\ \begin{bmatrix} x^+(t) \\ a^+(t) \end{bmatrix} = \Delta_{aux}(x^-(t), a^-(t)), & \begin{bmatrix} x^-(t) \\ a^-(t) \end{bmatrix} \in \mathcal{S}_{aux}, \end{cases} \quad (\text{C.30})$$

where the state space is $\mathcal{X}_{aux} := \mathcal{X} \times \mathcal{A}$, the impact surface is $\mathcal{S}_{aux} := \mathcal{S} \times \mathcal{A}$, and the differential equation and impact map are given by

$$f_{aux}(x, a) = \begin{bmatrix} f(x, a) \\ 0 \end{bmatrix} \quad (\text{C.31a})$$

$$\Delta_{aux}(x, a) = \begin{bmatrix} \Delta(x, v_1(x)) \\ v_1(x) \end{bmatrix}. \quad (\text{C.31b})$$

The hypotheses of Theorem 4.8 ensure that (C.30) and $\mathbf{Z} := \{(\mathcal{Z}_a, a) \mid a \in \mathcal{A}\}$ satisfy all the hypotheses of Corollary 4.2, and thus the existence and stability of orbits can be checked by evaluating the stability of fixed points of the discrete-time system associated with the restricted Poincaré map, namely

$$\begin{aligned} x[k+1] &= \rho(x[k], v_1(x[k])) \\ a[k+1] &= v_1(x[k]). \end{aligned} \quad (\text{C.32})$$

Since the stability properties of (C.32) are equivalent to those of

$$x[k+1] = \rho(x[k], v_1(x[k])), \quad (\text{C.33})$$

the result is proven.

For $\mathcal{W} \neq \emptyset$, the reasoning is essentially identical. The auxiliary system becomes

$$\Sigma_{aux} : \begin{cases} \begin{bmatrix} \dot{x}(t) \\ \dot{a}(t) \\ \dot{w}(t) \end{bmatrix} = f_{aux}(x(t), a(t), w(t)), & \begin{bmatrix} x^-(t) \\ a^-(t) \\ w^-(t) \end{bmatrix} \notin \mathcal{S}_{aux} \\ \begin{bmatrix} x^+(t) \\ a^+(t) \\ w^+(t) \end{bmatrix} = \Delta_{aux}(x^-(t), a^-(t), w^-(t)), & \begin{bmatrix} x^-(t) \\ a^-(t) \\ w^-(t) \end{bmatrix} \in \mathcal{S}_{aux}, \end{cases} \quad (\text{C.34})$$

where the state space is $\mathcal{X}_{aux} := \mathcal{X} \times \mathcal{A} \times \mathcal{W}$, the impact surface is $\mathcal{S}_{aux} := \mathcal{S} \times \mathcal{A} \times \mathcal{W}$ and the differential equation and impact map are given by

$$f_{aux}(x, a, w) = \begin{bmatrix} f(x, a) \\ 0 \\ 0 \end{bmatrix} \quad (\text{C.35a})$$

$$\Delta_{aux}(x, a, w) = \begin{bmatrix} \Delta(x, v_1(x, w)) \\ v_1(x, w) \\ v_2(x, w) \end{bmatrix}. \quad (\text{C.35b})$$

The hypotheses of Theorem 4.8 ensure that (C.34) and $\mathcal{Z}_{aux} := \mathbf{Z} \times \mathcal{W}$ satisfy all the hypotheses³ of Corollary 4.2 and thus the existence and stability of orbits can be checked by evaluating the stability of fixed points of the discrete-time system associated with the restricted Poincaré map, namely

$$\begin{aligned} x[k+1] &= \rho(x[k], v_1(x[k], w[k]), v_2(x[k], w[k])) \\ a[k+1] &= v_1(x[k], w[k]) \\ w[k+1] &= v_2(x[k], w[k]). \end{aligned} \quad (\text{C.36})$$

Since the stability properties of (C.36) are equivalent to those of

$$\begin{aligned} x[k+1] &= \rho(x[k], v_1(x[k], w[k]), v_2(x[k], w[k])) \\ w[k+1] &= v_2(x[k], w[k]), \end{aligned} \quad (\text{C.37})$$

the result is proven.

C.1.8 Proof of Theorem 4.9

The proof follows the same pattern as the proof of Theorem 4.8. For clarity, first assume that $\mathcal{W} = \emptyset$ and consider

$$\Sigma_{aux} : \begin{cases} \begin{bmatrix} \dot{x}(t) \\ \dot{a}_1(t) \\ \dot{a}_2(t) \end{bmatrix} = f_{aux}(x(t), a_1(t), a_2(t)) & \begin{bmatrix} x^-(t) \\ a_1^-(t) \\ a_2^-(t) \end{bmatrix} \notin \mathcal{S}_{aux} \\ \begin{bmatrix} x^+(t) \\ a_1^+(t) \\ a_2^+(t) \end{bmatrix} = \Delta_{aux}(x^-(t), a_1^-(t), a_2^-(t)) & \begin{bmatrix} x^-(t) \\ a_1^-(t) \\ a_2^-(t) \end{bmatrix} \in \mathcal{S}_{aux}, \end{cases} \quad (\text{C.38})$$

where the state space is $\mathcal{X}_{aux} := \mathcal{X} \times \mathcal{A}_1 \times \mathcal{A}_2$, the impact surface is $\mathcal{S}_{aux} := \mathcal{S} \times \mathcal{A}_1 \times \mathcal{A}_2$, and the differential equation and impact map are given by

$$\begin{aligned} f_{aux}(x, a_1, a_2) &= \begin{bmatrix} f(x, a_1, a_2) \\ 0 \\ 0 \end{bmatrix} \\ \Delta_{aux}(x, a_1, a_2) &= \begin{bmatrix} \Delta(x, \psi(a_2), v_1(x)) \\ \psi(a_2) \\ v_1(x) \end{bmatrix}. \end{aligned} \quad (\text{C.39})$$

³Note that local continuous finite-time attractivity of \mathbf{Z} in $\mathcal{X} \times \mathcal{A}$ immediately implies that of $\mathbf{Z} \times \mathcal{W}$ in $\mathcal{X} \times \mathcal{A} \times \mathcal{W}$.

The hypotheses of Theorem 4.9 ensure that (C.38) and $\mathcal{Z}_{aux} := \mathbf{Z}$ satisfy all the hypotheses of Corollary 4.2 and thus the existence and stability of orbits can be checked by evaluating the stability of fixed points of the discrete-time system associated with the restricted Poincaré map, namely

$$\begin{aligned} x[k+1] &= \rho(x[k], \psi(a_2[k]), v_1(x[k])) \\ a_1[k+1] &= \psi(a_2[k]) \\ a_2[k+1] &= v_1(x[k]) \end{aligned} \quad (\text{C.40})$$

Since the stability properties of (C.37) are equivalent to those of

$$\begin{aligned} x[k+1] &= \rho(x[k], \psi(a_2[k]), v_1(x[k])) \\ a_2[k+1] &= v_1(x[k]), \end{aligned} \quad (\text{C.41})$$

the result is proven. The simple modifications for including $\mathcal{W} \neq \emptyset$ are left to the reader.

C.2 Proofs Associated with Chapter 5

C.2.1 Proof of Theorem 5.4

Denote the closed-loop system consisting of (3.30) and (5.95) by

$$\Sigma : \begin{cases} \dot{x} = f_{cl}(x) & x^- \notin \mathcal{S} \\ x^+ = \Delta(x^-) & x^- \in \mathcal{S}, \end{cases} \quad (\text{C.42})$$

where

$$f_{cl}(x) := f_s(x) + g_s(x)u_{FT}(x). \quad (\text{C.43})$$

The proof consists in systematically showing that all of the hypotheses of Theorem 4.5 are met for (C.42).

Hypothesis HSH1 follows from $\mathcal{X} = T\mathcal{Q}$. Hypotheses HSH3 and HSH5 are immediate from (3.31), and HSH4 is met because the impact map in (3.25) is as smooth as the mechanical model, and hence, is analytic. Hypothesis HSH2 is shown to hold in the following lemma. Its proof is delayed until the end of the proof of Theorem 5.4.

Lemma C.6

Assume that Hypotheses HH1–HH4 hold. Then for the closed-loop system (C.43), Hypotheses HH2, HC1 and HC2 imply Hypothesis HSH2.

Continuing with the proof of the theorem, Lemma 5.1 and the definition of the hybrid zero dynamics establish Hypotheses HInv1 and HInv4. Hypothesis HH5 implies HInv2; see Remark 5.3. Finally, Hypothesis HInv3, that

is, the finite-time attractivity of the zero dynamics manifold, follows from Hypotheses HC3 and HC4. This concludes the proof.

Proof of Lemma C.6: The continuity portion of HSH2 is immediate. The existence and uniqueness portions of HSH2 are coordinate independent. From Hypotheses HH1–HH4, the swing phase dynamics can be written as in (5.43). Applying the feedback (5.95) to (5.43) yields that the closed-loop swing phase dynamics are

$$\begin{aligned}\dot{\eta}_1 &= \eta_2 \\ \dot{\eta}_2 &= v(\eta_1, \eta_2) \\ \dot{z} &= \Omega(\eta_1, \eta_2, z),\end{aligned}\tag{C.44}$$

where $\eta_1 = y$, $\eta_2 = \dot{y}$, $z = (\xi_1; \xi_2)$, v is given by (5.90), and Ω is a smooth function of its arguments (the smoothness comes from that of (3.8)). In particular, Ω is locally Lipschitz continuous. In these coordinates, the system is expressed as a cascade of a system that satisfies HSH2 feeding forward into a system that is locally Lipschitz. The Gronwall-Bellman inequality [138] can therefore be used to establish that HSH2 holds for the cascade.

C.2.2 Proof of Theorem 5.5

Denote the closed-loop system consisting of (3.30) and (5.96) by

$$\Sigma : \begin{cases} \dot{x} = f_{cl}(x) & x^- \notin \mathcal{S} \\ x^+ = \Delta(x^-) & x^- \in \mathcal{S}, \end{cases}\tag{C.45}$$

where

$$f_{cl}(x) := f_s(x) + g_s(x)u_{LIN}(x).\tag{C.46}$$

The proof consists in showing that all of the hypotheses of Theorem 4.6 are met for (C.45).

Hypothesis HSH1 follows from $\mathcal{X} = T\mathcal{Q}$. Hypothesis HSH2' follows from the smoothness of the mechanical model (3.31) and the feedback (5.96). Hypotheses HSH3 and HSH5 are immediate from (3.31), and HSH4' is met because the impact map in (3.25) is as smooth as the mechanical model, and hence, is analytic.

From Hypotheses HH1–HH4, the swing phase dynamics can be written as in (5.43). Applying the feedback (5.96) to (5.43) yields that the closed-loop swing phase dynamics are

$$\begin{aligned}\dot{\eta}_1 &= \eta_2 \\ \dot{\eta}_2 &= -\frac{1}{\epsilon^2}K_P\eta_1 - \frac{1}{\epsilon}K_D\eta_2 \\ \dot{z} &= \Omega(\eta_1, \eta_2, z),\end{aligned}\tag{C.47}$$

where $\eta_1 = y$, $\eta_2 = \dot{y}$, $z = (\xi_1; \xi_2)$, and Ω is a smooth function of its arguments (the smoothness comes from that of (3.8)). From this, Hypotheses HS1 and HS2, and HS6 are immediate. Because the hybrid zero dynamics is assumed to have a periodic orbit transversal to $\mathcal{S} \cap \mathcal{Z}$, Hypotheses HS3–HS5 are met. Hence, the exponential stability of the orbit in the hybrid zero dynamics implies that, for $\epsilon > 0$ sufficiently small, the orbit is also exponentially stable in (C.45).

C.3 Proofs Associated with Chapter 6

C.3.1 Proof of Proposition 6.1

The first part of (a) follows from the fact that the decoupling matrix in (6.65) is the sum of an identity matrix and the outer product of a column vector and a row vector; the second part follows by multiplying by the positive quantity $\tilde{d}_{N,N}$. The proof of (b) is a direct application of the Sherman-Morrison formula, more commonly known as the Matrix Inversion Lemma, which states that the matrix $(I_{n \times n} - PQ)$, $P \in \mathbb{R}^{n \times m}$, $Q \in \mathbb{R}^{m \times n}$ is invertible if, and only if, $(I_{m \times m} - QP)$ is invertible, in which case $(I_{n \times n} - PQ)^{-1} = I_{n \times n} + P(I_{m \times m} - QP)^{-1}Q$. In our case, the matrices involved are

$$P = \frac{\partial h_d(\theta)}{\partial \theta} \quad \text{and} \quad Q = -\tilde{J}^{\text{norm}}(q_b), \quad (\text{C.48})$$

and the dimensions are $n = N - 1$ and $m = 1$. Part (c) is immediate from (a) and (b). For part (d), because the MPFL-normal form is obtained by applying a change of coordinates and a regular state variable feedback, the decoupling matrix associated with (6.2) and (6.3) is invertible if, and only if, the decoupling matrix associated with (6.64) and (6.60) is invertible; see [Proposition B.7](#).

C.3.2 Proof of Theorem 6.2

The first part of the proof consists in showing that Hypotheses HH1–HH5 are satisfied, so that the swing phase zero dynamics exists. Hypothesis HH1 is trivially satisfied. By construction, on the periodic orbit, $\dot{q}_b(t) = \frac{\partial h_d}{\partial \theta}(t)\dot{\theta}(t)$ and hence

$$\sigma_1(t) = \bar{\sigma}_N(t) = I(\theta(t))\dot{\theta}(t). \quad (\text{C.49})$$

Thus, by Hypotheses HO3 and HO4, $I(\theta)$ is nonzero on the periodic orbit. It follows therefore by [Proposition 6.1](#) that the determinant of the decoupling matrix is nonzero on an open set about the periodic orbit, and hence by restricting \mathcal{Q} if necessary, Hypothesis HH2 is met. Hypotheses HH3 and HH4

are trivially satisfied due to the choice of $h(q) = q_b - h_d(\theta)$. Hypothesis HH5 is implied by Hypothesis HO2, in particular, by the fact that the orbit is transversal to \mathcal{S} . By Lemma 5.1, the swing phase zero dynamics exists.

To establish existence of the hybrid zero dynamics, it remains to establish impact invariance. Hypotheses HH5 and HO4 imply part (c) of Theorem 5.2, and part (a) of that theorem establishes impact invariance. This concludes the proof of part 1) of the theorem.

By construction of the output (6.83), \mathcal{O} is a solution of the hybrid zero dynamics (the invariance across the impact being part of the definition of periodicity). By the definition of δ_{zero} , it satisfies $\sigma_1^+ = \delta_{\text{zero}}\sigma_1^-$, establishing

$$\delta_{\text{zero}} = \lim_{t \rightarrow T} \frac{\sigma_1(0)}{\sigma_1(t)}. \quad (\text{C.50})$$

By Hypothesis HO4, $\delta_{\text{zero}} > 0$. Therefore, appealing to Corollary 5.1 establishes that \mathcal{O} is an exponentially stable periodic orbit of the hybrid zero dynamics when $\delta_{\text{zero}} < 1$. Indeed, condition (5.79) holds because the hybrid zero dynamics admits a solution and condition (5.80) is equivalent to (6.84).

C.4 Proof Associated with Chapter 7

C.4.1 Proof of Theorem 7.3

For $\Gamma_{\bar{\alpha}+w\delta\alpha}$ based on finite-time control, as in (5.95) and Theorem 5.4, the result is a corollary of Theorem 4.8. For $\Gamma_{\bar{\alpha}+w\delta\alpha}$ as in (5.96) and Theorem 5.5, the proof is given here.

Due to the form of the parameter dependence in the output (7.3), H_0 and $\theta(q)$ are independent of α . Hence, the coordinate transformation in (6.55) and (6.56) is independent of the parameters, is globally well-defined for all $\alpha \in \mathcal{A}$, and places the output in the form

$$y = h(\tilde{q}, \alpha) := q_b - h_d(\theta, \alpha). \quad (\text{C.51})$$

Based on (C.51), introduce the smooth global change of coordinates, valid for all $\alpha \in \mathcal{A}$,

$$\begin{bmatrix} q_b \\ \dot{q}_b \\ \theta \\ \dot{\theta} \end{bmatrix} \rightarrow \begin{bmatrix} v_1 \\ v_2 \\ \theta \\ \bar{\sigma}_N \end{bmatrix}, \quad (\text{C.52})$$

where $v_1 := y = h(\tilde{q}, \alpha) = q_b - h_d(\theta, \alpha)$ and $v_2 := \dot{y} = L_f h(\tilde{q}, \dot{\tilde{q}}, \alpha)$. For w in its domain of definition \mathcal{W} (from $\bar{\alpha}$ being a regular value of α), the decoupling

matrix is invertible, and hence, by (a) of Proposition 6.1, so is

$$\mathbf{I}_{(N-1) \times (N-1)} + \frac{\partial h_d(\theta, \bar{\alpha} + w\delta\alpha)}{\partial \theta} \tilde{J}^{\text{norm}}(q_b). \quad (\text{C.53})$$

In these coordinates, the system (7.25) becomes

$$\left. \begin{array}{l} \dot{v}_1 = v_2 \\ \dot{v}_2 = -\frac{1}{\epsilon^2} K_P v_1 - \frac{1}{\epsilon} K_D v_2 \\ \dot{\theta} = \frac{\bar{\sigma}_N}{d_{N,N}(q_b)} - \tilde{J}^{\text{norm}}(q_b) \dot{q}_b \\ \dot{\sigma}_N = -\frac{\partial \tilde{V}}{\partial \theta}(q_b, \theta) \\ \dot{e} = 0 \\ \dot{w} = 0 \\ \dot{\eta} = 0 \\ \dot{x}^+ = \check{\Delta}(\check{x}^-) \\ e^+ = e^- + (\eta^* - \eta^-) \\ w^+ = \bar{K}_P(\eta^* - \eta^-) + \bar{K}_I e^- \\ \eta^+ = \bar{\nu}(x^-, \bar{\alpha} + w^+ \delta\alpha) \end{array} \right\} \begin{array}{l} \check{x}^- \notin \mathcal{S} \\ \check{x}^- \in \mathcal{S} \end{array} \quad (\text{C.54})$$

where

$$\check{x} = (v_1; \theta; v_2; \bar{\sigma}_N) \quad (\text{C.55a})$$

$$q_b = v_1 + h_d(\theta, \alpha) \quad (\text{C.55b})$$

$$\begin{aligned} \dot{q}_b &= \left[\mathbf{I}_{(N-1) \times (N-1)} + \frac{\partial h_d(\theta, \alpha)}{\partial \theta} \tilde{J}^{\text{norm}}(q_b) \right]^{-1} \\ &\quad \left(v_2 + \frac{\partial h_d(\theta, \alpha)}{\partial \theta} \frac{\bar{\sigma}_N}{d_{N,N}(q_b)} \right) \end{aligned} \quad (\text{C.55c})$$

$$\alpha = \bar{\alpha} + w\delta\alpha, \quad (\text{C.55d})$$

and $\check{\Delta}$ is the representation of Δ in the new coordinates. Defining

$$\check{z} := (\theta; \bar{\sigma}_N; e; w; \eta) \quad (\text{C.56a})$$

$$\check{\eta} := (v_1; v_2) \quad (\text{C.56b})$$

$$\check{\mathcal{S}} := \mathcal{S} \times \mathbb{R}^3 \quad (\text{C.56c})$$

$$\check{\mathcal{Z}} := \{(\mathcal{Z}_{\bar{\alpha}+w\delta\alpha}, e, \bar{\alpha} + w\delta\alpha, \eta) \mid w \in \mathcal{W}, e \in \mathbb{R}, \eta \in \mathbb{R}\}, \quad (\text{C.56d})$$

it is straightforward to verify that all of the hypotheses of Theorem 4.6 are met, with the restricted Poincaré map given by (7.19) in closed loop with (7.23).

C.5 Proofs Associated with Chapter 9

C.5.1 Proof of Theorem 9.2

By (9.10), points in $\tilde{\mathcal{S}} \cap \mathcal{Z}_s$ are parameterized by $(q_0^{s-}; \dot{q}_0^{s-} \sigma_1^{s-})$. The position of the center of mass $(\mathbf{x}_{cm}^{s-}; \mathbf{y}_{cm}^{s-})$ is obtained by evaluating (3.86) at q_0^{s-} and its velocity is obtained from (9.15), $(\dot{\mathbf{x}}_{cm}^{s-}; \dot{\mathbf{y}}_{cm}^{s-}) = (\lambda_x(q_0^{s-})\sigma_1^{s-}; \lambda_y(q_0^{s-})\sigma_1^{s-})$. The angular momentum about the center of mass can be determined from (3.107) to be

$$\sigma_{cm}^{s-} = \sigma_1^{s-} - m_{tot} (\mathbf{y}_{cm}^{s-} \lambda_x(q_0^{s-})\sigma_1^{s-} - \mathbf{x}_{cm}^{s-} \lambda_y(q_0^{s-})\sigma_1^{s-}). \quad (C.57)$$

Since the transition map from the stance phase to the flight phase preserves positions and velocities, (C.57) is also the angular momentum at the *beginning* of the flight phase, σ_{cm}^{f+} , and because angular momentum is conserved during ballistic motion, (C.57) is also the value of the angular momentum at the *end* of the flight phase, σ_{cm}^{f-} . From the hypotheses $\Delta(\tilde{\mathcal{S}} \cap \mathcal{Z}_s) \subset \mathcal{Z}_s$ and $\pi \circ \Delta(\tilde{\mathcal{S}} \cap \mathcal{Z}_s)$ is a single point, the position of the center of mass at the end of the flight phase is known and equal to the position of the center of mass at the beginning of the subsequent stance phase, $(\mathbf{x}_{cm}^{s+}; \mathbf{y}_{cm}^{s+})$. From this, the flight time, t_f , can be computed

$$t_f = \frac{\dot{\mathbf{y}}_{cm}^{s-}}{g_0} + \frac{\sqrt{(\dot{\mathbf{y}}_{cm}^{s-})^2 - 2g_0(\mathbf{y}_{cm}^{s+} - \mathbf{y}_{cm}^{s-})}}{g_0}, \quad (C.58)$$

and from (3.105), the velocity of the center of mass at the end of the flight phase is determined

$$\begin{bmatrix} \dot{\mathbf{x}}_{cm}(t_f) \\ \dot{\mathbf{y}}_{cm}(t_f) \end{bmatrix} = \begin{bmatrix} \dot{\mathbf{x}}_{cm}^{s-} \\ -\sqrt{(\dot{\mathbf{y}}_{cm}^{s-})^2 - 2g_0(\mathbf{y}_{cm}^{s+} - \mathbf{y}_{cm}^{s-})} \end{bmatrix}. \quad (C.59)$$

Equations (C.57), (C.59), and (3.107) allow the angular momentum about the contact point at the end of the flight phase, σ_2^{f-} , to be evaluated, and then (3.115) allows the evaluation of the angular momentum about the stance leg at the beginning of the subsequent stance phase. This yields

$$\begin{aligned} \sigma_1^{s+} &= \sigma_1^{s-} - m_{tot} (\mathbf{y}_{cm}^{s-} \lambda_x(q_0^{s-})\sigma_1^{s-} - \mathbf{x}_{cm}^{s-} \lambda_y(q_0^{s-})\sigma_1^{s-}) + \\ &m_{tot} \left(\mathbf{y}_{cm}^{s+} \lambda_x(q_0^{s-})\sigma_1^{s-} + \mathbf{x}_{cm}^{s+} \sqrt{(\lambda_y(q_0^{s-})\sigma_1^{s-})^2 - 2g_0(\mathbf{y}_{cm}^{s+} - \mathbf{y}_{cm}^{s-})} \right), \end{aligned} \quad (C.60)$$

which, after simplification, completes the proof.

C.5.2 Proof of Theorem 9.3

From Section 5.4, in the coordinates $(\theta_s; K_{s,\text{zero}} = \frac{1}{2}(\sigma_1)^2)$ for \mathcal{Z}_s , the stance-phase zero dynamics can be integrated as

$$K_{s,\text{zero}}(\theta_s) = K_{s,\text{zero}}(\theta_s^+) - V_{s,\text{zero}}(\theta_s). \quad (\text{C.61})$$

Evaluating the above at θ_s^- and applying (9.36) yields the restricted Poincaré map

$$\rho(\zeta) = \delta_e(\zeta) - V_{s,\text{zero}}(\theta_s^-), \quad (\text{C.62})$$

where $\zeta = \frac{1}{2}(\sigma_1^{s-})^2$. The domain of ρ follows from Theorem 5.3 on page 129.

Remark C.1 The integration of the stance phase zero dynamics can also be expressed as

$$K_{s,\text{zero}}(\theta_s) + V_{s,\text{zero}}(\theta_s) = K_{s,\text{zero}}(\theta_s^+), \quad (\text{C.63})$$

for $\theta_s^+ \leq \theta_s < \theta_s^-$, which is conservation of total “pseudo-energy” during the stance phase; see also Fig. 9.4.

C.5.3 Proof of Theorem 9.4

By (d) of Corollary 9.2, the hypotheses imply that ρ is strictly convex, and by (c), $\frac{d\rho}{d\zeta} \leq (\chi - |\beta|)^2 < 1$. Hence, the graph of ρ can have at most one intersection with the graph of the identity function, which implies that there can exist at most one fixed point. Since δ_e and ρ differ by a constant, their derivatives are equal and Corollary 9.2 applies equally to δ_e . Therefore, δ_e is strictly increasing on $\tilde{\mathcal{D}}_\rho$, and thus, if $\zeta \in \tilde{\mathcal{D}}_\rho$, then $\zeta \in \tilde{\mathcal{D}}_\rho$ for all $\zeta > \zeta$. It follows that $\tilde{\mathcal{D}}_\rho$ is unbounded and connected. By Corollary 9.1, ζ^* is exponentially stable.

Let $\zeta \in \tilde{\mathcal{D}}_\rho$ be such that $\zeta < \zeta^*$. Then, since ρ is strictly increasing on $\tilde{\mathcal{D}}_\rho$, $\rho(\zeta) < \rho(\zeta^*) = \zeta^*$. Hence, $\rho^{(k)}(\zeta)$ is a strictly increasing sequence bounded from above, and therefore has a limit. By continuity of ρ , this limit is a fixed point of ρ , and by uniqueness of the fixed point, $\lim_{k \rightarrow \infty} \rho^{(k)}(\zeta) = \zeta^*$. Similarly, let $\zeta \in \tilde{\mathcal{D}}_\rho$ be such that $\zeta > \zeta^*$. Then $\zeta^* = \rho(\zeta^*) < \rho(\zeta)$, and similar reasoning shows that $\lim_{k \rightarrow \infty} \rho^{(k)}(\zeta) = \zeta^*$, with the convergence being monotonic.

Derivation of the Equations of Motion for Three-Dimensional Mechanisms

This appendix summarizes how to use the method of Lagrange in order to derive the equations of motion for robots comprised of N -link, open kinematic chains with N one-DOF revolute joints, moving in three dimensions. The purpose of including this material is to underline, in a more fundamental manner, the invariance of the kinetic energy under translations and rotations of the inertial frame, which is the source of cyclic variables of the kinetic energy. The mechanical portion of the planar bipedal robot models of this book are special cases of the models derived here. For the most part,¹ the calculations presented in this appendix parallel and, at points, duplicate the calculations performed in [164, pp. 161–171] and [219, pp. 136–141].

Remark D.1 Though not treated in this book, feedback control of three-dimensional legged robots is an active and important area of research. Some key references are [6, 57, 58, 80, 116, 143, 185, 212, 217].

D.1 The Lagrangian

The Lagrangian for an N -link, rigid body open-chain robot with N one-DOF revolute joints is a functional acting on points in the state space, $x = (q; \dot{q}) \in \mathcal{X} = T\mathcal{Q}$, where \mathcal{Q} is a simply connected, open subset of $\mathbb{T}^{N+3} \times \mathbb{R}^3$. The generalized coordinates $q \in \mathcal{Q}$ give the robot's shape, orientation, and position in three-dimensional space. The Lagrangian is defined to be the difference between the kinetic and potential energies

$$\mathcal{L}(q, \dot{q}) := K(q, \dot{q}) - V(q). \quad (\text{D.1})$$

¹An exception is that the center of mass (COM) of an individual link is not assumed to be coincident with the origin of its body coordinate frame (i.e., $\bar{r}_B \neq 0$ in Fig. D.1). This is interesting because while the origin of the link body coordinate frames may be designed to be collocated with their respective centers of mass, upon robot construction and parameter identification, collocation is unlikely to hold.

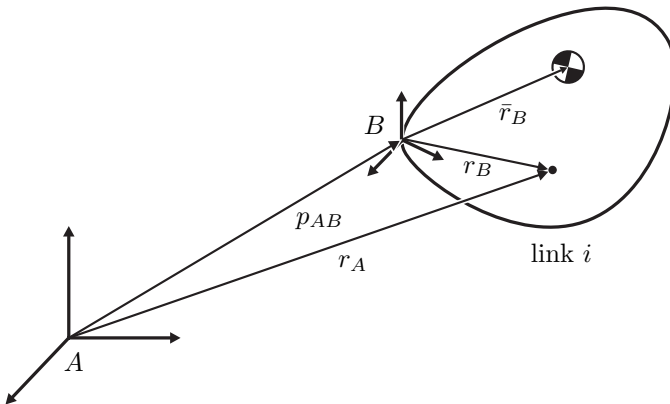


Figure D.1. A single link of an open-chain robot used to explain the method of Lagrange. A is an inertial coordinate frame and B is a body coordinate frame, i.e., it is affixed to the link. The vector \bar{r} is from the origin of B to the center of mass of the link. The vector r_A (resp. r_B) is from the origin of A (resp. B) to an arbitrary point in the link. The vector p_{AB} is from the origin of A to the origin of B .

From Hamilton's principle, the equations of motion can be calculated directly from the Lagrangian as

$$\frac{d}{dt} \frac{\partial \mathcal{L}}{\partial \dot{q}_i} - \frac{\partial \mathcal{L}}{\partial q_i} = f_i \quad (\text{D.2})$$

where f_i are joint torques and other nonconservative forces affecting the i -th generalized coordinate [90, pp. 34–45].

D.2 The Kinetic Energy

The first ingredient required to calculate the Lagrangian is the total kinetic energy. The kinetic energy of a single link will be calculated first and then the kinetic energy of the entire robot will be calculated. To prevent clutter, the subscripts indicating the link will be dropped until the end of the section.

The kinetic energy of an individual link (rigid body) is given by

$$K = \frac{1}{2} \int_V \rho(r_B) \|\dot{r}_A\|^2 dV \quad (\text{D.3})$$

where $V \subset \mathbb{R}^3$ is the region of three-dimensional space occupied by the link, $\rho(r_B)$, $r_B \in V$ is the density of the link at point r_B , and $\|\cdot\|$ is the two-norm.

The total mass of the link is

$$m = \int_V \rho(r) dV \quad (\text{D.4})$$

and the center of mass is then

$$\bar{r} = \frac{1}{m} \int_V \rho(r) r dV. \quad (\text{D.5})$$

Note that \bar{r} in (D.5) is in whatever coordinate frame the integral is performed.

Using the coordinate frames A and B as given in Fig. D.1, let $R_{AB} \in SO(3)$ denote the rotation matrix that takes vectors expressed in the coordinates of the body frame B into vectors expressed in the coordinates of the inertial frame A . Then r_A and \dot{r}_A may be expressed as

$$r_A = p_{AB} + R_{AB} r_B \quad (\text{D.6a})$$

$$\dot{r}_A = \dot{p}_{AB} + \dot{R}_{AB} r_B. \quad (\text{D.6b})$$

For $\omega = [\omega_1; \omega_2; \omega_3] \in \mathbb{R}^3$, let $\hat{\omega}$ denote the 3×3 skew-symmetric matrix

$$\begin{bmatrix} 0 & -\omega_3 & \omega_2 \\ \omega_3 & 0 & -\omega_1 \\ -\omega_2 & \omega_1 & 0 \end{bmatrix}. \quad (\text{D.7})$$

It follows that $\hat{\omega} \in so(3)$, the Lie algebra of $SO(3)$. Conversely, every 3×3 skew-symmetric matrix can be expressed in the form (D.5), and the “unpacking operation” is defined by

$$\begin{bmatrix} 0 & -\omega_3 & \omega_2 \\ \omega_3 & 0 & -\omega_1 \\ -\omega_2 & \omega_1 & 0 \end{bmatrix}^\vee := \begin{bmatrix} \omega_1 \\ \omega_2 \\ \omega_3 \end{bmatrix}, \quad (\text{D.8})$$

so that $(\hat{\omega})^\vee = \omega$.

Using this notation and the fact that $R_{AB}^{-1} \dot{R}_{AB}$ is skew symmetric [164, pp. 52], \dot{R}_{AB} can be rewritten as

$$\dot{R}_{AB} = R_{AB} R_{AB}^{-1} \dot{R}_{AB} \quad (\text{D.9a})$$

$$= R_{AB} \hat{\omega}_B \quad (\text{D.9b})$$

where

$$\hat{\omega}_B := R_{AB}^{-1} \dot{R}_{AB} \quad (\text{D.10})$$

and

$$\omega_B := \left(R_{AB}^{-1} \dot{R}_{AB} \right)^\vee \in \mathbb{R}^3 \quad (\text{D.11})$$

is the instantaneous angular velocity of the link in the body coordinate frame.

It follows that (D.6b) can be rewritten as

$$\dot{r}_A = \dot{p}_{AB} + R_{AB}\hat{\omega}_B r_B, \quad (\text{D.12})$$

and the total kinetic energy (D.3) may be expanded as

$$K = \frac{1}{2} \int_V \rho(r_B) \|\dot{p}_{AB} + \dot{R}_{AB}r_B\|^2 dV \quad (\text{D.13a})$$

$$= \frac{1}{2} \int_V \rho(r_B) \left(\|\dot{p}_{AB}\|^2 + \|\dot{R}_{AB}r_B\|^2 + 2\dot{p}'_{AB}\dot{R}_{AB}r_B \right) dV \quad (\text{D.13b})$$

$$= \frac{1}{2} \int_V \rho(r_B) \left(\|\dot{p}_{AB}\|^2 + \|R_{AB}\hat{\omega}_B r_B\|^2 + 2\dot{p}'_{AB}R_{AB}\hat{\omega}_B r_B \right) dV. \quad (\text{D.13c})$$

The first term of (D.13c) is due to translation of the link with respect to A . The term is

$$K_{\text{translation}} = \frac{1}{2} \int_V \rho(r_B) \|\dot{p}_{AB}\|^2 dV \quad (\text{D.14a})$$

$$= \frac{1}{2} m \|\dot{p}_{AB}\|^2. \quad (\text{D.14b})$$

The second term of (D.13c) is due to rotation of the link about the origin of B . The term is

$$K_{\text{rotation}} = \frac{1}{2} \int_V \rho(r_B) (R_{AB}\hat{\omega}_B r_B)' (R_{AB}\hat{\omega}_B r_B) dV \quad (\text{D.15a})$$

$$= \frac{1}{2} \int_V \rho(r_B) r'_B \hat{\omega}'_B R'_{AB} R_{AB} \hat{\omega}_B r_B dV \quad (\text{D.15b})$$

$$= \frac{1}{2} \int_V \rho(r_B) r'_B \hat{\omega}'_B \hat{\omega}_B r_B dV \quad (\text{D.15c})$$

$$= \frac{1}{2} \int_V \rho(r_B) (-\omega'_B \hat{r}'_B) (-\hat{r}_B \omega_B) dV \quad (\text{D.15d})$$

$$= \frac{1}{2} \omega'_B \left(\int_V \rho(r_B) \hat{r}'_B \hat{r}_B dV \right) \omega_B \quad (\text{D.15e})$$

$$= \frac{1}{2} \omega'_B I_{\text{rotation}} \omega_B \quad (\text{D.15f})$$

where I_{rotation} is the inertia tensor of the link expressed in the body frame. The third term of (D.13c) is due to non-collocation² of the origin of B and the COM of the link,

$$K_{\text{non-collocation}} = \int_V \rho(r_B) \dot{p}'_{AB} R_{AB} \hat{\omega}_B r_B dV \quad (\text{D.16a})$$

$$= m \dot{p}'_{AB} R_{AB} \hat{\omega}_B \bar{r}_B, \quad (\text{D.16b})$$

²If the origin of B is the COM of the link, then $\bar{r}_B = 0$ and this term is zero.

where \bar{r}_B is the link's center of mass in the coordinate frame B . Hence, the total kinetic energy for the link may be expressed as

$$K = \frac{1}{2} m \|\dot{p}_{AB}\|^2 + \frac{1}{2} \omega'_B I_{\text{rotation}} \omega_B + m \dot{p}'_{AB} R_{AB} \hat{\omega}_B \bar{r}_B \quad (\text{D.17})$$

The dependence of \dot{p}_{AB} , ω_B , R_{AB} and I_{rotation} upon q and \dot{q} has been suppressed up until this point. Each of these terms will be expressed in such a way that (D.17) may be written in quadratic form.

The translational velocity of the origin of B with respect to A is

$$\dot{p}_{AB}(q, \dot{q}) = \frac{\partial p}{\partial q} \dot{q} =: J_p(q) \dot{q}. \quad (\text{D.18})$$

Expanding (D.10) yields

$$\hat{\omega}_B(q, \dot{q}) = \sum_{i=1}^{N+6} R_{AB}^{-1}(q) \frac{\partial R_{AB}(q)}{\partial q_i} \dot{q}_i \quad (\text{D.19})$$

which may be rewritten as

$$\omega_B = J_{AB}(q) \dot{q} \quad (\text{D.20})$$

where

$$J_{AB}(q) := \left[\left(R_{AB}^{-1}(q) \frac{\partial R_{AB}(q)}{\partial q_1} \right)^{\vee} \dots \left(R_{AB}^{-1}(q) \frac{\partial R_{AB}(q)}{\partial q_{N+6}} \right)^{\vee} \right]. \quad (\text{D.21})$$

Now, the kinetic energy of link- i (D.17) may be expressed as

$$\begin{aligned} K_i(q, \dot{q}) &= \frac{1}{2} m \dot{q}' J'_p(q) J_p(q) \dot{q} + \frac{1}{2} \dot{q}' J'_{AB}(q) I_{\text{rotation}}(q) J_{AB}(q) \dot{q} \\ &\quad - m \dot{q}' J'_p(q) R_{AB}(q) \hat{r}_B J_{AB}(q) \dot{q} \end{aligned} \quad (\text{D.22a})$$

$$= \frac{1}{2} \dot{q}' \bar{D}_i(q) \dot{q} \quad (\text{D.22b})$$

where

$$\begin{aligned} \bar{D}_i(q) &= m J_p(q)' J_p(q) + J'_{AB}(q) I_{\text{rotation}}(q) J_{AB}(q) \\ &\quad - 2m J'_p(q) R_{AB}(q) \hat{r}_B J_{AB}(q) \end{aligned} \quad (\text{D.23})$$

is a symmetric, positive semi-definite matrix. The total kinetic energy of the robot is the sum of the kinetic energies of the individual links

$$K(q, \dot{q}) = \sum_{i=1}^N K_i(q, \dot{q}) = \frac{1}{2} \dot{q}' D(q) \dot{q} \quad (\text{D.24})$$

where $D(q) := \sum_{i=1}^N \bar{D}_i(q)$.

D.3 The Potential Energy

The second ingredient required to calculate the Lagrangian is the total potential energy of the robot. Calculation of the potential energy is considerably less complicated than calculation of the kinetic energy.

Let $p_{\text{cm},i}^{\text{v}}(q)$ be the height of the center of mass of link i . The potential energy for link i is simply

$$V_i(q) = g_0 m_i p_{\text{cm},i}^{\text{v}}(q), \quad (\text{D.25})$$

where g_0 is the acceleration due to gravity. The total potential energy of the robot is then

$$V(q) = \sum_{i=1}^N V_i(q). \quad (\text{D.26})$$

D.4 Equations of Motion

The equations of motion may now be directly calculated using (D.2). The two primary structural properties of the Lagrangian that will be exploited are the form of (D.22b) and the independence of the potential energy of \dot{q} . First, expand (D.2) as

$$\frac{d}{dt} \frac{\partial K(q, \dot{q})}{\partial \dot{q}_i} - \frac{\partial K(q, \dot{q})}{\partial q_i} + \frac{\partial V(q)}{\partial q_i} = f_i, \quad (\text{D.27})$$

where f_i are nonconservative forces affecting the i -th generalized coordinate. Expanding the first term of (D.27) yields

$$\frac{d}{dt} \frac{\partial K(q, \dot{q})}{\partial \dot{q}_i} = \frac{d}{dt} \left(\sum_{j=1}^{N+6} D_{ij}(q) \dot{q}_j \right) \quad (\text{D.28a})$$

$$= \sum_{j=1}^{N+6} D_{ij}(q) \ddot{q}_j + \sum_{j,k=1}^{N+6} \frac{\partial D_{ij}(q)}{\partial q_k} \dot{q}_j \dot{q}_k. \quad (\text{D.28b})$$

Expanding the second term of (D.27) yields

$$\frac{\partial K(q, \dot{q})}{\partial q_i} = \frac{1}{2} \sum_{j,k=1}^{N+6} \frac{\partial D_{kj}(q)}{\partial q_i} \dot{q}_j \dot{q}_k. \quad (\text{D.29})$$

Hence, (D.27) may be written as

$$\sum_{j=1}^{N+6} D_{ij}(q)\ddot{q}_j + \sum_{j,k=1}^{N+6} \left(\frac{\partial D_{ij}(q)}{\partial q_k} \dot{q}_j \dot{q}_k - \frac{1}{2} \frac{\partial D_{kj}(q)}{\partial q_i} \dot{q}_j \dot{q}_k \right) + \frac{\partial V(q)}{\partial q_i} = f_i. \quad (\text{D.30})$$

To write (D.30) in vector form, define the Christoffel symbols to be

$$\Gamma_{ijk} := \frac{1}{2} \left(\frac{\partial D_{ij}(q)}{\partial q_k} + \frac{\partial D_{ik}(q)}{\partial q_j} - \frac{\partial D_{kj}(q)}{\partial q_i} \right), \quad (\text{D.31})$$

and the Coriolis matrix $C(q, \dot{q}) \in \mathbb{R}^{(N+6) \times (N+6)}$ to be

$$C_{ij}(q, \dot{q}) := \sum_{k=1}^{N+6} \Gamma_{ijk}(q) \dot{q}_k, \quad (\text{D.32})$$

so that

$$\sum_{j,k=1}^{N+6} \left(\frac{\partial D_{ij}(q)}{\partial q_k} \dot{q}_j \dot{q}_k - \frac{1}{2} \frac{\partial D_{kj}(q)}{\partial q_i} \dot{q}_j \dot{q}_k \right) = \sum_{j=1}^{N+6} C_{ij} \dot{q}_j. \quad (\text{D.33})$$

The effect of the potential energy is represented by $G \in \mathbb{R}^{N+6}$ defined as

$$G_i(q) := \frac{\partial V(q)}{\partial q_i}. \quad (\text{D.34})$$

The torques and other nonconservative forces affecting the i -th generalized coordinate can often be decomposed as

$$f_i(q, \dot{q}, u) = F_i(q, \dot{q}) + E_i(q)F_{\text{ext}} + B_i(q)\tau, \quad (\text{D.35})$$

where F is a vector of frictional forces and $E_i(q)$ and B_i are the i -th rows of the matrices E and B which are defined as follows. Decompose $u \in \mathbb{R}^P$ into the torques and nonconservative forces, $u = (F_{\text{ext}}; \tau)$, where $F_{\text{ext}} \in \mathbb{R}^{(P-P_\tau)}$ and $\tau \in \mathbb{R}^{P_\tau}$. Let the nonconservative forces act at $p_j(q)$, $j = 1, \dots, (P - P_\tau)$ so that

$$E(q) = \left(\frac{\partial p(q)}{\partial q} \right)' . \quad (\text{D.36})$$

Similarly, let $\tilde{q}_j(q)$, $j = 1, \dots, P_\tau$, be the relative angles of the actuated joints so that

$$B(q) = \left(\frac{\partial \tilde{q}(q)}{\partial q} \right)' . \quad (\text{D.37})$$

Finally, assuming the decomposition of f_i given in (D.35), the equations of motion may be written in vector form as

$$D(q)\ddot{q} + C(q, \dot{q})\dot{q} + G(q) - F(q, \dot{q}) = E(q)F_{\text{ext}} + B(q)\tau. \quad (\text{D.38})$$

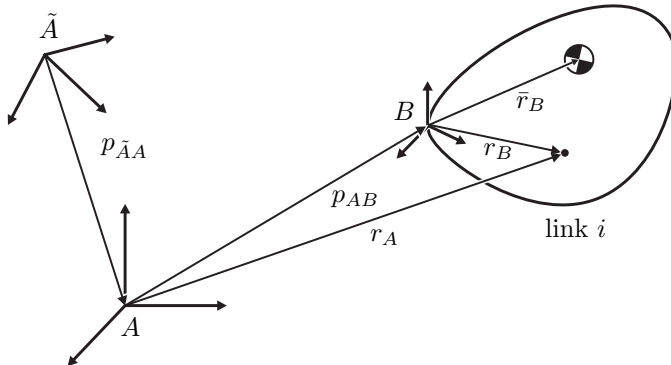


Figure D.2. The inertial frame \tilde{A} is translated by $p_{\tilde{A}A}$ and rotated by $R_{\tilde{A}A}$ with respect to A .

D.5 Invariance Properties of the Kinetic Energy

Consider now a new inertial frame \tilde{A} as in Fig. D.2, where $p_{\tilde{A}A}$ defines the translation of the origin with respect to the original inertial frame A and $R_{\tilde{A}A}$ defines the rotation. Let $r_{\tilde{A}}$, $p_{\tilde{A}B}$, and $R_{\tilde{A}B}$ be defined as in (D.6a), per

$$r_{\tilde{A}} = p_{\tilde{A}B} + R_{\tilde{A}B}r_B, \quad (\text{D.39})$$

so that

$$r_{\tilde{A}} = p_{\tilde{A}A} + R_{\tilde{A}A}r_A. \quad (\text{D.40})$$

It follows that

$$\dot{r}_{\tilde{A}} = R_{\tilde{A}A}\dot{r}_A \quad (\text{D.41})$$

because $p_{\tilde{A}A}$ and $R_{\tilde{A}A}$ are constant.

Computing the kinetic energy in the inertial frame \tilde{A} gives

$$\tilde{K} = \frac{1}{2} \int_V \rho(r_B) \|\dot{r}_{\tilde{A}}\|^2 dV = \frac{1}{2} \int_V \rho(r_B) \|R_{\tilde{A}A}\dot{r}_A\|^2 dV = K, \quad (\text{D.42})$$

because

$$\|R_{\tilde{A}A}\dot{r}_A\| = \|\dot{r}_A\|. \quad (\text{D.43})$$

Hence, the kinetic energy is invariant under translations and rotations of the inertial frame.

E

Single Support Equations of Motion of RABBIT

This appendix gives the details of the equations of motion for RABBIT during the swing phase. The intention is to impress upon the reader the complexity of the robot's dynamics. Chapter 5 demonstrates that despite this apparent complexity, the structure of the dynamics may be leveraged for controller design. The definition of the parameters in the model can be found in Section 6.6.2. The values of the constants used in the design of the controllers tested in the experiments can be found in Table 6.3.

The equations have the general matrix form

$$D(q)\ddot{q} + C(q, \dot{q})\dot{q} + G(q) = Bu \quad (\text{E.1})$$

where

$$\begin{aligned} (D(q))_{1,1} &= I_t + I_f + 4M_f l_f l_t \cos(q_3) + 2M_f l_t^2 + 2M_t l_f l_t \cos(q_3) + \\ &\quad 2M_t l_f l_t \cos(q_3) + I_{a,H} - 2p_f^M l_t \cos(q_3) + 2M_f l_f^2 - \\ &\quad 2p_t^M l_t + M_t l_f^2 + M_T l_f^2 + M_t l_t^2 - 2p_f^M l_f + 2M_t l_t^2 \\ (D(q))_{1,2} &= -p_t^M l_f \cos(-q_2 - q_4 + q_1) - M_t l_t l_f \cos(q_1 + q_3 - q_2) - \\ &\quad M_t l_f^2 \cos(q_1 - q_2) - p_f^M l_f \cos(q_1 - q_2) - \\ &\quad p_f^M l_t \cos(q_1 + q_3 - q_2) - p_t^M l_t \cos(-q_2 - q_4 + q_1 + q_3) \\ (D(q))_{1,3} &= -2p_t^M l_t + 2M_f l_t^2 + 2M_f l_f l_t \cos(q_3) + M_t l_f l_t \cos(q_3) + \\ &\quad 2M_t l_t^2 + M_t l_f l_t \cos(q_3) - p_f^M l_t \cos(q_3) + I_t + M_T l_t^2 \\ (D(q))_{1,4} &= -p_t^M l_t \cos(-q_2 - q_4 + q_1 + q_3) - p_f^M l_f \cos(-q_2 - q_4 + q_1) \\ (D(q))_{1,5} &= 2M_f l_t^2 - p_f^M l_f \cos(-q_2 - q_4 + q_1) - \\ &\quad M_t l_t l_f \cos(q_1 + q_3 - q_2) - M_t l_f^2 \cos(q_1 - q_2) - \\ &\quad p_f^M l_f \cos(q_1 - q_2) - p_f^M l_t \cos(q_1 + q_3 - q_2) + \\ &\quad 2M_t l_f l_t \cos(q_3) + 2M_t l_f l_t \cos(q_3) + 2M_f l_f^2 - 2p_f^M l_t + \\ &\quad M_t l_f^2 + M_T l_f^2 + M_t l_t^2 + 4M_f l_f l_t \cos(q_3) - 2p_f^M l_f + \\ &\quad 2M_t l_t^2 - p_f^M l_t \cos(q_1 + q_3) - p_f^M l_f \cos(q_1) - \\ &\quad 2p_f^M l_t \cos(q_3) - p_t^M l_t \cos(-q_2 - q_4 + q_1 + q_3) + I_f + I_t \\ (D(q))_{2,2} &= M_t l_f^2 + I_f + 2p_f^M l_f \cos(q_4) + I_{a,H} + I_t \\ (D(q))_{2,3} &= -l_t(p_f^M \cos(q_1 + q_3 - q_2) + M_t l_f \cos(q_1 + q_3 - q_2) + \\ &\quad p_t^M \cos(-q_2 - q_4 + q_1 + q_3)) \\ (D(q))_{2,4} &= I_t + p_t^M l_f \cos(q_4) \end{aligned}$$

$$\begin{aligned}
(D(q))_{2,5} &= M_t l_f^2 - p_f^M l_f \cos(q_1 - q_2) - M_t l_f^2 \cos(q_1 - q_2) + \\
&\quad 2p_t^M l_f \cos(q_4) - p_t^M l_t \cos(-q_2 - q_4 + q_1 + q_3) - \\
&\quad p_t^M l_f \cos(-q_2 - q_4 + q_1) + I_t + I_f - \\
&\quad p_f^M l_t \cos(q_1 + q_3 - q_2) - M_t l_t l_f \cos(q_1 + q_3 - q_2) \\
(D(q))_{3,3} &= -2p_t^M l_t + 2M_f l_t^2 + I_{a,K} + 2M_t l_t^2 + I_t + M_T l_t^2 \\
(D(q))_{3,4} &= -p_t^M l_t \cos(-q_2 - q_4 + q_1 + q_3) \\
(D(q))_{3,5} &= -2p_t^M l_t + 2M_f l_t^2 + 2M_t l_t^2 + M_T l_t^2 + M_t l_f l_t \cos(q_3) + \\
&\quad M_t l_f l_t \cos(q_3) + 2M_f l_f l_t \cos(q_3) - p_T^M l_t \cos(q_1 + q_3) - \\
&\quad p_t^M l_t \cos(-q_2 - q_4 + q_1 + q_3) - p_f^M l_t \cos(q_3) + I_t - \\
&\quad p_f^M l_t \cos(q_1 + q_3 - q_2) - M_t l_t l_f \cos(q_1 + q_3 - q_2) \\
(D(q))_{4,4} &= I_t + I_{a,K} \\
(D(q))_{4,5} &= p_t^M l_f \cos(q_4) - p_t^M l_t \cos(-q_2 - q_4 + q_1 + q_3) + I_t - \\
&\quad p_t^M l_f \cos(-q_2 - q_4 + q_1) \\
(D(q))_{5,5} &= 2p_t^M l_f \cos(q_4) + 2M_f l_t^2 - 2p_t^M l_f \cos(-q_2 - q_4 + q_1) - \\
&\quad 2M_t l_t l_f \cos(q_1 + q_3 - q_2) - 2M_t l_f^2 \cos(q_1 - q_2) - \\
&\quad 2p_f^M l_f \cos(q_1 - q_2) - 2p_f^M l_t \cos(q_1 + q_3 - q_2) + \\
&\quad 2M_t l_f l_t \cos(q_3) + 2M_T l_f l_t \cos(q_3) + 2M_f l_f^2 - 2p_t^M l_t + \\
&\quad 2M_t l_f^2 + M_T l_f^2 + M_t l_t^2 + 4M_f l_f l_t \cos(q_3) - 2p_f^M l_f + 2M_t l_f^2 - \\
&\quad 2p_T^M l_t \cos(q_1 + q_3) - 2p_f^M l_f \cos(q_1) - 2p_f^M l_t \cos(q_3) - \\
&\quad 2p_t^M l_t \cos(-q_2 - q_4 + q_1 + q_3) + I_T + 2I_f + 2I_t
\end{aligned}$$

$$\begin{aligned}
(C(q, \dot{q}))_{1,1} &= -l_t(2M_f l_f \sin(q_3) + M_t l_f \sin(q_3) + M_T l_f \sin(q_3) - \\
&\quad p_f^M \sin(q_3))\dot{q}_3 \\
(C(q, \dot{q}))_{1,2} &= -\dot{q}_4 p_t^M l_f \sin(-q_2 - q_4 + q_1) - \dot{q}_2 M_t l_f^2 \sin(q_1 - q_2) - \\
&\quad \dot{q}_2 p_t^M l_f \sin(-q_2 - q_4 + q_1) - \dot{q}_2 p_f^M l_f \sin(q_1 - q_2) - \\
&\quad \dot{q}_5 p_t^M l_f \sin(-q_2 - q_4 + q_1) - \dot{q}_5 p_f^M l_f \sin(q_1 - q_2) - \\
&\quad \dot{q}_5 M_t l_f^2 \sin(q_1 - q_2) - \dot{q}_5 M_t l_t l_f \sin(q_1 + q_3 - q_2) - \\
&\quad \dot{q}_5 p_t^M l_t \sin(-q_2 - q_4 + q_1 + q_3) - \\
&\quad \dot{q}_5 p_f^M l_t \sin(q_1 + q_3 - q_2) - \dot{q}_2 M_t l_t l_f \sin(q_1 + q_3 - q_2) - \\
&\quad \dot{q}_2 p_t^M l_t \sin(-q_2 - q_4 + q_1 + q_3) - \\
&\quad \dot{q}_2 p_f^M l_t \sin(q_1 + q_3 - q_2) - \dot{q}_4 p_t^M l_t \sin(-q_2 - q_4 + q_1 + q_3) \\
(C(q, \dot{q}))_{1,3} &= -l_t(\dot{q}_5 + \dot{q}_3 + \dot{q}_1)(2M_f l_f \sin(q_3) + M_t l_f \sin(q_3) + \\
&\quad M_T l_f \sin(q_3) - p_f^M \sin(q_3)) \\
(C(q, \dot{q}))_{1,4} &= (-\dot{q}_2 - \dot{q}_4 - \dot{q}_5)(p_t^M l_t \sin(-q_2 - q_4 + q_1 + q_3) + \\
&\quad p_t^M l_f \sin(-q_2 - q_4 + q_1))
\end{aligned}$$

$$\begin{aligned}
(C(q, \dot{q}))_{1,5} &= -2\dot{q}_3 M_f l_f l_t \sin(q_3) - \dot{q}_3 M_t l_f l_t \sin(q_3) - \\
&\quad \dot{q}_3 M_T l_f l_t \sin(q_3) + \dot{q}_3 p_f^M l_t \sin(q_3) - \dot{q}_2 p_f^M l_f \sin(q_1 - q_2) - \\
&\quad \dot{q}_2 M_t l_f^2 \sin(q_1 - q_2) - \dot{q}_2 p_t^M l_f \sin(-q_2 - q_4 + q_1) - \\
&\quad \dot{q}_4 p_f^M l_f \sin(-q_2 - q_4 + q_1) - \dot{q}_5 p_f^M l_f \sin(q_1) - \\
&\quad \dot{q}_5 p_f^M l_f \sin(q_1 - q_2) - \dot{q}_5 p_t^M l_f \sin(-q_2 - q_4 + q_1) - \\
&\quad \dot{q}_5 M_t l_f^2 \sin(q_1 - q_2) - \dot{q}_5 M_t l_f l_t \sin(q_1 + q_3 - q_2) - \\
&\quad \dot{q}_5 p_T^M l_t \sin(q_1 + q_3) - \dot{q}_5 p_t^M l_t \sin(-q_2 - q_4 + q_1 + q_3) - \\
&\quad \dot{q}_5 p_f^M l_t \sin(q_1 + q_3 - q_2) - \\
&\quad \dot{q}_4 p_t^M l_t \sin(-q_2 - q_4 + q_1 + q_3) - \\
&\quad \dot{q}_2 M_t l_f l_t \sin(q_1 + q_3 - q_2) - \\
&\quad \dot{q}_2 p_t^M l_t \sin(-q_2 - q_4 + q_1 + q_3) - \dot{q}_2 p_f^M l_t \sin(q_1 + q_3 - q_2) \\
(C(q, \dot{q}))_{2,1} &= \dot{q}_1 p_f^M l_f \sin(q_1 - q_2) + \dot{q}_3 M_t l_f l_t \sin(q_1 + q_3 - q_2) + \\
&\quad \dot{q}_1 M_t l_f l_t \sin(q_1 + q_3 - q_2) + \\
&\quad \dot{q}_3 p_t^M l_t \sin(-q_2 - q_4 + q_1 + q_3) + \\
&\quad \dot{q}_1 p_t^M l_f \sin(-q_2 - q_4 + q_1) + \dot{q}_1 M_t l_f^2 \sin(q_1 - q_2) + \\
&\quad \dot{q}_1 p_f^M l_t \sin(q_1 + q_3 - q_2) + \\
&\quad \dot{q}_1 p_t^M l_t \sin(-q_2 - q_4 + q_1 + q_3) + \\
&\quad \dot{q}_3 p_f^M l_t \sin(q_1 + q_3 - q_2) + \dot{q}_5 p_f^M l_f \sin(q_1 - q_2) + \\
&\quad \dot{q}_5 p_t^M l_f \sin(-q_2 - q_4 + q_1) + \dot{q}_5 M_t l_f^2 \sin(q_1 - q_2) + \\
&\quad \dot{q}_5 M_t l_f l_t \sin(q_1 + q_3 - q_2) + \\
&\quad \dot{q}_5 p_t^M l_t \sin(-q_2 - q_4 + q_1 + q_3) + \dot{q}_5 p_f^M l_t \sin(q_1 + q_3 - q_2) \\
(C(q, \dot{q}))_{2,2} &= -l_f \dot{q}_4 p_t^M \sin(q_4) \\
(C(q, \dot{q}))_{2,3} &= l_t (\dot{q}_5 + \dot{q}_3 + \dot{q}_1) (p_f^M \sin(q_1 + q_3 - q_2) + \\
&\quad M_t l_f \sin(q_1 + q_3 - q_2) + p_t^M \sin(-q_2 - q_4 + q_1 + q_3)) \\
(C(q, \dot{q}))_{2,4} &= -l_f (\dot{q}_2 + \dot{q}_4 + \dot{q}_5) p_t^M \sin(q_4) \\
(C(q, \dot{q}))_{2,5} &= \dot{q}_1 p_f^M l_f \sin(q_1 - q_2) + \dot{q}_3 M_t l_f l_t \sin(q_1 + q_3 - q_2) + \\
&\quad \dot{q}_1 M_t l_f l_t \sin(q_1 + q_3 - q_2) - l_f \dot{q}_4 p_t^M \sin(q_4) + \\
&\quad \dot{q}_3 p_t^M l_t \sin(-q_2 - q_4 + q_1 + q_3) + \\
&\quad \dot{q}_1 p_t^M l_f \sin(-q_2 - q_4 + q_1) + \dot{q}_1 M_t l_f^2 \sin(q_1 - q_2) + \\
&\quad \dot{q}_1 p_f^M l_t \sin(q_1 + q_3 - q_2) + \\
&\quad \dot{q}_1 p_t^M l_t \sin(-q_2 - q_4 + q_1 + q_3) + \\
&\quad \dot{q}_3 p_f^M l_t \sin(q_1 + q_3 - q_2) + \dot{q}_5 p_f^M l_f \sin(q_1 - q_2) + \\
&\quad \dot{q}_5 p_t^M l_f \sin(-q_2 - q_4 + q_1) + \dot{q}_5 M_t l_f^2 \sin(q_1 - q_2) + \\
&\quad \dot{q}_5 M_t l_f l_t \sin(q_1 + q_3 - q_2) + \\
&\quad \dot{q}_5 p_t^M l_t \sin(-q_2 - q_4 + q_1 + q_3) + \dot{q}_5 p_f^M l_t \sin(q_1 + q_3 - q_2) \\
(C(q, \dot{q}))_{3,1} &= l_t (\dot{q}_1 + \dot{q}_5) (2M_f l_f \sin(q_3) + M_t l_f \sin(q_3) + M_T l_f \sin(q_3) - \\
&\quad p_f^M \sin(q_3)) \\
(C(q, \dot{q}))_{3,2} &= -l_t (\sin(q_1 + q_3 - q_2) l_f M_t \dot{q}_2 + \\
&\quad \sin(-q_2 - q_4 + q_1 + q_3) p_t^M \dot{q}_2 + \sin(q_1 + q_3 - q_2) p_f^M \dot{q}_2 + \\
&\quad \sin(-q_2 - q_4 + q_1 + q_3) p_t^M \dot{q}_4 + \\
&\quad \dot{q}_5 p_t^M \sin(-q_2 - q_4 + q_1 + q_3) + \dot{q}_5 p_f^M \sin(q_1 + q_3 - q_2) + \\
&\quad \dot{q}_5 M_t l_f \sin(q_1 + q_3 - q_2))
\end{aligned}$$

$$\begin{aligned}
(C(q, \dot{q}))_{3,3} &= 0 \\
(C(q, \dot{q}))_{3,4} &= -l_t(\dot{q}_2 + \dot{q}_4 + \dot{q}_5)p_t^M \sin(-q_2 - q_4 + q_1 + q_3) \\
(C(q, \dot{q}))_{3,5} &= -l_t(-2 \sin(q_3)l_f M_f \dot{q}_1 - \sin(q_3)l_f M_t \dot{q}_1 - \sin(q_3)l_f M_T \dot{q}_1 + \\
&\quad \sin(q_3)p_f^M \dot{q}_1 + \sin(-q_2 - q_4 + q_1 + q_3)p_t^M \dot{q}_2 + \\
&\quad \sin(q_1 + q_3 - q_2)p_f^M \dot{q}_2 + \sin(q_1 + q_3 - q_2)l_f M_t \dot{q}_2 + \\
&\quad \sin(-q_2 - q_4 + q_1 + q_3)p_t^M \dot{q}_4 + \dot{q}_5 p_f^M \sin(q_3) + \\
&\quad \dot{q}_5 p_T^M \sin(q_1 + q_3) - 2\dot{q}_5 M_f l_f \sin(q_3) - \dot{q}_5 M_t l_f \sin(q_3) - \\
&\quad \dot{q}_5 M_T l_f \sin(q_3) + \dot{q}_5 p_t^M \sin(-q_2 - q_4 + q_1 + q_3) + \\
&\quad \dot{q}_5 M_t l_f \sin(q_1 + q_3 - q_2) + \dot{q}_5 p_f^M \sin(q_1 + q_3 - q_2)) \\
(C(q, \dot{q}))_{4,1} &= \dot{q}_1 p_t^M l_t \sin(-q_2 - q_4 + q_1 + q_3) + \\
&\quad \dot{q}_1 p_t^M l_f \sin(-q_2 - q_4 + q_1) + \\
&\quad \dot{q}_3 p_t^M l_t \sin(-q_2 - q_4 + q_1 + q_3) + \\
&\quad \dot{q}_5 p_t^M l_t \sin(-q_2 - q_4 + q_1 + q_3) + \\
&\quad \dot{q}_5 p_t^M l_f \sin(-q_2 - q_4 + q_1) \\
(C(q, \dot{q}))_{4,2} &= l_f(\dot{q}_2 + \dot{q}_5)p_t^M \sin(q_4) \\
(C(q, \dot{q}))_{4,3} &= l_t(\dot{q}_5 + \dot{q}_3 + \dot{q}_1)p_t^M \sin(-q_2 - q_4 + q_1 + q_3) \\
(C(q, \dot{q}))_{4,4} &= 0 \\
(C(q, \dot{q}))_{4,5} &= \dot{q}_1 p_t^M l_t \sin(-q_2 - q_4 + q_1 + q_3) + \\
&\quad \dot{q}_1 p_t^M l_f \sin(-q_2 - q_4 + q_1) + \dot{q}_2 p_t^M l_f \sin(q_4) + \\
&\quad \dot{q}_3 p_t^M l_t \sin(-q_2 - q_4 + q_1 + q_3) + \dot{q}_5 p_t^M l_f \sin(q_4) + \\
&\quad \dot{q}_5 p_t^M l_t \sin(-q_2 - q_4 + q_1 + q_3) + \\
&\quad \dot{q}_5 p_t^M l_f \sin(-q_2 - q_4 + q_1) \\
(C(q, \dot{q}))_{5,1} &= \dot{q}_1 p_f^M l_f \sin(q_1 - q_2) + \dot{q}_3 M_t l_t l_f \sin(q_1 + q_3 - q_2) + \\
&\quad \dot{q}_1 M_t l_t l_f \sin(q_1 + q_3 - q_2) - 2\dot{q}_3 M_f l_f l_t \sin(q_3) - \\
&\quad \dot{q}_3 M_t l_f l_t \sin(q_3) + \dot{q}_1 p_T^M l_t \sin(q_1 + q_3) - \dot{q}_3 M_T l_f l_t \sin(q_3) + \\
&\quad \dot{q}_3 p_f^M l_t \sin(q_3) + \dot{q}_3 p_T^M l_t \sin(q_1 + q_3) + \dot{q}_5 p_T^M l_f \sin(q_1) + \\
&\quad \dot{q}_1 p_T^M l_f \sin(q_1) + \dot{q}_3 p_t^M l_t \sin(-q_2 - q_4 + q_1 + q_3) + \\
&\quad \dot{q}_1 p_t^M l_f \sin(-q_2 - q_4 + q_1) + \dot{q}_1 M_t l_f^2 \sin(q_1 - q_2) + \\
&\quad \dot{q}_1 p_f^M l_t \sin(q_1 + q_3 - q_2) + \\
&\quad \dot{q}_1 p_t^M l_t \sin(-q_2 - q_4 + q_1 + q_3) + \\
&\quad \dot{q}_3 p_f^M l_t \sin(q_1 + q_3 - q_2) + \dot{q}_5 p_f^M l_f \sin(q_1 - q_2) + \\
&\quad \dot{q}_5 p_t^M l_f \sin(-q_2 - q_4 + q_1) + \dot{q}_5 M_t l_f^2 \sin(q_1 - q_2) + \\
&\quad \dot{q}_5 M_t l_t l_f \sin(q_1 + q_3 - q_2) + \dot{q}_5 p_T^M l_t \sin(q_1 + q_3) + \\
&\quad \dot{q}_5 p_f^M l_t \sin(-q_2 - q_4 + q_1 + q_3) + \dot{q}_5 p_t^M l_t \sin(q_1 + q_3 - q_2)
\end{aligned}$$

$$\begin{aligned}
(C(q, \dot{q}))_{5,2} &= -l_f \dot{q}_4 p_t^M \sin(q_4) - \dot{q}_2 p_f^M l_f \sin(q_1 - q_2) - \\
&\quad \dot{q}_2 M_t l_f^2 \sin(q_1 - q_2) - \dot{q}_2 p_t^M l_f \sin(-q_2 - q_4 + q_1) - \\
&\quad l_f \dot{q}_4 p_t^M \sin(-q_2 - q_4 + q_1) - \dot{q}_5 p_f^M l_f \sin(q_1 - q_2) - \\
&\quad \dot{q}_5 p_t^M l_f \sin(-q_2 - q_4 + q_1) - \dot{q}_5 M_t l_f^2 \sin(q_1 - q_2) - \\
&\quad \dot{q}_5 M_t l_f l_t \sin(q_1 + q_3 - q_2) - \\
&\quad \dot{q}_5 p_f^M l_t \sin(q_1 + q_3 - q_2) - \\
&\quad \dot{q}_4 p_t^M l_t \sin(-q_2 - q_4 + q_1 + q_3) - \\
&\quad \dot{q}_2 M_t l_f l_t \sin(q_1 + q_3 - q_2) - \\
&\quad \dot{q}_2 p_t^M l_t \sin(-q_2 - q_4 + q_1 + q_3) - \dot{q}_2 p_f^M l_t \sin(q_1 + q_3 - q_2) \\
(C(q, \dot{q}))_{5,3} &= l_t (\dot{q}_5 + \dot{q}_3 + \dot{q}_1) (M_t l_f \sin(q_1 + q_3 - q_2) - 2M_f l_f \sin(q_3) + \\
&\quad p_f^M \sin(q_1 + q_3 - q_2) - M_T l_f \sin(q_3) + \sin(q_1 + q_3) p_T^M + \\
&\quad p_f^M \sin(q_3) + p_t^M \sin(-q_2 - q_4 + q_1 + q_3) - M_t l_f \sin(q_3)) \\
(C(q, \dot{q}))_{5,4} &= (-\dot{q}_2 - \dot{q}_4 - \dot{q}_5) (p_t^M l_f \sin(q_4) + \\
&\quad p_t^M l_t \sin(-q_2 - q_4 + q_1 + q_3) + p_t^M l_f \sin(-q_2 - q_4 + q_1)) \\
(C(q, \dot{q}))_{5,5} &= \dot{q}_3 p_t^M l_t \sin(-q_2 - q_4 + q_1 + q_3) + \dot{q}_1 p_f^M l_f \sin(q_1 - q_2) + \\
&\quad \dot{q}_1 p_t^M l_f \sin(-q_2 - q_4 + q_1) + \dot{q}_1 M_t l_f^2 \sin(q_1 - q_2) + \\
&\quad \dot{q}_1 p_f^M l_t \sin(q_1 + q_3 - q_2) - l_f \dot{q}_4 p_t^M \sin(q_4) + \\
&\quad \dot{q}_1 p_t^M l_t \sin(-q_2 - q_4 + q_1 + q_3) - \\
&\quad \dot{q}_2 p_t^M l_f \sin(-q_2 - q_4 + q_1) - \dot{q}_2 M_t l_f^2 \sin(q_1 - q_2) - \\
&\quad \dot{q}_2 p_f^M l_f \sin(q_1 - q_2) - l_f \dot{q}_4 p_t^M \sin(-q_2 - q_4 + q_1) - \\
&\quad \dot{q}_4 p_t^M l_t \sin(-q_2 - q_4 + q_1 + q_3) - \\
&\quad \dot{q}_2 M_t l_f l_t \sin(q_1 + q_3 - q_2) - \dot{q}_2 p_f^M l_t \sin(q_1 + q_3 - q_2) - \\
&\quad \dot{q}_2 p_t^M l_t \sin(-q_2 - q_4 + q_1 + q_3) + \\
&\quad \dot{q}_3 p_f^M l_t \sin(q_1 + q_3 - q_2) + \dot{q}_1 p_T^M l_f \sin(q_1) + \\
&\quad \dot{q}_3 M_t l_f l_t \sin(q_1 + q_3 - q_2) + \dot{q}_1 M_t l_f l_t \sin(q_1 + q_3 - q_2) - \\
&\quad \dot{q}_3 M_T l_f l_t \sin(q_3) - \dot{q}_3 M_t l_f l_t \sin(q_3) + \dot{q}_1 p_T^M l_t \sin(q_1 + q_3) + \\
&\quad \dot{q}_3 p_T^M l_t \sin(q_1 + q_3) + \dot{q}_3 p_f^M l_t \sin(q_3) - 2\dot{q}_3 M_f l_f l_t \sin(q_3)
\end{aligned}$$

$$\begin{aligned}
(G(q))_{1,1} &= g_0 (l_f \sin(q_1 + q_5) M_T + l_t \sin(q_1 + q_3 + q_5) M_T + \\
&\quad 2l_f \sin(q_1 + q_5) M_f + 2l_t \sin(q_1 + q_3 + q_5) M_f - \\
&\quad \sin(q_1 + q_5) p_f^M + 2l_t \sin(q_1 + q_3 + q_5) M_t - \\
&\quad \sin(q_1 + q_3 + q_5) p_t^M + l_f \sin(q_1 + q_5) M_t) \\
(G(q))_{2,1} &= g_0 (-\sin(q_2 + q_5) p_f^M - l_f \sin(q_2 + q_5) M_t - \\
&\quad \sin(q_2 + q_4 + q_5) p_t^M) \\
(G(q))_{3,1} &= g_0 (l_t \sin(q_1 + q_3 + q_5) M_T + 2l_t \sin(q_1 + q_3 + q_5) M_f + \\
&\quad 2l_t \sin(q_1 + q_3 + q_5) M_t - \sin(q_1 + q_3 + q_5) p_t^M) \\
(G(q))_{4,1} &= -g_0 \sin(q_2 + q_4 + q_5) p_t^M
\end{aligned}$$

$$(G(q))_{5,1} = g_0(l_f \sin(q_1 + q_5)M_T + l_t \sin(q_1 + q_3 + q_5)M_T - \sin(q_5)p_T^M + 2l_f \sin(q_1 + q_5)M_f + 2l_t \sin(q_1 + q_3 + q_5)M_f - \sin(q_1 + q_5)p_f^M - \sin(q_2 + q_5)p_f^M + 2l_t \sin(q_1 + q_3 + q_5)M_t - \sin(q_1 + q_3 + q_5)p_t^M + l_f \sin(q_1 + q_5)M_t - l_f \sin(q_2 + q_5)M_t - \sin(q_2 + q_4 + q_5)p_t^M)$$

and

$$B = \begin{bmatrix} I \\ 0 \end{bmatrix}.$$

Nomenclature

| | |
|--------------------------------------|--|
| (x_1, x_2, \dots, x_m) | an m -tuple |
| $(x_1; x_2; \dots; x_m)$ | a column vector |
| $\mathcal{Q}, T\mathcal{Q}$ | configuration and state manifolds |
| K, V | kinetic and potential energies |
| D, C, G, B | matrices of the Lagrange equations of motion, the mass-inertia matrix, the matrix of Coriolis and centrifugal terms, the vector of terms associated with conservative potentials, and the input matrix |
| f, g, h | drift vector field, control vector field, output |
| q, \dot{q}, x, u | generalized configuration variables, generalized velocities, state ($x = (q; \dot{q})$), input |
| θ | function of configuration that is selected to be strictly monotonic over a step |
| $\Delta, \Delta_q, \Delta_{\dot{q}}$ | impact map, impact map for positions, impact map for velocities |
| \mathcal{O} | orbit |
| \mathcal{S} | Poincaré section |
| \mathcal{Z} | zero dynamics manifold |
| P | Poincaré map |
| ρ | restricted Poincaré map |
| \star^+, \star^- | denotes the beginning or end of phase \star |
| g_0 | gravitational constant |
| m_{tot} | total mass |
| N | number of links |
| $\sigma_\star, \bar{\sigma}_i$ | angular momentum about the point \star and generalized angular momentum conjugate to \dot{q}_i |
| p_\star^h, p_\star^v | horizontal and vertical positions of a point \star on the robot |
| $\mathbb{S}^1, \mathbb{T}^n$ | the unit circle and the n -torus: $\mathbb{T}^n = \underbrace{\mathbb{S}^1 \times \mathbb{S}^1 \times \cdots \times \mathbb{S}^1}_{n-\text{times}}$ |

End Notes

Notes on Chapter 1

The literature on bipedal robots is already quite extensive. The reader seeking a general overview would do well to start with [123, 180, 185, 224, 235], in that order. Some control-oriented works that we have found especially illuminating, because of their emphasis on analytical aspects of walking, running, and balancing are [28, 76, 143, 170, 184, 202, 216, 217]. For an insightful analysis of another system that exhibits limit cycles and impacts, see [193]. For a very simple and insightful analysis of a planar rimless wheel as a model of walking, see [56], and for the 3-D rimless wheel, see [210]. A rich literature is developing on feedback control design based on path following as a means to overcome performance limitations due to trajectory tracking; see [3, 61, 62] and references therein.

The reader seeking further information on the ZMP and other ground reference points, such as the FRI, is referred to [177, 234] and references therein.

Notes on Chapter 2

The description of RABBIT is taken from [43]. As pointed out in Chapter 1, for legged robots, the evolution of the individual joints during a walking or running gait is far from being uniquely specified by speed, step length, knee flexion direction, torso posture, etc. An often used criterion for defining a (time-based) reference trajectory is to minimize the energy consumed per distance traveled along a periodic orbit of the robot model. The determination of reference trajectories is important during the design phase of a walking robot in order to determine the sizes of links, mass distribution, and the choice of the actuators [44, 47, 49].

History of RABBIT: The CNRS research project that resulted in the construction of RABBIT began in 1997.

In 1997 and 1998, B. Espiau (Inria Rhône Alpes) and C. Canudas de Wit (Automatic Control Laboratory of Grenoble (LAG)) formulated the general specifications for a prototype biped under the PrC-GdR project entitled *Control of Walking Robots*. The following is a list of laboratories and personnel who contributed to this project: **Laboratoire de Mécanique des Solides de Poitiers (LMS)** (P. Sardain, G. Bessonnet, and M. Rostami), **LSIIT-GRAII, Strasbourg** (G. Abba and N. Chaillet), **INRIA Rhône-Alpes** (B. Espiau, A. Goswami, F. Génot, P. B. Wieber, and B.Thuilot), **INRIA Sophia-Antipolis** (C. Samson and C. François), **Laboratoire de Robotique de Paris (LRP)** (N. M'Sirdi, N. Manamami, N. Nadjar-Gauthier,

P. Blazevic, G. Beurier, F. B. Ouezdou, O. Bruneau), **Laboratoire d'Automatique de Grenoble (LAG)** (C. Canudas de Wit, A. Loria, L. Roussel, C. Acosta), and **Laboratoire d'Automatique de Nantes (LAN)** (C. Chevallereau, B. Perrin, A. Formal'sky, Y. Aoustin). Financial support was provided by the CNRS.

From September 1999 to September 2001, C. Chevallereau (IRCyN) and A. Loria (LAG) with the support of the Automatic Control Research Group under the project entitled *Control of Walking Robots* conducted activities that allowed the realization of the prototype RABBIT. The following is a list of laboratories and personnel who contributed to this project: **INRIA Rhône-Alpes** (B. Espiau, A. Goswami, P. B. Wieber, F. Genot, and E. Panтелей), **INRIA Sophia-Antipolis** (C. Samson and J.B. Pomet), **Institut de Recherche en Cybernétique de Nantes (IRCyN)** (C. Chevallereau, A. Formal'sky, and Y. Aoustin), **Laboratoire d'Automatique de Grenoble (LAG)** (C. Canudas de Wit, B. Brogliato, and A. Loria), **Laboratoire de Mécanique des Solides de Poitiers (LMS)** (G. Bessonnet, and P. Sardain), **LSIIT-GRAII** (G. Abba and F. Plestan), **Laboratoire de Robotique de Paris (LRP)** (N. M'Sirdi, N. Nadjar-Gauthier, F. B. Ouezdou, and P. Blazevic), and **Laboratoire Vision et Robotique (Bourges)** (P. Poignet, J. Fontaine, and J. Louboutin). This part of the project was funded from 1999–2001.

From November 2001 to November 2004, C. Chevallereau (IRCCyN) and A. Loria (LSS) with support of the CNRS project ROBEA (Robotique et Entités Artificielles) under the subproject *Control of a Walking and Running Biped Robot* directed a French national collaboration on a single walking robot, RABBIT. The following is a list of laboratories and personnel who contributed to this project: **Institut de Recherche en Communications et Cybernétique de Nantes (IRCCyN)** (Y. Aoustin, R. Chellali, C. Chevallereau, C. Moog, M. Gautier, A. Muraro, F. Plestan, S. Miossec, and D. Djoudi), **Laboratoire d'Automatique de Grenoble (LAG)** (G. Buche, C. Canudas de Wit, A. Chemouri, A. Franco, A. Loria, and C. Urrea), **Laboratoire de Génie Industriel et de Production Mécanique (LGIPM)** de l'université de Metz (G. Abba, C. Bop, D. Mihalachi, and A. Siadat), **Laboratoire d'Informatique, de Robotique et de Micro-électronique de Montpellier (LIRMM)** (P. Poignet and F. Lydoire), **Laboratoire de Mécanique des Solides (LMS)** de Poitiers (G. Bessonnet, S. Chesse, P. Sardain, and P. Seguin), **Laboratoire de Robotique de Paris (LRP)** (J.C. Cadiou, N. M'Sirdi, N. Nadjar-Gauthier, and P. Bonnin), **Laboratoire de Vision et Robotique (LVR)** de Bourges (D. Boutat, O. Bruneau, and C. Sabourin), and **Puis Laboratoire des Signaux et Systèmes (A. Loria)**. Funding was provided by the CNRS.

Notes on Chapter 3

The notion of a nonlinear system with impulse effects is taken from [13] and [250]. The first use of this class of models in legged locomotion was

in [98]. Prior to this paper, legged locomotion models were not described in such formal terms. Typically, the mechanical model of the robot was quite precisely specified, the impact model was described in less precise terms, and the desired properties of the gait were the least formally described. Formalizing the models is the first step toward developing a control theory of bipedal walking.

Systems with impulse effects have not been extensively studied. The stability analysis of equilibrium points can be found in [13, 250], using Lyapunov methods. Steady state walking and running gaits clearly correspond, however, to nontrivial periodic orbits, and not to equilibrium solutions of the model. This has motivated the use of Poincaré return maps to determine the existence and stability properties of periodic orbits in models of legged machines; see [74, 85, 86, 93, 120, 143].

The analysis carried out in this book is heavily dependent on the use of a rigid impact model. Alternatives to the rigid impact model are discussed in [25, 36, 176, 208, 236–238, 249].

Notes on Chapter 4

Haddad and coauthors have a very nice set of papers on Poincaré’s method for systems with impulse effects and for a more general class of systems called left-continuous systems [39, 104–107, 167]. For even more general methods of representing models of systems with unilateral constraints and impact behavior, the reader is referred to [12] and [24]. Section 4.2.1 is based on [98], with considerable inspiration coming from [173]. The stability analyses performed on the basis of finite-time convergence and the restricted Poincaré map are based on [98] and [245], while the result using sufficiently rapid exponential convergence was taken from [161]. The results on event-based control are inspired by [100, 243]; see also [95].

Notes on Chapter 5

Early definitions of the zero dynamics of a time-invariant nonlinear control system were proposed by Krener and Isidori in 1980 (using controlled-invariant distributions), by Byrnes and Isidori in 1984, and Marino in 1985 (using inverse systems) as a tool for feedback design and stability analysis. An important refinement of the concept was achieved by Isidori and Moog in 1988 [128], where three equivalent state-space characterizations of the zero dynamics of a linear time-invariant system were evaluated and compared for nonlinear systems. One of these characterizations was the now-familiar definition of the zero dynamics as the restriction dynamics to the largest controlled-invariant manifold contained in the zero set of the output. The role of the zero dynamics in the asymptotic stabilization of equilibrium points is very nicely treated in [32].

In the context of bipedal robots, early papers using the zero dynamics (of the swing phase) are [97, 99, 151, 176]; these papers did not address the invariance under the impact map. A method to obtain invariance under the impact map “in the limit” through high-gain feedback control was analyzed in

[98]. The notion of a hybrid zero dynamics was introduced in [244, 245]; these papers are the sources for most of the material in this chapter. Section 5.2.2 is taken from [242]; Section 5.5.1 draws on [98]; and Section 5.5.2 is taken from [161].

Notes on Chapter 6

The use of Bézier polynomials and parameter optimization for designing simultaneously a periodic orbit and a stabilizing controller was introduced in [245]. Section 6.3.1 is from [242]. Sections 6.4 and 6.5 are based on [246, 247]. [Figure 6.7](#) is from [43]. Section 6.6.1 is from [98]. Section 6.6.2 is from [245]. Section 6.6.3 is from [246, 247]. Further results on using virtual constraints are available in [34].

An interesting aspect of the paper [176] was that it showed how to go from a periodic solution of the robot's hybrid model to a set of holonomic constraints that would render invariant the same periodic orbit. Using this method, it is possible to transform many time-varying control algorithms based on trajectory tracking to time-invariant control algorithms based on virtual constraints. This can be carried out without explicitly computing the zero dynamics, as shown in Section 6.5. A quite different way to go from a periodic solution of a model to a time-invariant controller has been developed in [46] for systems with one degree of underactuation; see also [41, 42]. Consider a periodic solution of an N DOF model as a curve in the configuration space of the robot for a single step. The curve has a beginning and an end determined by the double support condition. Introduce a parameter, s , that is similar to arc-length in that $s = 0$ at the beginning of the curve and $s = 1$ at the end, with intermediate values of s parameterizing the posture of the robot, $q_d(s)$, as it progresses from the beginning of a step to the end. The condition $q(s) - q_d(s)$ defines the virtual constraints to be imposed by the control law. The freedom in how s itself evolves as a function of time, from its initial value of zero to its final value of one, can be used to augment the $N - 1$ joint torques (already available for control) with the acceleration \ddot{s} ; this makes the system now look like it is fully actuated: N degrees of motion freedom and N controls. Consequently, a dynamic state-feedback controller can be found that drives a vector of N outputs, $y = q(s) - q_d(s)$, asymptotically to zero. An advantage of this approach is that a monotonic parameter that replaces time is automatically produced, so the control designer does not have to find one *a priori*. From a theoretical perspective, this idea may be especially useful for applying the method of virtual constraints to mechanisms with a large number of degrees of freedom. A potential disadvantage is that, since the evolution of s must be determined from the model, it is unclear how sensitive the closed-loop system may be to model uncertainty. Further work is still needed to clarify this issue.

Notes on Chapter 7

The main idea of this chapter is to view parameters embedded in a within-stride controller as event-based control signals for a stride-to-stride controller. The underlying discrete-time model for event-based control design comes from

the Poincaré map. This idea was formalized in [243]. The results on switching control are taken from [243]. The results on PI control are from [100, 242, 243]; see also [95].

Notes on Chapter 8

The experiments reported for RABBIT are based solely on [242]. ERNIE took its first steps in December 2006; the reported experiments were performed January 2007 by Tao Yang and Jeff Wensink.

Notes on Chapter 9

Sections 9.8–9.9 are from [163]. The remainder of the chapter is based solely on [51].

Notes on Chapter 10

With the exception of Section 10.2.8, the work reported in the chapter is based on [52, 54].

An analysis of a robot with impulsive foot action is given in [52, 53]. This work extends the results of [Chapters 3, 5, and 6](#) to include the impulsive actuator model of Kuo [144]. An impulsive actuator is attached at each leg end in order to model push off on the toe just before impact of the swing foot; the actuator is assumed to be active only during the double support phase. A feedback design method based on the hybrid zero dynamics is proposed that integrates actuation in the single and double support phases. A complete stability analysis is performed. A more efficient gait is demonstrated with impulsive foot actuation.

An analysis of a robot with a foot rigidly connected at the ankle is given in [52]. This situation provides a simple hybrid system with two dynamic equations and with two algebraic transition maps. Walking is assumed to consist of four phases: a single support phase where the swing leg advances, a toe-roll phase where the robot rotates about the end of the stance foot, a double support phase where the swing foot impacts the ground at the heel of the swing foot, and a heel-roll phase where the robot rotates about the heel of the stance foot.

Notes on Chapter 11

The work presented in this chapter is based on [66–68]. The material has been rewritten to match the framework of the book.

Notes on Appendix B

The overview of notions from Differential Geometry given in [Appendix B.1](#) is deliberately very limited. Many complete treatments of this material are available. One excellent source is [22] and the overview in [127, Appendix A] is also highly recommended. The summary of nonlinear geometric control given in [Appendix B.2](#) is based on [127]; other excellent sources are [150, 168, 204].

The treatment of the method of Poincaré sections given [Appendix B.3](#) is deliberately informal and meant to aid the reader in building up an understanding of the basic concepts. A very nice treatment for ordinary differ-

ential equations (i.e., nonlinear systems without impulse effects) is available in [173, App. D]. Other sources are [102, 138].

The development of planar Lagrangian dynamics is given from a control theorist's point of view in a form that aids in the developments of [Chapters 3, 5, and 9](#). Other user-oriented sources on the use of Lagrange's method for the derivation of equations of motions for rigid-body mechanical systems from a roboticist's perspective are [60, 71, 164, 206, 218]. For a thorough treatment of the method see [[10, 90](#)].

References

- [1] G. Abba and N. Chaillet. Robot dynamic modeling using a power flow approach with application to biped locomotion. *Autonomous Robots*, 6(1):39–52, 1999.
- [2] J. Adolfsson, H. Dankowicz, and A. Nordmark. 3D passive walkers: finding periodic gaits in the presence of discontinuities. *Nonlinear Dynamics*, 24(2):205–29, 2001.
- [3] A. P. Aguiar, J. P. Hespanha, and P. V. Kokotovic. Path-following for nonminimum phase systems removes performance limitations. *IEEE Transactions on Automatic Control*, 50(2):234–9, Feb 2005.
- [4] M. Ahmadi and M. Bühler. Stable control of a simulated one-legged running robot with hip and leg compliance. *IEEE Transactions on Robotics and Automation*, 13(1):96–104, February 1997.
- [5] R. McN. Alexander. Three uses for springs in legged locomotion. *International Journal of Robotics Research*, 9(2):53–61, 1990.
- [6] Aaron D. Ames and Robert D. Gregg. Stably extending two-dimensional bipedal walking to three. In *Proc. of the 2007 American Control Conference, New York, NY*, 2007.
- [7] Y. Aoustin and A Formal'sky. Design of reference trajectory to stabilize desired nominal cyclic gait of a biped. In *Proc. of the First Workshop on Robot Motion and Control, Kiekrz, Poland*, pages 159–64, June 1999.
- [8] Y. Aoustin and A. Formal'sky. Stability of a cyclic biped gait and hastening of the convergence to it. In *Proc. of the 2001 Int. Conf. on Climbing and Walking Robots*, 2001.
- [9] Aristotle. *The Complete Works of Aristotle: the Revised Oxford Translation*, volume 1 of *Bollingen Series LXXI*, chapter Progression of Animals. Princeton University Press, 1984.
- [10] V. Arnold. *Mathematical Methods of Classical Mechanics*. New York NY Berlin Paris : Springer, 1989. translated by : Karen Vogtmann and Alan D. Weinstein.
- [11] F. Asano, M. Yamakita, N. Kamamichi, and Z.W. Luo. A novel gait generation for biped walking robots based on mechanical energy con-

- straint. In *Proc. of the IEEE/RSJ International Conference on Intelligent Robots and Systems*, pages 2637–44, 2002.
- [12] V.I. Babitsky. *Theory of Vibro-Impact Systems and Applications*. Foundations of Engineering Mechanics. Springer, Berlin, 1998.
 - [13] D.D. Bainov and P.S. Simeonov. *Systems with Impulse Effects : Stability, Theory and Applications*. Ellis Horwood Limited, Chichester, 1989.
 - [14] A. Banaszuk and J. Hauser. On control of planar periodic orbits. In *Proc. of the 1999 IEEE International Conference on Decision and Control, Phoenix, AZ*, pages 3830–36, December 1999.
 - [15] S. P. Banks. *Control Systems Engineering*. Prentice Hall, Englewood Cliffs, 1986.
 - [16] C. E. Bauby and A. D. Kuo. Active control of lateral balance in human walking. *Journal of Biomechanics*, 33(11):1433–1440, 2000.
 - [17] M.D. Berkemeier and R.S. Fearing. Sliding and hopping gaits for the underactuated Acrobot. *IEEE Transactions on Robotics and Automation*, 14(4):629–34, August 1998.
 - [18] K. Berns. The Walking Machine Catalogue. <http://www.walking-machines.org/>, 2007.
 - [19] P. Bézier. *Numerical Control: Mathematics and Applications*. John Wiley & Sons, New York, 1972.
 - [20] S. P. Bhat and D. S. Bernstein. Continuous finite-time stabilization of the translational and rotational double integrators. *IEEE Transactions on Automatic Control*, 43(5):678–682, 1998.
 - [21] S. P. Bhat and D. S. Bernstein. Finite-time stability of continuous autonomous systems. *SIAM Journal on Control and Optimization*, 38:751–766, 2000.
 - [22] W. M. Boothby. *An Introduction to Differentiable Manifolds and Riemannian Geometry*. Academic Press, New York, 1975.
 - [23] R.M. Brach. Rigid body collisions. *Journal of Applied Mechanics*, 56:133–8, 1989.
 - [24] B. Brogliato. *Nonsmooth Impact Dynamics: Models, Dynamics and Control*, volume 220 of *Lecture Notes in Control and Information Sciences*. Springer, London, 1996.
 - [25] B. Brogliato, S.-I. Niculescu, and P. Orhant. On the control of finite-dimensional mechanical systems with unilateral constraints. *IEEE Transactions on Automatic Control*, 42(2):200–15, 1997.

- [26] G. Buche. ROBEA Home Page. [http://robot-rabbit.lag.ensieg.inpg.fr/
English/](http://robot-rabbit.lag.ensieg.inpg.fr/English/), 2007.
- [27] M. Bühler, D. E. Koditschek, and P. J. Kindlmann. A family of robot control strategies for intermittent dynamical environments. *IEEE Control Systems Magazine*, 10(2):16–22, February 1990.
- [28] M. Bühler, D. E. Koditschek, and P. J. Kindlmann. Planning and control of a juggling robot. *International Journal of Robotics Research*, 13(2):101–18, 1994.
- [29] F. Bullo and K. M. Lynch. Kinematic controllability for decoupled trajectory planning in underactuated mechanical systems. *IEEE Transactions on Robotics and Automation*, 17(4):402–12, August 2001.
- [30] R. Burridge, A. Rizzi, and D. E. Koditschek. Sequential composition of dynamically dexterous robot behaviors. *International Journal of Robotics Research*, 18(6):534–55, June 1999.
- [31] C. Byrnes and A. Isidori. A frequency domain philosophy for nonlinear systems, with applications to stabilization and adaptive control. In *Proc. of the 1985 IEEE International Conference on Decision and Control, Fort Lauderdale, FL*, pages 1031–7, 1985.
- [32] C. Byrnes and A. Isidori. Asymptotic stabilization of nonlinear minimum phase systems. *IEEE Transactions on Automatic Control*, 37:1122–37, 1991.
- [33] G. Cabodevilla and G. Abba. Quasi optimal gait for a biped robot using genetic algorithm. In *Proc. of the IEEE International Conference on Systems, Man and Cybernetics, Computational Cybernetics and Simulations, Orlando, FL*, pages 3960–5, October 1997.
- [34] C. Canudas. On the concept of virtual constraints as a tool for walking robot control and balancing. *Annual Reviews in Control*, 28:157–66, 2004.
- [35] C. Canudas, B. Espiau, and C. Urrea. Orbital stabilization of underactuated mechanical systems. In *15th World Congress on Automatic Control, Barcelona, Spain*, July 2002.
- [36] C. Canudas, L. Roussel, and A. Goswami. Periodic stabilization of a 1-DOF hopping robot on nonlinear compliant surface. In *Proc. of IFAC Symposium on Robot Control, Nantes, France*, pages 405–10, September 1997.
- [37] R.E. Carlton and S.J. Bartholet. The evolution of the application of mobile robotics to nuclear facility operations and maintenance. In *Proc. of the 1987 IEEE International Conference on Robotics and Automation, Raleigh, NC*, pages 720–6, 1987.

- [38] P.H. Channon, S. Hopkins, and Pham. Optimal walking motions for a biped walking robot. *Robotica*, 10(2):165–72, 1990.
- [39] V. Chellaboina, S. P. Bhat, and W. M. Haddad. An invariance principle for nonlinear hybrid and impulsive dynamical systems. *Nonlinear Analysis*, 53:527–50, 2003.
- [40] C. T. Chen. *Linear System Theory and Design*. Oxford, New York, 1984.
- [41] C. Chevallereau. Parameterized control for an underactuated biped robot. In *15th World Congress on Automatic Control, Barcelona, Spain*, July 2002.
- [42] C. Chevallereau. Time-scaling control for an underactuated biped robot. *IEEE Transactions on Robotics and Automation*, 19(2):362–368, 2003.
- [43] C. Chevallereau, G. Abba, Y. Aoustin, F. Plestan, E. R. Westervelt, C. Canudas, and J. W. Grizzle. RABBIT: a testbed for advanced control theory. *IEEE Control Systems Magazine*, 23(5):57–79, October 2003.
- [44] C. Chevallereau and Y. Aoustin. Optimal reference trajectories for walking and running of a biped robot. *Robotica*, 19(5):557–69, September 2001.
- [45] C. Chevallereau, Y. Aoustin, and Formal'sky. Optimal walking trajectories for a biped. In *Proc. of the First Workshop on Robot Motion and Control, Kiekrz, Poland*, pages 171–6, June 1999.
- [46] C. Chevallereau, A. Formal'sky, and D. Djoudi. Tracking of a joint path for the walking of an underactuated biped. *Robotica*, 22:15–28, 2004.
- [47] C. Chevallereau, A. Formal'sky, and B. Perrin. Low energy cost reference trajectories for a biped robot. In *Proc. of the 1998 IEEE International Conference on Robotics and Automation, Leuven, Belgium*, pages 1398–404, 1998.
- [48] C. Chevallereau, J. W. Grizzle, and C. H. Moog. Nonlinear control of mechanical systems with one degree of underactuation. In *Proc. of the 2004 IEEE International Conference on Robotics and Automation, New Orleans, LA*, volume 3, pages 2222–8, 2004.
- [49] C. Chevallereau and P. Sardain. Design and actuation optimization of a 4 axes biped robot for walking and running. In *Proc. of the 2000 IEEE International Conference on Robotics and Automation, San Francisco, CA*, pages 3365–70, 2000.
- [50] C. Chevallereau, E. R. Westervelt, and J. W. Grizzle. Asymptotic stabilization of a five-link, four-actuator, planar bipedal runner. In *Proc. of the 2004 IEEE International Conference on Decision and Control, Nassau, Bahamas*, pages 303–10, 2004.

- [51] C. Chevallereau, E. R. Westervelt, and J. W. Grizzle. Asymptotically stable running for a five-link, four-actuator, planar bipedal robot. *International Journal of Robotics Research*, 24:431–464, 2005.
- [52] J. H. Choi. *Model-based Control and Analysis of Anthropomorphic Walking*. PhD thesis, University of Michigan, 2005.
- [53] J. H. Choi and J. W. Grizzle. Feedback control of an underactuated planar bipedal robot with impulsive foot action. *Robotica*, 23:567–80, September 2005.
- [54] Jun Ho Choi and J. W. Grizzle. Planar bipedal walking with foot rotation. In *Proc. of the 2005 American Control Conference, Portland, OR*, pages 4909–16, 2005.
- [55] C.K. Chow and D.H. Jacobson. Studies of human locomotion via optimal programming. *Mathematical Biosciences*, 10:239–306, 1971.
- [56] M. Coleman. *A Stability Study of a Three-Dimensional Passive-Dynamic Model of Human Gait*. PhD thesis, Cornell, 1998.
- [57] M. J. Coleman, A. Chatterjee, and A. Ruina. Motions of a rimless spoked wheel: a simple 3D system with impacts. In *Dynamics and Stability of Systems*, volume 12, pages 139–60, 1997.
- [58] S. H. Collins, A. Ruina, R. Tedrake, and M. Wisse. Efficient bipedal robots based on passive-dynamic walkers. *Science*, 307:1082–85, 2005.
- [59] S. H. Collins, M. Wisse, and A. Ruina. A three-dimensional passive-dynamic walking robot with two legs and knees. *International Journal of Robotics Research*, 20(7):607–15, July 2001.
- [60] J. J. Craig. *Introduction to Robotics: Mechanics and Control*. Pearson/Prentice-Hall, Upper Saddle River, N.J., 3rd ed edition, 2005.
- [61] D. B. Dacic, M. V. Subbotin, and P. V. Kokotovic. Path-following for a class of nonlinear systems with unstable zero dynamics. In *Proc. of the 2004 IEEE International Conference on Decision and Control, Nassau, Bahamas*, volume 5, pages 4915–20, 2004.
- [62] D. B. Dacic, M. V. Subbotin, and P. V. Kokotovic. Path-following approach to control effort reduction of tracking feedback laws. In *Proc. of the 2005 IEEE International Conference on Decision and Control / European Control Conference, Seville, Spain*, pages 7284–9, December 2005.
- [63] C. De Boor. *A Practical Guide to Splines*. Springer-Verlag, 1978.
- [64] J. B. Dingwell and J. P. Cusumano. Nonlinear time series analysis of normal and pathological human walking. *Chaos*, 10(4):848–863, 2000.

- [65] S. Diop, J. W. Grizzle, P. E. Moraal, and A. Stefanopoulou. Interpolation and numerical differentiation for observer design. In *Proc. of the 1994 American Control Conference, Baltimore, MD*, pages 1329–33, June 1994.
- [66] D. Djoudi. *Contribution à la Commande de Robots Marcheurs*. PhD thesis, Ecole Centrale de Nantes, Université de Nantes - France, January 2007.
- [67] D. Djoudi and C. Chevallereau. *Fast motions in Biomechanics and Robotics*, chapter Stability analysis of bipedal walking with control or monitoring of the center of pressure, pages 95–120. Lecture Notes in Control and Information Sciences. Springer, Heidelberg, Germany, 2006.
- [68] D. Djoudi and C. Chevallereau. Feet can improve the stability property of a control law for a walking robot. In *Proc. of the 2006 IEEE International Conference on Robotics and Automation, Orlando, FL*, pages 1206–1212, 2006.
- [69] D. Djoudi, C. Chevallereau, and Y. Aoustin. Optimal reference motions for walking of a biped robot. In *Proc. of the 2005 IEEE International Conference on Robotics and Automation, Barcelona, Spain*, pages 2002–7, Barcelona, Spain, April 2005.
- [70] Masahiro Doi, Y. Hasegawa, and T. Fukuda. Realization of 3-dimensional dynamic walking based on the assumption of point-contact. In *Proc. of the 2005 IEEE International Conference on Robotics and Automation, Barcelona, Spain*, pages 4120–4125, 2005.
- [71] E. Dombre and W. Khalil. *Modeling, Identification and Control of Robots*. Hermès Sciences, Europe. Paris, 2002.
- [72] J. M. Donelan, R. Kram, and A. D. Kuo. Mechanical work for step-to-step transitions is a major determinant of the metabolic cost of human walking. *Journal of Experimental Biology*, 205:3717–27, 2002.
- [73] B. Espiau. BIP: a joint project for the development of an anthropomorphic biped robot. In *Proc. of the International Conference on Advanced Robotics, Monterey, CA*, pages 267–72, July 1997.
- [74] B. Espiau and A. Goswami. Compass gait revisited. In *Proc. of the IFAC Symposium on Robot Control, Capri, Italy*, pages 839–846, September 1994.
- [75] A. Formal'sky. *Locomotion of Anthropomorphic Mechanisms*. Nauka. in Russian, Moscow, 1982.
- [76] C. Francois and C. Samson. A new approach to the control of the planar one-legged hopper. *International Journal of Robotics Research*, 17(11):1150–66, 1998.

- [77] Y. Fujimoto. Trajectory generation of biped running robot with minimum energy consumption. In *Proc. of the 2004 IEEE International Conference on Robotics and Automation, New Orleans, LA*, volume 4, pages 3803–8, 2004.
- [78] Y. Fujimoto and A. Kawamura. Simulation of an autonomous biped walking robot including environmental force interaction. *IEEE Robotics and Automation Magazine*, pages 33–42, June 1998.
- [79] Y. Fujimoto, S. Obata, and A. Kawamura. Robust biped walking with active interaction control between foot and ground. In *Proc. of the 1998 IEEE International Conference on Robotics and Automation, Leuven, Belgium*, pages 2030–5, 1998.
- [80] T. Fukuda, M. Doi, Y. Hasegawa, and H. Kajima. *Fast Motions Symposium on Biomechanics and Robotics*, chapter Multi-locomotion control of biped locomotion and brachiation robot, pages 121–145. Lecture Notes in Control and Information Sciences. Springer-Verlag, Heidelberg, Germany, 2006.
- [81] R. Full and D. E. Koditschek. Templates and anchors: Neuromechanical hypotheses of legged locomotion on land. *Journal of Experimental Biology*, 202:3325–32, December 1999.
- [82] J. Furusho and M. Masubuchi. Control of a dynamical biped locomotion system for steady walking. *Journal of Dynamic Systems, Measurement and Control*, 108:111–8, 1986.
- [83] J. Furusho and A. Sano. Sensor-based control of a nine-link biped. *International Journal of Robotics Research*, 9(2):83–98, 1990.
- [84] M. Garcia. *Stability, Scaling, and Chaos in Passive-Dynamic Gait Models*. PhD thesis, Cornell University, 1999.
- [85] M. Garcia, A. Chatterjee, and A. Ruina. Efficiency, speed, and scaling of two-dimensional passive-dynamic walking. *Dynamics and Stability of Systems*, 15(2):75–99, June 2000.
- [86] M. Garcia, A. Chatterjee, A. Ruina, and M. Coleman. The simplest walking model: Stability, complexity, and scaling. *ASME Journal of Biomechanical Engineering*, 120(2):281–8, April 1998.
- [87] M. Gienger, K. Löffler, and F. Pfeiffer. A biped robot that jogs. In *Proc. of the 2000 IEEE International Conference on Robotics and Automation, San Francisco, CA*, pages 3334–9, 2000.
- [88] J. M. Godhavn, A. Balluchi, L. Crawford, and S. Sastry. Path planning for nonholonomic systems with drift. In *Proc. of the 1997 American Control Conference, Albuquerque, NM*, pages 532–6, 1997.

- [89] W. Goldsmith. *Impact: The Theory and Physical Behaviour of Colliding Solids*. Arnold, London, 1960.
- [90] H. Goldstein, C. Poole, and J. Safko. *Classical Mechanics*. Addison-Wesley, San Francisco, third edition, 2002.
- [91] J. M. Goncalves, A. Megretski, and M. A. Dahleh. Global stability of relay feedback systems. *IEEE Transactions on Automatic Control*, 46(4):550–62, April 2001.
- [92] A. Goswami. Postural stability of biped robots and the foot-rotation indicator (FRI) point. *International Journal of Robotics Research*, 18(6):523–33, June 1999.
- [93] A. Goswami, B. Espiau, and A. Keramane. Limit cycles and their stability in a passive bipedal gait. In *Proc. of the 1996 IEEE International Conference on Robotics and Automation, Minneapolis, MN*, pages 246–51, 1996.
- [94] A. A. Grishin, A. M. Formal'sky, A. V. Lensky, and S. V. Zhitomirsky. Dynamical walking of a vehicle with two telescopic legs controlled by two drives. *International Journal of Robotics Research*, 13(2):137–47, 1994.
- [95] J. W. Grizzle. Remarks on event-based stabilization of periodic orbits in systems with impulse effects. In *Second International Symposium on Communications, Control and Signal Processing*, 2006.
- [96] J. W. Grizzle. Jessy Grizzle's publications. <http://www.eecs.umich.edu/~grizzle/papers/robotics.html>, 2007.
- [97] J. W. Grizzle, G. Abba, and F. Plestan. Proving asymptotic stability of a walking cycle for a five DOF biped robot model. In *Proc. of the 1999 Int. Conf. on Climbing and Walking Robots*, pages 69–81, September 1999.
- [98] J. W. Grizzle, G. Abba, and F. Plestan. Asymptotically stable walking for biped robots: Analysis via systems with impulse effects. *IEEE Transactions on Automatic Control*, 46:51–64, January 2001.
- [99] J. W. Grizzle, F. Plestan, and G. Abba. Poincaré's method for systems with impulse effects: Application to mechanical biped locomotion. In *Proc. of the 1999 IEEE International Conference on Decision and Control, Phoenix, AZ*, 1999.
- [100] J. W. Grizzle, E. R. Westervelt, and C. Canudas. Event-based PI control of an underactuated biped walker. In *Proc. of the 2003 IEEE International Conference on Decision and Control, Maui, HI*, pages 3091–6, 2003.

- [101] J. Guckenheimer. Sensitive dependence to initial conditions for one dimensional maps. *Communications in Mathematical Physics*, 70:133–60, 1979.
- [102] J. Guckenheimer and P. Holmes. *Nonlinear Oscillations, Dynamical Systems, and Bifurcations of Vector Fields*, volume 42 of *Applied Mathematical Sciences*. Springer-Verlag, New York, 1996.
- [103] J. Guckenheimer and S. Johnson. Planar hybrid systems. In *Hybrid Systems II, Lecture Notes in Computer Science*, pages 203–25. Springer-Verlag, 1995.
- [104] W. Haddad and V. Chellaboina. Dissipativity theory and stability of feedback interconnections for hybrid dynamical systems. In *Mathematical Problems in Engineering*, volume 7, pages 299–335. 2001.
- [105] W. M. Haddad, V. Chellaboina, and N. Kablar. Non-linear impulsive dynamical systems. Part I: Stability and dissipativity. *International Journal of Control*, 74(17):1631–58, 2001.
- [106] W. M. Haddad, V. Chellaboina, and N. Kablar. Non-linear impulsive dynamical systems. Part II: Stability of feedback interconnections and optimality. *International Journal of Control*, 74(17):1659–77, 2001.
- [107] W. M. Haddad, S. G. Nersesova, and V. Chellaboina. Energy-based control for hybrid port-controlled hamiltonian systems. *Automatica*, 39:1425–35, 2003.
- [108] V. T. Haimo. Finite time controllers. *SIAM J. Contr. Optim.*, 24(4):760–70, 1986.
- [109] M. W. Hardt. *Multibody Dynamical Algorithms, Numerical Optimal Control, with Detailed Studies in the Control of Jet Engine Compressors and Biped Walking*. PhD thesis, University of California, San Diego, 1999.
- [110] P. Hartman. *Ordinary Differential Equations*. Birkhauser, Boston, 2nd edition, 1982.
- [111] Y. Hasegawa, T. Arakawa, and T. Fukuda. Trajectory generation for biped locomotion. *Mechatronics*, 10(1–2):67–89, March 2000.
- [112] S. Hashimoto, S. Narita, H. Kasahara, K. Shirai, T. Kobayashi, A. Takanishi, S. Sugano, and et al. Humanoid robots in Waseda University—Hadaly-2 and WABIAN. *Advanced Robotics*, 12(1):25–38, 2002.
- [113] H. Hatze. The complete optimization of a human motion. *Mathematical Biosciences*, 28:99–135, 1976.
- [114] K. Hirai, M. Hirose, Y. Haikawa, and T. Takenaka. The development of Honda humanoid robot. In *Proc. of the 1998 IEEE International*

Conference on Robotics and Automation, Leuven, Belgium, pages 1321–26, 1998.

- [115] I. A. Hiskens. Stability of hybrid limit cycles: application to the compass gait biped robot. In *Proc. of the 40th IEEE Conf. Dec. and Control, Orlando, FL*, pages 774–9, December 2001.
- [116] J.K. Hodgins and M.H. Raibert. Adjusting step length for rough terrain locomotion. *IEEE Transactions on Robotics and Automation*, 7(3):289–98, June 1991.
- [117] Honda Corporation. ASIMO’s Homepage. <http://world.honda.com/ASIMO/>, 2007.
- [118] G.W. Howell and J. Baillieul. Simple controllable walking mechanisms which exhibit bifurcations. In *Proc. of the 1998 IEEE International Conference on Decision and Control, Tampa, FL*, pages 3027–32, December 1998.
- [119] Q. Huang, S. Kajita, N. Koyachi, K. Kaneko, K. Yokoi, H. Arai, Komoriya K., and K. Tanie. A high stability, smooth walking pattern for a biped robot. In *Proc. of the 1999 IEEE International Conference on Robotics and Automation, Detroit, MI*, pages 65–71, 1999.
- [120] Y. Hürmüzlü. Dynamics of bipedal gait—Part 1: objective functions and the contact event of a planar five-link biped. *Journal of Applied Mechanics*, 60(2):331–6, 1993.
- [121] Y. Hürmüzlü. Dynamics of bipedal gait—Part 2: stability analysis of a planar five-link biped. *Journal of Applied Mechanics*, 60(2):337–43, 1993.
- [122] Y. Hürmüzlü, C. Basdogan, and J.J. Carollo. Presenting joint kinematics of human locomotion using phase plane portraits and Poincaré maps. 27(12):1495–9, 1994.
- [123] Y. Hürmüzlü, F. Génot, and B. Brogliato. Modeling, stability and control of biped robots - a general framework. *Automatica*, 40(10):1647–1664, 2004.
- [124] Y. Hürmüzlü and D. B. Marghitu. Rigid body collisions of planar kinematic chains with multiple contact points. *International Journal of Robotics Research*, 13(1):82–92, 1994.
- [125] Y. Hürmüzlü and D. Moskowitz. The role of impact in the stability of bipedal locomotion. *Dynamics and Stability of Systems*, 1(3):217–34, 1986.
- [126] S.-H. Hyon and T. Emura. Running control of a planar biped robot based on energy-preserving strategy. In *Proc. of the 2004 IEEE International Conference on Robotics and Automation, New Orleans, LA*, volume 4, pages 3791–6, 2004.

- [127] A. Isidori. *Nonlinear Control Systems*. Springer-Verlag, Berlin, third edition, 1995.
- [128] A. Isidori and C. H. Moog. On the nonlinear equivalent of the notion of transmission zeros. In C. Byrnes and A. Kurzhanski, editors, *Proc. of the IIASA Conference: Modeling and Adaptive Control*, pages 146–57, Berlin, 1988. Springer-Verlag.
- [129] S. Kajita, F. Kanehiro, K. Kaneko, K. Fujiwara, K. Yokoi, and H. Hirukawa. A realtime pattern generator for biped walking. In *Proc. of the 2002 IEEE International Conference on Robotics and Automation, Washington, D.C.*, pages 31–7, 2002.
- [130] S. Kajita, F. Kanehiro, K. Kaneko, K. Yokoi, and H. Hirukawa. The 3D linear inverted pendulum mode: a simple modeling for a biped walking pattern generation. In *Proc. of the 2001 IEEE/RSJ International Conference on Intelligent Robots and Systems, Maui, HI*, pages 239–46, November 2001.
- [131] S. Kajita and T. Nagasaki. Running pattern generation for a humanoid robot. In *Proc. of the 2002 IEEE International Conference on Robotics and Automation, Washington, D.C.*, pages 2755–61, May 2002.
- [132] S. Kajita, T. Nagasaki, K. Kaneko, K. Yokoi, and K. Tanie. A hop towards running humanoid biped. In *Proc. of the 2004 IEEE International Conference on Robotics and Automation, New Orleans, LA*, pages 629–35, 2004.
- [133] S. Kajita and K. Tani. Experimental study of biped dynamic walking. *IEEE Control Systems Magazine*, 16(1):13–9, February 1996.
- [134] S. Kajita, T. Yamaura, and A. Kobayashi. Dynamic walking control of biped robot along a potential energy conserving orbit. *IEEE Transactions on Robotics and Automation*, 8(4):431–37, August 1992.
- [135] K. Kaneko, F. Kanehiro, S. Kajita, K. Yokoyama, K. Akachi, T. Kawasaki, S. Ota, and T. Isozumi. Design of prototype humanoid robotics platform for HRP. In *Proc. of the 2002 IEEE/RSJ International Conference on Intelligent Robots and Systems, Lausanne, Switzerland*, pages 2431–6, 2002.
- [136] I. Kato and H. Tsuiki. The hydraulically powered biped walking machine with a high carrying capacity. In *Proc. of the Fourth International Symposium on External Control of Human Extremities, Dubrovnik, Yugoslavia*, pages 410–21, September 1972.
- [137] R. Katoh and M. Mori. Control method of biped locomotion giving asymptotic stability of trajectory. *Automatica*, 20(4):405–14, 1984.
- [138] H. K. Khalil. *Nonlinear Systems - 3rd Edition*. Upper Saddle River, NJ, 2002.

- [139] D. E. Koditschek and M. Bühler. Analysis of a simplified hopping robot. *International Journal of Robotics Research*, 10(6):587–605, 1991.
- [140] P. V. Kokotovic, H. K. Khalil, and J. O'Reilly. *Singular Perturbation Methods in Control: Analysis and Design*. Academic Press, London, 1986.
- [141] I. Kolmanovsky, N.H. McClamroch, and V.T. Coppola. New results on control of multibody systems which conserve angular momentum. *Journal of Dynamical and Control Systems*, 1(4):447–62, 1995.
- [142] V.R. Kumar and K.J. Waldron. A review of research on walking vehicles. In O. Khatib, J.J. Craig, and T. Lozano-Pérez, editors, *The robotics review 1*, pages 243–66. MIT Press, Cambridge, MA, 1989.
- [143] A. D. Kuo. Stabilization of lateral motion in passive dynamic walking. *International Journal of Robotics Research*, 18(9):917–30, 1999.
- [144] A. D. Kuo. Energetics of actively powered locomotion using the simplest walking model. *Journal of Biomechanical Engineering*, 124(1):113–20, 2002.
- [145] H. Lim, Y. Yamamoto, and A. Takanishi. Control to realize human-like walking of a biped humanoid robot. In *Proc. of the IEEE International Conference on Systems, Man and Cybernetics, Computational Cybernetics and Simulations, Nashville, TN*, pages 3271–76, June 2000.
- [146] R.A. Liston and Mosher R.S. A versatile walking truck. In *Proceedings of the Transportation Engineering Conference*. Institution of Civil Engineers, London, 1968.
- [147] K. Löffler, M. Gienger, and F. Pfeiffer. Sensors and control concept of walking “Johnnie.” *International Journal of Robotics Research*, 22(3–4):229–39, 2003.
- [148] K. Löffler, M. Gienger, F. Pfeiffer, and H. Ulbrich. Sensors and control concept of a biped robot. *IEEE Transactions on Industrial Electronics*, 51(5):972–80, 2004.
- [149] D. W. Marhefka and D. Orin. Simulation of contact using a nonlinear damping model. In *Proc. of the 1996 IEEE International Conference on Robotics and Automation, Minneapolis, MN*, pages 1662–8, 1996.
- [150] T. Marino and P. Tomei. *Nonlinear Control Design*. Prentice Hall, London, 1995.
- [151] T. G. McGee and M. W. Spong. Trajectory planning and control of a novel walking biped. In *IEEE International Conference on Control Applications, Mexico City, Mexico*, pages 1099–104, September 2001.

- [152] T. McGeer. Stability and control of two-dimensional biped walking. Technical Report 1, Center for Systems Science, Simon Fraser University, Burnaby, B.C., Canada V5A 1S6, 1988.
- [153] T. McGeer. Passive dynamic walking. *International Journal of Robotics Research*, 9(2):62–82, April 1990.
- [154] T. McGeer. Dynamics and control of bipedal locomotion. *Journal of Theoretical Biology*, 166(3):277–314, August 1993.
- [155] M. Meinders, A. Gitter, and J. M. Czerniecki. The role of ankle plantar flexor muscle work during walking. *Scandinavian Journal of Rehabilitation Medicine*, 30:39–46, 1998.
- [156] K. Mitobe, N. Mori, K. Aida, and Y. Nasu. Nonlinear feedback control of a biped walking robot. In *Proc. of the 1995 IEEE International Conference on Robotics and Automation, Nagoya, Japan*, pages 2865–70, 1995.
- [157] H. Miura and I. Shimoyama. Dynamic walk of a biped. *International Journal of Robotics Research*, 3(2):60–74, 1984.
- [158] M. Miyazaki, M. Sampei, and M. Koga. Control of a motion of an Acrobot approaching a horizontal bar. *Advanced Robotics*, 15(4):467–80, 2001.
- [159] K.D. Mombaur, H.G. Bock, J.P. Schloder, and R.W. Longman. Self-stabilizing somersaults. *IEEE Transactions on Robotics*, 21(6):1148–57, 2005.
- [160] M. Morisawa, Y. Fujimoto, T. Murakami, and K. Ohnishi. A walking pattern generation for biped robot with parallel mechanism by considering contact force. In *Proc. of the IEEE Annual Conference on Industrial Electronics Society, Denver, CO*, pages 2184–9, 2001.
- [161] B. Morris and J. W. Grizzle. A restricted Poincaré map for determining exponentially stable periodic orbits in systems with impulse effects: Application to bipedal robots. In *Proc. of the 2005 IEEE International Conference on Decision and Control / European Control Conference, Seville, Spain*, pages 4199–206, 2005.
- [162] B. Morris and J.W. Grizzle. Hybrid invariance in bipedal robots with series compliant actuators. pages 4793–800, December 2006.
- [163] B. Morris, E. R. Westervelt, C. Chevallereau, G. Buche, and J. W. Grizzle. *Fast Motions Symposium on Biomechanics and Robotics*, chapter Achieving Bipedal Running with RABBIT: Six Steps toward Infinity, pages 277–97. Lecture Notes in Control and Information Sciences. Springer-Verlag, Heidelberg, Germany, 2006.

- [164] R. M. Murray, Z. Li, and S. Sastry. *A Mathematical Introduction to Robotic Manipulation*. CRC Press, 1994.
- [165] J. Nakanishi, T. Fukuda, and D. E. Koditschek. A brachiating robot controller. *IEEE Transactions on Robotics and Automation*, 16(2):109–23, April 2000.
- [166] R. R. Neptune, S. A. Kautz, and F. E. Zajac. Contributions of the individual ankle plantar flexors to support, forward progression and swing initiation during walking. *Journal of Biomechanics*, 34(11):1387–98, 2001.
- [167] S. G. Nersesov, V. Chellaboina, and W. M. Haddad. A generalization of Poincaré’s theorem to hybrid and impulsive dynamical systems. *International Journal of Hybrid Systems*, 2:39–55, 2002.
- [168] H. Nijmeijer and A. J. van der Schaft. *Nonlinear Dynamical Control Systems*. Springer-Verlag, Berlin, 1989.
- [169] K. Ono, R. Takahashi, and T. Shimada. Self-excited walking of a biped mechanism. *International Journal of Robotics Research*, 20(12):953–66, December 2001.
- [170] K. Ono, K. Yamamoto, and A. Imaud. Control of giant swing motion of a two-link horizontal bar gymnastic robot. *Advanced Robotics*, 15(4):449–65, 2001.
- [171] J. H. Park. Impedance control for biped robot locomotion. *IEEE Transactions on Robotics and Automation*, 17(6):870–82, December 2001.
- [172] J. H. Park and K. D. Kim. Biped robot walking using gravity-compensated inverted pendulum mode and computed torque control. In *Proc. of the 1998 IEEE International Conference on Robotics and Automation, Leuven, Belgium*, pages 3528–33, 1998.
- [173] T. S. Parker and L. O. Chua. *Practical Numerical Algorithms for Chaotic Systems*. Springer-Verlag, New York, 1989.
- [174] F. Pfeiffer and C. Glocker. *Multi-Body Dynamics with Unilateral Constraints*. Wiley Series in Nonlinear Science. John Wiley & Sons, New York, 1996.
- [175] F. Pfeiffer, K. Löffler, and M. Gienger. The concept of Jogging JOHN-NIE. In *Proc. of the 2002 IEEE International Conference on Robotics and Automation, Washington, D.C.*, pages 3129–35, 2002.
- [176] F. Plestan, J. W. Grizzle, E. R. Westervelt, and G. Abba. Stable walking of a 7-DOF biped robot. *IEEE Transactions on Robotics and Automation*, 19(4):653–68, August 2003.

- [177] M. B. Popovic, A. Goswami, and H. Herr. Ground reference points in legged locomotion: definitions, biological trajectories and control implications. *International Journal of Robotics Research*, 24(12):1013–32, 2005.
- [178] G. A. Pratt. MIT Leg Lab. <http://www.ai.mit.edu/projects/leglab>, 2007.
- [179] G. A. Pratt and M. M. Williamson. Series elastic actuators. In *Proc. of the 1995 IEEE/RSJ International Conference on Intelligent Robots and Systems, Pittsburgh, PA*, pages 399–406, August 1995.
- [180] J. E. Pratt. *Exploiting Inherent Robustness and Natural Dynamics in the Control of Bipedal Walking Robots*. PhD thesis, Massachusetts Institute of Technology, June 2000.
- [181] J. E. Pratt, M. C. Chee, A. Torres, P. Dilworth, and G. A. Pratt. Virtual model control: an intuitive approach for bipedal locomotion. *International Journal of Robotics Research*, 20(2):129–43, February 2001.
- [182] J. E. Pratt and G. A. Pratt. Intuitive control of a planar bipedal walking robot. In *Proc. of the 1998 IEEE International Conference on Robotics and Automation, Leuven, Belgium*, pages 2014–21, 1998.
- [183] M. H. Raibert. Hopping in legged systems—modeling and simulation for the two-dimensional one-legged case. *IEEE Transactions on Systems, Man and Cybernetics*, 14(3):451–63, June 1984.
- [184] M. H. Raibert. Legged robots. *Communications of the ACM*, 29(6):499–514, 1986.
- [185] M. H. Raibert. *Legged Robots that Balance*. MIT Press, Cambridge, MA, 1986.
- [186] M. H. Raibert, S. Tzafestas, and C. Tzafestas. Comparative simulation study of three control techniques applied to a biped robot. In *Proc. of the IEEE International Conference on Systems, Man and Cybernetics Systems Engineering in the Service of Humans, Le Touquet, France*, pages 494–502, October 1993.
- [187] M. Reyhanoglu, A. van der Schaft, N.H. McClamroch, and I. Kolmanovsky. Dynamics and control of a class of underactuated mechanical systems. *IEEE Transactions on Automatic Control*, 44(9):1663–71, 1999.
- [188] A. Rizzi and D. E. Koditschek. An active visual estimator for dexterous manipulation. *IEEE Transactions on Robotics and Automation*, 12(5):697–713, October 1996.
- [189] D.F. Rogers and J.A. Adams. *Mathematical Elements for Computer Graphics*. McGraw-Hill, New York, second edition, 1990.

- [190] M. E. Rosheim. *Robot Evolution: The Development of Anthrobotics*. Wiley, New York, 1994.
- [191] M. Rostami and G. Bessonnet. Sagittal gait of a biped robot during the single support phase. part 1: passive motion. *Robotica*, 19:163–176, 2001.
- [192] M. Rostami and G. Bessonnet. Sagittal gait of a biped robot during the single support phase. part 2: optimal motion. *Robotica*, 19:241–53, 2001.
- [193] A. V. Roup, D. S. Bernstein, S. G. Nersesov, W. M. Haddad, and V. Chellaboina. Limit cycle analysis of the verge and foliot clock escapement using impulsive differential equations and Poincaré maps. *International Journal of Control*, 76(17):1685–98, 2003.
- [194] L. Roussel. *Génération de Trajectoires de Marche Optimales Pour un Robot Bipède*. PhD thesis, Institut National Polytechnique, Grenoble, France, November 1998.
- [195] L. Roussel, C. Canudas, and A. Goswami. Generation of energy optimal complete gait cycles for biped robots. In *Proc. of the 1998 IEEE International Conference on Robotics and Automation, Leuven, Belgium*, pages 2036–41, 1998.
- [196] M. Russell. ODEX I: the first functionoid. *Robotics Age*, 5(5):12–8, 1983.
- [197] L.A. Rygg. Mechanical horse. *US Patent*, February 14, 1893.
- [198] C. Sabourin, O. Bruneau, and G. Buche. Control strategy for the robust dynamic walk of a biped robot. *International Journal of Robotics Research*, 25(9):843–60, September 2006.
- [199] M. Sampei, H. Kiyota, and M. Ishikawa. Control strategies for mechanical systems with various constraints-control of non-holonomic systems. In *Proc. of the IEEE International Conference on Systems, Man and Cybernetics, Tokyo, Japan*, pages 158–65, October 1999.
- [200] A. Sano and J. Furusho. Realization of natural dynamic walking using the angular momentum information. In *Proc. of the 1990 IEEE International Conference on Robotics and Automation, Cincinnati, OH*, pages 1476–81, 1990.
- [201] U. Saranli. *Dynamic Locomotion with a Hexapod Robot*. PhD thesis, University of Michigan, 2002.
- [202] U. Saranli, W. Schwind, and D. E. Koditschek. Toward the control of a multi-jointed, monoped runner. In *Proc. of the 1998 IEEE International Conference on Robotics and Automation, Leuven, Belgium*, pages 2676–82, 1998.

- [203] P. Sardain and G. Bessonnet. Gait analysis of a human walker wearing robot feet as shoes. In *Proc. of the 2001 IEEE International Conference on Robotics and Automation, Seoul, Korea*, pages 2285–92, May 2001.
- [204] S. Sastry. *Nonlinear Systems: Analysis, Stability, and Control*. Springer, 1999.
- [205] W. J. Schwind. *Spring Loaded Inverted Pendulum Running: A Plant Model*. PhD thesis, University of Michigan, 1998.
- [206] L. Sciavicco and B. Siciliano. *Modelling and Control of Robot Manipulators*. Springer, London, 2000.
- [207] C.-L. Shih. Ascending and descending stairs for a biped robot. *IEEE Transactions on Systems, Man and Cybernetics*, 29(3):255–68, 1999.
- [208] C.-L. Shih and W. A. Gruver. Control of a biped robot in the double-support phase. *IEEE Transactions on Systems, Man and Cybernetics*, 22(4):729–35, 1992.
- [209] D. Singer. Stable orbits and bifurcations of maps of the interval. *SIAM Journal of Applied Mathematics*, 35(2):260–7, 1978.
- [210] A.C. Smith and M.D. Berkemeier. The motion of a finite-width wheel in 3D. In *Proc. of the 1998 IEEE International Conference on Robotics and Automation, Leuven, Belgium*, pages 2345–50, 1998.
- [211] G. Song and M. Zefran. Stabilization of hybrid periodic orbits with application to bipedal walking. In *Proc. of the 2006 American Control Conference, Minneapolis, MN*, pages 2504–9, 2006.
- [212] G. Song and M. Zefran. Underactuated dynamic three-dimensional bipedal walking. In *Proc. of the 2006 IEEE International Conference on Robotics and Automation, Orlando, FL*, pages 854–9, 2006.
- [213] S. Song and K.J. Waldron. *Machines that Walk: The Adaptive Suspension Vehicle*. MIT Press Series in Artificial Intelligence. MIT Press, Cambridge, MA, 1989.
- [214] Sony Corporation. QRIO’s Homepage. <http://www.sony.net/SonyInfo/QRIO/>, 2007.
- [215] M. W. Spong. The swing up control problem for the Acrobot. *IEEE Control Systems Magazine*, 15(1):49–55, February 1995.
- [216] M. W. Spong. Passivity based control of the compass gait biped. In *Proc. of IFAC World Congress, Beijing, China*, July 1999.
- [217] M. W. Spong and F. Bullo. Controlled symmetries and passive walking. *Automatic Control, IEEE Transactions on*, 50(7):1025–31, 2005.
- [218] M. W. Spong, S. Hutchinson, and M Vidyasagar. *Robot Modeling and Control*. John Wiley & Sons, 2005.

- [219] M. W. Spong and M. Vidyasagar. *Robot Dynamics and Control*. John Wiley & Sons, New York, 1989.
- [220] M.W. Spong. Energy based control of a class of underactuated mechanical systems. In *Proc. of IFAC World Congress, San Francisco, CA*, pages 431–5, 1996.
- [221] D. E. Stewart. Convergence of a time-stepping scheme for rigid body dynamics and resolution of Painlevé’s problem. *Archive for Rational Mechanics and Analysis*, 145:215–60, 1998.
- [222] D. H. Sutherland, K. R. Kaufman, and J. R. Moitoza. Kinematics of normal human walking. In J. Rose and J.G. Gamble, editors, *Human Walking*, pages 23–44. Williams and Wilkins, second edition, 1994.
- [223] T. Takahashi and A. Kawamura. Posture control using foot toe and sole for biped walking robot “Ken.” In *Proc. of the 2002 IEEE International Workshop on Advanced Motion Control, Maribor, Slovenia*, pages 437–42, 2002.
- [224] A. Takanishi. Humanoid robots and animal robots — towards entertainment robot market in 21st century. In *International Symposium on Robotics, Seoul, Korea*, April 2001.
- [225] A. Takanishi, M. Ishida, Y. Yamazaki, and I. Kato. The realization of dynamic walking by the biped walking robot WL-10RD. In *Proc. of the International Conference on Advanced Robotics*, pages 459–66, September 1985.
- [226] H. Takanobu, H. Tabayashi, S. Narita, A. Takanishi, E. Guglielmelli, and P. Dario. Remote interaction between human and humanoid robot. *Autonomous Robots*, 25(4):371–85, August 1999.
- [227] R. Tedrake, T. W. Zhang, and H. S. Seung. Stochastic policy gradient reinforcement learning on a simple 3D biped. In *Proc. of the 2004 IEEE/RSJ International Conference on Intelligent Robots and Systems*, volume 3, pages 2849–54, 2004.
- [228] B. Thuilot, A. Goswami, and B. Espiau. Bifurcation and chaos in a simple passive bipedal gait. In *Proc. of the 1997 IEEE International Conference on Robotics and Automation, Albuquerque, NM*, pages 792–8, 1997.
- [229] D. J. Todd. *Walking Machines: An Introduction to Legged Robotics*. Chapman & Hall, 1985.
- [230] R.Q. van der Linde. Active leg compliance for passive walking. In *Proc. of the 1998 IEEE International Conference on Robotics and Automation, Leuven, Belgium*, pages 2339–44, 1998.

- [231] B. Vanderborght, B. Verrelst, R. van Ham, J. Vermeulen, and D. Lefeber. Dynamic control of a bipedal walking robot actuated with pneumatic artificial muscles. In *Proc. of the 2005 IEEE International Conference on Robotics and Automation, Barcelona, Spain*, pages 1–6, 2005.
- [232] O. von Stryk. *DIRCOL User's Guide*. Technische Universität München, Zentrum Mathematik (SCB), Lehrstuhl M2 Höhere Mathematik und Numerische Mathematik, D-80290, München, Germany, 2.1 edition, 1999.
- [233] M. Vukobratović and B. Borovac. Zero-moment point—thirty five years of its life. *International Journal of Humanoid Robotics*, 1(1):157–73, 2004.
- [234] M. Vukobratović, B. Borovac, and V. Potkonjak. ZMP: A review of some basic misunderstandings. *International Journal of Humanoid Robotics*, 3(2):153–75, June 2006.
- [235] M. Vukobratović, B. Borovac, D. Surla, and D. Stokic. *Biped Locomotion*. Springer-Verlag, Berlin, 1990.
- [236] Q. F. Wei. *Modeling and Control of Dynamical Effects due to Impact on Flexible Structures*. PhD thesis, University of Maryland, 1994.
- [237] Q. F. Wei, W. P. Dayawansa, and P. S. Krishnaprasad. Approximation of dynamical effects due to impact on flexible bodies. In *Proc. of the 1994 American Control Conference, Baltimore, MD*, pages 1841–5, June 1994.
- [238] Q. F. Wei, P. S. Krishnaprasad, and W. P. Dayawansa. Modeling of impact on a flexible beam. In *Proc. of the 1993 IEEE International Conference on Decision and Control, San Antonio, TX*, pages 1377–82, December 1993.
- [239] E. R. Westervelt. Eric Westervelt's publications. <http://www.mecheng.osu.edu/~westerve/publications/>, 2007.
- [240] E. R. Westervelt. Feedback Control of Dynamic Bipedal Robot Locomotion Webpage. http://www.mecheng.osu.edu/~westerve/biped_book/, 2007.
- [241] E. R. Westervelt, G. Buche, and J. W. Grizzle. Experimental validation of a framework for the design of controllers that induce stable walking in planar bipeds. *International Journal of Robotics Research*, 23(6):559–82, 2004.
- [242] E. R. Westervelt, G. Buche, and J. W. Grizzle. Inducing dynamically stable walking in an underactuated prototype planar biped. In *Proc. of the 2004 IEEE International Conference on Robotics and Automation, New Orleans, LA*, pages 4234–9, 2004.

- [243] E. R. Westervelt, J. W. Grizzle, and C. Canudas. Switching and PI control of walking motions of planar biped walkers. *IEEE Transactions on Automatic Control*, 48(2):308–12, February 2003.
- [244] E. R. Westervelt, J. W. Grizzle, and D. E. Koditschek. Zero dynamics of underactuated planar biped walkers. In *15th World Congress on Automatic Control, Barcelona, Spain*, July 2002.
- [245] E. R. Westervelt, J. W. Grizzle, and D. E. Koditschek. Hybrid zero dynamics of planar biped walkers. *IEEE Transactions on Automatic Control*, 48(1):42–56, January 2003.
- [246] E. R. Westervelt, B. Morris, and K. D. Farrell. Sample-based HZD control for robustness and slope invariance of planar passive bipedal gaits. In *Proc. of the 14th Mediterranean Conference on Control and Automation*, 2006.
- [247] E. R. Westervelt, B. Morris, and K. D. Farrell. Analysis results and tools for the control of planar bipedal gaits using hybrid zero dynamics. *Autonomous Robots*, 2007. In press.
- [248] J. Yamaguchi, E. Soga, S. Inoue, and A. Takanishi. Development of a bipedal humanoid robot: control method of whole body cooperative dynamic biped walking. In *Proc. of the 1999 IEEE International Conference on Robotics and Automation, Detroit, MI*, pages 368–74, 1999.
- [249] H. Yamamoto and K. Ohnishi. An approach to stable walking on unknown slippery floor for biped robot. In *Proc. of the IEEE Annual Conference on Industrial Electronics Society, Denver, CO*, pages 1728–33, 2001.
- [250] H. Ye, A. N. Michel, and L. Hou. Stability theory for hybrid dynamical systems. *IEEE Transactions on Automatic Control*, 43(4):461–74, April 1998.
- [251] K. Y. Yi. Walking of a biped robot with compliant ankle joints: implementation with KUBCA. In *Proc. of the 2000 IEEE International Conference on Decision and Control, Sydney, Australia*, volume 5, pages 4809–14, 2000.